July 2021

Modeling of Island Block Scatter for Intensity Modulated Bolus Electron Conformal Therapy

JOSEPH G. SCOTTO
Louisiana State University and Agricultural and Mechanical College

MODELING OF ISLAND BLOCK SCATTER FOR INTENSITY MODULATED BOLUS ELECTRON CONFORMAL THERAPY

A Thesis

Submitted to the Graduate Faculty of the
Louisiana State University and
Agricultural and Mechanical College
in partial fulfillment of the
requirements for the degree of
Master of Science

in

The Department of Physics and Astronomy

by
Joseph G Scotto
B.S., Portland State University, 2018
August 2021

ჩემო ერთადერთო სიყვარულო და სულის სიხარულო
ჩვენი შეუსრულებელი მომავლისთვის ვიშრომე
გედძებ, ჩემს გვერდით იყო არადა ვერ გიპოვე
სადაც იქნები, ყველა სუნთვით და ფიქრით
მიყვარხააარ
მიყვარხააარ
მი
ყვარ
ხარ
მრგვალად და მთლიანად

Acknowledgments

I thank my committee members for their patience and assistance throughout this project: Dr. Garrett Pitcher for his continual guidance and mentorship, Dr. Kenneth Hogstrom for spending many of his afternoons and weekends in discussion, Dr. Robert Carver for his assistance with the PBRA, and Dr. James Matthews for his physics perspective. I also thank my colleague Andrew McGuffey for his assistance in continuing this project.

The research reported in this work was supported by the National Cancer Institute of the National Institutes of Health (NIH) under Award Number R44CA199838. The content is solely the responsibility of me and my supervisory committee and does not necessarily represent the official views of the National Institutes of Health.

I am grateful for the support of the faculty and staff at Mary Bird Perkins Cancer Center and LSU. I thank Katelynn Fontenot, Yao Zeng, Susan Hammond, and Paige Whittington, with special thanks to Katelynn for scheduling clinic access during quarantine. I appreciate Drs. Pitcher, Jonas Fontenot, and Wayne Newhauser for their professional advocacy of my career and Dr. Kip Matthews for his instruction, guidance, and the many ways he supports our program.

I thank my peers Chia-Lung Chien, Ana Dieguez, Ivan Hidrovo, Maryam Naseri, Michael Stock, and Jared Taylor for their friendship and collaboration, and special thanks to Ana and Michael without whom I would have caused costly havoc in the clinic. I extend my sincere gratitude to my dear friends Charles “Ramekin” LeBlanc and Huevo Loco who kept me sane and fed during quarantine, Ivan for his exemplary virtue and abnegation, Maryam for her academic assistance and teaching me humility, Jeff Bentz for continually inspiring me in countless ways, Nika Ananidze for setting me on this path, and Lena and Henry Harkness for their wit, humor, and unmatched battle prowess. I am especially grateful to Ana for being an amazing friend and driving

me to be a better scientist. I would also like to acknowledge my parents and family for always supporting me throughout my education.

Table of Contents

List of Tables

List of Figures

Abstract

Purpose: Bolus electron conformal therapy (BECT) benefits treatment of the post-mastectomy chest wall, head and neck, paraspinal muscles, and extremities. Patient dose heterogeneities caused by bolus can be reduced through intensity modulation (IM) across the incident electron beam. This requires passive radiotherapy intensity modulation for electrons (PRIME) devices, which utilize tungsten pins (island blocks) imbedded in machinable foam. IM-BECT treatment planning requires accurate dose calculation using the pencil beam redefinition dose algorithm (PBRA). Currently, the PBRA models island blocks as perfect collimators. This work explores models to account for electrons scattering into and out of the sides of island blocks.

Methods: A pencil beam model was used to compute a pin diameter (d_{IS}) that corrected for in-scatter for a given beam energy and physical (nominal) pin diameter (d_{nom}). Percent depth-dose and off-axis profiles in water were measured for each of 36 combinations of four PRIME devices, each with uniform pin diameters (0.0, 0.158, 0.273, 0.352 cm), three beam energies (7, 13, 20 MeV), and three SSDs (100, 105, 110 cm). Similarly, out-scattered electrons were modeled by modifying pin diameter. An initial model based on Monte Carlo calculating a pin's effect on the dose distribution failed to improve accuracy of the PBRA-calculated dose relative to that calculated using d_{nom}. Therefore, a second model was developed, which estimated out-scatter as the difference between measured and in-scatter-adjusted PBRA-calculated dose distributions. Then, a single out-scatter dose correction was determined using a least squares minimization, from which a new pin diameter (d_{IS+OS}) was determined.

Results: A table of d_{IS+OS} values was generated as a function of beam energy, SSD, and d_{nom}. For the 27 combinations, passing rates (3%/3 mm) for the PBRA-calculated versus measured

dose distributions were determined; compared to those using d_{nom}, those using d_{IS+OS} improved for 11, remained the same for 13, and worsened for 3.

Conclusions: The hypothesis was only conditionally met. However, upon study completion it was discovered that PRIME devices used for measurement were incorrectly fabricated. Future measurements and data analysis with correctly fabricated devices will refine scatter corrections, possibly making both Monte Carlo and measurement methods acceptable.

Chapter 1. Introduction

1.1. Background and significance

1.1.1. Electron conformal therapy

Therapeutic electron beams with energies between 7-20 MeV are used to treat superficial lesions up to 6 cm depth in tissue (Hogstrom and Almond, 2006). Electron beam dose distributions are characterized by a fairly uniform plateau region near the surface and a sharp distal fall-off at depth. Figure 1.1 shows a typical percent depth dose (PDD) curve for an electron beam. The defining features of the electron PDD curve include the surface dose (D_s), depth of maximum dose (R_{100}), dose from bremsstrahlung x-ray production (D_x), practical range (R_p), depth of distal 90% dose (R_{90}), and the distal dose falloff ($R_{90\text{-}10}$), each indicated in Figure 1.1. AAPM Task Group 25 recommends that the beam specifications be chosen such that the target be contained within the 90% isodose line (Gerbi *et al.*, 2009).

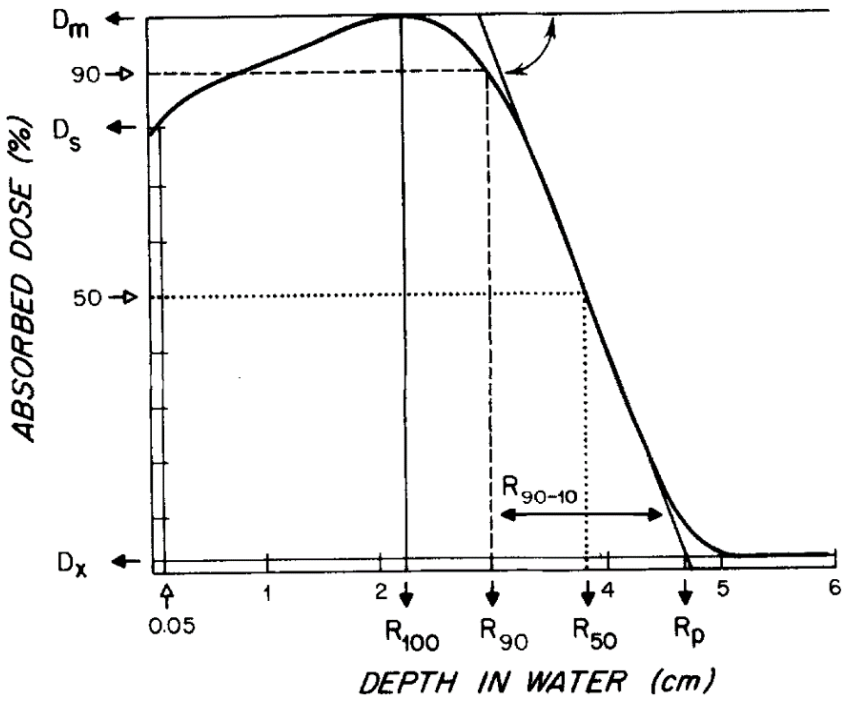

Figure 1.1. Example electron percent depth dose curve. Modified from AAPM TG Report No. 25 (Khan *et al.*, 1991).

The sharp dose fall-off beyond the treatment region allows distal critical structures and healthy tissues to be spared, reducing radiation-induced complications. These features make electron therapy advantageous for many treatment sites, including head and neck (Richaud and Tapley, 1979; Wang, 1991; Million *et al.*, 1991), post-mastectomy chest wall (Tapley and Montague, 1976; Gaffney *et al.*, 2001), post-lumpectomy boost (Recht *et al.*, 1991; Gerbi *et al.*, 2009), and skin (Tapley and Fletcher, 1973; Perez *et al.*, 1991).

The beam energy selected for treatment should be sufficient for the 90% isodose surface to reach the deepest portions of the planning target volume (PTV). Distal PTV surface irregularities can cause healthy tissues immediately distal to shallower portions of the PTV to receive the full prescription dose as shown in Figure 1.2. Electron Conformal Therapy (ECT) techniques mitigate this effect and improve treatment for many sites (Hogstrom *et al.*, 2003) by conforming the prescription isodose surface to the distal PTV surface. ECT involves beam and treatment device

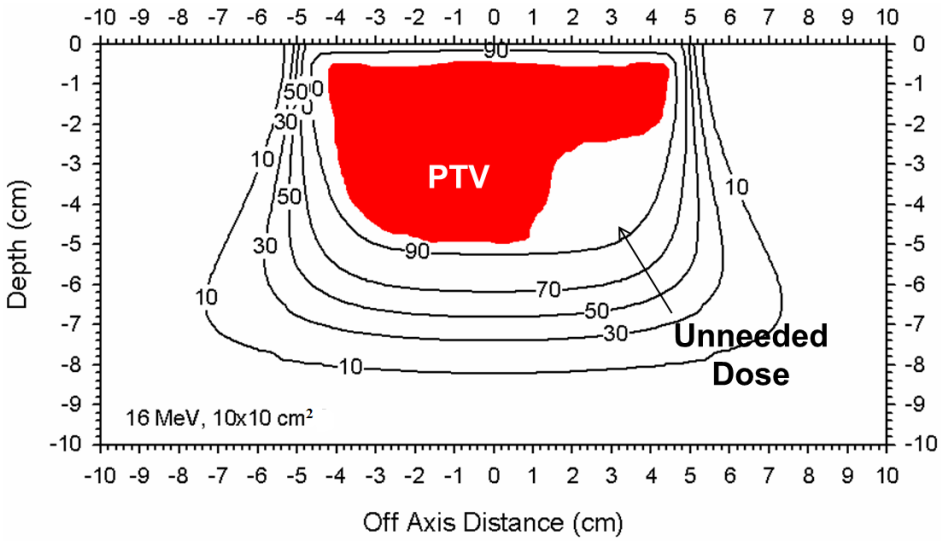

Figure 1.2. Irregular distal PTV surface and non-conformal dose distribution. The figure displays an example open field electron isodose distribution for a given PTV, shown in red, with the 90% isodose line covering the deepest portions of the target volume. Irregularities in the distal surface of the PTV result in prescription dose being delivered unnecessarily to healthy tissue immediately distal to the shallower portions of the target surface as indicated. Reproduced from Chambers (2016).

selection to fulfill three criteria: (1) the PTV is encompassed by the 90% isodose line; (2) the PTV dose uniformity is within ±10%; (3) dose to healthy tissue is minimized. Several methods to improve PTV dose conformity have been proposed, including segmented-field ECT (Richert *et al.*, 2007; Perrin, 2008; Eley *et al.*, 2011) and bolus ECT (BECT).

BECT utilizes a variable-thickness bolus of machinable wax or wax-like material to modulate the electron range within the patient to conform the 90% isodose surface for a given beam energy to the distal surface of the PTV. Previous studies have shown the benefits of BECT in the treatment of post-mastectomy chest wall (Perkins *et al*., 2001; Kudchadker *et al*., 2002; Kim *et al*., 2012; Opp *et al*., 2013; Park *et al*., 2017; Doiron, 2018), head and neck cancer (Kudchadker *et al*., 2003; Zeidan *et al*., 2011; Lin *et al.*, 2016; Łukowiak *et al*., 2017), paraspinal muscles (Low *et al*., 1995), and extremities (Su *et al.*, 2014). Figure 1.3 contains a clinical example of bolus for a right ear concha treatment with the calculated dose distribution.

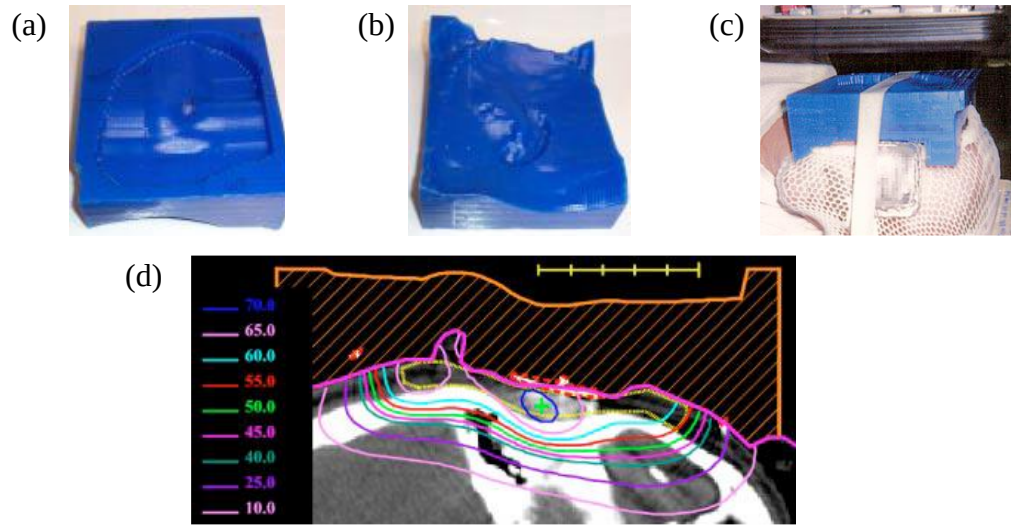

Figure 1.3. Right ear concha BECT treatment. The figure illustrates a bolus treatment of the right ear concha using a machined wax bolus. The bolus was designed using COPPERPlan's bolus design software based on Low *et al*. (1992) and fabricated using a computer-controlled milling machine. Images (a) and (b) show the proximal and distal bolus surfaces, respectively. The patient setup is shown in image (c), and the calculated isodose distributions are shown in image (d). The bolus (hatched orange) conforms the prescription (90%) isodose line (cyan) to the PTV (yellow). Modified from Kudchadker *et al.* (2003).

Though BECT improves dose conformity, gradients in the upstream bolus surface can exacerbate PTV dose spread (heterogeneity), which can be as severe as 30% (Kudchadker *et al.*, 2002). This is in addition to other sources of dose spread, such as internal heterogeneities. Kudchadker *et al*. (2002) demonstrated that introducing intensity modulation and then slightly modifying the shape of the bolus can reduce dose heterogeneity within the PTV to within ±10% while maintaining conformity of the 90% dose surface to the PTV, achieving the PTV dose uniformity criterion of ECT. The PTV dose uniformity of BECT treatments planned with and without intensity modulation are exemplified in Figure 1.4.

Electron multileaf collimators (eMLCs) have been proposed as one method of achieving intensity modulation. Prototype eMLCs have been designed and explored by several groups (Ma *et al.*, 2000; Hogstrom *et al.*, 2004; Gauer *et al.*, 2006; Vatanen *et al.*, 2008; Eldib *et al*., 2010). Though an add-on from Euromechanics Medical was commercially developed, eMLCs have not seen widespread adoption compared to their photon counterparts, which may be attributed to the added costs, inability of the eMLC to retract, lack of treatment planning software integration, and comparatively lower clinical workload of electron patients (Hogstrom *et al.*, 2017).

1.1.2. Passive radiotherapy intensity modulation for electrons

Hogstrom *et al*. (2017) developed Passive Radiotherapy Intensity Modulation for Electrons (PRIME) devices as an alternative to eMLCs for electron intensity modulation (Hogstrom and Carver, 2020). In this technique, high-density cylindrical tungsten island blocks, or pins, are positioned in a hexagonal pattern within the field to passively modulate the beam intensity. Pins are imbedded in low-density, machinable foam such that their cylinder axis back projects to the virtual source of the electron beam; the resulting intensity modulator is then placed into a

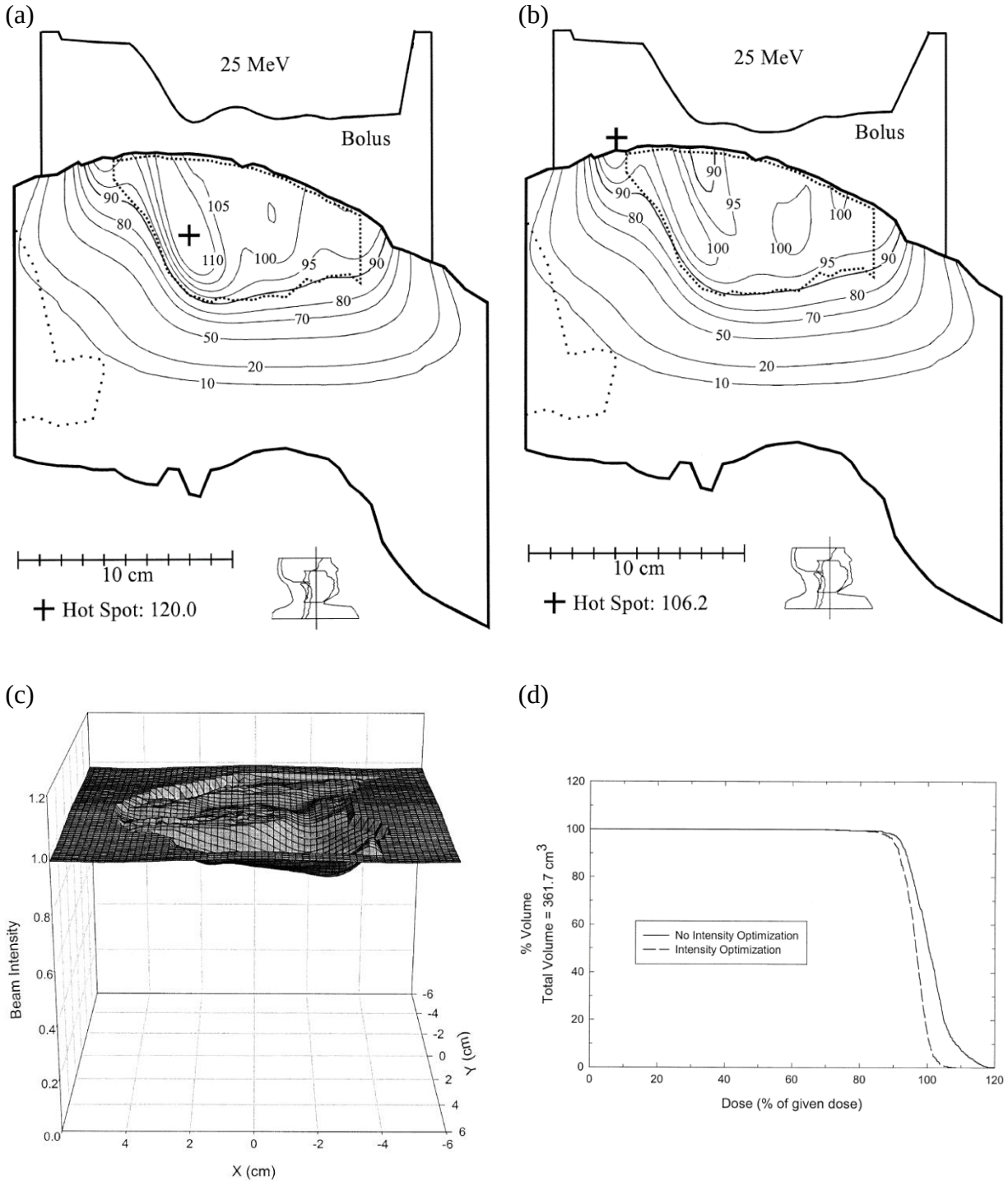

Figure 1.4. Comparison of BECT dose distributions with and without intensity modulation. Isodose distributions for a BECT head and neck treatment planned without (a) and with (b) intensity modulation are shown. The spatial distribution of the planar fluence required to achieve the distribution in (b) is shown in (c). By implementing intensity modulation, dose homogeneity is improved, reducing the maximum dose from 120.0% to 106.2% and $\Delta D_{90\%\text{-}10\%}$ from 14.9% to 9.2%. The PTV dose volume histograms of these treatments with (dashed) and without (solid) intensity modulation are compared in (d). Modified from Kudchadker *et al.* (2002).

patient-specific collimating insert. Incident electrons are absorbed by the pins, and the fluence is reduced by approximately the fraction of the cross-sectional area of the field covered by the blocks in the plane perpendicular to the beam. Multiple coulomb scattering (MCS) causes the electrons to scatter laterally behind the pins, restoring downstream planar fluence uniformity but with the planar fluence (intensity) reduced approximately to the intensity reduction factor (IRF), which is the unblocked fraction of the beam cross section. For cylindrical pins of diameter d arranged on a hexagonal grid with packing radius r, the IRF is geometrically computed to be:

$$\mathrm{IRF}(r,d) = 1 - \left(\frac{\pi}{2\sqrt{3}}\right)\left(\frac{d}{r}\right)^2. \qquad 1.1$$

This hexagonal grid pin spacing is illustrated in Figure 1.5. The pin diameters and packing radii are selected to yield the necessary local intensity reduction. As noted by Hogstrom *et al.* (2017), a circular block face minimizes the ratio of lateral surface area to upstream cross-sectional area, minimizing the scatter into and out of the pin. The height of the pin must be sufficient to stop the most energetic electrons, i.e. 0.6 cm of tungsten (ρ = 19.30 g·cm^{-3}) is sufficient to stop 28 MeV electrons (R_{CSDA}) (Svensson *et al*. 1984).

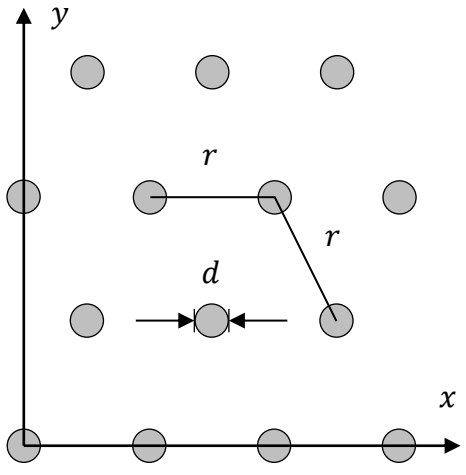

Figure 1.5. Depiction of PRIME modulator pin layout. The image shows a beam's eye view of the hexagonally arranged pins of diameter d and packing radius r. Modified from Chambers (2016).

Intensity modulated bolus electron conformal therapy (IM-BECT) combines the intensity modulation of PRIME and the energy modulation of BECT to meet the three criteria of ECT. In particular, IM-BECT reduces the undesirable PTV dose spread, improving treatment to sites such as head and neck (Kudchadker *et al.*, 2002) and post-mastectomy chest wall (Doiron, 2018). Chambers (2016) determined suitability of packing radius and block diameter combinations for PRIME IRFs of 70-100% for electron energies of 7-20 MeV at source-to-surface distances (SSDs) of 100 and 103 cm. A design tool software based on the pencil beam algorithm (PBA) (Hogstrom *et al.*, 1981) was developed to generate pin arrangements from an intensity distribution input, illustrated in Figure 1.6.

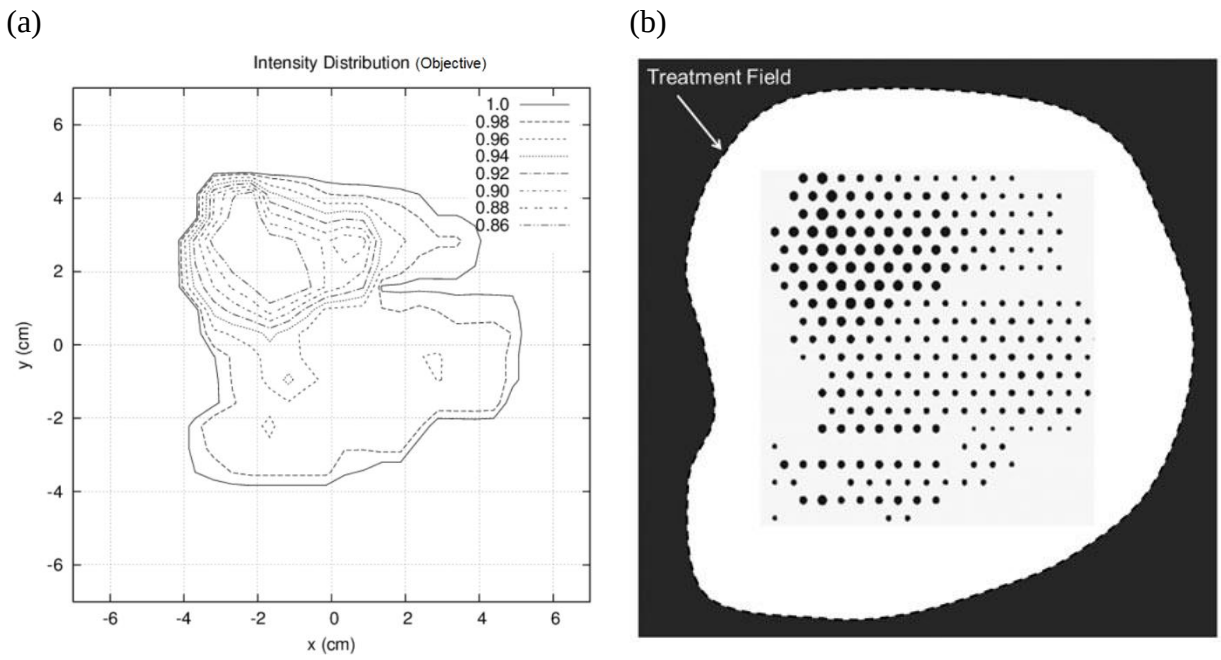

Figure 1.6. Passive intensity modulation for electrons. From an input intensity distribution retrieved from Kudchadker *et al.* (2002), (a) target isodose contours were generated, from which (b) a pin arrangement was determined. Modified from Hogstrom *et al.* (2017).

IM-BECT treatment planning requires accurate dose calculations in the presence of intensity modulators. Hilliard (2018) modified the input parameters to the pencil beam redefinition algorithm (PBRA) (Shiu and Hogstrom, 1991; Boyd *et al.*, 1998) based on empirical data to

account for scatter and energy loss in the machinable foam in which the pins are imbedded. Specifically, $\sigma_{\theta x}$ was increased by 50% and the R_{90} range was reduced by 0.1 cm. Also, the island blocks (cylindrical pins) comprising the intensity modulator were assumed to be perfect collimators that were squares of area equal to the circular face of the pin. Validation of these modifications and this assumption was performed using a prototype modulator fabricated by .decimal and shown in Figure 1.7.a-b. In comparing the intensity modulated PBRA (IM-PBRA) calculations to measurement, Hilliard found that differences varied with pin diameter, beam energy, and depth. Dose profiles showing these differences are illustrated in Figure 1.7.c-f for 9 and 16 MeV beams.

Hilliard's calculations assumed an idealized, binary treatment in which electrons incident on the proximal surface of the island blocks were removed while all others were unaffected and transmitted to the patient as illustrated in Figure 1.8.a. In validating the IM-PBRA, Hilliard noted that differences between the calculated and measured doses could be attributed to scatter into and out of the pins.

In-scatter refers to the scattering of electrons into the lateral surface of the block and being absorbed as shown in Figure 1.8.b. This results in reduced dose to the patient as these electrons are removed from the beam planar fluence. The effect is observed at all depths because it does not affect the energy distribution of the transmitted electrons. In-scattering is most prominent at lower beam energies due to the increased lateral MCS in air and foam of lower energy electrons. Figures 1.7.c and d compare the measured and calculated profiles for a 9 MeV beam at depths in water of 0.5 and 2.0 cm, respectively. Believed to be due to in-scattering at this lower energy, the measured dose is lower than the calculated value at both depths.

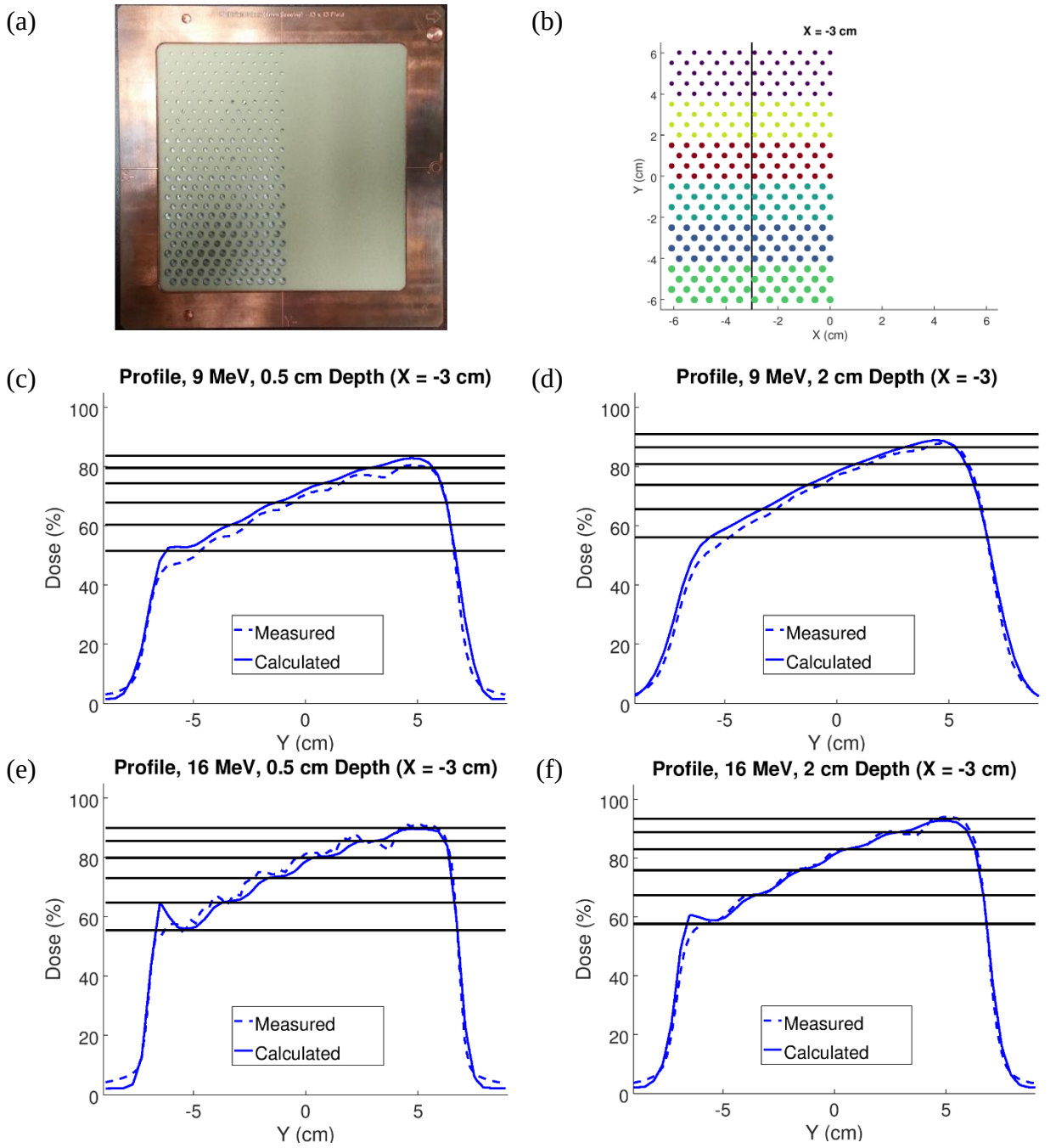

Figure 1.7. PRIME prototype and dose measurements for 9 and 16 MeV beams. The PRIME prototype device shown in (a), fabricated by .decimal and used by Hilliard (2018), features pin diameters yielding IRFs from approximately 60% to 95% at a packing radius of 0.579 cm within a 13×13 cm^2 field. The positions and diameters of the pins of this device are shown in (b) with the vertical line positioned at x = -3 cm indicating the measurement plane for the lateral relative dose profiles plotted in (c-f). These plots compare measured (dashed) and IM-PBRA-calculated (solid) profiles for 9 (c and d) and 16 MeV (e and f) beams acquired at 0.5 (c and e) and 2.0 cm (d and f) depth in water and normalized to the dose measured at R_{100} and x = 3 cm in the unmodulated portion of the beam. Modified from Hilliard (2018).

Out-scatter refers to electrons that enter either the side or upstream surface of the block and then scatter out of the sides as illustrated in Figure 1.8.c. Out-scattered electrons contribute to the fluence, increasing the dose to the patient. The effect is more pronounced at shallower depths due to the reduced range of the energy-degraded electrons exiting the pin. Out-scattering is believed to increase with beam energy as higher energy electrons with increased range are more likely to escape the pin. Figures 1.7.e and f compare calculation to measurement for a 16 MeV beam at 0.5 and 2.0 cm depth. Due to increased out-scattering at this energy, calculation underpredicts the dose at 0.5 cm depth. At 2.0 cm, the effects of in-scatter and out-scatter seem to balance, and the profiles agree more closely.

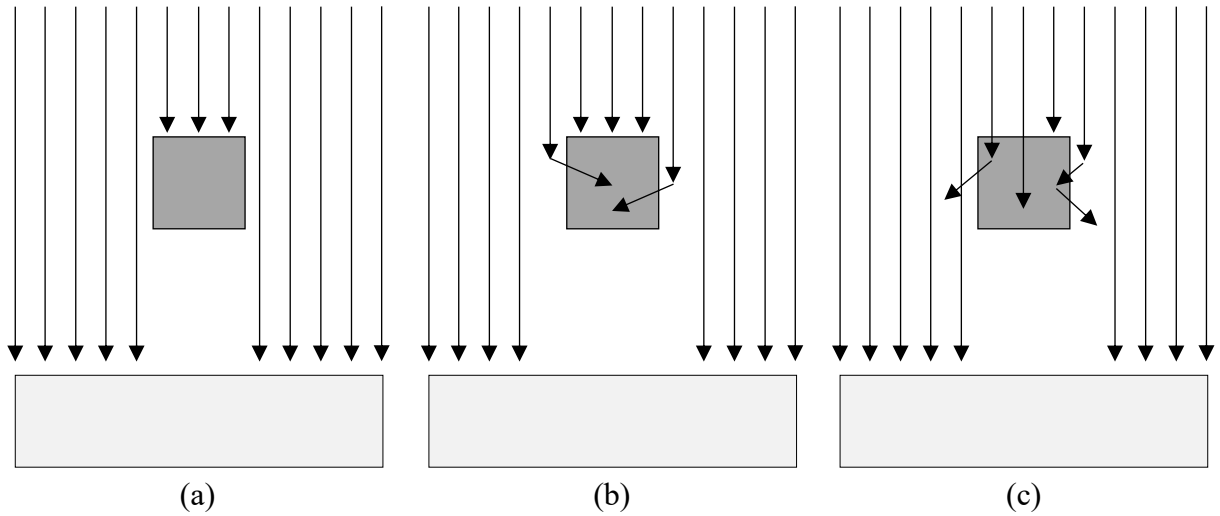

Figure 1.8. Scattering considerations for intensity modulator pins. A simplified treatment of the electron beam shown in (a) assumes the block to be a perfect collimator. Electrons, indicated by arrows, incident on the upstream surface of the pin are removed from the beam, and all others are transmitted to the patient. The effect of in-scattering is illustrated in image (b) in which electrons that scatter into the sides are absorbed and removed from the beam. Out-scattering is shown in image (c) in which some electrons entering the side and upstream pin surface scatter out of the sides of the block and are transmitted.

1.2. Purpose

To improve the accuracy of dose calculations, the effects of scatter into and out of the island blocks will be quantified and empirical modifications will be incorporated into the PBRA. Improvement of accuracy will be assessed by comparison of modified IM-PBRA calculations with measured dose distributions.

1.3. Hypothesis and specific aims

1.3.1. Hypothesis

Incorporating island block diameter correction factors, which approximately account for electron scatter into and out of the sides of island blocks constituting PRIME devices, will improve accuracy of IM-PBRA dose calculations with 3% or 3 mm criteria for all measured dose points up to approximately R_p in depth and ±12 cm off-axis (21-cm-wide field) for each of the 27 measurement conditions of beam energy (7, 13, and 20 MeV), SSD (100, 105, and 110 cm), and pin diameter (0.158, 0.273, and 0.352 cm). The correction factors will be a function of beam energy ($E_{p,0}$), SSD, and island block diameter over the range of 7-20 MeV, 100-110 cm, and 0.158-0.352 cm, respectively. Island blocks will be spaced 0.6 cm on a hexagonal grid, for which these diameters result in nominal intensity reduction factors ranging from 0.688 to 0.937.

1.3.2. Aim 1: analytical modification of PBRA pin modeling to account for in-scatter

Analytical corrections accounting for scattering into the sides of the island blocks will be determined for beam energies of 7, 9, 10, 11, 13, 16, and 20 MeV for nominal (physical) island block diameters of 0.352, 0.315, 0.273, 0.223, and 0.158 cm. These diameters correspond to nominal IRFs of 0.688, 0.750, 0.812, 0.875, and 0.937 respectively, for a 0.6-cm packing radius. Each pin will be modeled as 0.6-cm in length and embedded in machinable foam (ρ = 0.096 g·cm^{-3}). The fraction of electrons scattering into each pin along its axis at a given energy will be

determined by applying pencil beam theory. This additional loss in electron fluence will be modeled as an increase in pin diameter. The in-scatter-adjusted pin diameters will be functions of both beam energy ($E_{p,0}$) and pin diameter (d), which can be computed or implemented into the PBRA as a lookup table for future use.

1.3.3. Aim 2: modeling of out-scatter using measurement and in-scatter-adjusted PBRA calculation

Modification of pin diameter will be determined from the change in dose required to increase the results of Aim 1 (in-scatter-adjusted pin diameter) to best match measured dose downstream of the modulated portion of the beam and at depths up to R_{90}. The change in dose required as a function of beam energy, SSD, and pin diameter will be determined for use in calculating pin diameters modified for both in-scatter and out-scatter. Scanning tank measurements will be performed using sample PRIME devices at beam energies of 7, 13, and 20 MeV and at 100, 105, and 110 cm SSD. Three sample devices will feature 8.4×8.4 cm^2 matrices of pins (0.6 cm packing radius) having equal diameters of 0.158, 0.273, and 0.352 cm, and a fourth device will have machinable foam only (unmodulated). In-scatter-adjusted PBRA calculations will be performed with the same pin arrangements as the sample devices, including foam only, and the same beam energy and SSD combinations as measurement. At corresponding beam energy, SSD, modulator, and depth conditions, the in-scatter-adjusted PBRA profile will be subtracted from measurement to yield an out-scatter profile. For each set of profiles, a least squares minimization between measurement and in-scatter-adjusted PBRA differences will be performed to determine the out-scatter component. The solution will be parameterized and then extended to intermediate beam energy and diameter combinations. The out-scatter adjustment will be combined with the in-scatter correction to create a lookup table of diameters adjusted for both in-scatter and out-scatter. The IM-PBRA corrections will be a function of beam energy, SSD, and pin diameter.

1.3.4. Aim 3: validation of the modified IM-BECT PBRA dose calculation

Accuracy of modified IM-PBRA dose calculations will be evaluated by comparison with 2D dose measurements in water for the three sample PRIME devices at beam energies of 7, 13, and 20 MeV at 100, 105, and 110 cm SSD. Passing rates and locations of failure for 3% or 3 mm distance-to-agreement criteria at all measured points will be determined using corresponding measured and calculated 2D dose distributions.

1.4. Impact of fabrication error in PRIME island block divergence

The axes of the pins of PRIME devices used in this study were believed to be colinear with rays diverging from the virtual source as discussed by Hilliard (2018). However, due to a fabrication error, the island blocks of the devices used in this work were arranged converging with respect to the beam. This error was discovered upon completion of the thesis research and likely explains a larger-than-expected difference between measured and both PBRA and MC dose distributions. This is expected to have a measurable impact on the results of this thesis, both the proposed pin diameter corrections and the resulting accuracy of the PBRA. Preliminary results presented in Appendix E suggest that the hypothesis will likely be true once the methods of this thesis are applied to data measured with the properly fabricated intensity modulators.

Chapter 2. Aim 1: Analytical Modification of PBRA Pin Modeling to Account for In-Scatter

2.1. Methods

2.1.1. Current status of IM-PBRA

The PBRA functions by using a PBA calculation to propagate the open field planar fluence, specified within the beam model, from the plane of the collimating insert to the patient surface. At the patient surface, the first three moments of each pencil beam are redefined. The pencil beams are then transported to the next depth within the patient in 0.5-cm increments and redefined again. This process continues until the planar fluence reaches a clinically negligible value (Shiu and Hogstrom, 1991).

In the current version of the IM-PBRA, each tungsten pin comprising the beam modulator is treated as a square pencil beam having area equal to the area occupied by the circular island block and having negative planar fluence. Each such beam is included in the initial transport of the broad beam from the collimator to the initial plane of the patient surface (water surface in this study). That calculation is included in the planar fluence calculation used to calculate the first three scattering moments of each redefined pencil beam.

As described by Chambers (2016), the relative electron intensity (i.e. planar fluence) distribution of the modulated field is given by

$$I_{\text{blocks}}^{WX,WY}(x,y,z) = I_{\text{no block}}^{WX,WY}(x,y,z) - \sum_{i=1}^{N} I_{\text{block},i}(x,y,z;x_i,y_i). \quad 2.1$$

For the present work, a square beam ($WX \times WX$) incident on a water phantom, the relative intensity of an open field (no pins) is

$$I_{\text{no block}}^{WX,WX}(x,y,z) = \frac{1}{4}\left[\text{erf}\left(\frac{\frac{WX_z}{2}+x}{\sqrt{2}\sigma_{x,\text{beam}}}\right)+\text{erf}\left(\frac{\frac{WX_z}{2}-x}{\sqrt{2}\sigma_{x,\text{beam}}}\right)\right] \times\left[\text{erf}\left(\frac{\frac{WX_z}{2}+y}{\sqrt{2}\sigma_{x,\text{beam}}}\right)+\text{erf}\left(\frac{\frac{WX_z}{2}-y}{\sqrt{2}\sigma_{x,\text{beam}}}\right)\right]\cdot\left(\frac{1}{f}\right)^2, \quad (2.2)$$

where $\sigma_{x,\text{beam}}$, which is due to the initial angular spread (σ_{θ_x}) of electrons at each point in the beam at the collimator, is the root mean square (RMS) of the resulting spatial distribution at the collimator insert. It is given by $\sigma_{x,\text{beam}} = \sigma_{\theta_x}(SSD - SCD + z)$, where *SCD* is the nominal source to collimator distance. The geometric divergence of the beam is accounted for by $f = (SSD + z)/SCD$. WX_z is the collimator width projected to depth *z*, *SSD* is the nominal SSD (100, 105, or 110 cm) where $z = 0$ cm. The intensity reduction of the *i*th pin centered at (x_i , y_i) is calculated for a square pencil beam by

$$I_{\text{block},i}(x,y,z;x_i,y_i) = \frac{1}{4}\left[\text{erf}\left(\frac{f\cdot\left(x_i+\frac{s_i}{2}\right)-x}{\sqrt{2}\sigma_{x,\text{beam}}}\right)+\text{erf}\left(\frac{f\cdot\left(x_i-\frac{s_i}{2}\right)-x}{\sqrt{2}\sigma_{x,\text{beam}}}\right)\right] \times\left[\text{erf}\left(\frac{f\cdot\left(y_i+\frac{s_i}{2}\right)-y}{\sqrt{2}\sigma_{x,\text{beam}}}\right)+\text{erf}\left(\frac{f\cdot\left(y_i-\frac{s_i}{2}\right)-y}{\sqrt{2}\sigma_{x,\text{beam}}}\right)\right]\cdot\left(\frac{1}{f}\right)^2, \quad (2.3)$$

with *f* accounting for geometric divergence at depth *z* and s_i being the side of a square having the same area as the upstream face of a pin of diameter d_i.

Equation 2.1 makes the perfect collimator assumption that all electrons incident on the upstream surface of the modulator pin are absorbed and all others are transmitted to the patient. This approach ignores the effects of in-scatter and out-scatter, treating the pins as both infinitely thin and infinitely dense. The planar fluence distribution can be corrected for in-scatter and out-

scatter by adding these planar fluence contributions to the primary fluence, expressed for the *E*th energy bin as

$$\phi'_{0,E} = \phi_{0,E} - \Delta\phi_E^{\mathrm{IS}} + \Delta\phi_E^{\mathrm{OS}}, \qquad 2.4$$

where $\phi_{0,E}$ is the planar fluence under the perfect collimator assumption, $\Delta\phi_E^{\mathrm{IS}}$ represents the change in planar fluence due to in-scattering, and $\Delta\phi_E^{\mathrm{OS}}$ is the change in fluence due to out-scattering. The effects of in-scatter on the beam fluence can be determined analytically as these electrons are removed from the fluence and are assumed not to affect the energy distribution.

2.1.2. Derivation of analytical in-scatter correction

If a uniform planar fluence is incident on a homogeneous slab medium, side-scatter equilibrium is established, and the number of electrons scattering into and out of some subvolume within the slab are equal. If that subvolume is replaced with a medium absorbing all electrons (e.g. tungsten pin), the number of in-scattered electrons remains unchanged. The number of electrons scattering into the subvolume can be calculated as the number scattering out of the subvolume, which are equal under equilibrium conditions. This concept is illustrated in Figure 2.1.

The electrons in (a) which scatter into the boxed subvolume are represented as the shaded region in (b). The electrons in (c) which have entered the upstream surface of the subvolume and scattered out are shaded in (d). Under conditions of side scatter equilibrium, the shaded region of (b) can be inferred by calculating the shaded region in (d). This latter quantity can be determined analytically using pencil beam theory. These in-scattered electrons are absorbed in a dense absorber like the tungsten island blocks (pins).

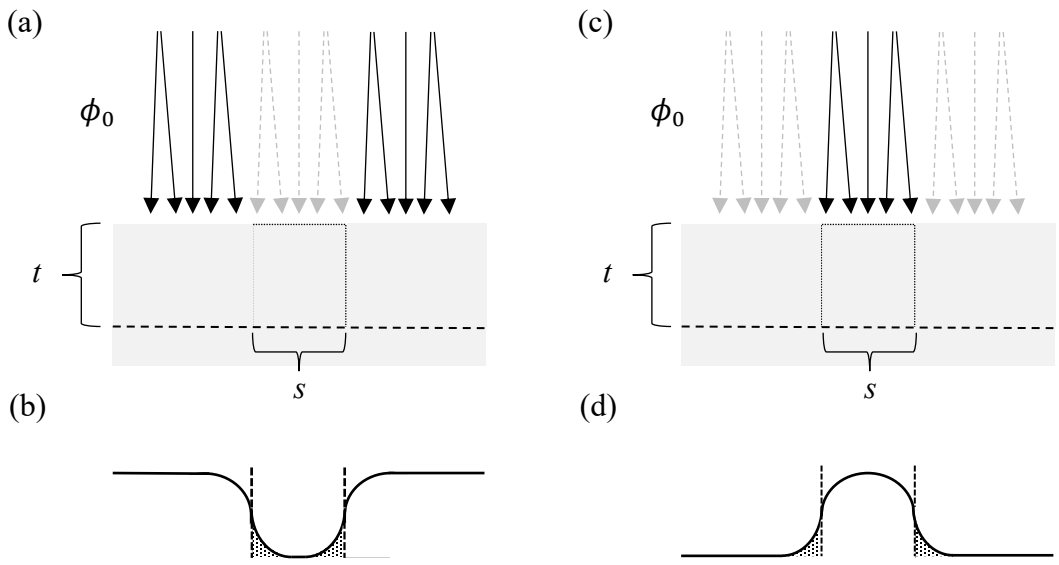

Figure 2.1. Scattered electron planar fluences. A uniform planar fluence of electrons, ϕ_0, depicted as arrows, is incident on a medium in (a) and (c). Subsets of the fluence incident on the slab inside (a) and outside (c) a cuboid of side *s* are indicated by the bolded arrows. The lateral fluence distribution at depth *t*, indicated by the dotted line, from the fluence subsets (a) and (c) are depicted in (b) and (d), respectively. A portion of the planar fluence in (a) scatters laterally into the boxed subvolume, illustrated as the shaded region in (b). Likewise, some electrons in (c) scatter out of the subvolume, with these electrons shaded in (d). Due to side scatter equilibrium, the number of electrons in the shaded parts of (b) and (d) are equal.

The average electron planar fluence (ϕ_t) transmitted from the upstream surface of the subvolume to the downstream surface of the subvolume, i.e. at the dashed line in Figure 2.1.c, can be calculated using pencil beam theory (Hogstrom, private communication) as

$$\phi_t = \frac{\phi_0}{s^2}\left\{\int_{-s/2}^{+s/2}\left[\frac{1}{2}\mathrm{erf}\left(\frac{\frac{s}{2}-x}{\sqrt{2}\sigma_x}\right)+\frac{1}{2}\mathrm{erf}\left(\frac{\frac{s}{2}+x}{\sqrt{2}\sigma_x}\right)\right]dx\right\}^2, \qquad 2.5$$

where ϕ_0 is the planar fluence incident on the upstream subvolume surface, σ_x is the RMS of the pencil beam's spatial distribution (see Section 2.1.3), and *s* is the side of a square having the same face area as a pin of diameter *d*. Note that this equation models the right cylinder (island block) as a cuboid with bases of equal area ($s^2 = \pi d^2/4$) and neglects beam divergence. Also note that σ_x in Equation 2.5 differs from $\sigma_{x,\mathrm{beam}}$ in Equations 2.2 and 2.3.

The average planar fluence incident on the downstream slab surface outside the subvolume arising from electrons incident on the upstream surface of the subvolume, i.e. the shaded portion beneath the plotted curve in Figure 2.1.d, is the difference between the initial planar fluence and the average planar fluence transmitted within the subvolume:

$$\phi_{\mathrm{IS}} = \phi_0 - \phi_t. \tag{2.6}$$

This portion of electrons scattering out of the subvolume, indicated by the shaded region in Figure 2.1.d, is equal to those scattering into the subvolume, indicated by the shaded region in Figure 2.1.b. This additional fraction of electrons scattering into the block, *f*, can be determined. This fraction is relative to the fluence incident on the block (i.e. 1 – *IRF*), and can be calculated as

$$f(E,d) = 1 - \frac{1}{s^2}\left\{\int_{-s/2}^{+s/2}\left[\frac{1}{2}\mathrm{erf}\left(\frac{\frac{s}{2}-x}{\sqrt{2}\sigma_x}\right) + \frac{1}{2}\mathrm{erf}\left(\frac{\frac{s}{2}+x}{\sqrt{2}\sigma_x}\right)\right]dx\right\}^2. \tag{2.7}$$

Evaluating the integral, this can be expressed as

$$f(E,d) = 1 - \frac{2\sigma_x^2}{s^2}\left\{\frac{s}{\sqrt{2}\sigma_x}\mathrm{erf}\left(\frac{s}{\sqrt{2}\sigma_x}\right) + \frac{1}{\sqrt{\pi}}\left[\exp\left(-\frac{s^2}{2\sigma_x^2}\right) - 1\right]\right\}^2. \tag{2.8}$$

Note that the dependence on the beam energy is contained within σ_x.

An in-scatter-adjusted IRF, IRF_{IS}, represents the intensity reduction due to the primary collimation plus losses from scattering into the sides of the island block. This can be determined based on the *f*-factor (Equation 2.8) and the nominal IRF (Equation 1.1), expressed here as IRF_{nom}:

$$IRF_{\mathrm{IS}} = IRF_{\mathrm{nom}} - f \cdot (1 - IRF_{\mathrm{nom}}). \tag{2.9}$$

The blocked area of the beam cross section (i.e. 1 – IRF_{nom}) is directly proportional to the pin face area, so the pin diameter is upscaled to account for the intensity reduction arising from in-scatter, i.e. by substituting Equation 1.1 into Equation 2.9, yielding:

$$d_{\mathrm{IS}}(E,d) = d\sqrt{1 + f(E,d)}. \tag{2.10}$$

The in-scatter-adjusted IRF then relates to this diameter by

$$IRF_{\mathrm{IS}}(d_{\mathrm{IS}}) = 1 - \left(\frac{\pi}{2\sqrt{3}}\right)\left(\frac{d_{\mathrm{IS}}}{0.6\ \mathrm{cm}}\right)^2, \tag{2.11}$$

where 0.6 cm is the hexagonal packing radius.

2.1.3. Determination of σ_x and scatter considerations due to machinable foam

The dual scattering foils, air, and the machinable foam contribute to the root mean square of the spatial distribution at the bottom of the pin for an electron beam originating at the top of the pin according to

$$\sigma_x^2 = \sigma_{\theta_x,\mathrm{clinical}}^2 \cdot t^2 + \sigma_{x,\mathrm{foam}}^2, \tag{2.12}$$

where t is the pin length of 0.6 cm, $\sigma_{\theta_x,\mathrm{clinical}}$ is the angular spread due to scattering in the foils and the air and is determined by measurement, and $\sigma_{x,\mathrm{foam}}$ is calculated from Fermi Eyges theory (Hogstrom *et al.*, 1981):

$$\sigma_{x,\mathrm{foam}}^2 = \frac{1}{2}\int_0^t T(z') \cdot (t - z')^2 \, dz', \tag{2.13}$$

where T is the linear angular scattering power in the foam and z is the depth within the foam from the pin surface. Since the energy loss due to the foam is negligible, the scattering power is approximately constant. Evaluating this integral yields

$$\sigma_{x,\mathrm{foam}}^2 = \frac{1}{6}\left(\frac{T}{\rho}\right)_{\mathrm{foam}} \cdot \rho_{\mathrm{foam}} t^3. \tag{2.14}$$

Combining Equations 2.12 and 2.14 results in the RMS of the spatial distribution:

$$\sigma_x(t) = \left[\sigma^2_{\theta_x,\text{clinical}} \cdot t^2 + \frac{1}{6}\left(\frac{T}{\rho}\right)_{\text{foam}} \cdot \rho_{\text{foam}} t^3\right]^{1/2}. \quad 2.15$$

Values of $\sigma_{\theta_x,\text{clinical}}$ are contained in Table 2.1. Hilliard (2018) assumed the foam to be atomically equivalent to polyethylene with density of 0.096 g·cm^{-3} when calculating the scattering power, for which the mass scattering powers are listed in Table 2.2.

Table 2.1. Measured values of $\sigma_{\theta x,\text{clinical}}$ for the Elekta electron beam models at MBPCC.

Beam Energy (MeV)	$\sigma_{\theta x,\text{clinical}}$ (radians)
7	0.0626
9	0.0535
10	0.0476
11	0.0420
13	0.0383
16	0.0296
20	0.0234

Table 2.2. Mass scattering powers for polyethylene. The mass scattering powers for polyethylene are partially reproduced from Table 2.6 of ICRU 35 (Svensson *et al.*, 1984).

Beam Energy (MeV)	Mass Scattering Power (radians^2 · cm^2 · g^{-1})
6.0	1.27E-1
8.0	7.74E-2
10.0	5.22E-2
15.0	2.53E-2
20.0	1.50E-2

2.2. Results

Table 2.3 contains the RMS of the spatial distribution of the planar fluence for a point beam propagating from the top to the bottom of the pin at clinically relevant energies. According to Equation 2.15, the second term, which accounts for the machinable foam, was found to increase σ_x by 10-13% with respect to the $\sigma_{\theta_x,\text{clinical}} \cdot t$ value.

The in-scatter-adjusted quantities for all nominal (physical) block diameters and clinical beam energies are listed in Table 2.4 and compared to nominal *d* and IRF. The additional fraction of planar fluence lost, *f*, ranged from 0.079 to 0.420, indicating that the planar fluence loss increases by as much as 42% due to in-scattering. As expected, this value was greater at lower energies and smaller diameters. The extent of the diameter upscaling correction (i.e. difference between *d* and d_{IS}) is likewise most significant at the lower energies.

Table 2.3. Impact of machinable foam on in-scatter sigma. The contribution of the foam is calculated by Equation 2.14 from the tabulated mass scattering power data in Table 2.2 with intermediate values determined by interpolation. The RMS of the spatial distribution is evaluated using these data and Equation 2.15. The results with and without the foam in place are compared in the last column. The pin height, *t*, is 0.6 cm.

Beam Energy (MeV)	$\sigma_{\theta_x,\text{clinical}}$ (radians)	$\sigma_{x,\text{foam}}$ (cm)	σ_x (cm)	$\frac{\sigma_x}{\sigma_{\theta_x,\text{clinical}} \cdot t}$
7	0.0626	0.0184	0.0418	1.11
9	0.0535	0.0148	0.0353	1.10
10	0.0476	0.0134	0.0315	1.10
11	0.0420	0.0124	0.0281	1.12
13	0.0383	0.0107	0.0253	1.10
16	0.0296	0.0088	0.0198	1.11
20	0.0234	0.0072	0.0158	1.13

Table 2.4. Nominal and in-scatter-adjusted diameters and IRFs for 7-20 MeV. The nominal pin diameters are tabulated along with their IRFs according to Equation 1.1. The *f*-factors are calculated from Equation 2.8 and the data in Table 2.3 for beam energies 7-20 MeV. The in-scattered-adjusted diameters and IRFs were computed using these values with Equations 2.10 and 2.11, respectively.

Beam Energy (MeV)	d (cm)	IRF_{nom}	f	d_{IS} (cm)	IRF_{IS}
7	0.158	0.937	0.420	0.188	0.911
7	0.223	0.875	0.309	0.255	0.836
7	0.273	0.812	0.257	0.306	0.764
7	0.315	0.750	0.225	0.349	0.694
7	0.352	0.688	0.202	0.386	0.625
9	0.158	0.937	0.362	0.184	0.914
9	0.223	0.875	0.265	0.251	0.842
9	0.273	0.812	0.219	0.301	0.771
9	0.315	0.750	0.192	0.344	0.702
9	0.352	0.688	0.172	0.381	0.634
10	0.158	0.937	0.328	0.182	0.916
10	0.223	0.875	0.239	0.248	0.845
10	0.273	0.812	0.198	0.299	0.775
10	0.315	0.750	0.172	0.341	0.707
10	0.352	0.688	0.155	0.378	0.640
11	0.158	0.937	0.295	0.180	0.918
11	0.223	0.875	0.214	0.246	0.848
11	0.273	0.812	0.177	0.296	0.779
11	0.315	0.750	0.154	0.338	0.712
11	0.352	0.688	0.139	0.376	0.645
13	0.158	0.937	0.268	0.178	0.920
13	0.223	0.875	0.194	0.244	0.851
13	0.273	0.812	0.160	0.294	0.782
13	0.315	0.750	0.139	0.336	0.715
13	0.352	0.688	0.125	0.373	0.649

(table cont'd.)

Beam Energy (MeV)	d (cm)	IRF_{nom}	f	d_{IS} (cm)	IRF_{IS}
16	0.158	0.937	0.213	0.174	0.924
16	0.223	0.875	0.153	0.239	0.856
16	0.273	0.812	0.126	0.290	0.788
16	0.315	0.750	0.110	0.332	0.723
16	0.352	0.688	0.099	0.369	0.657
20	0.158	0.937	0.172	0.171	0.926
20	0.223	0.875	0.124	0.236	0.860
20	0.273	0.812	0.101	0.286	0.793
20	0.315	0.750	0.088	0.329	0.728
20	0.352	0.688	0.079	0.366	0.663

2.3. Discussion

Equations 2.8 and 2.10 provide an analytical solution to model planar fluence losses due to in-scatter in IM-BECT. Consistent with expectation, the diameter upscaling is more significant at lower energies where MCS is greater. This lookup table (Table 2.4) provides a simple solution that will insignificantly increase computation time of PBRA calculations.

However, this correction alone is likely insufficient. In-scatter losses (i.e. the *f*-factor) may be overestimated since the correction was derived under the perfect collimator assumption, i.e. all laterally scattered electrons entering the side of the pin are assumed to be absorbed. However, data show a large amount of electrons will scatter back out of the block. In other words, both those entering near the edge of the top surface and those entering the side at grazing angles can escape. Therefore, further correction for out-scatter will be necessary to improve accuracy.

Chapter 3. Aim 2: Modeling of Out-Scatter Using Measurement and In-Scatter-Adjusted PBRA Calculation

3.1. Methods

3.1.1. Separation of scattering components

As Equation 2.4 delineates, the modulated component of the dose calculation can be considered in terms of three components: primary modulation, in-scatter, and out-scatter. Incorporation of the primary modulation into the PBRA was described by Chambers (2016), and a semi-empirical model for incorporating in-scatter was described in Chapter 2. Therefore, the out-scatter component can be deduced as the difference between in-scatter-corrected theoretical calculation and measurement, which inherently includes the combined effects of all three components.

3.1.2. Intensity modulator devices

Four PRIME devices (Hogstrom *et al.*, 2017) were manufactured by .decimal (Sanford, FL) for PBRA validation. The devices imbedded 0.6-cm-long tungsten pins of various diameters into a 1.27-cm-thick slab of machinable foam that was placed in a 21×21 cm^2 copper insert. One device contained no pins, and the other three contained an 8.4×8.4 cm^2 matrix of 247 pins of uniform diameter packed on a 0.6-cm hexagonal grid with diameters of 0.158, 0.273, and 0.352 cm, corresponding to nominal IRFs of 0.937, 0.812, and 0.688, respectively. The devices used for validation are shown in Figure 3.1.

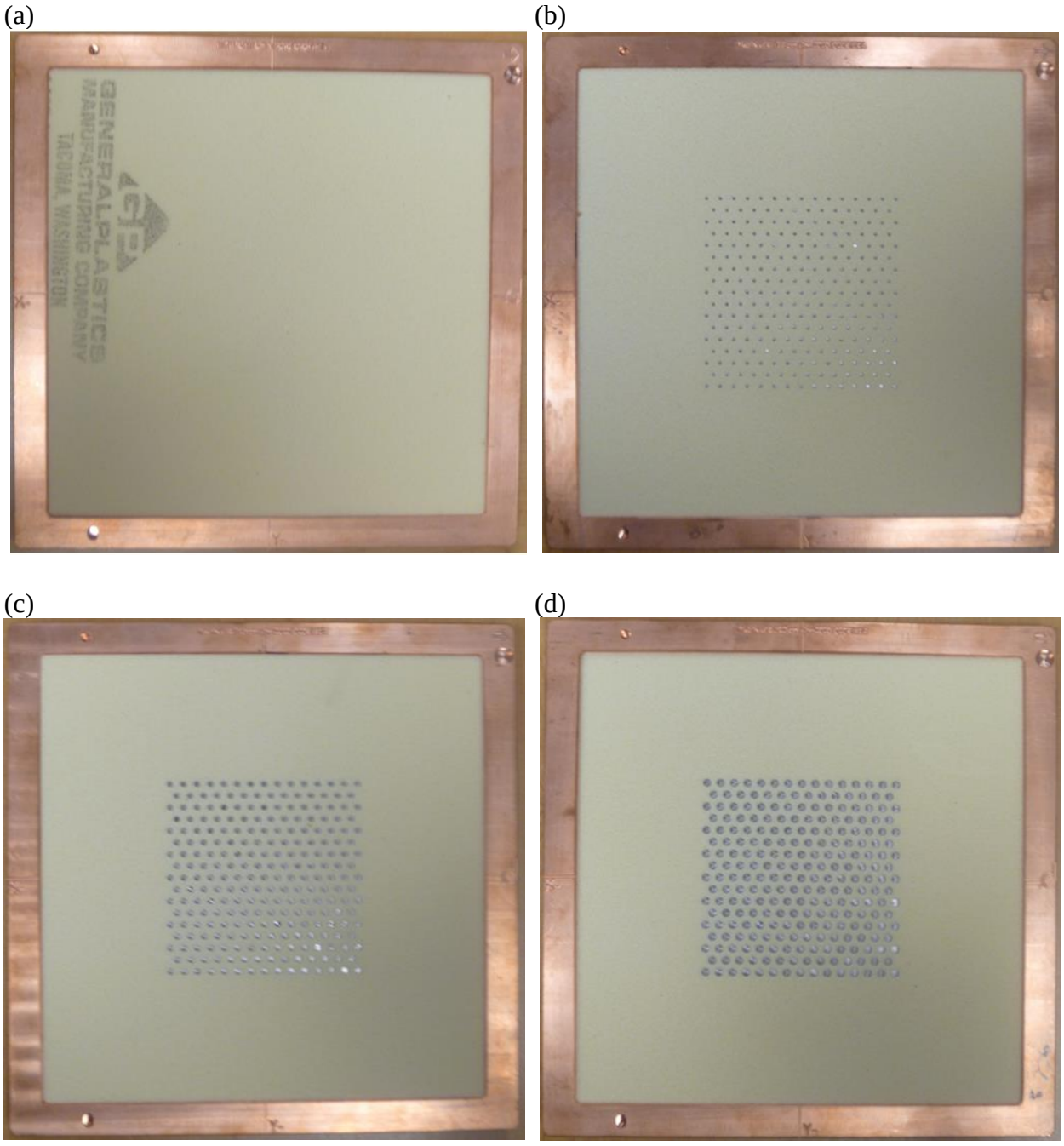

Figure 3.1. Beam's eye view of intensity modulator devices used for validation of the IM-PBRA. Each device contains machinable foam within a copper 21×21 cm^2 insert to fit within the nominal 20×20 cm^2 Elekta applicator. One device contains (a) foam only, while the others each contain 247 pins with uniform diameters of (b) 0.158 cm, (c) 0.273 cm, and (d) 0.352 cm. Pins were separated 0.6 cm on a hexagonal grid.

3.1.3. Measurement setup

All measurements were made on the Elekta Agility at Mary Bird Perkins Cancer Center (MBPCC) using an IBA Blue Phantom Compact 2D scanning system with IBA myQA Accept control software (IBA Dosimetry, Bartlett, TN). IBA CC13 ionization chambers (0.13 cm^3 cavity volume; 5.8 mm cavity length, 3.0 mm radius) were used as both field and reference detectors. All scanning was performed in the inplane direction as shown in Figure 3.2, which illustrates the tank setup.

Figure 3.2: Measurement beam scanning setup. Measurement was performed using Elekta Agility at MBPCC. The tank is oriented for inplane scanning.

3.1.4. Beam scanning quality assurance

Both before and after collecting IM scans at a given SSD, an open-field percent depth ionization (PDI) curve was collected at each energy and converted to a PDD curve using TG-25 protocol (Khan *et al.*, 1991) and renormalized such that the maximum dose on central axis (CAX), D_{max}, was 100%. To verify consistency of accelerator performance over the measurement period, the R_{90} and R_{50} values of the initial and final PDDs were compared with 0.5 mm tolerance. The scanning speed was set at 0.30 cm/s for all PDI curves.

3.1.5. Measurement acquisition

Scans were performed with the 7, 13, and 20 MeV beams at 100, 105, and 110 cm SSD for each of the four intensity modulators (foam only, 0.158-cm pins, 0.273-cm pins, 0.352-cm pins). For all setup combinations, PDI curves were collected from the surface to a depth of 12 cm, and off-axis profiles (in the bending plane containing isocenter) at various depths were acquired from -12 to +12 cm off axis in the inplane dimension (plane of bending) as shown in Figure 3.3. For the 7 MeV beam, measured profiles were acquired at depths of 0.5 to 3.5 cm in increments of 0.5 cm. For the 13 MeV beam, profiles were acquired at depths of 0.5, 1.5, 2.5, 3.0, 3.5, 4.0, 4.5, 5.5, and 6.5 cm. For the 20 MeV beam, profiles were acquired at depths of 0.5, 1.5, 2.5, 3.5, 4.5, 5.0, 5.5, 6.0, 6.5, 7.5, 8.5, and 9.5 cm. A scanning speed of 0.30 cm/s was used for all PDI measurements and 0.8 cm/s for all profile measurements.

Measurements at all energies for a given insert were collected sequentially to minimize room reentries, and all measurements for a given SSD were taken sequentially. All PDI curves were converted to PDDs using TG-25 protocol (Khan *et al.*, 1991) using the E_0 value calculated from the foam-only PDI data at the same energy and SSD. All depths were corrected to the effective point of measurement to account for the curvature of the cylindrical chamber.

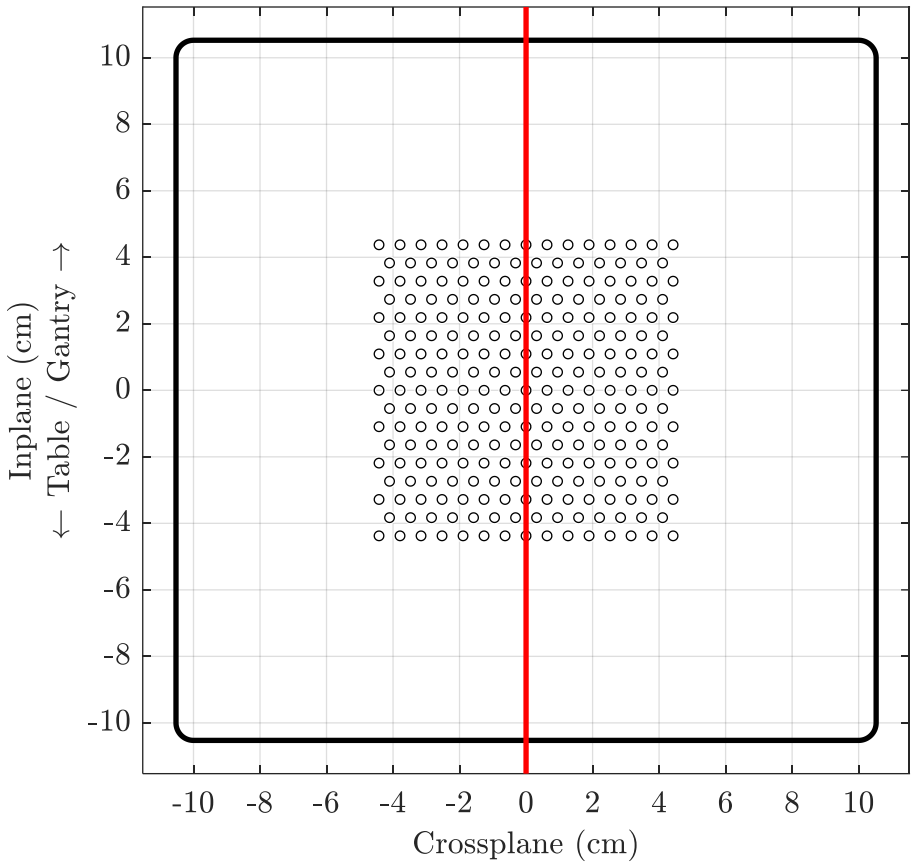

Figure 3.3. Plane of measurement for inplane profiles. The schematic of the PRIME device shows the pin positions and sizes as projected to isocenter. This example contains 0.273-cm pins. Pins are represented by circles and the inner edge of the insert by the bold black line. All profiles were measured in the inplane at x = 0 cm, depicted as the bold red line.

3.1.6. PDD and profile normalization

Since the beam scanning reference chamber reading can vary after changing the IM device and realigning the chamber, normalization factors were measured using a 1D water phantom. Ionization was measured for water at each combination of beam energy, SSD, and modulator (foam only, 0.158-cm pins, 0.273-cm pins, and 0.352-cm pins) with an Elekta Agility at MBPCC. Measurements were performed with a Standard Imaging 1D Water Scanning System using the same IBA CC13 detector as used for scanning measurements and a CNMC 206 electrometer. The setup is shown in Figure 3.4, and the physical depth of measurement at each energy is indicated in Table 3.1.

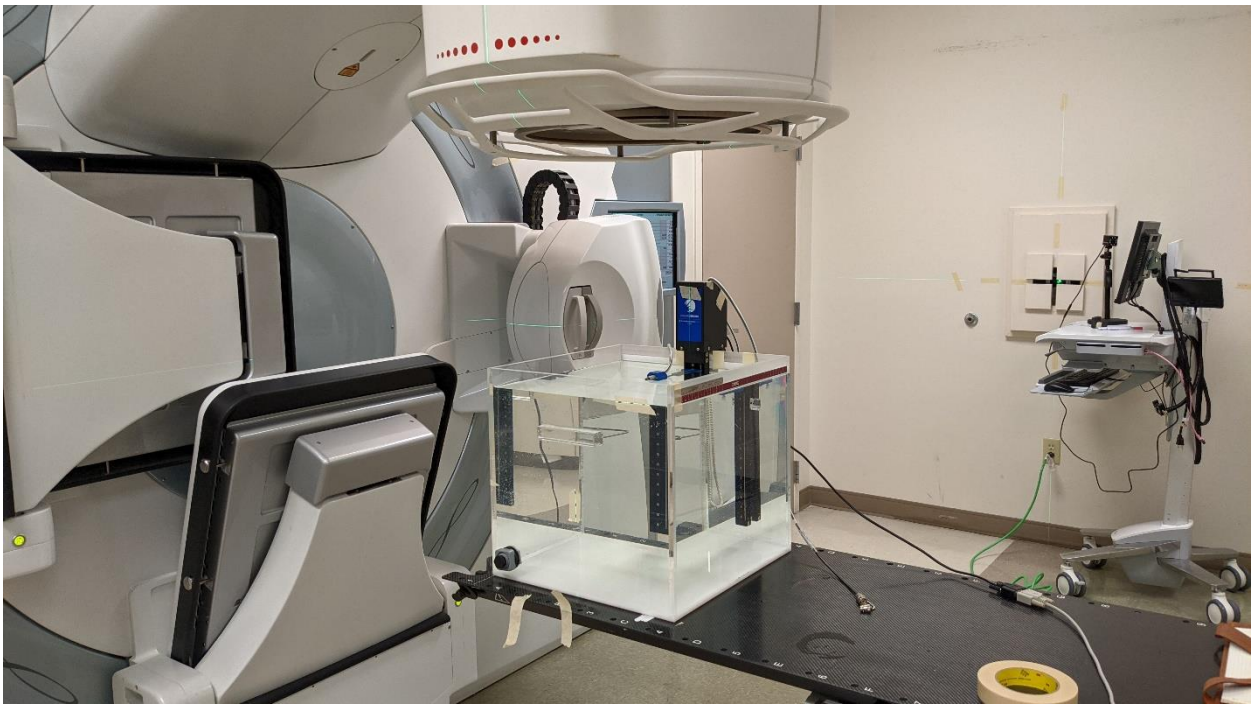

Figure 3.4. Ionization ratio measurement setup. The aligned tank and chamber are shown here prior to attaching the applicator.

Table 3.1. Measurement depths for ionization ratios. Ionization at a given beam energy was measured with the chamber on CAX at the physical depth shown. The effective point of measurement includes an upstream shift of 0.15 cm ($0.5r_{cav}$) due to the curvature of the cylindrical ionization chamber (Khan *et al.*, 1991). These depths are approximately equal to the reference depth, z_{ref} (Almond *et al.*, 1999), for each beam and are those used clinically for routine output measurement.

Beam Energy (MeV)	Physical Depth (cm)	Effective Depth (cm)
7	1.7	1.55
13	3.2	3.05
20	5.0	4.85

Ionization was measured on CAX. 100 MUs were delivered per collection. Ionization ratios, *R*, were calculated relative to the foam-only field at the same energy and SSD for each modulation device:

$$R(E, SSD, d) = \frac{\bar{Q}(E, SSD, d, z_{\mathrm{ref}})}{\bar{Q}(E, SSD, 0, z_{\mathrm{ref}})}, \qquad 3.1$$

where $\bar{Q}$ is the collected charge, d is the pin diameter, 0 indicates the foam-only modulator (pin diameter of 0 cm), and z_{ref} is the reference depth for a given energy as listed in Table 3.1.

All PDDs were initially scaled such that D_{max} was equal to 100%. The modulated PDDs were then normalized such that the modulated to unmodulated dose ratio at z_{ref} was equal to the corresponding ionization ratio of Equation 3.1. That is, the normalized PDD value, PDD_N, was calculated as

$$PDD_N(E, SSD, d, z) = \left[R(E, SSD, d) \cdot \frac{PDD(E, SSD, 0, z_{\mathrm{ref}})}{PDD(E, SSD, d, z_{\mathrm{ref}})}\right] \cdot PDD(E, SSD, d, z), \qquad 3.2$$

where R is the ionization ratio of Equation 3.2, $PDD(E, SSD, 0, z_{\mathrm{ref}})$ is the unmodulated PDD value at z_{ref}, $PDD(E, SSD, d, z_{\mathrm{ref}})$ and $PDD(E, SSD, d, z)$ are the modulated PDD values at z_{ref} and z, respectively, and 100% is the foam-only value at R_{100}.

Variations in tank filling and water level can result in small depth errors in PDD measurements. To account for this, each measured PDD was shifted such that its R_{20} value agreed with the in-scatter adjusted PBRA R_{20} under the same conditions. As normalization depends on the PDD value at the reference depth, the normalization and depth adjustment were applied iteratively until the modulated to foam-only PDD ratio at z_{ref} was within 0.0001% of the ionization ratio R and the measured-PBRA R_{20} agreement was within 0.0001%. The maximum shift required was 0.15 cm for 20 MeV at 110 cm SSD for 0.352-cm-diameter pins.

Off-axis profiles were normalized such that CAX dose was equal to the PDD value at the same measurement depth. Profiles were centered so that the points in the outer penumbrae where the dose was equal to 50% of the unmodulated PDD at that depth were equidistant from CAX.

3.1.7. Isodose contours

Isodose contours were composed from a 2D dose matrix that was constructed from the inplane profiles at each depth. Isodose line segments were calculated by bilinear interpolation between bracketing inplane position and depth values.

3.1.8. PBRA calculations

Dose calculations were performed in water using an in-house research version of the PBRA model commissioned using the clinical commissioning data at MBPCC. Calculations were performed for the 7, 13, and 20 MeV beams at 100, 105, and 100 cm SSD for a 21×21 cm^2 field containing foam only and with modulators with nominal and in-scatter-adjusted diameters as listed in Table 3.2. This research version of the PBRA reads in pin arrangements from a text file containing the total number of island blocks and their inplane and crossplane positions and diameters as defined at 100 cm. Pin geometries, including both position and diameter, were identical to those in the sample devices.

To minimize the error due to accelerator fluctuations in this analysis, the measured foam-only PDDs at 100 cm SSD were used as input for the PBRA calculations. The R_{90} shift for the foam in the PBRA, as used by Hilliard, was removed as foam was present during measurement of the PDD used as input for the calculations. Hilliard's σ_{θ_x} scaling was retained, i.e. $\sigma_{\theta_x} = 1.5 \cdot \sigma_{\theta_x,\text{clinical}}$. The most probable energy at the surface, $E_{p,0}$, was calculated from the measured PDDs at each energy according to TG-70 protocol (Gerbi *et al*., 2009) and entered manually into the PBRA input tables.

All dose values under a given setup were normalized such that the maximum CAX dose of the foam-only setup at the same beam energy and SSD was equal to 100%.

Table 3.2. Nominal and in-scatter-adjusted diameters used in PBRA calculations. The nominal pin diameters and their corresponding in-scatter-adjusted diameters are given for beam energies of 7, 13, and 20 MeV. The data here are partially reproduced from the relevant portions of Table 2.4. Since the PBRA assumes pin dimensions at 100 cm, these diameters were scaled in the input file to account for geometric divergence.

Beam Energy (MeV)	d_{nom} (cm)	d_{IS} (cm)
7	0.158	0.188
7	0.273	0.306
7	0.352	0.386
13	0.158	0.178
13	0.273	0.294
13	0.352	0.373
20	0.158	0.171
20	0.273	0.286
20	0.352	0.366

Initial PBRA calculations assumed a virtual source position of 100 cm upstream of isocenter, which differs from the value of 94 cm from isocenter for the Elekta Agility at MBPCC for the 7 MeV beam determined by Pitcher *et al.* (2017); the value at other energies was assumed to be within 1 cm of that. To account for this difference and improve calculation accuracy in sharp gradient regions in the off-axis profiles, a geometric scaling factor at a given depth *z* and SSD was applied to all PBRA position values:

$$x_{\text{corr}}(SSD, z) = x \cdot \left(\frac{IP - SAD_{\text{nom}}}{SSD_{\text{nom}} + z}\right)\left(\frac{[SSD_{\text{nom}} - (SAD_{\text{nom}} - SAD_{\text{virt}})] + z}{IP - SAD_{\text{virt}}}\right), \qquad 3.3$$

where x_{corr} is the corrected position, x is the nominal position, SSD_{nom} is the nominal SSD value under the 100 cm virtual source assumption, $IP - SAD_{\text{nom}}$ is the distance between the insert plane and the assumed virtual source position on CAX (95 cm), $SAD_{\text{nom}} - SAD_{\text{virt}}$ is the difference

between the nominal and actual virtual source positions from isocenter (6 cm), and $IP - SAD_{virt}$ is the distance between the virtual source and the modulating insert (89 cm).

3.1.9. Validation of PBRA beam modeling

In order to treat the modulated components of Equation 2.4 as separable, accuracy of the PBRA calculations in the absence of any modulation is critical so that any discrepancies between measurement and PBRA calculations are due to pin modeling. For each energy and SSD, PBRA calculations were performed for foam only, i.e. without any pins, and PDDs, profiles, and isodose distributions were generated from the dose matrix.

The PBRA uses off-axis weighting factors which are determined from commissioning at a single depth, $0.5 \cdot R_{90}$. In calculation, these weights are constant, but the actual ratios may vary with depth. Depth-specific ratios cannot be applied in PBRA calculations, so an off-axis dose adjustment for PBRA calculations, ΔD_{OAR}, is calculated as

$$\Delta D_{\mathrm{OAR}}(E, SSD, y, z) = D_{\mathrm{meas,foam}}(E, SSD, y, z) - D_{\mathrm{PBRA,foam}}(E, SSD, y, z), \qquad 3.4$$

where $D_{\mathrm{meas,foam}}$ and $D_{\mathrm{PBRA,foam}}$ are the measured and PBRA-calculated unmodulated dose values, respectively, at depth z. This quantity describes the off-axis difference at each depth between measurement and PBRA calculations in the inplane.

The foam-only measurement and PBRA (without the off-axis correction) isodose distributions were compared under 3% or 3 mm distance-to-agreement (3%/3mm DTA) criteria. A dose point was considered to have passed agreement criteria if either: (1) the measured and calculated dose values agree within 3% at the same point, or (2) the dose values were equal within 3 mm. If neither criterion was satisfied, the dose point was considered to have failed. The sign of the dose comparison of each failure was recorded, and a difference histogram was generated from

the passes and failures in binning increments of 1%. The passing rate for all points was also found. The greatest magnitude differences for points with 80% dose or greater were also determined.

3.1.10. Correction method

Investigation of the measured data revealed that measured dose exceeded in-scatter corrected calculations by several percent due to these calculations neglecting out-scatter dose. Additionally, the measured profiles did not produce a flat field within the modulated region, with the CAX dose being higher.

The difference between measurement and in-scatter-adjusted PBRA calculations approximates the out-scatter dose component as discussed in Section 3.1.1. To account for out-scatter, the diameter was empirically scaled down to minimize least squares differences between measured data and calculation within the modulated region. Equation 3.5 illustrates the optimization process. For N_y off-axis points at N_z depths, the optimal value for ΔD_{OS}, which minimizes the sum of the squares of the measured-PBRA differences, was determined according to

$$\min = \sum_{i,j}^{N_y,N_z} \left[D_{\text{meas}}(y_i, z_j) - \left(D_{\text{PBRA,IS}}(y_i, z_j) + \Delta D_{\text{OS}}\right)\right]^2 \quad 3.5$$

where D_{meas} and $D_{PBRA,IS}$ are the measured and in-scatter-adjusted PBRA dose values, respectively, at positions (y_i, z_j). The minimization was performed over the modulated region, specified as within ±3.5 of CAX. The dose profiles within the plateau region of the PDD, i.e. up to a depth of approximately R_{90}, were included in the analysis. The profiles for each SSD and modulator combination included were: 0.5, 1.0, 1.5, 2.0 cm at 7 MeV; 0.5, 1.5, 2.5, 3.5, and 4.5 cm at 13 MeV; 0.5, 1.5, 2.5, 3.5, 4.5, 5.5, and 6.5 cm at 20 MeV. ΔD_{OS} was determined for each combination of beam energy, SSD, and modulator combination.

To extend the solution to intermediate energies, SSD, and diameter combinations, a quadratic fit was applied to values of ΔD_{OS} against most probable energy at the surface, $E_{p,0}$, for each nominal beam energy and SSD combination. Each fit had the form of

$$\Delta D_{\mathrm{OS,fit}}\left(E_{p,0}, SSD, d\right) = A_1(SSD, d) \cdot E_{p,0}^2 + A_2(SSD, d) \cdot E_{p,0} + A_3(SSD, d), \qquad 3.6$$

where coefficients A_1, A_2, and A_3 were specific to a given SSD and diameter combination. The value of $\Delta D_{\mathrm{OS,fit}}$ was determined for each beam energy and pin diameter combination contained in Table 2.4 at each SSD. For pin diameters without corresponding measurement, the results were determined by interpolation between fitted values.

The value of $\Delta D_{\mathrm{OS,fit}}$ indicated relative dose to be reincorporated into the in-scatter-adjusted PBRA calculations to approximately account for out-scatter dose within the modulated region. This was equated to a change in IRF_{IS} to yield the IRF corrected for both in-scatter and out-scatter, $IRF_{\mathrm{IS+OS}}$, under a given set of conditions:

$$IRF_{\mathrm{IS+OS}}(E, SSD, d) = IRF_{\mathrm{IS}}(E, d) + \Delta D_{\mathrm{OS,fit}}(E, SSD, d). \qquad 3.7$$

Note that the out-scatter correction $\Delta D_{\mathrm{OS,fit}}$ is calculated from the corresponding $E_{p,0}$ value for a given nominal beam energy. The fully corrected (IS+OS) diameter for a given beam energy, SSD, and pin diameter combination was found according to the geometric relation between diameter and IRF:

$$d_{\mathrm{IS+OS}}(E, SSD, d) = (0.6\ \mathrm{cm})\left[\left(\frac{2\sqrt{3}}{\pi}\right)\left(1 - IRF_{\mathrm{IS+OS}}(E, SSD, d)\right)\right]^{1/2}. \qquad 3.8$$

IS+OS diameters were evaluated for each beam energy and pin diameter combination in Table 2.4 at each SSD.

3.2. Results

Table 3.3 contains the normalization ratios measured in the 1D water scanning tank. Table 3.4 lists $E_{p,0}$ values of the beam exiting the foam as determined from the measured foam-only PDDs at 100 cm SSD, which were used as input for PBRA calculations.

The foam-only measured and PBRA-calculated CAX PDDs are plotted in Figure 3.5, which demonstrate excellent agreement for the 7, 13, and 20 MeV beams at 100 cm SSD. 7, 13, and 20 MeV inplane off-axis profiles at depths of 1.0, 2.5, and 3.5 cm, respectively, are plotted in Figure 3.6. These depths correspond approximately to the depths at which the PBRA beam weights are determined ($0.5 \cdot R_{90}$): 1.0, 2.0, and 3.0 cm for the 7, 13, and 20 MeV beam energies, respectively. These profiles show good agreement within 7.5 cm of CAX. Outside of 7.5 cm from CAX, the calculated dose decreases relative to measurement, creating discrepancies as great as 6.4% (-10.71 cm off-axis) at 20 MeV and 0.5 cm depth. Note that these discrepancies are outside the modulated regions for the IM measurements. Foam-only PDD and profile comparisons at 105 and 110 cm SSD, plotted in Appendix A, show similar or better agreement.

Table 3.5 contains an overall comparison of PBRA-calculated and measured foam-only distributions at every energy and SSD, including the maximum magnitude point differences for doses greater than 80%. The average passing rate was 99.7% for all points within a given distribution under 3%/3mm DTA criteria. The PBRA and measured isodose contours are plotted in Figure 3.7 with difference histograms under the same 3%/3mm DTA criteria at 7 MeV and 100 cm SSD. This comparison represented the worst case with a passing rate of 98.3%. Figures 3.8 and 3.9 compare unmodulated measurement and PBRA calculations for 13 and 20 MeV, respectively, at 100 cm SSD, and show better overall agreement. Similar plots for at 105 and 110 cm SSD are found in Appendix A. Discrepancies for all distributions were generally confined to the high gradient penumbra with few exceptions.

Figures 3.10-12 compare the measured PDDs for 7-20 MeV beam energies at 100 cm SSD to the nominal and in-scatter-adjusted PBRA-calculated PDDs for all modulators. The estimated out-scatter component is also plotted. Figures 3.13-15 plot measured, nominal PBRA, and in-scatter-adjusted PBRA calculated profiles with the out-scatter estimation, which includes the off-axis weighting adjustment of Equation 3.4, for all modulators for 7-20 MeV at 100 cm SSD. Similar PDDs and off-axis profiles are plotted in Appendix A at 105 and 110 cm SSD.

Figures 3.16-18 plot the PDD and off-axis profiles at various depths for measurement, nominal PBRA, in-scatter-adjusted PBRA, and out-scatter estimation with off-axis adjustment for the largest pin diameter (0.352 cm) for 7-20 MeV beam energies at 100 cm SSD. Table 3.6 contains the minimizing dose adjustments calculated from Equation 3.5, and the fits to those data are listed in Table 3.7. The contents of these tables are plotted in Figure 3.19. Diameter correction factors at all beam energy, SSD, and nominal diameter combinations are tabulated in Appendix A.

PDDs comparing measurement to nominal and IS+OS-corrected PBRA calculations are plotted in Figures 3.20-22 for 7-20 MeV and all pin diameters at 100 cm SSD. Figures 3.23-25 contain off-axis profiles for measurement and IS+OS-corrected calculations for beam energies of 7, 13, and 20 MeV at depths of 1.0, 1.5, and 1.5 cm, respectively, at 100 cm SSD. Similar plots at 105 and 110 cm SSD are located in Appendix A.

Figures 3.26-28 compare the PDDs and off-axis profiles over various depths for measurement, nominal PBRA, and IS+OS-corrected PBRA for 7-20 MeV at 100 cm SSD for 0.352-cm pins, demonstrating the effect of the out-scatter dose adjustment. The measured CAX dose exceeds the corrected PBRA dose over most of the plateau region. In the off-axis profiles at shallow depths, measurement generally exceeds the IS+OS-corrected IM-PBRA calculations within the modulated region (±3.5 cm). At intermediate depths, measured dose is below calculation

in the lateral portions of the modulated profile and above near CAX. At deeper depths, the IS+OS-corrected calculation is above measurement.

Table 3.3. Normalization ratios. The normalization ratios at a given setup were computed according to Equation 3.1 from the average of three measurements for each setup.

SSD (cm)	Insert	Normalization Ratios		
		7 MeV	13 MeV	20 MeV
100	Foam Only	1.0000	1.0000	1.0000
	0.158-cm Pins	0.9355	0.9458	0.9500
	0.273-cm Pins	0.8122	0.8325	0.8412
	0.352-cm Pins	0.6907	0.7200	0.7299
105	Foam Only	1.0000	1.0000	1.0000
	0.158-cm Pins	0.9352	0.9459	0.9486
	0.273-cm Pins	0.8141	0.8312	0.8352
	0.352-cm Pins	0.6966	0.7193	0.7286
110	Foam Only	1.0000	1.0000	1.0000
	0.158-cm Pins	0.9361	0.9439	0.9458
	0.273-cm Pins	0.8174	0.8297	0.8321
	0.352-cm Pins	0.7018	0.7154	0.7216

Table 3.4. Foam-only most probable energy at the surface for PBRA input and out-scatter correction fits. The PBRA beam tables were updated with the $E_{p,0}$ values below, which correspond to the measured foam-only PDDs that were used as input for PBRA calculations. The quadratic fitting expressions to ΔD_{OS} use the $E_{p,0}$ values here rather than the corresponding nominal beam energy.

Beam Energy (MeV)	$E_{p,0}$ (MeV)
7	6.52
13	13.42
20	20.80

Table 3.5. Validation metrics for measured and PBRA-calculated foam-only dose distributions. 3%/3mm DTA criteria were applied for all points within the dose distribution, including the penumbra region. The greatest single point dose discrepancies for doses greater than 80% are listed in the right to columns (calculated minus measured).

SSD (cm)	Beam Energy (MeV)	Passing Rate	Maximum Differences	
100	7	98.3%	-4.80%	1.08%
100	13	100.0%	-3.16%	1.20%
100	20	99.7%	-3.12%	1.11%
105	7	99.6%	-2.72%	1.52%
105	13	100.0%	-2.29%	1.21%
105	20	99.8%	-0.72%	2.09%
110	7	99.7%	-1.65%	2.26%
110	13	100.0%	-1.18%	2.39%
110	20	99.9%	-0.67%	2.52%

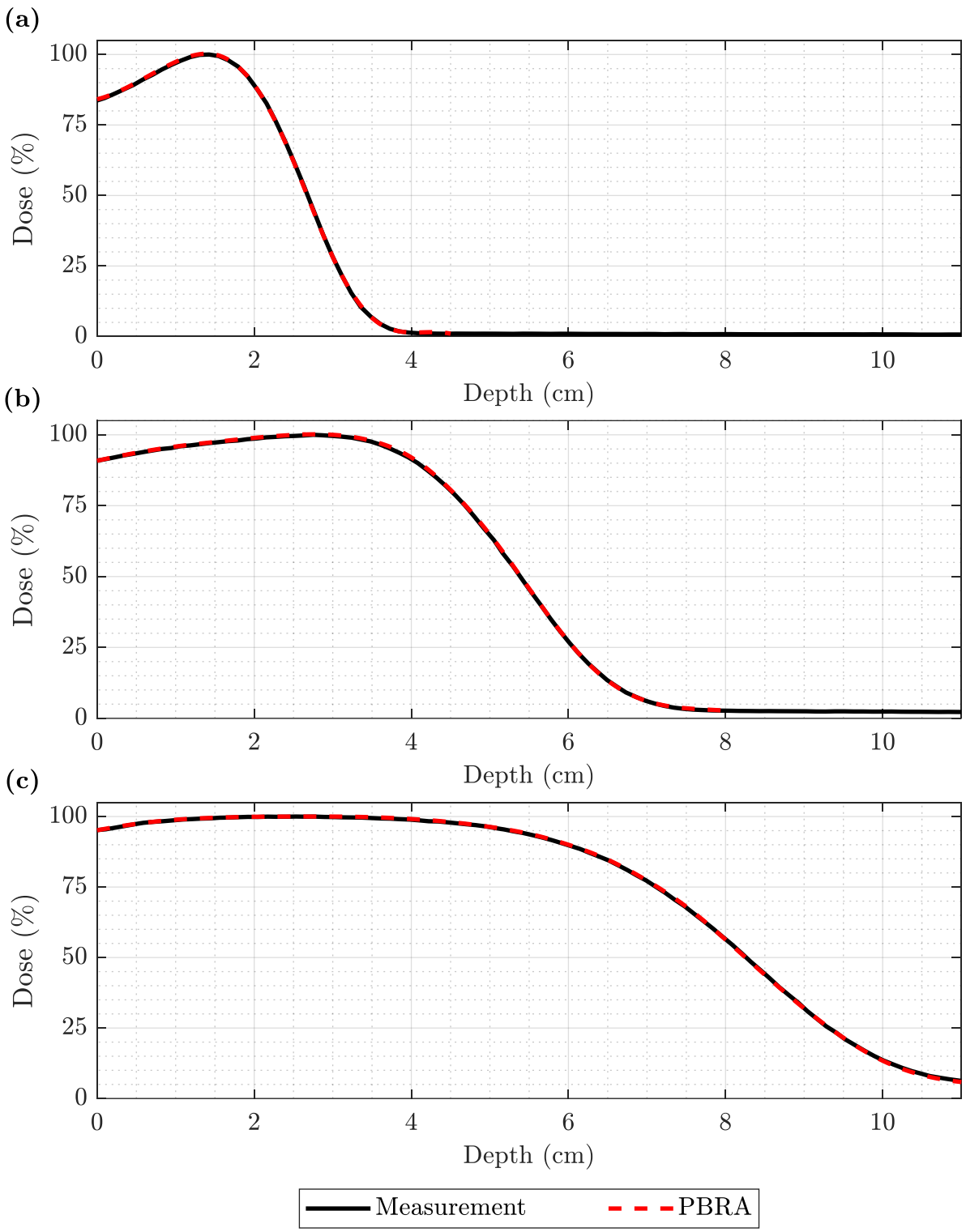

Figure 3.5. PDDs of foam-only measurement and PBRA calculation for each beam energy at 100 cm SSD. Foam-only PDDs are plotted for measurement (solid black) and PBRA (dashed red) at (a) 7, (b) 13, and (c) 20 MeV at 100 cm SSD for a 21×21 cm^2 field size.

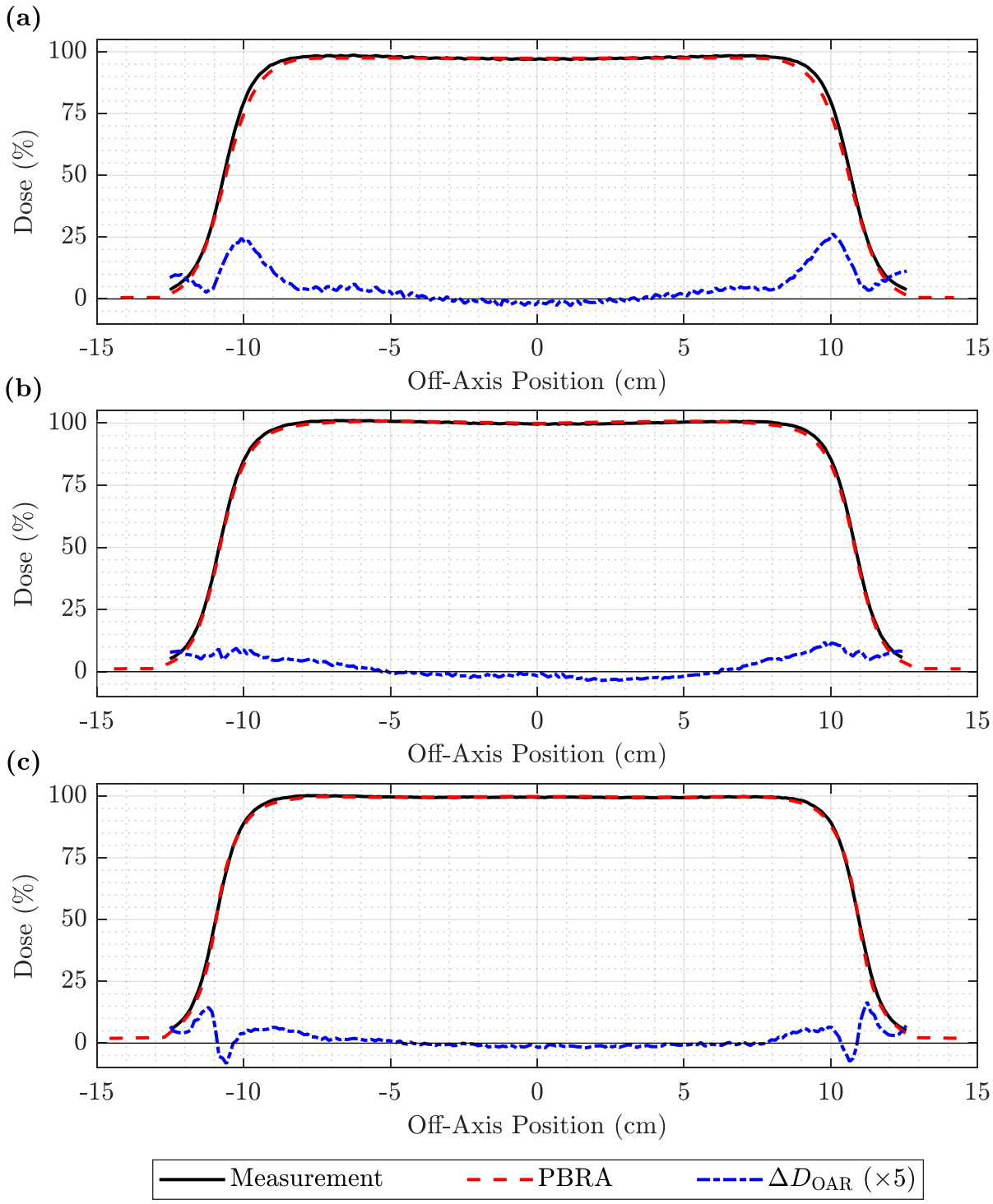

Figure 3.6. Off-axis profiles of foam-only measurement and PBRA calculation for each beam energy at 100 cm SSD. Foam-only inplane profiles are plotted for measurement (solid black) and PBRA (dashed red) at (a) 7 MeV and 1.0 cm depth, (b) 13 MeV and 2.5 cm depth, and (c) 20 MeV and 3.5 cm depth at 100 cm SSD for a 21×21 cm^2 field size. The off-axis weight adjustment of Equation 3.4 (dashed-dotted blue) is the difference between measured and PBRA-calculated profiles, plotted here with ×5 magnification for clarity.

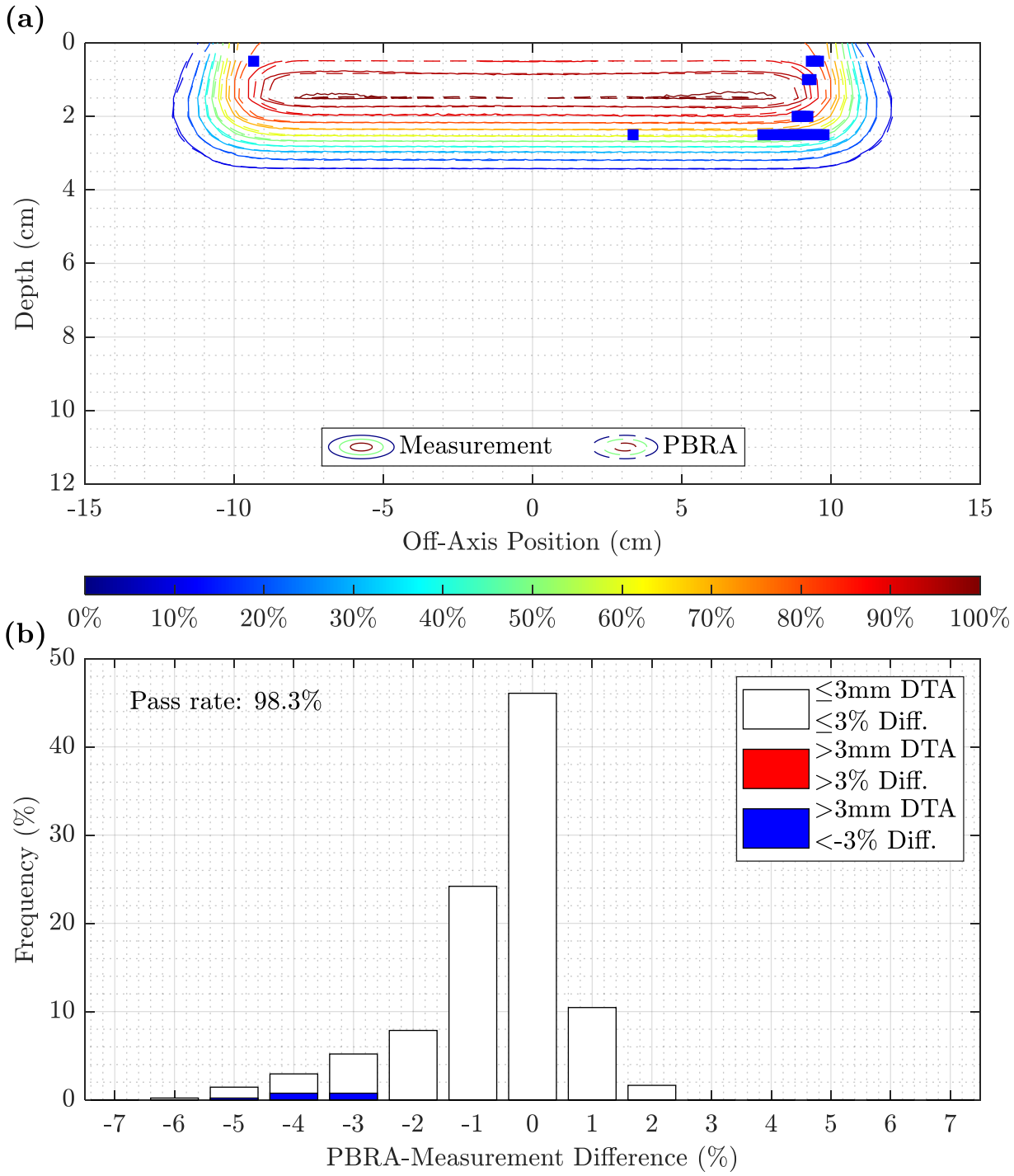

Figure 3.7. Measurement and PBRA foam-only isodose comparison and difference histogram for 7 MeV at 100 cm SSD. The isodose contours in (a) compare the measured (solid) and PBRA-calculated (dashed) isodose distributions, and (b) contains the histogram of differences between measurement and PBRA calculations for foam-only at 7 MeV and 100 cm SSD. In both (a) and (b), points where the PBRA underpredicted the dose relative to measurement are shown in blue, while those where the PBRA overpredicted dose are plotted as red. The 3%/3mm criteria yielded a passing rate of 98.3% for all points for this setup.

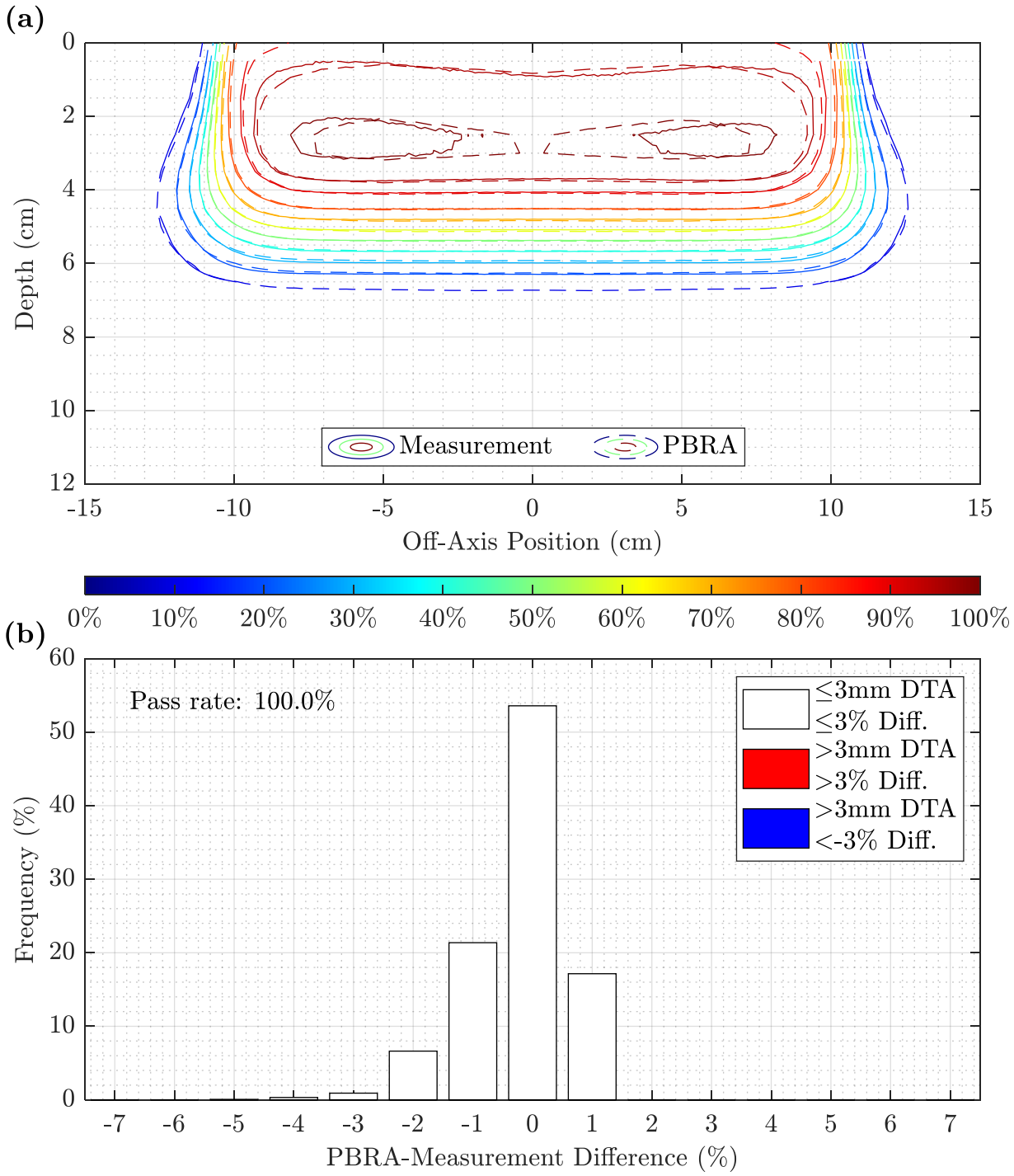

Figure 3.8. Measurement and PBRA foam-only isodose comparison and difference histogram for 13 MeV at 100 cm SSD. The isodose contours in (a) compare the measured (solid) and PBRA-calculated (dashed) isodose distributions, and (b) contains the histogram of differences between measurement and PBRA calculations for foam-only at 13 MeV and 100 cm SSD. In both (a) and (b), points where the PBRA underpredicted the dose relative to measurement are shown in blue, while those where the PBRA overpredicted dose are plotted as red. The 3%/3mm criteria yielded a passing rate of 100% for all points for this setup.

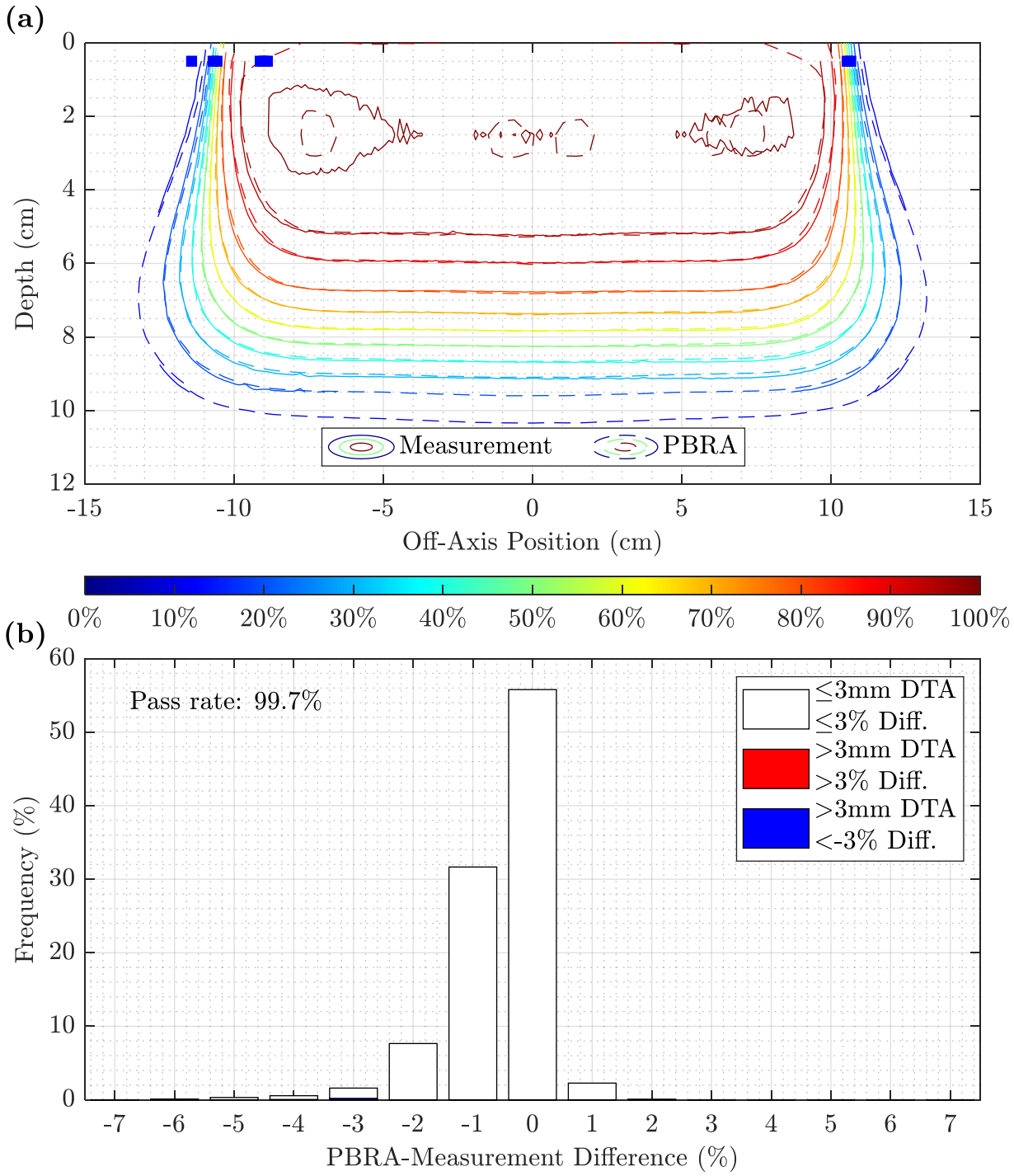

Figure 3.9. Measurement and PBRA foam-only isodose comparison and difference histogram for 20 MeV at 100 cm SSD. The isodose contours in (a) compare the measured (solid) and PBRA-calculated (dashed) isodose distributions, and (b) contains the histogram of differences between measurement and PBRA calculations for foam-only at 20 MeV and 100 cm SSD. In both (a) and (b), points where the PBRA underpredicted the dose relative to measurement are shown in blue, while those where the PBRA overpredicted dose are plotted as red. The 3%/3mm criteria yielded a passing rate of 99.7% for all points this setup.

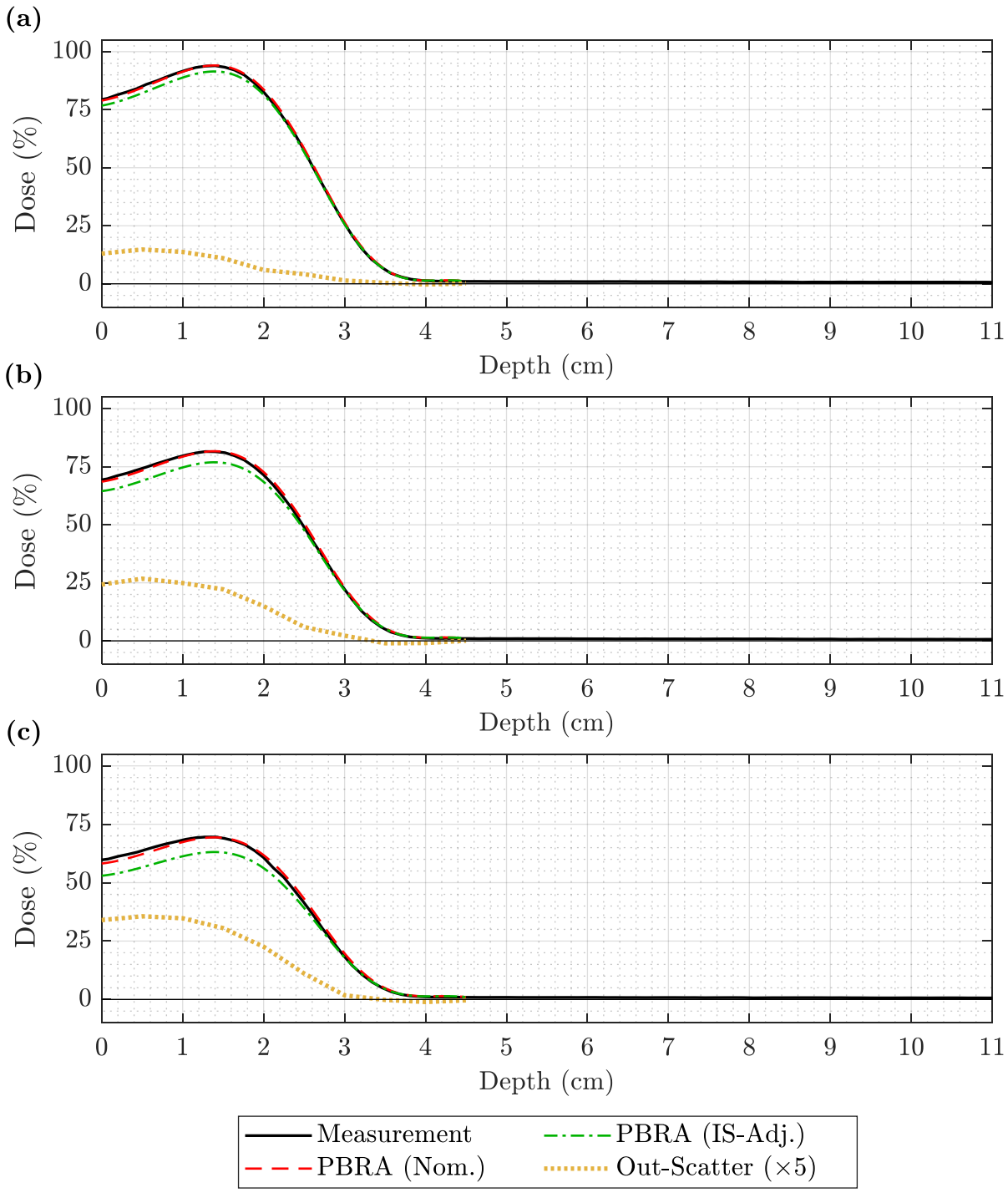

Figure 3.10. PDD comparison of measurement, nominal PBRA, and in-scatter-adjusted PBRA calculations at 7 MeV and 100 cm SSD. Measurement (solid black) is compared to the nominal PBRA (dashed red) and PBRA corrected for in-scatter only (dashed-dotted green) for a 7 MeV beam at 100 cm SSD for (a) 0.158-cm, (b) 0.273-cm, and (c) 0.352-cm pins. The out-scatter estimation (dotted yellow) is the difference between measurement and the in-scatter-adjusted PBRA, plotted here with ×5 magnification for clarity.

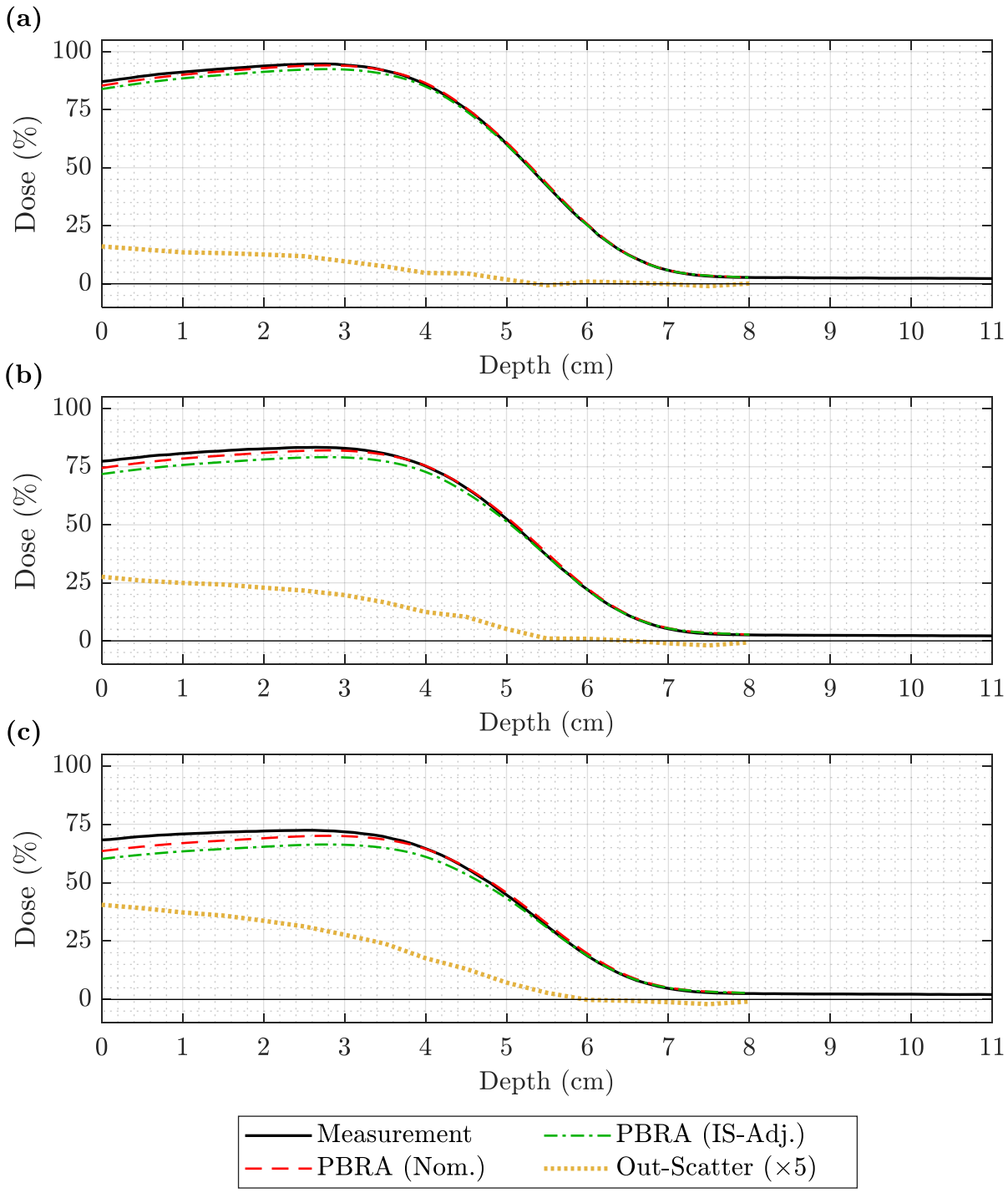

Figure 3.11. PDD comparison of measurement, nominal PBRA, and in-scatter-adjusted PBRA calculations at 13 MeV and 100 cm SSD. Measurement (solid black) is compared to the nominal PBRA (dashed red) and PBRA corrected for in-scatter only (dashed-dotted green) for a 13 MeV beam at 100 cm SSD for (a) 0.158-cm, (b) 0.273-cm, and (c) 0.352-cm pins. The out-scatter estimation (dotted yellow) is the difference between measurement and the in-scatter-adjusted PBRA, plotted here with ×5 magnification for clarity.

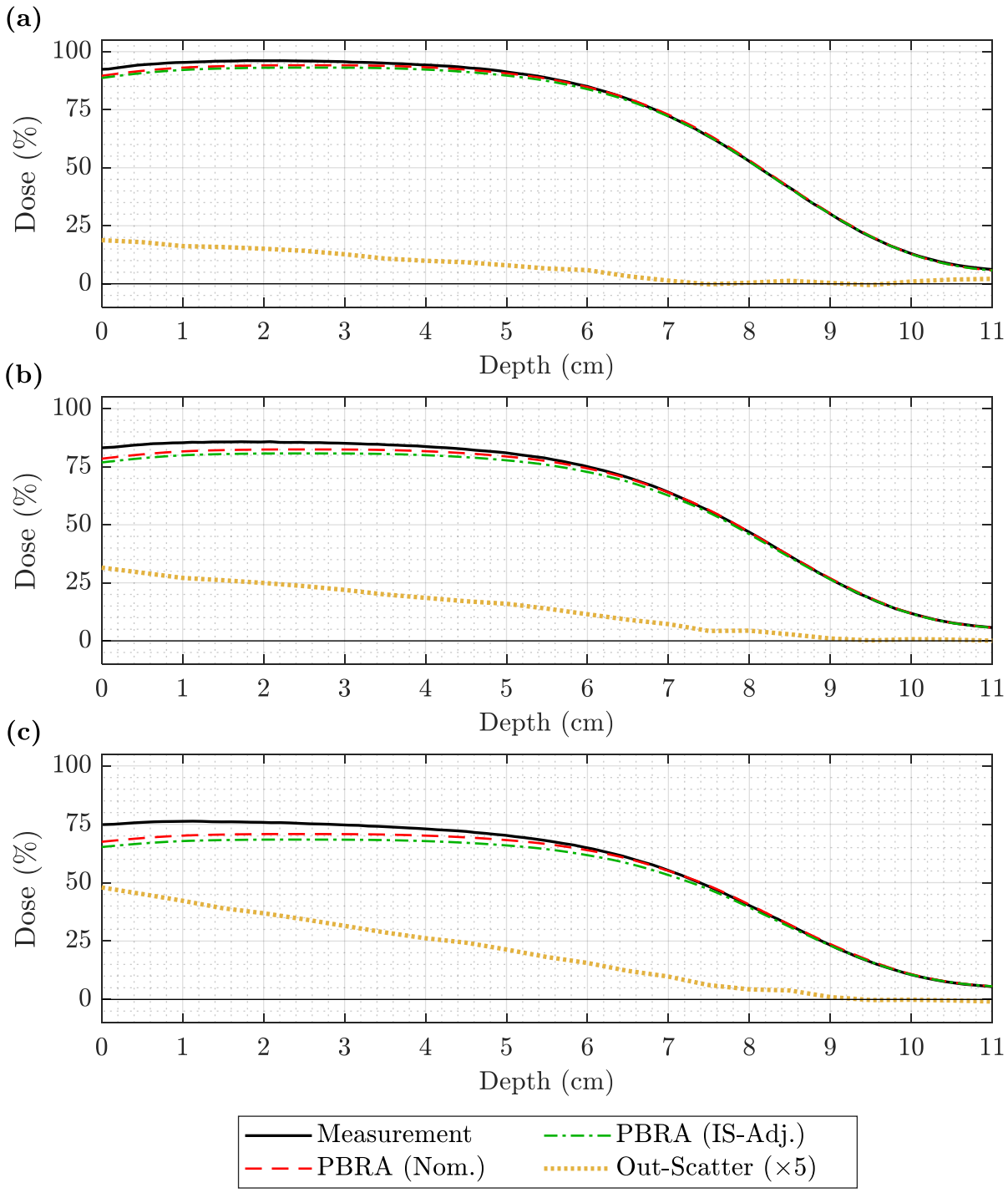

Figure 3.12. PDD comparison of measurement, nominal PBRA, and in-scatter-adjusted PBRA calculations at 20 MeV and 100 cm SSD. Measurement (solid black) is compared to the nominal PBRA (dashed red) and PBRA corrected for in-scatter only (dashed-dotted green) for a 20 MeV beam at 100 cm SSD for (a) 0.158-cm, (b) 0.273-cm, and (c) 0.352-cm pins. The out-scatter estimation (dotted yellow) is the difference between measurement and the in-scatter-adjusted PBRA, plotted here with ×5 magnification for clarity.

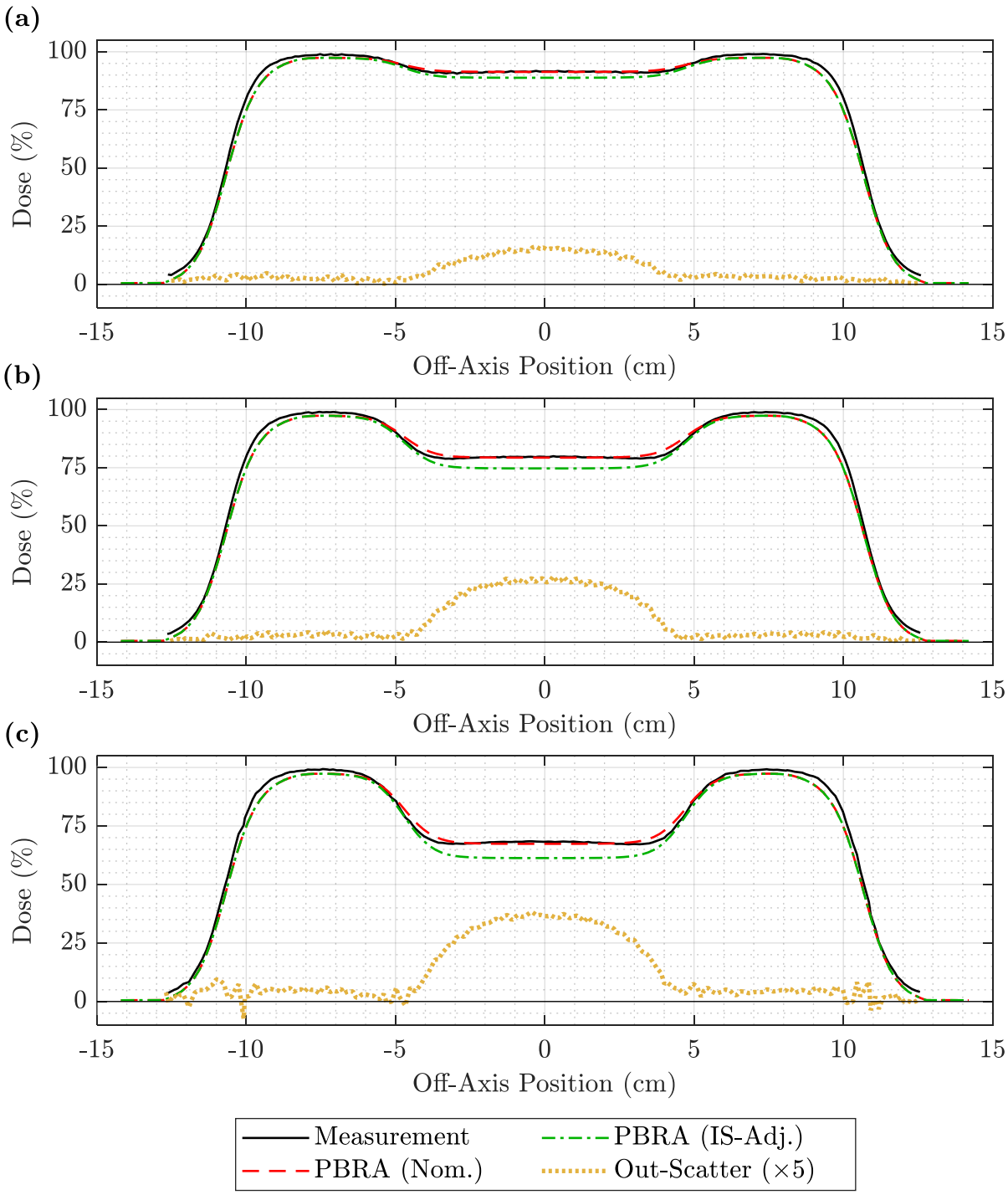

Figure 3.13. Off-axis profile comparison of measurement, nominal PBRA, and in-scatter-adjusted PBRA calculations for the 7 MeV beam at 100 cm SSD and 1.0 cm depth. Measurement (solid black) is compared to the nominal PBRA (dashed red) and PBRA corrected for in-scatter only (dashed-dotted green) for a 7 MeV beam at 100 cm SSD for (a) 0.158-cm, (b) 0.273-cm, and (c) 0.352-cm pins at a depth of 1.0 cm. The out-scatter estimation (dotted yellow) is the difference between measurement and the in-scatter-adjusted PBRA with the off-axis weight adjustment of Equation 3.4, plotted here with ×5 magnification for clarity.

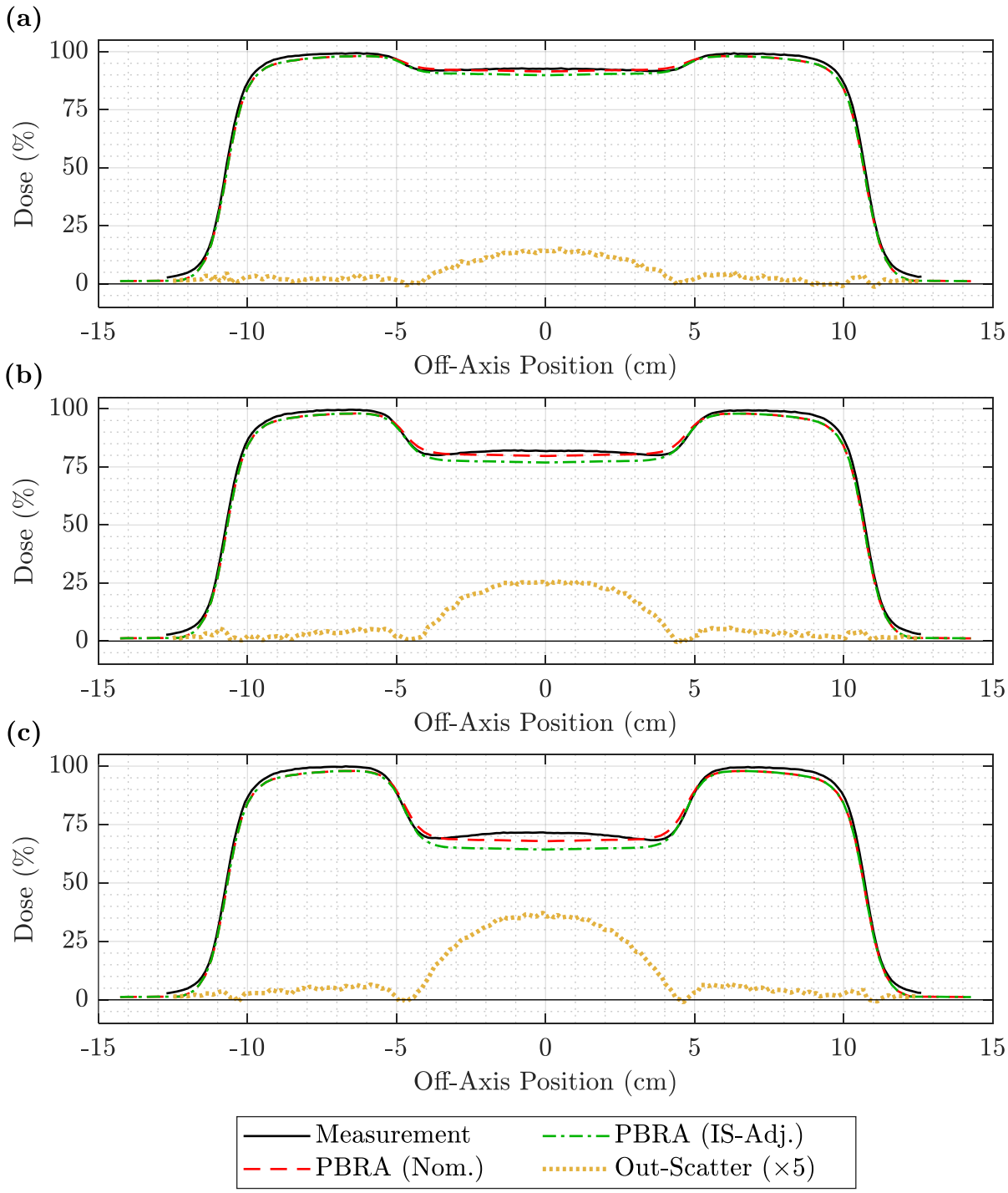

Figure 3.14. Off-axis profile comparison of measurement, nominal PBRA, and in-scatter-adjusted PBRA calculations for the 13 MeV beam at 100 cm SSD and 1.5 cm depth. Measurement (solid black) is compared to the nominal PBRA (dashed red) and PBRA corrected for in-scatter only (dashed-dotted green) for a 13 MeV beam at 100 cm SSD for (a) 0.158-cm, (b) 0.273-cm, and (c) 0.352-cm pins at a depth of 1.5 cm. The out-scatter estimation (dotted yellow) is the difference between measurement and the in-scatter-adjusted PBRA with the off-axis weight adjustment of Equation 3.4, plotted here with ×5 magnification for clarity.

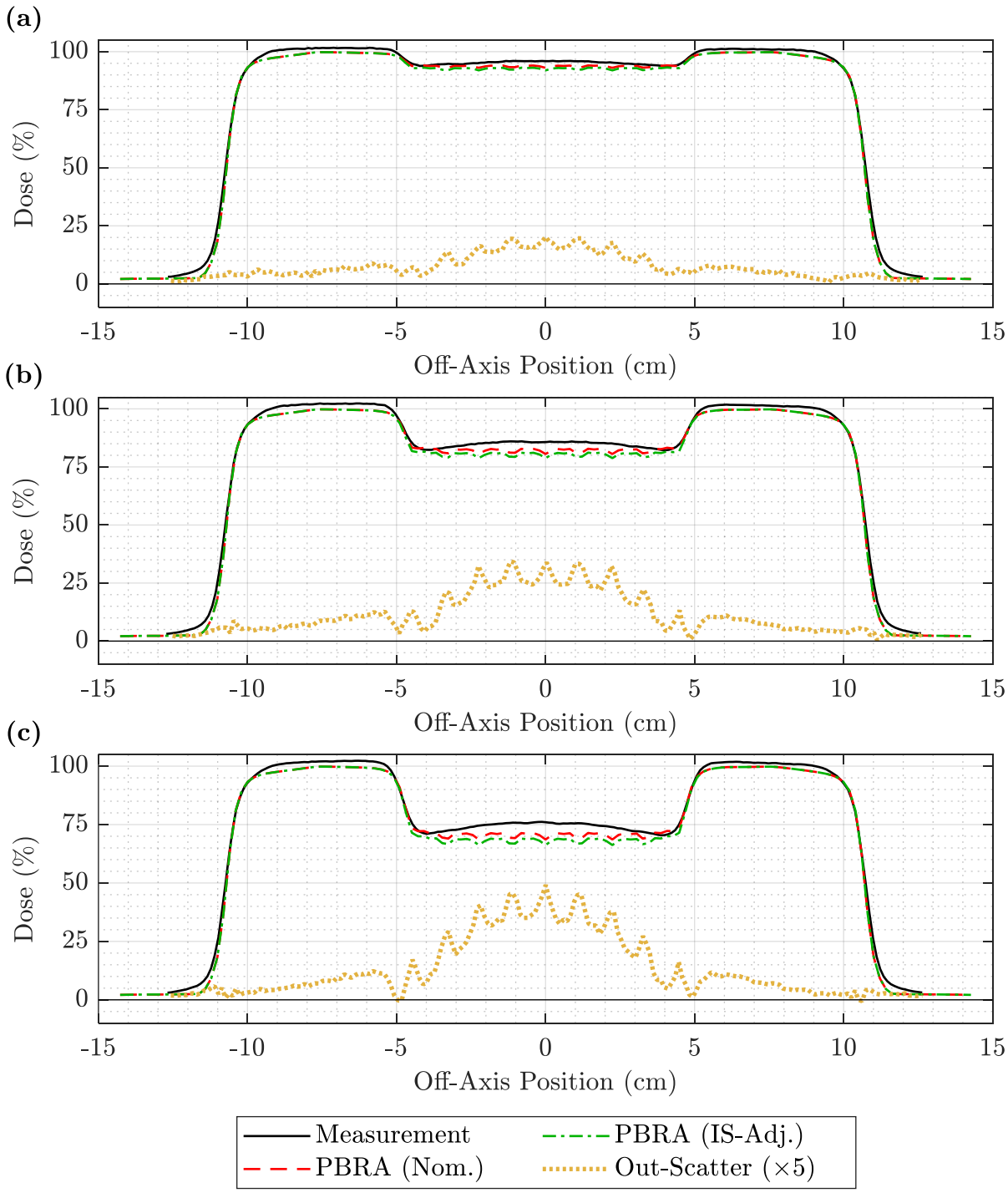

Figure 3.15. Off-axis profile comparison of measurement, nominal PBRA, and in-scatter-adjusted PBRA calculations for the 20 MeV beam at 100 cm SSD and 1.5 cm depth. Measurement (solid black) is compared to the nominal PBRA (dashed red) and PBRA corrected for in-scatter only (dashed-dotted green) for a 20 MeV beam at 100 cm SSD for (a) 0.158-cm, (b) 0.273-cm, and (c) 0.352-cm pins at a depth of 1.5 cm. The out-scatter estimation (dotted yellow) is the difference between measurement and the in-scatter-adjusted PBRA with the off-axis weight adjustment of Equation 3.4, plotted here with ×5 magnification for clarity.

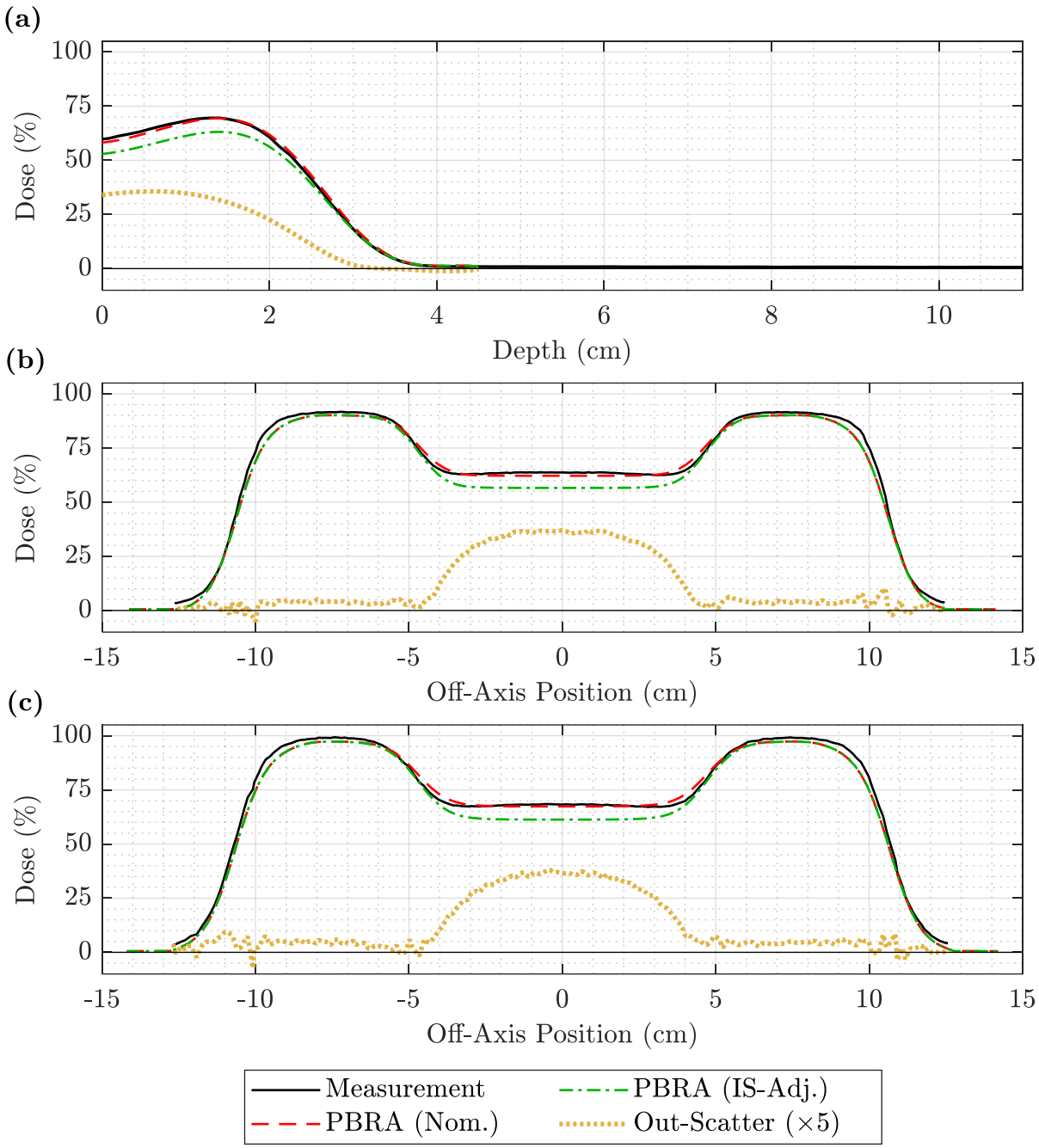

Figure 3.16. PDD and off-axis profiles for the 7 MeV beam at 100 cm SSD and 0.352-cm pins. The PDD in (a) and off-axis profiles at depths of (b) 0.5, (c) 1.0, (d) 1.5, and (e) 2.0 cm compare measurement (solid black) to the nominal PBRA (dashed red) and PBRA corrected for in-scatter only (dashed-dotted green) for a 7 MeV beam at 100 cm SSD for 0.352-cm-diameter pins. The out-scatter estimation (dotted yellow) is the difference between measurement and the in-scatter-adjusted PBRA with the off-axis weight adjustment of Equation 3.4, plotted here with ×5 magnification for clarity.

(figure cont'd.)

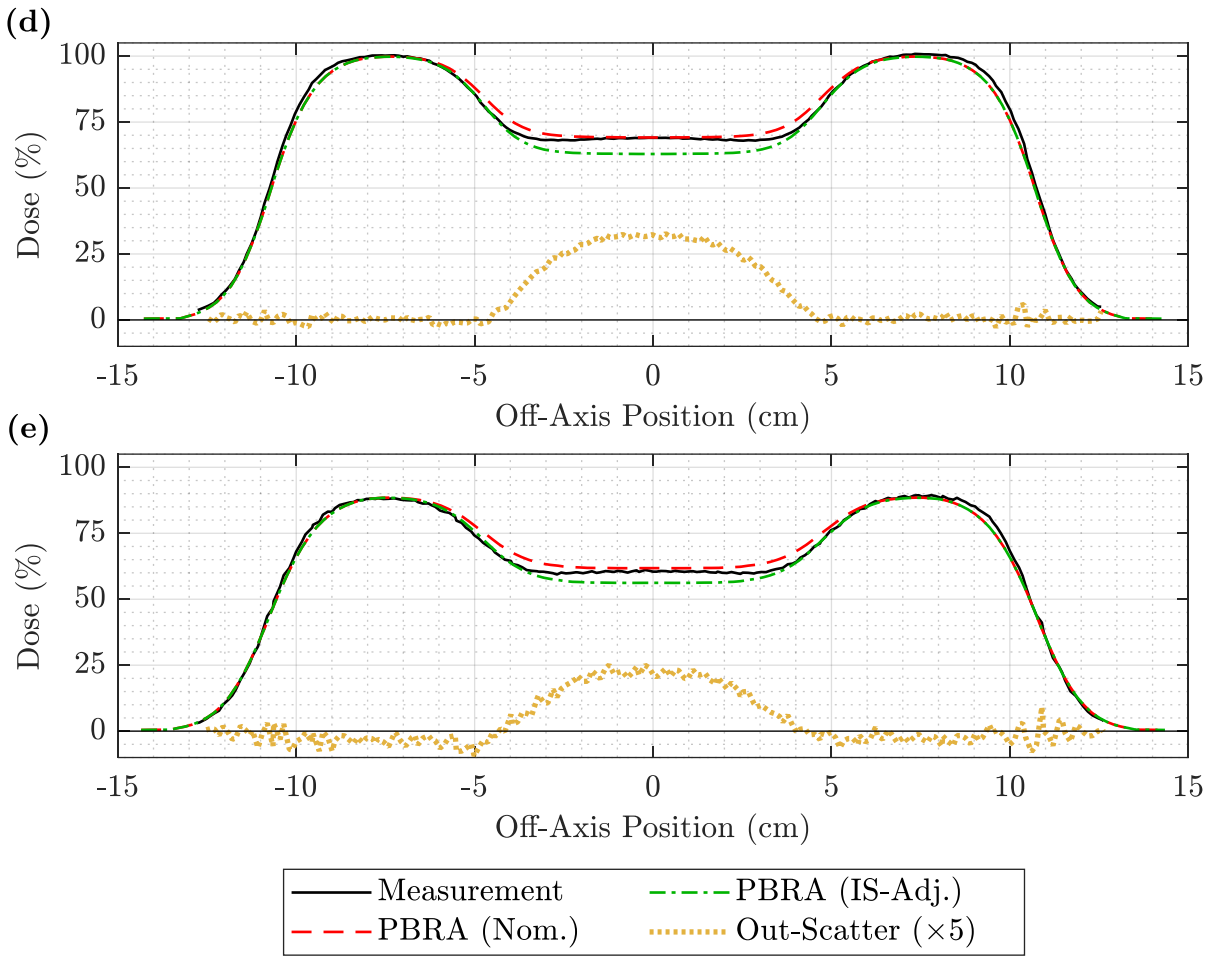
(d)
100
75
50
25
0
Dose (%)
-15
-10
-5
0
5
10
15
Off-Axis Position (cm)
(e)
100
75
50
25
0
Dose (%)
-15
-10
-5
0
5
10
15
Off-Axis Position (cm)
Measurement
PBRA (IS-Adj.)
PBRA (Nom.)
Out-Scatter (×5)

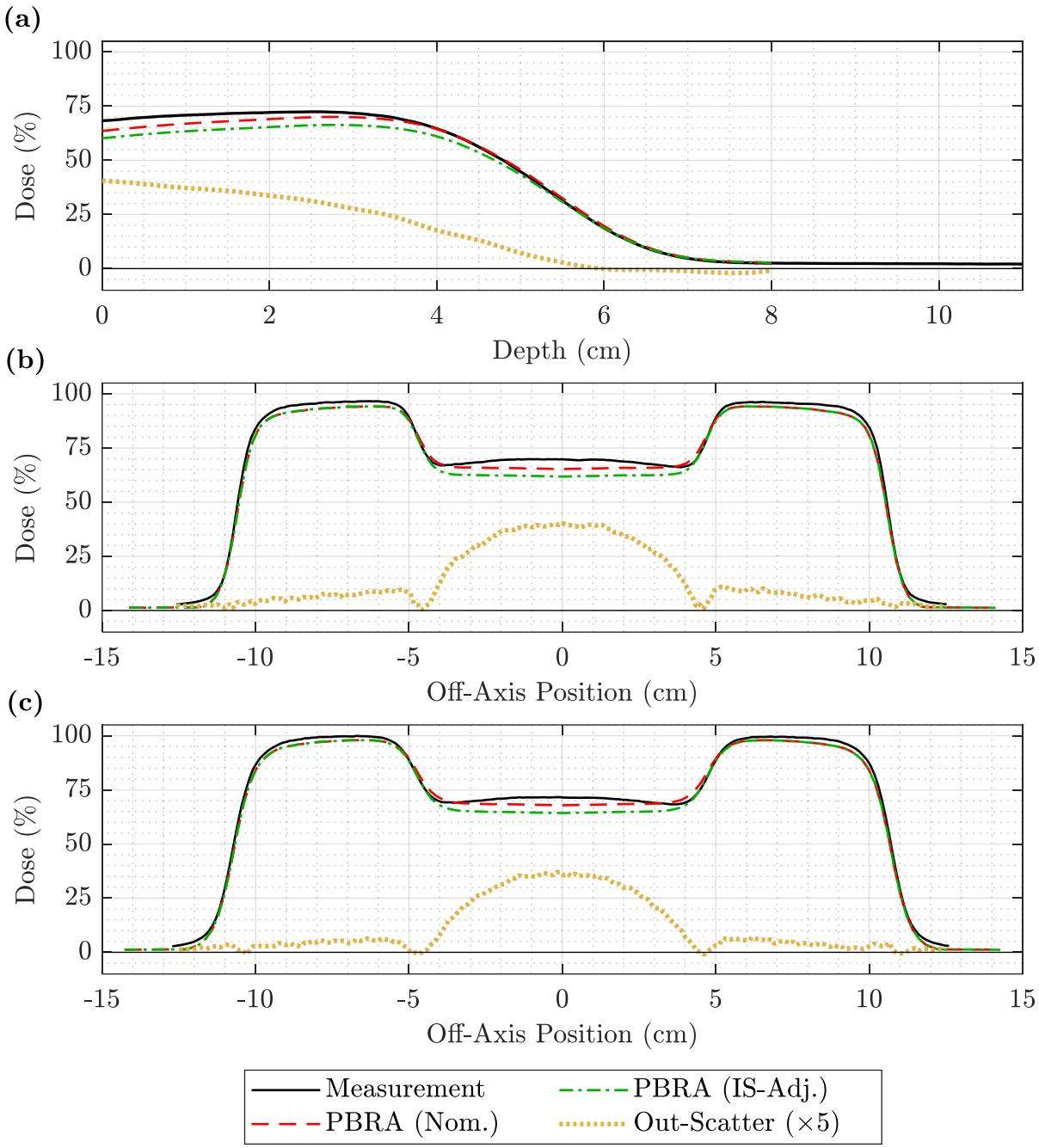

Figure 3.17. PDD and off-axis profiles for the 13 MeV beam at 100 cm SSD and 0.352-cm pins. The (a) PDD and off-axis profiles at depths of (b) 0.5, (c) 1.5, (d) 3.0, (e) 3.5, and (f) 4.0 cm compare measurement (solid black) to the nominal PBRA (dashed red) and PBRA corrected for in-scatter only (dashed-dotted green) for a 13 MeV beam at 100 cm SSD for 0.352-cm-diameter pins. The out-scatter estimation (dotted yellow) is the difference between measurement and the in-scatter-adjusted PBRA with the off-axis weight adjustment of Equation 3.4, plotted here with ×5 magnification for clarity.

(figure cont'd.)

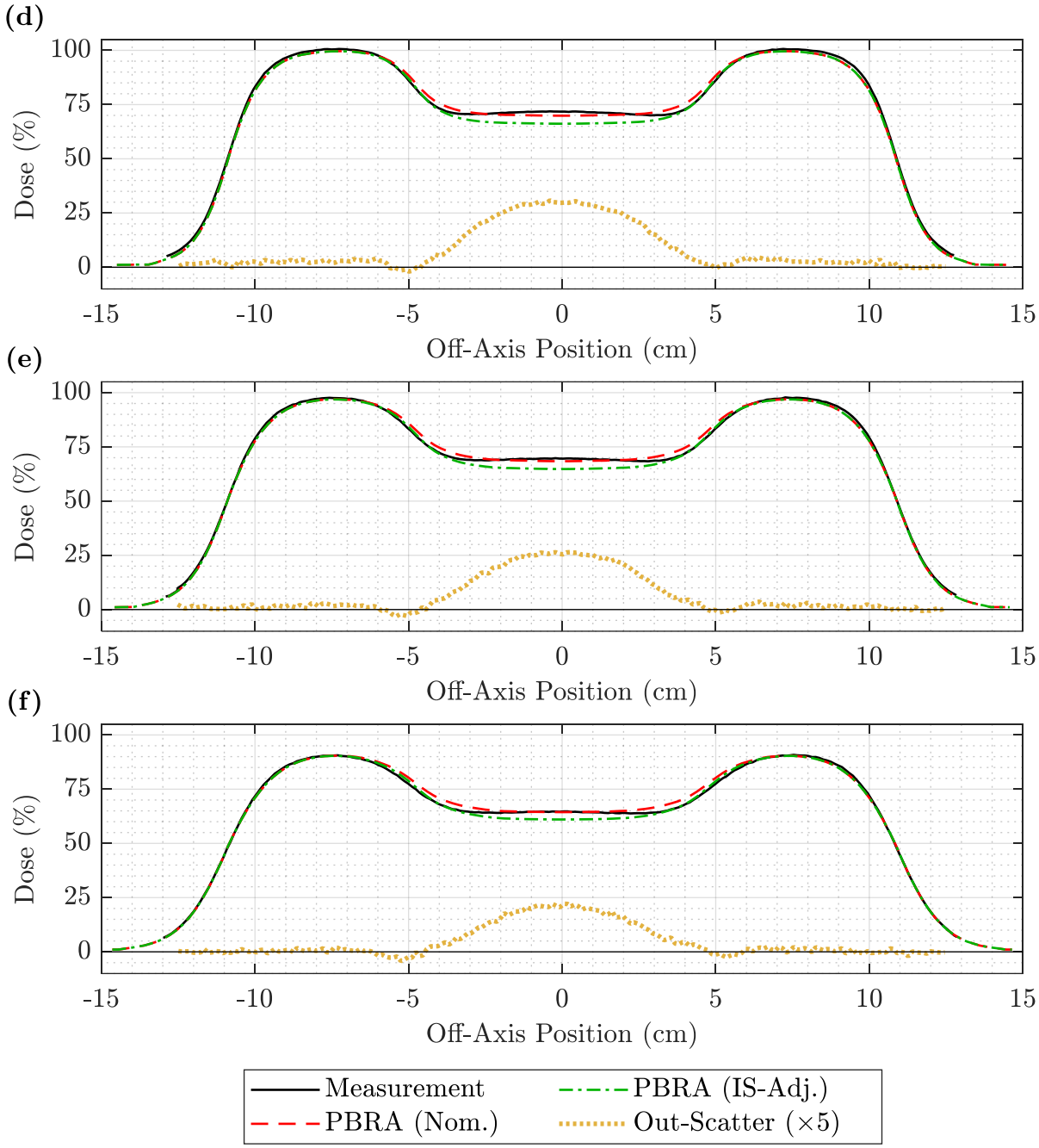
(d)
Dose (%)
100
75
50
25
0
-15
-10
-5
0
5
10
15
Off-Axis Position (cm)
(e)
Dose (%)
Off-Axis Position (cm)
(f)
Dose (%)
Off-Axis Position (cm)
Measurement
PBRA (Nom.)
PBRA (IS-Adj.)
Out-Scatter (×5)

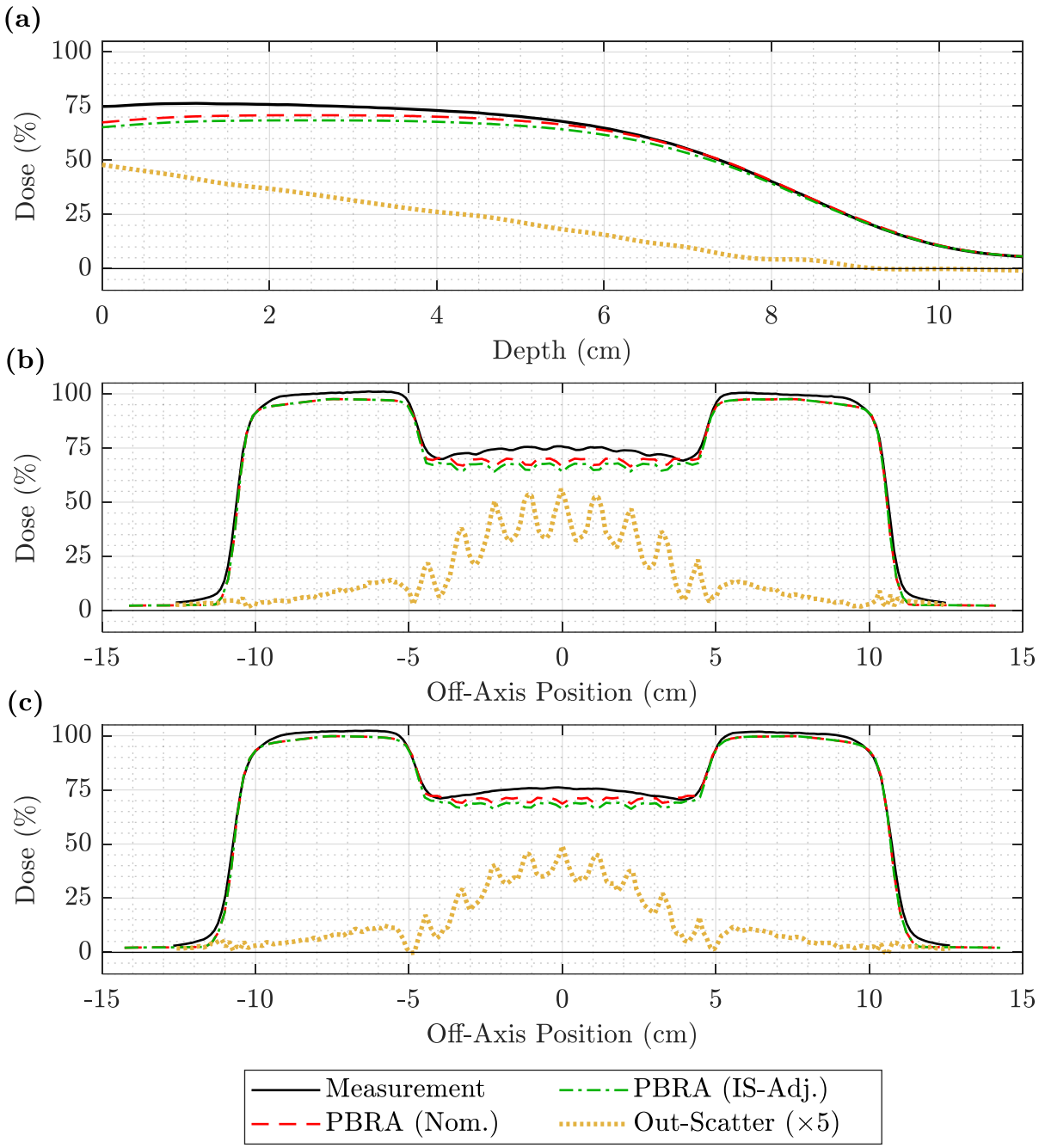

Figure 3.18. PDD and off-axis profiles for the 20 MeV beam at 100 cm SSD and 0.352-cm pins. The (a) PDD and off-axis profiles at depths of (b) 0.5, (c) 1.5, (d) 3.5, (e) 5.0, and (f) 6.0 cm compare measurement (solid black) to the nominal PBRA (dashed red) and PBRA corrected for in-scatter only (dashed-dotted green) for a 20 MeV beam at 100 cm SSD for 0.352-cm-diameter pins. The out-scatter estimation (dotted yellow) is the difference between measurement and the in-scatter-adjusted PBRA with the off-axis weight adjustment of Equation 3.4, plotted here with ×5 magnification for clarity.

(figure cont'd.)

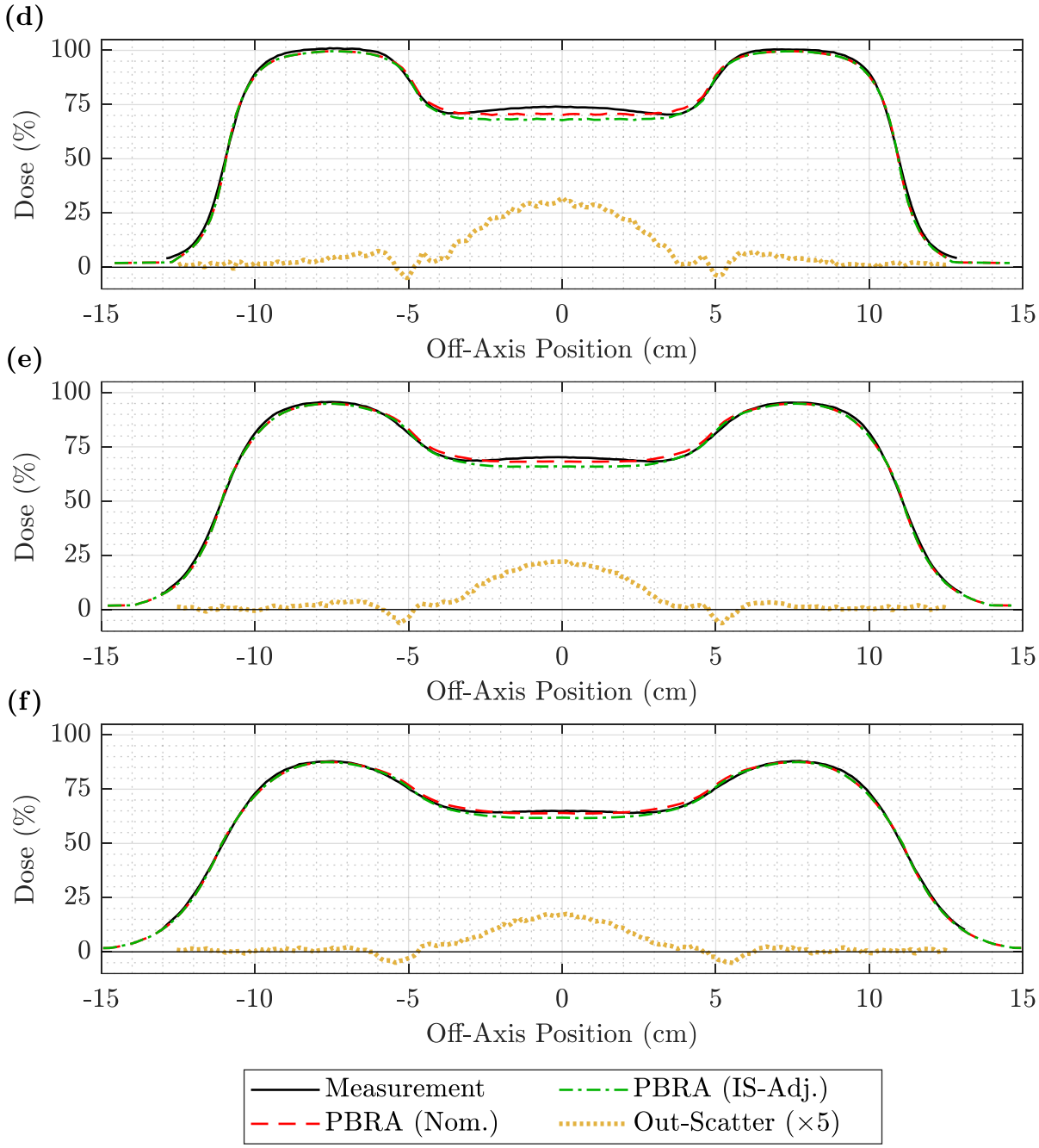
(d)
Dose (%)
100
75
50
25
0
-15
-10
-5
0
5
10
15
Off-Axis Position (cm)
(e)
Dose (%)
Off-Axis Position (cm)
(f)
Dose (%)
Off-Axis Position (cm)
Measurement
PBRA (IS-Adj.)
PBRA (Nom.)
Out-Scatter (×5)

Table 3.6. Minimization dose adjustment. The discretely calculated dose adjustments, ΔD_{OS}, which minimize the least squares summation of Equation 3.5, are expressed as a percentage of the unmodulated, foam-only beam, and are calculated for every measured beam energy, SSD, and diameter combination.

Beam Energy (MeV)	Nominal Diameter (cm)	Minimization Dose Adjustment, ΔD_{OS}		
		100 cm	105 cm	110 cm
7	0.158	2.03%	1.63%	1.39%
13	0.158	1.48%	1.10%	0.90%
20	0.158	1.73%	1.30%	0.65%
7	0.273	3.89%	3.90%	3.64%
13	0.273	3.16%	2.79%	2.44%
20	0.273	3.30%	2.14%	1.56%
7	0.352	5.35%	5.53%	5.38%
13	0.352	4.52%	4.03%	3.56%
20	0.352	4.51%	3.66%	2.58%

Table 3.7. Fits to minimization dose adjustment. Quadratic fits versus $E_{p,0}$ (Table 3.4) were calculated from the values in Table 3.6 for each beam energy and pin diameter combination.

SSD (cm)	Nominal Diameter (cm)	A_1	A_2	A_3
100	0.158	7.856E-05	-2.353E-03	3.227E-02
100	0.273	8.805E-05	-2.813E-03	5.345E-02
100	0.352	8.300E-05	-2.857E-03	6.862E-02
105	0.158	7.297E-05	-2.221E-03	2.765E-02
105	0.273	5.099E-05	-2.623E-03	5.389E-02
105	0.352	1.183E-04	-4.540E-03	7.989E-02
110	0.158	2.649E-05	-1.244E-03	2.088E-02
110	0.273	3.813E-05	-2.494E-03	5.103E-02
110	0.352	9.075E-05	-4.443E-03	7.891E-02

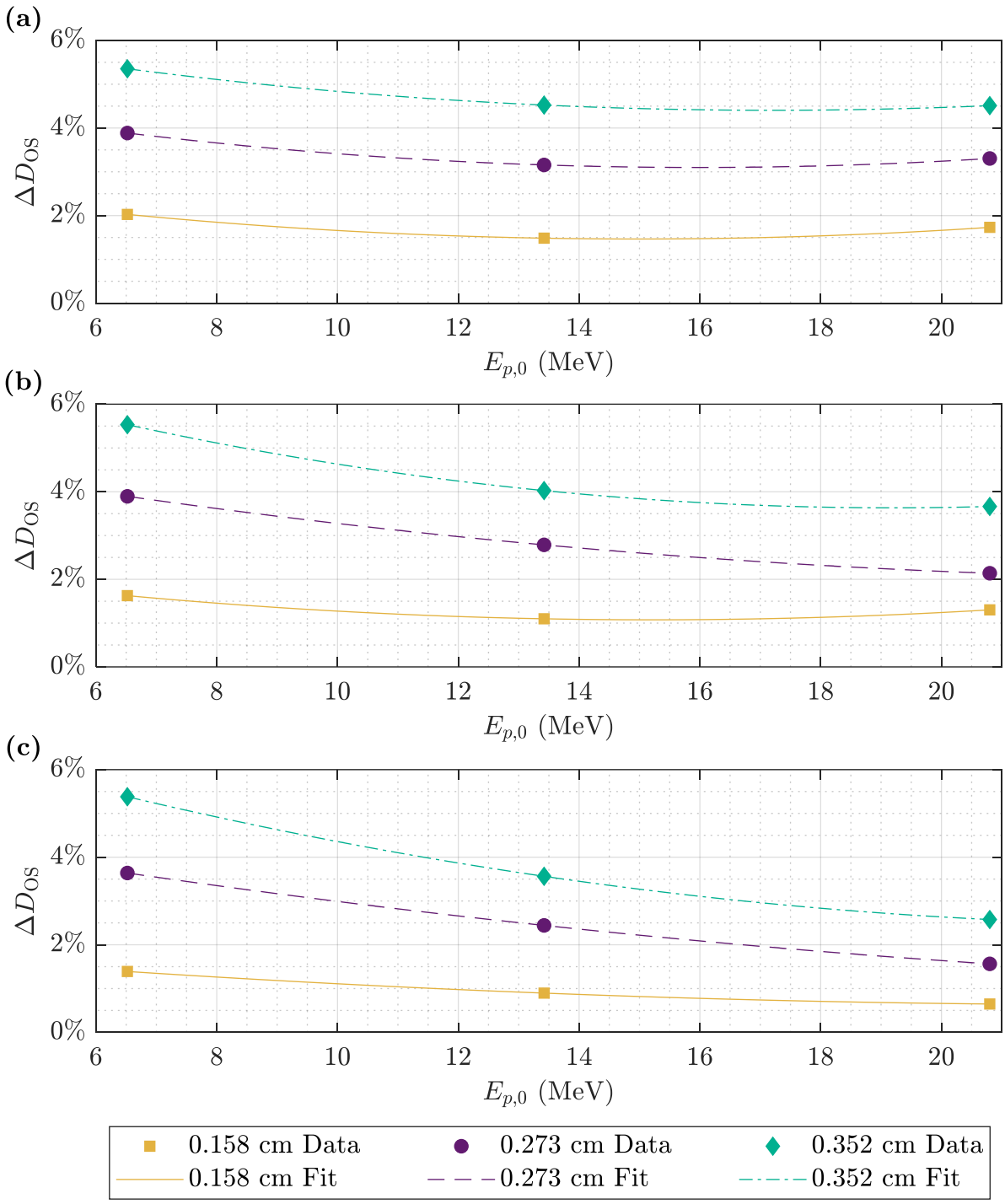

Figure 3.19. Out-scatter dose adjustments and fits versus $E_{p,0}$ for 0.158-0.352 cm island block diameters at 100-110 cm SSD. The minimizing dose adjustments, ΔD_{OS}, from Table 3.6 and the corresponding fits from Table 3.7 are plotted against beam energy at (a) 100, (b) 105, and (c) 110 cm SSD for 0.158 (yellow), 0.273 (purple), and 0.352 cm (green) pin diameters. Values of ΔD_{OS} are plotted as markers and fits are plotted as quadratic curves.

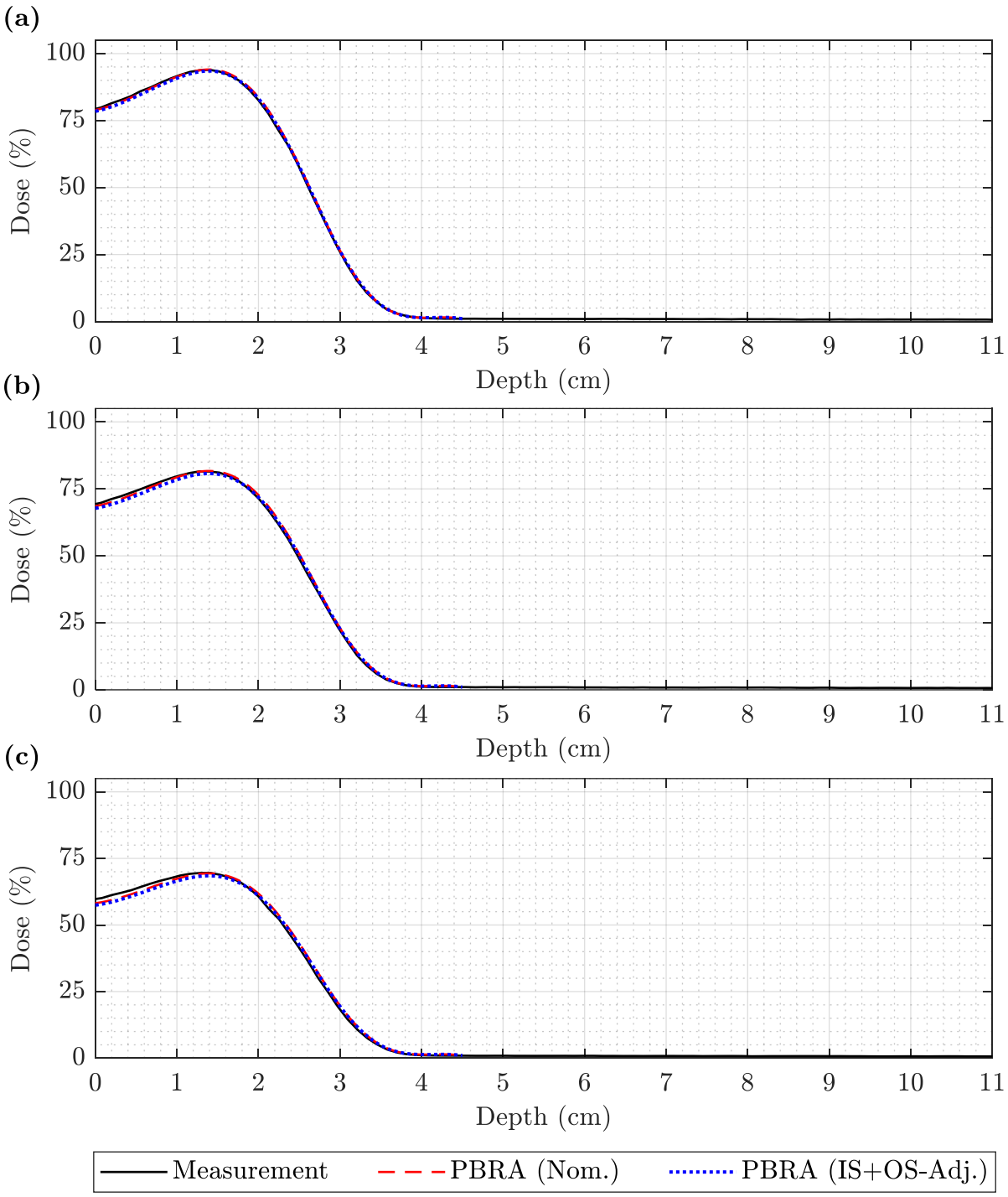

Figure 3.20. PDD comparison of measurement, nominal PBRA, and IS+OS-corrected PBRA at 7 MeV and 100 cm SSD. Measurement (solid black) is compared to the nominal PBRA (dashed red) and PBRA adjusted for both in-scatter and out-scatter (dotted blue) for a 7 MeV beam at 100 cm SSD for (a) 0.158-cm, (b) 0.273-cm, and (c) 0.352-cm pins.

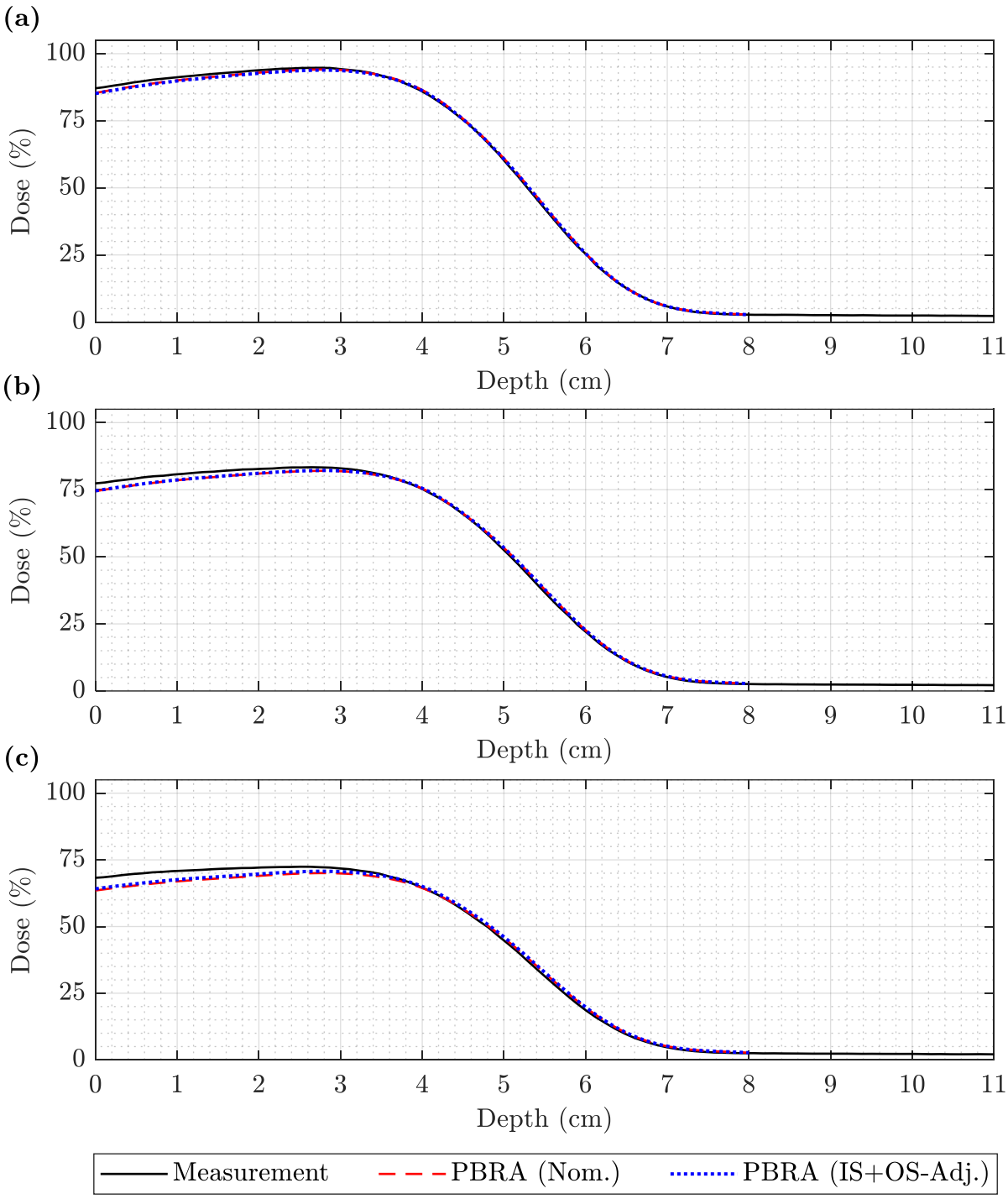

Figure 3.21. PDD comparison of measurement, nominal PBRA, and IS+OS-corrected PBRA at 13 MeV and 100 cm SSD. Measurement (solid black) is compared to the nominal PBRA (dashed red) and PBRA adjusted for both in-scatter and out-scatter (dotted blue) for a 13 MeV beam at 100 cm SSD for (a) 0.158-cm, (b) 0.273-cm, and (c) 0.352-cm pins.

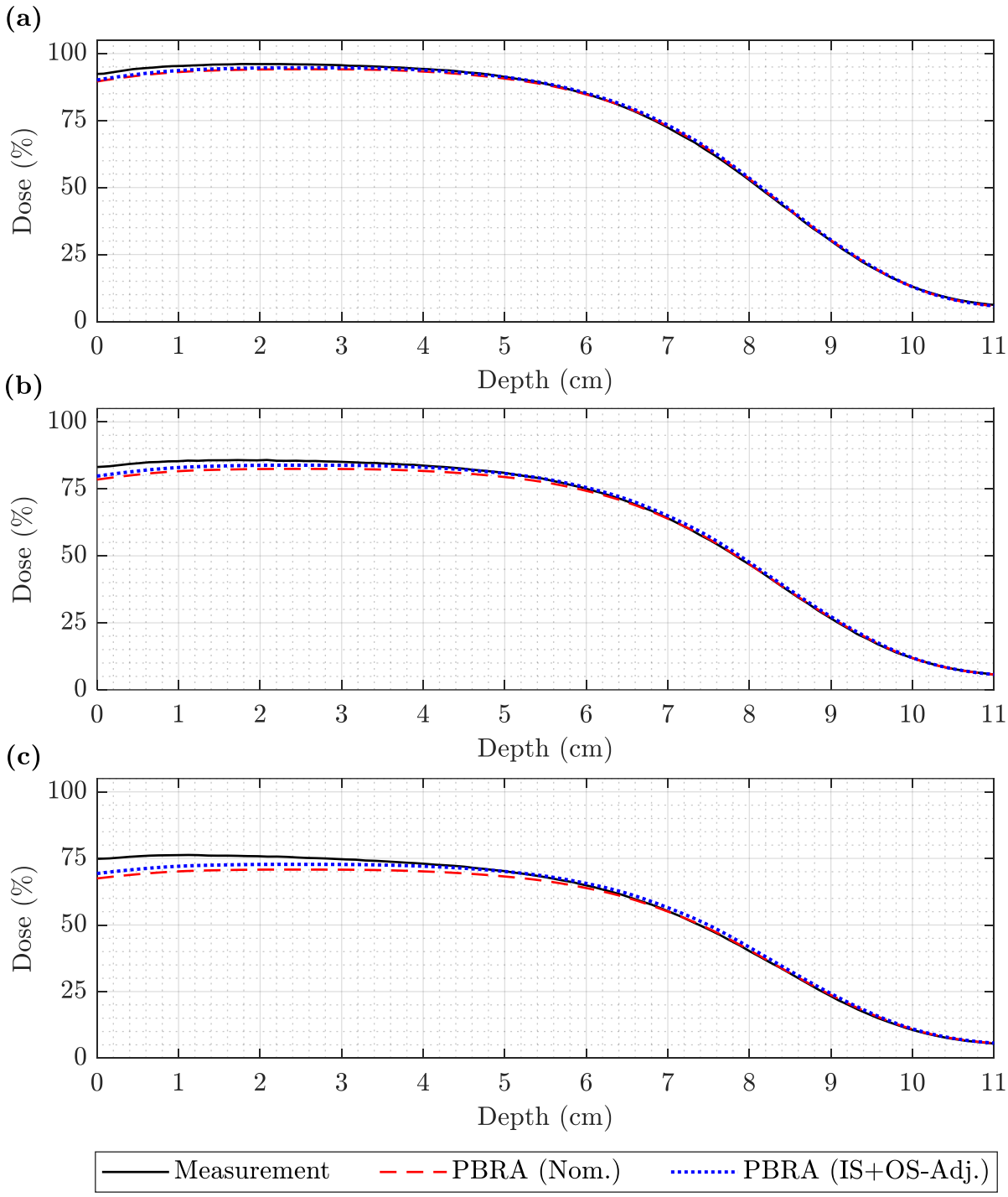

Figure 3.22. PDD comparison of measurement, nominal PBRA, and IS+OS-corrected PBRA at 20 MeV and 100 cm SSD. Measurement (solid black) is compared to the nominal PBRA (dashed red) and PBRA adjusted for both in-scatter and out-scatter (dotted blue) for a 20 MeV beam at 100 cm SSD for (a) 0.158-cm, (b) 0.273-cm, and (c) 0.352-cm pins.

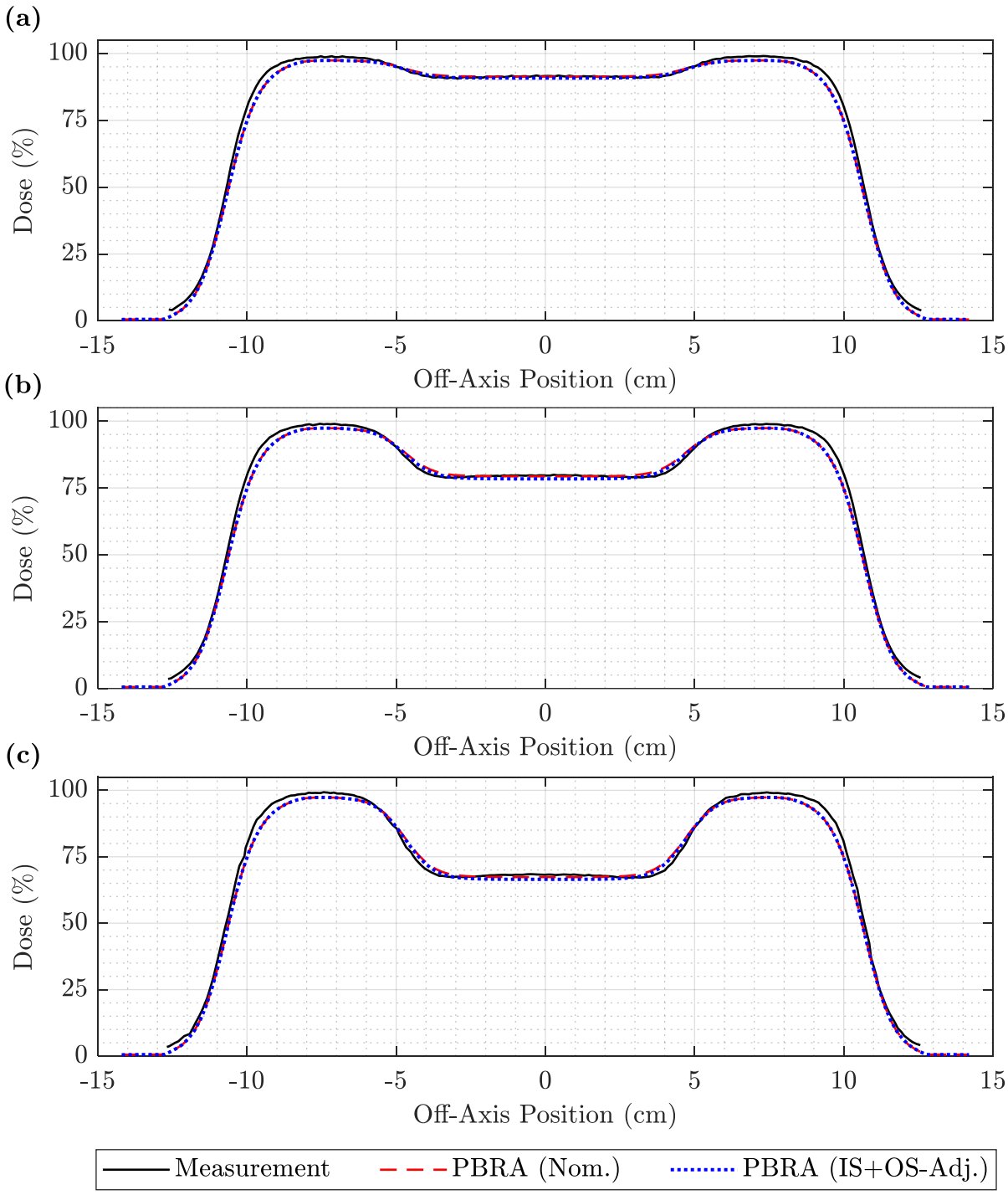

Figure 3.23. Off-axis profile comparison of measurement, nominal PBRA, and IS+OS-corrected PBRA at 7 MeV and 100 cm SSD. Measurement (solid black) is compared to the nominal PBRA (dashed red) and PBRA adjusted for both in-scatter and out-scatter (dotted blue) for a 7 MeV beam at 100 cm SSD for pin diameters of (a) 0.158 cm, (b) 0.273 cm, and (c) 0.352 cm at a depth of 1.0 cm.

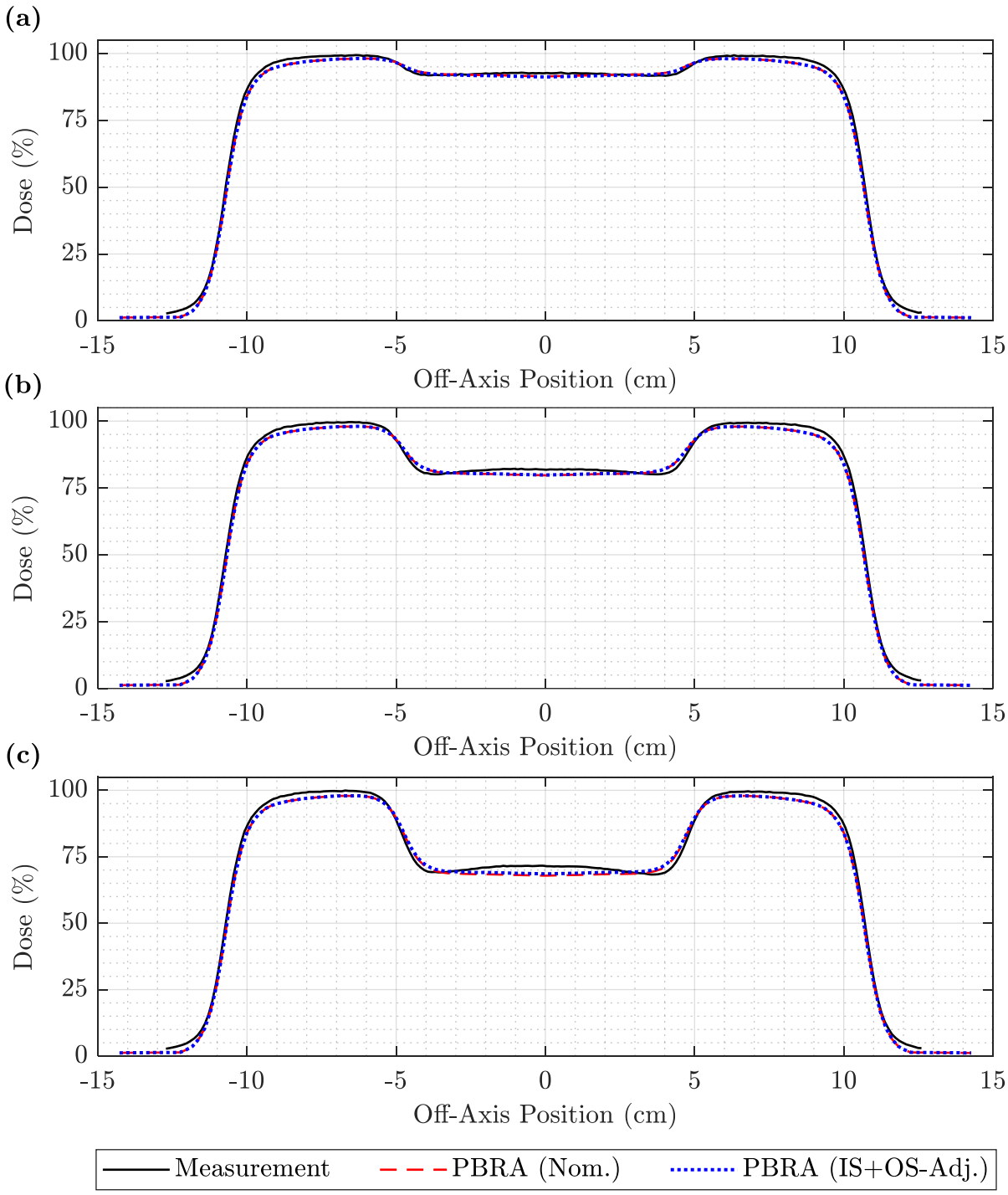

Figure 3.24. Off-axis profile comparison of measurement, nominal PBRA, and IS+OS-corrected PBRA at 13 MeV and 100 cm SSD. Measurement (solid black) is compared to the nominal PBRA (dashed red) and PBRA adjusted for both in-scatter and out-scatter (dotted blue) for a 13 MeV beam at 100 cm SSD for pin diameters of (a) 0.158 cm, (b) 0.273 cm, and (c) 0.352 cm at a depth of 1.5 cm.

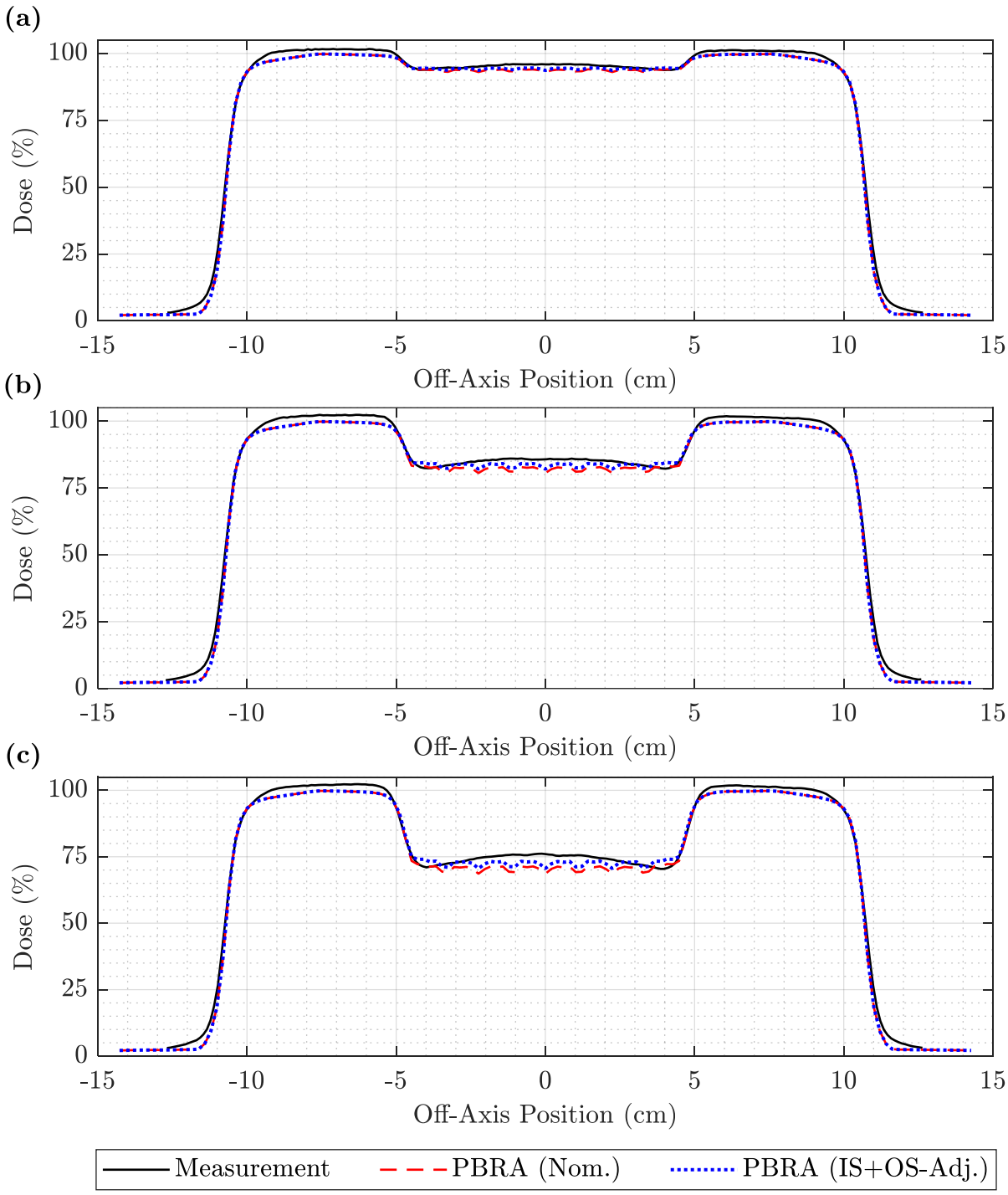

Figure 3.25. Off-axis profile comparison of measurement, nominal PBRA, and IS+OS-corrected PBRA at 20 MeV and 100 cm SSD. Measurement (solid black) is compared to the nominal PBRA (dashed red) and PBRA adjusted for both in-scatter and out-scatter (dotted blue) for a 20 MeV beam at 100 cm SSD for pin diameters of (a) 0.158 cm, (b) 0.273 cm, and (c) 0.352 cm at a depth of 1.5 cm.

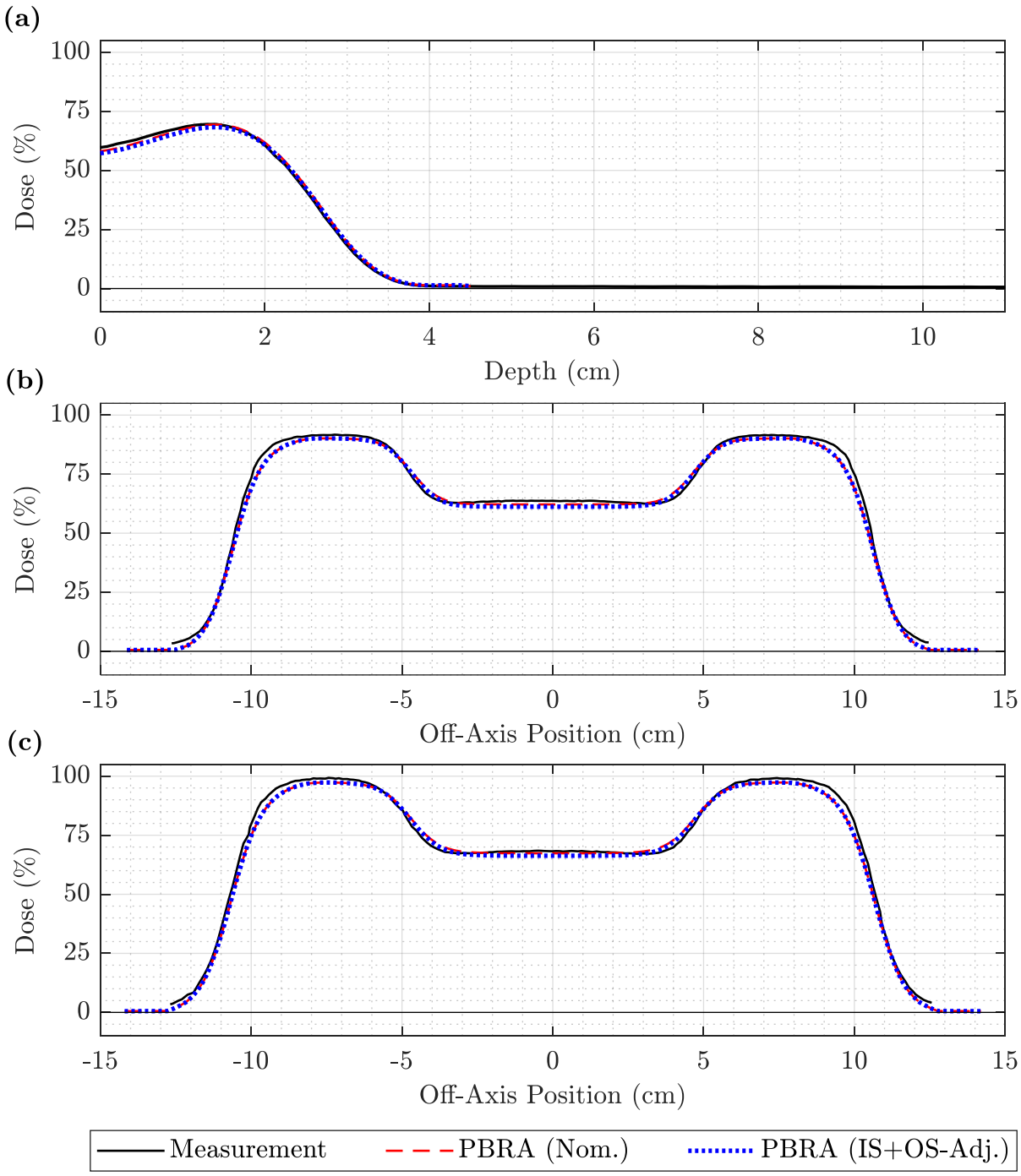

Figure 3.26. PDD and off-axis profile comparison of measurement, nominal PBRA, and IS+OS-corrected PBRA for the 7 MeV beam at 100 cm SSD and 0.352-cm pins. The PDD in (a) and off-axis profiles at depths of (b) 0.5, (c) 1.0, (d) 1.5, and (e) 2.0 cm compare measurement (solid black) to the nominal PBRA (dashed red) and PBRA adjusted for both in-scatter and out-scatter (dotted blue) for a 7 MeV beam at 100 cm SSD for 0.352-cm-diameter pins.

(figure cont'd.)

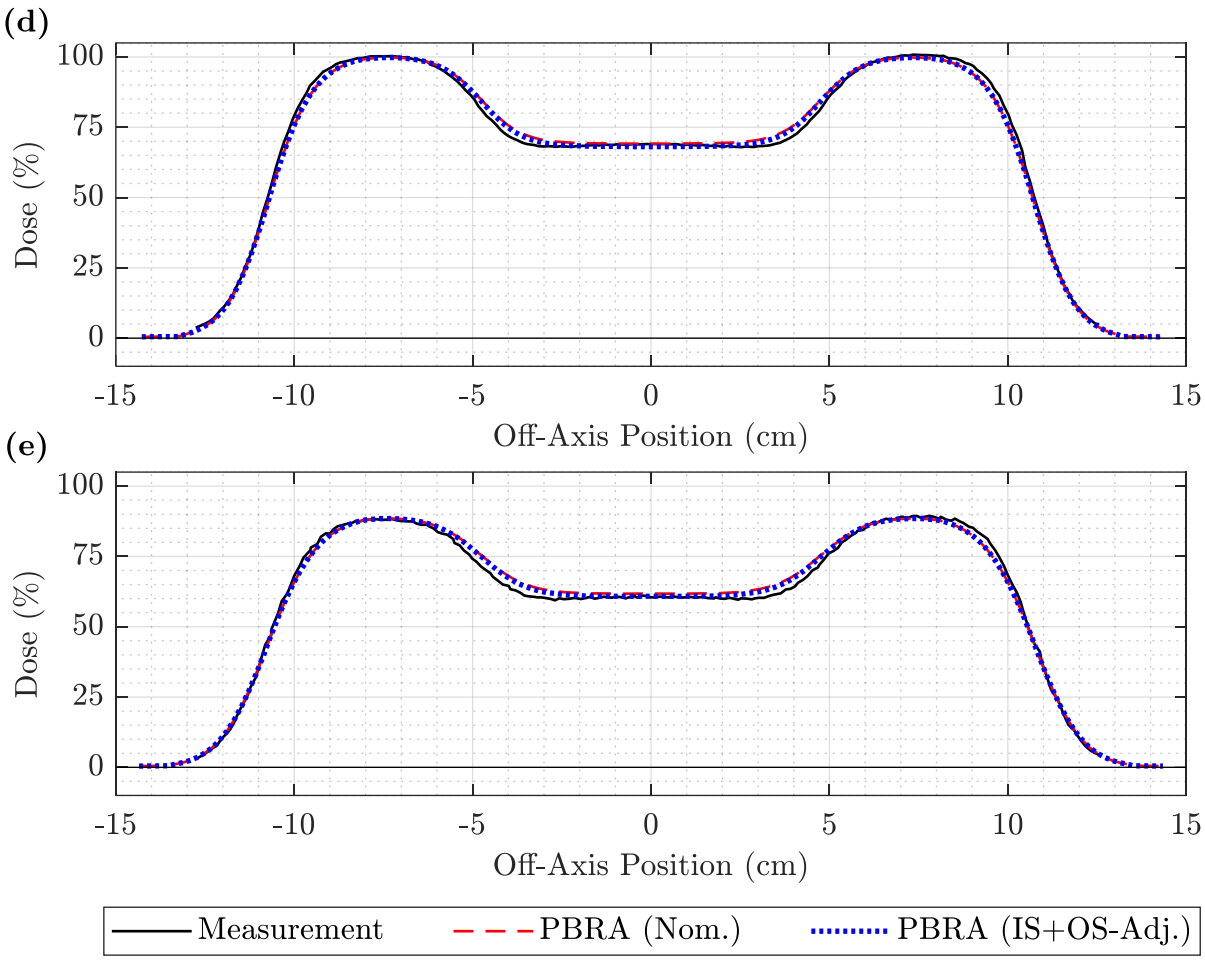
(d)
100
75
50
25
0
Dose (%)
-15
-10
-5
0
5
10
15
Off-Axis Position (cm)
(e)
100
75
50
25
0
Dose (%)
-15
-10
-5
0
5
10
15
Off-Axis Position (cm)
Measurement
PBRA (Nom.)
PBRA (IS+OS-Adj.)

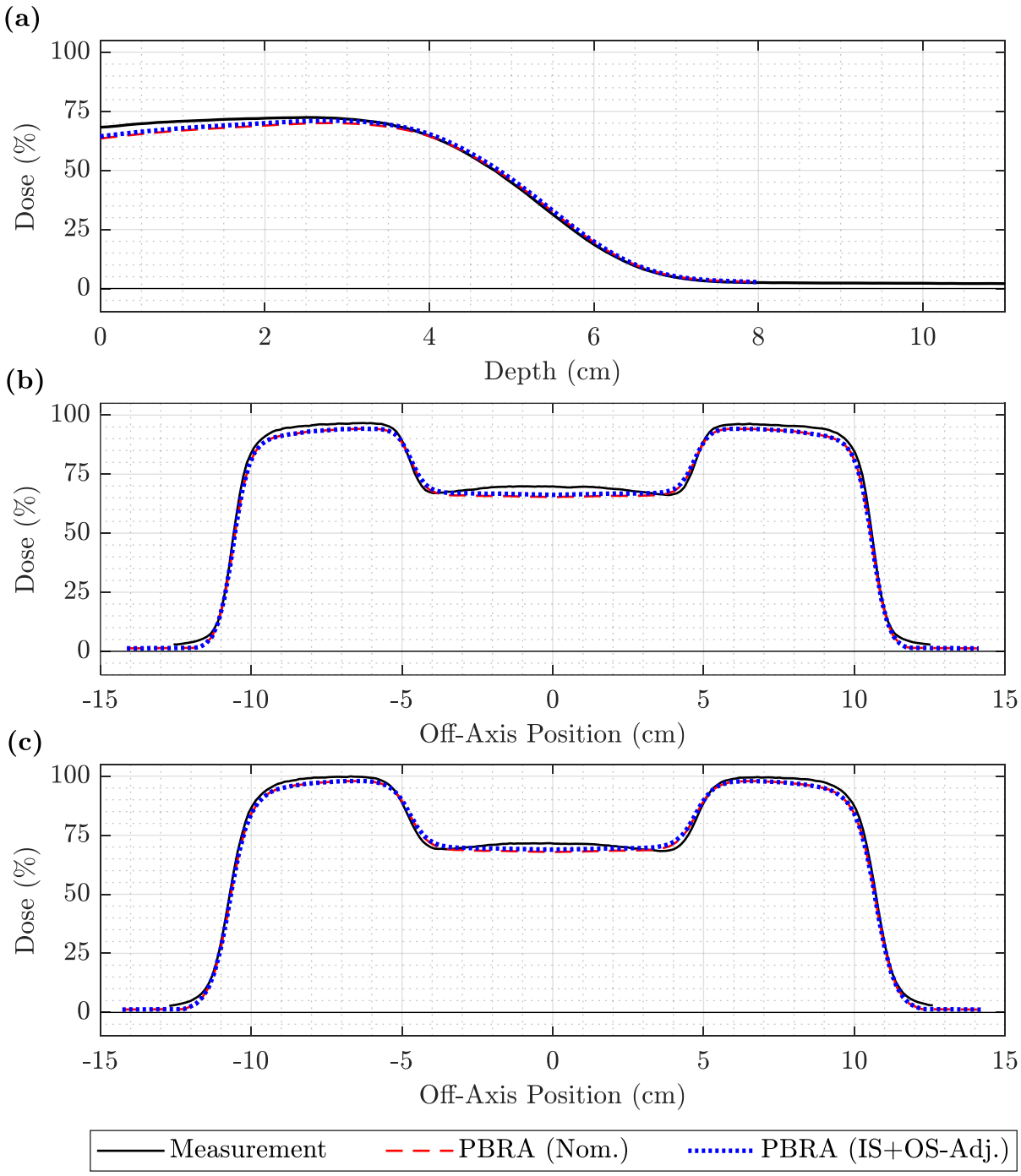

Figure 3.27. PDD and off-axis profile comparison of measurement, nominal PBRA, and IS+OS-corrected PBRA for the 13 MeV beam at 100 cm SSD and 0.352-cm pins. The PDD in (a) and off-axis profiles at depths of (b) 0.5, (c) 1.5, (d) 3.0, (e) 3.5, and (f) 4.0 cm compare measurement (solid black) to the nominal PBRA (dashed red) and PBRA adjusted for both in-scatter and out-scatter (dotted blue) for a 13 MeV beam at 100 cm SSD for 0.352-cm-diameter pins.

(figure cont'd.)

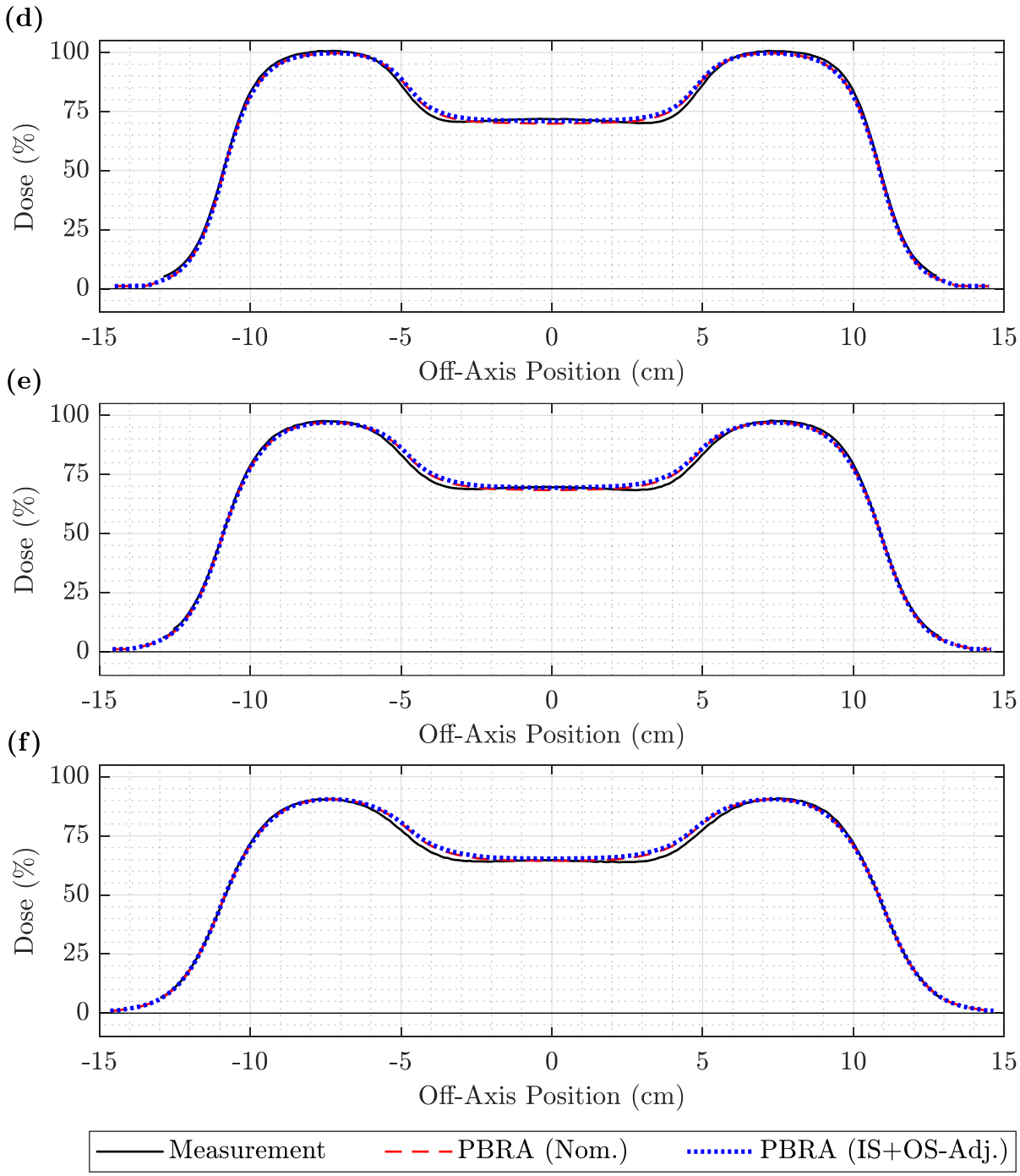
(d)
100
75
50
25
0
Dose (%)
-15
-10
-5
0
5
10
15
Off-Axis Position (cm)
(e)
100
75
50
25
0
Dose (%)
-15
-10
-5
0
5
10
15
Off-Axis Position (cm)
(f)
100
75
50
25
0
Dose (%)
-15
-10
-5
0
5
10
15
Off-Axis Position (cm)
Measurement
PBRA (Nom.)
PBRA (IS+OS-Adj.)

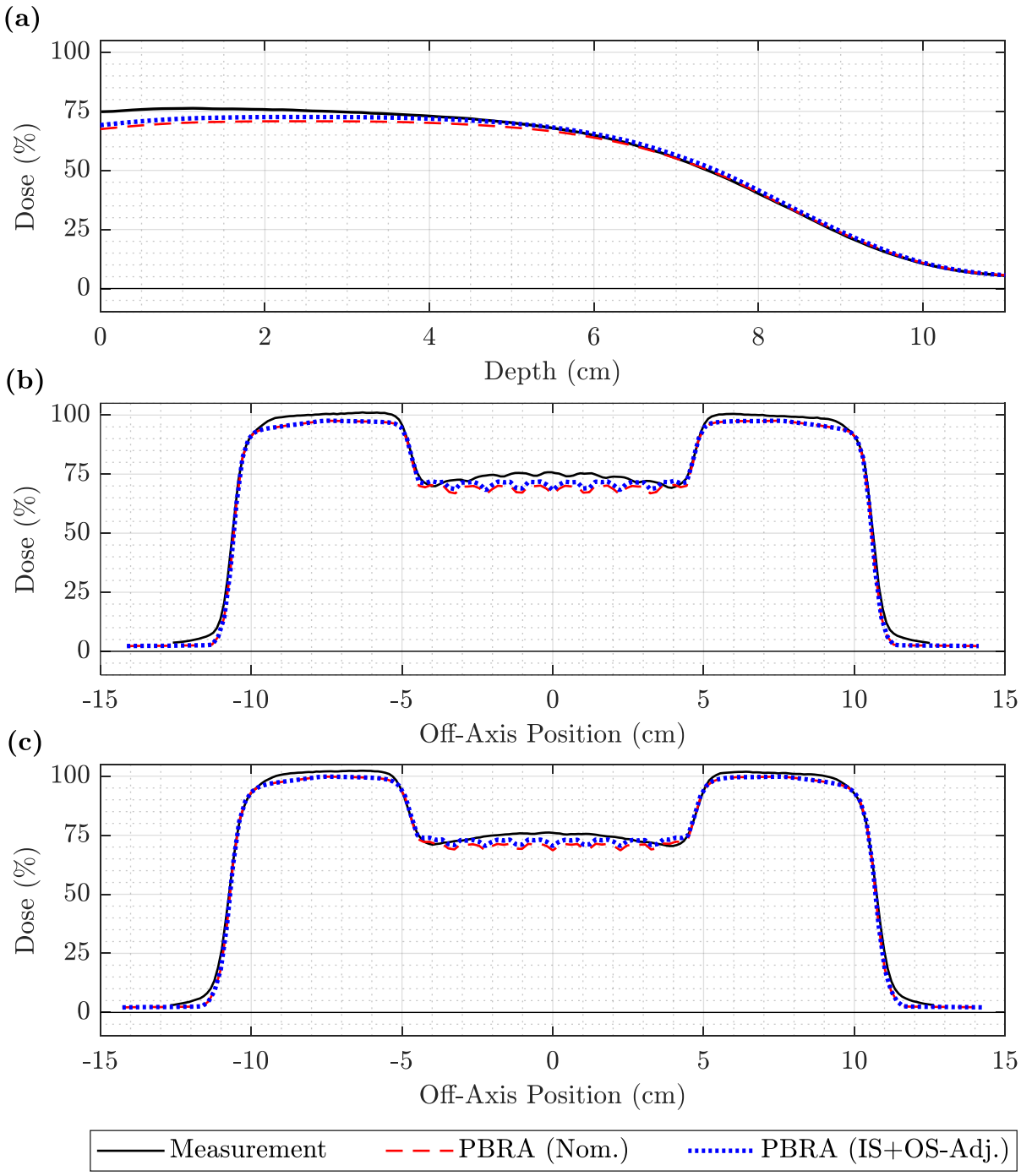

Figure 3.28. PDD and off-axis profile comparison of measurement, nominal PBRA, and IS+OS-corrected PBRA for the 20 MeV beam at 100 cm SSD and 0.352-cm pins. The PDD in (a) and off-axis profiles at depths of (b) 0.5, (c) 1.5, (d) 3.5, (e) 5.0, and (f) 6.0 cm compare measurement (solid black) to the nominal PBRA (dashed red) and PBRA adjusted for both in-scatter and out-scatter (dotted blue) for a 20 MeV beam at 100 cm SSD for 0.352-cm-diameter pins.

(figure cont'd.)

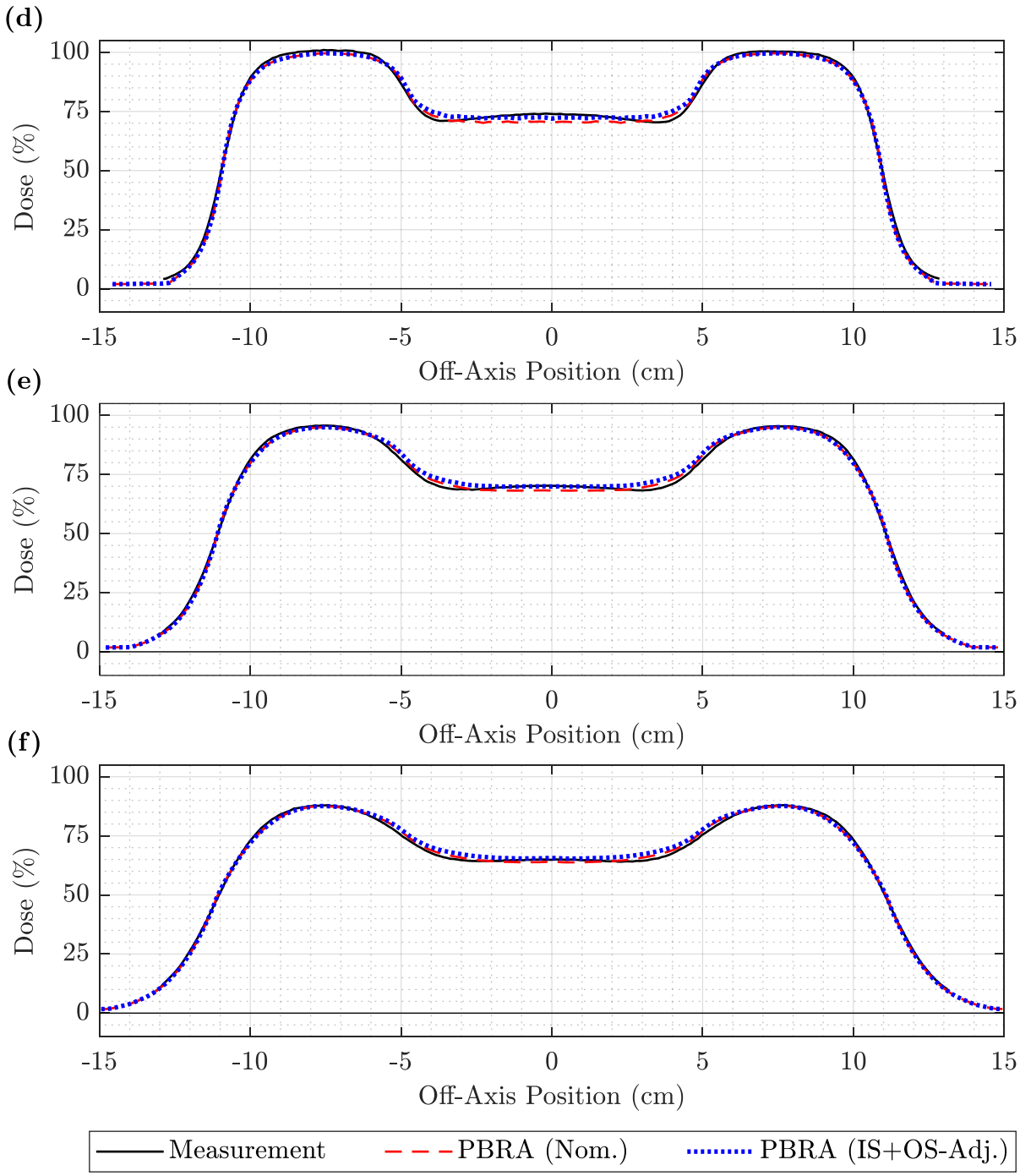
(d)
100
75
50
25
0
Dose (%)
-15
-10
-5
0
5
10
15
Off-Axis Position (cm)
(e)
100
75
50
25
0
Dose (%)
-15
-10
-5
0
5
10
15
Off-Axis Position (cm)
(f)
100
75
50
25
0
Dose (%)
-15
-10
-5
0
5
10
15
Off-Axis Position (cm)
Measurement
PBRA (Nom.)
PBRA (IS+OS-Adj.)

3.3. Discussion

The PBRA exhibits good agreement with measurement in the foam-only comparison, demonstrating that PBRA calculations accurately reproduce dose distributions in the absence of a modulator. Under 3%/3mm DTA criteria, calculations achieved an average passing rate of 99.7% for all points under all beam energy and SSD combinations. Eight of nine setups achieve 99.6% or better. Points of failure are focused in high-gradient regions, such as the penumbra and distal falloff regions, where accurate matching is difficult. The outlying case of 7 MeV and 100 cm SSD had the lowest foam-only passing rate at 98.3%. Although the 3%/3mm DTA criteria may be appropriate as a final validation metric, a high passing rate of the foam-only distributions should not be conflated with equivalence of unmodulated measurement and calculation since the differences typically fall within these criteria. The purpose of this comparison was to verify agreement along CAX and that the central portion of the field (±3.5 cm from CAX) following modifications to the PBRA input data.

There are several limitations in the PBRA modeling which contribute to the off-axis differences. PBRA calculations use a single set of off-axis beam weights for all depths, defined from commissioning data at depth of $0.5 \cdot R_{90}$, but the actual values can vary with depth. Moreover, PBRA calculations in this work used the values determined during commissioning rather than the foam-only measurements. Another source of inaccuracy is the modeling of σ_{θ_x}. Hilliard used a single, empirical scaling factor of 1.5 for σ_{θ_x} at all beam energies, but the actual value likely varies with beam energy. This simplification causes misalignment of the inflection points in the measured and PBRA-calculated penumbrae, which is highlighted by fluctuations in ΔD_{OAR} at the field edges in Figure 3.6. Electron scatter off of the collimator is not modeled in the PBRA and contributes to the unmodulated measurement-PBRA difference (Rusk *et al.*, 2016). Another source is possible

asymmetry in the inplane (bending plane) due to the bending magnet. Foam-only calculations could be improved by symmetrizing the inplane measurements, incorporating the measured off-axis ratios into the PBRA input, or incorporating energy-specific modifications to σ_{θ_x}.

These differences are collectively described by the off-axis weighting correction, ΔD_{OAR} (Equation 3.4). Incorporation of this term into calculations reduces the systematic discrepancies due to limitations in PBRA modeling. Once these issues have been accounted for, the out-scatter component can be more reliably separated.

An inspection of measured profiles under the three tested intensity modulators revealed that the validation devices did not produce a flat field within the modulated region as predicted by PBRA calculations, with the CAX dose being a few percent higher. The effect of diameter on the out-scatter component can be seen in the PDDs (Figures 3.10-12 and Figures A.11-16) and off-axis profiles (Figures 3.13-15 and Figures A.17-22). The magnitude of the out-scatter component increases with pin diameter, a trend which is consistent across beam energies and SSDs. The width of the off-axis out-scatter peak is not affected by changes in pin diameter. The dependence of the out-scatter component on beam energy, SSD, and depth can be seen in Figures 3.16-18 for 100 cm SSD and in Figures A.23-28 for 105 and 110 cm SSD. At a depth of the magnitude on CAX decreases with increasing SSD for 13 and 20 MeV beams, with ranges of 6-8% and 5-9%, respectively. At 7 MeV, the out-scatter was greatest at 105 cm SSD and the least at 100 cm SSD, with a range of 7-8%. The out-scatter component at 0.5 cm depth increases with beam energy at 100 cm SSD, but decreases with beam energy at 105 and 110 cm SSD. In all cases, the out-scatter component goes to zero between 1-2 cm beyond R_{90}. At 7 MeV and all SSDs, the out-scatter PDD has a similar shape to the primary PDD. For the 13 and 20 MeV beams at 100 cm SSD, the out-

scatter component decreases linearly. At other SSDs, the out-scatter component and dose distribution have similar PDDs.

This complex behavior could not be rectified through the chosen approach of a simple diameter scaling. Thus, rather than matching each of the measured profiles as accurately as possible, the correction method minimized least squares dose differences across a range of depths and off-axis positions to determine the best estimate of the out-scatter dose. As determining corrections purely from CAX measurements, where modulated dose is highest, would overpredict dose off-axis, off-axis profiles were included into the fitting region. However, minimization to a single plane rather than a 3D region still gives greater weight to the central region.

At 7 MeV and all SSDs, the IS+OS-corrected diameters were greater than the nominal values in all cases, consistent with the expectation of in-scatter being predominant. At 13 MeV, the IS+OS-corrected diameters were comparable (±0.008 cm) to the nominal values. In half of the measured combinations, the IS+OS-corrected diameter was smaller (≤ 0.004 cm) than nominal; this occurred with the largest and intermediate pin diameters, consistent with the expectation that blocks with greater circumference will result in more out-scatter. For 10 of 12 combinations at 20 MeV, the IS+OS-corrected diameter was smaller (≤ 0.012 cm) than nominal. This trend is generally consistent with the expectation that out-scatter increases with beam energy. Figures 3.20-25 illustrate the extent of the correction for all beam energy and block diameter combinations at 100 cm SSD.

Figures 3.26-28 illustrate the effect of the out-scatter correction over a wider range of depths for the largest pin diameter where correction was typically most significant. Measurement generally exceeded corrected PBRA calculations at shallow depths within the modulated region,

particularly on CAX. At deeper depths, this difference decreased until calculation was consistently greater than measurement within the modulated region.

Chapter 4. Aim 3: Validation of the Modified IM-BECT PBRA Dose Calculation

4.1. Method

4.1.1. IM-PBRA calculations

For each measured dose distribution at a given beam energy, SSD, and modulator combination, a corresponding dose distribution was calculated using the PBRA with the IS+OS-corrected pin diameter for the given conditions as listed in Tables A.1-3. PBRA calculations were performed for the 7, 13, and 20 MeV beams at 100, 105, and 110 cm SSD using both nominal (physical) diameters and diameters corrected for both in- and out-scatter, $d_{\mathrm{IS+OS}}$. The input pin arrangement, shown in Figure 3.3, was identical to the PRIME devices previously used for measurement and PBRA calculations. Corrections for virtual source position as described in Section 3.1.8 were again applied.

4.1.2. Validation metrics

All validation metrics were evaluated for the PBRA dose distributions under both nominal and IS+OS-corrected pin diameters. Each of the 27 measured isodose distributions was compared to the PBRA-calculated distributions using 3%/3mm DTA criteria for all measured dose points as discussed in Section 3.1.9. Dose difference histograms were generated showing both the passes and failures.

Also, the maximum magnitude differences between PBRA calculations and measurement within the modulated volume were evaluated according to

$$\Delta D^{+}_{\mathrm{mod}} = \max\big(D_{\mathrm{PBRA}}(y,z) - D_{\mathrm{meas}}(y,z)\big), \tag{4.1}$$

and

$$\Delta D_{\mathrm{mod}}^{-} = \min\left(D_{\mathrm{PBRA}}(y,z) - D_{\mathrm{meas}}(y,z)\right), \quad 4.2$$

where $|y| \leq 3.5$ cm and $z \leq 2.0$ cm at 7 MeV, $z \leq 4.5$ cm at 13, and $z \leq 6.5$ cm at 20 MeV. This was performed for PBRA dose distributions under both nominal and IS+OS-corrected diameters.

4.2. Results

Table 4.1 shows the overall passing rates for all points within the entire domain of the measured dose distribution for each setup. The adjustments to the nominal 0.158-cm-diameter pin (IRF_{nom} = 0.937) produced no changes in passing rates for all combinations of beam energy and SSD, except for 20 MeV and 100 cm SSD, where the passing rate increased slightly (98.8% to 99.1%). However, the passing rate for the smallest diameter was already 100% for 4 of 9 combinations and at least 99.4% for 3 others. For the intermediate diameter (0.273 cm, IRF_{nom} = 0.812), the agreement increased at 7 and 20 MeV at 100 cm SSD, did not change at any energy at 105 cm SSD, and increased minimally at 13 and 20 MeV at 110 cm SSD. The largest block size (0.352 cm, IRF_{nom} = 0.688) had mixed results. The passing rate increased by 1.3-2.5% in the case of 7 MeV at all SSDs. At 13 MeV, the passing rate decreased at 100 and 105 cm SSD, but increased at 110 cm SSD. For the 20 MeV beam with the 0.352-cm pin, the passing rate increased at 100 and 105 cm SSD, but decreased at 110 cm SSD.

Table 4.2 shows the passing rates for points within the modulated volume over which the optimization (Equation 3.5) was performed. The average nominal and IS+OS-corrected PBRA passing rates were 96.2% and 98.5%, respectively. There was no improvement in 16 of the 27 combinations where the average rate was 100%. In the remaining cases, the average increase in passing rate was 5.8%, with a maximum of 16.9% for the 0.352-cm diameter at 20 MeV and 100 cm SSD. The improvements were most significant for the largest pin diameter.

Table 4.3 contains the maximum magnitude differences between calculation and measurement within the modulated region. As expected, the change in the spread between minimum and maximum dose differences was minor as modifying pin diameter simply raised or lowered calculated dose under the modulated region. The corrected IM-PBRA decreased the maximum absolute difference for 24 of the 27 measurement combinations, but produced no change for 2 combinations. The correction increased the maximum difference for 20 MeV at 110 cm SSD under the 0.273-cm pins. The correction provided an average reduction of the maximum difference of 0.8%, 0.4%, and 0.3% at 100, 105, and 110 cm SSD, respectively; 0.6%, 0.2%, and 0.6% for 7, 13, and 20 MeV, respectively; 0.4%, 0.4%, and 0.6% for diameters of 0.158, 0.273, and 0.352 cm, respectively.

Isodose comparisons of measurement to nominal and IS+OS-corrected PBRA are plotted along with their dose difference histograms in Figures 4.1-3 for three selected beam energy and modulator combinations at 100 cm SSD. These illustrate that common points of failure are in the penumbra and dose falloff regions. Similar plots for all measured combinations are contained in Appendix B.

Table 4.1. Comparison of overall passing rates under 3%/3mm DTA criteria for nominal and corrected IM-PBRA calculations. PBRA calculations were compared to measurement for all points in the dose distribution with 3%/3mm DTA criteria, and overall passing rates were evaluated.

Beam Energy (MeV)	SSD (cm)	*d* (cm)	Nominal PBRA	Corrected PBRA	Change
7	100	0.158	97.5%	97.5%	0.0%
7	100	0.273	96.4%	97.8%	1.4%
7	100	0.352	93.7%	96.2%	2.5%
13	100	0.158	100.0%	100.0%	0.0%
13	100	0.273	100.0%	100.0%	0.0%
13	100	0.352	96.5%	93.9%	-2.6%
20	100	0.158	98.8%	99.1%	0.3%
20	100	0.273	94.6%	97.1%	2.5%
20	100	0.352	91.7%	93.1%	1.4%
7	105	0.158	99.8%	99.8%	0.0%
7	105	0.273	99.1%	99.1%	0.0%
7	105	0.352	96.6%	97.9%	1.3%
13	105	0.158	100.0%	100.0%	0.0%
13	105	0.273	99.9%	99.9%	0.0%
13	105	0.352	97.3%	96.8%	-0.5%
20	105	0.158	99.4%	99.4%	0.0%
20	105	0.273	99.2%	99.2%	0.0%
20	105	0.352	95.7%	97.6%	1.9%
7	110	0.158	100.0%	100.0%	0.0%
7	110	0.273	99.9%	99.9%	0.0%
7	110	0.352	97.9%	99.2%	1.3%
13	110	0.158	100.0%	100.0%	0.0%
13	110	0.273	99.7%	100.0%	0.3%
13	110	0.352	96.7%	98.0%	1.3%
20	110	0.158	99.5%	99.5%	0.0%
20	110	0.273	99.3%	99.4%	0.1%
20	110	0.352	98.7%	98.3%	-0.4%
		Average	98.1%	98.2%	0.1%

Table 4.2. Comparison of passing rates within the modulated region under 3%/3mm DTA criteria for nominal and corrected IM-PBRA calculations. PBRA calculations were compared to measurement for all points in the modulated region ($|y| \leq 3.5$ cm and $z \leq R_p$) of the dose distribution with 3%/3mm DTA criteria, and the passing rates were evaluated.

Beam Energy (MeV)	SSD (cm)	*d* (cm)	Nominal PBRA	Corrected PBRA	Change
7	100	0.158	100.0%	100.0%	0.0%
7	100	0.273	97.8%	100.0%	2.2%
7	100	0.352	94.4%	99.6%	5.2%
13	100	0.158	100.0%	100.0%	0.0%
13	100	0.273	100.0%	100.0%	0.0%
13	100	0.352	84.7%	89.1%	4.4%
20	100	0.158	98.5%	100.0%	1.5%
20	100	0.273	83.5%	95.0%	11.5%
20	100	0.352	70.9%	87.7%	16.9%
7	105	0.158	100.0%	100.0%	0.0%
7	105	0.273	100.0%	100.0%	0.0%
7	105	0.352	94.8%	98.7%	3.9%
13	105	0.158	100.0%	100.0%	0.0%
13	105	0.273	100.0%	100.0%	0.0%
13	105	0.352	91.4%	92.9%	1.5%
20	105	0.158	100.0%	100.0%	0.0%
20	105	0.273	100.0%	100.0%	0.0%
20	105	0.352	83.1%	96.7%	13.6%
7	110	0.158	100.0%	100.0%	0.0%
7	110	0.273	100.0%	100.0%	0.0%
7	110	0.352	97.8%	100.0%	2.2%
13	110	0.158	100.0%	100.0%	0.0%
13	110	0.273	100.0%	100.0%	0.0%
13	110	0.352	99.8%	99.8%	0.0%
20	110	0.158	100.0%	100.0%	0.0%
20	110	0.273	100.0%	100.0%	0.0%
20	110	0.352	99.4%	100.0%	0.6%
		Average	96.2%	98.5%	2.3%

Table 4.3. Maximum magnitude dose differences in the modulated volume. The maximum magnitude dose differences between measurement and either nominal or IS+OS-corrected PBRA calculations were determined within the modulated region where the minimization routine was performed. Dose differences greater than 3% are shaded. The greatest dose difference for a given beam energy, SSD, and nominal diameter combination are bolded. Cases where there was no positive or negative difference are noted as "N/A".

SSD (cm)	Beam Energy (MeV)	*d* (cm)	Nominal		IS+OS-Corrected	
			$\Delta D^{+}_{\mathrm{mod}}$	$\Delta D^{-}_{\mathrm{mod}}$	$\Delta D^{+}_{\mathrm{mod}}$	$\Delta D^{-}_{\mathrm{mod}}$
100	7	0.158	**2.3%**	-0.7%	1.8%	-1.2%
100	7	0.273	**3.3%**	-1.1%	2.5%	-1.9%
100	7	0.352	**3.8%**	-1.6%	3.1%	-2.4%
100	13	0.158	**2.1%**	-1.7%	1.9%	-2.0%
100	13	0.273	2.4%	**-2.9%**	2.5%	-2.7%
100	13	0.352	2.8%	**-4.5%**	3.4%	-3.9%
100	20	0.158	1.2%	**-3.6%**	1.6%	-2.9%
100	20	0.273	1.2%	**-6.3%**	2.5%	-4.9%
100	20	0.352	1.9%	**-8.9%**	3.6%	-7.0%
105	7	0.158	**2.6%**	-0.6%	1.9%	-1.5%
105	7	0.273	**2.4%**	-1.1%	1.7%	-2.1%
105	7	0.352	**3.7%**	-2.4%	3.1%	-3.0%
105	13	0.158	**2.1%**	-1.2%	1.6%	-1.8%
105	13	0.273	**2.6%**	-2.4%	2.4%	**-2.6%**
105	13	0.352	3.0%	**-3.7%**	3.1%	-3.6%
105	20	0.158	1.0%	**-1.7%**	1.2%	-1.6%
105	20	0.273	1.9%	**-2.4%**	2.1%	-2.2%
105	20	0.352	1.8%	**-4.5%**	2.9%	-3.3%
110	7	0.158	**2.3%**	N/A	1.3%	-0.9%
110	7	0.273	**2.2%**	-0.6%	1.4%	-1.7%
110	7	0.352	**3.2%**	-2.1%	2.6%	-2.9%
110	13	0.158	**2.0%**	-0.7%	1.4%	-1.5%
110	13	0.273	**2.7%**	-2.0%	2.4%	-2.5%
110	13	0.352	**3.0%**	-2.8%	2.9%	**-3.0%**
110	20	0.158	**1.7%**	-1.2%	1.4%	-1.6%
110	20	0.273	2.0%	-1.9%	1.8%	**-2.2%**
110	20	0.352	2.5%	**-3.1%**	2.7%	-2.9%

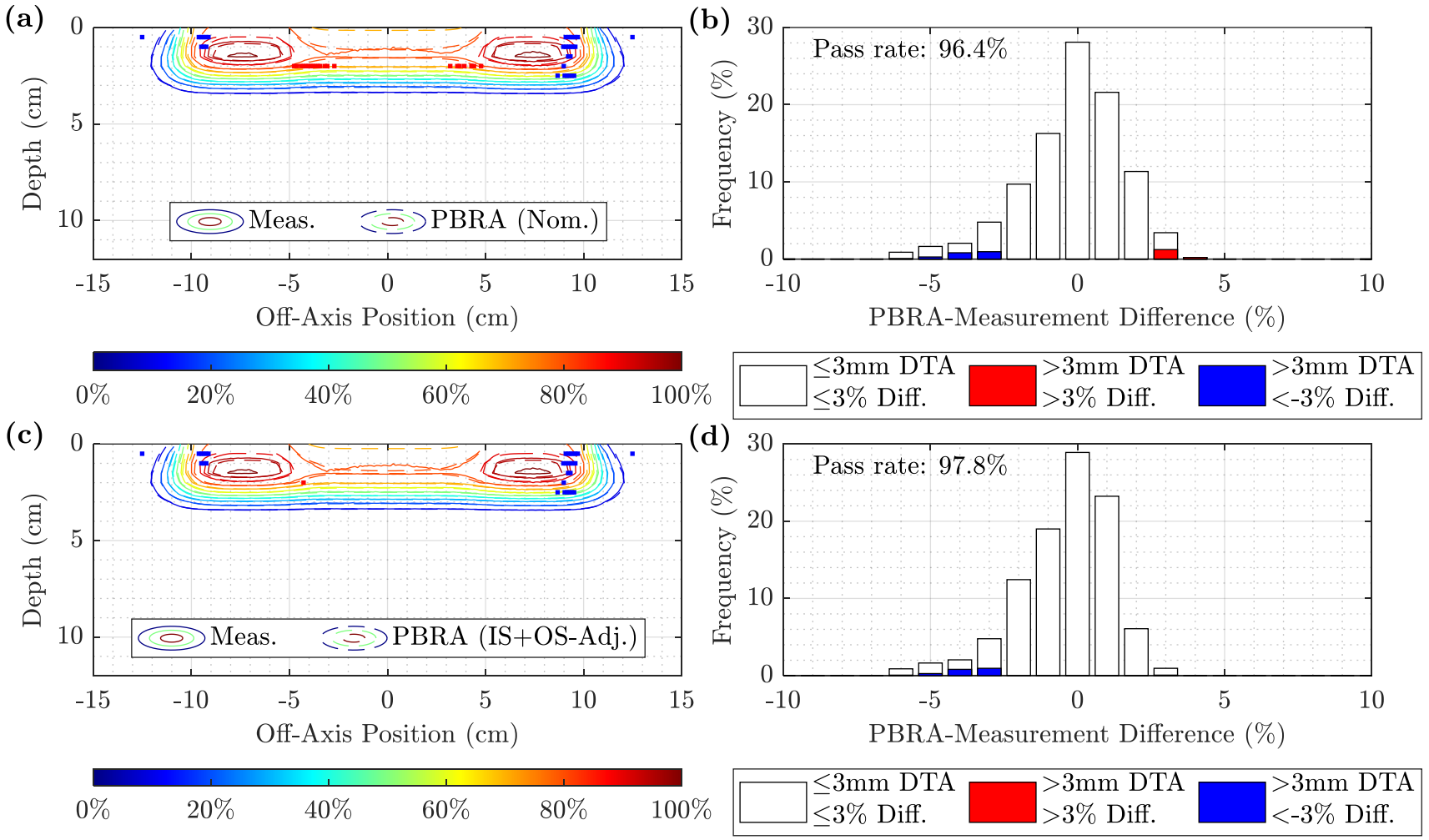

Figure 4.1. Measured and PBRA-calculated isodose comparison and difference histogram for 0.273-cm pins at 7 MeV and 100 cm SSD. The isodose contours for measurement (solid) are compared to the PBRA calculations with (a) nominal and (c) IS+OS-corrected pin diameters. Difference histograms under 3%/3mm DTA criteria are plotted for (b) nominal and (d) IS+OS-corrected PBRA diameters. Points at which the PBRA underpredicted and overpredicted the dose relative to measurement are shown in blue and red, respectively. The nominal and corrected passing rates were 96.4% and 97.8%, respectively.

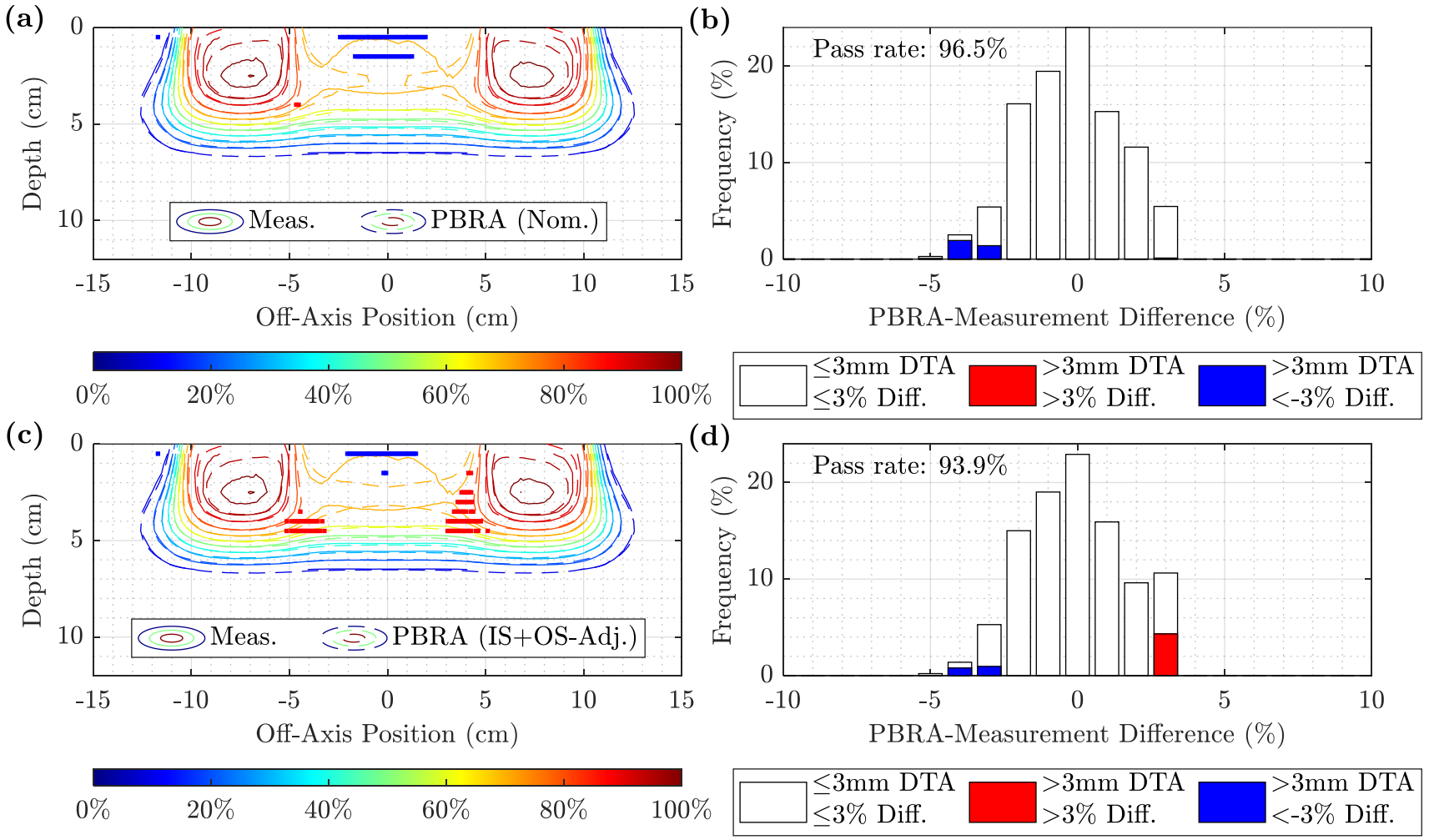

Figure 4.2. Measured and PBRA-calculated isodose comparison and difference histogram for 0.352-cm pins at 13 MeV and 100 cm SSD. The isodose contours for measurement (solid) are compared to the PBRA calculations with (a) nominal and (c) IS+OS-corrected pin diameters. Difference histograms under 3%/3mm DTA criteria are plotted for (b) nominal and (d) IS+OS-corrected PBRA diameters. Points at which the PBRA underpredicted and overpredicted the dose relative to measurement are shown in blue and red, respectively. The nominal and corrected passing rates were 96.5% and 93.9%, respectively.

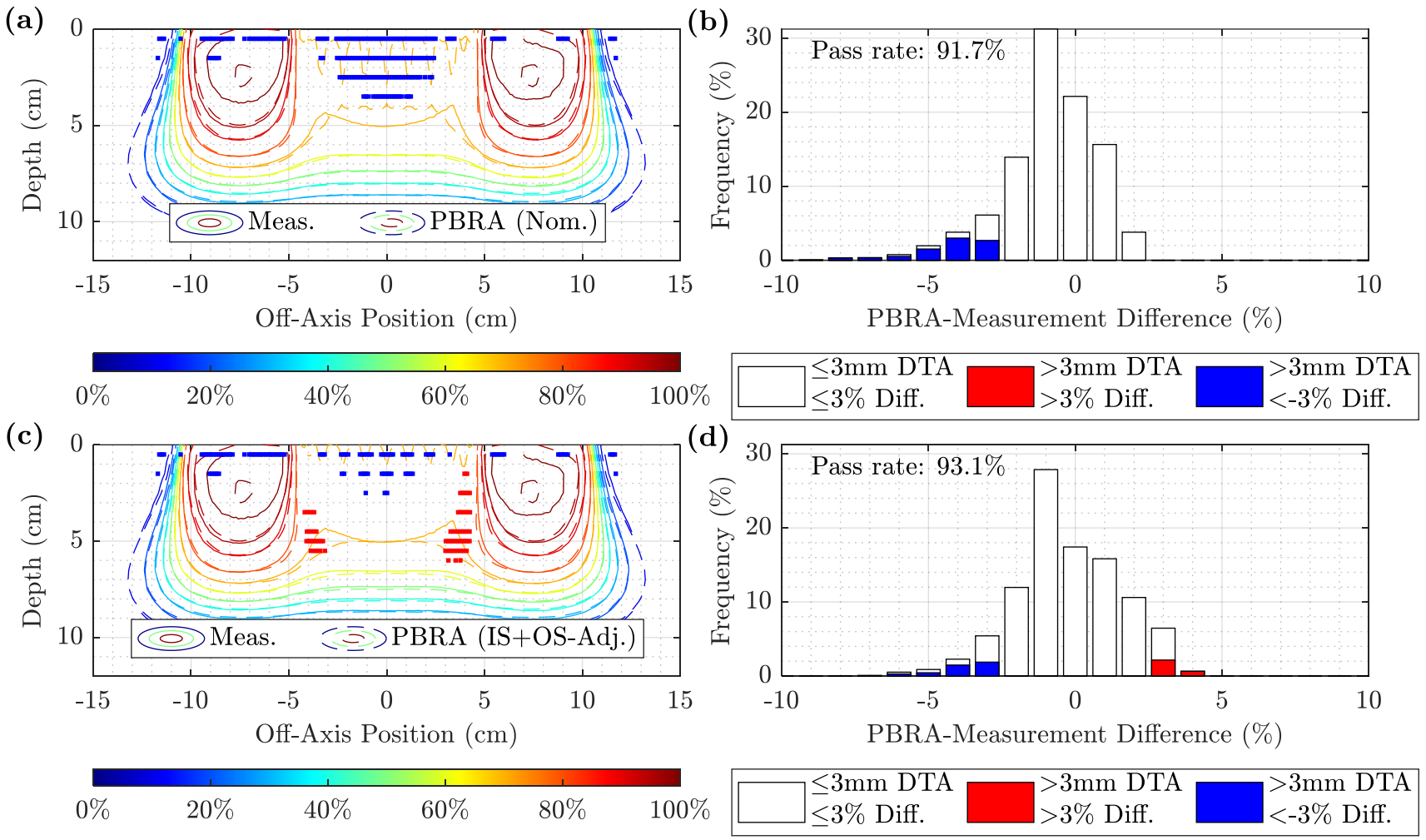

Figure 4.3. Measured and PBRA-calculated isodose comparison and difference histogram for 0.352-cm pins at 20 MeV and 100 cm SSD. The isodose contours for measurement (solid) are compared to the PBRA calculations with (a) nominal and (c) IS+OS-corrected pin diameters. Difference histograms under 3%/3mm DTA criteria are plotted for (b) nominal and (d) IS+OS-corrected PBRA diameters. Points at which the PBRA underpredicted and overpredicted the dose relative to measurement are shown in blue and red, respectively. The nominal and corrected passing rates were 91.7% and 93.1%, respectively.

4.3. Discussion

The objective of this Aim was to determine an optimal pin diameter that fit IM-PBRA calculations most closely to measured data. The resulting benefits are most clearly illustrated in the case of 0.352-cm island blocks at 20 MeV and 100 cm SSD (Figure 4.3). The nominal PBRA calculation initially underpredicts measurement in the modulated region due to what was initially thought to be the significant out-scatter component, initially hypothesized to be a result of both the large block diameter and high beam energy. The correction improves agreement of passing rates for IM-PBRA calculated and measured dose comparisons over nominal within the modulated region by 1.4% overall and as much as 16.9% in the most extreme case. The out-scatter dose adjustment improves agreement most significantly at shallow depths in the modulated region, but worsens agreement at the edge of the modulated region at deeper depths where the out-scattered fluence is ranging out. Hence, the minimization is a tradeoff in agreement within these regions.

The PBRA calculations with nominal diameters without any corrections for in-scatter and out-scatter have an average passing rate of 98.1% under the 3%/3mm DTA criteria for the distributions compared here. Introducing the correction increased this average to 98.5%. While the passing rate improved for some cases, it was reduced for others, most notably at 13 MeV. In the three cases with a decrease in the overall passing rate (13 MeV, 100 cm SSD, 0.352-cm diameter; 13 MeV, 105 cm SSD, 0.352-cm diameter; 20 MeV, 110 cm SSD, 0.352-cm diameter), the correction decreases the points of failure within the modulated field, but increases the failure rate in the unmodulated region. Another reason for the worsening passing rates is that the minimization was performed over the modulated volume while the 3%/3mm DTA validation metric was calculated over the entire dose distribution. An inspection of the isodose plots with such failures (e.g. Figure 4.4) reveals that many of the failure points are within the penumbra and falloff region, outside the 3.5 cm off-axis and R_{90} depth limits of the minimization.

Another benefit of the diameter corrections is the reduction of the modulated maximum dose difference as described by Equations 4.1 and 4.2. Of the 27 measurement conditions, the diameter correction reduced the maximum difference for 24 combinations, produced no change in 2 cases, and increased the difference by 0.2% for one setup. The case at 20 MeV, 100 cm SSD, and the 0.352-cm diameter showed the greatest improvement, with the maximum difference reduced from 8.9% to 7.0%. At 20 MeV, 110 cm SSD and the 0.273-cm diameter, the maximum difference worsened by 0.2% with the correction, but the overall passing rate still improved by 0.1%.

Chapter 5. Summary of Results and Conclusions

5.1. Benefits of pin diameter corrections

Using 3%/3mm DTA criteria, the nominal IM-PBRA returns an average passing rate of 98.1% for all points within the distribution with a worst-case value of 91.7%. For points in the modulated volume, the average and worst-case values are 96.2% and 70.9%, respectively. With IS+OS scattering corrections, the overall average passing rate improved to 98.5% and the worst-case passing rate increased to 93.1%. For points in the modulated region ($|y| \leq 3.5$ cm and $z \leq R_p$), these values increased to 98.5% and 87.7%, respectively. Of the 27 cases compared, 13 had no improvement from nominal, 11 saw some improvement with an average increase of 1.3%, and three resulted in agreement worsening by 1.2% when considering the full dose distribution. When considering only the modulated region, 16 cases had no improvement, 11 had some improvement with an average increase of 5.8%, and 0 saw worsened agreement. The hypothesis of this work, that incorporating island block scatter diameter correction factors will improve accuracy of IM-PBRA dose calculations, was found to be conditionally true.

25 of 27 IM-PBRA calculations with IS+OS-corrected pin diameters agreed to within ±4% of measurement in the modulated volume, with the exceptions being 20 MeV and 100 cm SSD for diameters of 0.273 and 0.352 cm. The IS+OS corrections also reduced the maximum dose differences in the modulated volume in 24 of 27 cases. There was no change for 2 combinations, and an increased difference in the remaining case at 20 MeV and 110 cm SSD for 0.273-cm island blocks.

5.2. Shortcomings and possible improvements on diameter scaling method

A comparison of off-axis profiles (Figures A.21-28) reveals that PBRA calculations produce a relatively uniform dose in the modulated area while measured dose profiles feature a

peak centered on CAX within the modulated area. The peak-to-trough amplitude of this peak increases with beam energy and pin diameter and decreases with increasing SSD. In the most extreme case at 20 MeV and 100 cm SSD for 0.352-cm pins, this difference can be as much as 6%. The magnitude of this effect is most clearly seen on the CAX PDDs (Figures A.13-20). Another notable feature of the off-axis profiles is that measurement is typically greater than calculation in the unmodulated portion of the field, i.e. the region between the modulated area and the penumbra. The magnitude of this difference generally increases with beam energy and pin diameter.

These two features, the CAX dose peak and higher measured dose in the unmodulated area, were initially attributed to large-angle scattering from the pin and the degraded energy distribution of the out-scattered electrons (Appendix C). The PBRA approximates the angular distribution as a Gaussian, characterized by σ_{θ_x}. Therefore, a simple model of subtracted fluence removed by a particular pin will assume the same distribution.

A single pin diameter scaling, which approximately accounts for in-scatter losses and out-scatter contributions, was chosen as the correction method due to the simplicity of its implementation and negligible impact on calculation time. Since PBRA calculations will not be able to exactly reproduce the measured distribution, the primary goal was to minimize differences across the modulated volume.

The primary limitation of the simple diameter scaling is that it assumes similar angular and energy fluence distributions between the primary and out-scattered electrons. Using MC calculations, the incident and out-scattered energy spectra were determined for 7, 13, and 20 MeV beams incident on a 0.315-cm pin as shown in Appendix C. The out-scattered spectra differed substantially from the incident, with a broader, more uniform energy distribution and a lower mean

energy. This would result in differing dose deposition with depth with respect to that of the primary beam. Additionally, it is expected that the angular distribution of these out-scattered electrons would differ significantly from the primary electrons, likely having a much broader angular distribution.

In-scattering removes electrons from the incident spectrum and does not affect the energy distribution. A more complex phase space approach to account for out-scattering could be combined with the in-scatter adjustments to improve calculation accuracy. A simple pin diameter scaling is unable to reproduce the measured dose distribution since it does not account for changes in the energy and angular spectra. MC calculations could be used to extract information on the phase space of out-scattered electrons, which could then be used to determine the initial PBRA pencil beam parameters for a supplemental PBRA calculation which can be added to the regular dose calculation using the in-scatter-adjusted diameters. Additional corrections could also include an analytical model to calculate attenuation of the x-ray component due to the island blocks, though preliminary investigation indicated that this effect was less than 1% of D_{max}.

5.3. Effect of fabrication error in PRIME island block divergence

The corrections and discussion presented in this work were based on measurements made under intensity modulators having pins incorrectly converging, rather than correctly diverging, axes with respect to the beam. Both Hilliard (2018) and the preliminary analysis in Appendix E demonstrate that the pin orientation had a measurable, significant effect. Therefore, the IS+OS-corrected diameters presented in Tables A.1-3 should not be used, and the methodology of Chapter 3 should be repeated with measurements under intensity modulators with correct pin divergence. Preliminary data for correct pin divergence is shown in Appendix E. This orientation error, which

resulted from a change in the manufacturing process, was discovered following data acquisition and analysis. Its effect should explain some unexpected differences in the dose measurement.

Appendix A. Comparison of Measurement and Nominal and In-Scatter-Adjusted PBRA Calculations

Measured and PBRA-calculated foam-only PDDs are compared in Figure A.1 and Figure A.2 at 105 and 110 cm SSD, respectively. Foam-only measured and PBRA-calculated profiles are plotted in Figure A.3 and Figure A.4 at 105 and 110 cm, respectively. Measured and PBRA-calculated isodose contours for foam only with difference histograms under 3%/3mm DTA criteria are plotted in Figures A.5-10 for beam energy 7-20 MeV at 105 and 110 cm SSD. Comparison of modulated measurement to nominal and in-scatter-adjusted PBRA calculations are plotted in Figures A.11-16 for PDDs and Figures A.17-22 for off-axis profiles. Figures A.23-28 plot the PDD and off-axis profiles at various depths for measurement, nominal PBRA, in-scatter-adjusted PBRA, and out-scatter estimation for the 0.352-cm diameter for 7-20 MeV beam energies at 105 and 110 cm SSD.

Tables A.1-3 contain the IS+OS diameter corrections described in Chapter 3 for nominal beam energies 7-20 MeV. The out-scatter dose corrections are calculated using $E_{p,0}$ and Equation 3.6 with the corresponding coefficients from Table 3.7 for a given beam energy. For the measured conditions, the measured foam-only $E_{p,0}$ value was used (Table 3.4). For the other beam energies, the $E_{p,0}$ values were taken from the commissioning data for Elekta Agility at MBPCC and reduced by 0.2 MeV to account for the machinable foam (Hilliard, 2018).

Figures A.29-34 compare measurement to nominal and IS+OS-corrected PBRA calculations for 7-20 MeV and all pin diameters at 105 and 110 cm SSD. Figures A.35-40 contain off-axis profiles of measurement and IS+OS-corrected calculations for beam energies of 7, 13, and 20 MeV at depths of 1.0, 1.5, and 1.5 cm, respectively, at 105 and 110 cm SSD. Figures A.41-46 compare the PDDs and off-axis profiles over various depths for measurement, nominal PBRA, and IS+OS-corrected PBRA for 7-20 MeV at 105 and 110 cm SSD for 0.352-cm pins.

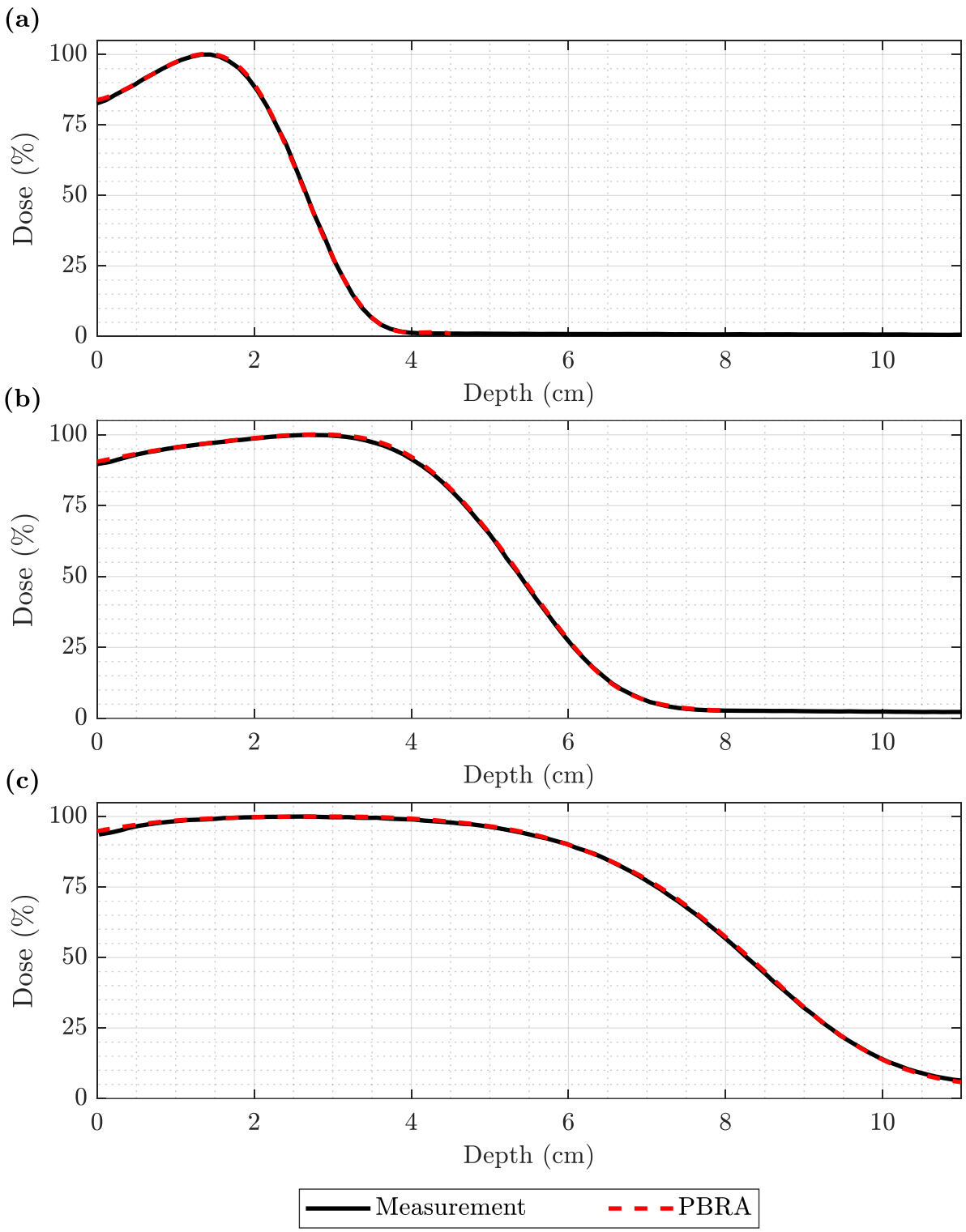

Figure A.1. PDDs of foam-only measurement and PBRA calculation for each beam energy at 105 cm SSD. Foam-only PDDs are plotted for measurement (solid black) and PBRA (dashed red) at (a) 7, (b) 13, and (c) 20 MeV at 105 cm SSD for a 21×21 cm^2 field size.

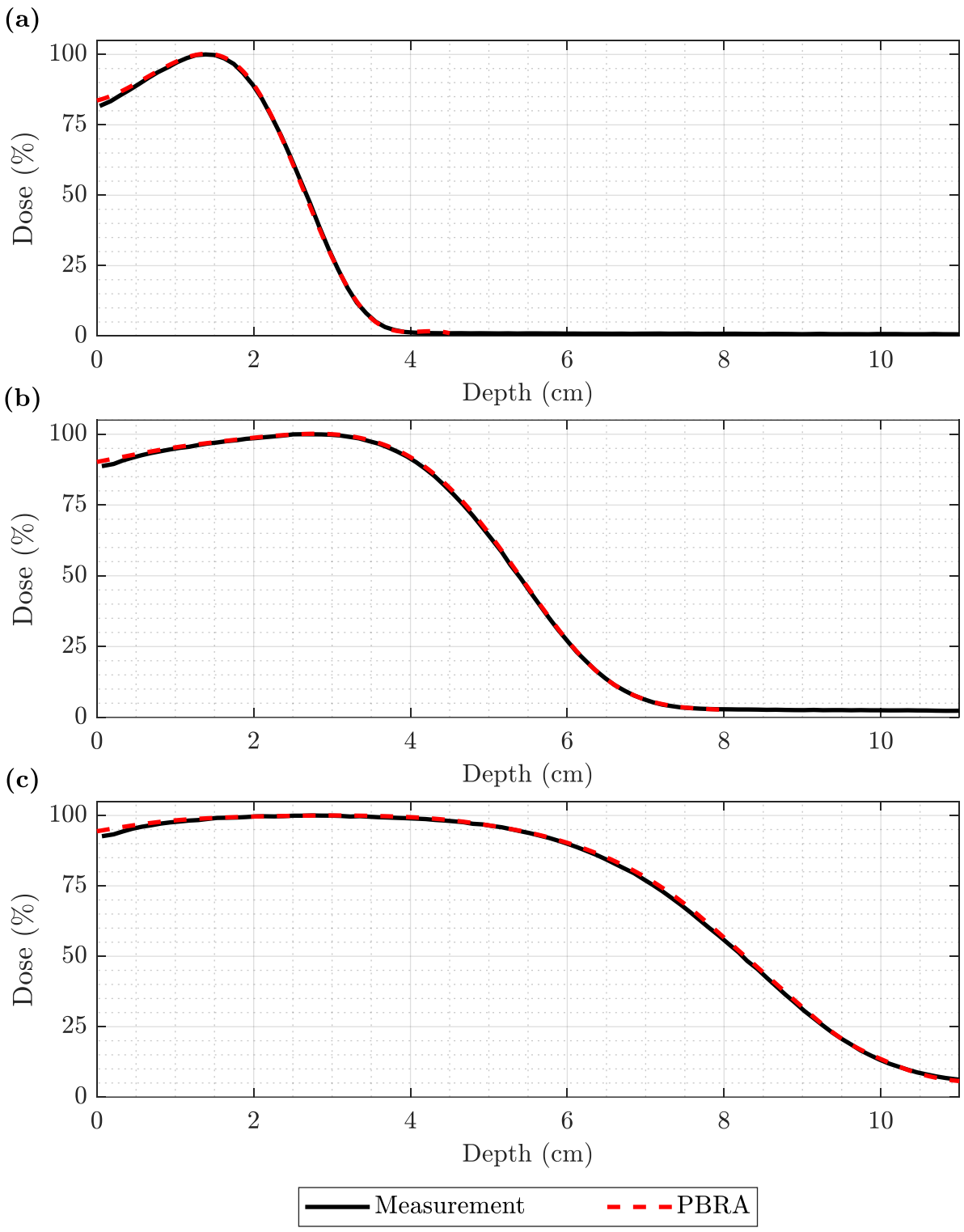

Figure A.2. PDDs of foam-only measurement and PBRA calculation for each beam energy at 110 cm SSD. Foam-only PDDs are plotted for measurement (solid black) and PBRA (dashed red) at (a) 7, (b) 13, and (c) 20 MeV at 110 cm SSD for a 21×21 cm^2 field size.

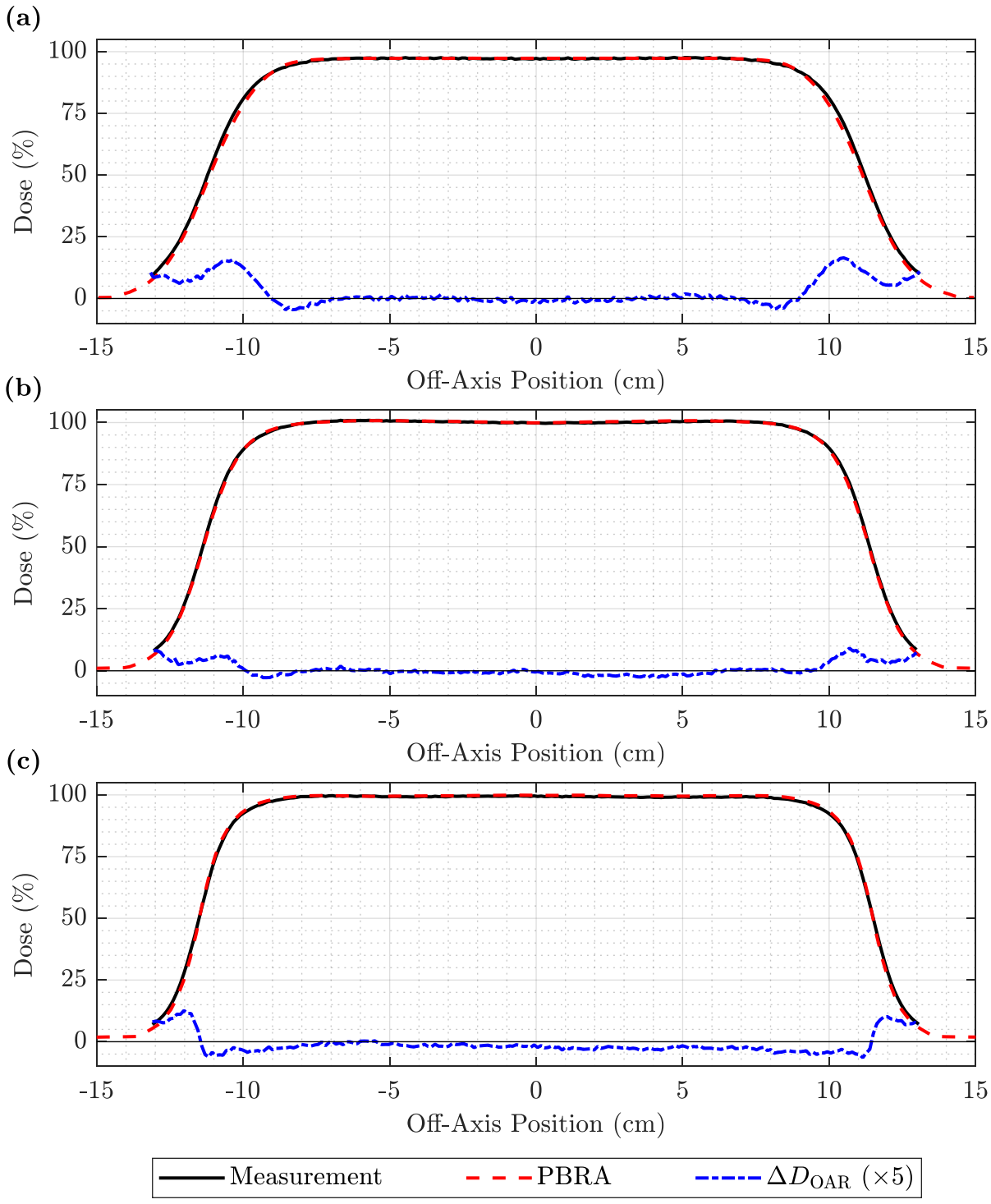

Figure A.3. Off-axis profiles of foam-only measurement and PBRA calculation for each beam energy at 105 cm SSD. Foam-only inline profiles are plotted for measurement (solid black) and PBRA (dashed red) at (a) 7 MeV and 1.0 cm depth, (b) 13 MeV and 2.5 cm depth, and (c) 20 MeV and 3.5 cm depth at 105 cm SSD for a 21×21 cm^2 field size. The off-axis weight adjustment of Equation 3.4 (dashed-dotted blue) is the difference between measured and PBRA-calculated profiles, plotted here with ×5 magnification for clarity.

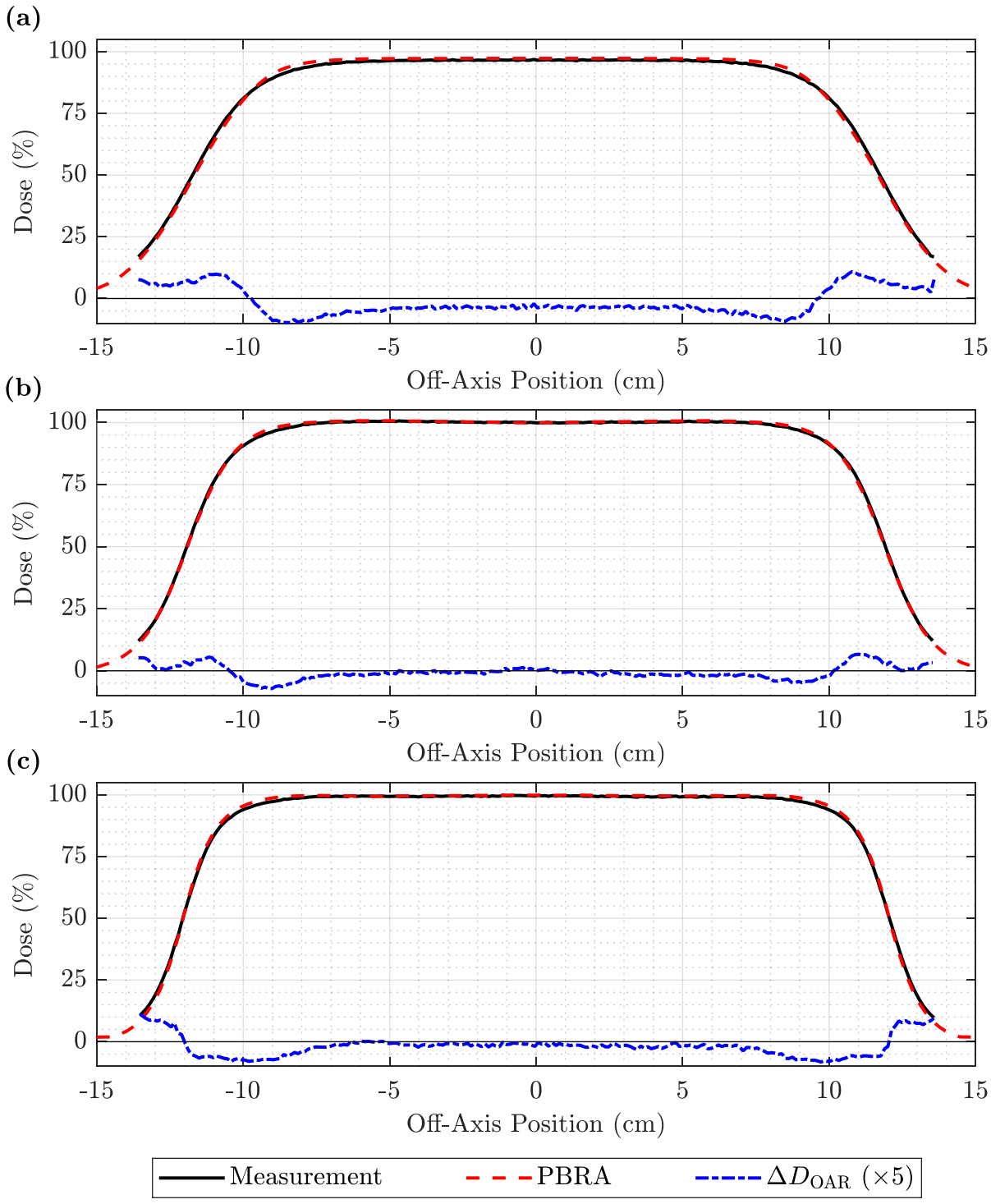

Figure A.4. Off-axis profiles of foam-only measurement and PBRA calculation for each beam energy at 110 cm SSD. Foam-only inline profiles are plotted for measurement (solid black) and PBRA (dashed red) at (a) 7 MeV and 1.0 cm depth, (b) 13 MeV and 2.5 cm depth, and (c) 20 MeV and 3.5 cm depth at 110 cm SSD for a 21×21 cm^2 field size.. The off-axis weight adjustment of Equation 3.4 (dashed-dotted blue) is the difference between measured and PBRA-calculated profiles, plotted here with ×5 magnification for clarity.

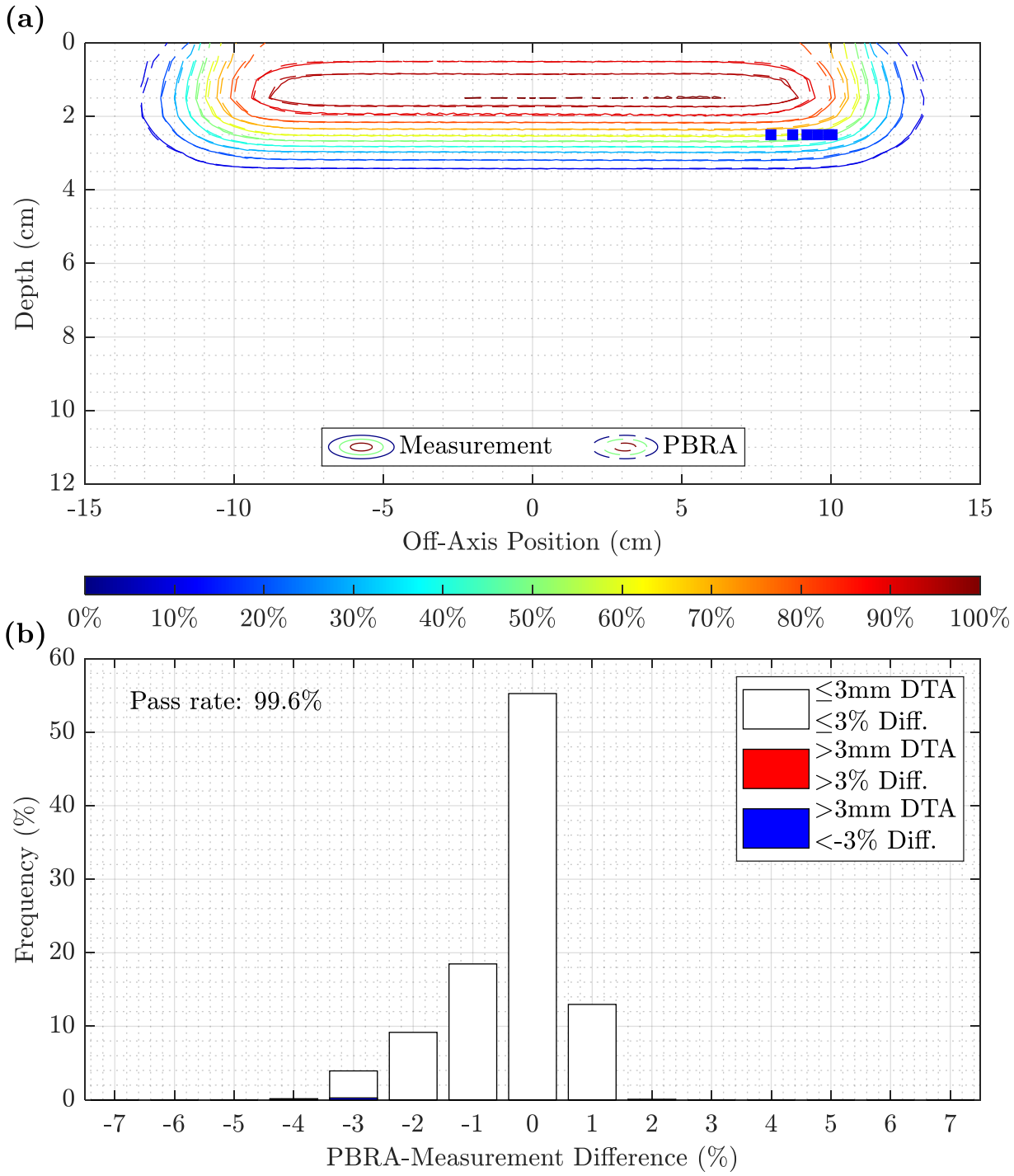

Figure A.5. Measurement and PBRA foam-only isodose comparison and difference histogram for 7 MeV at 105 cm SSD. The isodose contours in (a) compare the measured (solid) and PBRA-calculated (dashed) isodose distributions, and (b) contains the histogram of differences between measurement and PBRA calculations for foam-only at 7 MeV and 105 cm SSD. In both (a) and (b), points where the PBRA underpredicted the dose relative to measurement are shown in blue, while those where the PBRA overpredicted dose are plotted as red. The 3%/3mm DTA criteria yielded a passing rate of 99.6% for all points for this setup.

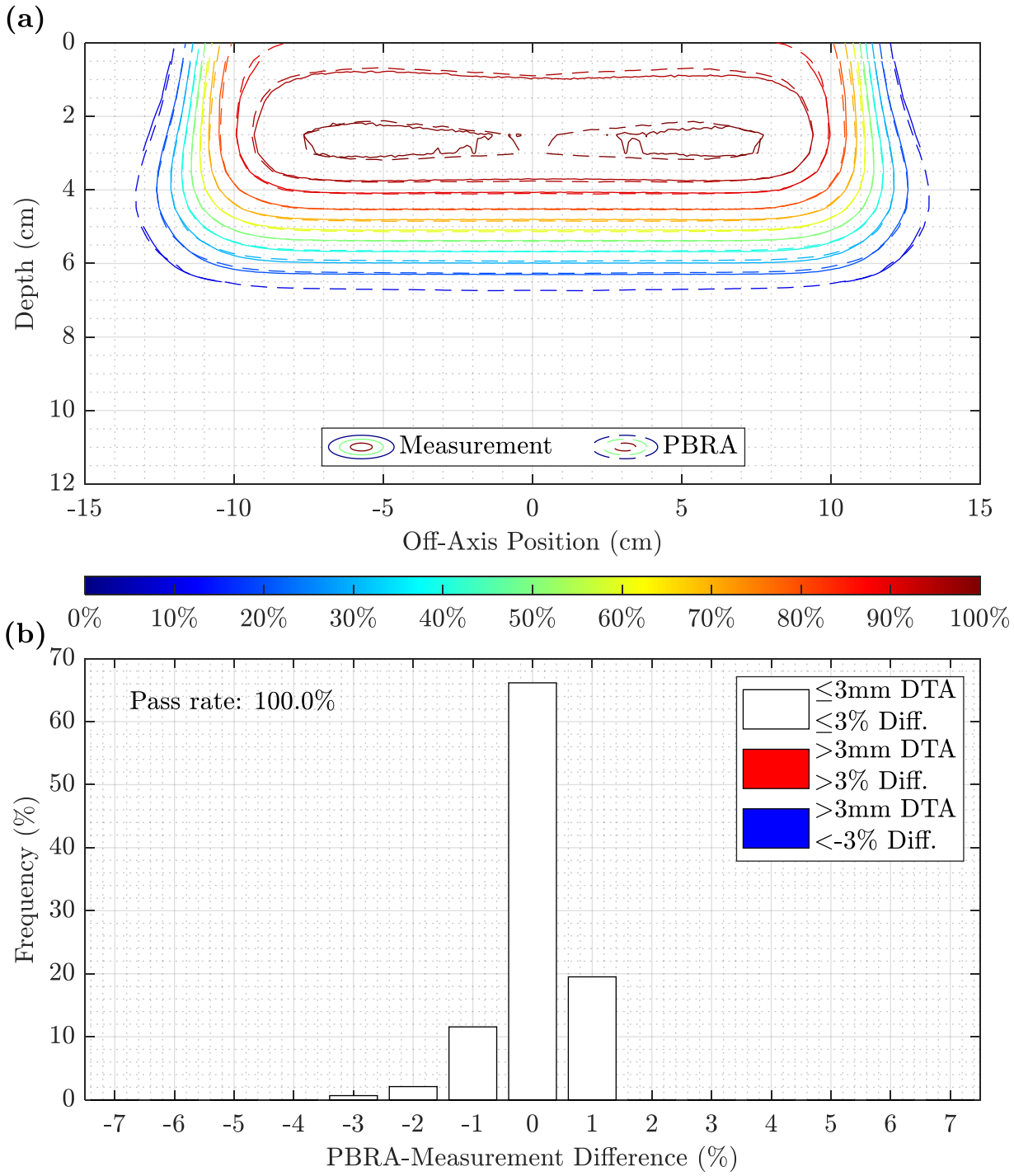

Figure A.6. Measurement and PBRA foam-only isodose comparison and difference histogram for 13 MeV at 105 cm SSD. The isodose contours in (a) compare the measured (solid) and PBRA-calculated (dashed) isodose distributions, and (b) contains the histogram of differences between measurement and PBRA calculations for foam-only at 13 MeV and 105 cm SSD. In both (a) and (b), points where the PBRA underpredicted the dose relative to measurement are shown in blue, while those where the PBRA overpredicted dose are plotted as red. The 3%/3mm DTA criteria yielded a passing rate of 100% for all points for this setup.

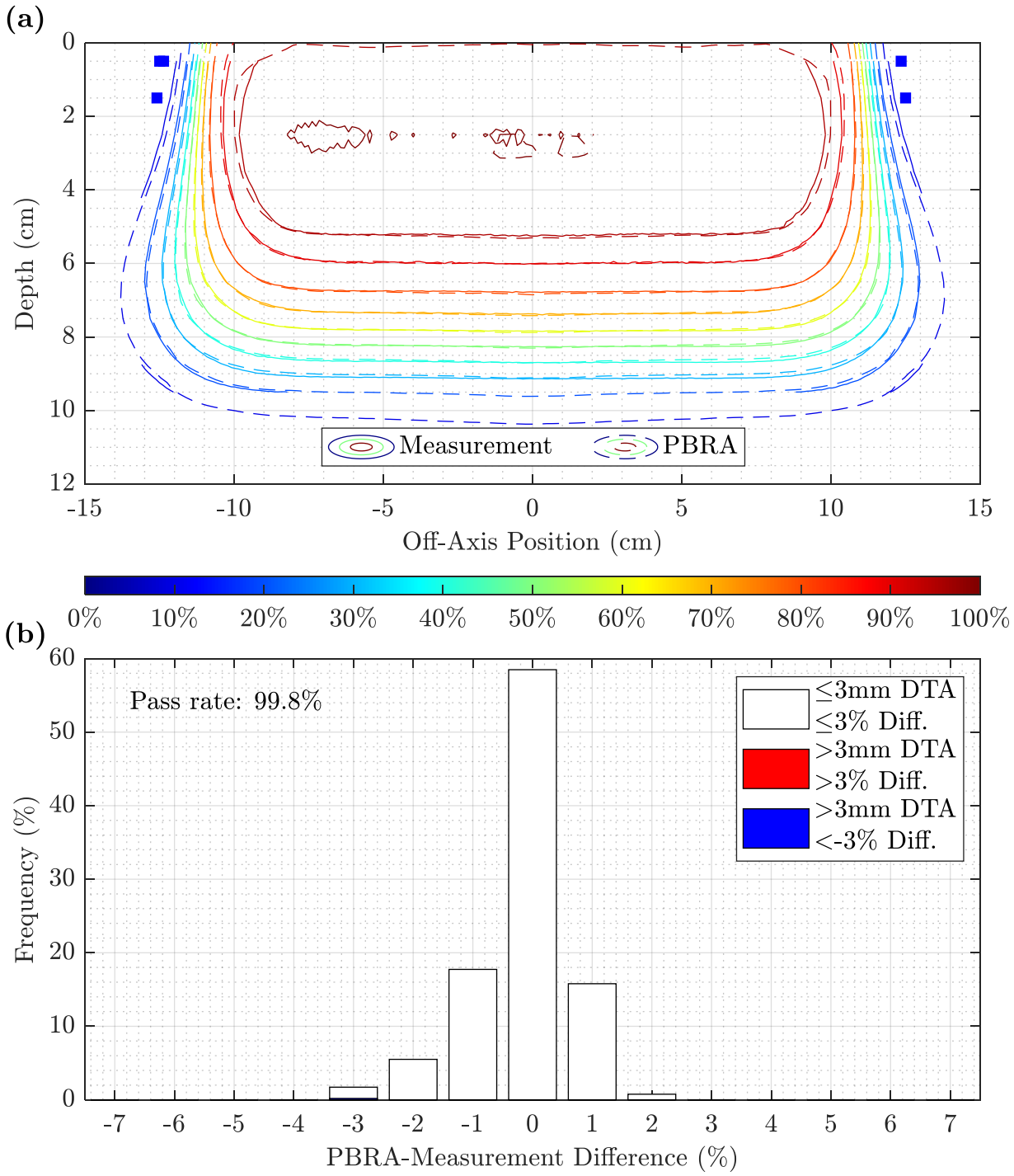

Figure A.7. Measurement and PBRA foam-only isodose comparison and difference histogram for 20 MeV at 105 cm SSD. The isodose contours in (a) compare the measured (solid) and PBRA-calculated (dashed) isodose distributions, and (b) contains the histogram of differences between measurement and PBRA calculations for foam-only at 20 MeV and 105 cm SSD. In both (a) and (b), points where the PBRA underpredicted the dose relative to measurement are shown in blue, while those where the PBRA overpredicted dose are plotted as red. The 3%/3mm DTA criteria yielded a passing rate of 99.8% for all points for this setup.

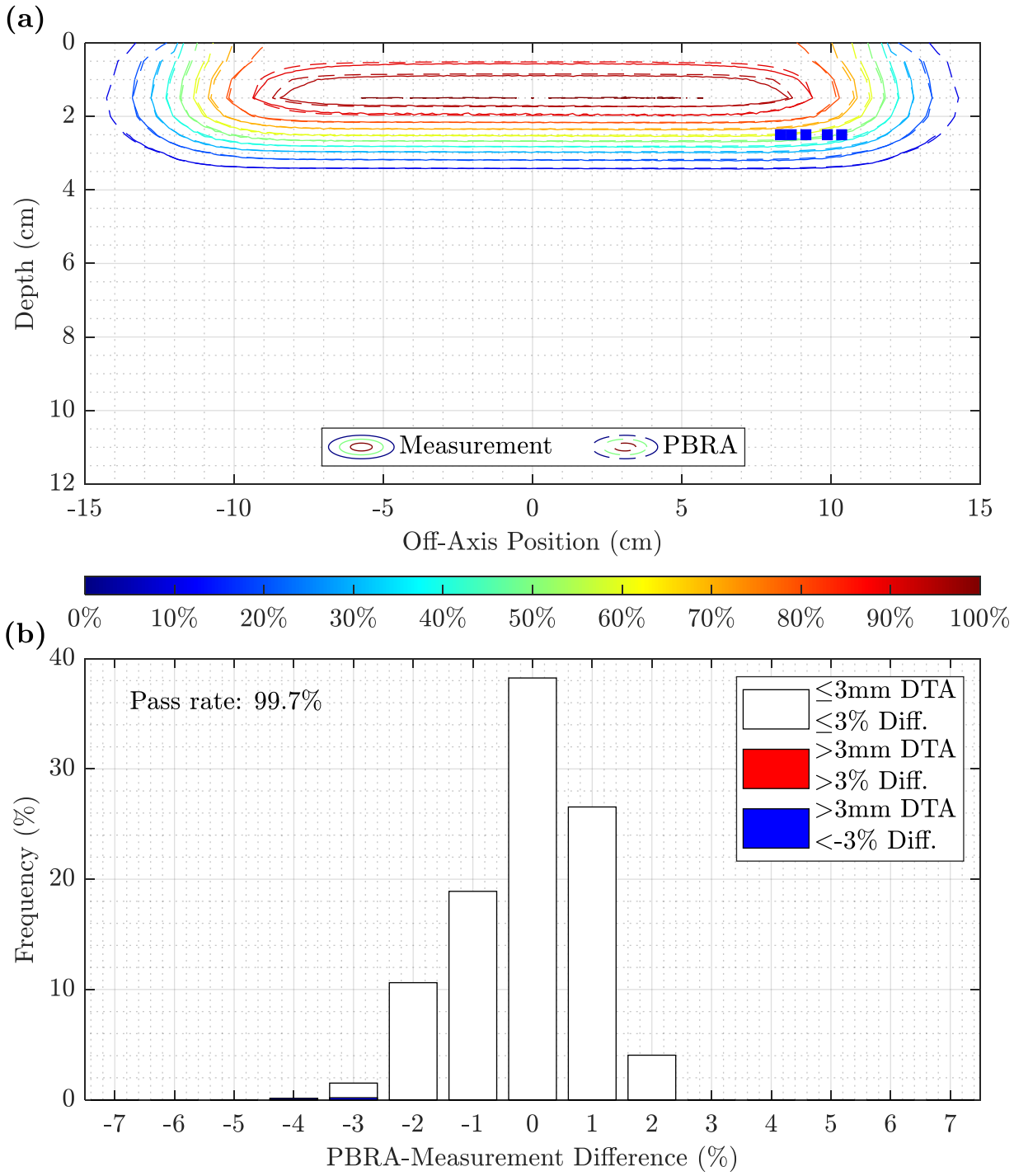

Figure A.8. Measurement and PBRA foam-only isodose comparison and difference histogram for 7 MeV at 110 cm SSD. The isodose contours in (a) compare the measured (solid) and PBRA-calculated (dashed) isodose distributions, and (b) contains the histogram of differences between measurement and PBRA calculations for foam-only at 7 MeV and 110 cm SSD. In both (a) and (b), points where the PBRA underpredicted the dose relative to measurement are shown in blue, while those where the PBRA overpredicted dose are plotted as red. The 3%/3mm DTA criteria yielded a passing rate of 99.7% for all points for this setup.

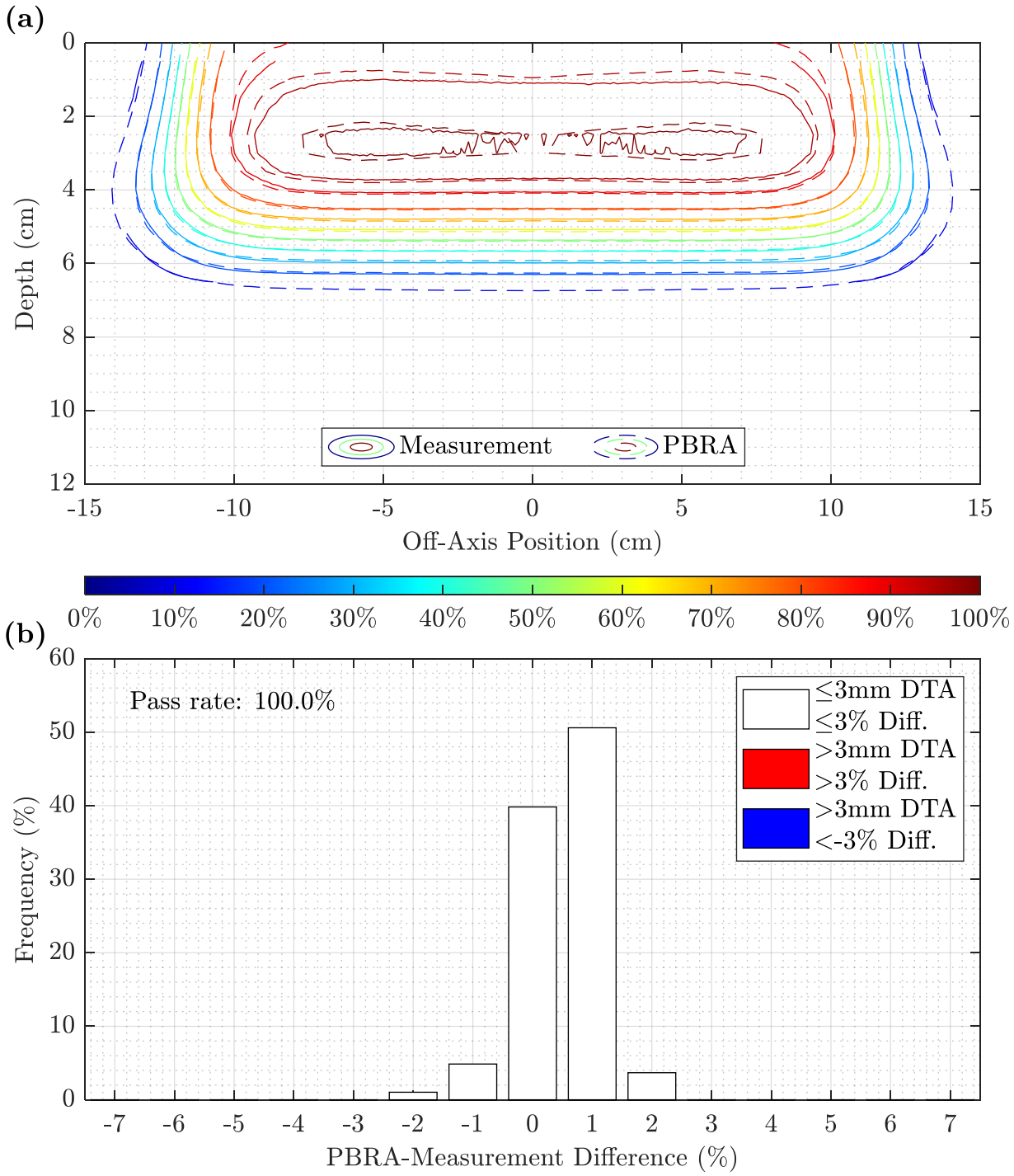

Figure A.9. Measurement and PBRA foam-only isodose comparison and difference histogram for 13 MeV at 110 cm SSD. The isodose contours in (a) compare the measured (solid) and PBRA-calculated (dashed) isodose distributions, and (b) contains the histogram of differences between measurement and PBRA calculations for foam-only at 13 MeV and 110 cm SSD. In both (a) and (b), points where the PBRA underpredicted the dose relative to measurement are shown in blue, while those where the PBRA overpredicted dose are plotted as red. The 3%/3mm DTA criteria yielded a passing rate of 100% for all points for this setup.

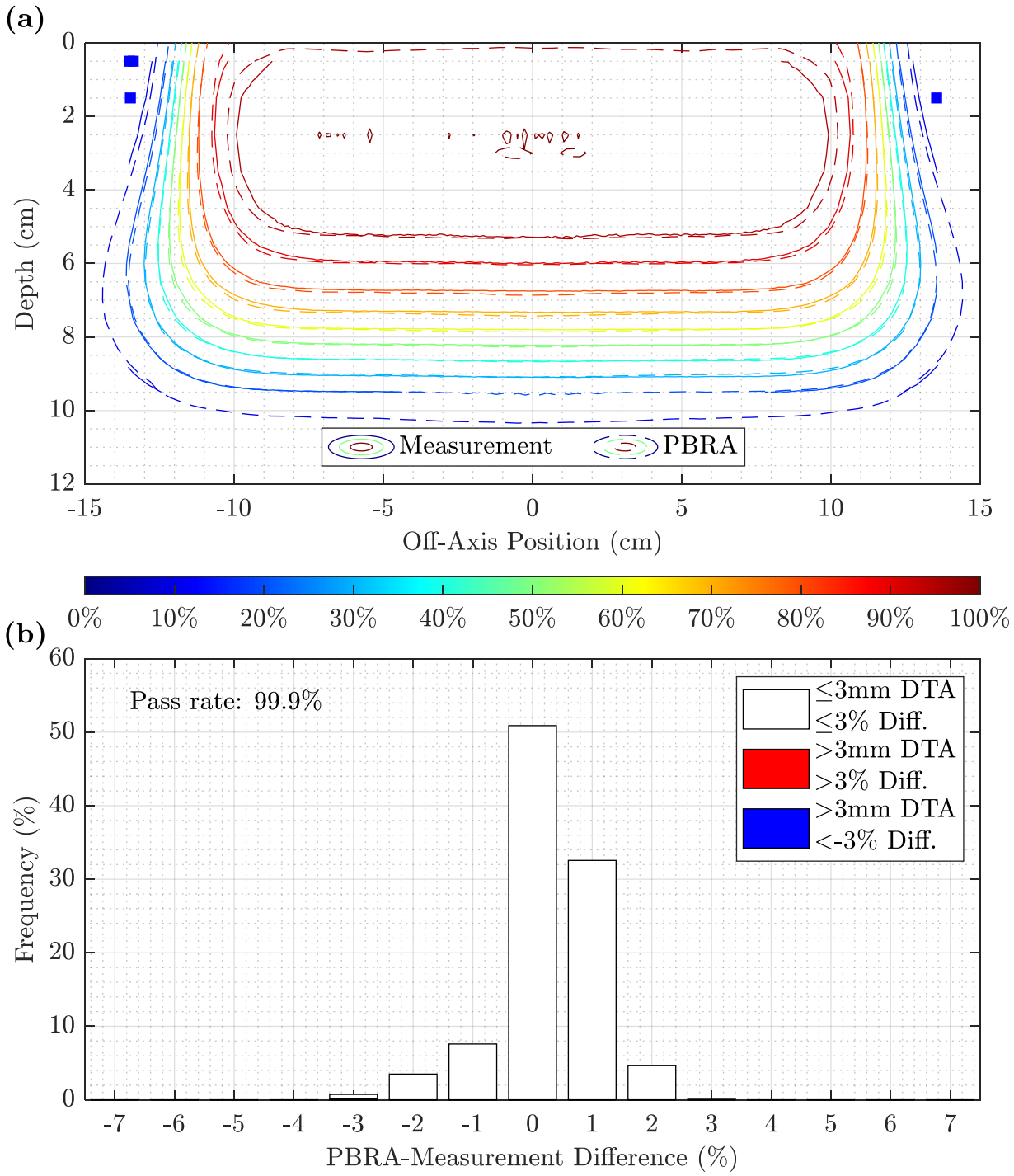

Figure A.10. Measurement and PBRA foam-only isodose comparison and difference histogram for 20 MeV at 110 cm SSD. The isodose contours in (a) compare the measured (solid) and PBRA-calculated (dashed) isodose distributions, and (b) contains the histogram of differences between measurement and PBRA calculations for foam-only at 20 MeV and 110 cm SSD. In both (a) and (b), points where the PBRA underpredicted the dose relative to measurement are shown in blue, while those where the PBRA overpredicted dose are plotted as red. The 3%/3mm DTA criteria yielded a passing rate of 99.9% for all points for this setup.

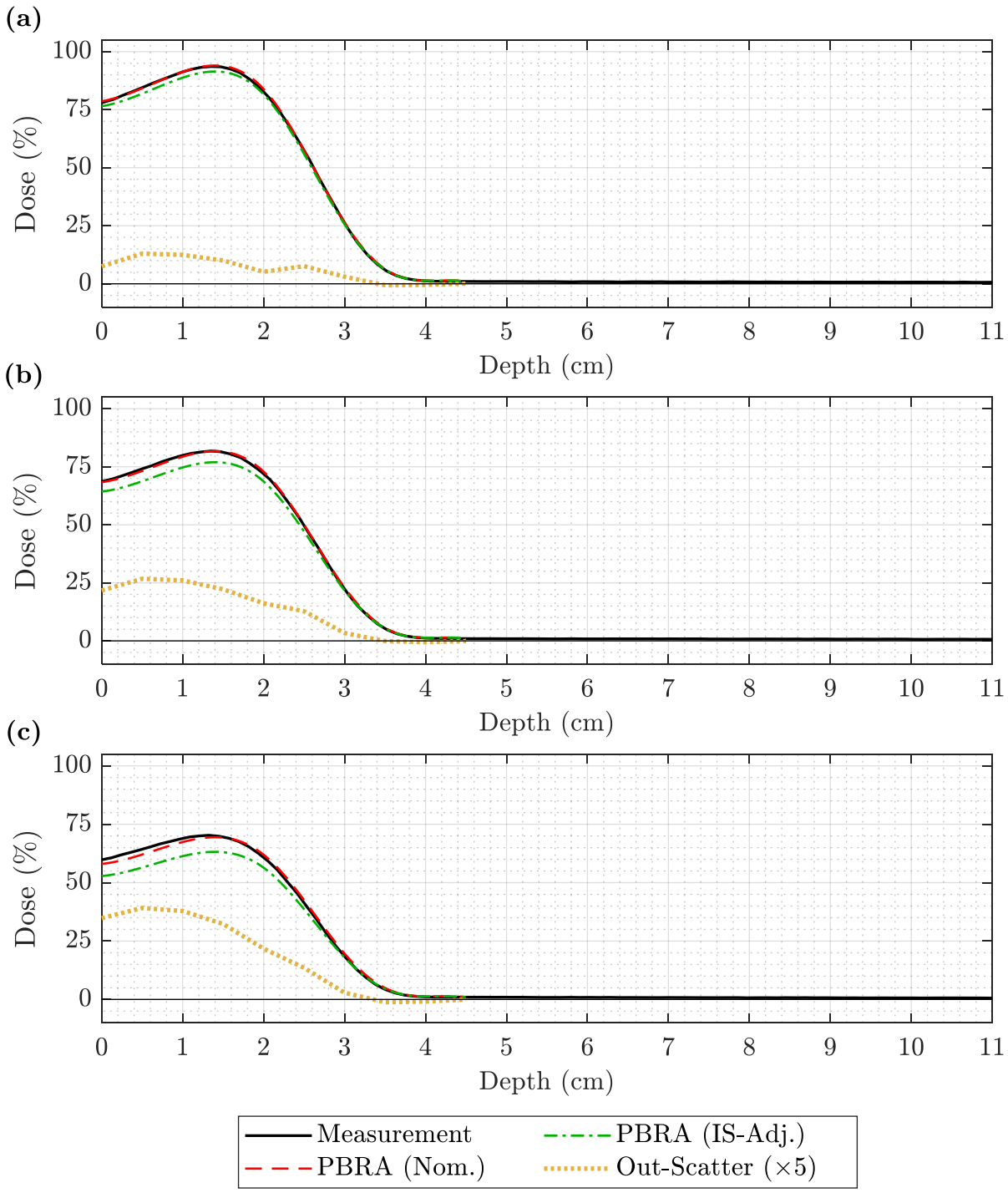

Figure A.11. PDD comparison of measurement, nominal PBRA, and in-scatter-adjusted PBRA calculations at 7 MeV and 105 cm SSD. Measurement (solid black) is compared to the nominal PBRA (dashed red) and PBRA corrected for in-scatter only (dashed-dotted green) for a 7 MeV beam at 105 cm SSD for (a) 0.158-cm, (b) 0.273-cm, and (c) 0.352-cm pins. The out-scatter estimation (dotted yellow) is the difference between measurement and the in-scatter-adjusted PBRA, plotted here with ×5 magnification for clarity.

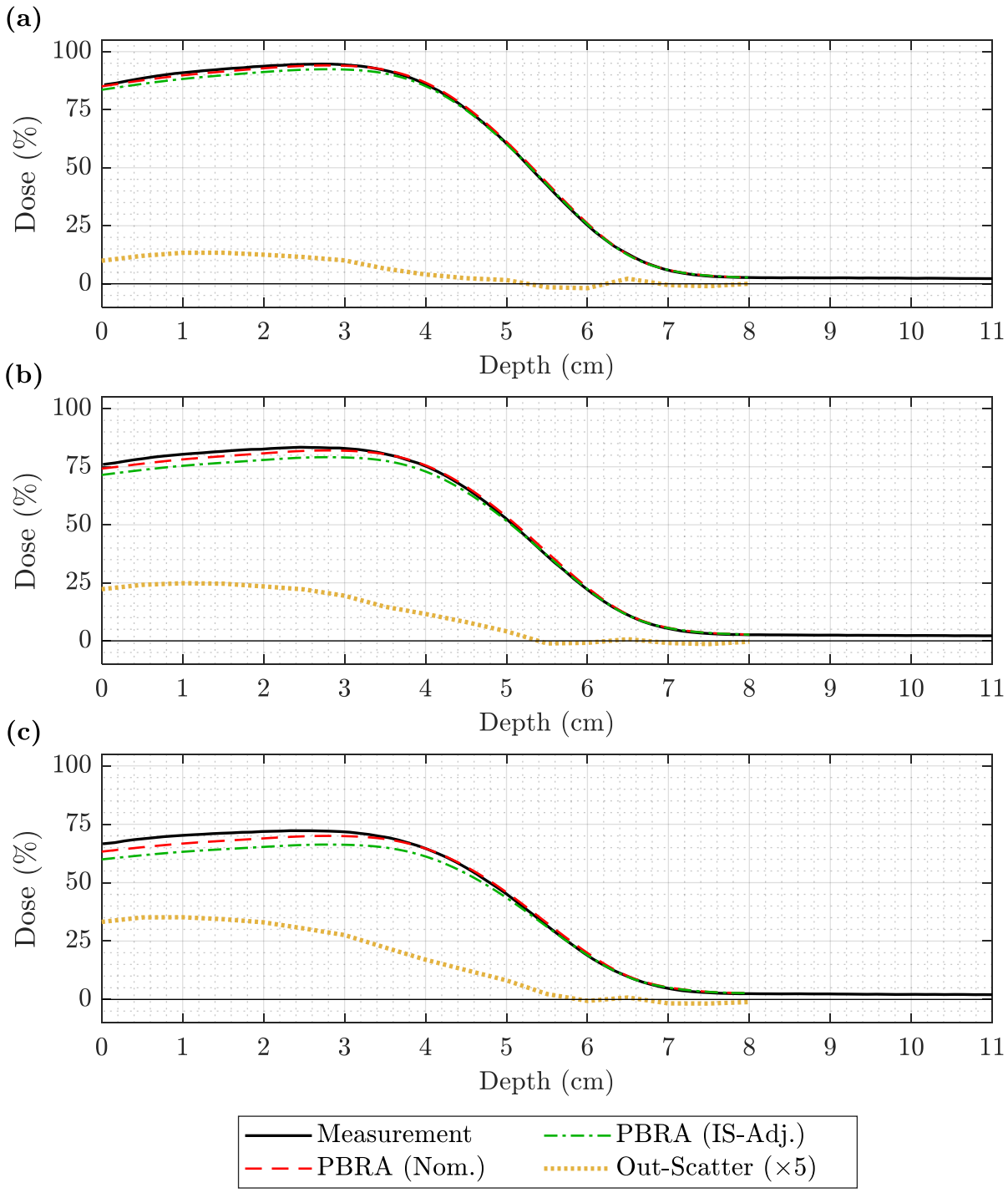

Figure A.12. PDD comparison of measurement, nominal PBRA, and in-scatter-adjusted PBRA calculations at 13 MeV and 105 cm SSD. Measurement (solid black) is compared to the nominal PBRA (dashed red) and PBRA corrected for in-scatter only (dashed-dotted green) for a 13 MeV beam at 105 cm SSD for (a) 0.158-cm, (b) 0.273-cm, and (c) 0.352-cm pins. The out-scatter estimation (dotted yellow) is the difference between measurement and the in-scatter-adjusted PBRA, plotted here with ×5 magnification for clarity.

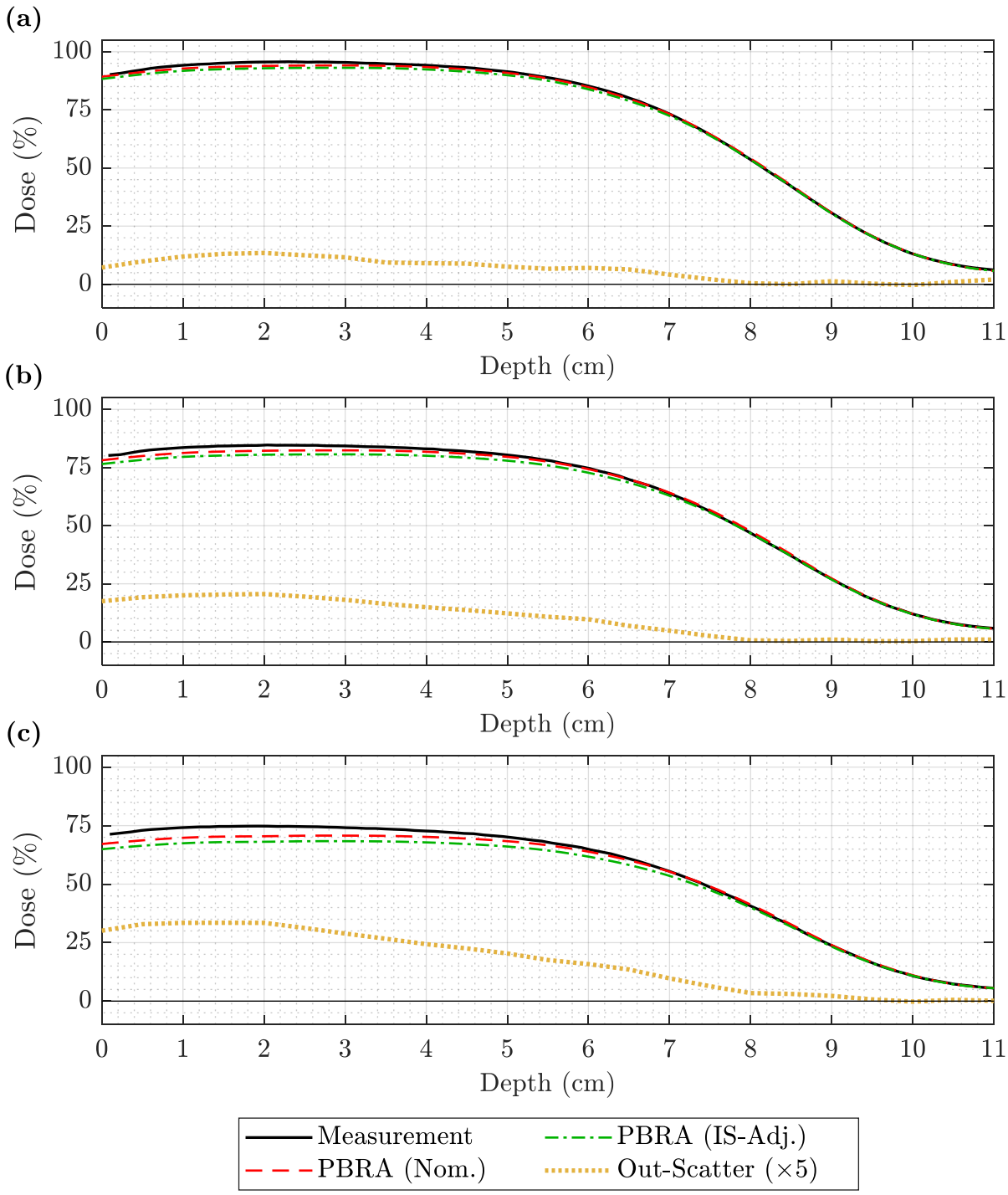

Figure A.13. PDD comparison of measurement, nominal PBRA, and in-scatter-adjusted PBRA calculations at 20 MeV and 105 cm SSD. Measurement (solid black) is compared to the nominal PBRA (dashed red) and PBRA corrected for in-scatter only (dashed-dotted green) for a 20 MeV beam at 105 cm SSD for (a) 0.158-cm, (b) 0.273-cm, and (c) 0.352-cm pins. The out-scatter estimation (dotted yellow) is the difference between measurement and the in-scatter-adjusted PBRA, plotted here with ×5 magnification for clarity.

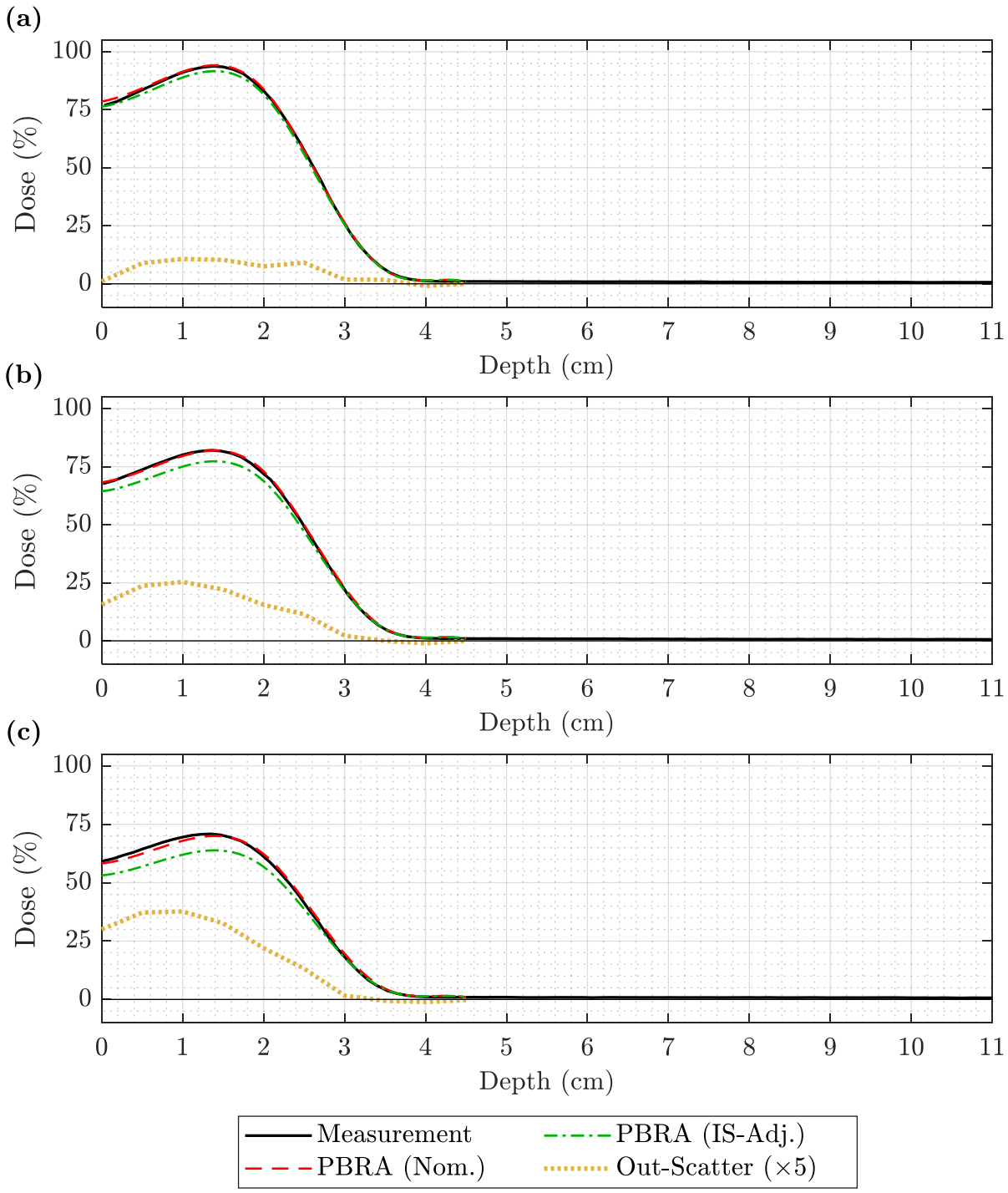

Figure A.14. PDD comparison of measurement, nominal PBRA, and in-scatter-adjusted PBRA calculations at 7 MeV and 110 cm SSD. Measurement (solid black) is compared to the nominal PBRA (dashed red) and PBRA corrected for in-scatter only (dashed-dotted green) for a 7 MeV beam at 110 cm SSD for (a) 0.158-cm, (b) 0.273-cm, and (c) 0.352-cm pins. The out-scatter estimation (dotted yellow) is the difference between measurement and the in-scatter-adjusted PBRA, plotted here with ×5 magnification for clarity.

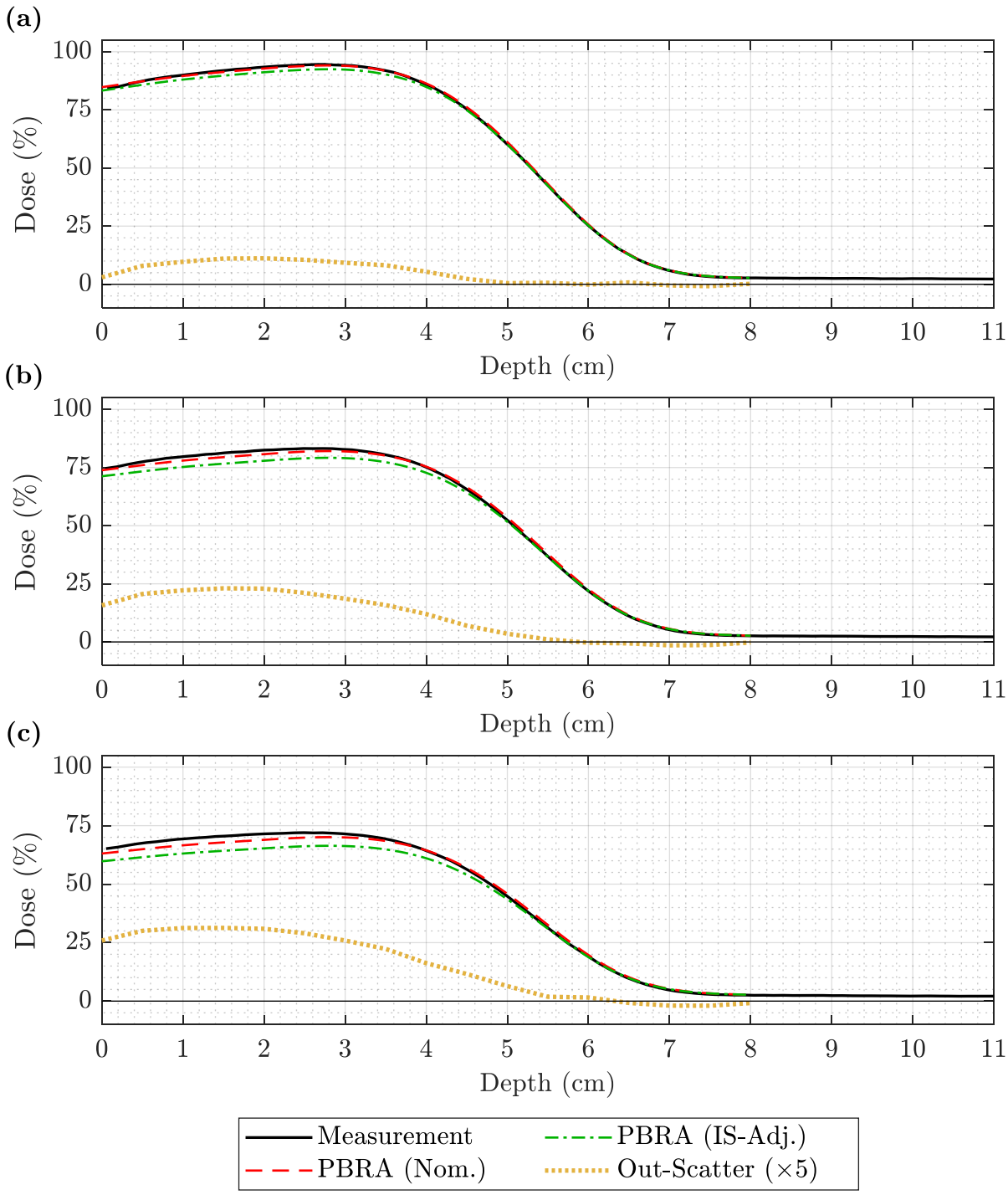

Figure A.15. PDD comparison of measurement, nominal PBRA, and in-scatter-adjusted PBRA calculations at 13 MeV and 110 cm SSD. Measurement (solid black) is compared to the nominal PBRA (dashed red) and PBRA corrected for in-scatter only (dashed-dotted green) for a 13 MeV beam at 110 cm SSD for (a) 0.158-cm, (b) 0.273-cm, and (c) 0.352-cm pins. The out-scatter estimation (dotted yellow) is the difference between measurement and the in-scatter-adjusted PBRA, plotted here with ×5 magnification for clarity.

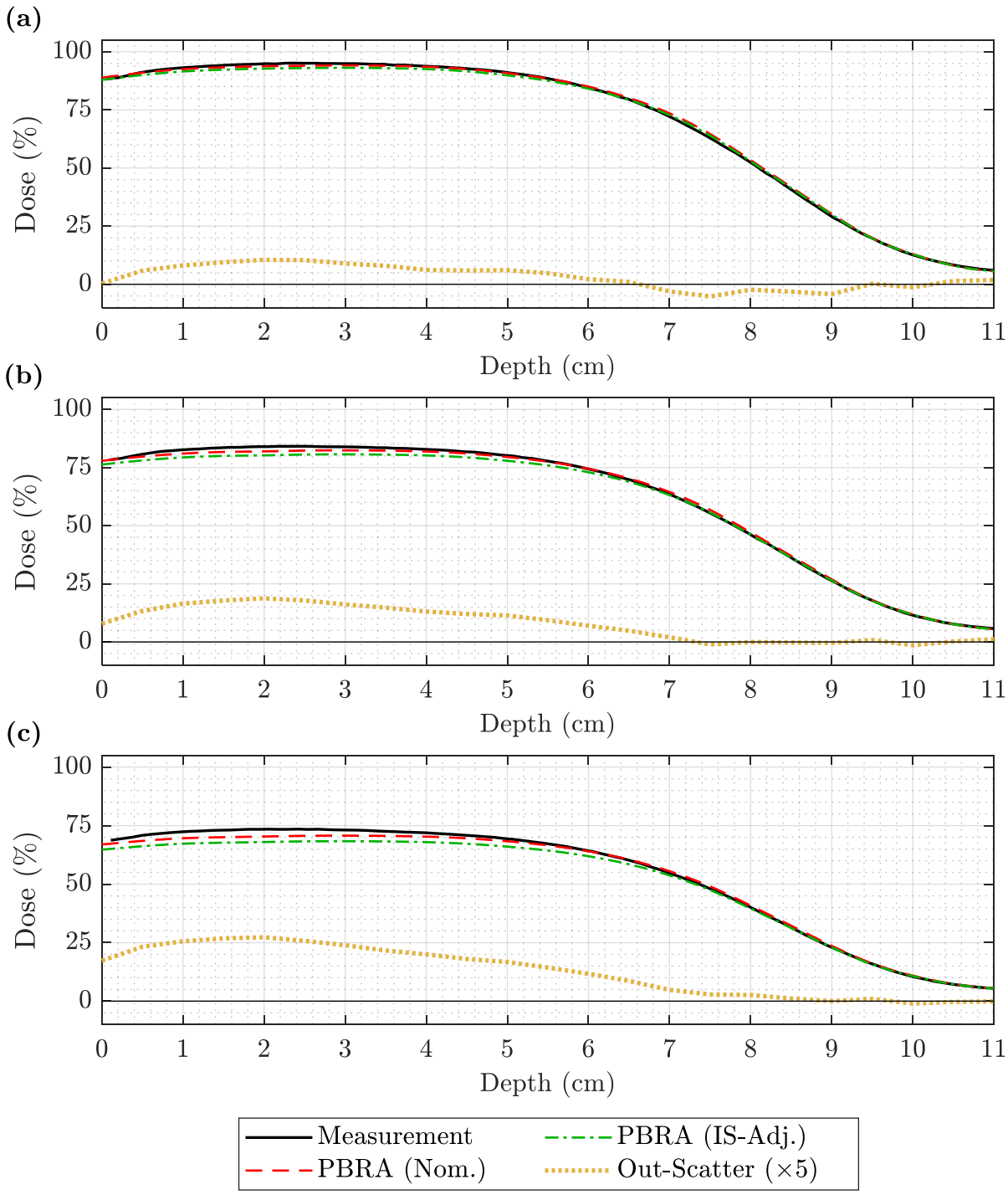

Figure A.16. PDD comparison of measurement, nominal PBRA, and in-scatter-adjusted PBRA calculations at 20 MeV and 110 cm SSD. Measurement (solid black) is compared to the nominal PBRA (dashed red) and PBRA corrected for in-scatter only (dashed-dotted green) for a 20 MeV beam at 110 cm SSD for (a) 0.158-cm, (b) 0.273-cm, and (c) 0.352-cm pins. The out-scatter estimation (dotted yellow) is the difference between measurement and the in-scatter-adjusted PBRA, plotted here with ×5 magnification for clarity.

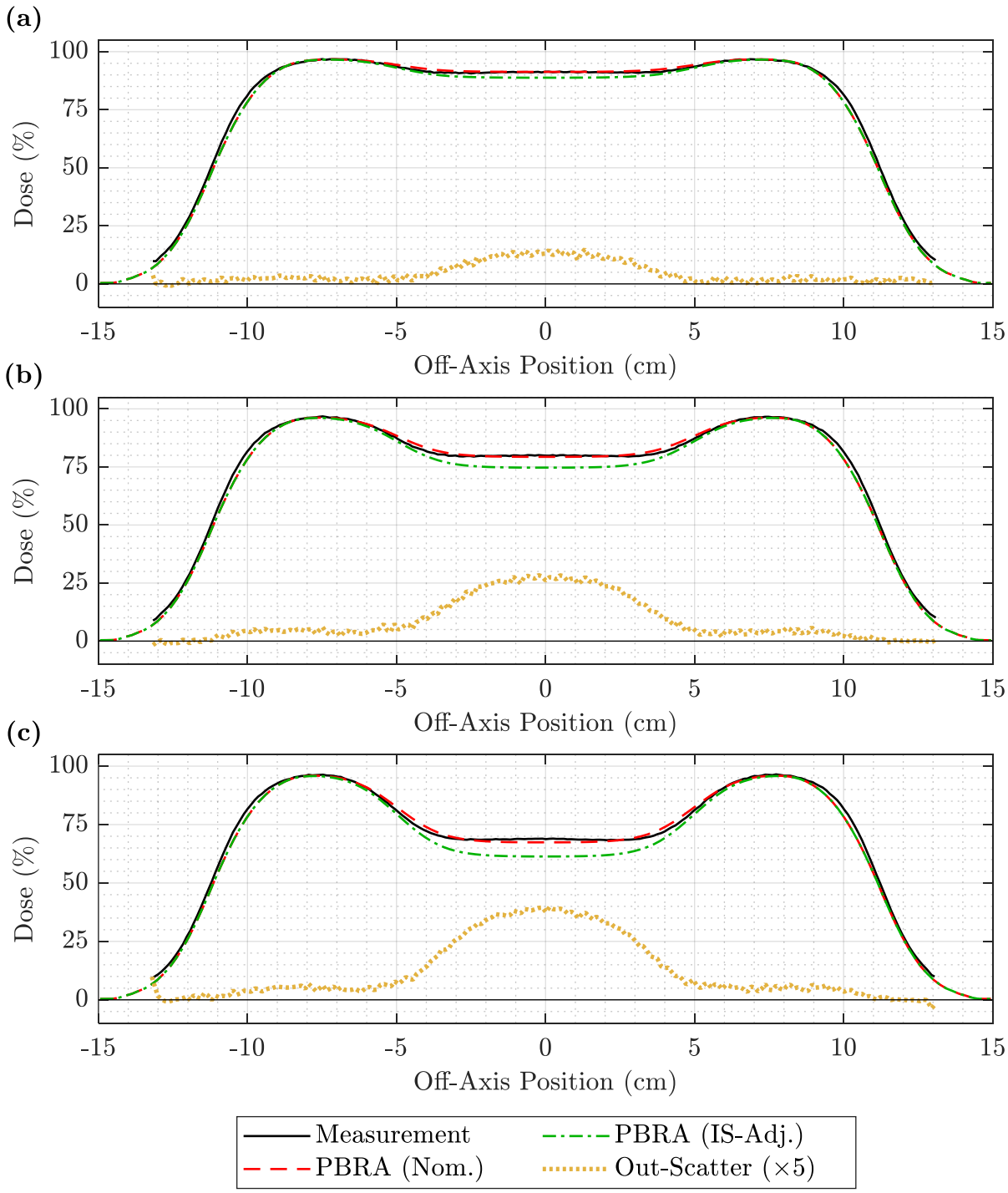

Figure A.17. Off-axis profile comparison of measurement, nominal PBRA, and in-scatter-adjusted PBRA calculations for the 7 MeV beam at 105 cm SSD and 1.0 cm depth. Measurement (solid black) is compared to the nominal PBRA (dashed red) and PBRA corrected for in-scatter only (dashed-dotted green) for a 7 MeV beam at 105 cm SSD for (a) 0.158-cm, (b) 0.273-cm, and (c) 0.352-cm pins at a depth of 1.0 cm. The out-scatter estimation (dotted yellow) is the difference between measurement and the in-scatter-adjusted PBRA with the off-axis weight adjustment of Equation 3.4, plotted here with ×5 magnification for clarity.

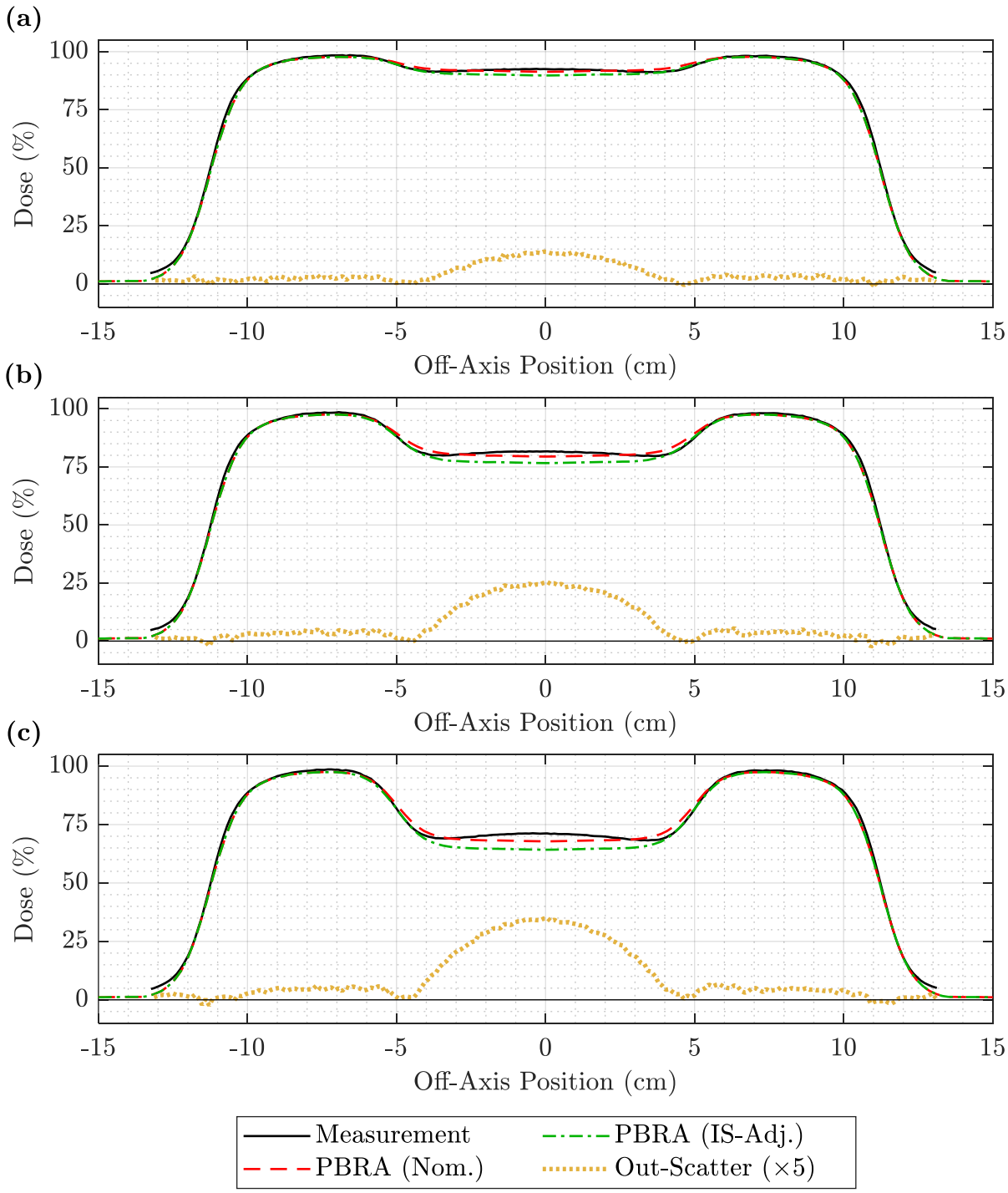

Figure A.18. Off-axis profile comparison of measurement, nominal PBRA, and in-scatter-adjusted PBRA calculations for the 13 MeV beam at 105 cm SSD and 1.5 cm depth. Measurement (solid black) is compared to the nominal PBRA (dashed red) and PBRA corrected for in-scatter only (dashed-dotted green) for a 13 MeV beam at 105 cm SSD for (a) 0.158-cm, (b) 0.273-cm, and (c) 0.352-cm pins at a depth of 1.5 cm. The out-scatter estimation (dotted yellow) is the difference between measurement and the in-scatter-adjusted PBRA with the off-axis weight adjustment of Equation 3.4, plotted here with ×5 magnification for clarity.

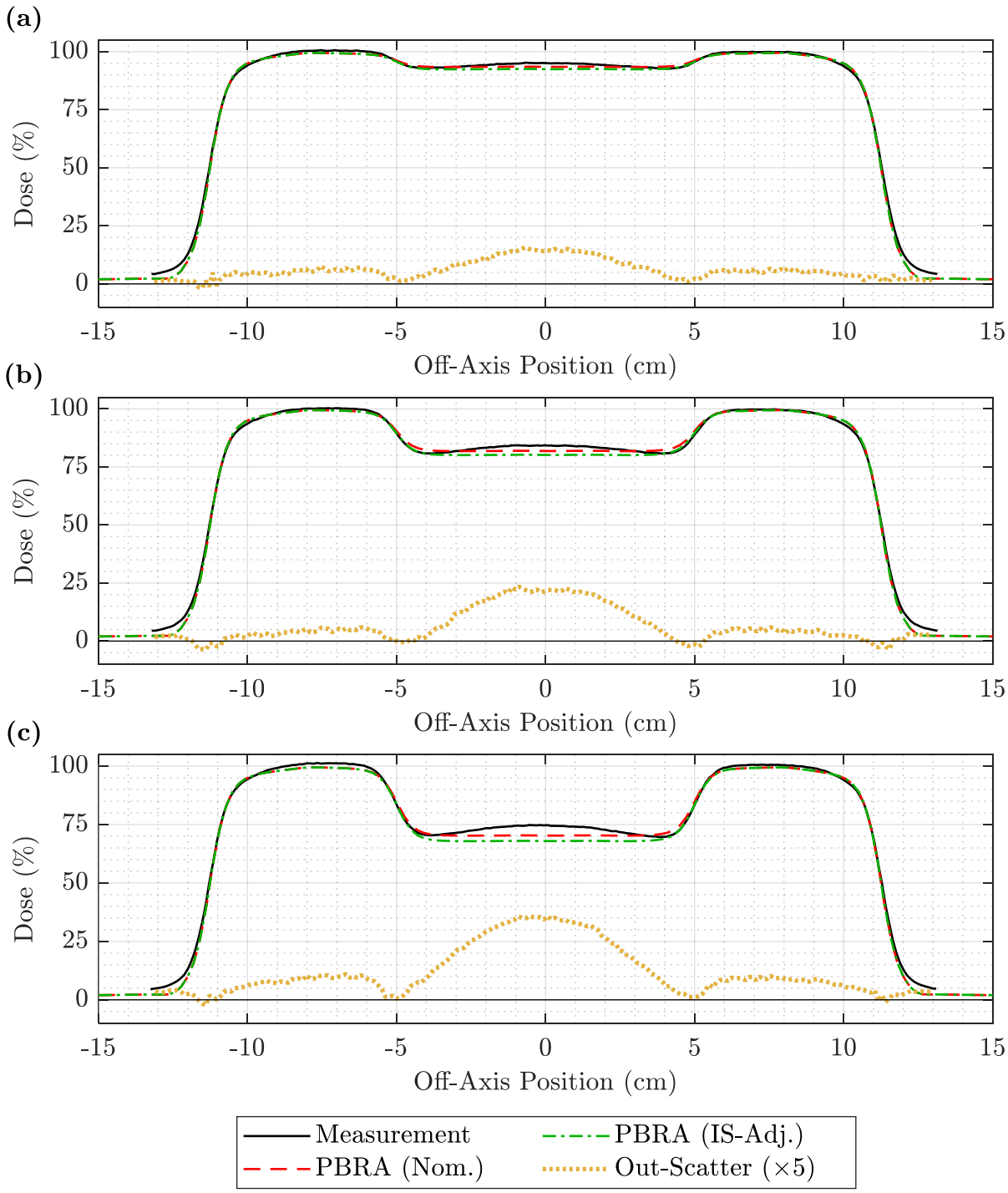

Figure A.19. Off-axis profile comparison of measurement, nominal PBRA, and in-scatter-adjusted PBRA calculations for the 20 MeV beam at 105 cm SSD and 1.5 cm depth. Measurement (solid black) is compared to the nominal PBRA (dashed red) and PBRA corrected for in-scatter only (dashed-dotted green) for a 20 MeV beam at 105 cm SSD for (a) 0.158-cm, (b) 0.273-cm, and (c) 0.352-cm pins at a depth of 1.5 cm. The out-scatter estimation (dotted yellow) is the difference between measurement and the in-scatter-adjusted PBRA with the off-axis weight adjustment of Equation 3.4, plotted here with ×5 magnification for clarity.

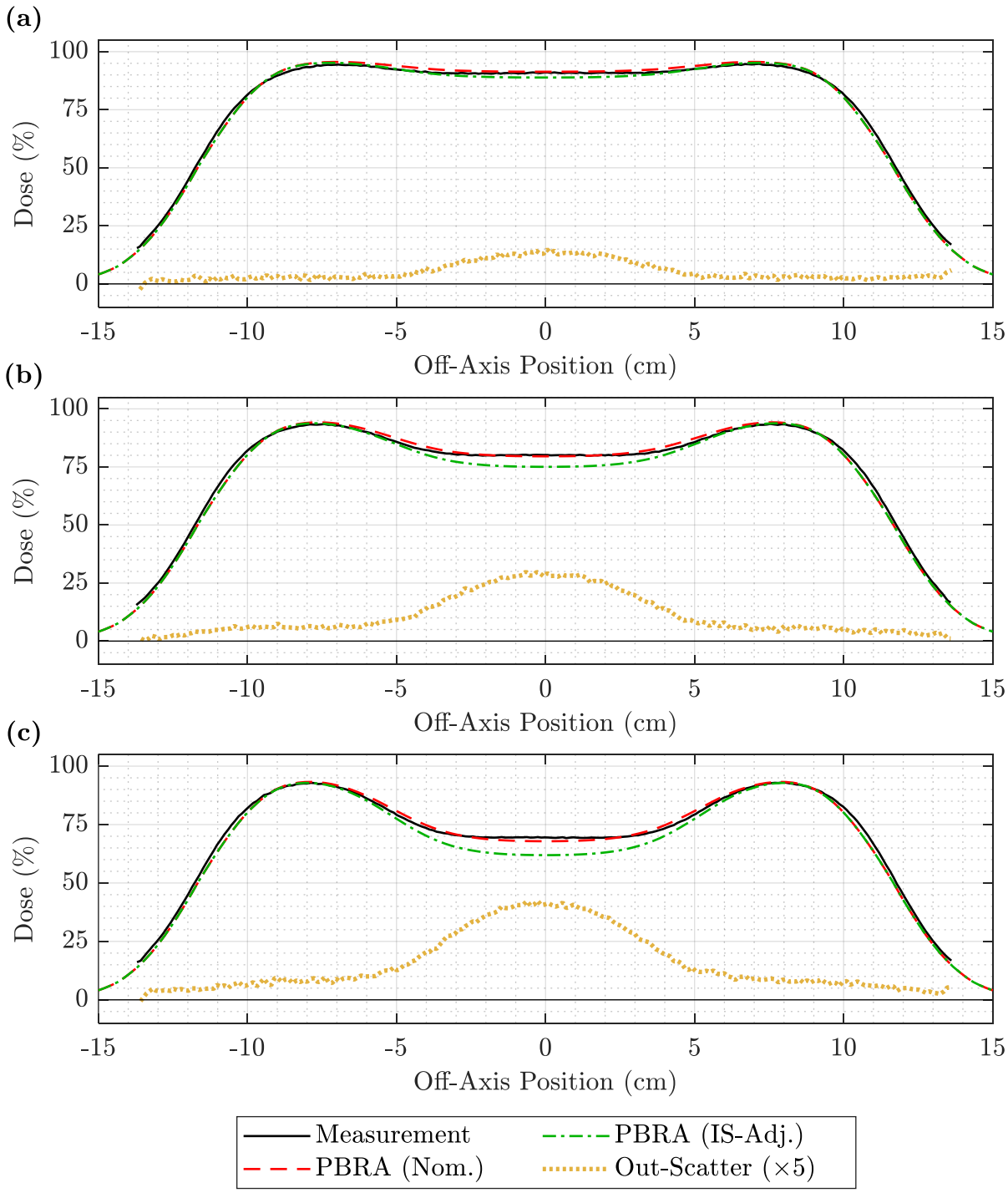

Figure A.20. Off-axis profile comparison of measurement, nominal PBRA, and in-scatter-adjusted PBRA calculations for the 7 MeV beam at 110 cm SSD and 1.0 cm depth. Measurement (solid black) is compared to the nominal PBRA (dashed red) and PBRA corrected for in-scatter only (dashed-dotted green) for a 7 MeV beam at 110 cm SSD for (a) 0.158-cm, (b) 0.273-cm, and (c) 0.352-cm pins at a depth of 1.0 cm. The out-scatter estimation (dotted yellow) is the difference between measurement and the in-scatter-adjusted PBRA with the off-axis weight adjustment of Equation 3.4, plotted here with ×5 magnification for clarity.

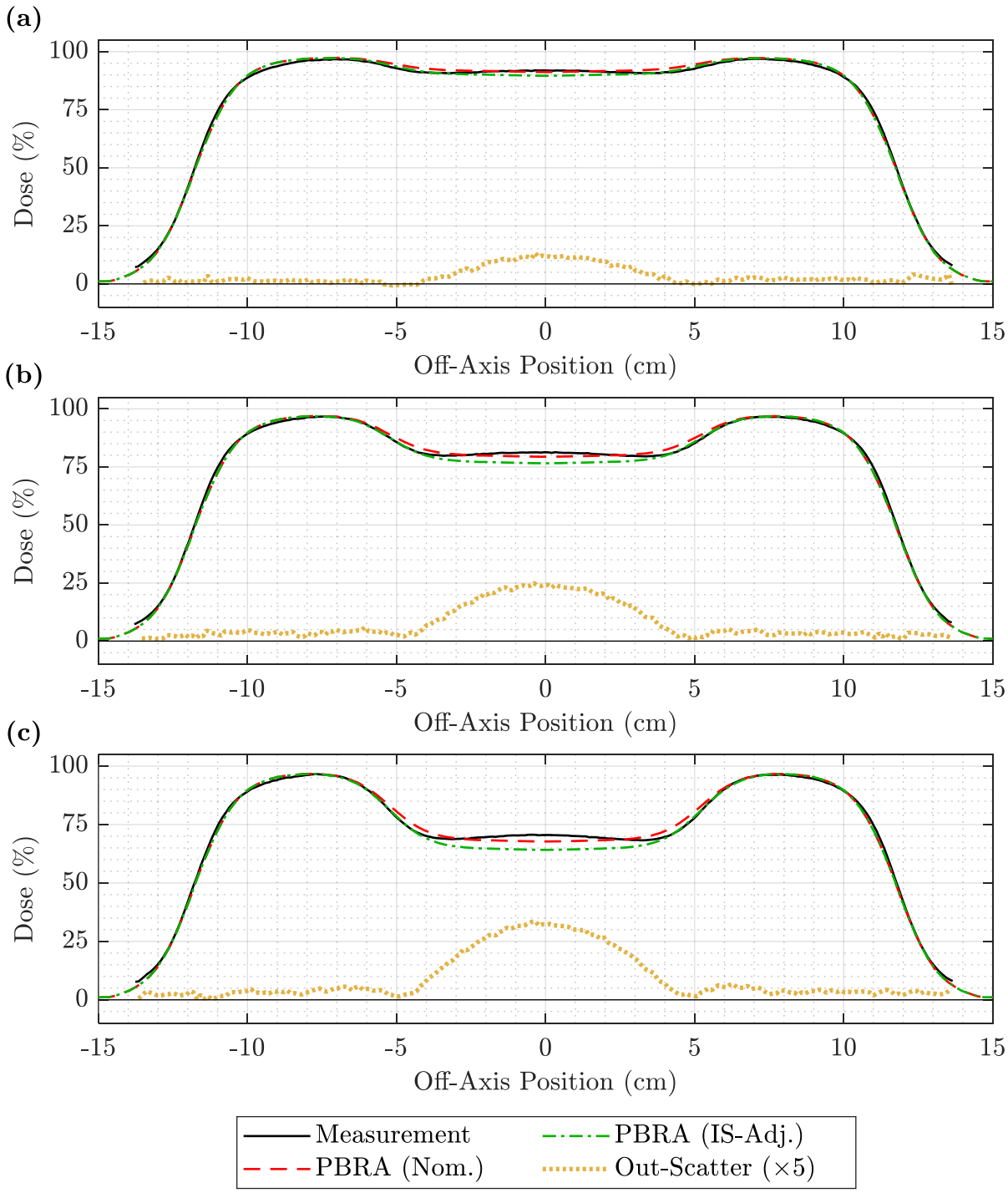

Figure A.21. Off-axis profile comparison of measurement, nominal PBRA, and in-scatter-adjusted PBRA calculations for the 13 MeV beam at 110 cm SSD and 1.5 cm depth. Measurement (solid black) is compared to the nominal PBRA (dashed red) and PBRA corrected for in-scatter only (dashed-dotted green) for a 13 MeV beam at 110 cm SSD for (a) 0.158-cm, (b) 0.273-cm, and (c) 0.352-cm pins at a depth of 1.5 cm. The out-scatter estimation (dotted yellow) is the difference between measurement and the in-scatter-adjusted PBRA with the off-axis weight adjustment of Equation 3.4, plotted here with ×5 magnification for clarity.

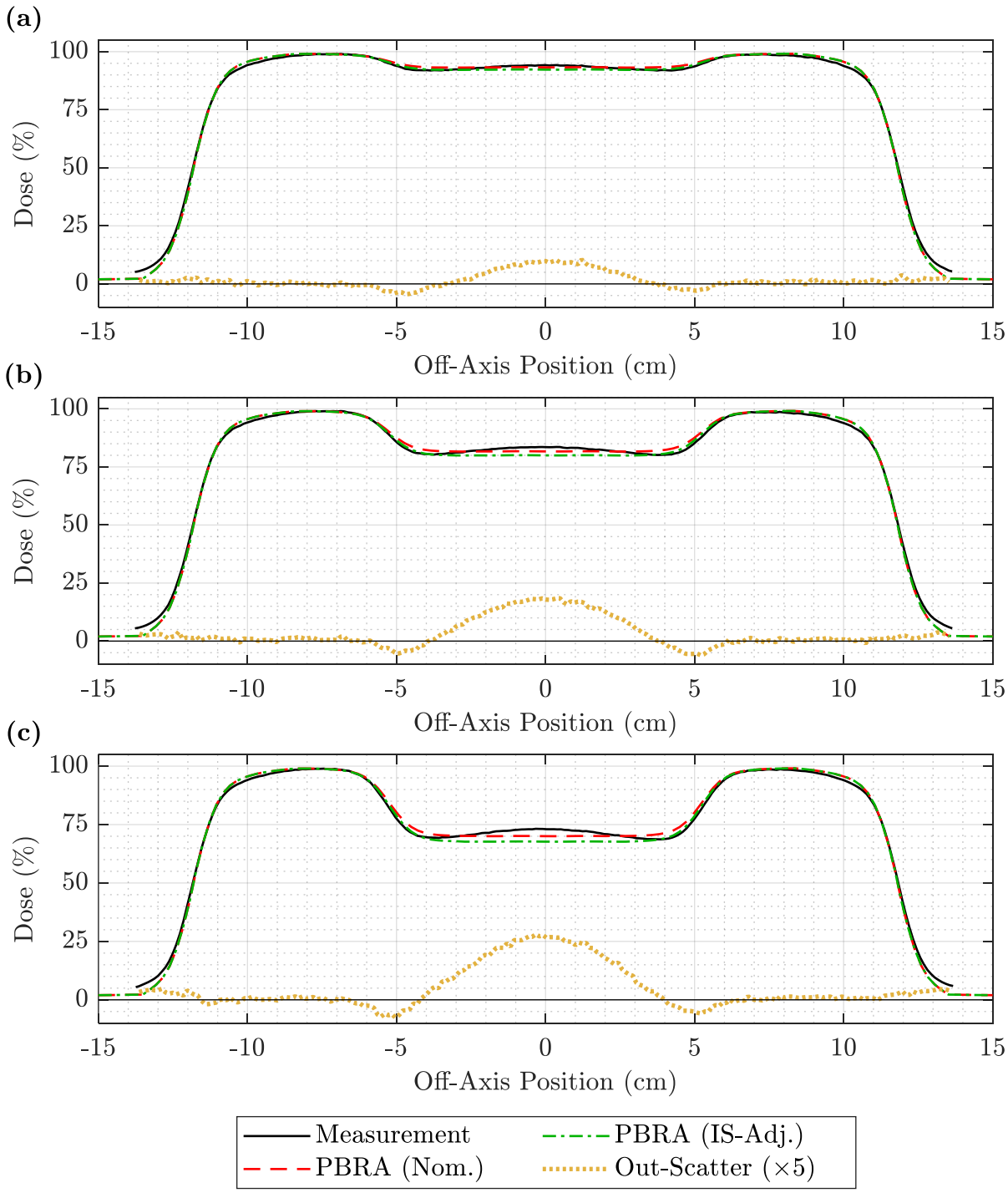

Figure A.22. Off-axis profile comparison of measurement, nominal PBRA, and in-scatter-adjusted PBRA calculations for the 20 MeV beam at 110 cm SSD and 1.5 cm depth. Measurement (solid black) is compared to the nominal PBRA (dashed red) and PBRA corrected for in-scatter only (dashed-dotted green) for a 20 MeV beam at 110 cm SSD for (a) 0.158-cm, (b) 0.273-cm, and (c) 0.352-cm pins at a depth of 1.5 cm. The out-scatter estimation (dotted yellow) is the difference between measurement and the in-scatter-adjusted PBRA with the off-axis weight adjustment of Equation 3.4, plotted here with ×5 magnification for clarity.

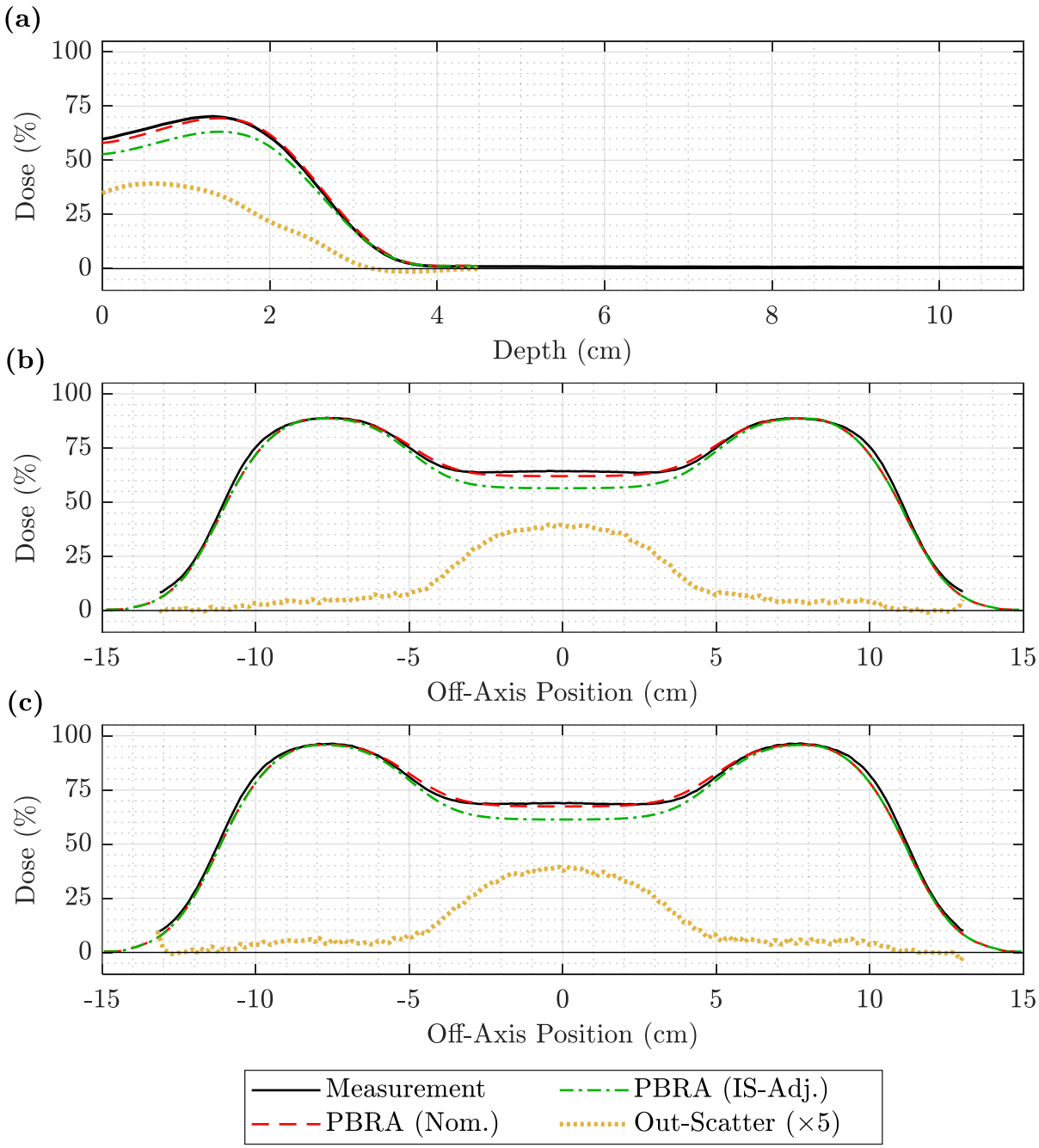

Figure A.23. PDD and off-axis profiles for the 7 MeV beam at 105 cm SSD and 0.352-cm pins. The PDD in (a) and off-axis profiles at depths of (b) 0.5, (c) 1.0, (d) 1.5, and (e) 2.0 cm compare measurement (solid black) to the nominal PBRA (dashed red) and PBRA corrected for in-scatter only (dashed-dotted green) for a 7 MeV beam at 105 cm SSD for 0.352-cm-diameter pins. The out-scatter estimation (dotted yellow) is the difference between measurement and the in-scatter-adjusted PBRA with the off-axis weight adjustment of Equation 3.4, plotted here with ×5 magnification for clarity.

(figure cont'd.)

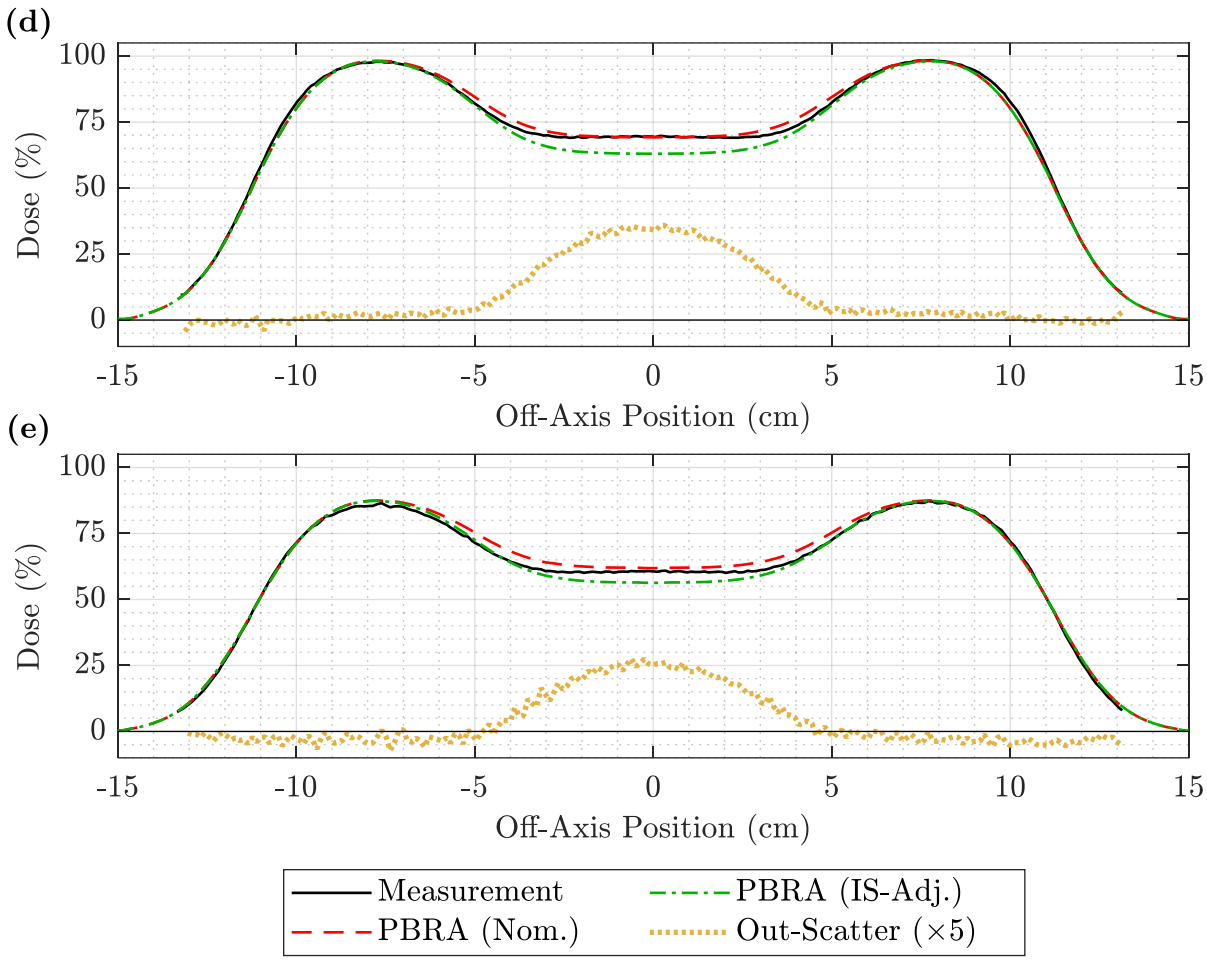
(d)
100
75
50
25
0
Dose (%)
-15
-10
-5
0
5
10
15
Off-Axis Position (cm)
(e)
100
75
50
25
0
Dose (%)
-15
-10
-5
0
5
10
15
Off-Axis Position (cm)
Measurement
PBRA (IS-Adj.)
PBRA (Nom.)
Out-Scatter (×5)

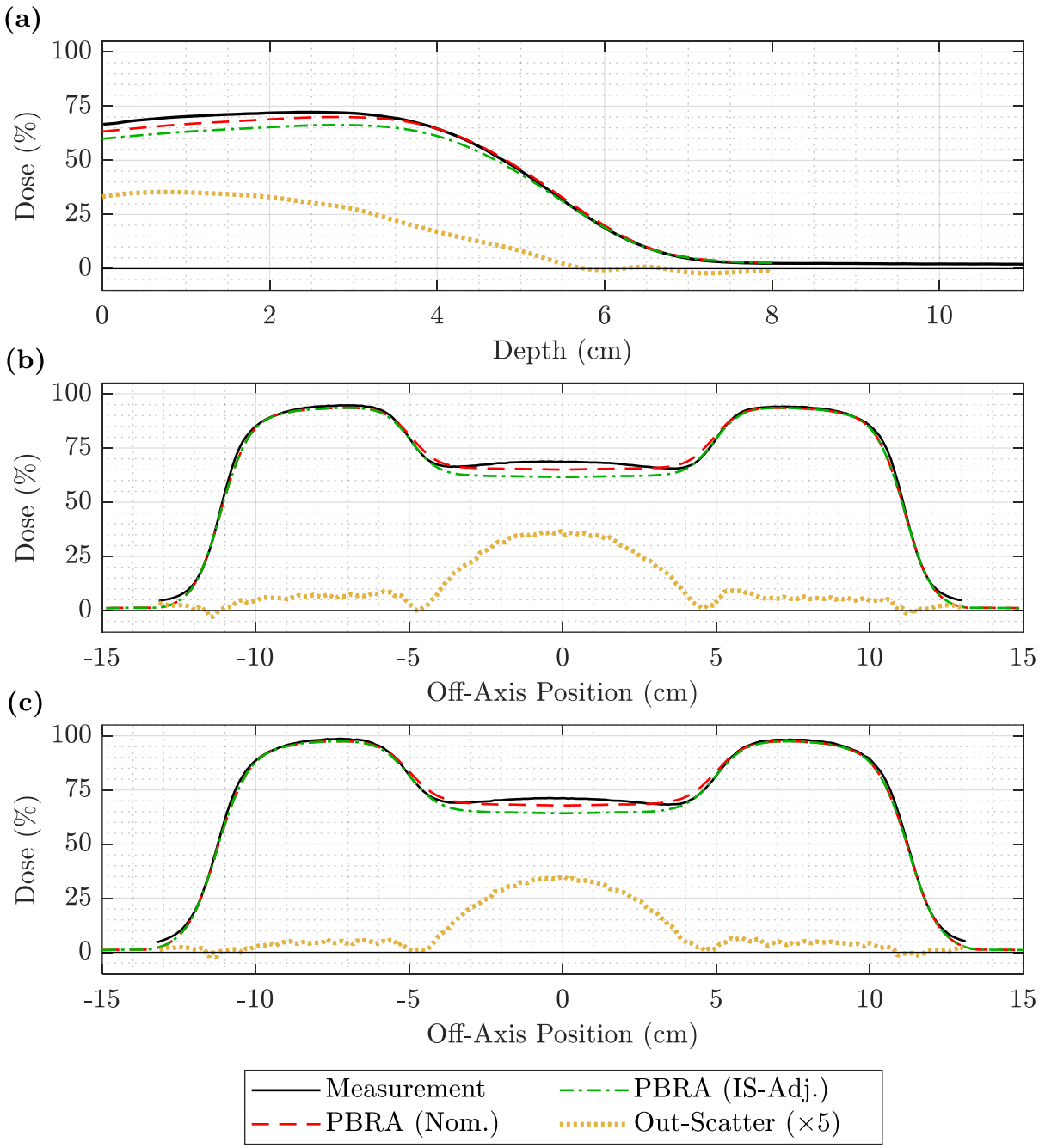

Figure A.24. PDD and off-axis profiles for the 13 MeV beam at 105 cm SSD and 0.352-cm pins. The (a) PDD and off-axis profiles at depths of (b) 0.5, (c) 1.5, (d) 3.0, (e) 3.5, and (f) 4.0 cm compare measurement (solid black) to the nominal PBRA (dashed red) and PBRA corrected for in-scatter only (dashed-dotted green) for a 13 MeV beam at 105 cm SSD for 0.352-cm-diameter pins. The out-scatter estimation (dotted yellow) is the difference between measurement and the in-scatter-adjusted PBRA with the off-axis weight adjustment of Equation 3.4, plotted here with ×5 magnification for clarity.

(figure cont'd.)

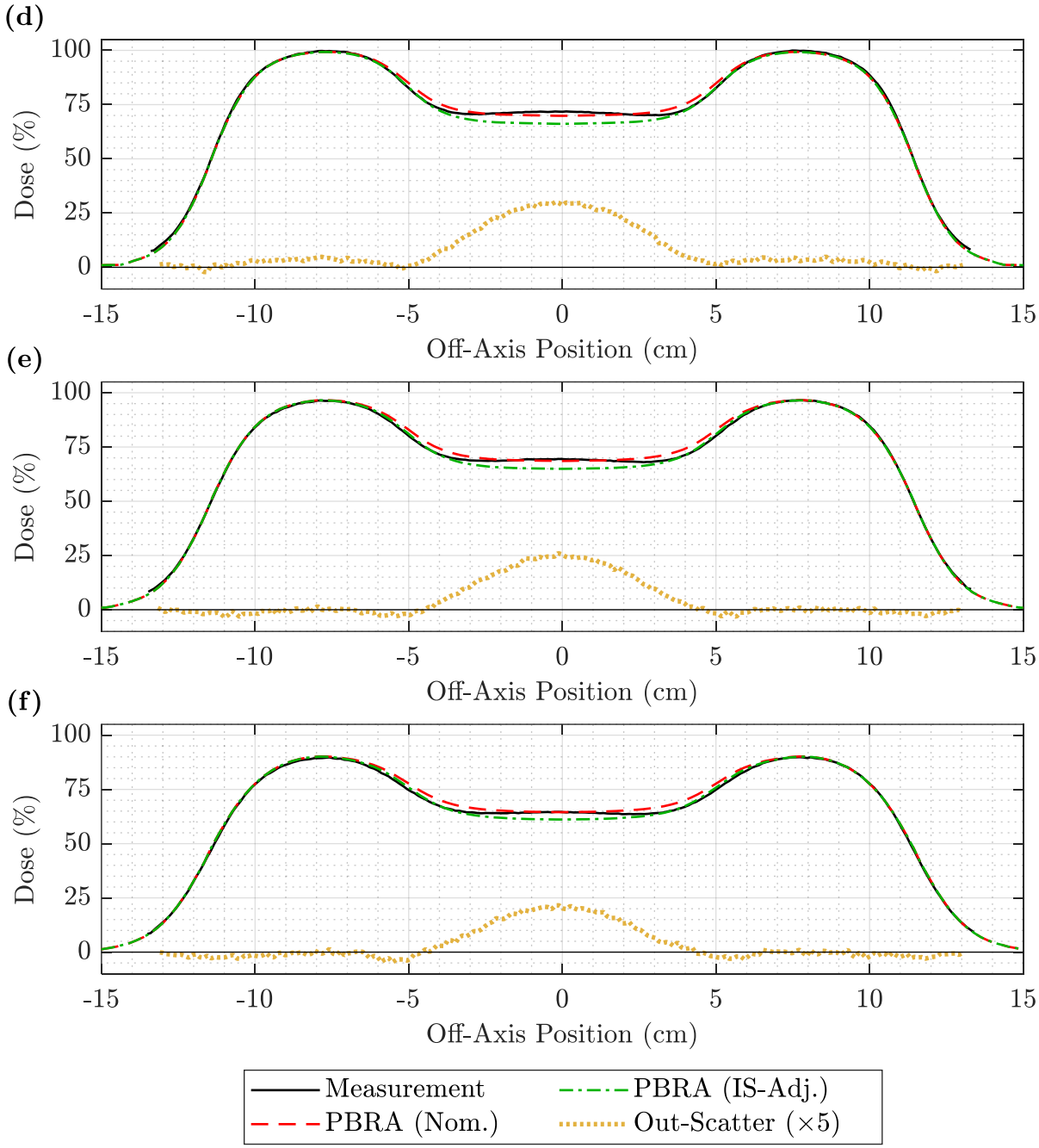
(d)
100
75
50
25
0
Dose (%)
-15
-10
-5
0
5
10
15
Off-Axis Position (cm)
(e)
100
75
50
25
0
Dose (%)
-15
-10
-5
0
5
10
15
Off-Axis Position (cm)
(f)
100
75
50
25
0
Dose (%)
-15
-10
-5
0
5
10
15
Off-Axis Position (cm)
Measurement
PBRA (IS-Adj.)
PBRA (Nom.)
Out-Scatter (×5)

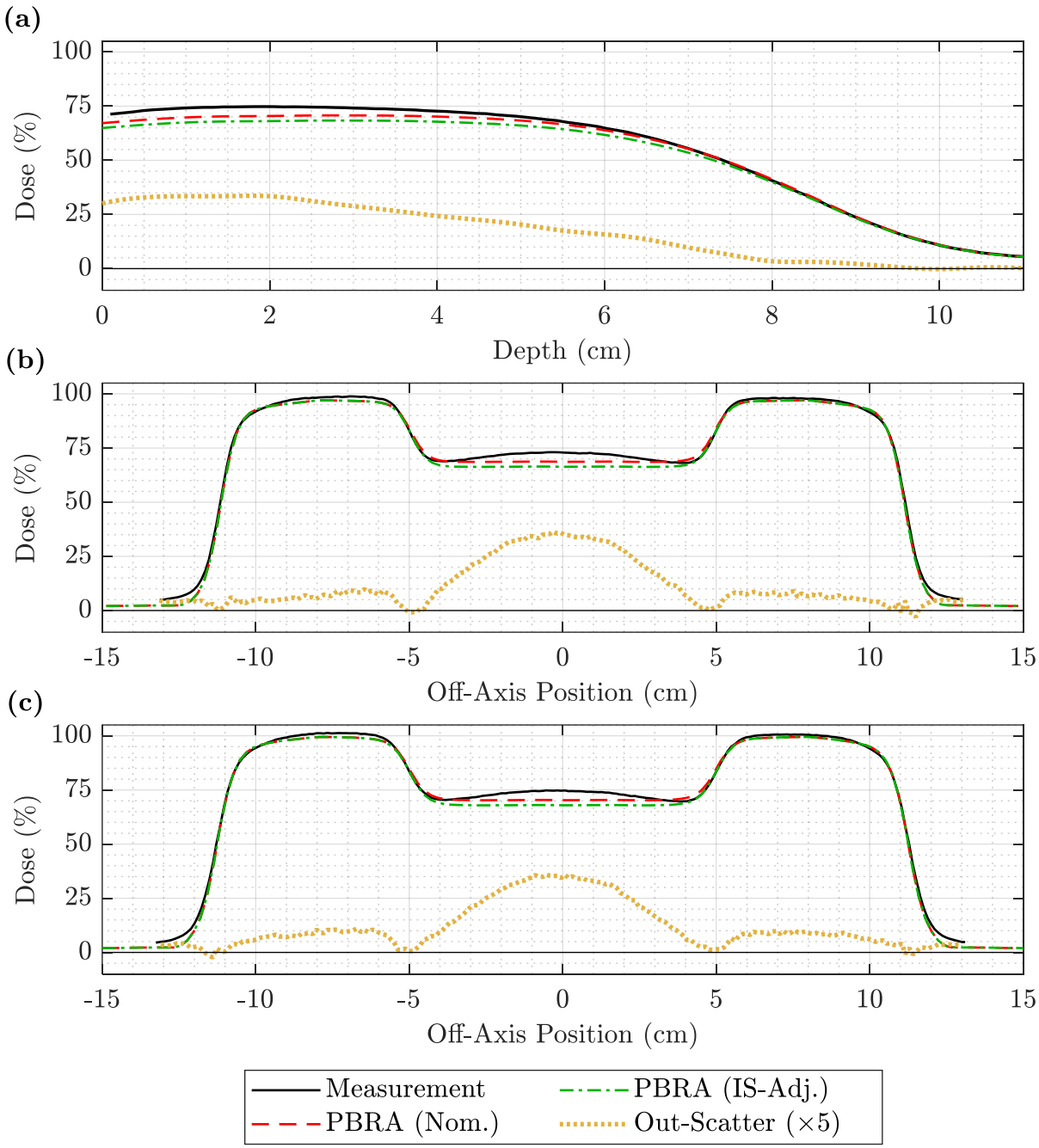

Figure A.25. PDD and off-axis profiles for the 20 MeV beam at 105 cm SSD and 0.352-cm pins. The (a) PDD and off-axis profiles at depths of (b) 0.5, (c) 1.5, (d) 3.5, (e) 5.0, and (f) 6.0 cm compare measurement (solid black) to the nominal PBRA (dashed red) and PBRA corrected for in-scatter only (dashed-dotted green) for a 20 MeV beam at 105 cm SSD for 0.352-cm-diameter pins. The out-scatter estimation (dotted yellow) is the difference between measurement and the in-scatter-adjusted PBRA with the off-axis weight adjustment of Equation 3.4, plotted here with ×5 magnification for clarity.

(figure cont'd.)

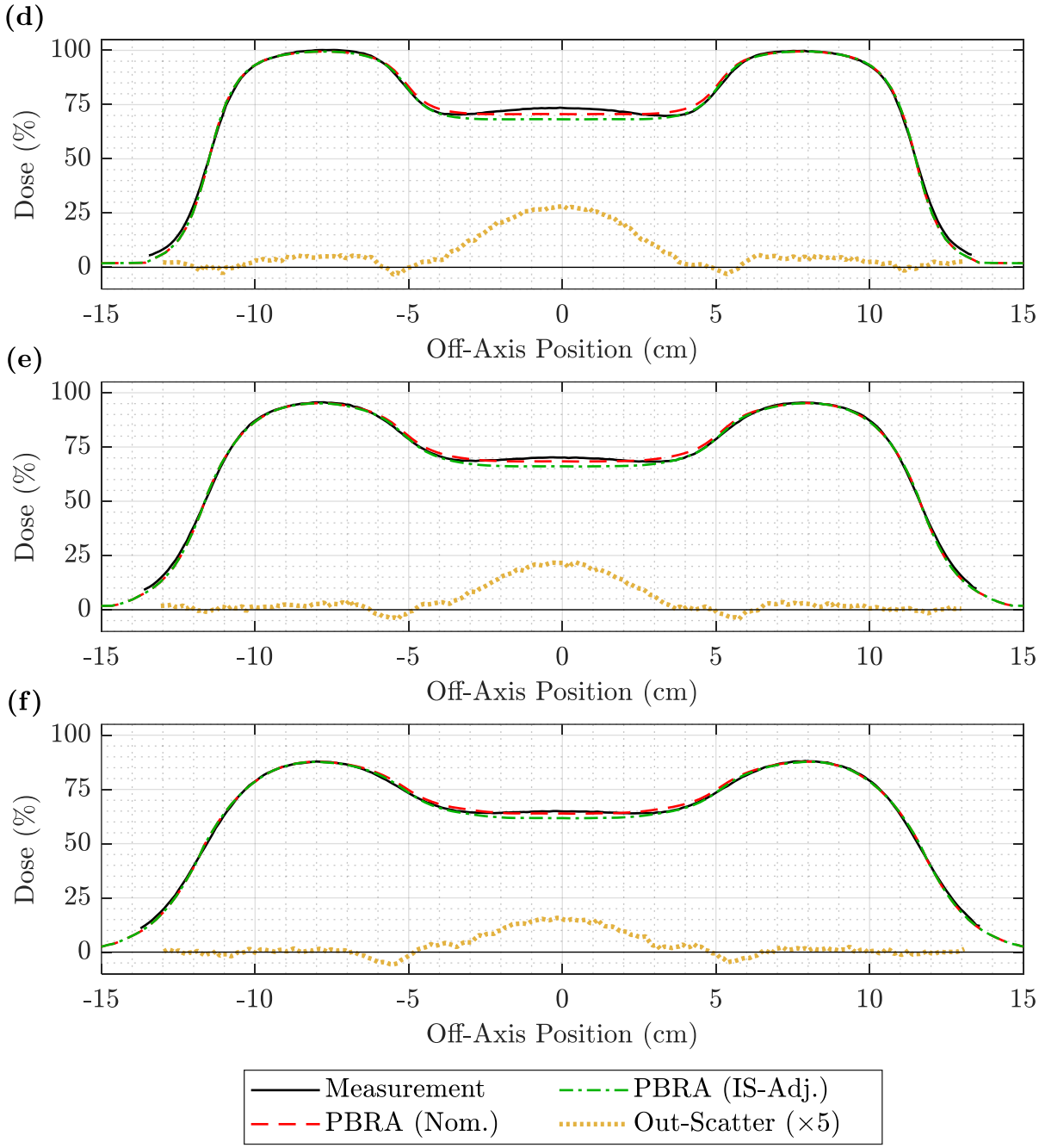
(d)
Dose (%)
100
75
50
25
0
-15
-10
-5
0
5
10
15
Off-Axis Position (cm)
(e)
Dose (%)
Off-Axis Position (cm)
(f)
Dose (%)
Off-Axis Position (cm)
Measurement
PBRA (IS-Adj.)
PBRA (Nom.)
Out-Scatter (×5)

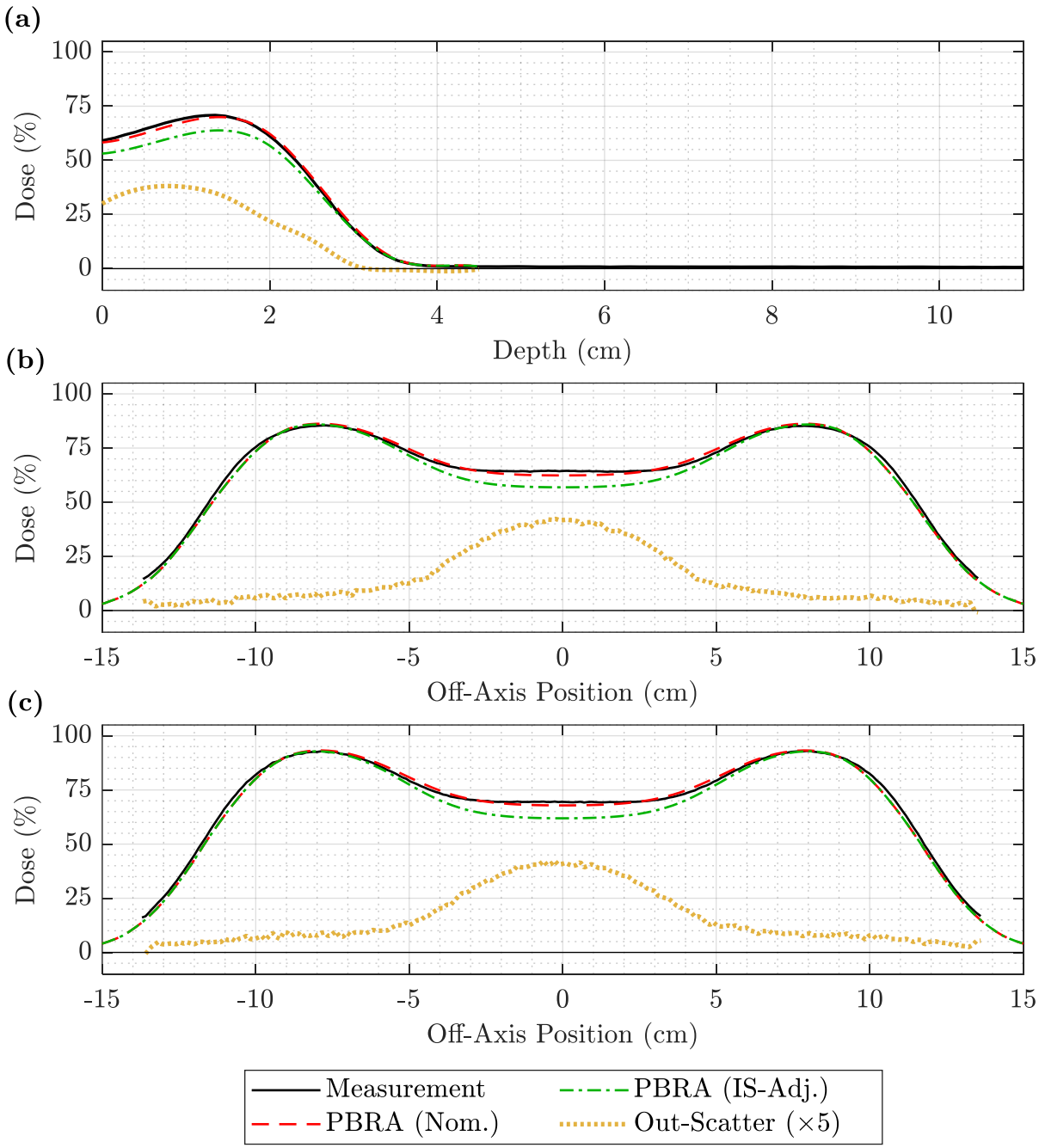

Figure A.26. PDD and off-axis profiles for the 7 MeV beam at 110 cm SSD and 0.352-cm pins. The PDD in (a) and off-axis profiles at depths of (b) 0.5, (c) 1.0, (d) 1.5, and (e) 2.0 cm compare measurement (solid black) to the nominal PBRA (dashed red) and PBRA corrected for in-scatter only (dashed-dotted green) for a 7 MeV beam at 110 cm SSD for 0.352-cm-diameter pins. The out-scatter estimation (dotted yellow) is the difference between measurement and the in-scatter-adjusted PBRA with the off-axis weight adjustment of Equation 3.4, plotted here with ×5 magnification for clarity.

(figure cont'd.)

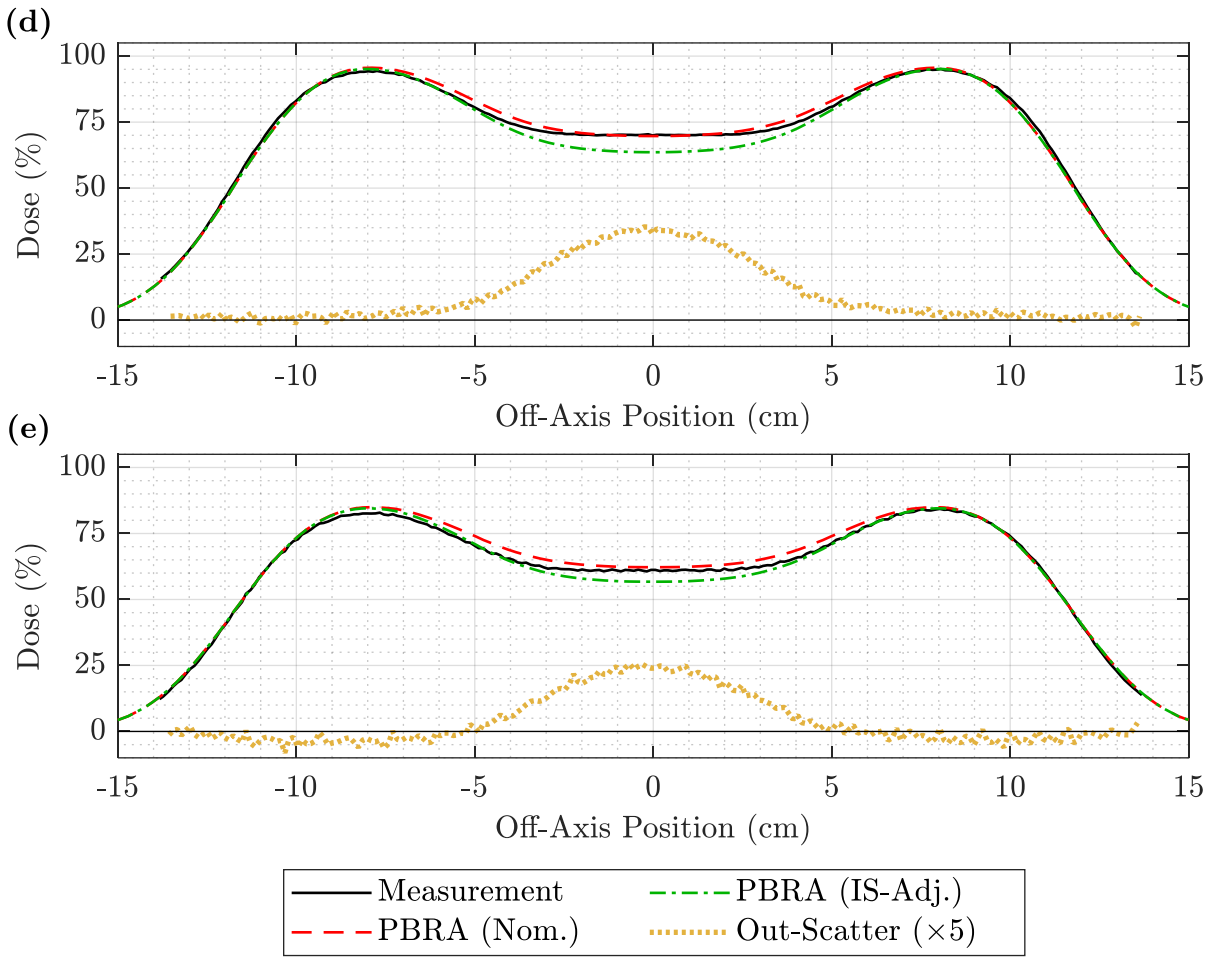
(d)
100
75
50
25
0
Dose (%)
-15
-10
-5
0
5
10
15
Off-Axis Position (cm)
(e)
100
75
50
25
0
Dose (%)
-15
-10
-5
0
5
10
15
Off-Axis Position (cm)
Measurement
PBRA (IS-Adj.)
PBRA (Nom.)
Out-Scatter (×5)

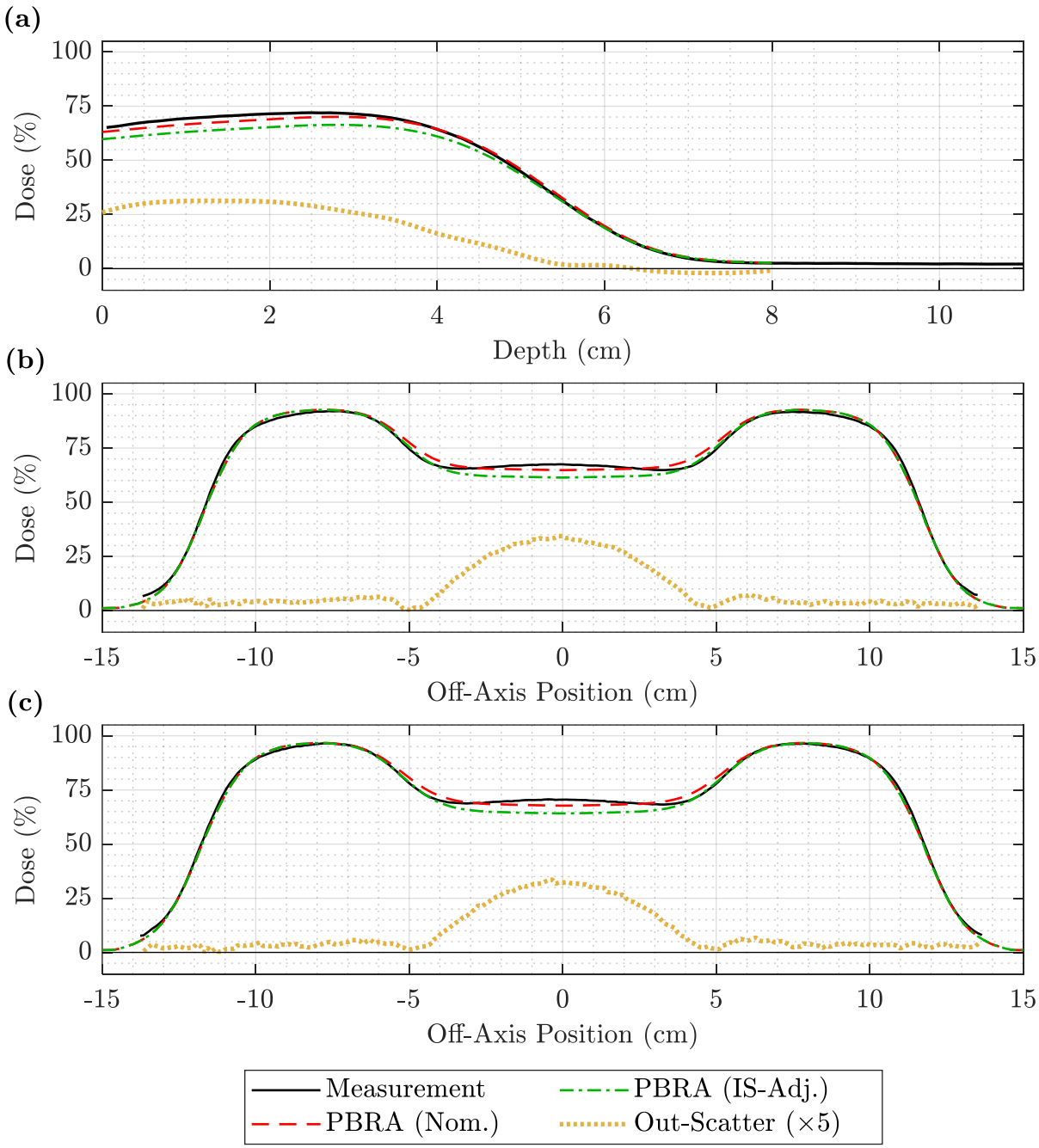

Figure A.27. PDD and off-axis profiles for the 13 MeV beam at 110 cm SSD and 0.352-cm pins. The (a) PDD and off-axis profiles at depths of (b) 0.5, (c) 1.5, (d) 3.0, (e) 3.5, and (f) 4.0 cm compare measurement (solid black) to the nominal PBRA (dashed red) and PBRA corrected for in-scatter only (dashed-dotted green) for a 13 MeV beam at 110 cm SSD for 0.352-cm-diameter pins. The out-scatter estimation (dotted yellow) is the difference between measurement and the in-scatter-adjusted PBRA with the off-axis weight adjustment of Equation 3.4, plotted here with ×5 magnification for clarity.

(figure cont'd.)

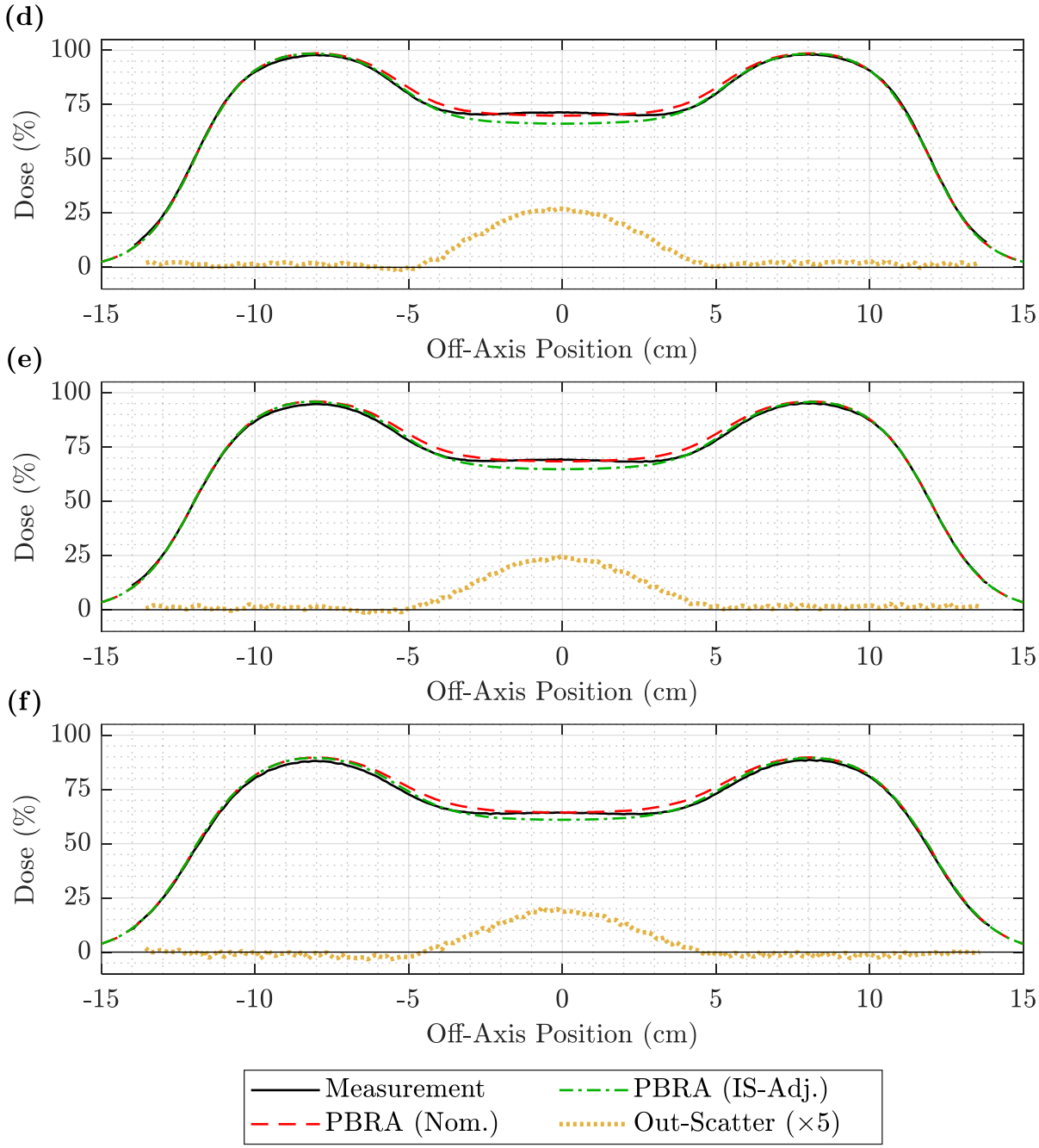
(d)
100
75
50
25
0
Dose (%)
-15
-10
-5
0
5
10
15
Off-Axis Position (cm)
(e)
100
75
50
25
0
Dose (%)
-15
-10
-5
0
5
10
15
Off-Axis Position (cm)
(f)
100
75
50
25
0
Dose (%)
-15
-10
-5
0
5
10
15
Off-Axis Position (cm)
Measurement
PBRA (IS-Adj.)
PBRA (Nom.)
Out-Scatter (×5)

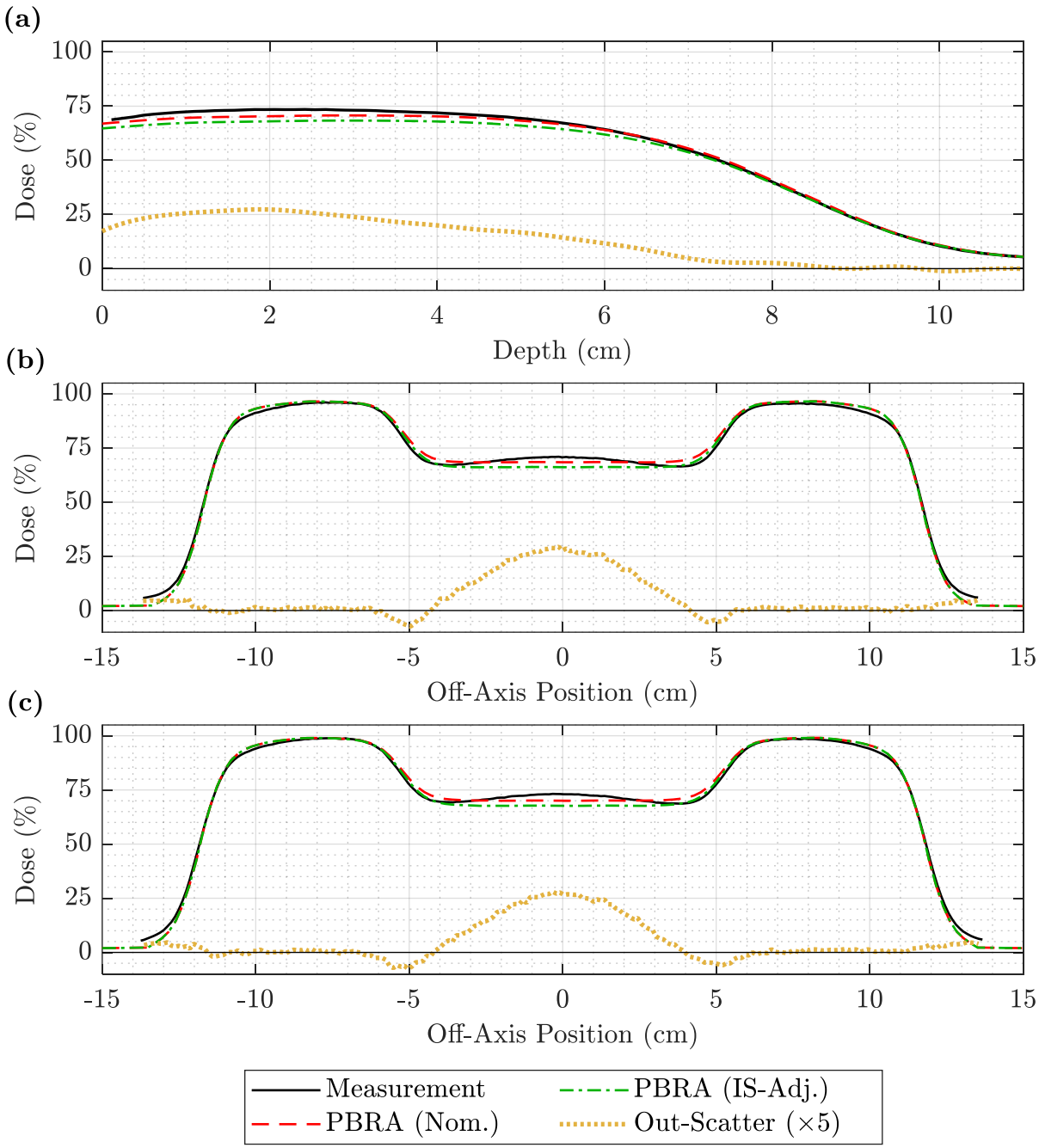

Figure A.28. PDD and off-axis profiles for the 20 MeV beam at 110 cm SSD and 0.352-cm pins. The (a) PDD and off-axis profiles at depths of (b) 0.5, (c) 1.5, (d) 3.5, (e) 5.0, and (f) 6.0 cm compare measurement (solid black) to the nominal PBRA (dashed red) and PBRA corrected for in-scatter only (dashed-dotted green) for a 20 MeV beam at 110 cm SSD for 0.352-cm-diameter pins. The out-scatter estimation (dotted yellow) is the difference between measurement and the in-scatter-adjusted PBRA with the off-axis weight adjustment of Equation 3.4, plotted here with ×5 magnification for clarity.

(figure cont'd.)

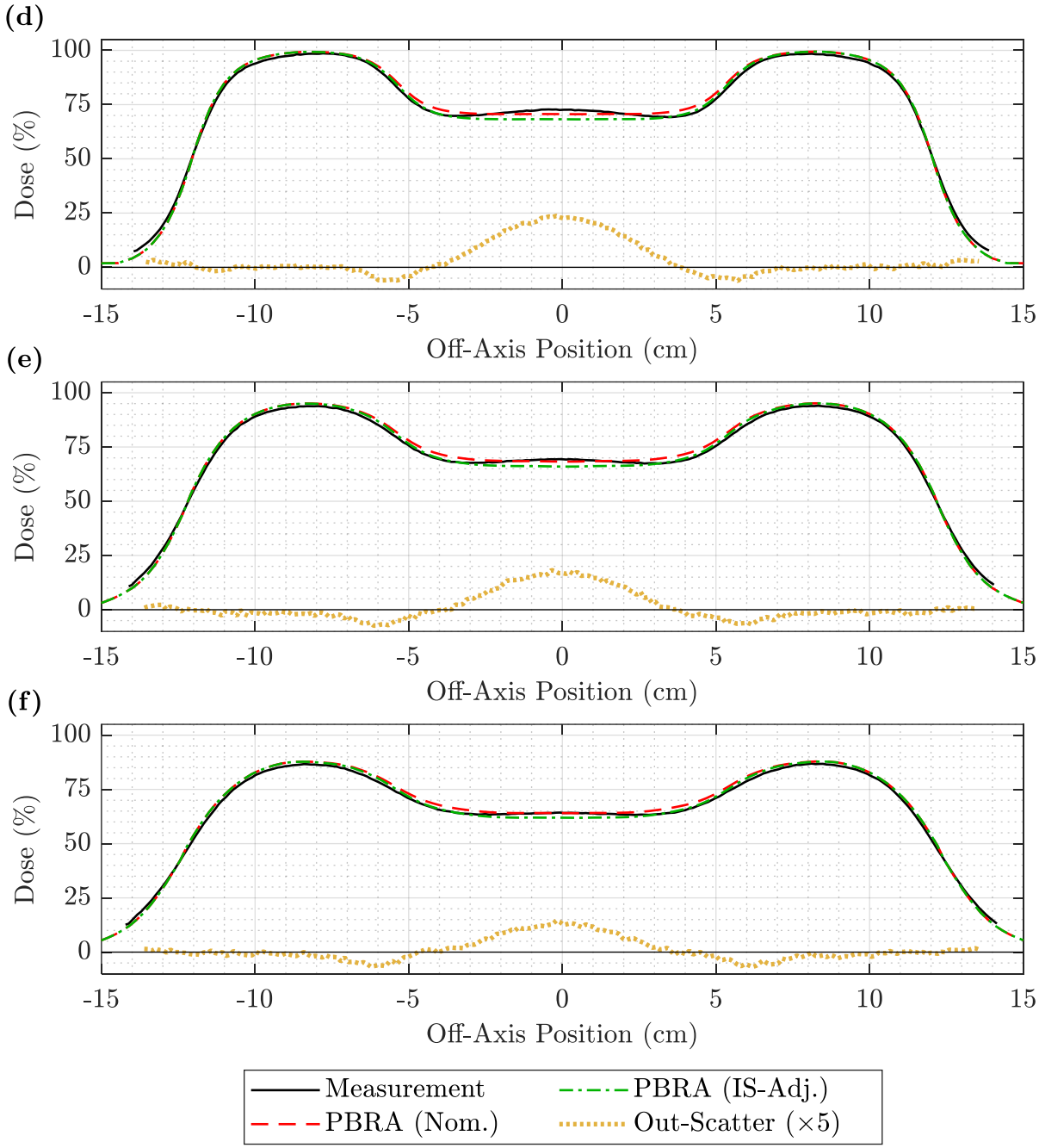
(d)
100
75
50
25
0
Dose (%)
-15
-10
-5
0
5
10
15
Off-Axis Position (cm)
(e)
100
75
50
25
0
Dose (%)
-15
-10
-5
0
5
10
15
Off-Axis Position (cm)
(f)
100
75
50
25
0
Dose (%)
-15
-10
-5
0
5
10
15
Off-Axis Position (cm)
Measurement
PBRA (IS-Adj.)
PBRA (Nom.)
Out-Scatter (×5)

Table A.1. Diameter corrections for nominal beam energies 7-20 MeV and pin diameters 0.158-352 cm at 100 cm SSD. The IS+OS diameter corrections and intermediate quantities are tabulated for all available pin diameters at all energies available on the Elekta Agility accelerator at MBPCC.

Beam Energy (MeV)	$E_{p,0}$ (MeV)	d (cm)	d_{IS} (cm)	IRF_{IS}	$\Delta D_{OS,fit}$	IRF_{IS+OS}	d_{IS+OS} (cm)
7	6.52	0.158	0.188	0.911	2.03%	0.931	0.165
7	6.52	0.223	0.255	0.836	3.08%	0.867	0.230
7	6.52	0.273	0.306	0.764	3.89%	0.803	0.280
7	6.52	0.315	0.349	0.693	4.67%	0.740	0.321
7	6.52	0.352	0.386	0.625	5.35%	0.679	0.357
9	8.79	0.158	0.184	0.915	1.77%	0.933	0.164
9	8.79	0.223	0.251	0.841	2.78%	0.869	0.228
9	8.79	0.273	0.301	0.772	3.55%	0.808	0.276
9	8.79	0.315	0.344	0.702	4.32%	0.745	0.318
9	8.79	0.352	0.381	0.634	4.99%	0.684	0.354
10	9.87	0.158	0.182	0.917	1.67%	0.934	0.162
10	9.87	0.223	0.248	0.845	2.66%	0.872	0.226
10	9.87	0.273	0.299	0.775	3.43%	0.809	0.275
10	9.87	0.315	0.341	0.707	4.18%	0.749	0.316
10	9.87	0.352	0.378	0.640	4.85%	0.689	0.352
11	11.17	0.158	0.180	0.918	1.58%	0.934	0.162
11	11.17	0.223	0.246	0.848	2.55%	0.874	0.224
11	11.17	0.273	0.296	0.779	3.30%	0.812	0.273
11	11.17	0.315	0.338	0.712	4.05%	0.752	0.313
11	11.17	0.352	0.376	0.644	4.71%	0.691	0.350
13	13.42	0.158	0.178	0.920	1.48%	0.935	0.161
13	13.42	0.223	0.244	0.850	2.43%	0.874	0.223
13	13.42	0.273	0.294	0.782	3.16%	0.814	0.272
13	13.42	0.315	0.336	0.716	3.88%	0.755	0.312
13	13.42	0.352	0.373	0.650	4.52%	0.695	0.348
16	15.80	0.158	0.174	0.924	1.47%	0.939	0.156
16	15.80	0.223	0.239	0.856	2.39%	0.880	0.218
16	15.80	0.273	0.290	0.788	3.10%	0.819	0.268
16	15.80	0.315	0.332	0.722	3.80%	0.760	0.309
16	15.80	0.352	0.369	0.657	4.42%	0.701	0.344
20	20.80	0.158	0.171	0.926	1.73%	0.943	0.150
20	20.80	0.223	0.236	0.860	2.62%	0.886	0.213
20	20.80	0.273	0.286	0.794	3.30%	0.827	0.262
20	20.80	0.315	0.329	0.727	3.95%	0.766	0.304
20	20.80	0.352	0.366	0.663	4.51%	0.708	0.340

Table A.2. Diameter corrections for nominal beam energies 7-20 MeV and pin diameters 0.158-352 cm at 105 cm SSD. The IS+OS diameter corrections and intermediate quantities are tabulated for all available pin diameters at all energies available on the Elekta Agility accelerator at MBPCC.

Beam Energy (MeV)	$E_{p,0}$ (MeV)	d (cm)	d_{IS} (cm)	IRF_{IS}	$\Delta D_{OS,fit}$	IRF_{IS+OS}	d_{IS+OS} (cm)
7	6.52	0.158	0.188	0.911	1.63%	0.927	0.170
7	6.52	0.223	0.255	0.836	2.91%	0.865	0.231
7	6.52	0.273	0.306	0.764	3.90%	0.803	0.280
7	6.52	0.315	0.349	0.693	4.77%	0.741	0.321
7	6.52	0.352	0.386	0.625	5.53%	0.680	0.356
9	8.79	0.158	0.184	0.915	1.38%	0.929	0.168
9	8.79	0.223	0.251	0.841	2.56%	0.867	0.230
9	8.79	0.273	0.301	0.772	3.48%	0.807	0.277
9	8.79	0.315	0.344	0.702	4.24%	0.744	0.319
9	8.79	0.352	0.381	0.634	4.91%	0.683	0.355
10	9.87	0.158	0.182	0.917	1.28%	0.930	0.167
10	9.87	0.223	0.248	0.845	2.42%	0.869	0.228
10	9.87	0.273	0.299	0.775	3.30%	0.808	0.276
10	9.87	0.315	0.341	0.707	4.02%	0.747	0.317
10	9.87	0.352	0.378	0.640	4.66%	0.687	0.353
11	11.17	0.158	0.180	0.918	1.19%	0.930	0.167
11	11.17	0.223	0.246	0.848	2.27%	0.871	0.227
11	11.17	0.273	0.296	0.779	3.09%	0.810	0.275
11	11.17	0.315	0.338	0.712	3.78%	0.750	0.315
11	11.17	0.352	0.376	0.644	4.39%	0.688	0.352
13	13.42	0.158	0.178	0.920	1.10%	0.931	0.166
13	13.42	0.223	0.244	0.850	2.05%	0.871	0.227
13	13.42	0.273	0.294	0.782	2.79%	0.810	0.275
13	13.42	0.315	0.336	0.716	3.45%	0.750	0.315
13	13.42	0.352	0.373	0.650	4.03%	0.690	0.351
16	15.80	0.158	0.174	0.924	1.08%	0.935	0.161
16	15.80	0.223	0.239	0.856	1.89%	0.875	0.223
16	15.80	0.273	0.290	0.788	2.52%	0.813	0.272
16	15.80	0.315	0.332	0.722	3.18%	0.754	0.313
16	15.80	0.352	0.369	0.657	3.77%	0.695	0.348
20	20.80	0.158	0.171	0.926	1.30%	0.939	0.156
20	20.80	0.223	0.236	0.860	1.78%	0.878	0.220
20	20.80	0.273	0.286	0.794	2.14%	0.815	0.271
20	20.80	0.315	0.329	0.727	2.95%	0.756	0.311
20	20.80	0.352	0.366	0.663	3.66%	0.700	0.345

Table A.3. Diameter corrections for nominal beam energies 7-20 MeV and pin diameters 0.158-352 cm at 110 cm SSD. The IS+OS diameter corrections and intermediate quantities are tabulated for all available pin diameters at all energies available on the Elekta Agility accelerator at MBPCC.

Beam Energy (MeV)	$E_{p,0}$ (MeV)	d (cm)	d_{IS} (cm)	IRF_{IS}	$\Delta D_{OS,fit}$	IRF_{IS+OS}	d_{IS+OS} (cm)
7	6.52	0.158	0.188	0.911	1.39%	0.925	0.173
7	6.52	0.223	0.255	0.836	2.66%	0.863	0.234
7	6.52	0.273	0.306	0.764	3.64%	0.800	0.281
7	6.52	0.315	0.349	0.693	4.56%	0.739	0.322
7	6.52	0.352	0.386	0.625	5.38%	0.679	0.357
9	8.79	0.158	0.184	0.915	1.20%	0.927	0.170
9	8.79	0.223	0.251	0.841	2.33%	0.864	0.232
9	8.79	0.273	0.301	0.772	3.20%	0.804	0.279
9	8.79	0.315	0.344	0.702	3.99%	0.742	0.320
9	8.79	0.352	0.381	0.634	4.69%	0.681	0.356
10	9.87	0.158	0.182	0.917	1.12%	0.928	0.169
10	9.87	0.223	0.248	0.845	2.19%	0.867	0.230
10	9.87	0.273	0.299	0.775	3.01%	0.805	0.278
10	9.87	0.315	0.341	0.707	3.75%	0.744	0.318
10	9.87	0.352	0.378	0.640	4.39%	0.684	0.354
11	11.17	0.158	0.180	0.918	1.03%	0.928	0.169
11	11.17	0.223	0.246	0.848	2.03%	0.868	0.229
11	11.17	0.273	0.296	0.779	2.79%	0.807	0.277
11	11.17	0.315	0.338	0.712	3.47%	0.747	0.317
11	11.17	0.352	0.376	0.644	4.06%	0.685	0.354
13	13.42	0.158	0.178	0.920	0.90%	0.929	0.168
13	13.42	0.223	0.244	0.850	1.77%	0.868	0.229
13	13.42	0.273	0.294	0.782	2.44%	0.806	0.277
13	13.42	0.315	0.336	0.716	3.04%	0.746	0.317
13	13.42	0.352	0.373	0.650	3.56%	0.686	0.353
16	15.80	0.158	0.174	0.924	0.78%	0.932	0.164
16	15.80	0.223	0.239	0.856	1.54%	0.871	0.226
16	15.80	0.273	0.290	0.788	2.11%	0.809	0.275
16	15.80	0.315	0.332	0.722	2.66%	0.749	0.316
16	15.80	0.352	0.369	0.657	3.14%	0.688	0.352
20	20.80	0.158	0.171	0.926	0.65%	0.932	0.164
20	20.80	0.223	0.236	0.860	1.17%	0.872	0.226
20	20.80	0.273	0.286	0.794	1.56%	0.810	0.275
20	20.80	0.315	0.329	0.727	2.10%	0.748	0.316
20	20.80	0.352	0.366	0.663	2.58%	0.689	0.351

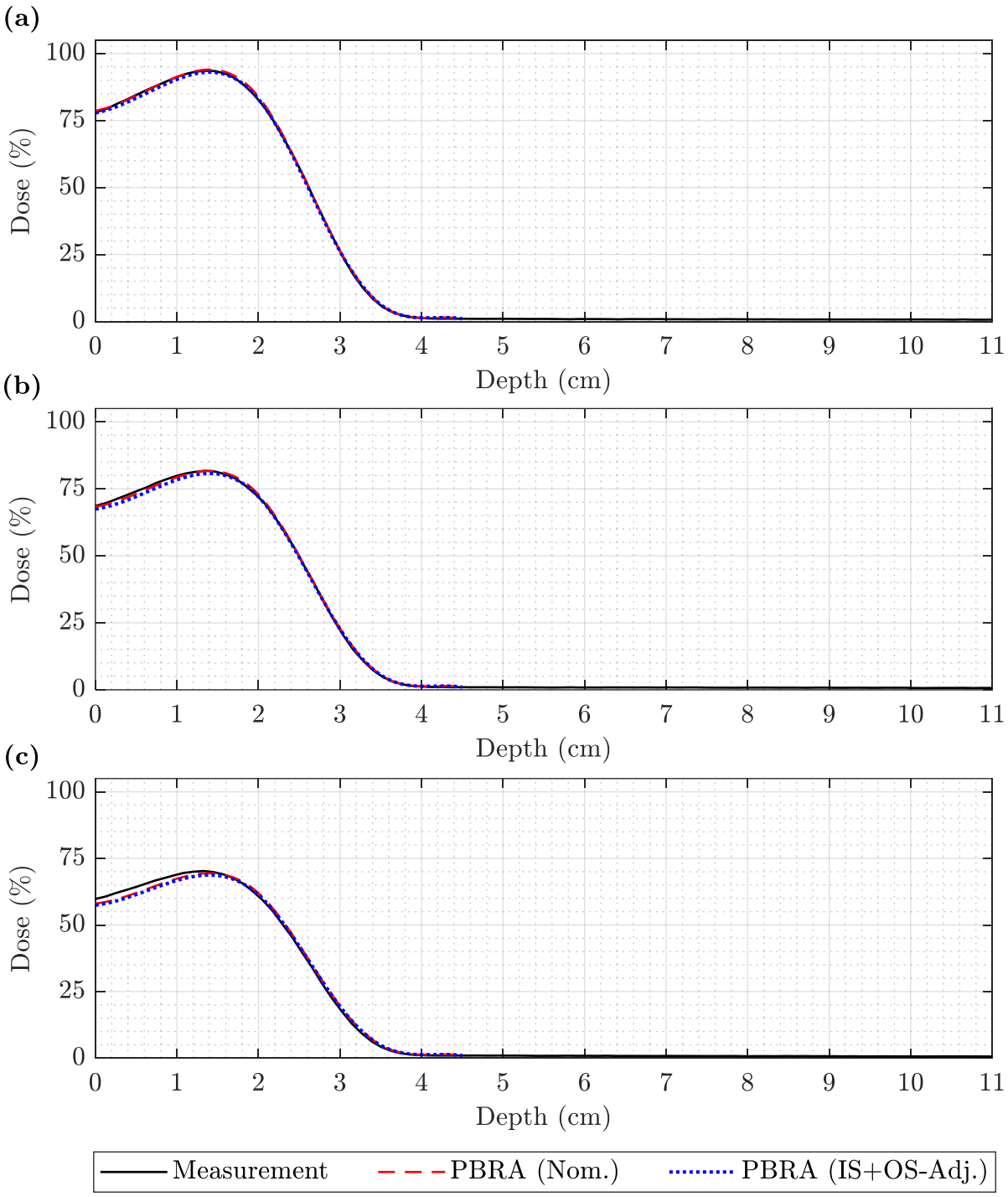

Figure A.29. PDD comparison of measurement, nominal PBRA, and IS+OS-corrected PBRA at 7 MeV and 105 cm SSD. Measurement (solid black) is compared to the nominal PBRA (dashed red) and PBRA adjusted for both in-scatter and out-scatter (dotted blue) for a 7 MeV beam at 105 cm SSD for (a) 0.158-cm, (b) 0.273-cm, and (c) 0.352-cm pins.

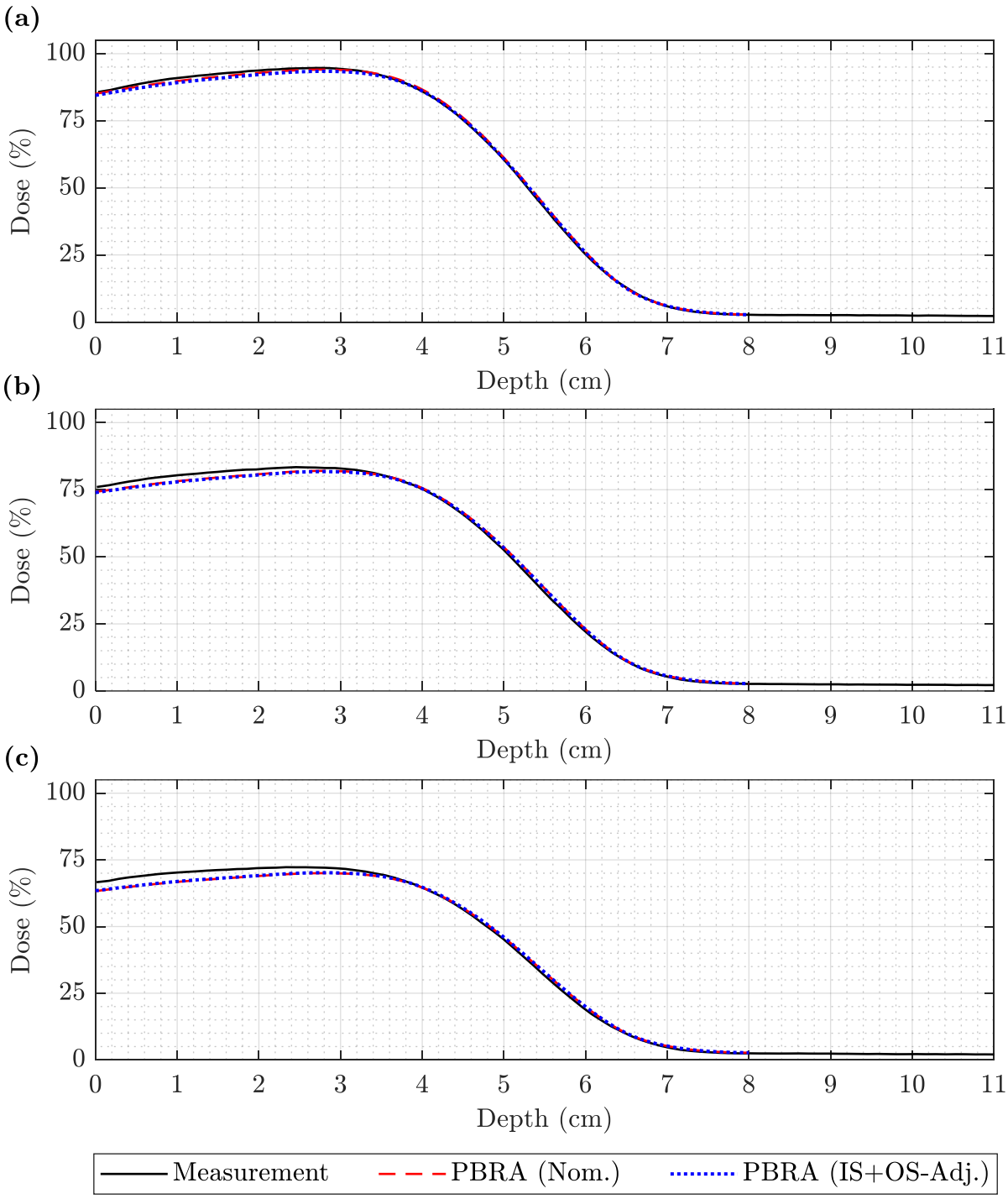

Figure A.30. PDD comparison of measurement, nominal PBRA, and IS+OS-corrected PBRA at 13 MeV and 105 cm SSD. Measurement (solid black) is compared to the nominal PBRA (dashed red) and PBRA adjusted for both in-scatter and out-scatter (dotted blue) for a 13 MeV beam at 105 cm SSD for (a) 0.158-cm, (b) 0.273-cm, and (c) 0.352-cm pins.

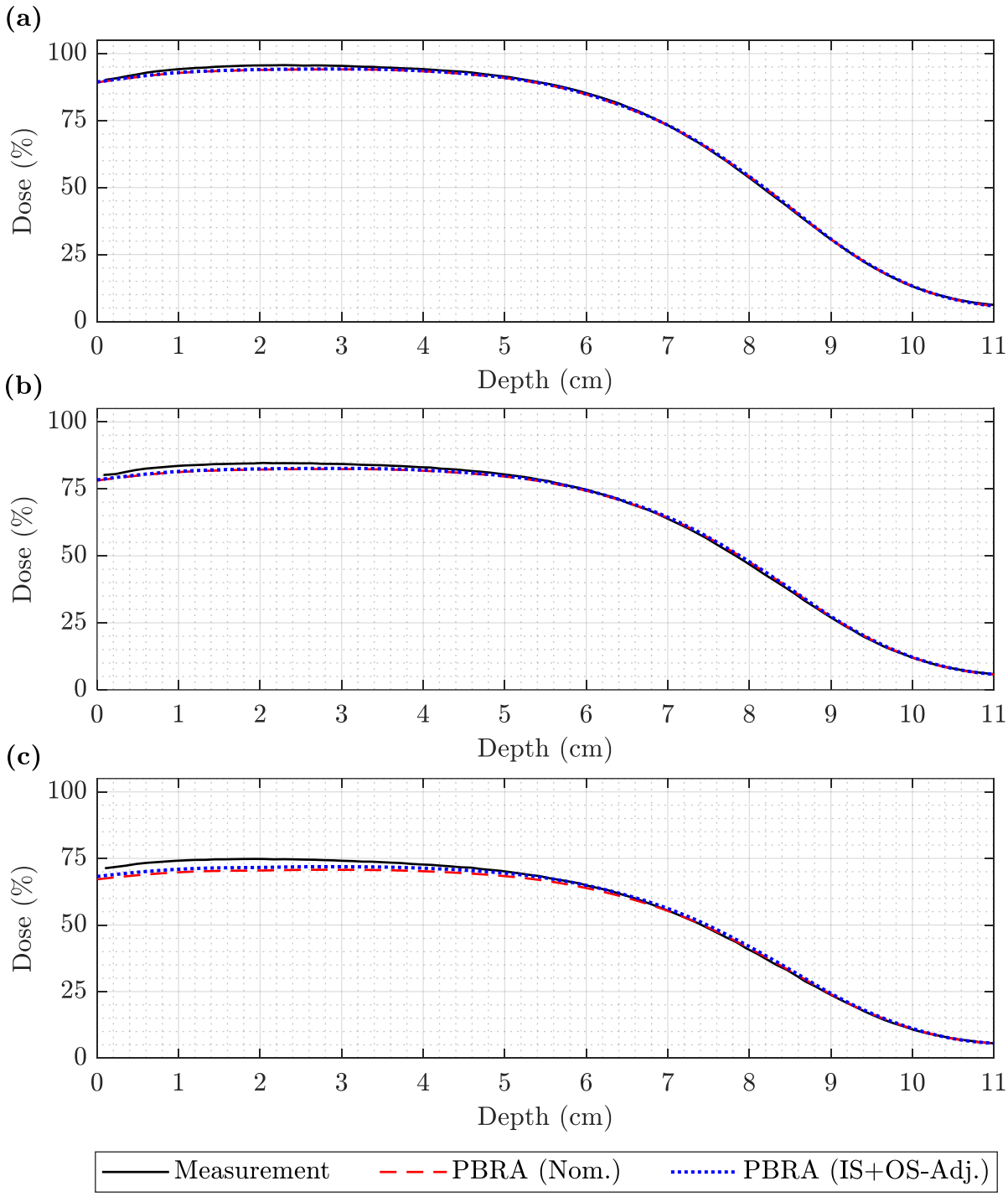

Figure A.31. PDD comparison of measurement, nominal PBRA, and IS+OS-corrected PBRA at 20 MeV and 105 cm SSD. Measurement (solid black) is compared to the nominal PBRA (dashed red) and PBRA adjusted for both in-scatter and out-scatter (dotted blue) for a 20 MeV beam at 105 cm SSD for (a) 0.158-cm, (b) 0.273-cm, and (c) 0.352-cm pins.

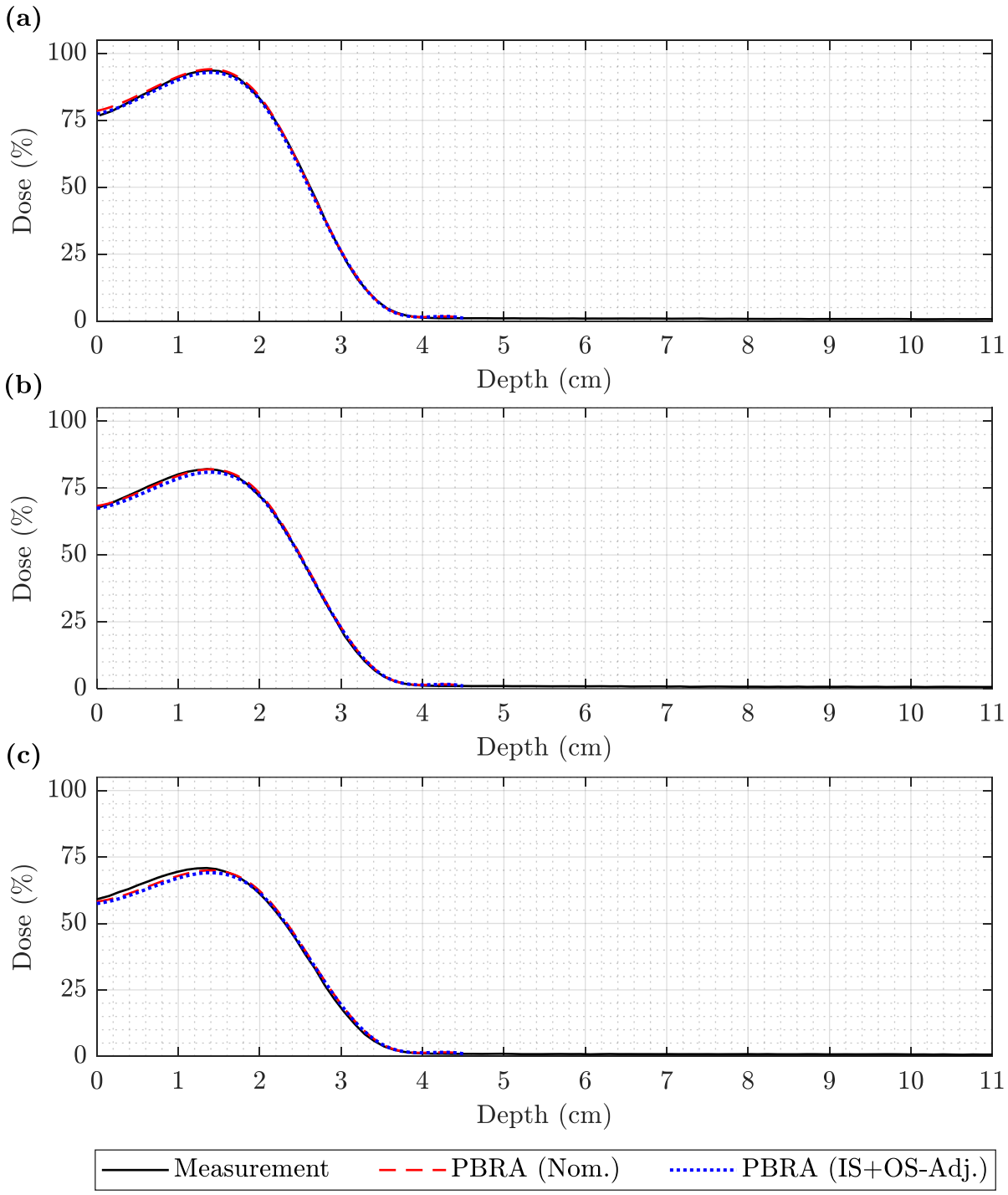

Figure A.32. PDD comparison of measurement, nominal PBRA, and IS+OS-corrected PBRA at 7 MeV and 110 cm SSD. Measurement (solid black) is compared to the nominal PBRA (dashed red) and PBRA adjusted for both in-scatter and out-scatter (dotted blue) for a 7 MeV beam at 110 cm SSD for (a) 0.158-cm, (b) 0.273-cm, and (c) 0.352-cm pins.

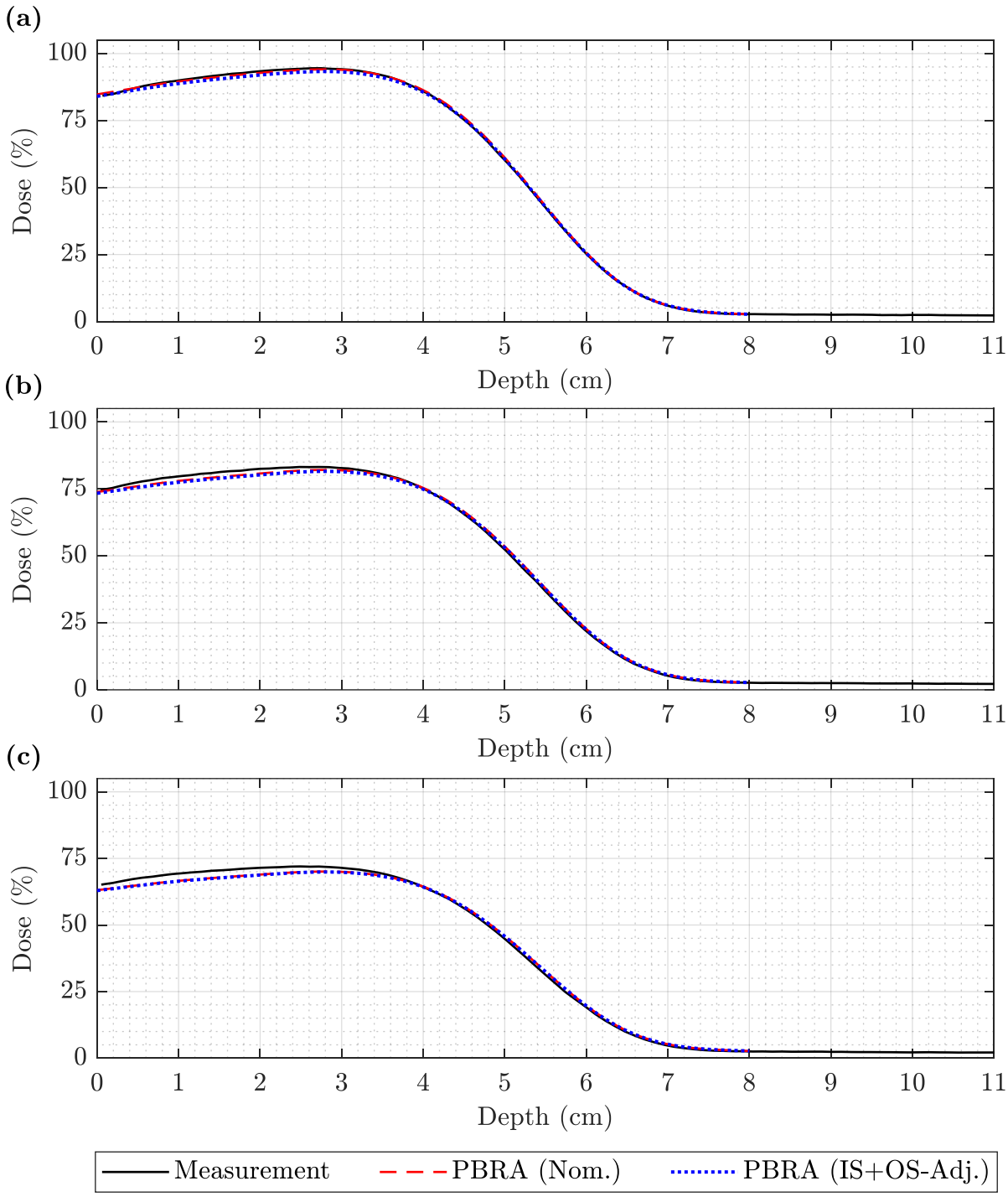

Figure A.33. PDD comparison of measurement, nominal PBRA, and IS+OS-corrected PBRA at 13 MeV and 110 cm SSD. Measurement (solid black) is compared to the nominal PBRA (dashed red) and PBRA adjusted for both in-scatter and out-scatter (dotted blue) for a 13 MeV beam at 110 cm SSD for (a) 0.158-cm, (b) 0.273-cm, and (c) 0.352-cm pins.

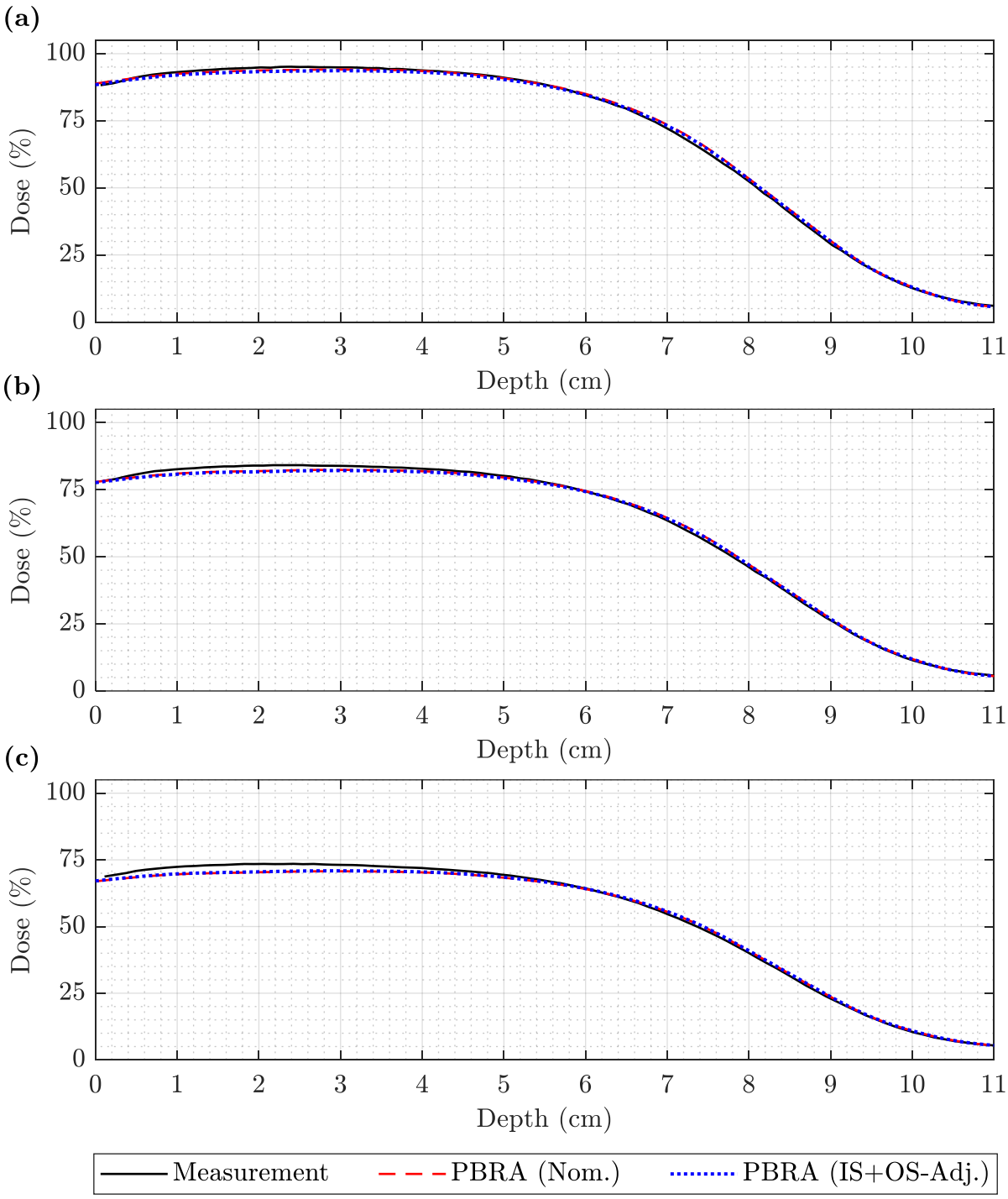

Figure A.34. PDD comparison of measurement, nominal PBRA, and IS+OS-corrected PBRA at 20 MeV and 110 cm SSD. Measurement (solid black) is compared to the nominal PBRA (dashed red) and PBRA adjusted for both in-scatter and out-scatter (dotted blue) for a 20 MeV beam at 110 cm SSD for (a) 0.158-cm, (b) 0.273-cm, and (c) 0.352-cm pins.

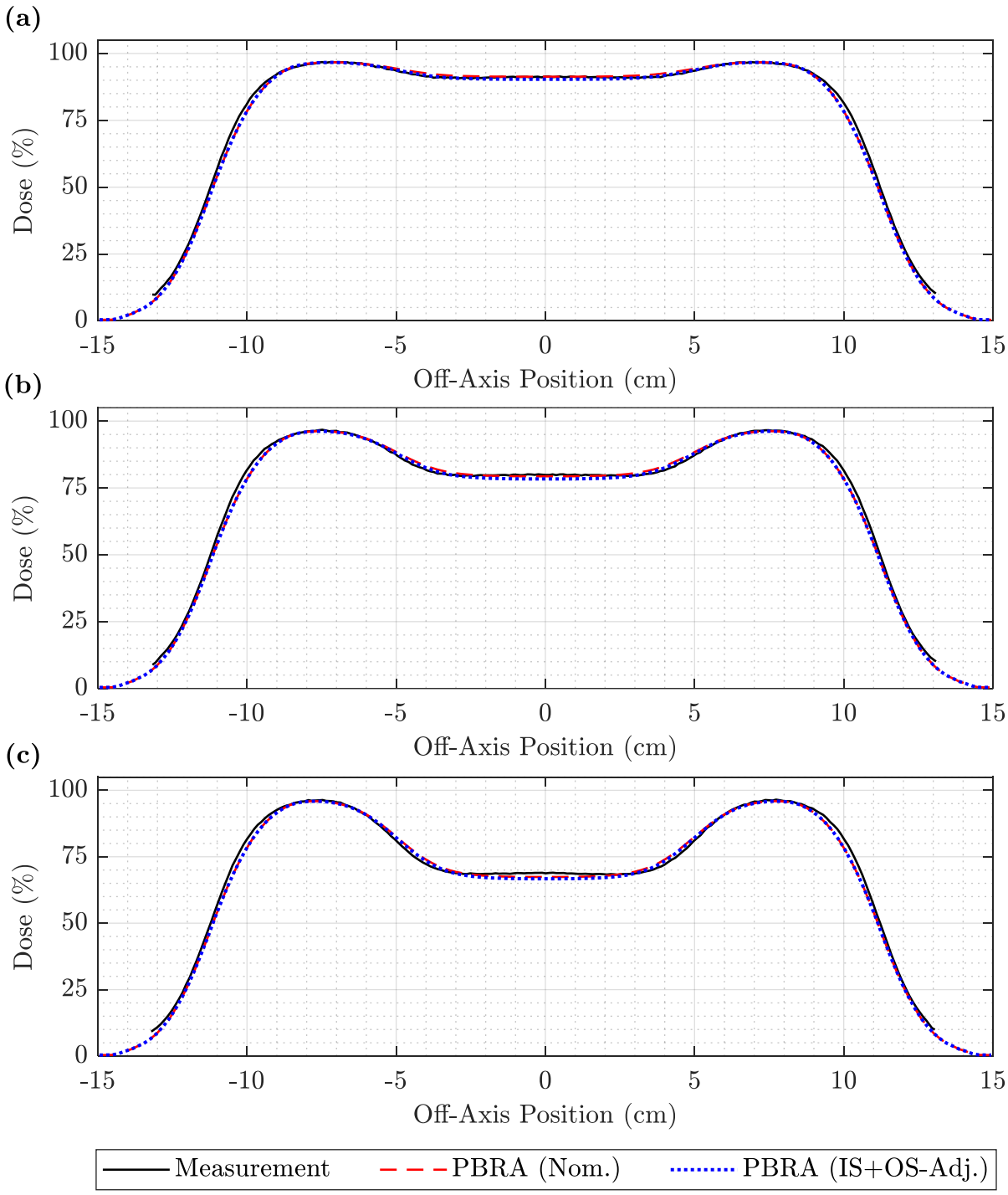

Figure A.35. Off-axis profile comparison of measurement, nominal PBRA, and IS+OS-corrected PBRA at 7 MeV and 105 cm SSD. Measurement (solid black) is compared to the nominal PBRA (dashed red) and PBRA adjusted for both in-scatter and out-scatter (dotted blue) for a 7 MeV beam at 105 cm SSD for pin diameters of (a) 0.158 cm, (b) 0.273 cm, and (c) 0.352 cm at a depth of 1.0 cm.

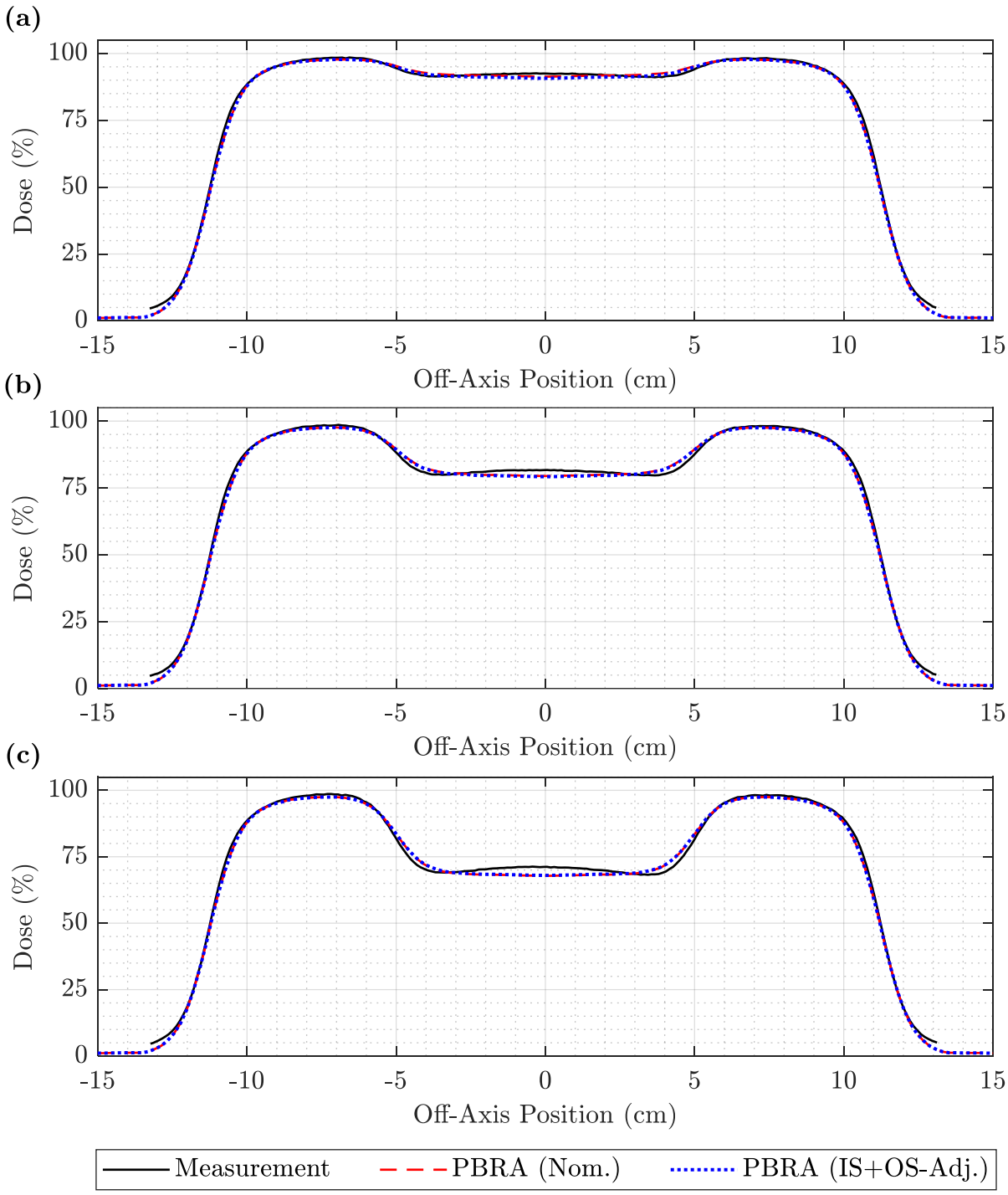

Figure A.36. Off-axis profile comparison of measurement, nominal PBRA, and IS+OS-corrected PBRA at 13 MeV and 105 cm SSD. Measurement (solid black) is compared to the nominal PBRA (dashed red) and PBRA adjusted for both in-scatter and out-scatter (dotted blue) for a 13 MeV beam at 105 cm SSD for pin diameters of (a) 0.158 cm, (b) 0.273 cm, and (c) 0.352 cm at a depth of 1.5 cm.

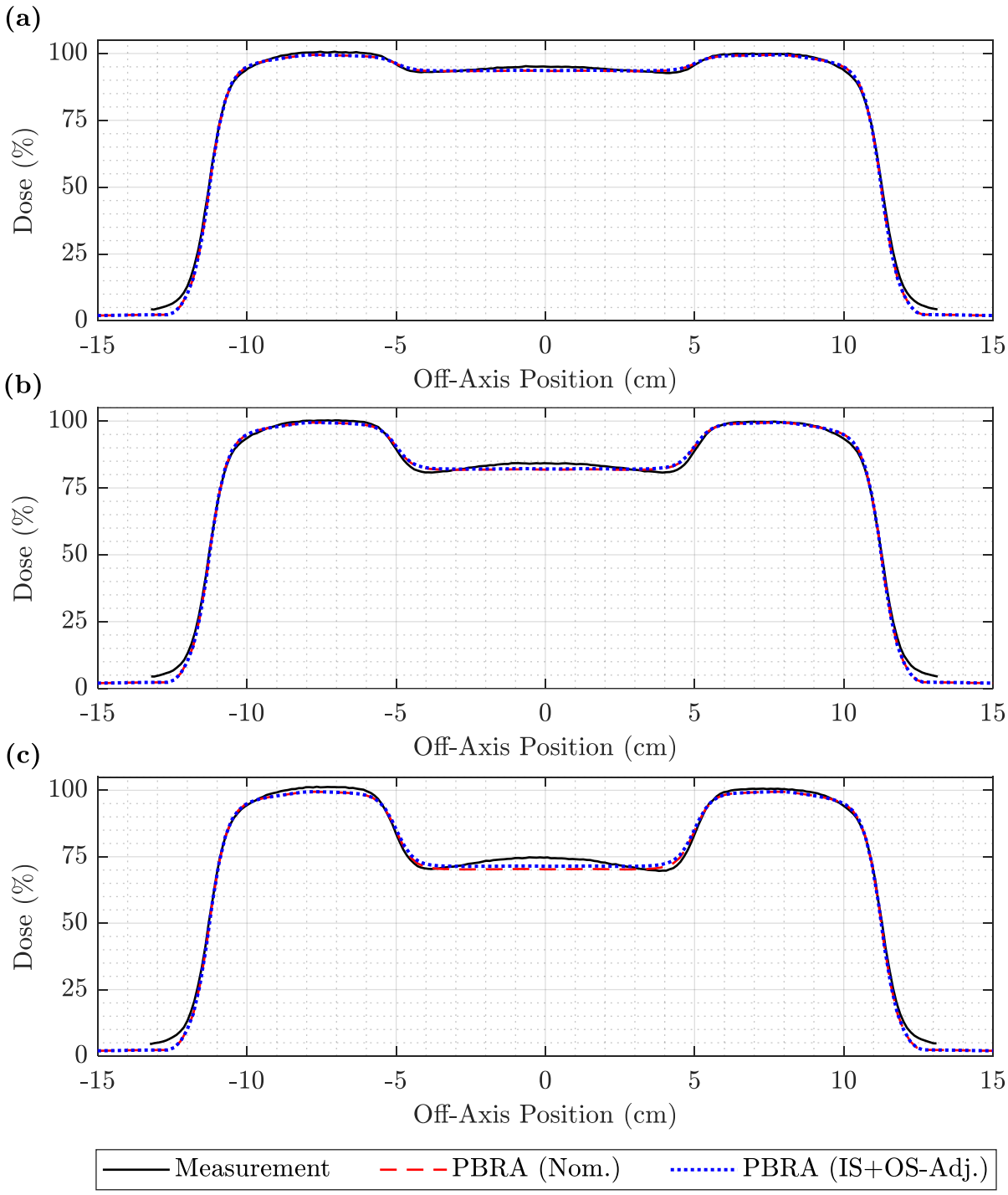

Figure A.37. Off-axis profile comparison of measurement, nominal PBRA, and IS+OS-corrected PBRA at 20 MeV and 105 cm SSD. Measurement (solid black) is compared to the nominal PBRA (dashed red) and PBRA adjusted for both in-scatter and out-scatter (dotted blue) for a 20 MeV beam at 105 cm SSD for pin diameters of (a) 0.158 cm, (b) 0.273 cm, and (c) 0.352 cm at a depth of 1.5 cm.

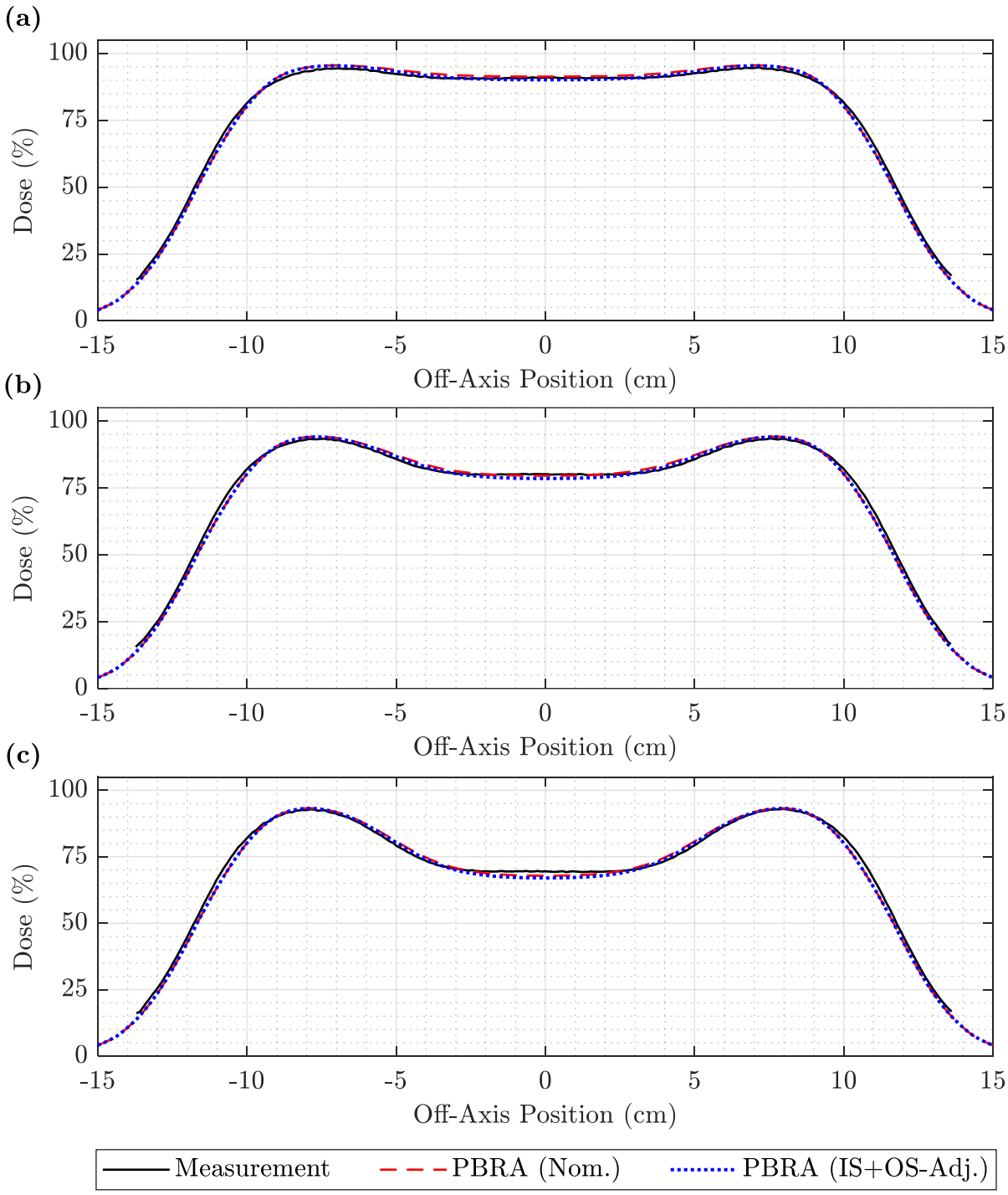

Figure A.38. Off-axis profile comparison of measurement, nominal PBRA, and IS+OS-corrected PBRA at 7 MeV and 110 cm SSD. Measurement (solid black) is compared to the nominal PBRA (dashed red) and PBRA adjusted for both in-scatter and out-scatter (dotted blue) for a 7 MeV beam at 110 cm SSD for pin diameters of (a) 0.158 cm, (b) 0.273 cm, and (c) 0.352 cm at a depth of 1.0 cm.

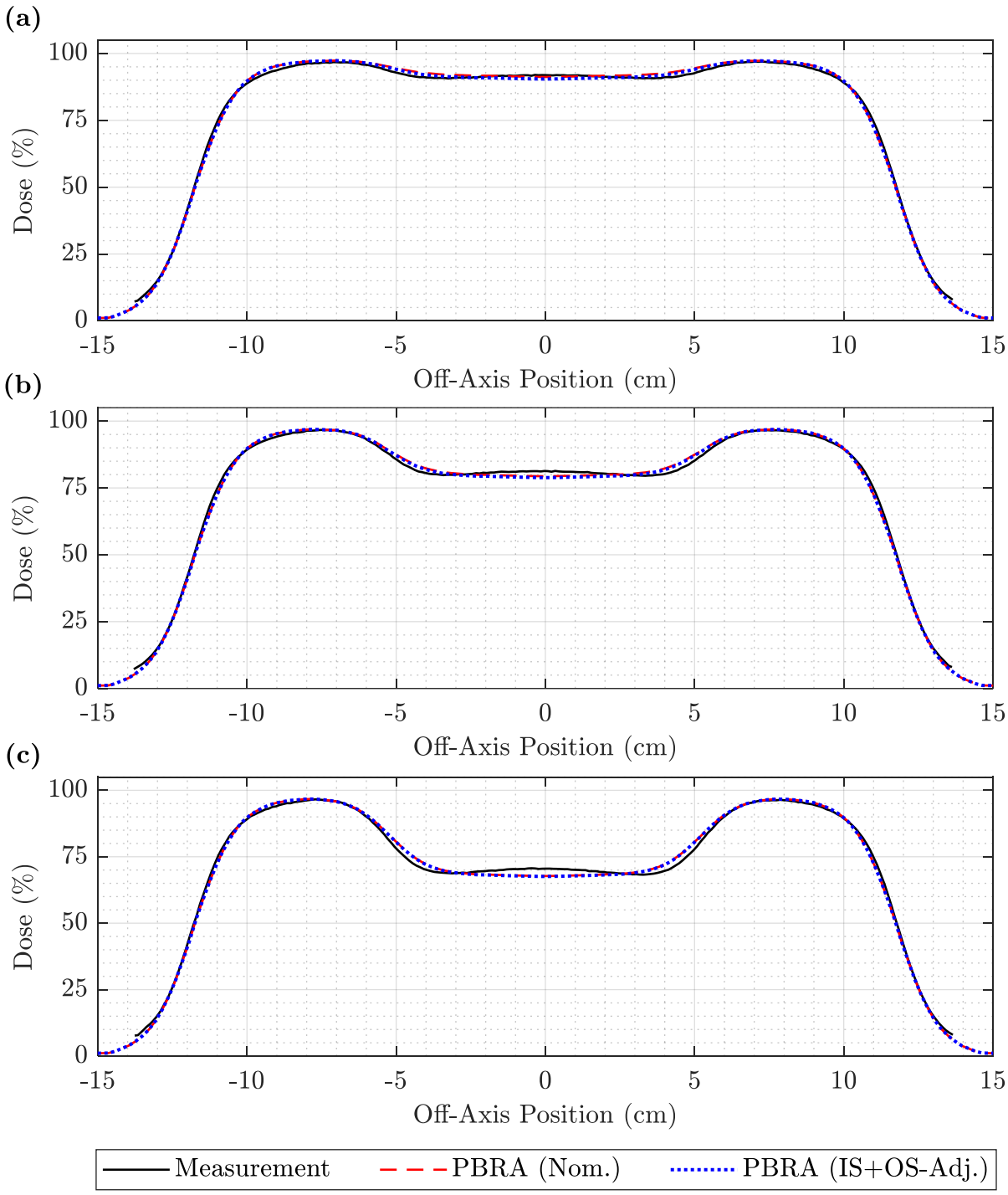

Figure A.39. Off-axis profile comparison of measurement, nominal PBRA, and IS+OS-corrected PBRA at 13 MeV and 110 cm SSD. Measurement (solid black) is compared to the nominal PBRA (dashed red) and PBRA adjusted for both in-scatter and out-scatter (dotted blue) for a 13 MeV beam at 110 cm SSD for pin diameters of (a) 0.158 cm, (b) 0.273 cm, and (c) 0.352 cm at a depth of 1.5 cm.

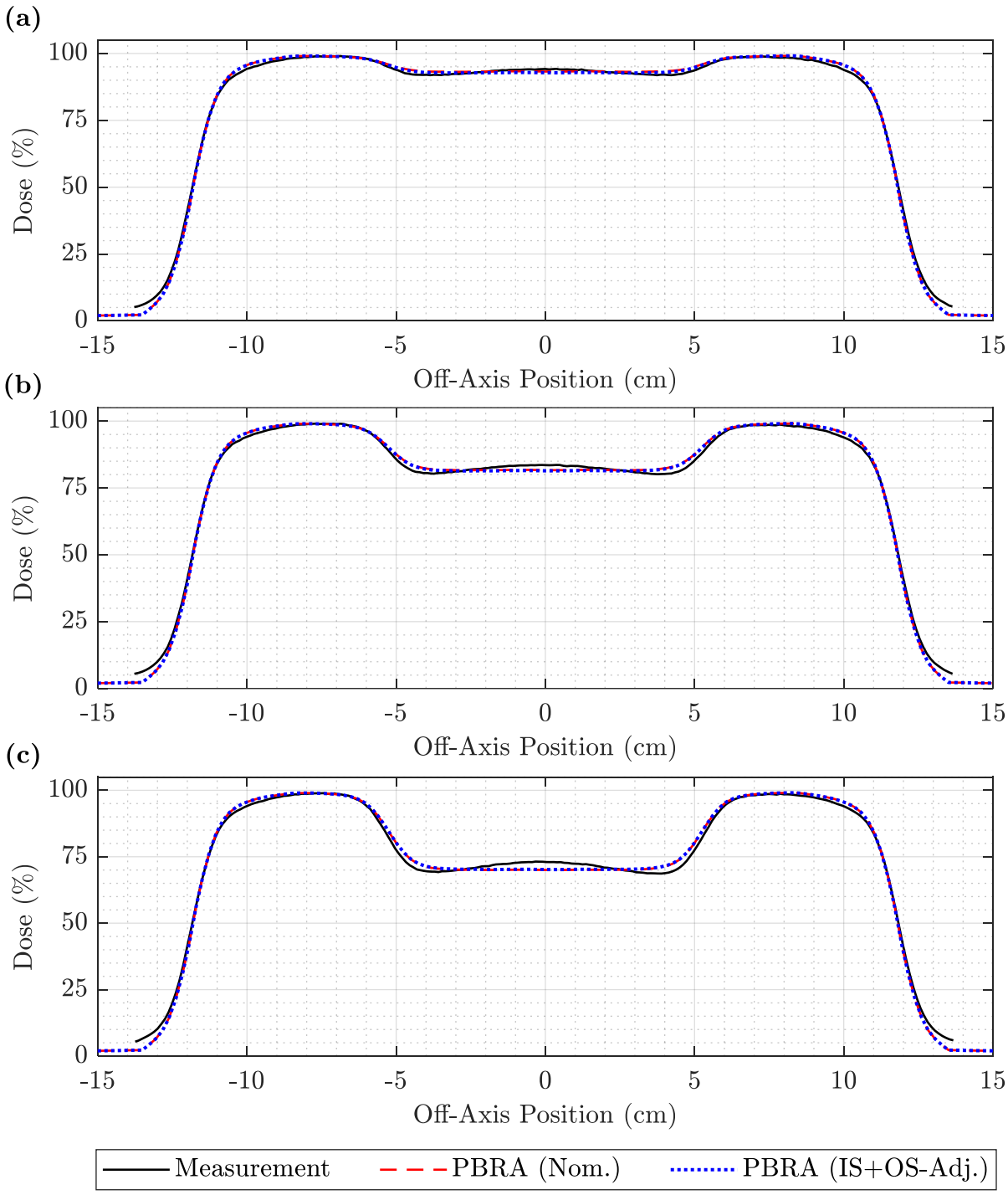

Figure A.40. Off-axis profile comparison of measurement, nominal PBRA, and IS+OS-corrected PBRA at 20 MeV and 110 cm SSD. Measurement (solid black) is compared to the nominal PBRA (dashed red) and PBRA adjusted for both in-scatter and out-scatter (dotted blue) for a 20 MeV beam at 110 cm SSD for pin diameters of (a) 0.158 cm, (b) 0.273 cm, and (c) 0.352 cm at a depth of 1.5 cm.

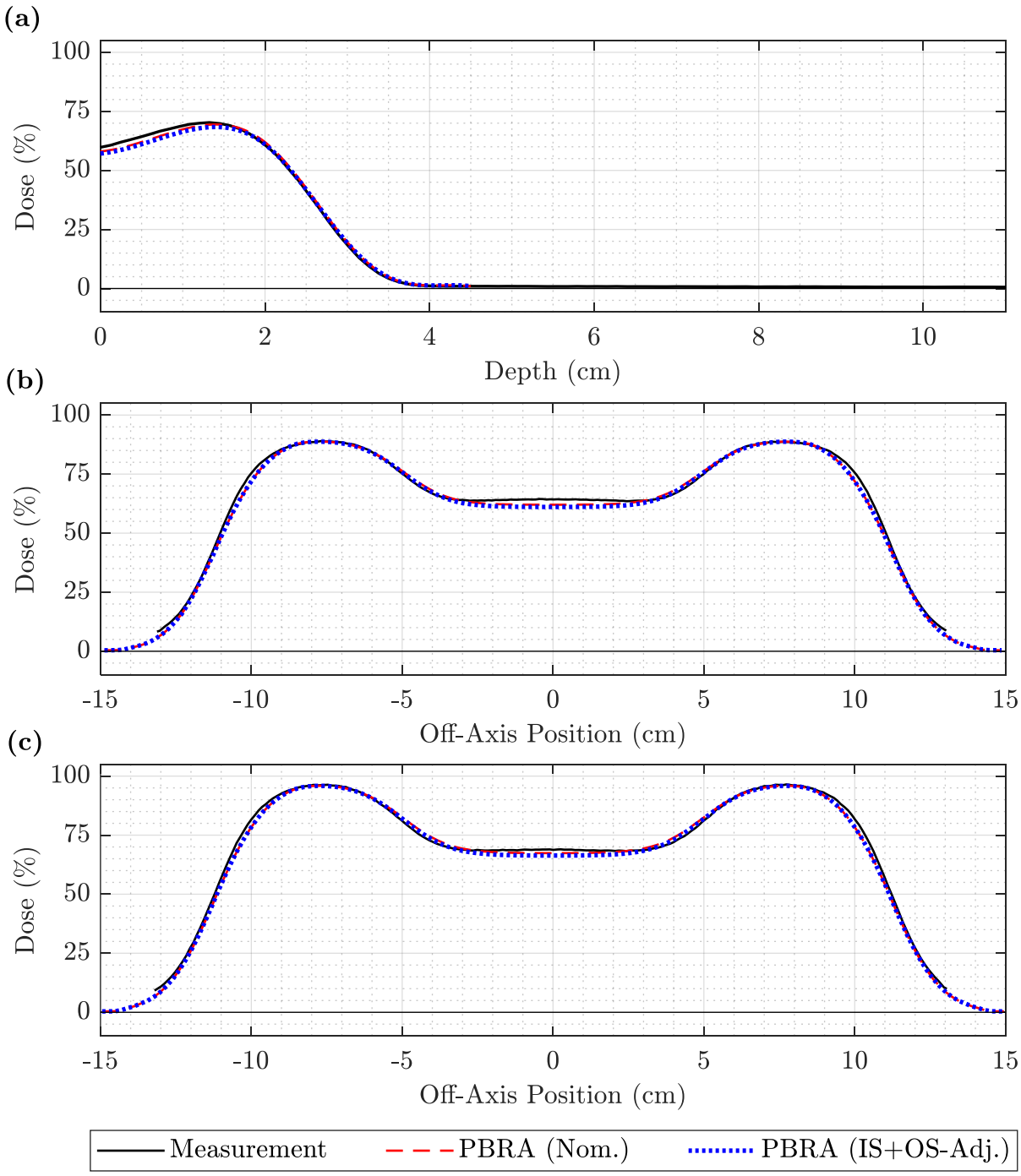

Figure A.41. PDD and off-axis profile comparison of measurement, nominal PBRA, and IS+OS-corrected PBRA for the 7 MeV beam at 105 cm SSD and 0.352-cm pins. The PDD in (a) and off-axis profiles at depths of (b) 0.5, (c) 1.0, (d) 1.5, and (e) 2.0 cm compare measurement (solid black) to the nominal PBRA (dashed red) and PBRA adjusted for both in-scatter and out-scatter (dotted blue) for a 7 MeV beam at 105 cm SSD for 0.352-cm-diameter pins.

(figure cont'd.)

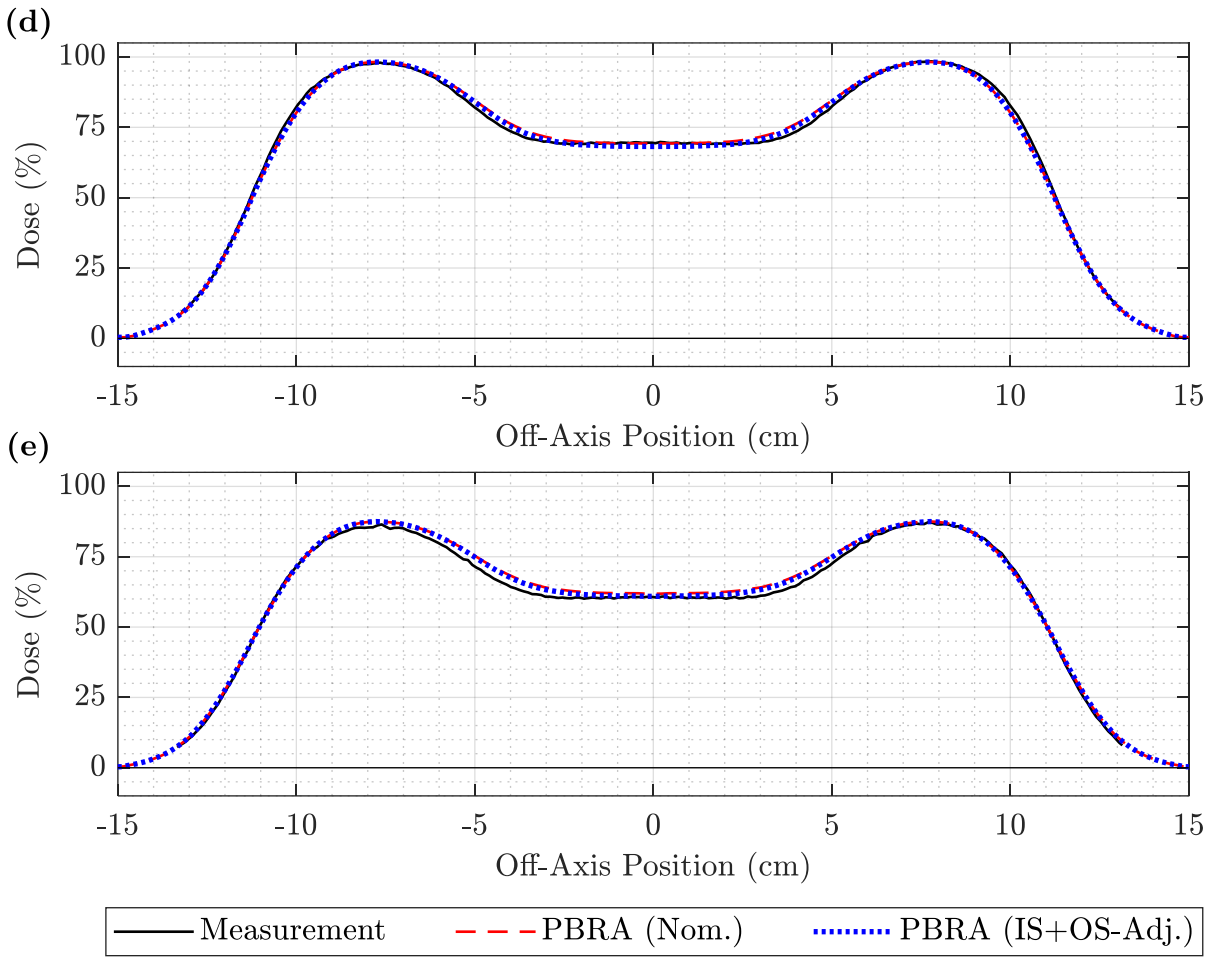
(d)
100
75
50
25
0
Dose (%)
-15
-10
-5
0
5
10
15
Off-Axis Position (cm)
(e)
100
75
50
25
0
Dose (%)
-15
-10
-5
0
5
10
15
Off-Axis Position (cm)
Measurement
PBRA (Nom.)
PBRA (IS+OS-Adj.)

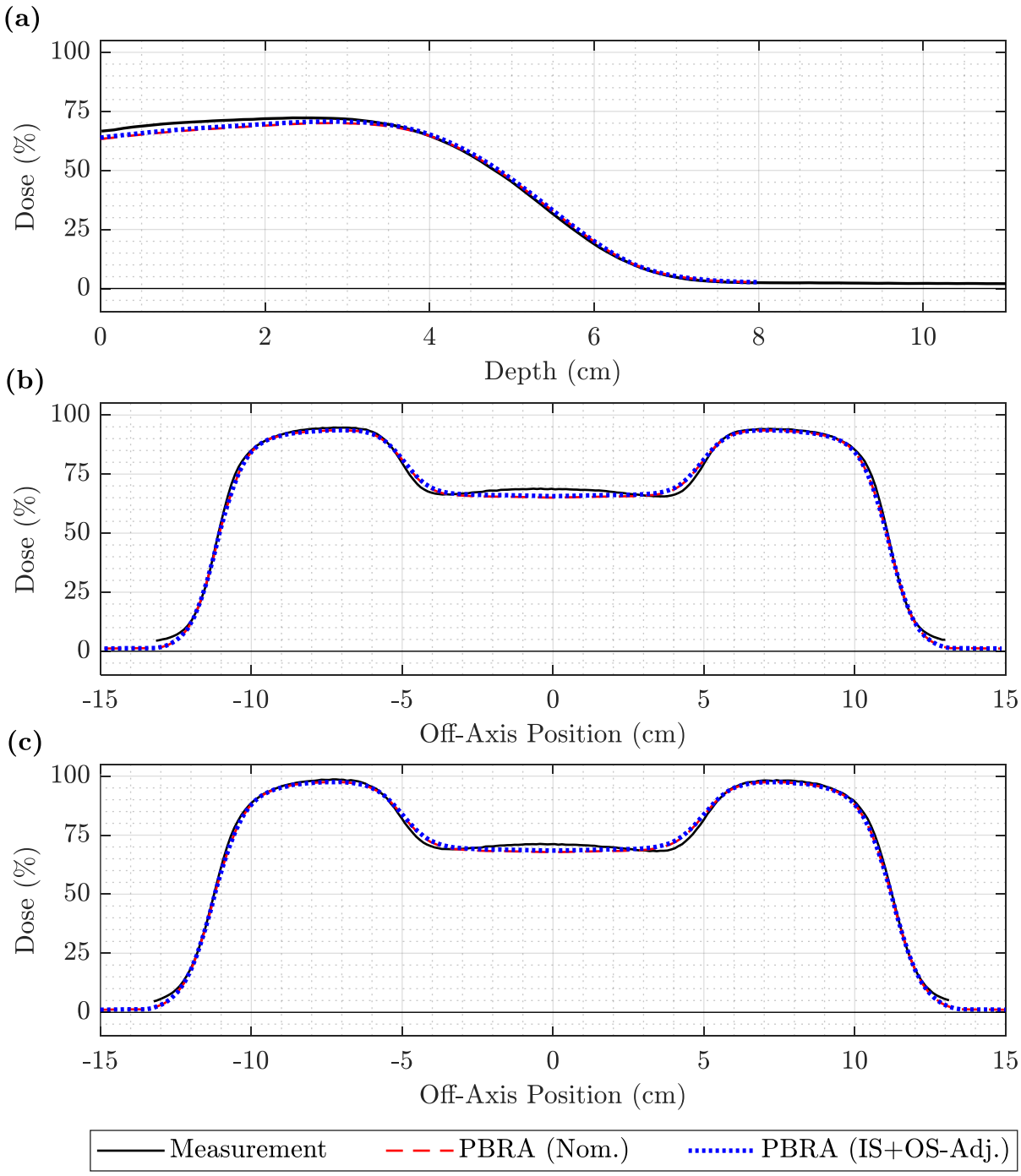

Figure A.42. PDD and off-axis profile comparison of measurement, nominal PBRA, and IS+OS-corrected PBRA for the 13 MeV beam at 105 cm SSD and 0.352-cm pins. The PDD in (a) and off-axis profiles at depths of (b) 0.5, (c) 1.5, (d) 3.0, (e) 3.5, and (f) 4.0 cm compare measurement (solid black) to the nominal PBRA (dashed red) and PBRA adjusted for both in-scatter and out-scatter (dotted blue) for a 13 MeV beam at 105 cm SSD for 0.352-cm-diameter pins.

(figure cont'd.)

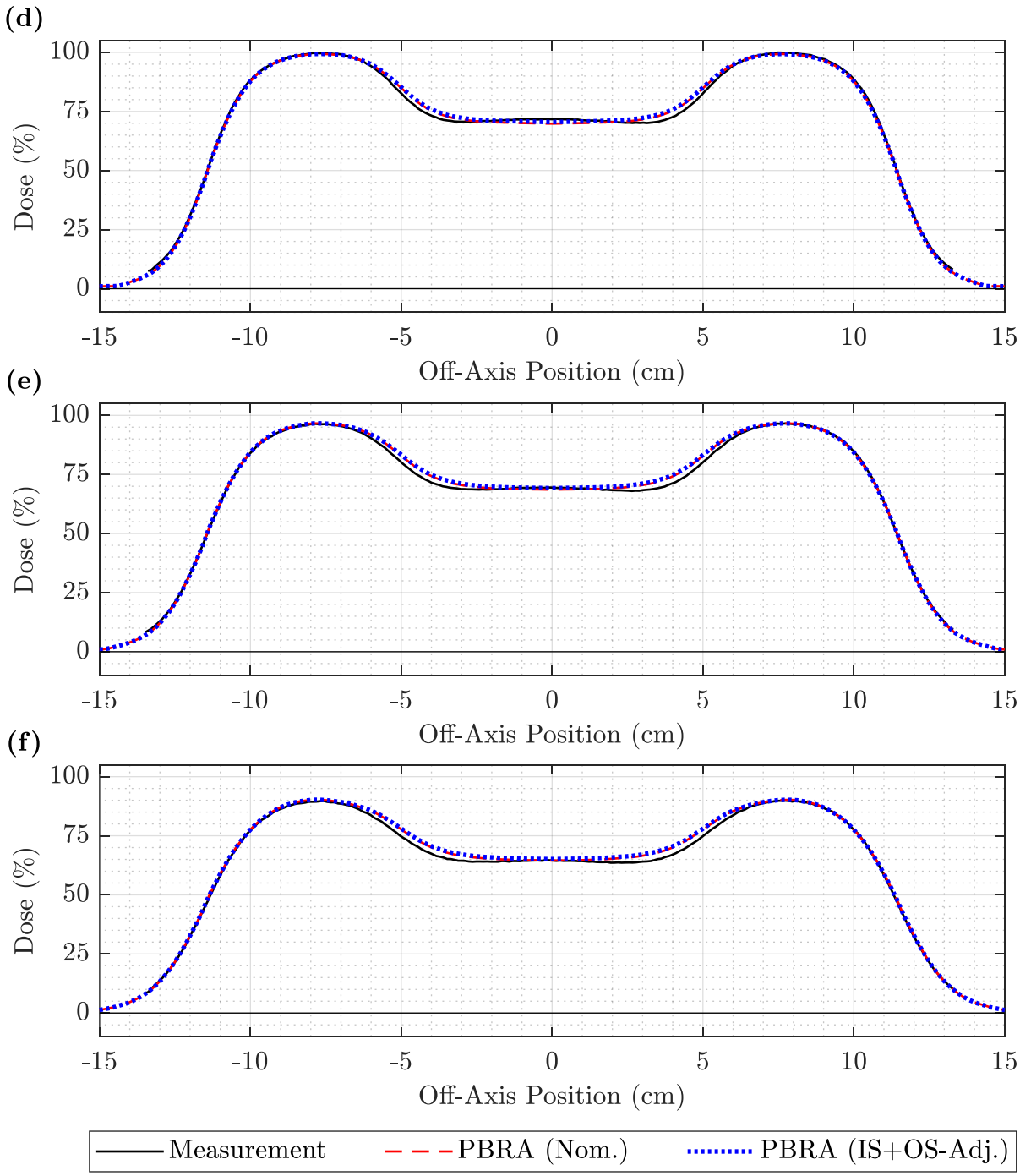
(d)
100
75
50
25
0
Dose (%)
-15
-10
-5
0
5
10
15
Off-Axis Position (cm)
(e)
100
75
50
25
0
Dose (%)
-15
-10
-5
0
5
10
15
Off-Axis Position (cm)
(f)
100
75
50
25
0
Dose (%)
-15
-10
-5
0
5
10
15
Off-Axis Position (cm)
Measurement
PBRA (Nom.)
PBRA (IS+OS-Adj.)

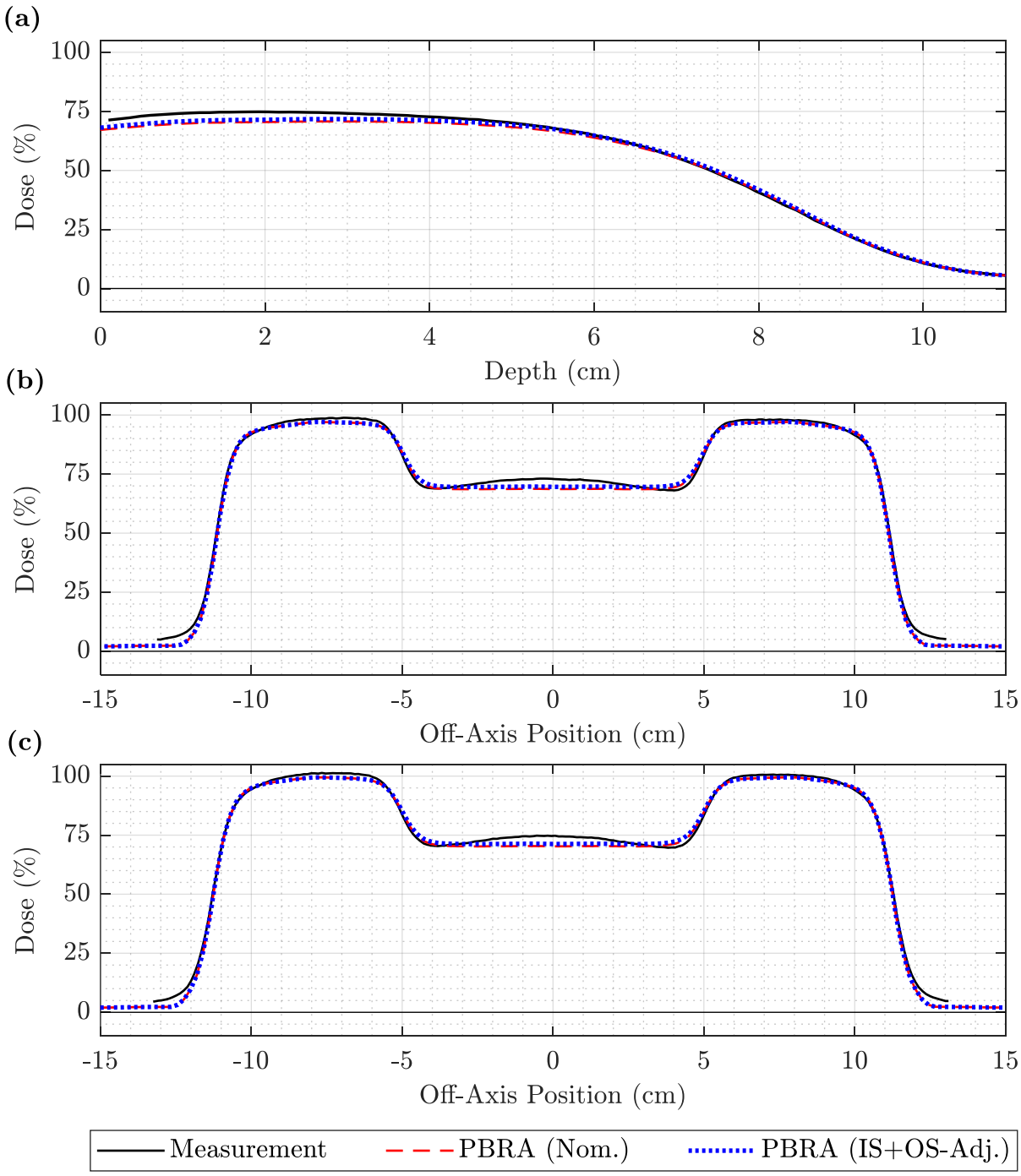

Figure A.43. PDD and off-axis profile comparison of measurement, nominal PBRA, and IS+OS-corrected PBRA for the 20 MeV beam at 105 cm SSD and 0.352-cm pins. The PDD in (a) and off-axis profiles at depths of (b) 0.5, (c) 1.5, (d) 3.5, (e) 5.0, and (f) 6.0 cm compare measurement (solid black) to the nominal PBRA (dashed red) and PBRA adjusted for both in-scatter and out-scatter (dotted blue) for a 20 MeV beam at 105 cm SSD for 0.352-cm-diameter pins.

(figure cont'd.)

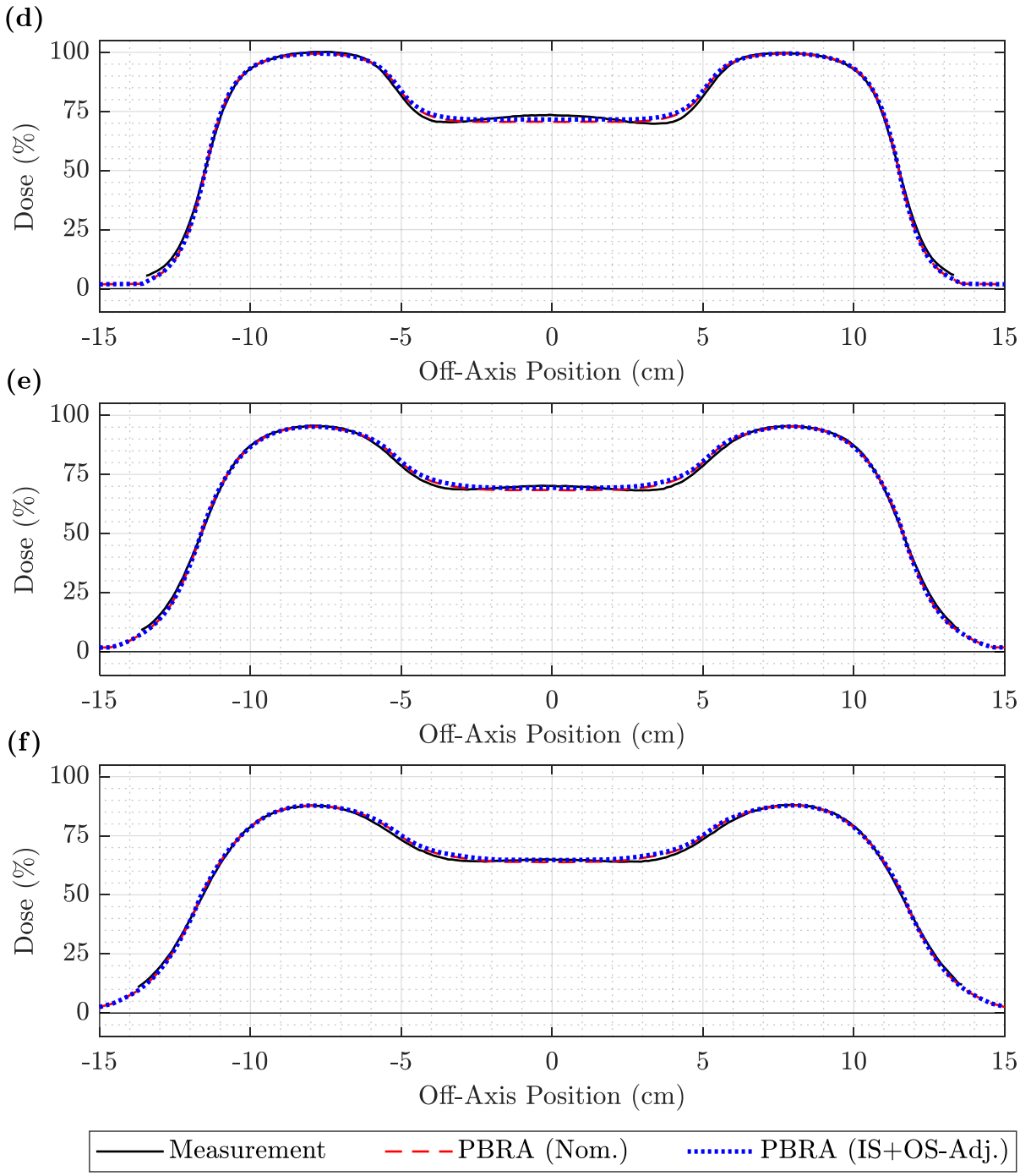
(d)
100
75
50
25
0
Dose (%)
-15
-10
-5
0
5
10
15
Off-Axis Position (cm)
(e)
100
75
50
25
0
Dose (%)
-15
-10
-5
0
5
10
15
Off-Axis Position (cm)
(f)
100
75
50
25
0
Dose (%)
-15
-10
-5
0
5
10
15
Off-Axis Position (cm)
Measurement
PBRA (Nom.)
PBRA (IS+OS-Adj.)

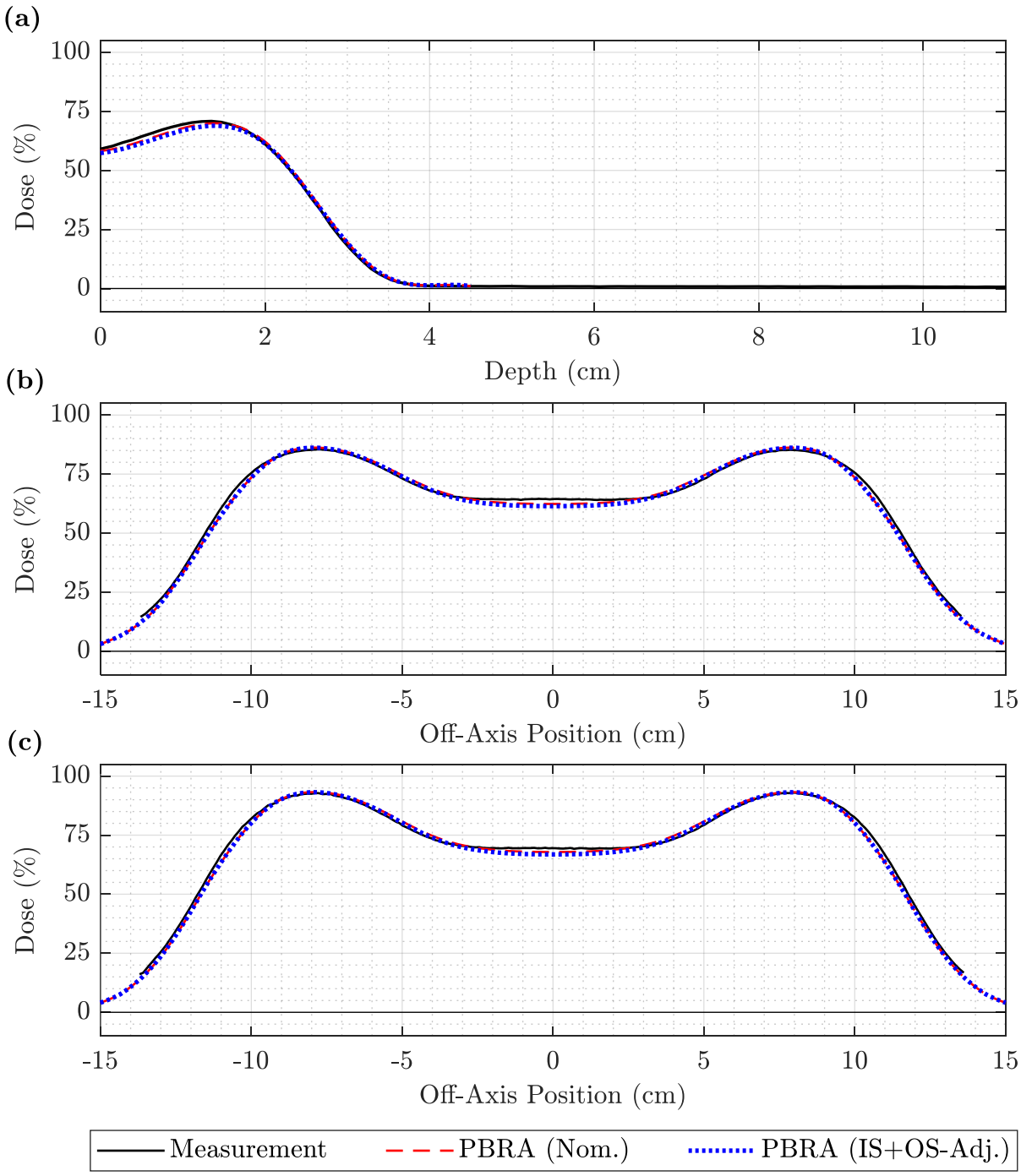

Figure A.44. PDD and off-axis profile comparison of measurement, nominal PBRA, and IS+OS-corrected PBRA for the 7 MeV beam at 110 cm SSD and 0.352-cm pins. The PDD in (a) and off-axis profiles at depths of (b) 0.5, (c) 1.0, (d) 1.5, and (e) 2.0 cm compare measurement (solid black) to the nominal PBRA (dashed red) and PBRA adjusted for both in-scatter and out-scatter (dotted blue) for a 7 MeV beam at 110 cm SSD for 0.352-cm-diameter pins.

(figure cont'd.)

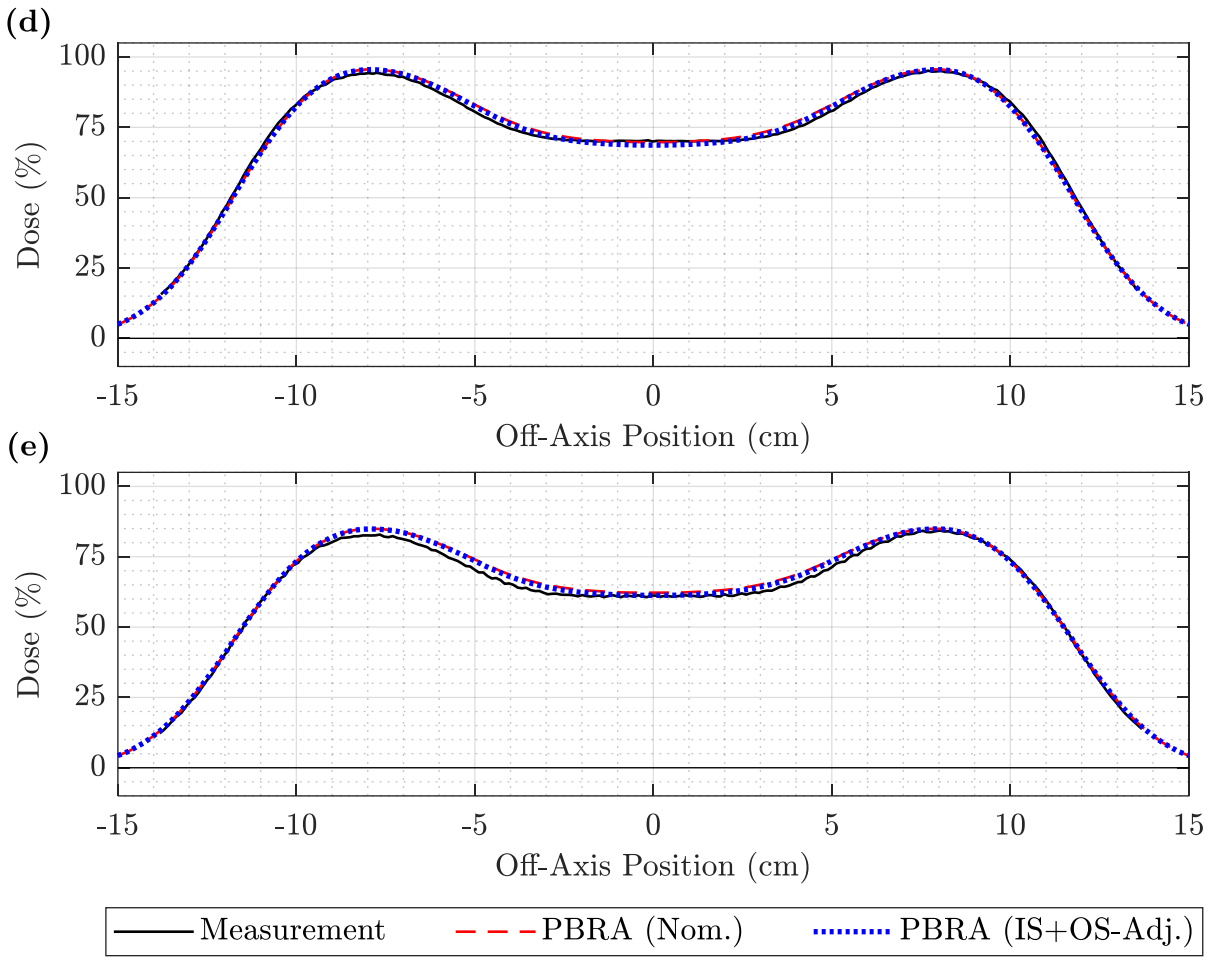
(d)
100
75
50
25
0
Dose (%)
-15
-10
-5
0
5
10
15
Off-Axis Position (cm)
(e)
100
75
50
25
0
Dose (%)
-15
-10
-5
0
5
10
15
Off-Axis Position (cm)
Measurement
PBRA (Nom.)
PBRA (IS+OS-Adj.)

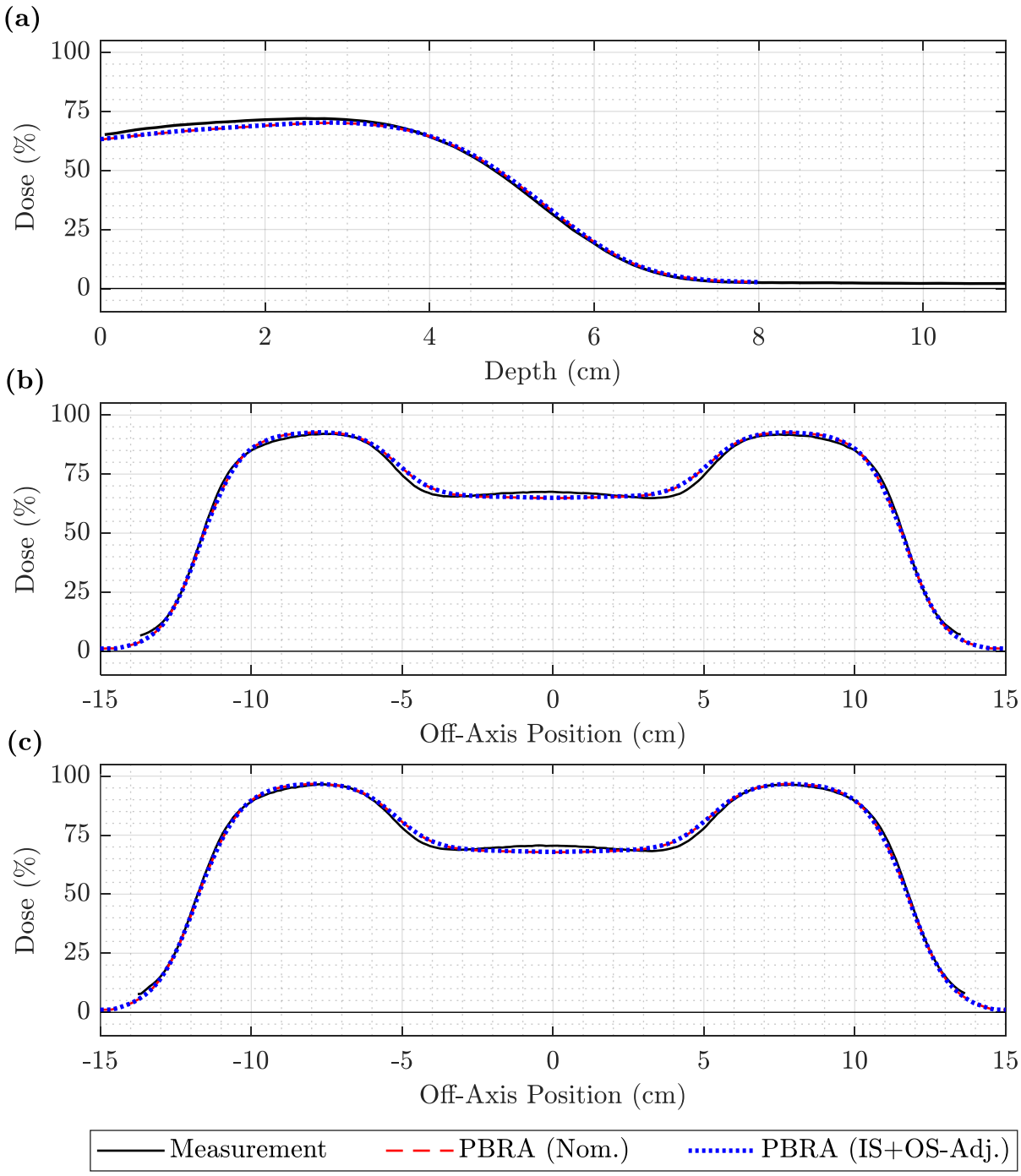

Figure A.45. PDD and off-axis profile comparison of measurement, nominal PBRA, and IS+OS-corrected PBRA for the 13 MeV beam at 110 cm SSD and 0.352-cm pins. The PDD in (a) and off-axis profiles at depths of (b) 0.5, (c) 1.5, (d) 3.0, (e) 3.5, and (f) 4.0 cm compare measurement (solid black) to the nominal PBRA (dashed red) and PBRA adjusted for both in-scatter and out-scatter (dotted blue) for a 13 MeV beam at 110 cm SSD for 0.352-cm-diameter pins.

(figure cont'd.)

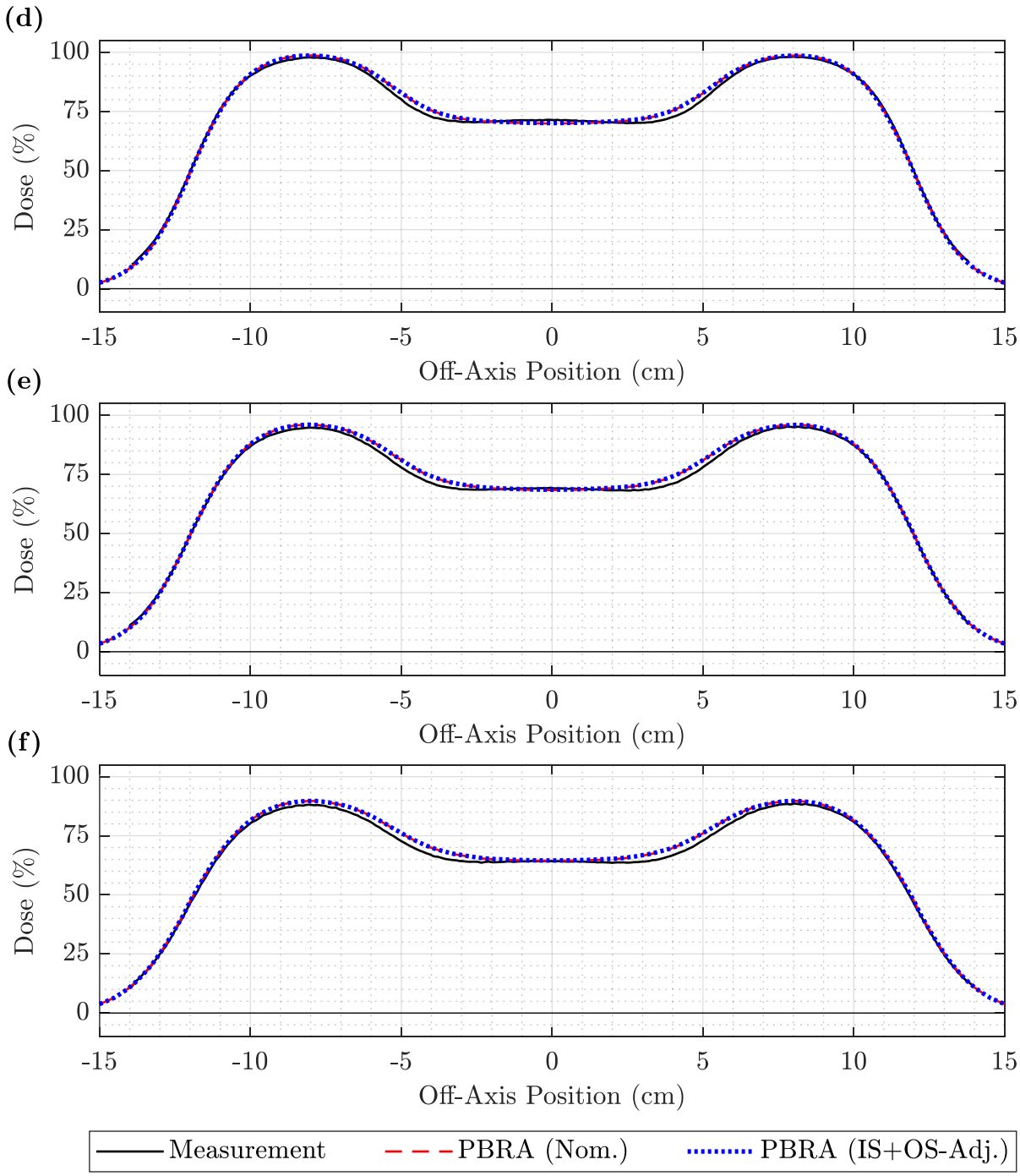
(d)
100
75
50
25
0
Dose (%)
-15
-10
-5
0
5
10
15
Off-Axis Position (cm)
(e)
100
75
50
25
0
Dose (%)
-15
-10
-5
0
5
10
15
Off-Axis Position (cm)
(f)
100
75
50
25
0
Dose (%)
-15
-10
-5
0
5
10
15
Off-Axis Position (cm)
Measurement
PBRA (Nom.)
PBRA (IS+OS-Adj.)

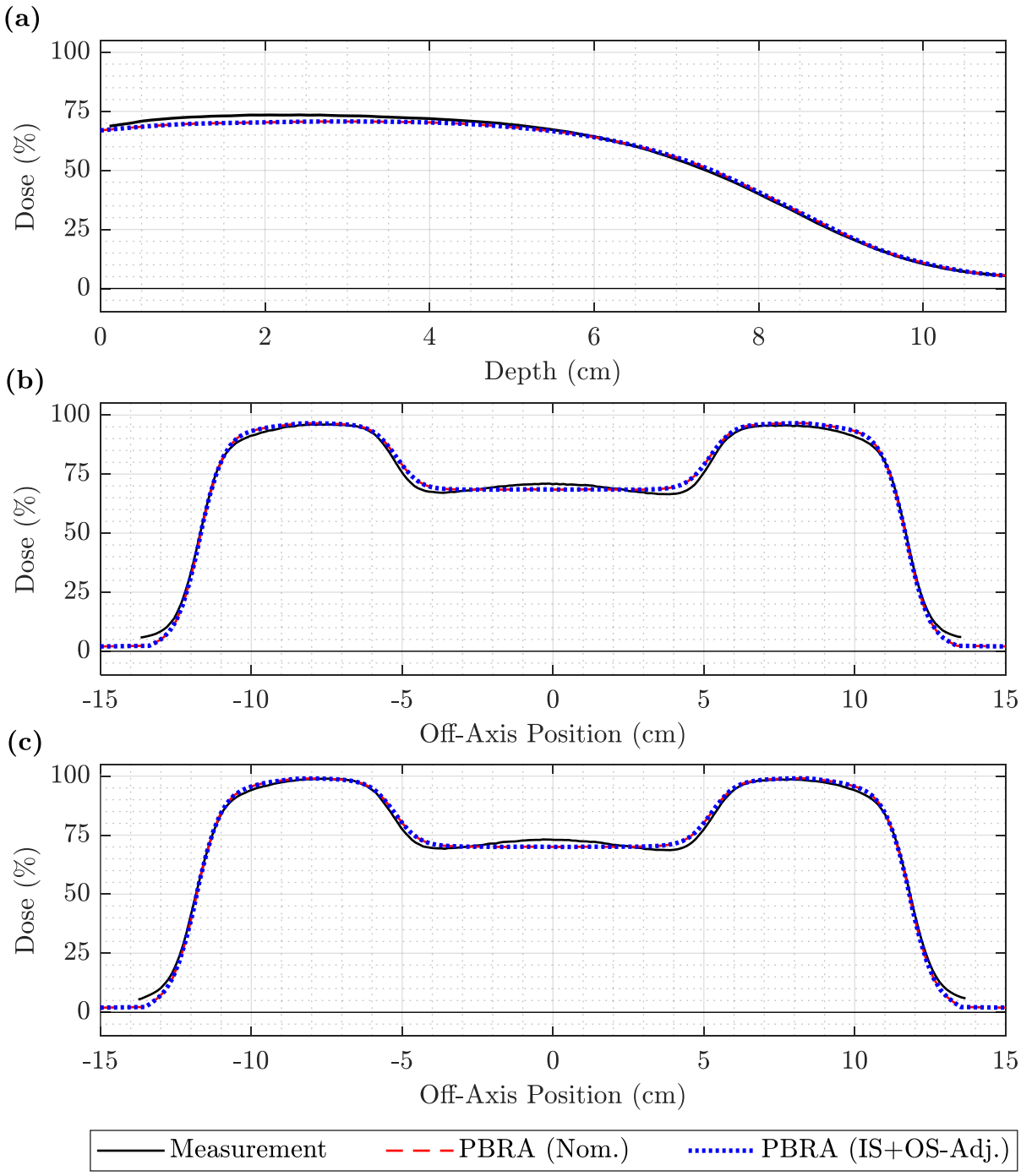

Figure A.46. PDD and off-axis profile comparison of measurement, nominal PBRA, and IS+OS-corrected PBRA for the 20 MeV beam at 110 cm SSD and 0.352-cm pins. The PDD in (a) and off-axis profiles at depths of (b) 0.5, (c) 1.5, (d) 3.5, (e) 5.0, and (f) 6.0 cm compare measurement (solid black) to the nominal PBRA (dashed red) and PBRA adjusted for both in-scatter and out-scatter (dotted blue) for a 20 MeV beam at 110 cm SSD for 0.352-cm-diameter pins.

(figure cont'd.)

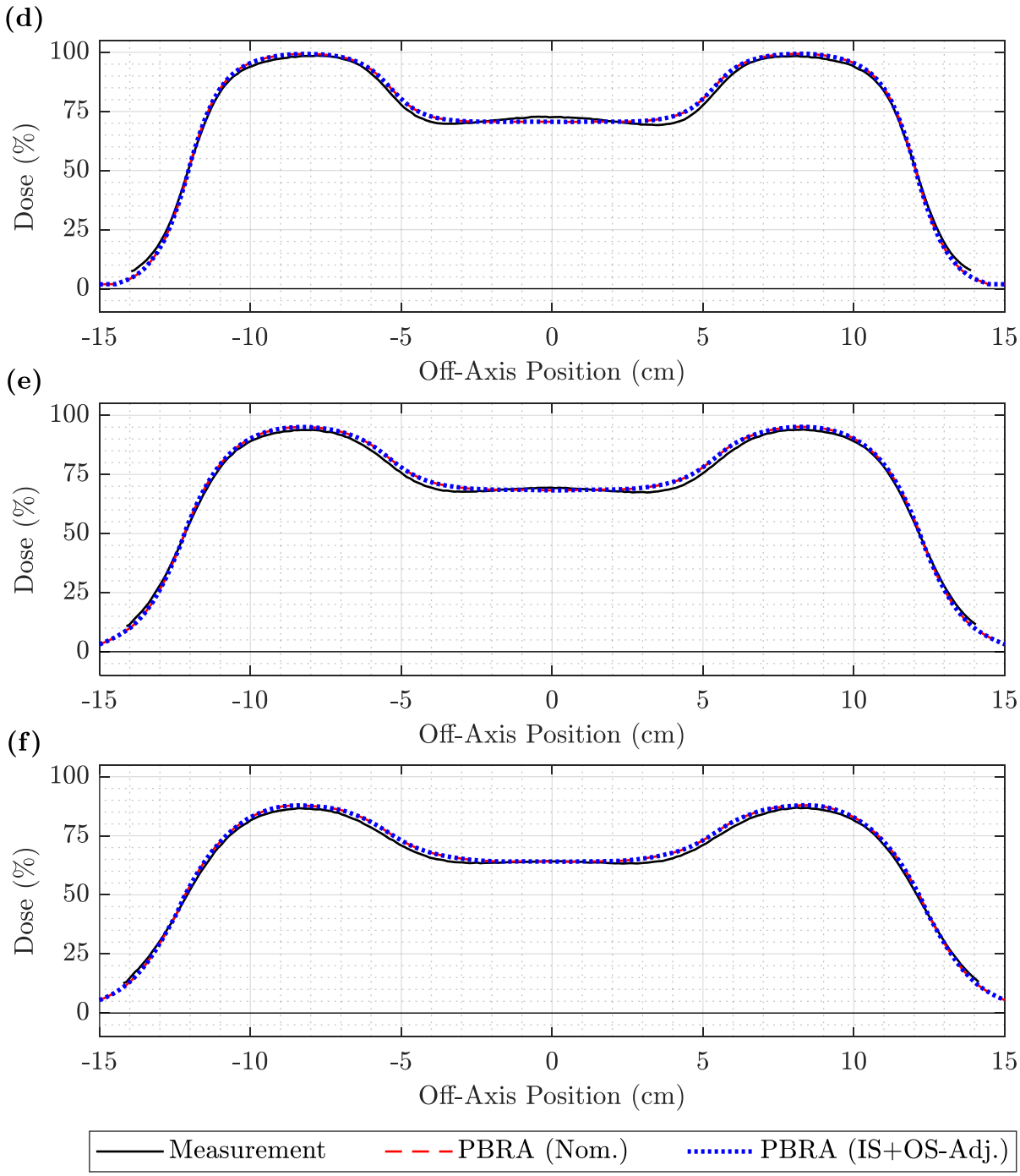
(d)
100
75
50
25
0
Dose (%)
-15
-10
-5
0
5
10
15
Off-Axis Position (cm)
(e)
100
75
50
25
0
Dose (%)
-15
-10
-5
0
5
10
15
Off-Axis Position (cm)
(f)
100
75
50
25
0
Dose (%)
-15
-10
-5
0
5
10
15
Off-Axis Position (cm)
Measurement
PBRA (Nom.)
PBRA (IS+OS-Adj.)

Appendix B. Comparison of Measurement and Corrected PBRA Calculations

Isodose comparisons of measurement to nominal and IS+OS-corrected PBRA calculations are plotted with the corresponding dose difference histograms in Figures B.1-24 for various beam specifications and modulator combinations.

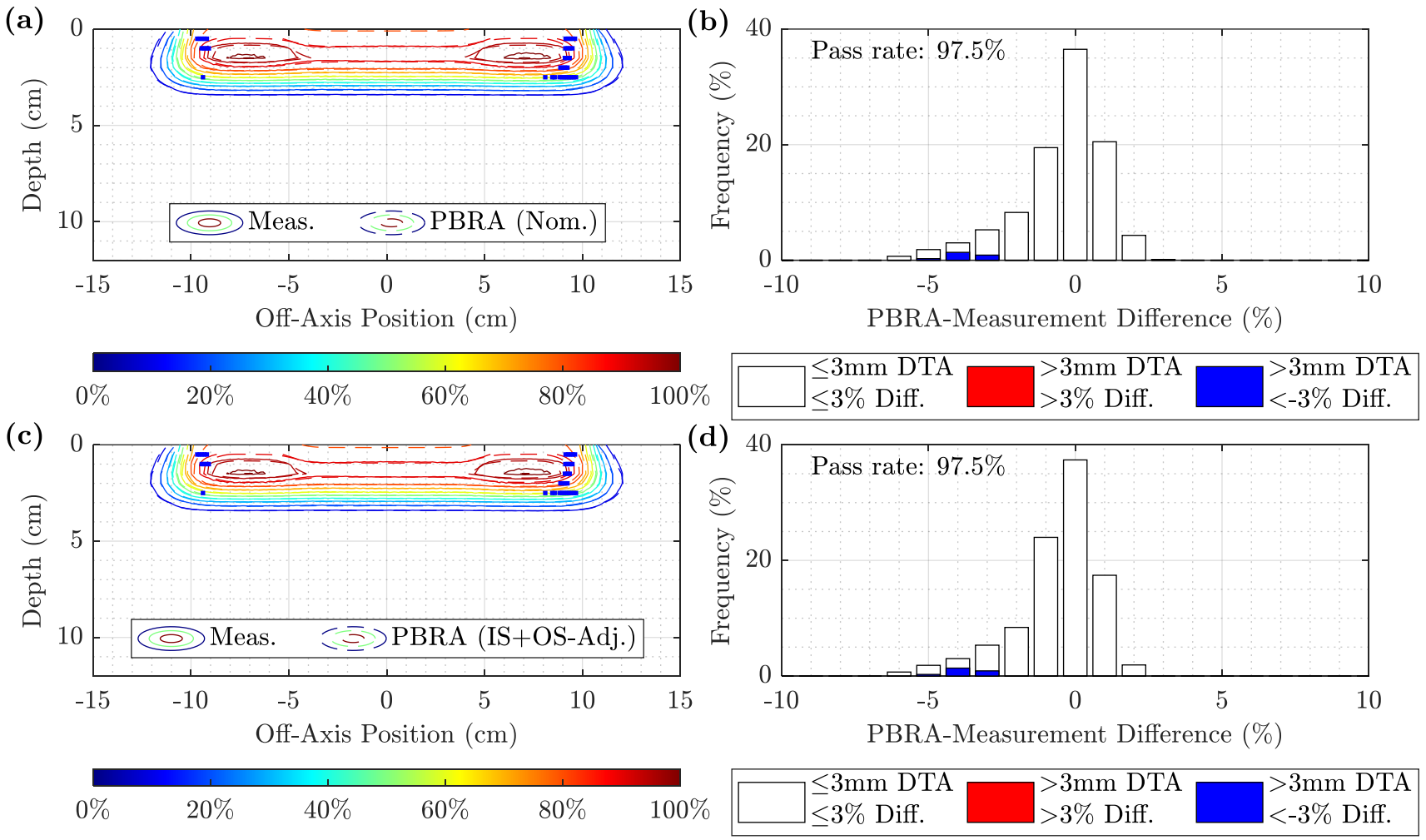

Figure B.1. Measured and PBRA-calculated isodose comparison and difference histogram for 0.158-cm pins at 7 MeV and 100 cm SSD. The isodose contours for measurement (solid) are compared to the PBRA calculations with (a) nominal and (c) IS+OS-corrected pin diameters. Difference histograms under 3%/3mm DTA criteria are plotted for (b) nominal and (d) IS+OS-corrected PBRA diameters. Points at which the PBRA underpredicted and overpredicted the dose relative to measurement are shown in blue and red, respectively. The nominal and corrected passing rates were both 97.5%.

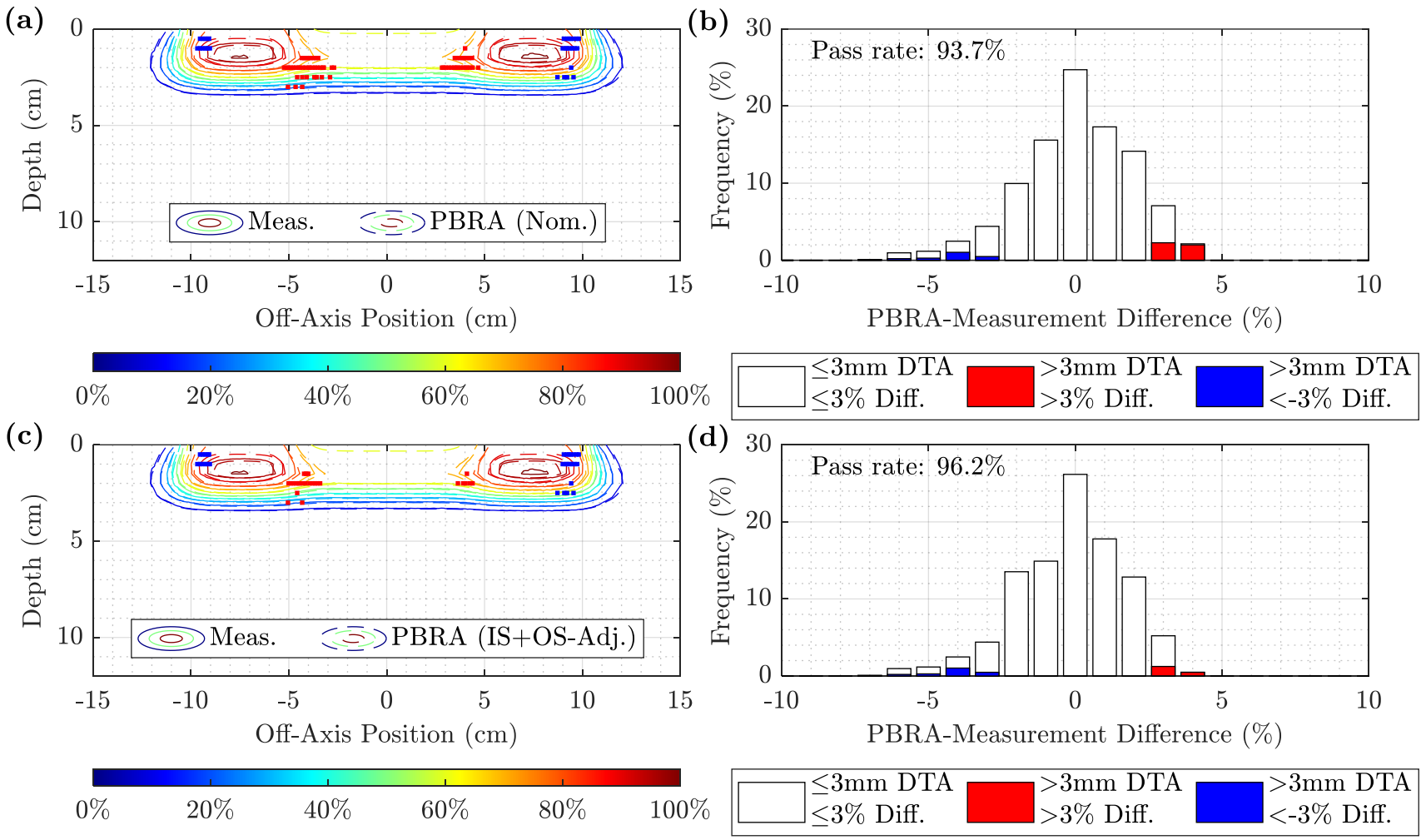

Figure B.2. Measured and PBRA-calculated isodose comparison and difference histogram for 0.352-cm pins at 7 MeV and 100 cm SSD. The isodose contours for measurement (solid) are compared to the PBRA calculations with (a) nominal and (c) IS+OS-corrected pin diameters. Difference histograms under 3%/3mm DTA criteria are plotted for (b) nominal and (d) IS+OS-corrected PBRA diameters. Points at which the PBRA underpredicted and overpredicted the dose relative to measurement are shown in blue and red, respectively. The nominal and corrected passing rates were 93.7% and 96.2%, respectively.

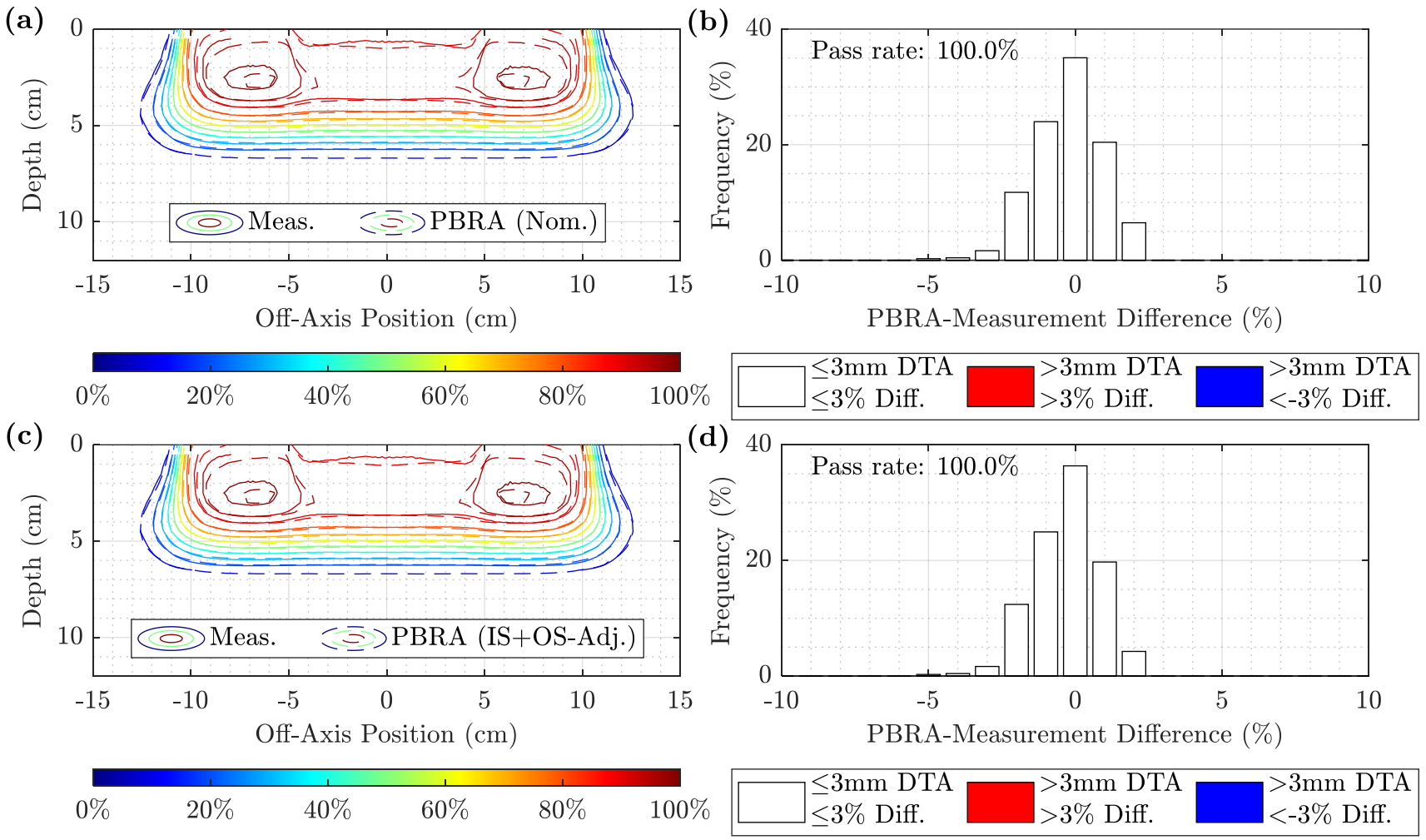

Figure B.3. Measured and PBRA-calculated isodose comparison and difference histogram for 0.158-cm pins at 13 MeV and 100 cm SSD. The isodose contours for measurement (solid) are compared to the PBRA calculations with (a) nominal and (c) IS+OS-corrected pin diameters. Difference histograms under 3%/3mm DTA criteria are plotted for (b) nominal and (d) IS+OS-corrected PBRA diameters. Points at which the PBRA underpredicted and overpredicted the dose relative to measurement are shown in blue and red, respectively. The nominal and corrected passing rates were both 100%.

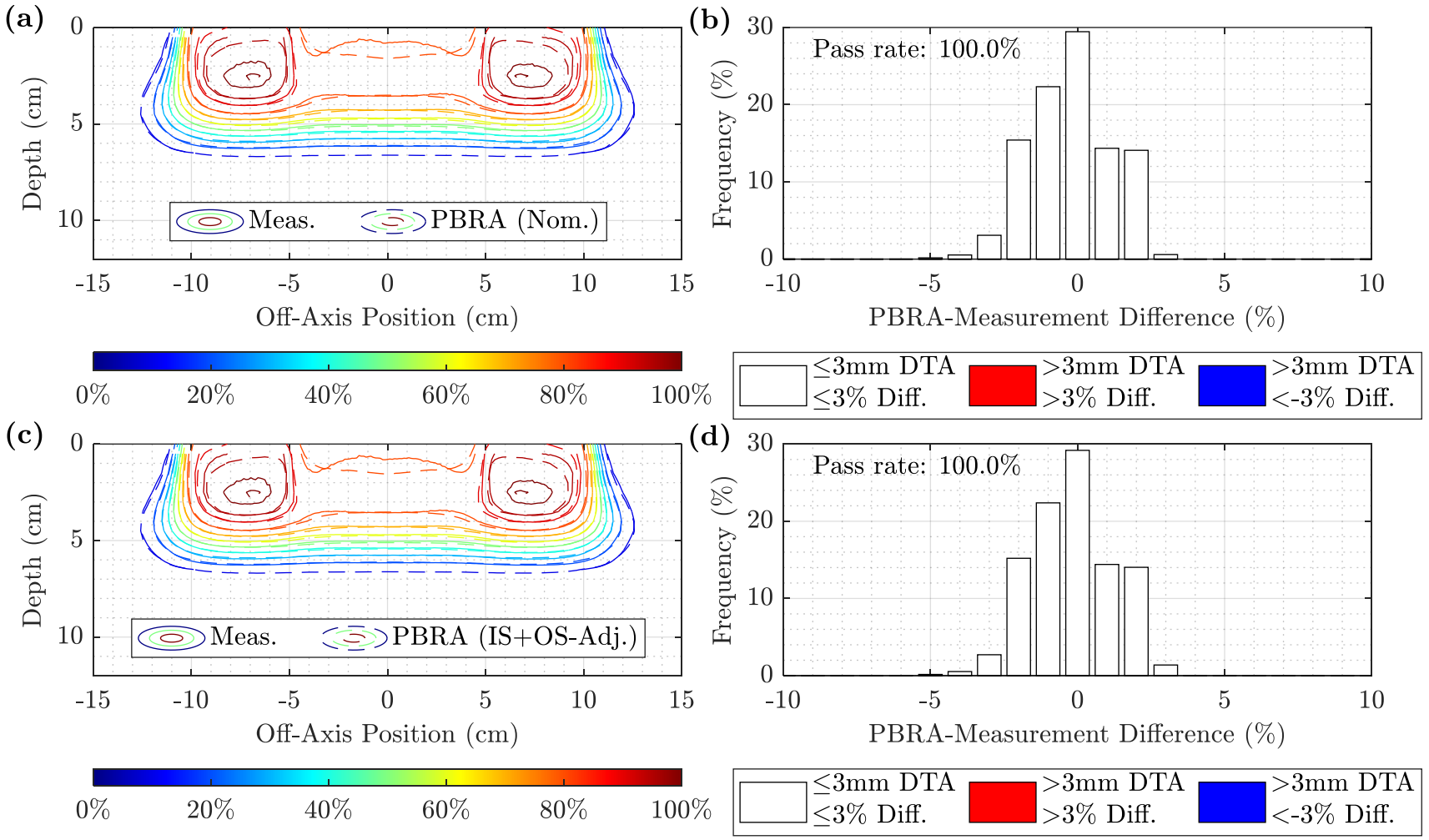

Figure B.4. Measured and PBRA-calculated isodose comparison and difference histogram for 0.273-cm pins at 13 MeV and 100 cm SSD. The isodose contours for measurement (solid) are compared to the PBRA calculations with (a) nominal and (c) IS+OS-corrected pin diameters. Difference histograms under 3%/3mm DTA criteria are plotted for (b) nominal and (d) IS+OS-corrected PBRA diameters. Points at which the PBRA underpredicted and overpredicted the dose relative to measurement are shown in blue and red, respectively. The nominal and corrected passing rates were both 100%.

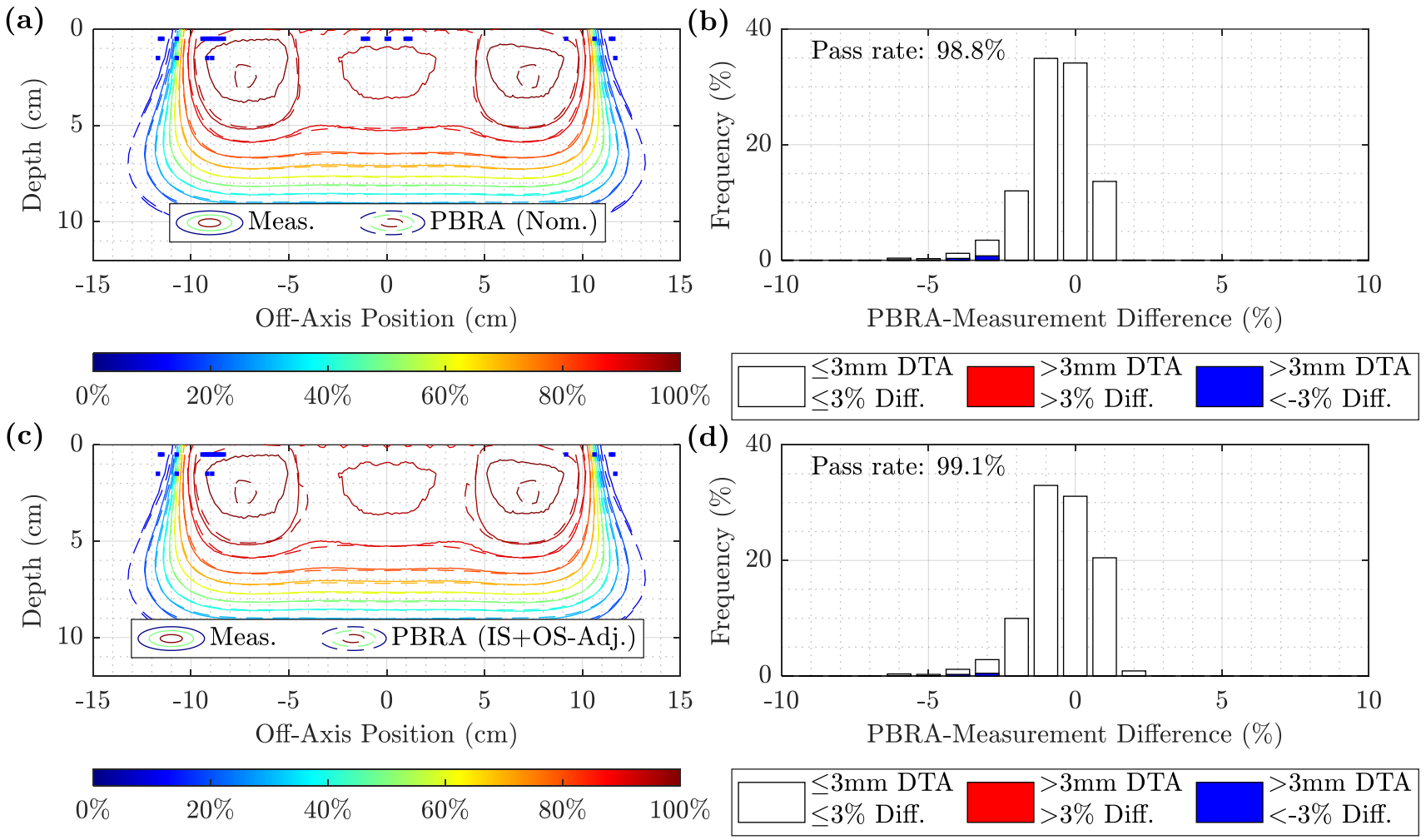

Figure B.5. Measured and PBRA-calculated isodose comparison and difference histogram for 0.158-cm pins at 20 MeV and 100 cm SSD. The isodose contours for measurement (solid) are compared to the PBRA calculations with (a) nominal and (c) IS+OS-corrected pin diameters. Difference histograms under 3%/3mm DTA criteria are plotted for (b) nominal and (d) IS+OS-corrected PBRA diameters. Points at which the PBRA underpredicted and overpredicted the dose relative to measurement are shown in blue and red, respectively. The nominal and corrected passing rates were 98.8% and 99.1%, respectively.

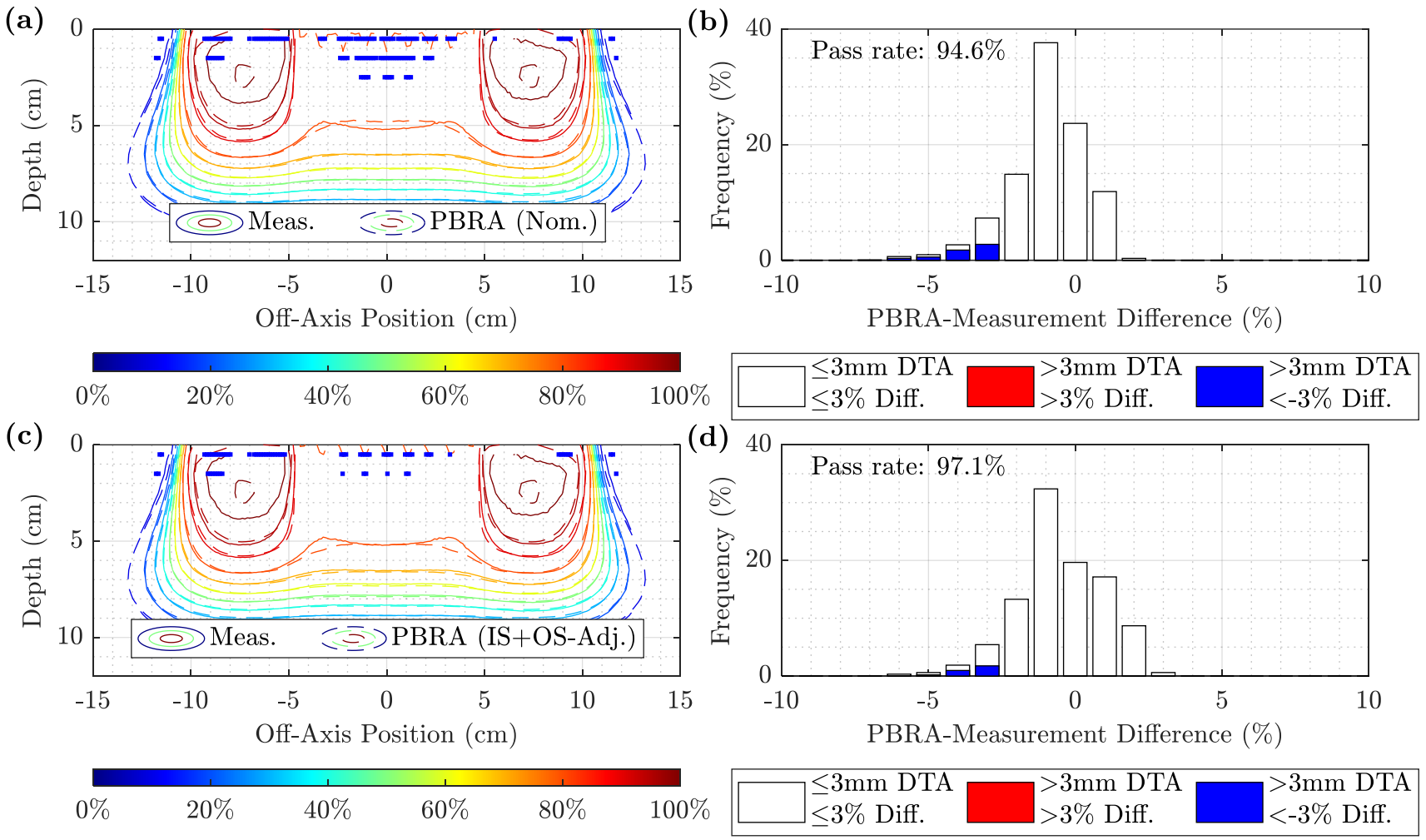

Figure B.6. Measured and PBRA-calculated isodose comparison and difference histogram for 0.273-cm pins at 20 MeV and 100 cm SSD. The isodose contours for measurement (solid) are compared to the PBRA calculations with (a) nominal and (c) IS+OS-corrected pin diameters. Difference histograms under 3%/3mm DTA criteria are plotted for (b) nominal and (d) IS+OS-corrected PBRA diameters. Points at which the PBRA underpredicted and overpredicted the dose relative to measurement are shown in blue and red, respectively. The nominal and corrected passing rates were 94.6% and 97.1%, respectively.

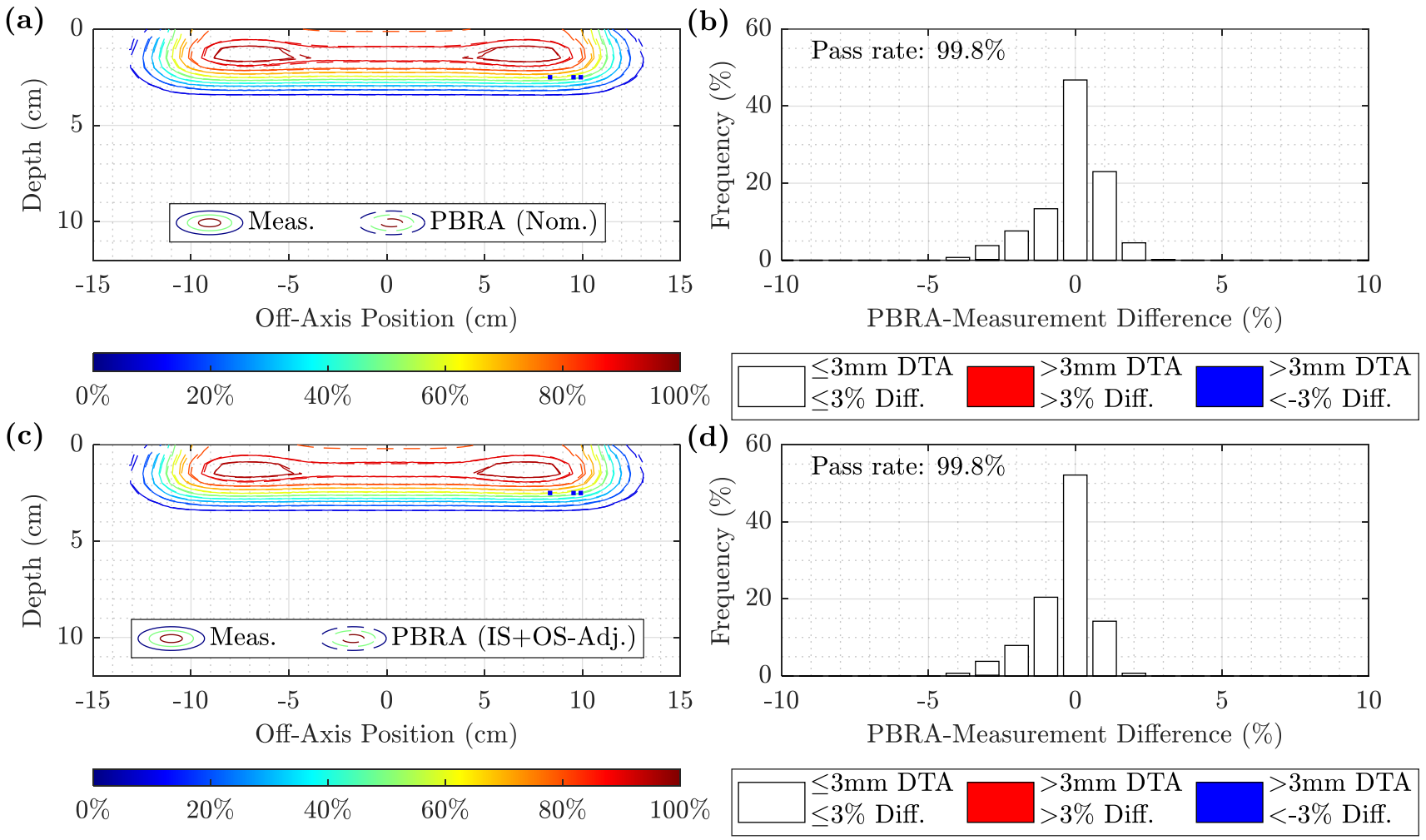

Figure B.7. Measured and PBRA-calculated isodose comparison and difference histogram for 0.158-cm pins at 7 MeV and 105 cm SSD. The isodose contours for measurement (solid) are compared to the PBRA calculations with (a) nominal and (c) IS+OS-corrected pin diameters. Difference histograms under 3%/3mm DTA criteria are plotted for (b) nominal and (d) IS+OS-corrected PBRA diameters. Points at which the PBRA underpredicted and overpredicted the dose relative to measurement are shown in blue and red, respectively. The nominal and corrected passing rates were both 99.8%.

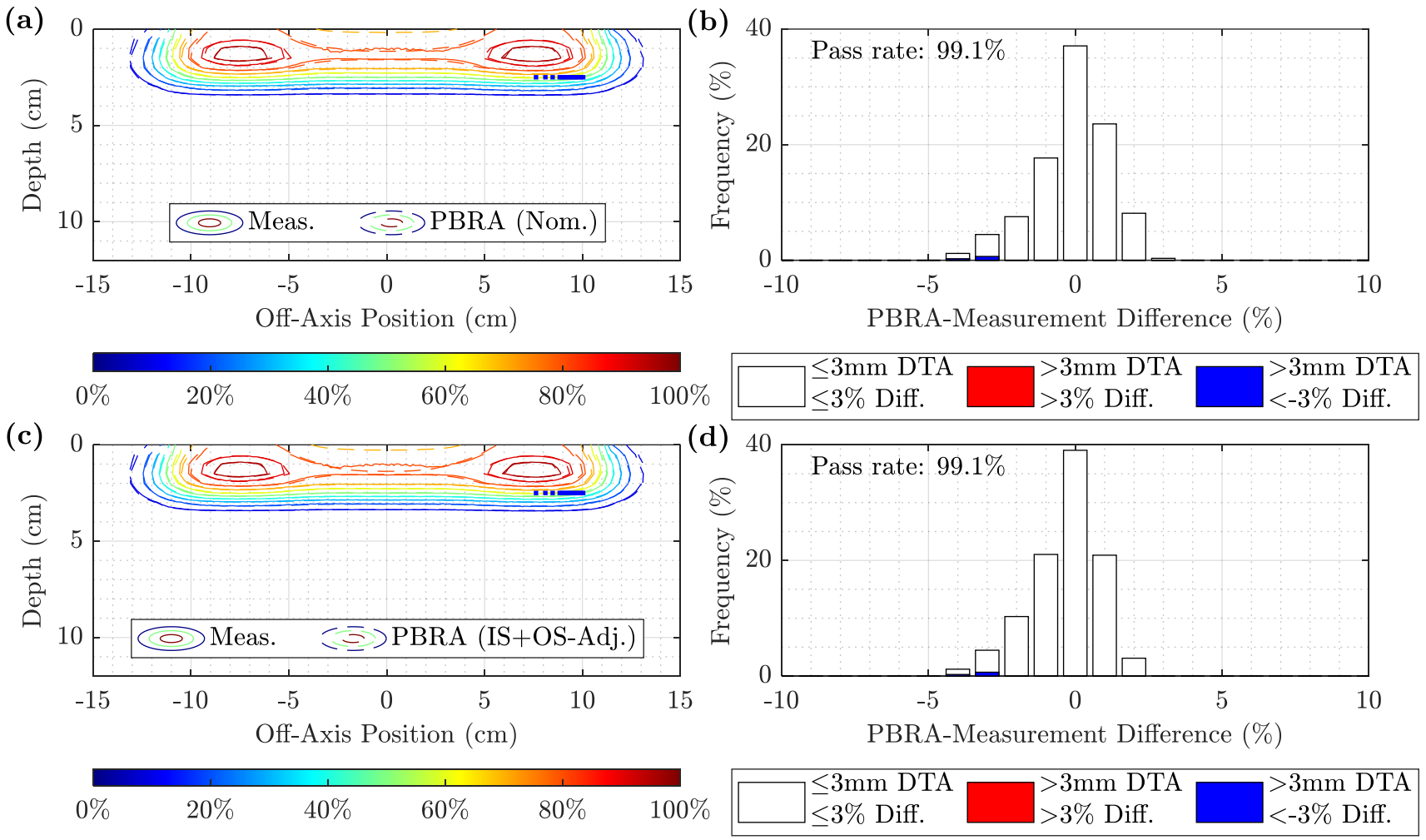

Figure B.8. Measured and PBRA-calculated isodose comparison and difference histogram for 0.273-cm pins at 7 MeV and 105 cm SSD. The isodose contours for measurement (solid) are compared to the PBRA calculations with (a) nominal and (c) IS+OS-corrected pin diameters. Difference histograms under 3%/3mm DTA criteria are plotted for (b) nominal and (d) IS+OS-corrected PBRA diameters. Points at which the PBRA underpredicted and overpredicted the dose relative to measurement are shown in blue and red, respectively. The nominal and corrected passing rates were both 99.1%.

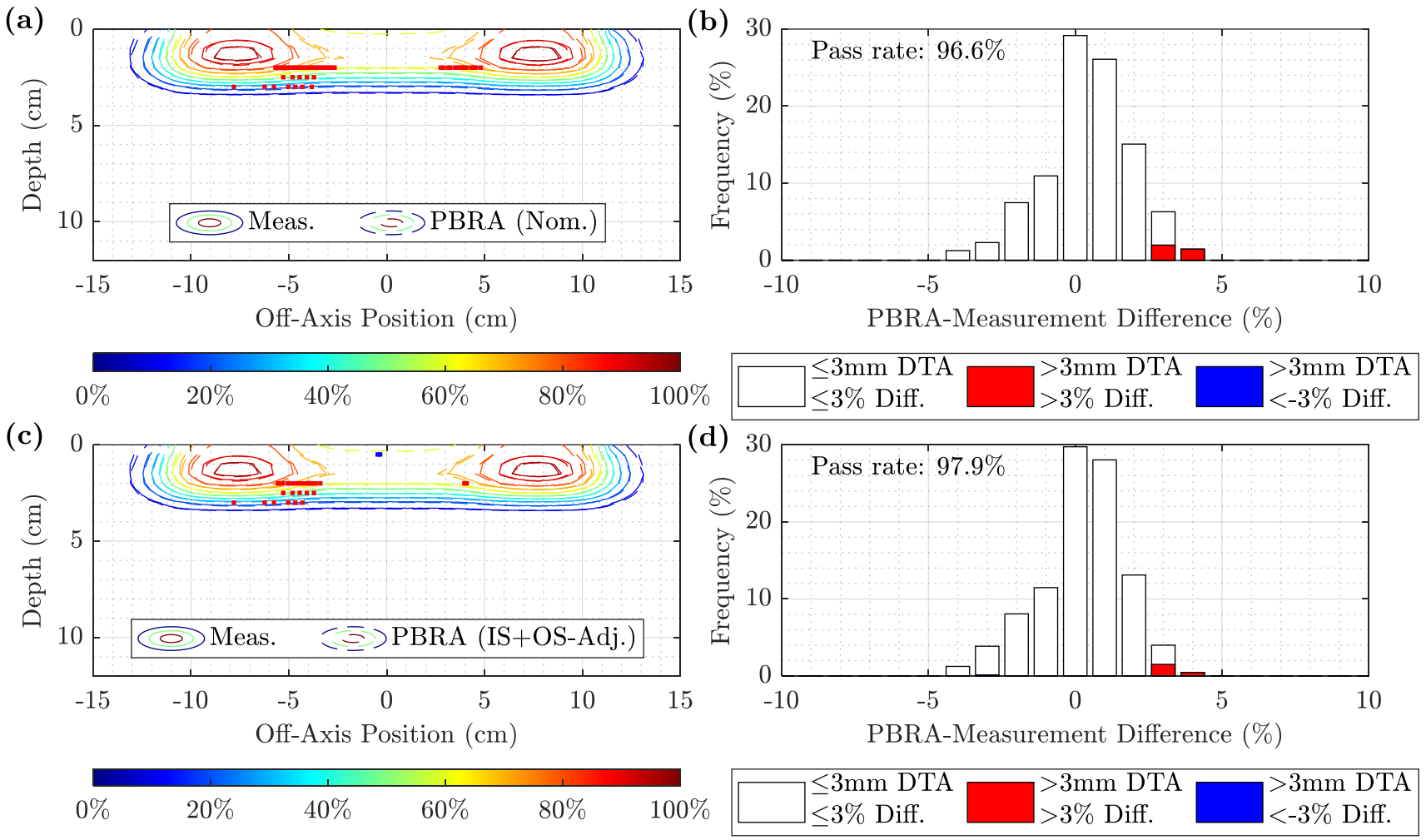

Figure B.9. Measured and PBRA-calculated isodose comparison and difference histogram for 0.352-cm pins at 7 MeV and 105 cm SSD. The isodose contours for measurement (solid) are compared to the PBRA calculations with (a) nominal and (c) IS+OS-corrected pin diameters. Difference histograms under 3%/3mm DTA criteria are plotted for (b) nominal and (d) IS+OS-corrected PBRA diameters. Points at which the PBRA underpredicted and overpredicted the dose relative to measurement are shown in blue and red, respectively. The nominal and corrected passing rates were 96.6% and 97.9%, respectively.

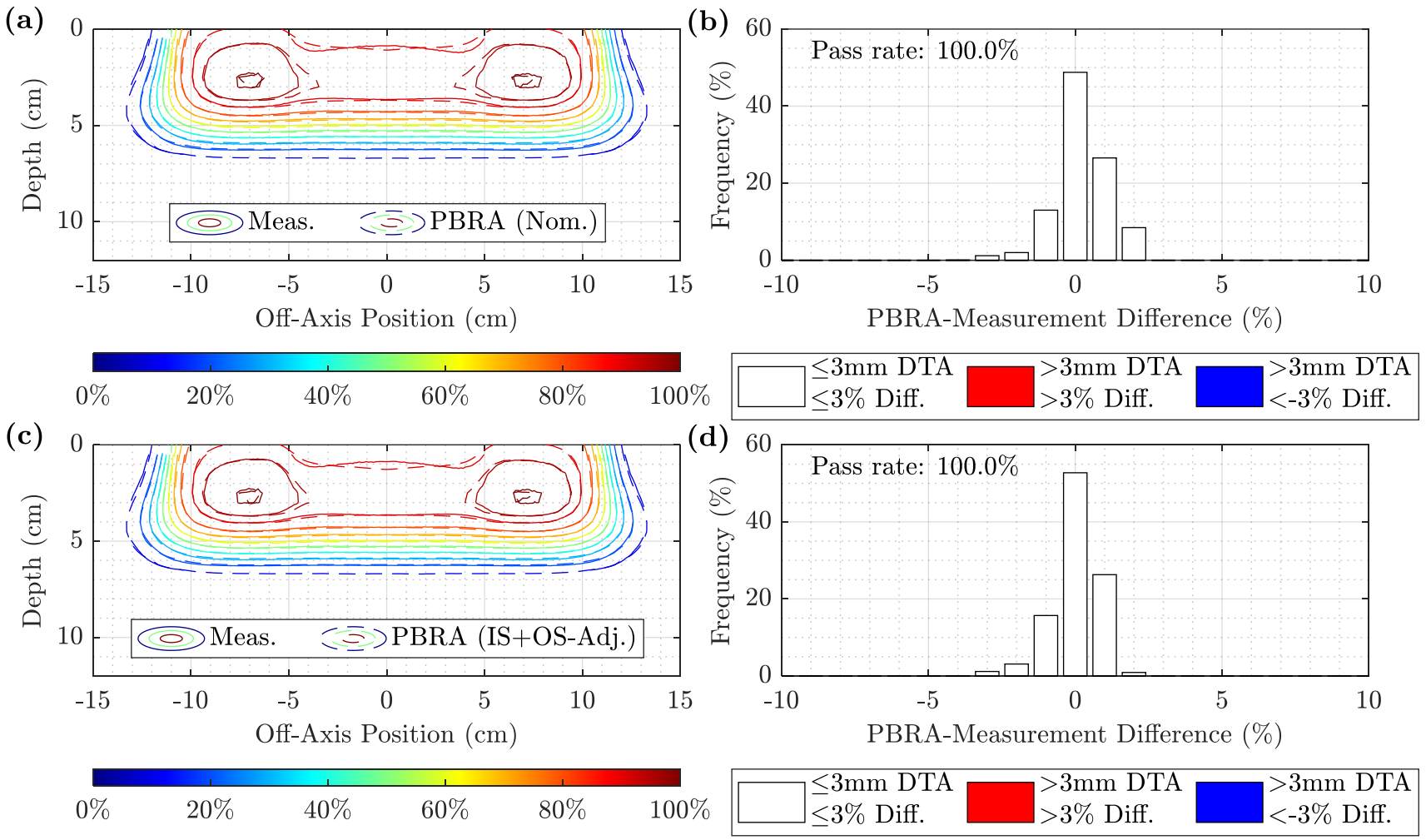

Figure B.10. Measured and PBRA-calculated isodose comparison and difference histogram for 0.158-cm pins at 13 MeV and 105 cm SSD. The isodose contours for measurement (solid) are compared to the PBRA calculations with (a) nominal and (c) IS+OS-corrected pin diameters. Difference histograms under 3%/3mm DTA criteria are plotted for (b) nominal and (d) IS+OS-corrected PBRA diameters. Points at which the PBRA underpredicted and overpredicted the dose relative to measurement are shown in blue and red, respectively. The nominal and corrected passing rates were both 100%.

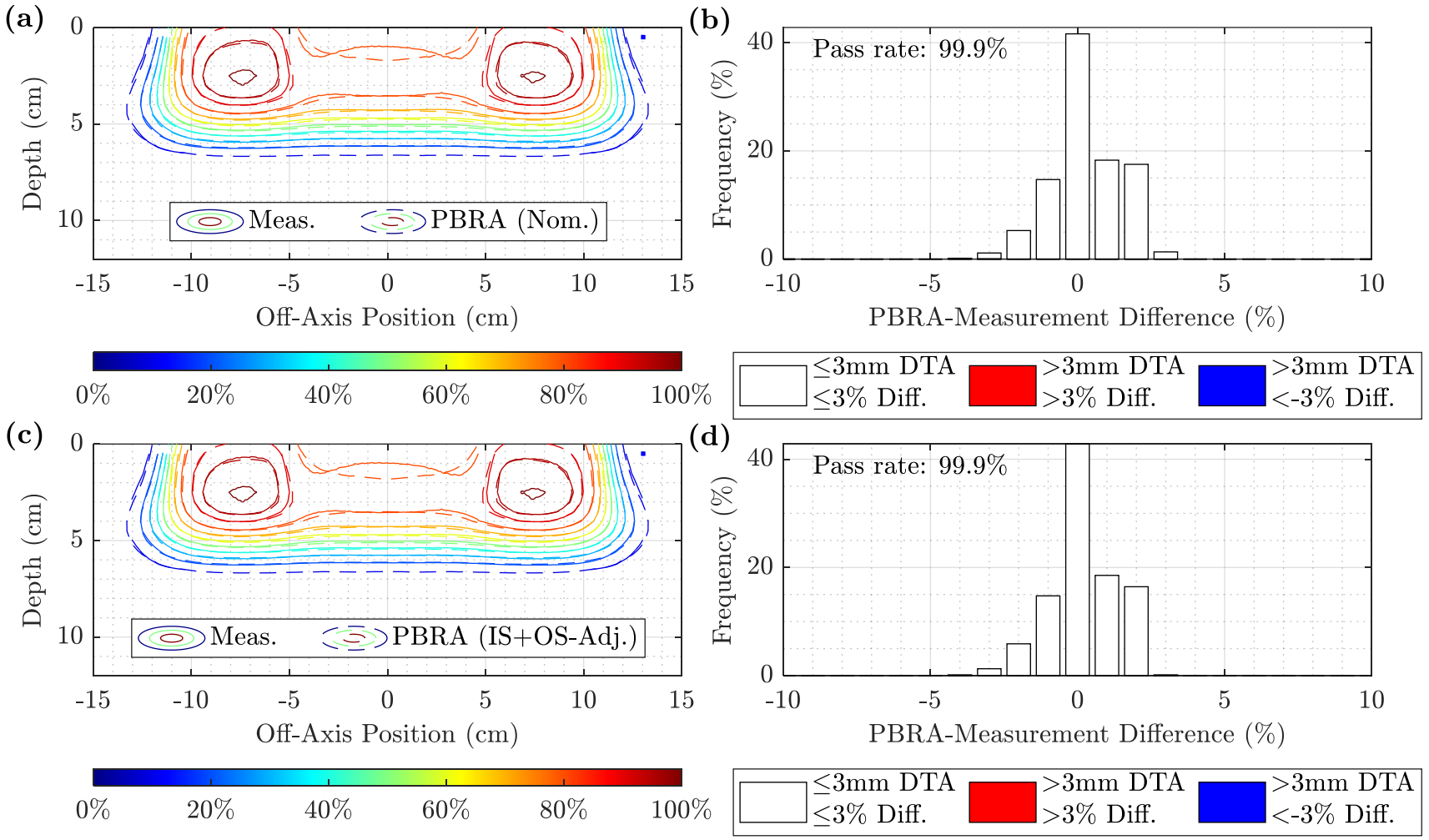

Figure B.11. Measured and PBRA-calculated isodose comparison and difference histogram for 0.273-cm pins at 13 MeV and 105 cm SSD. The isodose contours for measurement (solid) are compared to the PBRA calculations with (a) nominal and (c) IS+OS-corrected pin diameters. Difference histograms under 3%/3mm DTA criteria are plotted for (b) nominal and (d) IS+OS-corrected PBRA diameters. Points at which the PBRA underpredicted and overpredicted the dose relative to measurement are shown in blue and red, respectively. The nominal and corrected passing rates were both 99.9%.

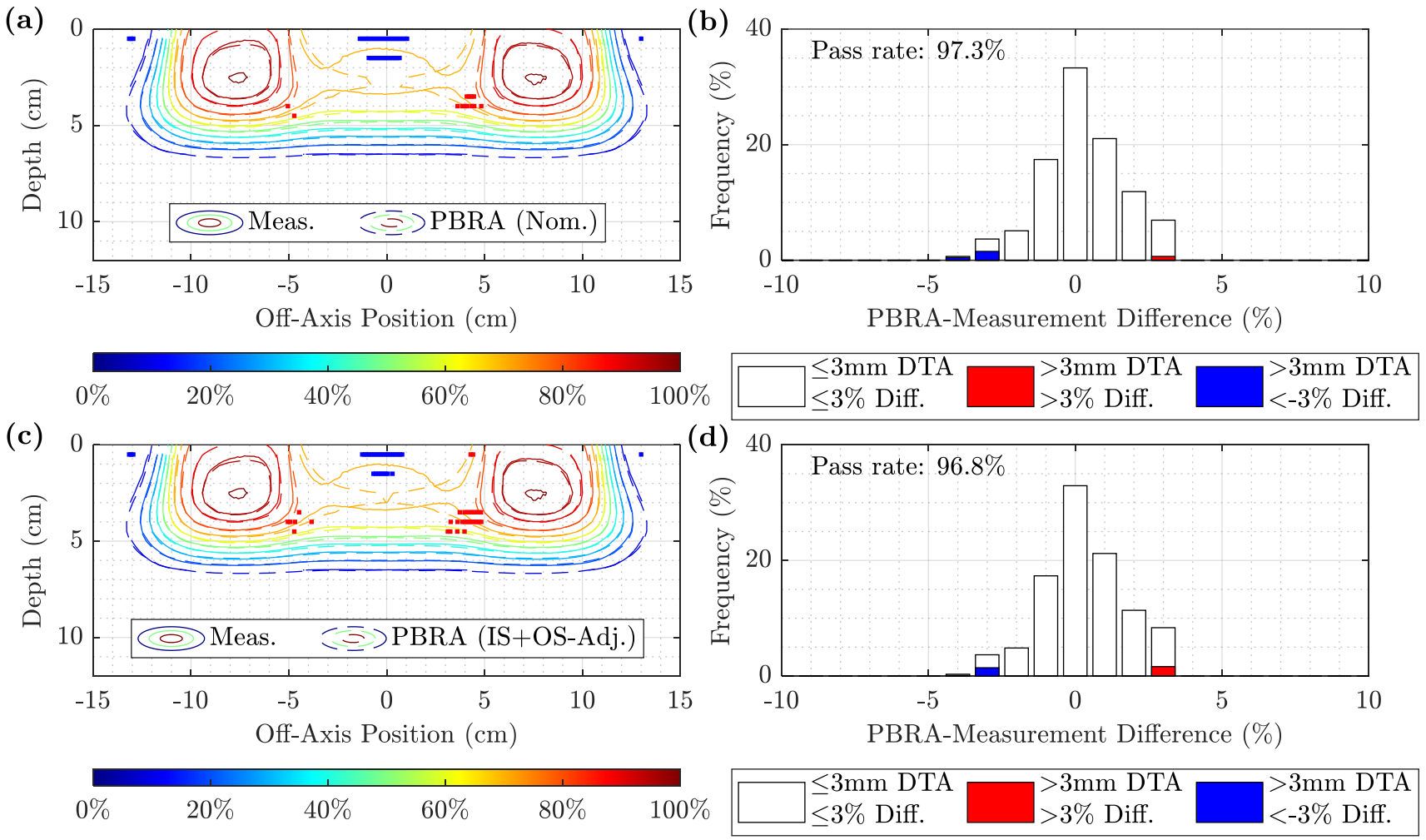

Figure B.12. Measured and PBRA-calculated isodose comparison and difference histogram for 0.352-cm pins at 13 MeV and 105 cm SSD. The isodose contours for measurement (solid) are compared to the PBRA calculations with (a) nominal and (c) IS+OS-corrected pin diameters. Difference histograms under 3%/3mm DTA criteria are plotted for (b) nominal and (d) IS+OS-corrected PBRA diameters. Points at which the PBRA underpredicted and overpredicted the dose relative to measurement are shown in blue and red, respectively. The nominal and corrected passing rates were 97.3% and 96.8%, respectively.

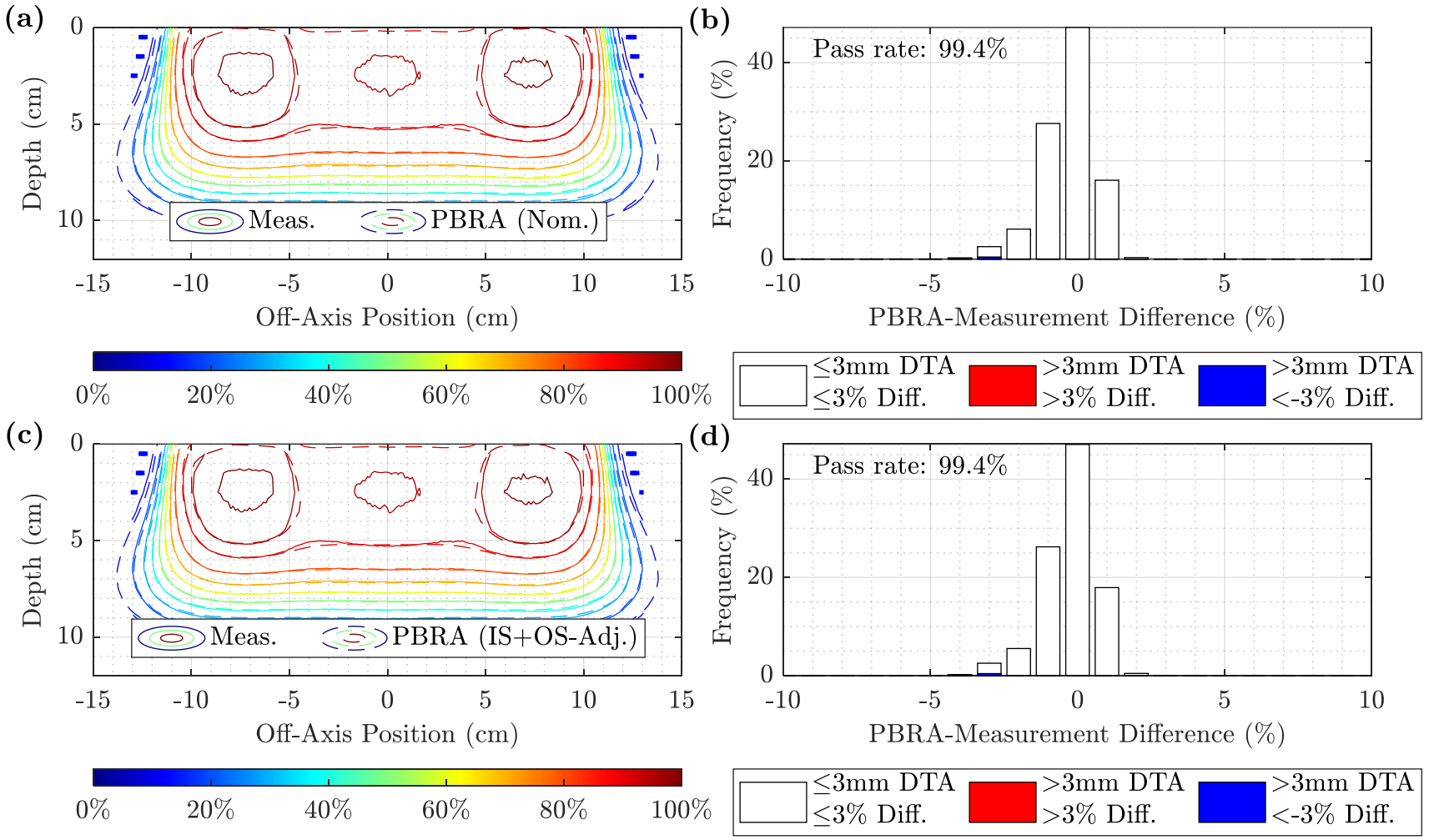

Figure B.13. Measured and PBRA-calculated isodose comparison and difference histogram for 0.158-cm pins at 20 MeV and 105 cm SSD. The isodose contours for measurement (solid) are compared to the PBRA calculations with (a) nominal and (c) IS+OS-corrected pin diameters. Difference histograms under 3%/3mm DTA criteria are plotted for (b) nominal and (d) IS+OS-corrected PBRA diameters. Points at which the PBRA underpredicted and overpredicted the dose relative to measurement are shown in blue and red, respectively. The nominal and corrected passing rates were both 99.4%.

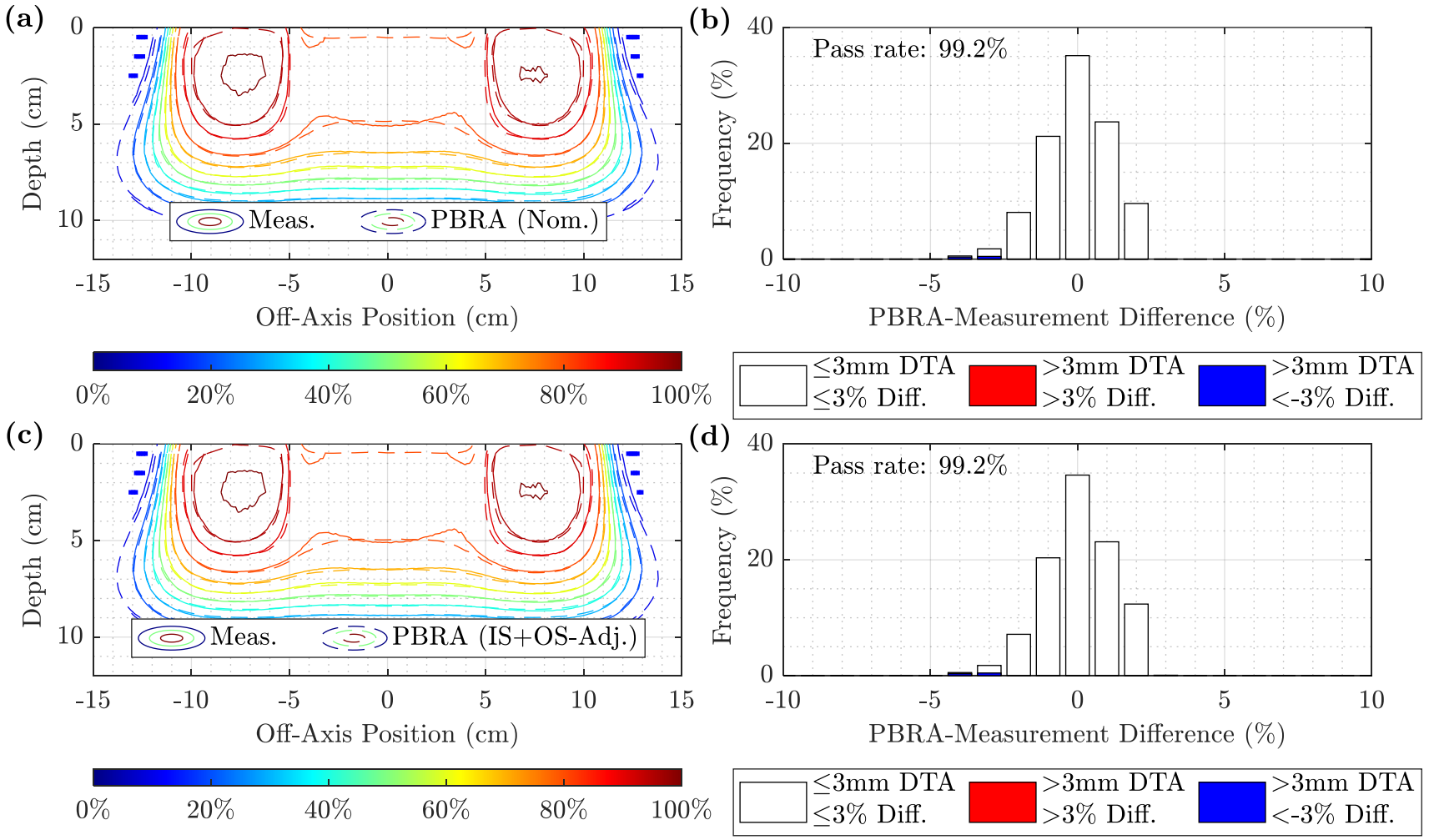

Figure B.14. Measured and PBRA-calculated isodose comparison and difference histogram for 0.273-cm pins at 20 MeV and 105 cm SSD. The isodose contours for measurement (solid) are compared to the PBRA calculations with (a) nominal and (c) IS+OS-corrected pin diameters. Difference histograms under 3%/3mm DTA criteria are plotted for (b) nominal and (d) IS+OS-corrected PBRA diameters. Points at which the PBRA underpredicted and overpredicted the dose relative to measurement are shown in blue and red, respectively. The nominal and corrected passing rates were both 99.2%.

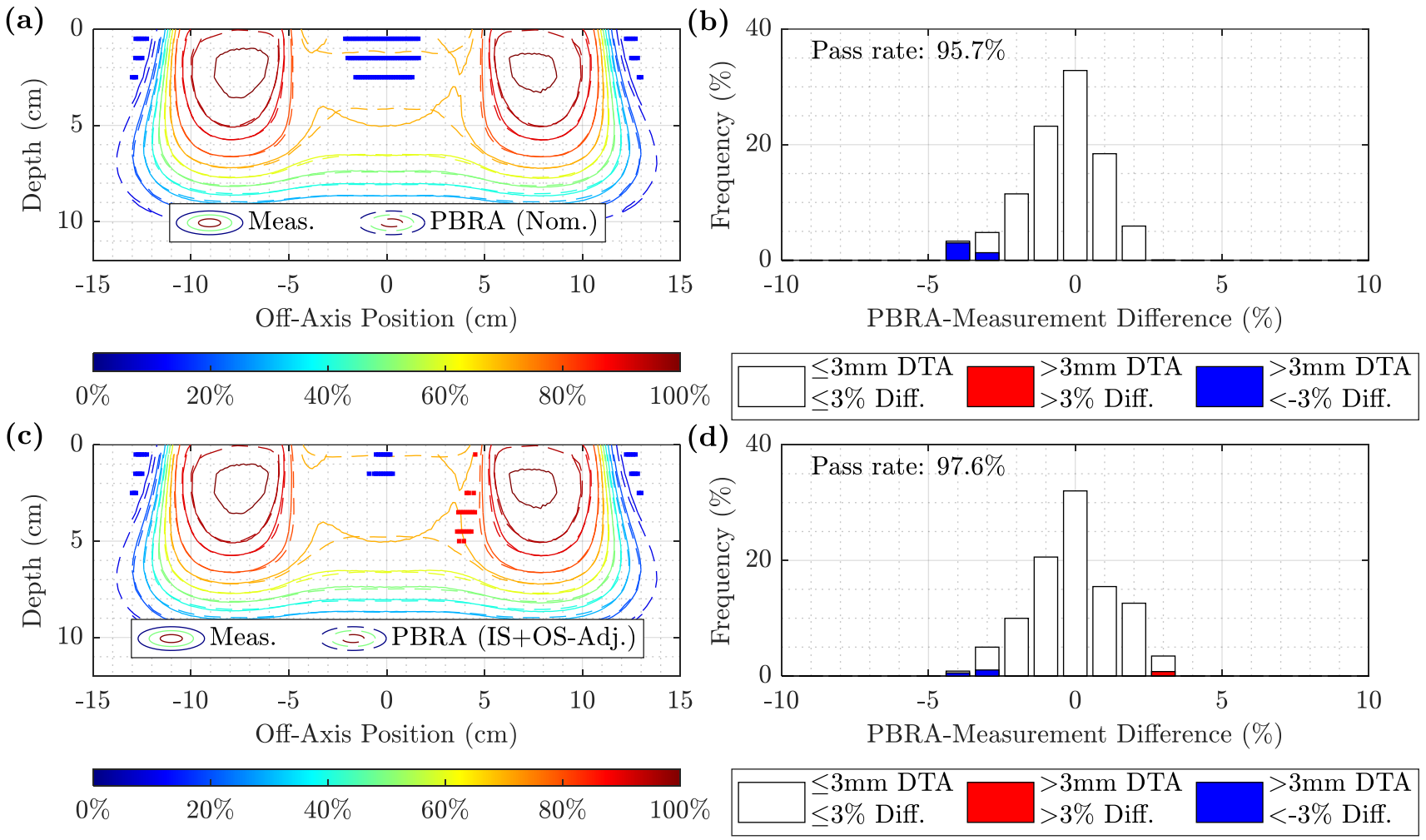

Figure B.15. Measured and PBRA-calculated isodose comparison and difference histogram for 0.352-cm pins at 20 MeV and 105 cm SSD. The isodose contours for measurement (solid) are compared to the PBRA calculations with (a) nominal and (c) IS+OS-corrected pin diameters. Difference histograms under 3%/3mm DTA criteria are plotted for (b) nominal and (d) IS+OS-corrected PBRA diameters. Points at which the PBRA underpredicted and overpredicted the dose relative to measurement are shown in blue and red, respectively. The nominal and corrected passing rates were 95.7% and 97.6%, respectively.

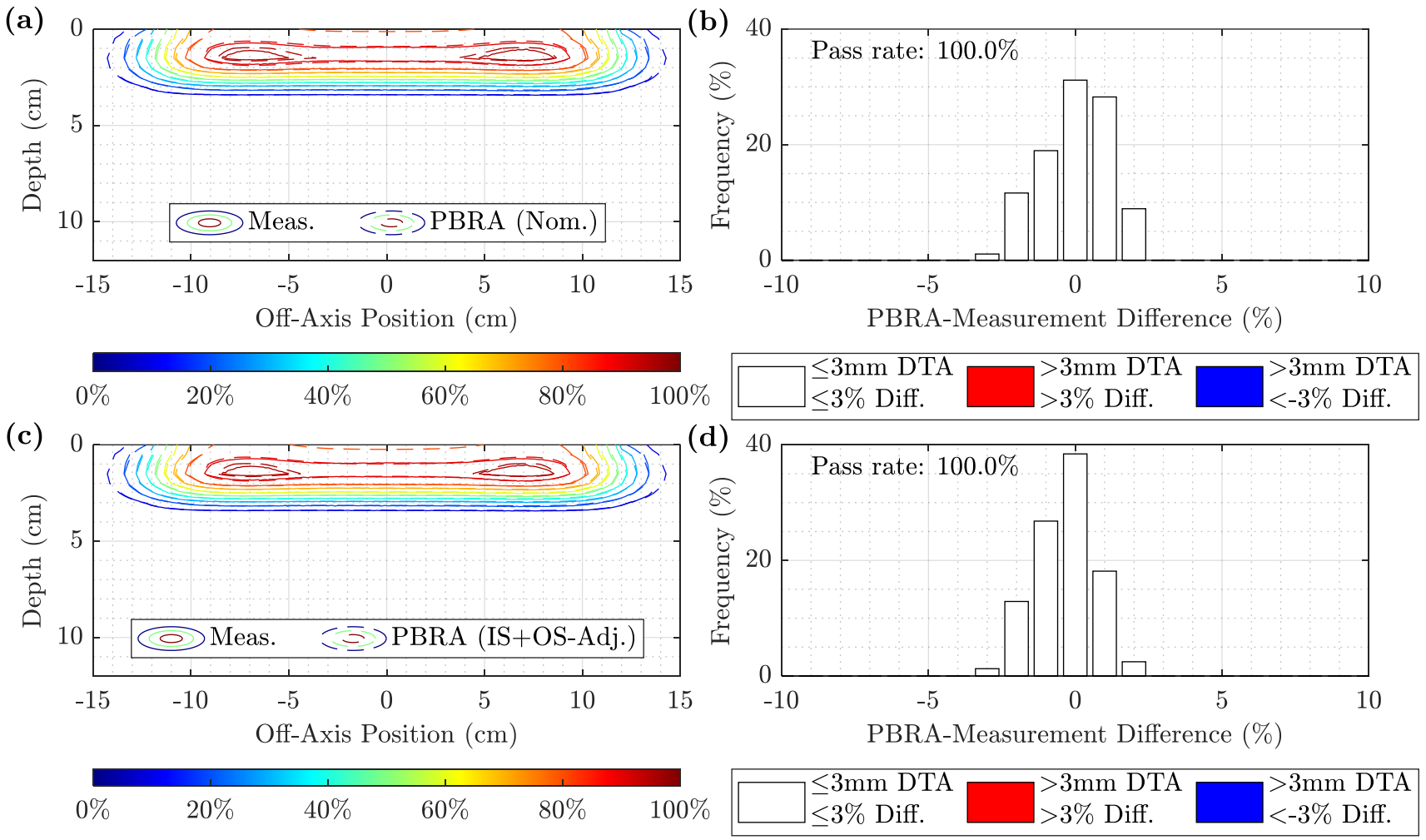

Figure B.16. Measured and PBRA-calculated isodose comparison and difference histogram for 0.158-cm pins at 7 MeV and 110 cm SSD. The isodose contours for measurement (solid) are compared to the PBRA calculations with (a) nominal and (c) IS+OS-corrected pin diameters. Difference histograms under 3%/3mm DTA criteria are plotted for (b) nominal and (d) IS+OS-corrected PBRA diameters. Points at which the PBRA underpredicted and overpredicted the dose relative to measurement are shown in blue and red, respectively. The nominal and corrected passing rates were both 100%.

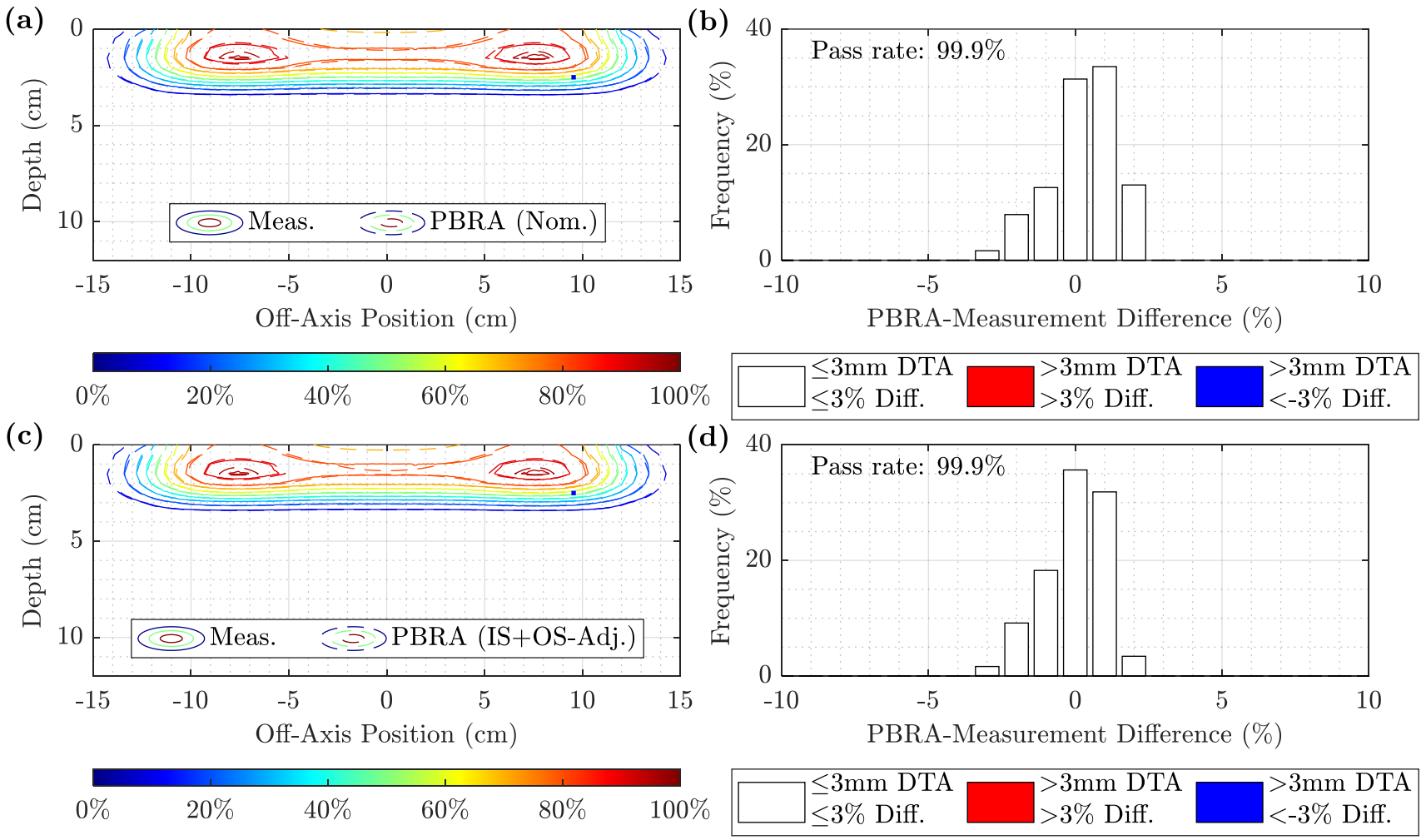

Figure B.17. Measured and PBRA-calculated isodose comparison and difference histogram for 0.273-cm pins at 7 MeV and 110 cm SSD. The isodose contours for measurement (solid) are compared to the PBRA calculations with (a) nominal and (c) IS+OS-corrected pin diameters. Difference histograms under 3%/3mm DTA criteria are plotted for (b) nominal and (d) IS+OS-corrected PBRA diameters. Points at which the PBRA underpredicted and overpredicted the dose relative to measurement are shown in blue and red, respectively. The nominal and corrected passing rates were both 99.9%.

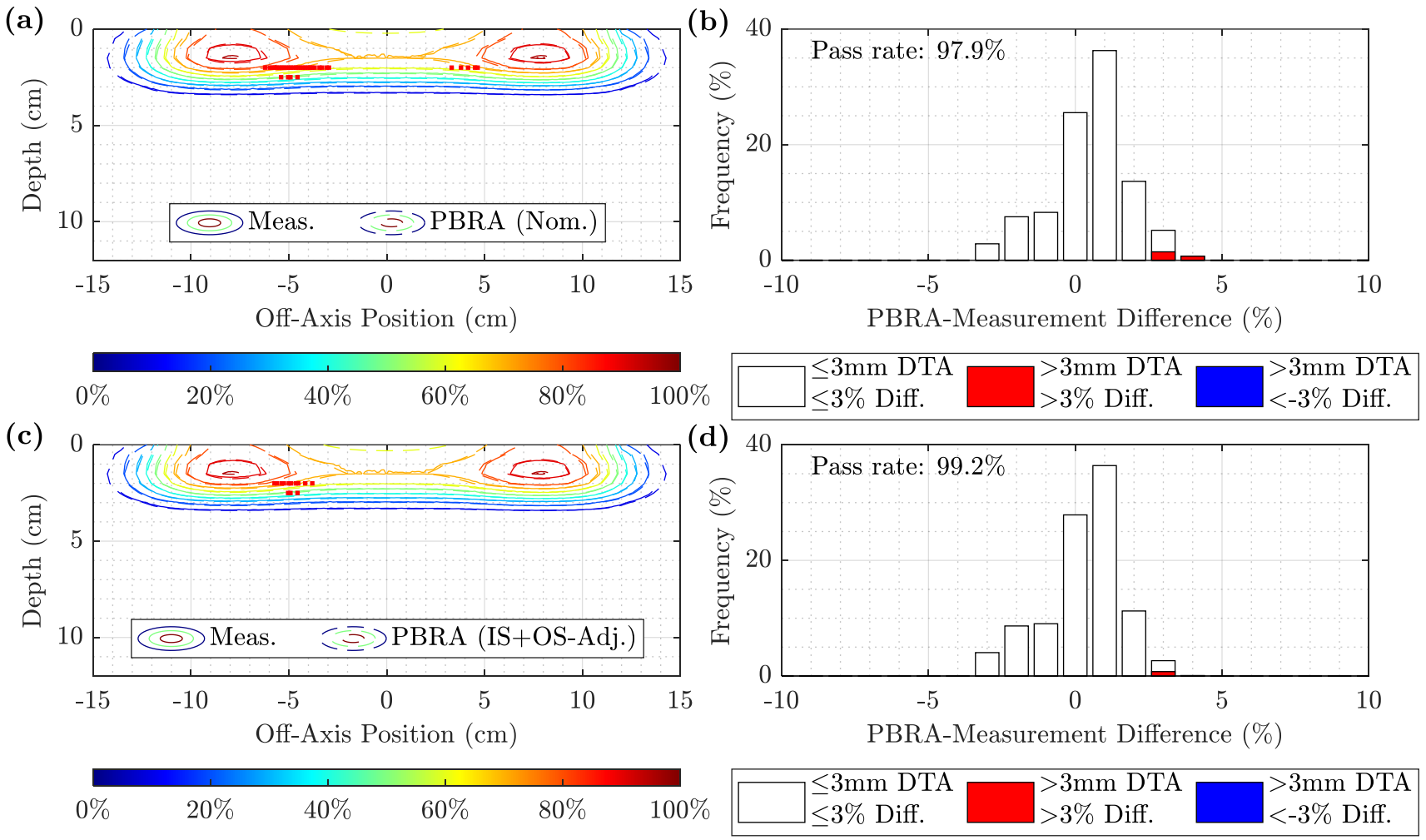

Figure B.18. Measured and PBRA-calculated isodose comparison and difference histogram for 0.352-cm pins at 7 MeV and 110 cm SSD. The isodose contours for measurement (solid) are compared to the PBRA calculations with (a) nominal and (c) IS+OS-corrected pin diameters. Difference histograms under 3%/3mm DTA criteria are plotted for (b) nominal and (d) IS+OS-corrected PBRA diameters. Points at which the PBRA underpredicted and overpredicted the dose relative to measurement are shown in blue and red, respectively. The nominal and corrected passing rates were 97.9% and 99.2%, respectively.

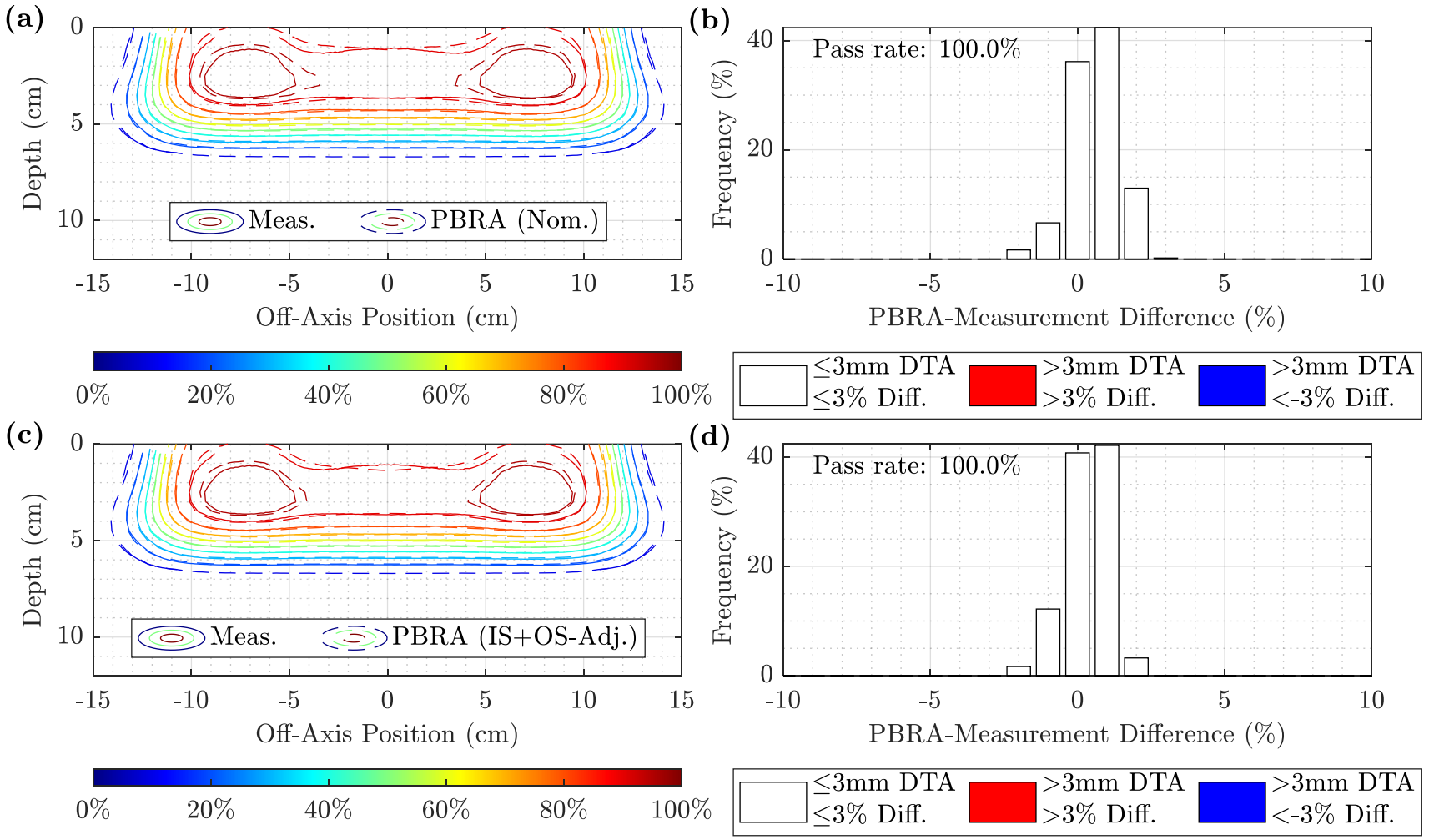

Figure B.19. Measured and PBRA-calculated isodose comparison and difference histogram for 0.158-cm pins at 13 MeV and 110 cm SSD. The isodose contours for measurement (solid) are compared to the PBRA calculations with (a) nominal and (c) IS+OS-corrected pin diameters. Difference histograms under 3%/3mm DTA criteria are plotted for (b) nominal and (d) IS+OS-corrected PBRA diameters. Points at which the PBRA underpredicted and overpredicted the dose relative to measurement are shown in blue and red, respectively. The nominal and corrected passing rates were both 100%.

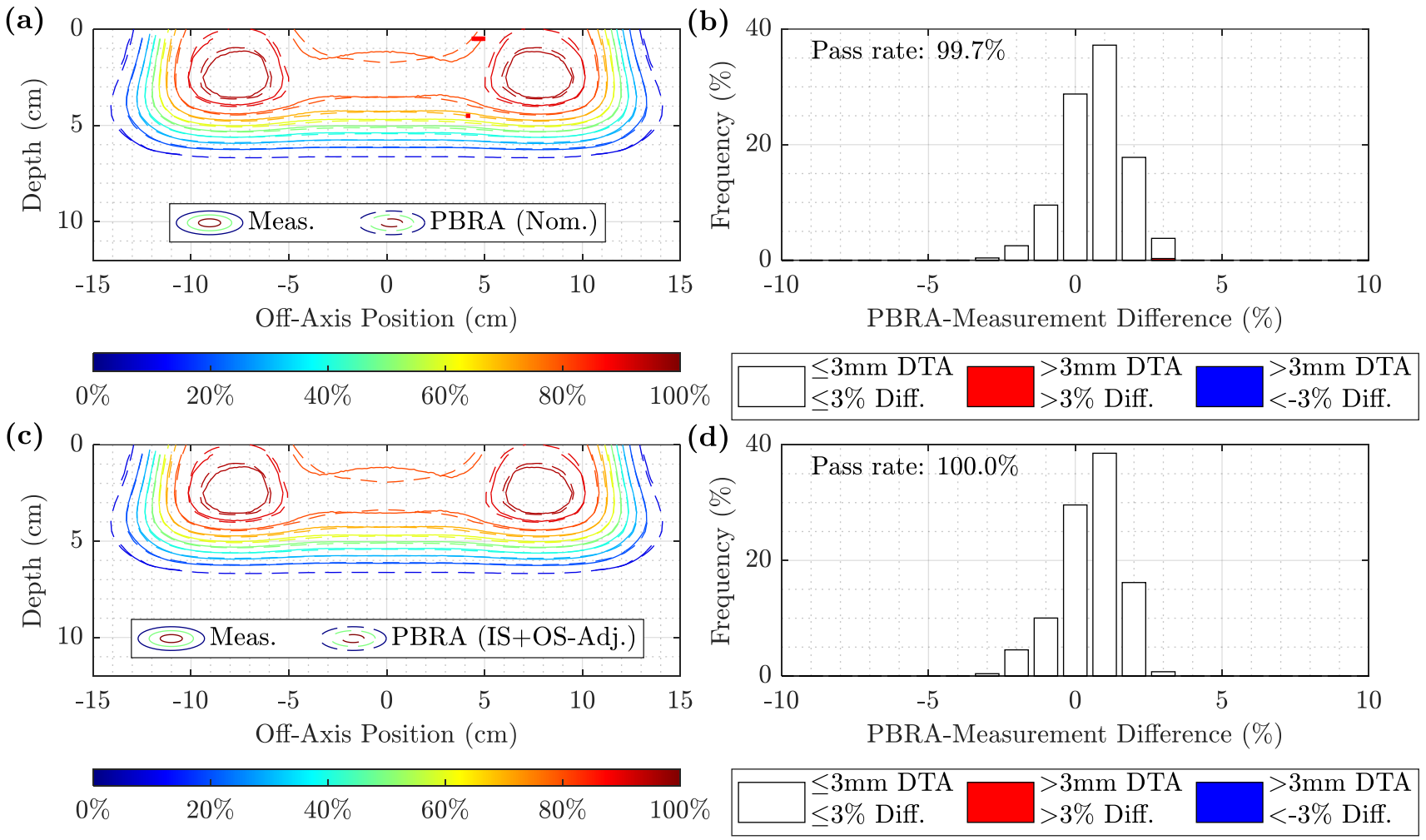

Figure B.20. Measured and PBRA-calculated isodose comparison and difference histogram for 0.273-cm pins at 13 MeV and 110 cm SSD. The isodose contours for measurement (solid) are compared to the PBRA calculations with (a) nominal and (c) IS+OS-corrected pin diameters. Difference histograms under 3%/3mm DTA criteria are plotted for (b) nominal and (d) IS+OS-corrected PBRA diameters. Points at which the PBRA underpredicted and overpredicted the dose relative to measurement are shown in blue and red, respectively. The nominal and corrected passing rates were 99.7% and 100%, respectively.

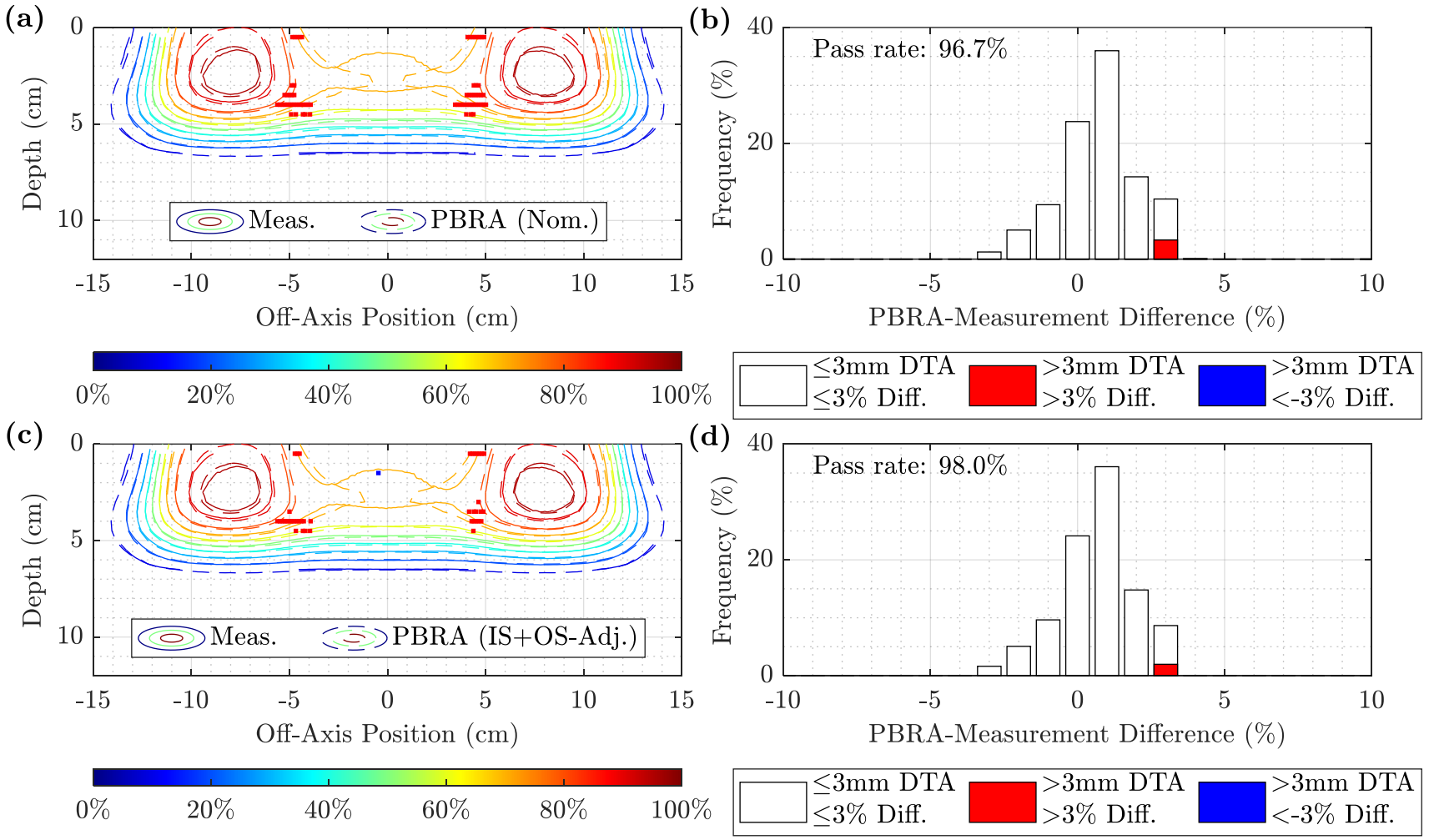

Figure B.21. Measured and PBRA-calculated isodose comparison and difference histogram for 0.352-cm pins at 13 MeV and 110 cm SSD. The isodose contours for measurement (solid) are compared to the PBRA calculations with (a) nominal and (c) IS+OS-corrected pin diameters. Difference histograms under 3%/3mm DTA criteria are plotted for (b) nominal and (d) IS+OS-corrected PBRA diameters. Points at which the PBRA underpredicted and overpredicted the dose relative to measurement are shown in blue and red, respectively. The nominal and corrected passing rates were 96.7% and 98.0%, respectively.

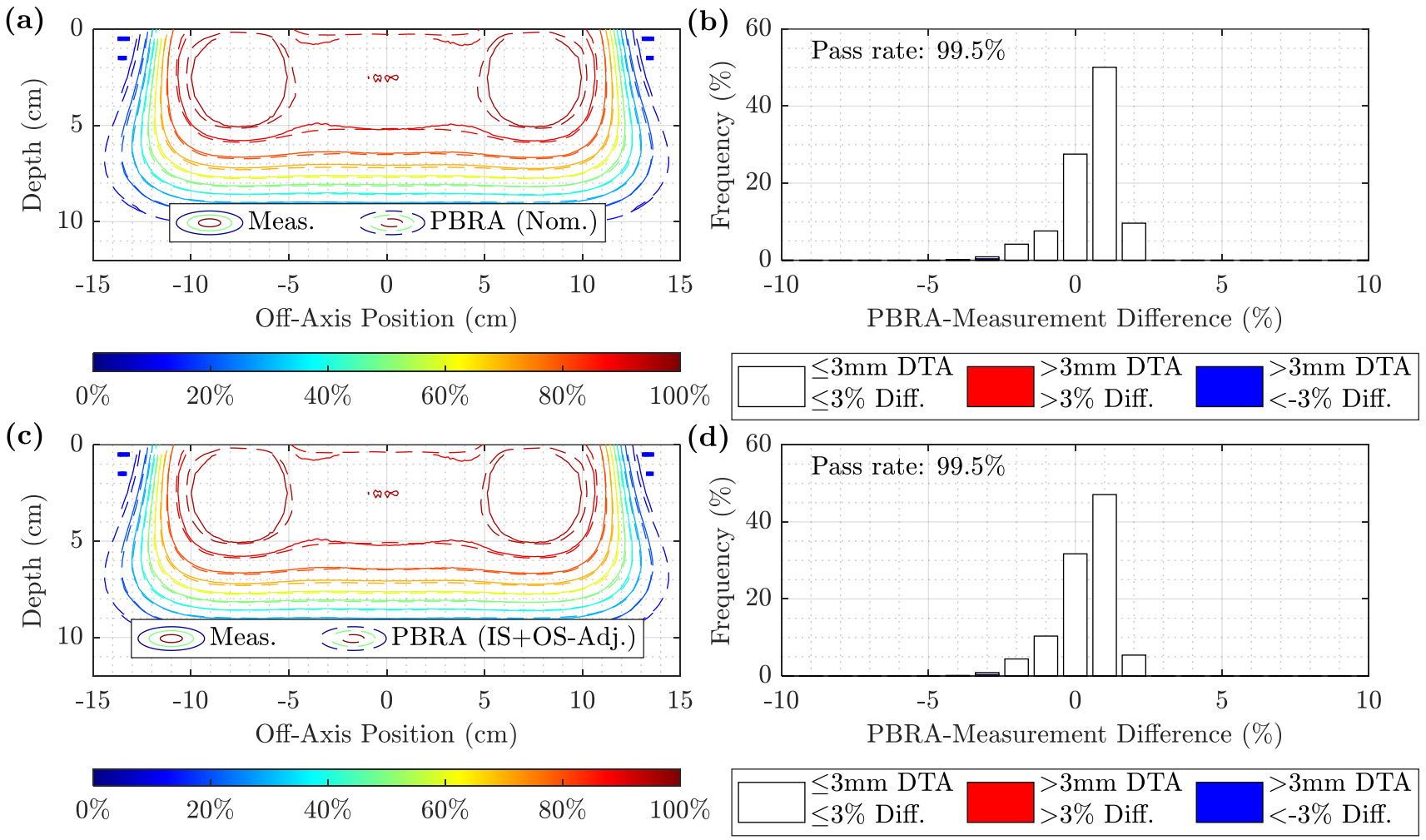

Figure B.22. Measured and PBRA-calculated isodose comparison and difference histogram for 0.158-cm pins at 20 MeV and 110 cm SSD. The isodose contours for measurement (solid) are compared to the PBRA calculations with (a) nominal and (c) IS+OS-corrected pin diameters. Difference histograms under 3%/3mm DTA criteria are plotted for (b) nominal and (d) IS+OS-corrected PBRA diameters. Points at which the PBRA underpredicted and overpredicted the dose relative to measurement are shown in blue and red, respectively. The nominal and corrected passing rates were both 99.5%.

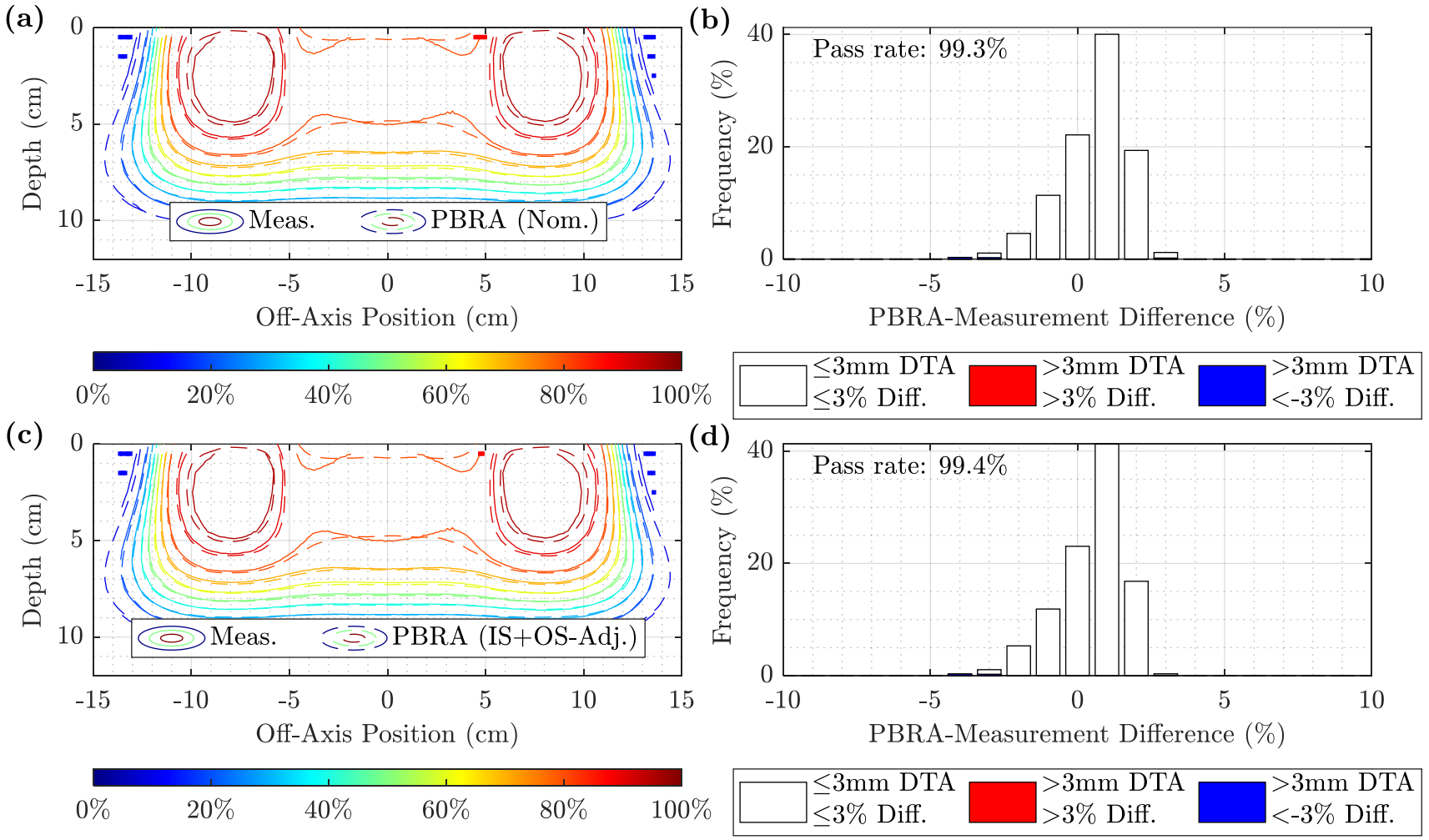

Figure B.23. Measured and PBRA-calculated isodose comparison and difference histogram for 0.273-cm pins at 20 MeV and 110 cm SSD. The isodose contours for measurement (solid) are compared to the PBRA calculations with (a) nominal and (c) IS+OS-corrected pin diameters. Difference histograms under 3%/3mm DTA criteria are plotted for (b) nominal and (d) IS+OS-corrected PBRA diameters. Points at which the PBRA underpredicted and overpredicted the dose relative to measurement are shown in blue and red, respectively. The nominal and corrected passing rates were 99.3% and 99.4%, respectively.

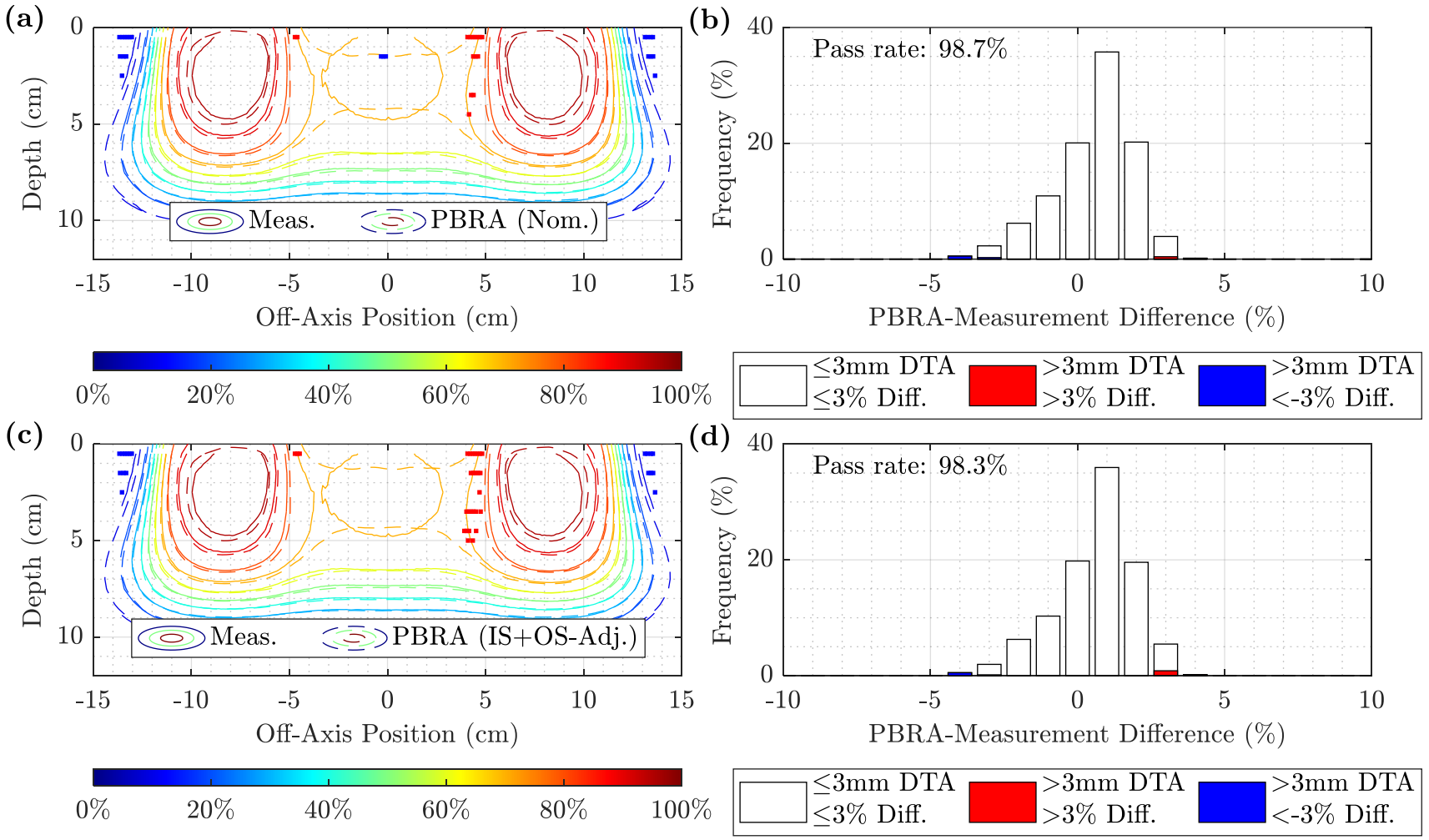

Figure B.24. Measured and PBRA-calculated isodose comparison and difference histogram for 0.352-cm pins at 20 MeV and 110 cm SSD. The isodose contours for measurement (solid) are compared to the PBRA calculations with (a) nominal and (c) IS+OS-corrected pin diameters. Difference histograms under 3%/3mm DTA criteria are plotted for (b) nominal and (d) IS+OS-corrected PBRA diameters. Points at which the PBRA underpredicted and overpredicted the dose relative to measurement are shown in blue and red, respectively. The nominal and corrected passing rates were 98.7% and 98.3%, respectively.

Appendix C. Fluence Energy Spectra

C.1. Methods

MC energy distributions were generated for incident and pin-scattered electrons at each beam energy using the phase spaces scored at 97 cm SSD, with the scattered spectrum being calculated from the 0.315-cm pin. These phases spaces were used as input to BEAMDP (Ma and Rogers, 2020) to generate the spectra. Energy binning was set to 0.5-MeV increments from 0 to 21 MeV and normalized to total counts. The mean energy of each distribution at each beam energy was calculated using the histogram data.

C.2. Results

Table C.1 shows the mean energy of each distribution. The results are plotted in Figure C.1 at each beam energy for the 0.315-cm pin. At all beam energies, the mean energy of the scattered distribution is less than that of the incident spectrum due to scattering within the tungsten block with the relative magnitude of the decrease greatest at higher energies. The uniformity of the energy distribution increases with beam energy.

Table C.1. Average energy of incident and scattered energy spectra for 0.315-cm pin for beam energies 7-20 MeV.

Beam Energy (MeV)	Average Energy (MeV)	
	Incident	Scattered
7	6.16	4.42
13	11.60	7.21
20	17.50	9.72

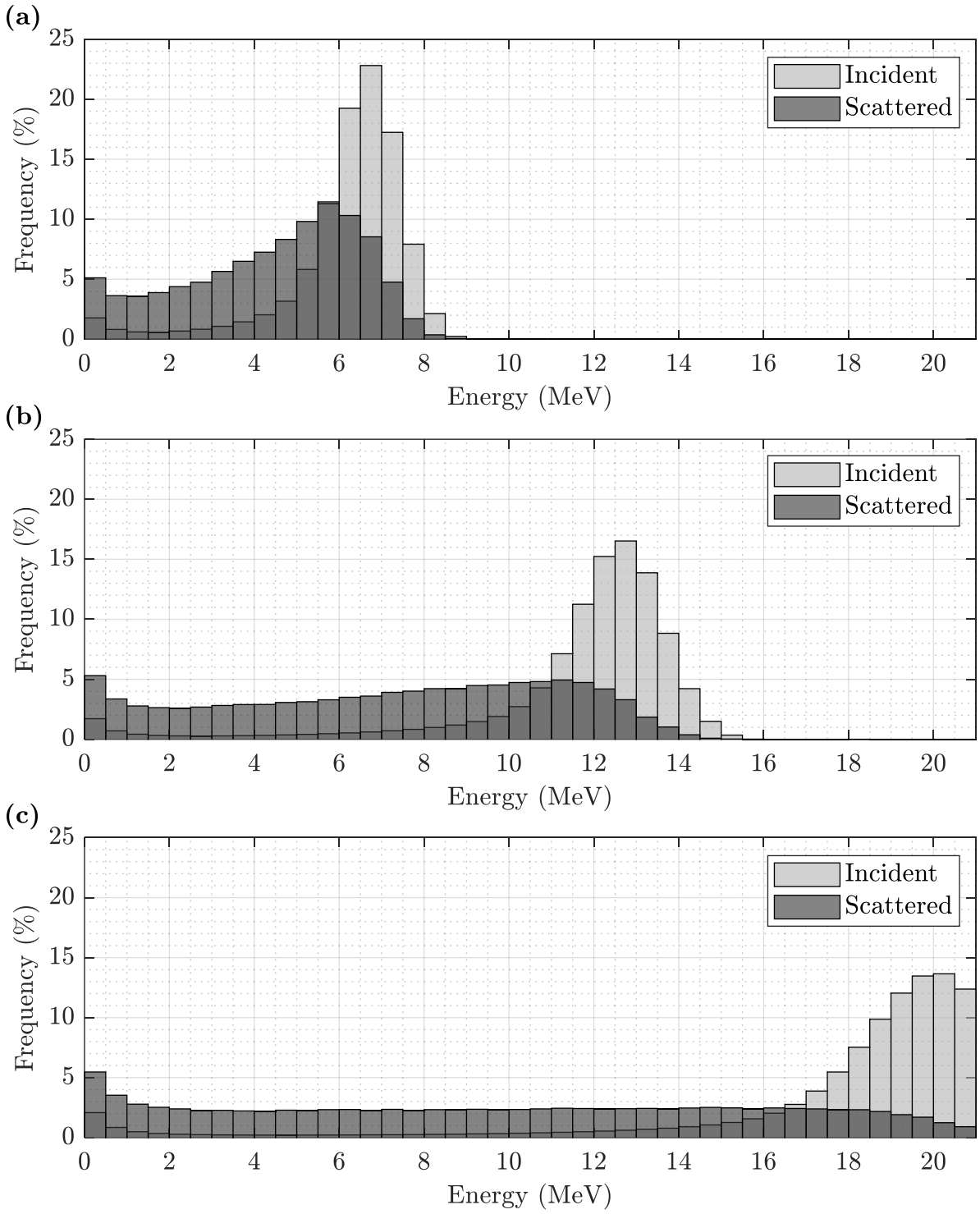

Figure C.1. Incident and pin-scattered energy distributions for 7-20 MeV beams. Energy histograms for incident (light gray) and pin-scattered (dark gray) electrons were calculated for (a) 7, (b) 13, and (c) 20 MeV beam energies using the 0.315-cm pin phase spaces scored at 97 cm SSD. Binning was performed in 0.5-MeV increments and frequencies are normalized to total counts. The uniformity of the pin-scattered spectrum increases with energy.

C.3. Discussion

The out-scattered spectrum differs substantially from the incident distribution, being both lower in mean energy and more uniform. This will cause the scattered electrons to range out at shallower depths, altering the depth dose distribution. Therefore, a simple pin diameter scaling to account for out-scattered electrons will likely be insufficient to accurately match the depth-dependent dose effect.

Appendix D. MC-Based Corrections

A MC-based approach was initially adopted to determine the out-scatter correction, but the MC methodology presented here was unable to produce dose distributions that matched measurement. Hence, the empirical correction discussed in Chapter 3 was taken in favor of the approach discussed here.

MC simulations were performed to determine the effect a single pin of a given nominal (physical) diameter, *d*, has on the dose distribution at a given energy and SSD, referred to as a perturbation kernel. Perturbation kernels were also calculated from the in-scatter-adjusted PBRA (IS-PBRA) described in Chapter 2 for each energy, SSD, and nominal diameter. These extracted kernels were used to estimate the dose distribution for an arbitrary arrangement of pins of uniform diameter. The MC-estimated and IS-PBRA-calculated dose distributions under corresponding conditions were used to evaluate a global parameterization of the out-scatter component as a function of beam energy, SSD, pin diameter, and depth. This expression was used to determine out-scatter dose corrections for each beam energy, SSD, and pin diameter combination. The out-scatter corrections were applied as a change in dose from the IS-PBRA to determine diameters corrected for both in-scatter and out-scatter. This was implemented as a lookup table of IM-PBRA diameter corrections as a function of beam energy, SSD, and pin diameter.

D.1. Determination of the perturbation from the PRIME tungsten pins using EGSnrc Monte Carlo

D.1.1. Monte Carlo model

All simulations were performed on the High Performance Computing SuperMike-II computing cluster at Louisiana State University. The MC calculations were made in three distinct steps, each indicated in Figure D.1.

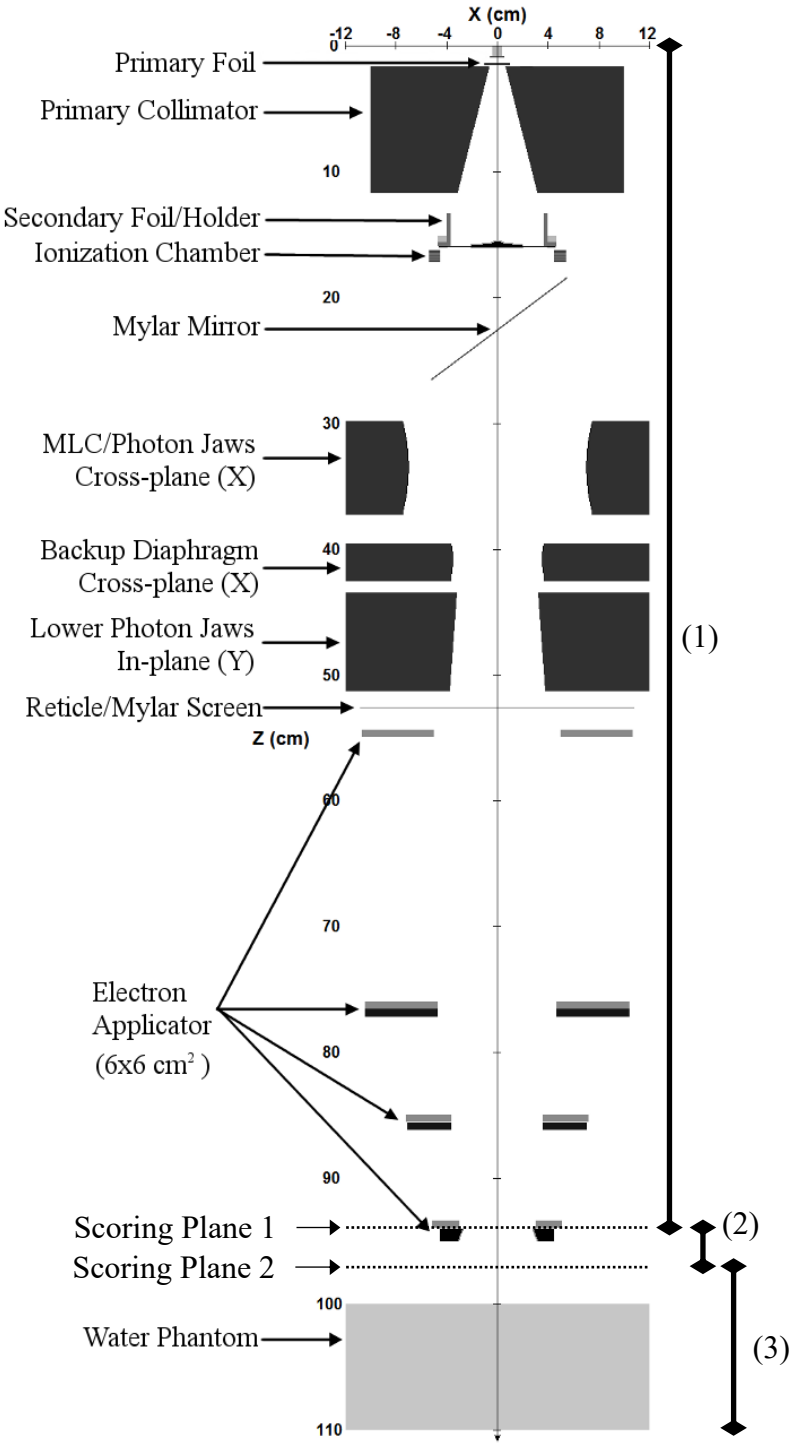

Figure D.1. MC model and calculation steps. (1) The beam is transported to 93.98 cm where the phase space is scored at Scoring Plane 1. (2) Using this first phase space as input, the beam is then transported through the intensity modulator with a pin and foam, foam only, or air only, and a second phase space is scored at 97 cm. (3) Using the phase space from the previous step, the dose up to 10 cm in water is calculated for a given SSD. Modified from Harris (2012).

First, MC simulations using the EGSnrc (Kawrakow *et al.*, 2011) model of the Elekta Infinity model developed by Harris (2012) were performed to score phase spaces containing the direction, position, and energy of each particle in the plane perpendicular to CAX immediately upstream of the collimating insert, 93.98 cm from the nominal source along CAX. The beam characteristics of this Elekta Infinity are identical to those of the current Elekta Agility. These simulations were performed at nominal beam energies of 7, 13, and 20 MeV ($E_{p,0}$ = 6.16, 11.60, and 17.50 MeV, respectively) with the 14×14 cm^2 applicator, modified by removing the bottom trimmer. Initial histories varied with beam energy: 220 million histories at 7 MeV, 400 million histories at 13 MeV, and 800 million histories at 20 MeV.

Using the phase space from the previous step as input, the beam was transported from the initial scoring plane to 97 cm SSD, where a second phase space was scored. This step was performed using 4, 8, and 12 million histories for the 7, 13, and 20 MeV beams, respectively, with three distinct simulation geometries:

1. *Pin and foam*. The first simulation geometry contained a pin and the machinable foam as shown in Figure D.2.a. A single tungsten intensity modulator block of a given diameter (0.158, 0.223, 0.273, 0.315, or 0.352 cm) and 0.6 cm in length was placed on CAX with the upstream surface at 94.2 cm. The 1.27-cm-thick machinable foam (ρ = 0.096 g·cm^{-3}) was modeled as a water slab 0.11-cm thick at the downstream pin surface. Phase spaces were scored with this geometry for each beam energy and pin diameter combination. Note that this geometry does not model scatter from the foam into the pin side, which was shown to increase in-scatter by 10-13% (Table D.18). Also, modeling the foam as water overestimates scatter behind the pin. This is discussed further in Section D.4.

2. *Foam only*. The second simulation geometry featured the machinable foam only, depicted in Figure D.2.b. A 0.11-cm-thick water slab was placed with the upstream face at 94.8 cm. All other volume was air at SATP conditions (ρ = 1.2048×10^{-3} g·cm^{-3}).
3. *Air only*. The third simulation geometry was only air at SATP conditions for the entire volume, illustrated in Figure D.2.c. These calculations were performed at each energy and 100 cm SSD only.

In the third and final step of the MC calculations, phase spaces scored at 97 cm SSD were used as input to DOSXYZnrc (Walters *et al.*, 2011) to calculate the dose in water to a depth of 10 cm. The first proximal layer of voxels was comprised of air with thicknesses of 3.0, 8.0, and 13.0 cm, corresponding respectively to water phantom calculations at 100, 105, and 110 cm SSD. All other downstream voxels were comprised of water, with the first proximal layer having a thickness (z) of 0.25 cm, and all subsequent layers being 0.50 cm thick. This geometry results in voxel centers at depths of 0.125 cm and 0.5-10.0 cm in 0.5-cm increments. In lateral dimensions (x and y), voxels were uniformly sized at 0.2×0.2 cm^2, with the central voxel center on CAX.

D.1.2. MC analysis

DOSXYZnrc outputs a Cartesian dose matrix containing the voxel center (x, y, z), the dose value, and the standard error relative to the dose value. The origin was defined as the point on the CAX at the surface with z increasing with depth in the phantom. The mean voxel dose value was considered equal to the point dose deposited at the center of the voxel.

For the "pin and foam" and "foam only" calculations, the Cartesian dose matrix was converted to a radial dose matrix by averaging the dose of Cartesian points positioned equal distance from CAX, with $r = 0$ being on CAX and z increasing with depth. The standard deviation

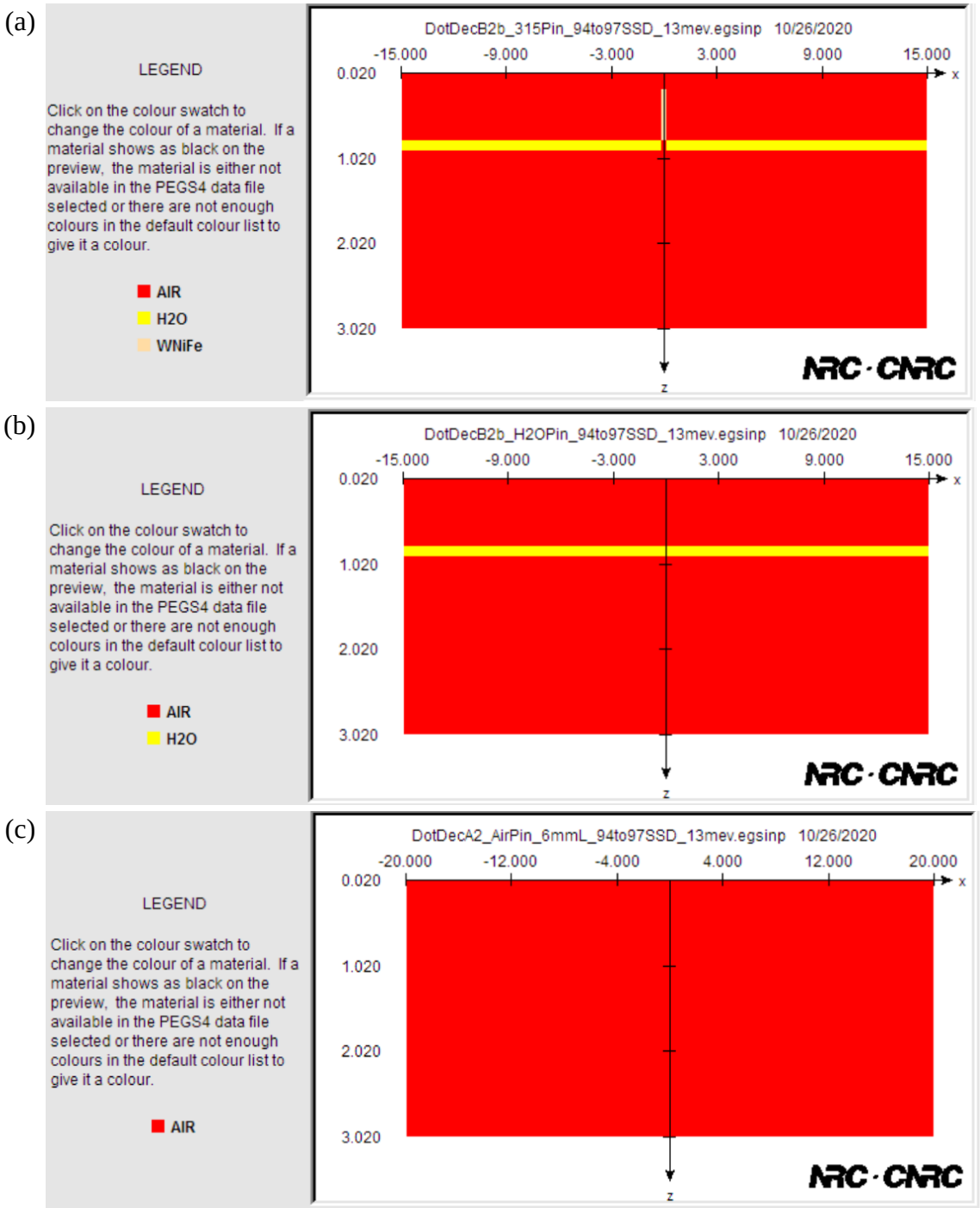

Figure D.2. BEAMnrc simulation geometries, 93.98 to 97 cm. Screenshots from the accelerator preview in BEAMnrc (Rogers *et al.*, 2011) show the three simulation geometries for the second step in the beam transport. Image (a) shows the "pin and foam" simulation geometry with a single 0.6-cm-long tungsten pin (beige) of a given diameter on CAX with the machinable foam modeled as a 0.11-cm-thick water slab (yellow) placed at the downstream surface of the pin. The remaining volume is air (red). Image (b) shows the "foam only" simulation geometry with only the water slab present. Image (c) shows the "air only" simulation geometry. In all images, 93.98 cm SSD corresponds to 0.00 cm in the *z*-direction.

was calculated for each radial dose value. This step assumed azimuthal symmetry in the vicinity of CAX.

A radial dose perturbation kernel, D_p, was calculated for each combination of beam energy, SSD, and pin diameter by subtracting the "foam only" dose distribution from the "pin and foam" dose distribution, i.e.

$$D_P(r,z) = D_{\text{block}}(r,z) - D_{\text{foam}}(r,z), \quad \text{D.1}$$

where D_{block} and D_{foam} represent the radial dose for the "pin and foam" and "foam only" simulation geometries, respectively, normalized to CAX D_{max} of D_{foam}. D_p describes the dose reduction in the water phantom caused by a single intensity modulator pin. D_p was calculated on a grid bound from CAX to a radial distance of 5 cm and from the surface to depths of 4.5, 8.0, and 10.0 cm for the 7, 13, and 20 MeV beams, respectively.

D.1.3. Foam energy loss validation

Hilliard measured a 0.1-cm average upstream shift of R_{90} when performing validation measurements with and without the foam in place as demonstrated in Figure D.3. A 0.1-cm R_{90} shift was applied in IM-PBRA calculations to emulate this energy loss. As shown in Figure D.2, the machinable foam in the MC model was simulated as a 0.11-cm-thick water slab at the downstream surface of the pin to account for the same energy loss observed by Hilliard. To validate the usage of this water slab in the MC model, R_{50} was calculated from the PDD at each energy at 100 cm SSD for the "foam only" and "air only" simulation geometries. The difference between these R_{50} values at a given energy was compared to the expected shift.

D.1.4. MC PDD perturbation

The radial dose perturbation kernels were used to approximate the dose beneath an arrangement of pins within a modulator device. For each pin in the device, the perturbation was

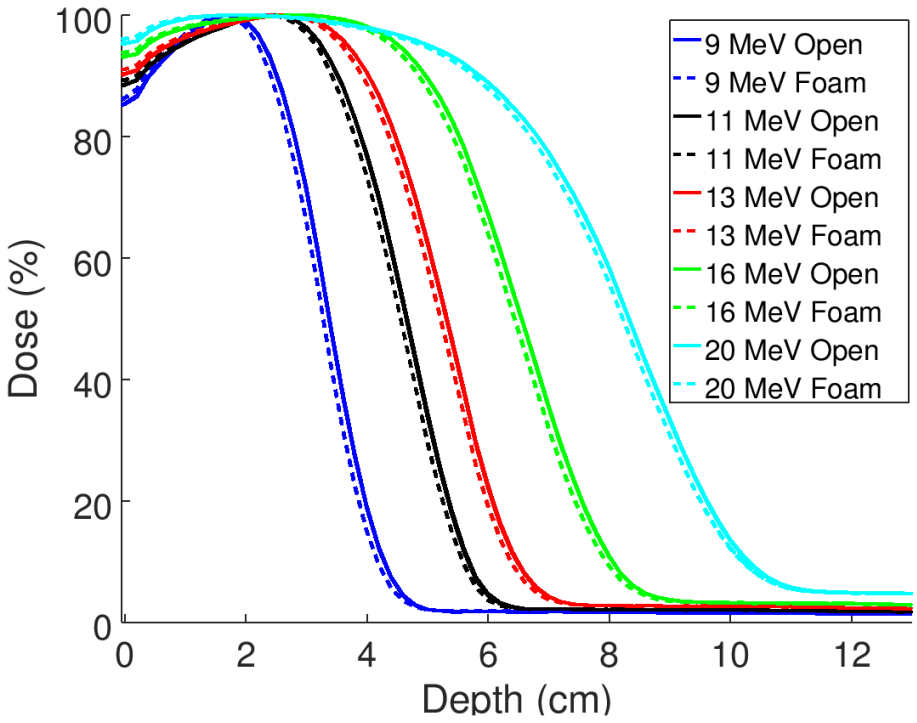

Figure D.3. Comparison of "foam only" and "open field" CAX PDDs. The PDDs were measured by Hilliard for a 10×10 cm^2 field for 9-20 MeV beam energies both with (dashed) and without (solid) the machinable foam in place. Reproduced from Hilliard (2018).

successively summed for voxels up to a radial limit of 5 cm from a given pin position. For a given beam energy and SSD, the dose perturbation to a voxel at (x, y, z) due to N intensity modulator pins was calculated as

$$\Delta D_{\text{matrix}}(x, y, z) = \sum_{i=1}^{N} D_P(r_i, z) \mid r_i^2 = (x - f \cdot x_i)^2 + (y - f \cdot y_i)^2, \qquad \text{D.2}$$

where D_P is the radial dose perturbation described by Equation D.1, the center of the ith pin is (x_i, y_i) defined nominally at 95 cm, and f is the geometric divergence (f = (SSD + z) / 95 cm). The resultant multipin dose perturbation matrix, ΔD_{matrix}, estimates the reduction in dose caused by the IM device relative to the unmodulated (foam only) dose distribution. As such, dose calculations using the kernels are specifically referred to as "MC estimation" or "MC prediction" rather than "MC calculation" because these dose distributions are not directly calculated by DOSXYZnrc.

ΔD_{matrix} was calculated for IM devices containing an 8.4×8.4 cm^2 matrix of pins of uniform diameter arranged with a uniform spacing of 0.6-cm on a rectilinear grid as depicted in Figure D.4. The dose grid was spaced 0.2 cm laterally and 0.5 cm with depth to be consistent with the spacing of the MC kernels. The pin arrangement and dose grid were chosen to minimize error due to interpolation between data points of the kernel. Calculations were performed for the 7, 13, and 20 MeV beams at 100, 105, and 110 cm SSD with pins 0.158, 0.223, 0.273, 0.315, and 0.352 cm in diameter, resulting in 45 total calculations. For each beam energy, SSD, and pin matrix

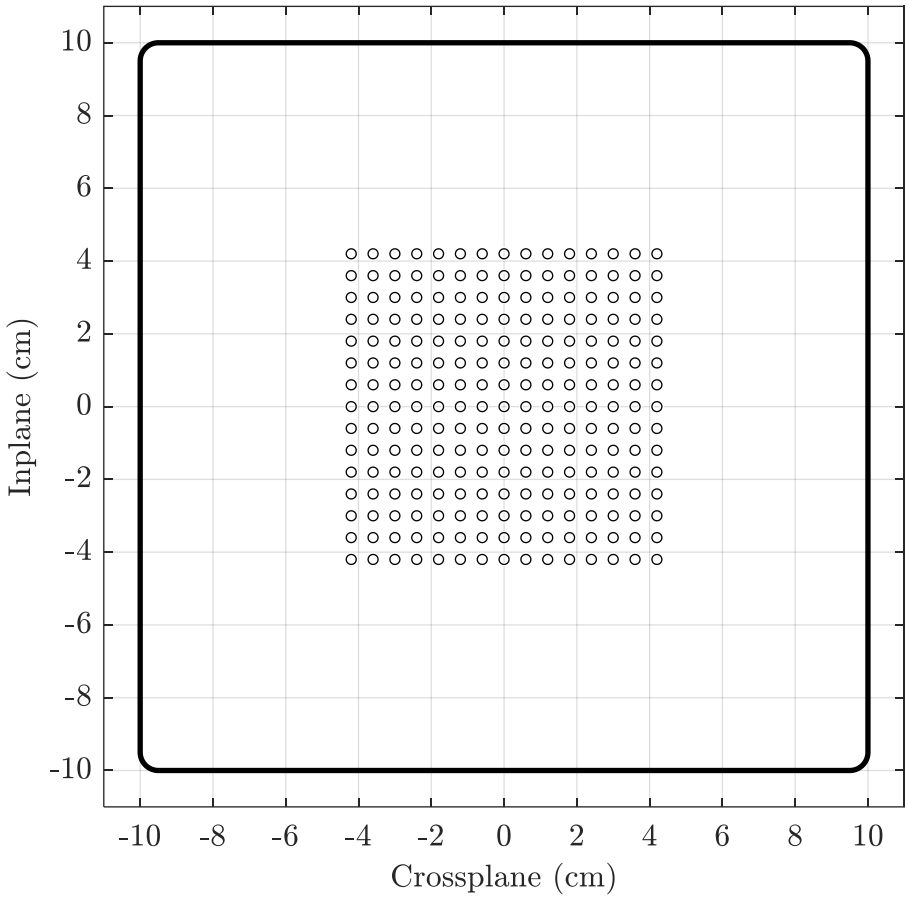

Figure D.4. Example square pin matrix for MC PDD perturbation calculations. The 8.4×8.4 cm^2 matrix consisted of 225 pins of uniform diameter, shown as circles, with centers spaced every 0.6 cm in both lateral directions within a 20×20 cm^2 insert, depicted as the bolded square. This example is comprised of 0.273-cm-diameter pins.

combination, the average perturbation in the PDD was taken from the central 2×2 cm^2 cross section, corresponding to the central 121 voxels, at each depth to yield a MC perturbation PDD, ΔPDD:

$$\Delta PDD(E,d,z) = \frac{1}{121}\sum_{i=1}^{121} \Delta D_{\text{matrix}}(x_i, y_i, z) \mid x_i \leq 2 \text{ cm}, y_i \leq 2 \text{ cm}. \quad \text{D.3}$$

ΔPDD was then added to the measured foam-only PDD to produce an estimated modulated PDD, PDD_{mod}:

$$PDD_{\text{mod}}(E,d,z) = PDD_{\text{meas}}(E,0,z) + \Delta PDD(E,d,z). \quad \text{D.4}$$

The modulated field PDD is estimated with respect to the measured foam-only PDD because Equation D.3 predicts the dose perturbation from the unmodulated field rather than the full dose distribution itself. Note that Equation D.4 is used for comparison of MC estimation and measurement rather than derivation of scattering corrections. The measured foam-only PDD included the adjustments discussed in Section 3.1.6.

D.1.5. Validation of the MC dose perturbation estimation method

Using the MC perturbation kernels, the dose under the hexagonal pin arrangement shown in Figure 3.3 was calculated for pin diameters of 0.158, 0.273, and 0.352 cm at 7, 13, and 20 MeV and 100, 105, and 110 cm SSD. The hexagonal spacing was used to be consistent with the devices used with measurement. The dose matrix, D_{matrix}, was estimated from each setup according to:

$$D_{\text{matrix}}(x,y,z) = PDD_{\text{meas}}(E,0,z) + \Delta D_{\text{matrix}}(x,y,z). \quad \text{D.5}$$

The modulated PDD (Equations D.3-4) is estimated by averaging a 2×2 cm^2 cross-sectional area of the field rather than taking the CAX dose from Equation D.5 as the CAX is directly beneath an island block which could overestimate the perturbation in the surrounding field.

The first term of Equation D.5 assumes that the field incident is uniformly infinite and flat beyond the modulated region. Consequently, the MC-estimated dose away from CAX unrealistically converges to the foam-only PDD value at a given depth, and thus there is no penumbra. This assumption does not affect calculations within the modulated region, and distant portions of the field were omitted from comparison metrics.

Central inplane *y* profiles and *yz* isodose curves (x = 0 cm), the latter within 8 cm of CAX ($|y| \leq 8.0$ cm), were extracted from D_{matrix} for each setup. The MC-based dose estimation at each setup was compared to measurement under corresponding conditions using 3%/3mm DTA criteria. Overall passing rates were calculated for points within 8 cm of CAX, and a histogram of dose differences (MC estimation minus measurement) was generated for each comparison. This 8-cm off-axis limit was chosen as it is just inside the penumbra, and the kernel-based method here did not simulate the penumbra. Thus, significant disagreement in this region would be expected.

Depths of R_{90}, R_{50}, and R_{20} were evaluated from measured and MC-predicted modulated PDDs at each beam energy, SSD, and modulator combination. The maximum modulated dose was also compared. The same was done from the foam-only PDDs at each beam energy and SSD combination.

D.1.6. Pin perturbation results

The MC PDDs for the air and foam only setups are plotted for each energy in Figure D.5. The calculated R_{50} values and the shifts are contained in Table D.1. The difference between the average shift of 0.104 cm and the expected 0.11 cm is less than 0.01 cm, which is clinically insignificant.

Representative examples of the MC radial dose profiles and perturbations, as described by Equation D.1, are presented to demonstrate the dependence on beam energy (Figures D.6-8), pin

diameter (Figures D.9-11), and depth (Figures D.12-14). The radial dose perturbations were also plotted in the *rz*-plane as isodose perturbations, demonstrating the perturbation with depth (Figure D.15). As expected, the magnitude of the perturbation below the pin increased with beam energy, a result of decreased MCS, and pin diameter. The perturbation was generally found to decrease with increasing SSD and depth, due to increased MCS. The radial isodose plots show that the effect of the pin is most pronounced at shallow depths and close to the pin, but the effect persists off-axis.

Figures D.16-18 compare the measured and MC-calculated foam-only PDDs, showing good agreement for all energies at all SSDs. The measured and MC-predicted R_{90}, R_{50}, and R_{20} values (Table D.2) for all energy and SSD combinations agree within 0.01 cm.

Measured and MC-estimated modulated PDDs are plotted in Figures D.19-21 for all measured beam energy and block diameter combinations at 100 cm SSD. Table D.3 compares the MC-estimated R_{90}, R_{50}, and R_{20} values under modulated conditions. Agreement is generally good at 7 MeV with R_{90} values within 0.08 cm in all but one case, all R_{50} values within 0.06 cm, and R_{20} values within 0.04 cm. At 13 MeV, the agreement is best for the smallest pin size (within 0.05 cm for all values), but discrepancies emerge as the diameter increases. At the largest diameter, the average difference between the MC and measured depths is 0.15 cm. Similar behavior is observed at 20 MeV; the average difference for the 0.158-cm diameter is 0.04 cm, but increases to 0.14 cm for 0.352-cm pins. The average difference for these depths under all setups was 0.07 cm. Table D.4 contains the modulated CAX dose values for measurement and MC estimations along with their differences. The average magnitude difference (within 8 cm of CAX and up to R_p in depth) was found to be 1.6%, with a maximum difference of 3.6% for 20 MeV at 105 cm SSD under 0.352-cm pins. The difference in the CAX dose typically increases with increasing pin diameter.

Measured off-axis dose profiles are compared to the MC prediction at select depths at 100 cm SSD in Figures D.22-24. Measured and MC-estimated isodose contours and their histogram of differences with 3%/3mm DTA criteria are plotted in Figures D.25-33 for all measured setups at 100 cm SSD. Table D.5 compares the overall passing rates for of the 27 combinations of beam energy, SSD, and diameter. The passing rates at 100, 105, and 110 cm SSD were 97.8%, 95.6%, and 94.9%, respectively. The overall average passing rate was 96.1%.

Table D.1. MC machinable foam shift validation for 100 cm SSD. R_{50} values for air and foam were determined from the CAX PDDs for MC calculations at 7, 13, and 20 MeV. The difference in R_{50} values between the two simulation geometries was calculated to validate the usage of the water slab to model the energy loss due to the machinable foam.

Energy (MeV)	R_{50} (cm)		Shift (cm)
	Air	Foam	
7	2.730 ± 0.001	2.626 ± 0.001	0.104 ± 0.001
13	5.273 ± 0.001	5.169 ± 0.001	0.104 ± 0.001
20	8.256 ± 0.001	8.152 ± 0.001	0.103 ± 0.002

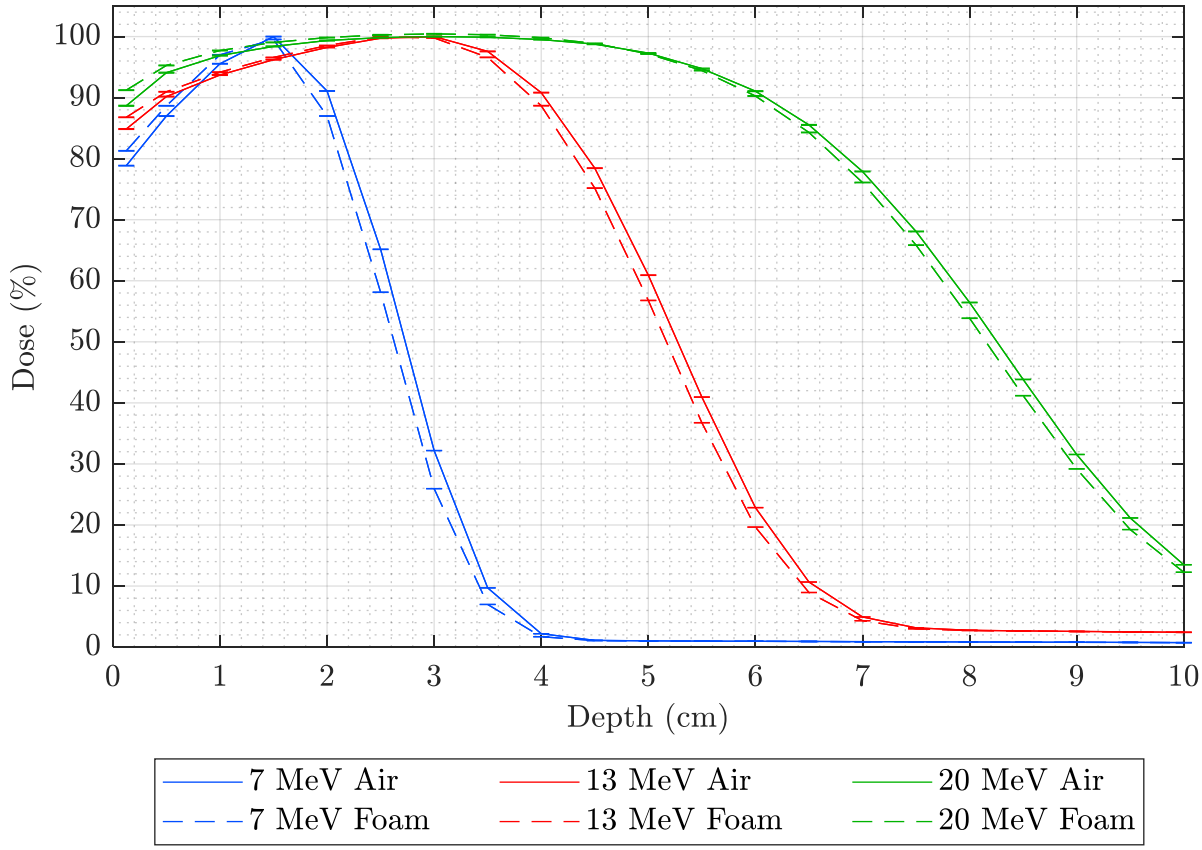

Figure D.5. MC open field PDD curves with and without foam. The PDD curves at 100 cm SSD for the MC calculations were calculated for air only (solid) and with foam (dashed) for 7 (blue), 13 (red), and 20 MeV (green). In all cases, the foam curve has an upstream shift of approximately 0.1 cm from the air curve at the same energy. Displayed uncertainties are 1σ.

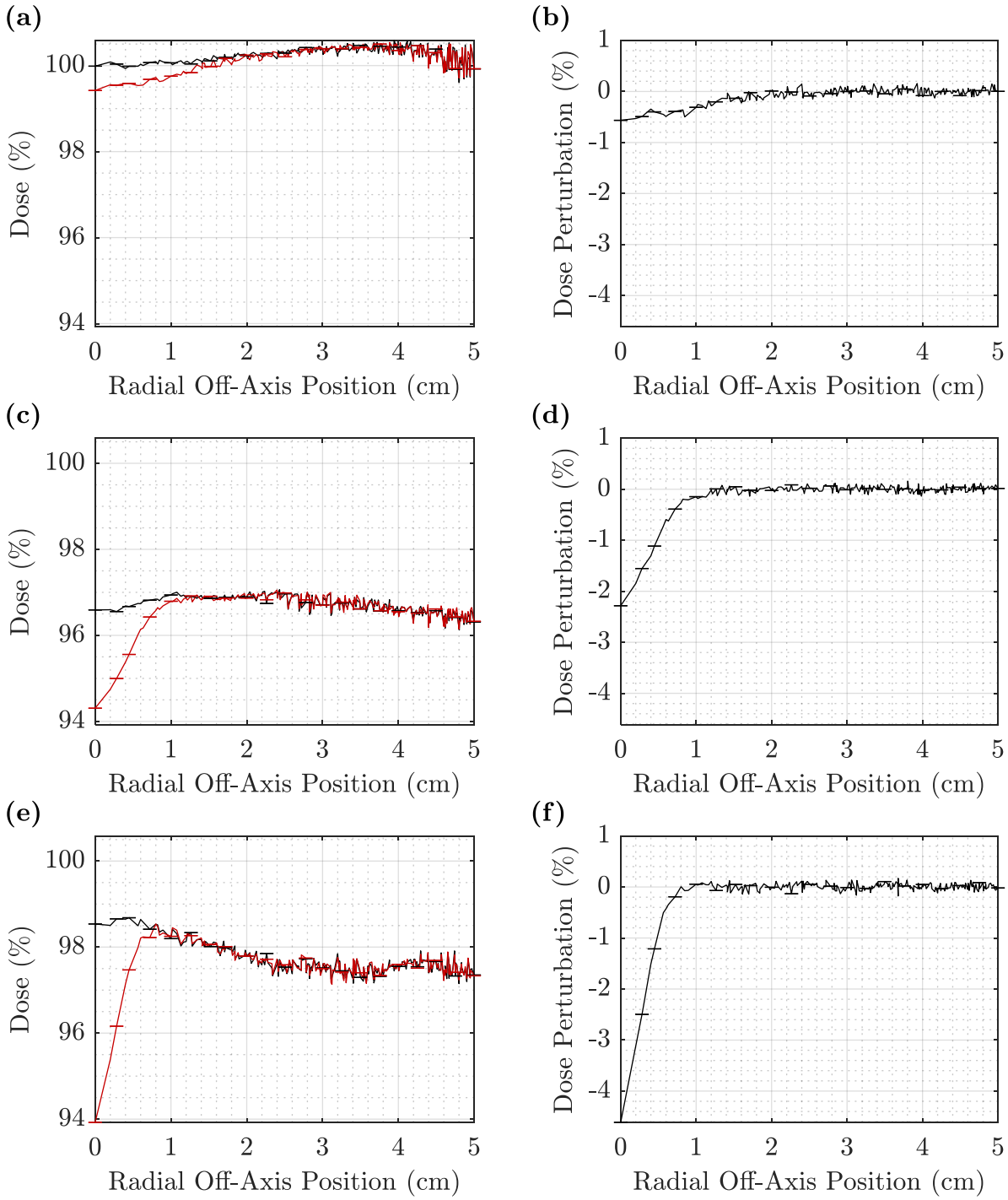

Figure D.6. Energy dependence of MC radial dose profiles and dose perturbation kernels at 7-20 MeV for a single 0.158-cm pin at 100 cm SSD at a depth of 1.5 cm. The radial dose profiles, in the first column, for foam only (black) and 0.158-cm single pin (red) are shown at (a) 7, (c) 13, and (e) 20 MeV at 1.5 cm depth and 100 cm SSD. The radial dose perturbation is the difference between these profiles, shown in the second column, for (b) 7, (d) 13, and (f) 20 MeV. Error bars represent 1σ.

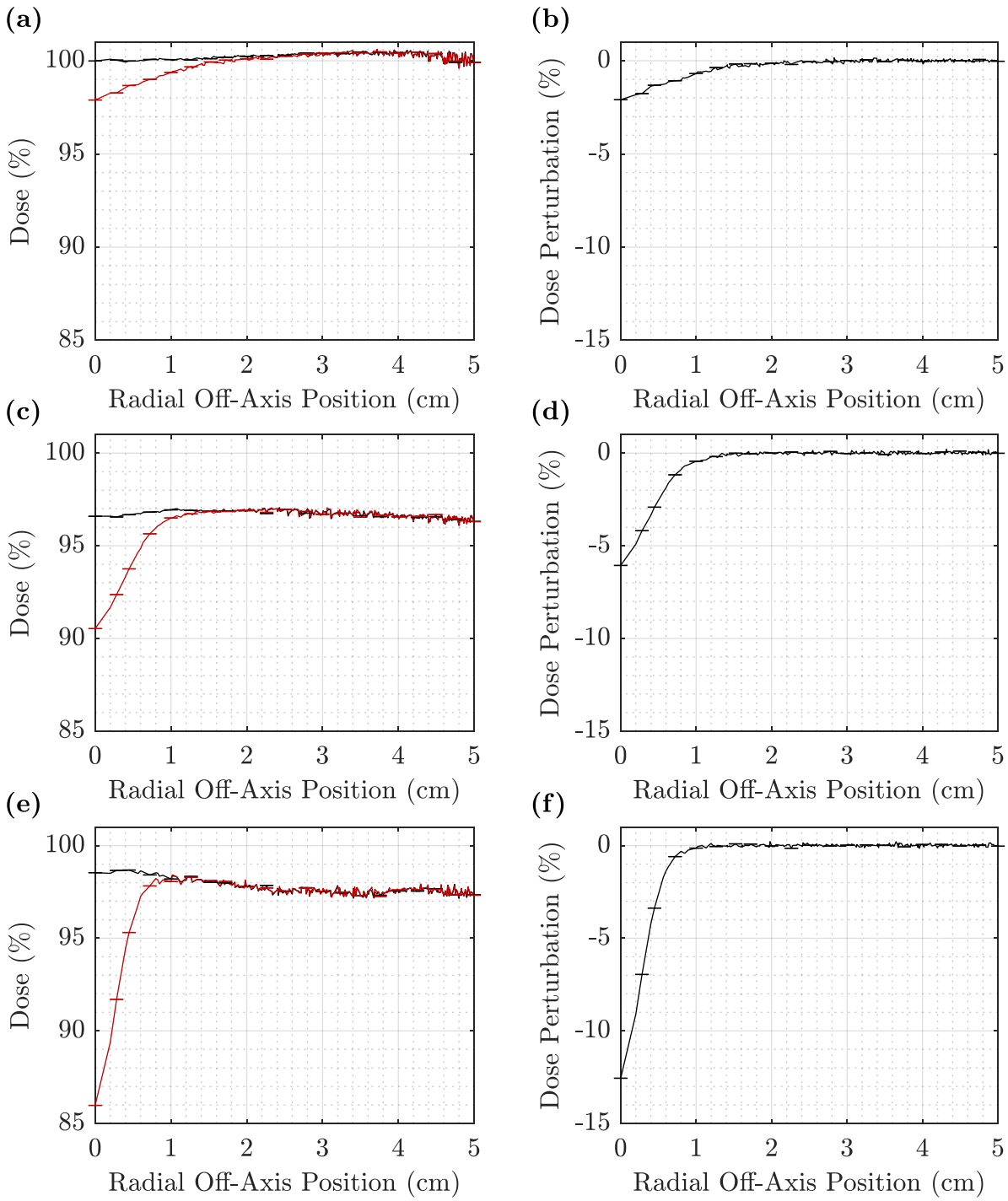

Figure D.7. Energy dependence of MC radial dose profiles and dose perturbation kernels at 7-20 MeV for a single 0.273-cm pin at 100 cm SSD at a depth of 1.5 cm. The radial dose profiles, in the first column, for foam only (black) and 0.273-cm single pin (red) are shown at (a) 7, (c) 13, and (e) 20 MeV at 1.5 cm depth and 100 cm SSD. The radial dose perturbation is the difference between these profiles, shown in the second column, for (b) 7, (d) 13, and (f) 20 MeV. Error bars represent 1σ.

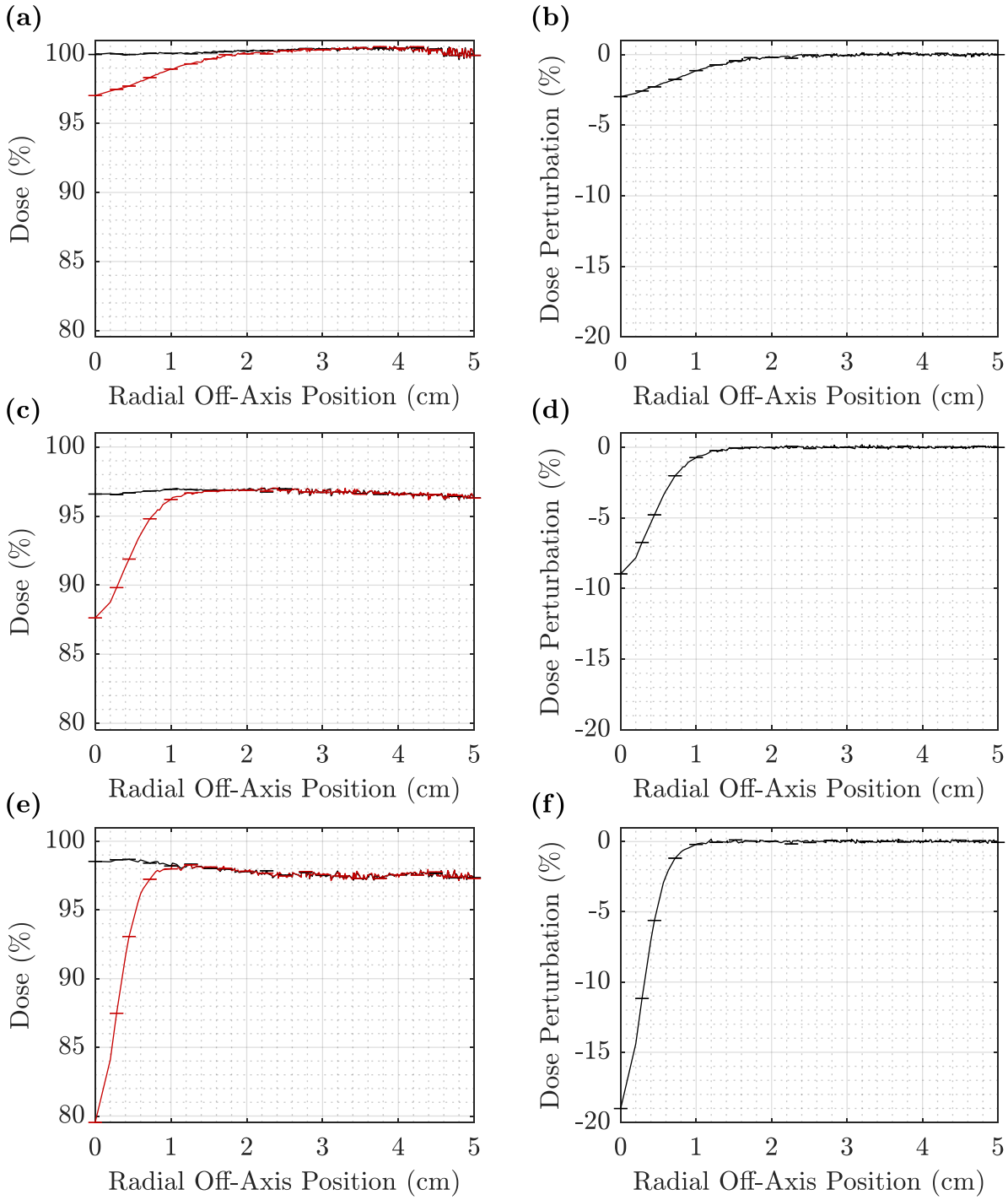

Figure D.8. Energy dependence of MC radial dose profiles and dose perturbation kernels at 7-20 MeV for a single 0.352-cm pin at 100 cm SSD at a depth of 1.5 cm. The radial dose profiles, in the first column, for foam only (black) and 0.352-cm single pin (red) are shown at (a) 7, (c) 13, and (e) 20 MeV at 1.5 cm depth and 100 cm SSD. The radial dose perturbation is the difference between these profiles, shown in the second column, for (b) 7, (d) 13, and (f) 20 MeV. Error bars represent 1σ.

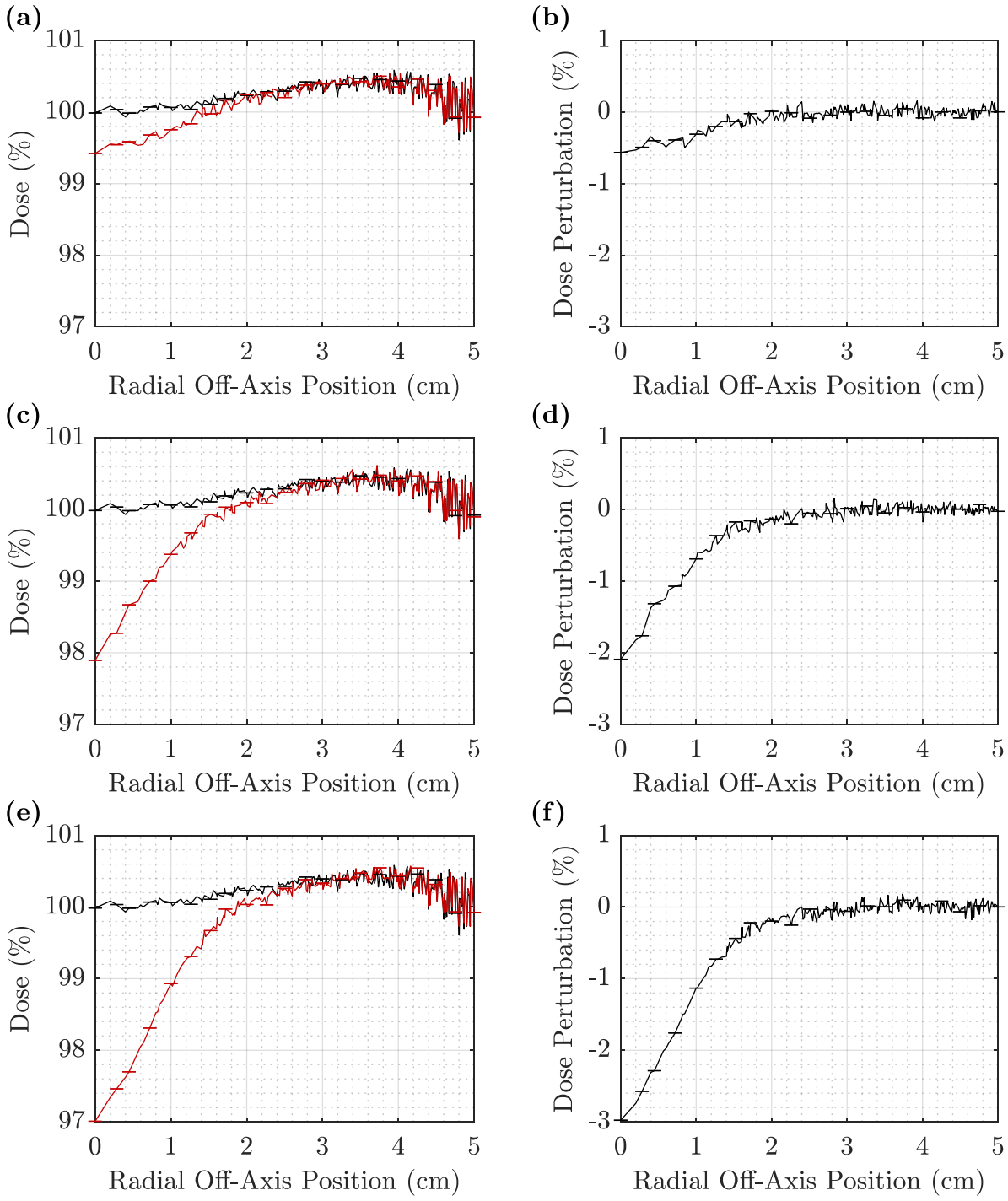

Figure D.9. Diameter dependence of MC radial dose profiles and dose perturbation kernels at 7 MeV for single pins 0.158-0.273 cm in diameter at 100 cm SSD at a depth of 1.5 cm. The radial dose profiles, in the first column, for foam only (black) and single pin (red) are shown at diameters of (a) 0.158, (c) 0.273, and (e) 0.352 cm at 1.5 cm depth for a 7 MeV beam at 100 cm SSD. The radial dose perturbation is the difference between these profiles, shown in the second column, for diameters of (b) 0.158, (d) 0.273, and (f) 0.352 cm. Error bars represent 1σ.

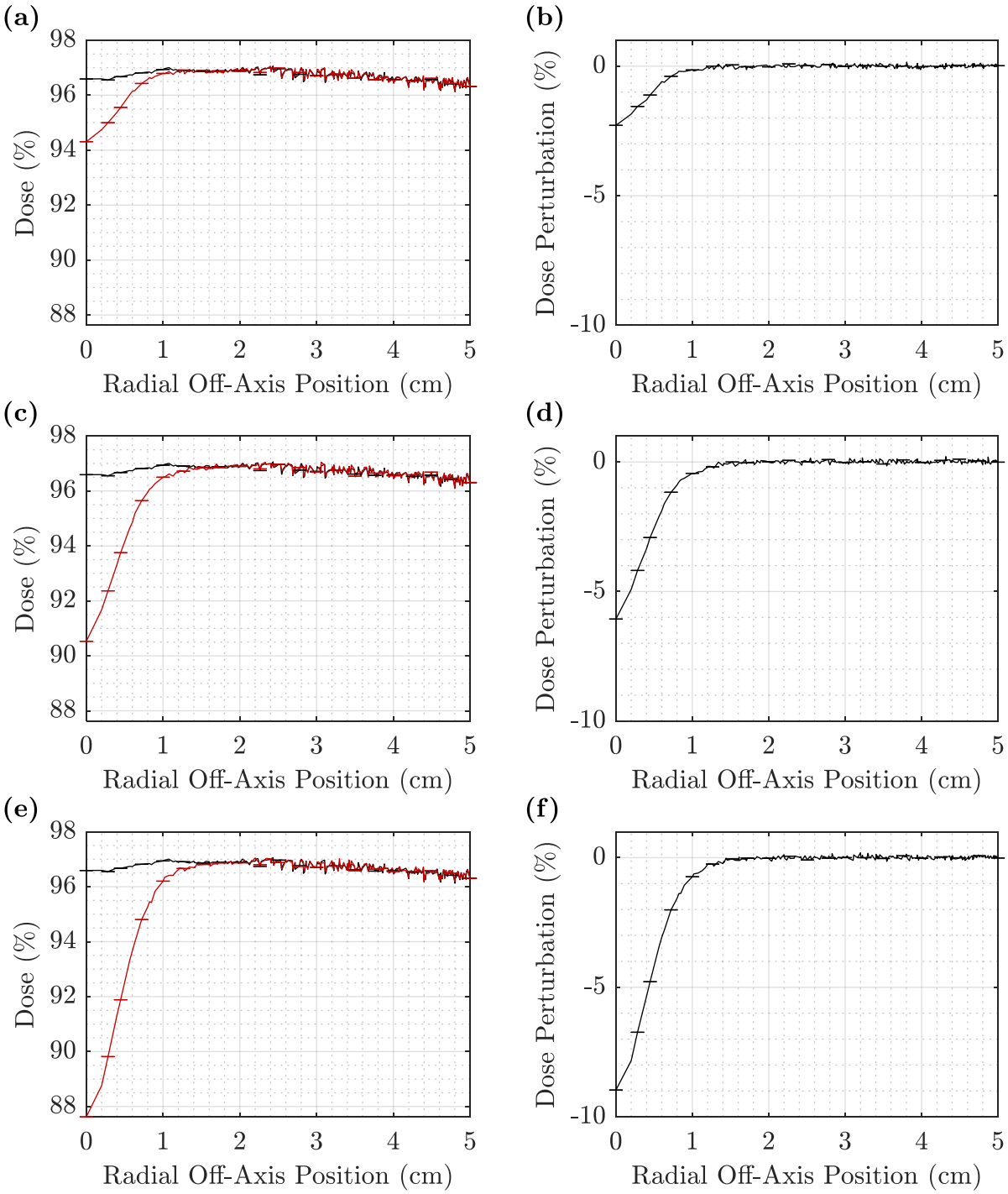

Figure D.10. Diameter dependence of MC radial dose profiles and dose perturbation kernels at 13 MeV for single pins 0.158-0.273 cm in diameter at 100 cm SSD at a depth of 1.5 cm. The radial dose profiles, in the first column, for foam only (black) and single pin (red) are shown at diameters of (a) 0.158, (c) 0.273, and (e) 0.352 cm at 1.5 cm depth for a 13 MeV beam at 100 cm SSD. The radial dose perturbation is the difference between these profiles, shown in the second column, for diameters of (b) 0.158, (d) 0.273, and (f) 0.352 cm. Error bars represent 1σ.

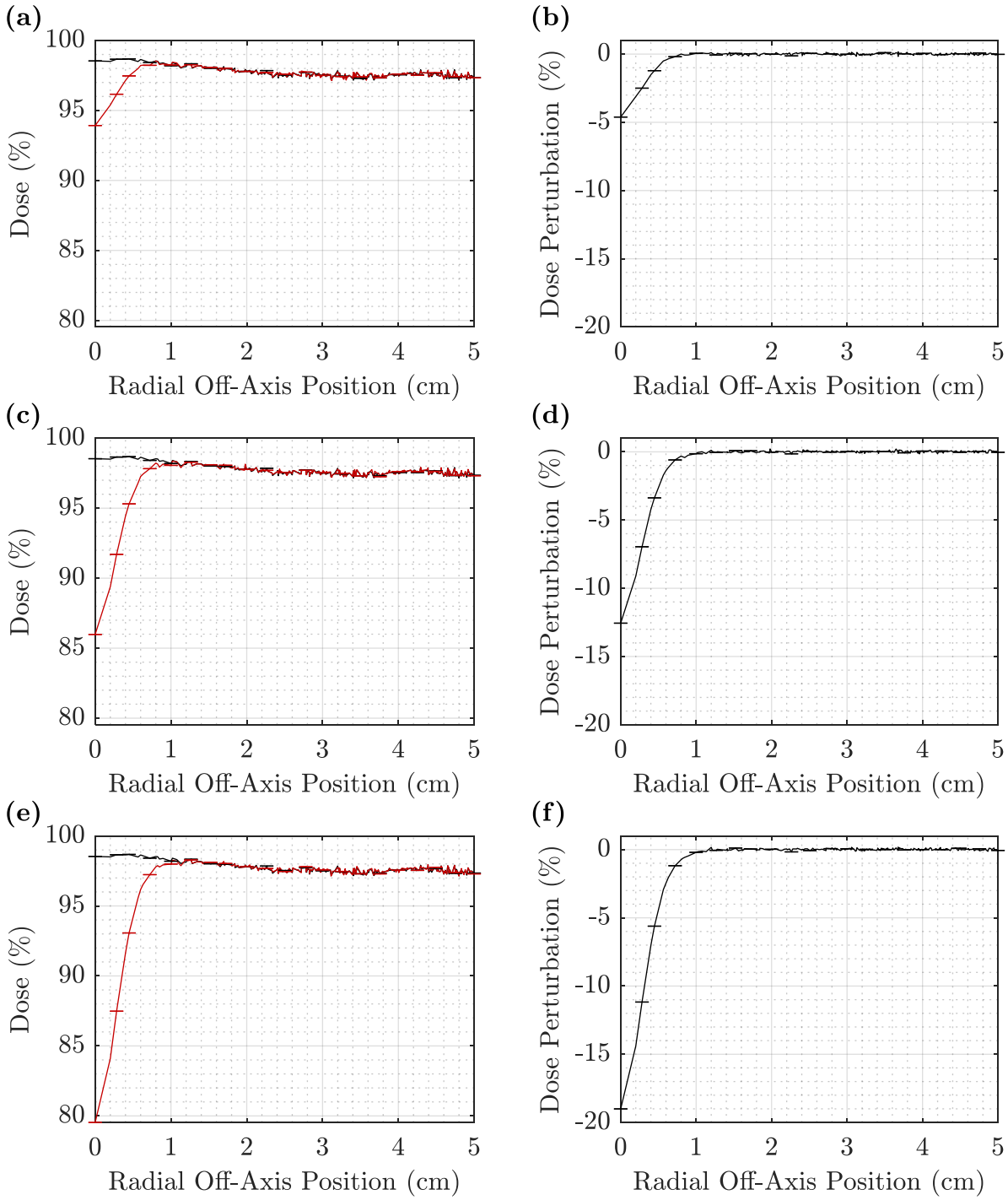

Figure D.11. Diameter dependence of MC radial dose profiles and dose perturbation kernels at 20 MeV for single pins 0.158-0.273 cm in diameter at 100 cm SSD at a depth of 1.5 cm. The radial dose profiles, in the first column, for foam only (black) and single pin (red) are shown at diameters of (a) 0.158, (c) 0.273, and (e) 0.352 cm at 1.5 cm depth for a 20 MeV beam at 100 cm SSD. The radial dose perturbation is the difference between these profiles, shown in the second column, for diameters of (b) 0.158, (d) 0.273, and (f) 0.352 cm. Error bars represent 1σ.

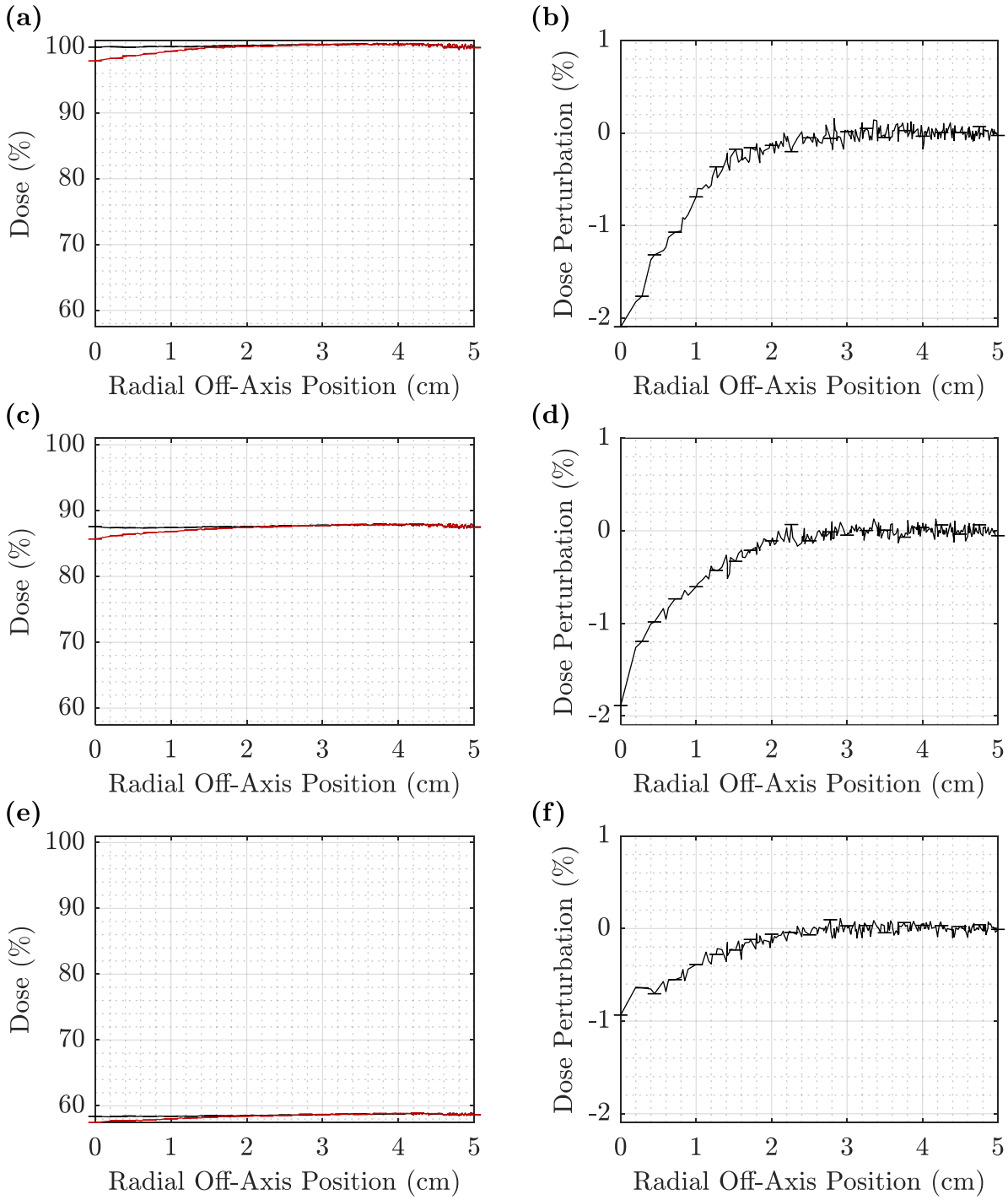

Figure D.12. Depth dependence of MC radial dose profiles and dose perturbation kernels at 7 MeV for a single 0.273-cm pin at 100 cm SSD at depths of R_{100} to R_{50}. The radial dose profiles, in the first column, for foam only (black) and 0.273-cm single pin (red) are shown for a 7 MeV beam at 100 cm SSD at depths of (a) 1.5, (c) 2.0, and (e) 2.5 cm, corresponding approximately to R_{100}, R_{90}, and R_{50}, respectively. The radial dose perturbation is the difference between these profiles, shown in the second column, at (b) 1.5, (d) 2.0, and (f) 2.5 cm depth. Error bars represent 1σ.

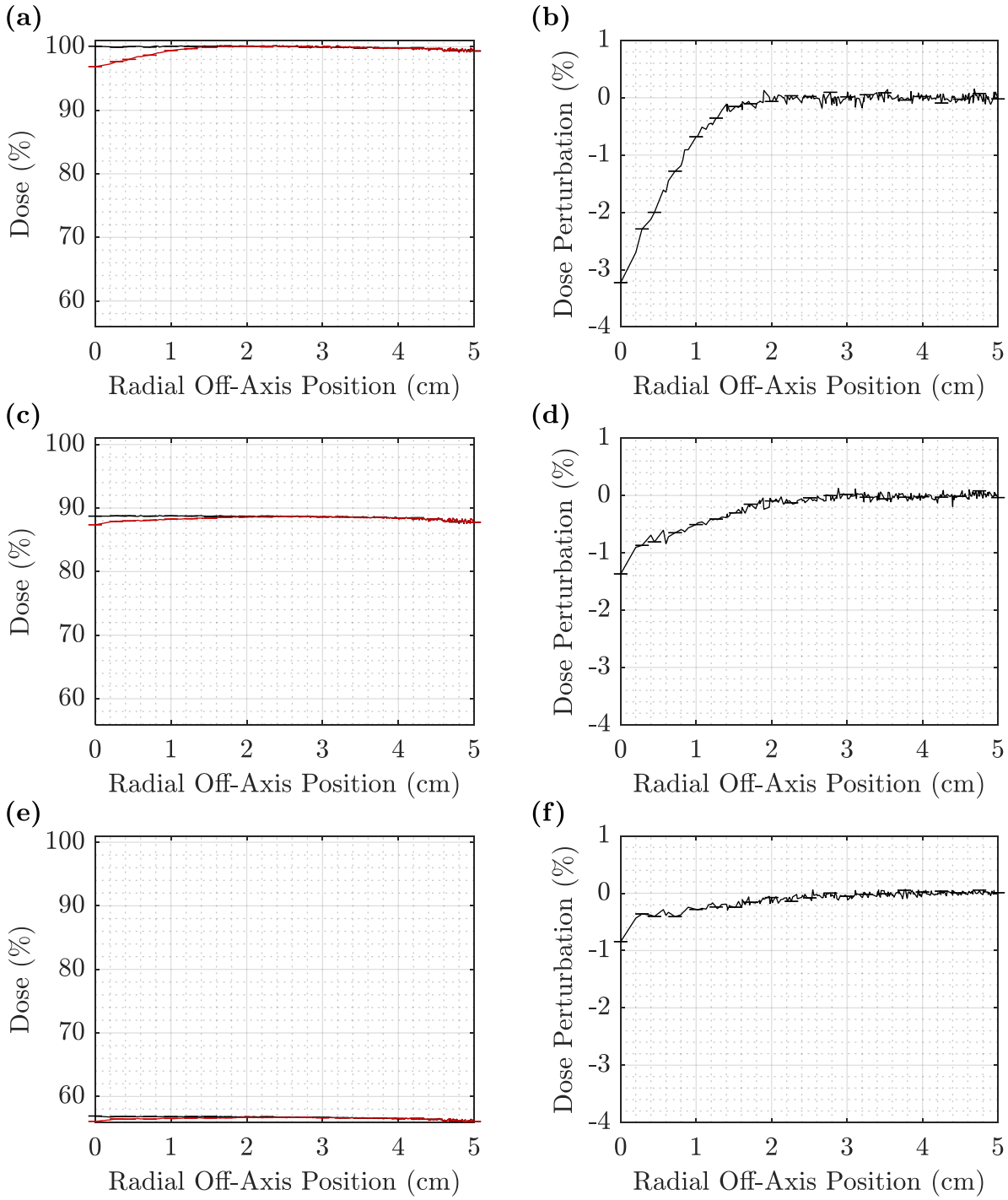

Figure D.13. Depth dependence of MC radial dose profiles and dose perturbation kernels at 13 MeV for a single 0.273-cm pin at 100 cm SSD at depths of R_{100} to R_{50}. The radial dose profiles, in the first column, for foam only (black) and 0.273-cm single pin (red) are shown for a 13 MeV beam at 100 cm SSD at depths of (a) 2.5, (c) 4.0, and (e) 5.0 cm, corresponding approximately to R_{100}, R_{90}, and R_{50}, respectively. The radial dose perturbation is the difference between these profiles, shown in the second column, at (b) 2.5, (d) 4.0, and (f) 5.0 cm depth. Error bars represent 1σ.

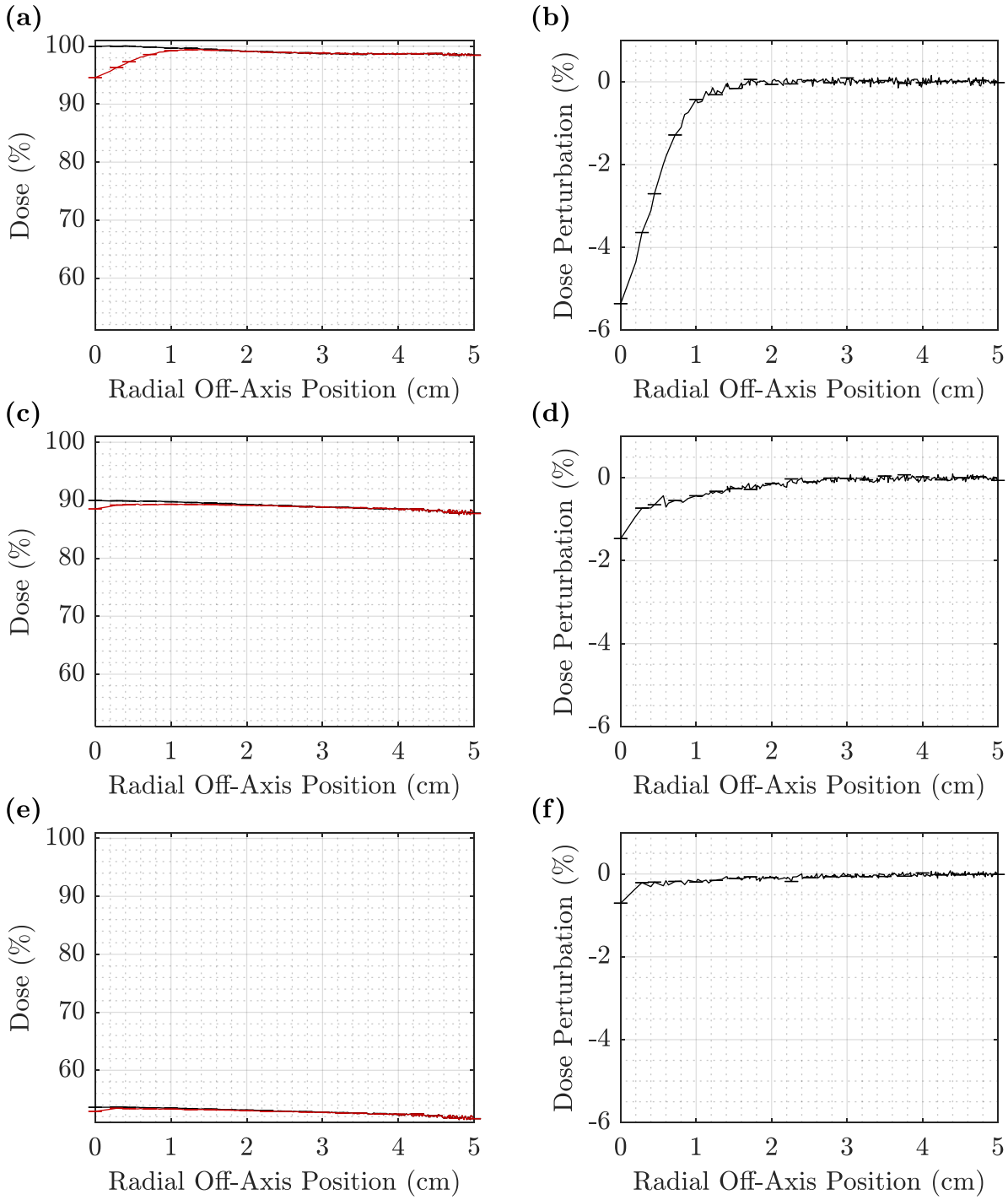

Figure D.14. Depth dependence of MC radial dose profiles and dose perturbation kernels at 20 MeV for a single 0.273-cm pin at 100 cm SSD at depths of R_{100} to R_{50}. The radial dose profiles, in the first column, for foam only (black) and 0.273-cm single pin (red) are shown for a 20 MeV beam at 100 cm SSD at depths of (a) 3.0, (c) 6.0, and (e) 8.0 cm, corresponding approximately to R_{100}, R_{90}, and R_{50}, respectively. The radial dose perturbation is the difference between these profiles, shown in the second column, at (b) 3.0, (d) 6.0, and (f) 8.0 cm depth. Error bars represent 1σ.

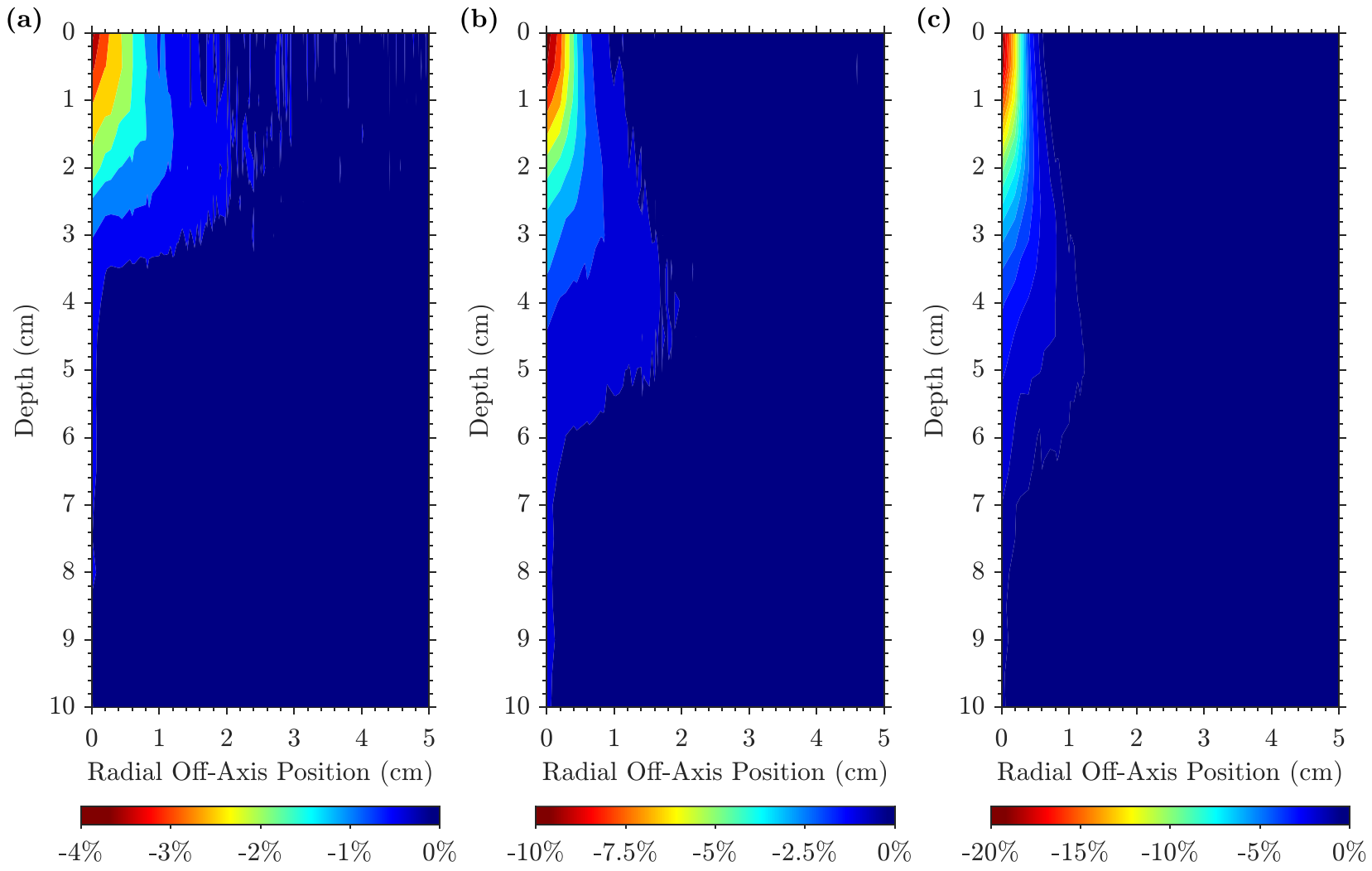

Figure D.15. MC radial isodose perturbation for a single 0.273-cm pin at 7-20 MeV at 100 cm SSD. The radial dose perturbation profiles for the 0.273-cm pin are plotted in the *rz*-plane to yield the radial isodose contours shown here for the (a) 7, (b) 13, and (c) 20 MeV beams at 100 cm SSD. The isodose plot describes the dose perturbation due to a single pin on CAX at a given set of conditions. The effect up to a radial distance of 5 cm and a depth of 10 cm is plotted here.

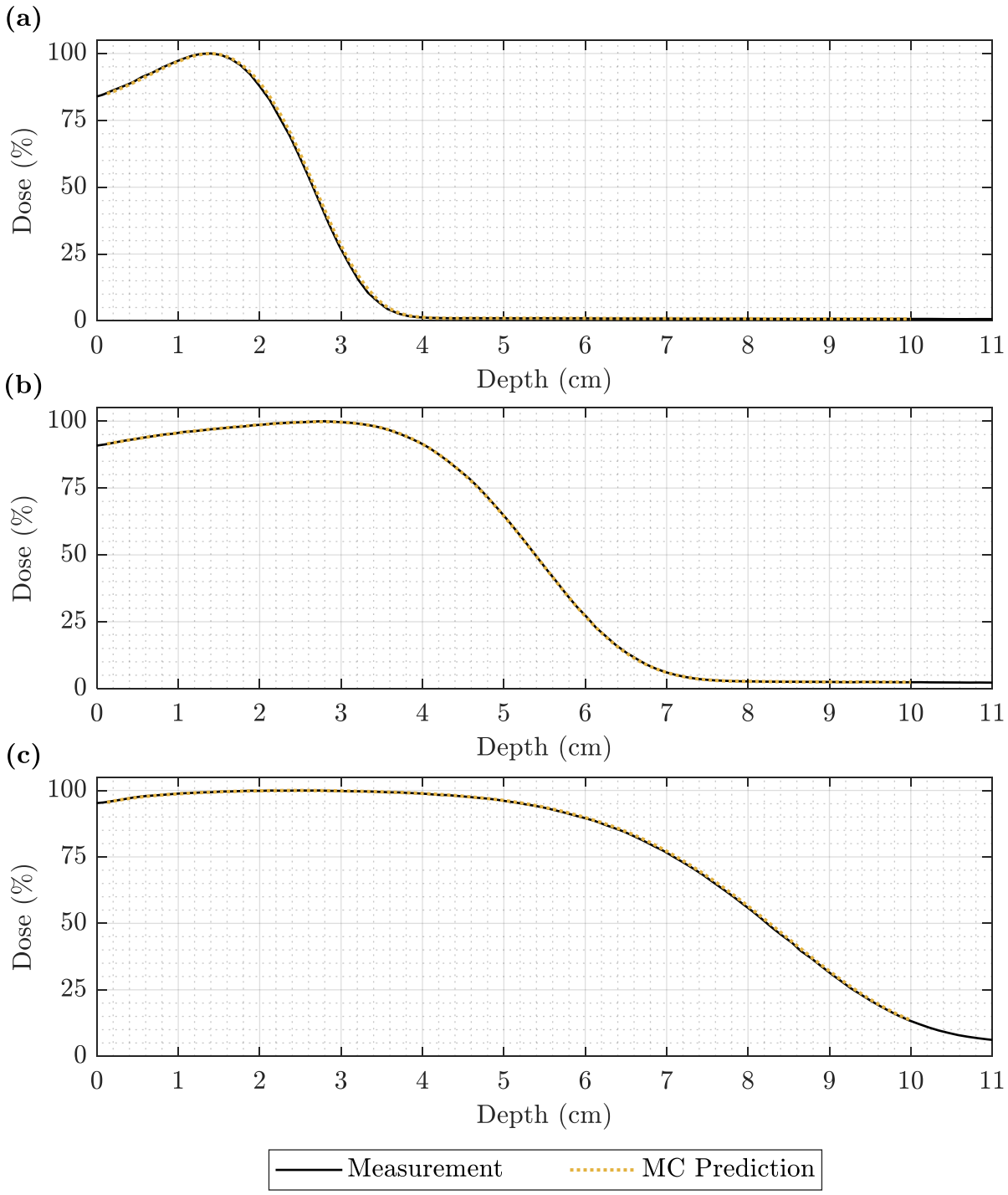

Figure D.16. PDD comparison of foam-only measurement and MC calculation for each beam energy at 100 cm SSD. Foam-only PDDs are plotted for measurement (solid black) and MC calculation (dotted yellow) at (a) 7, (b) 13, and (c) 20 MeV at 100 cm SSD.

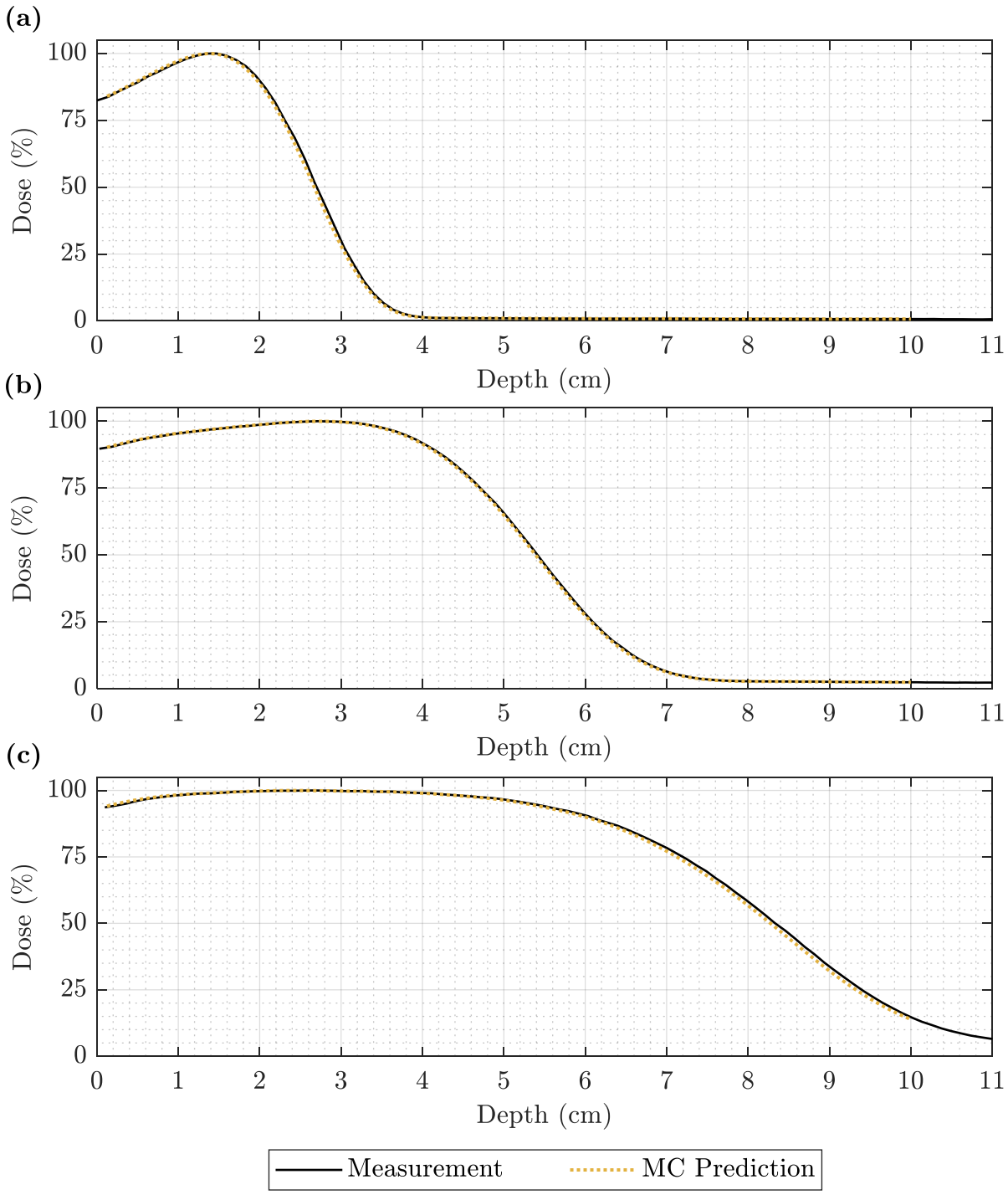

Figure D.17. PDD comparison of foam-only measurement and MC calculation for each beam energy at 105 cm SSD. Foam-only PDDs are plotted for measurement (solid black) and MC calculation (dotted yellow) at (a) 7, (b) 13, and (c) 20 MeV at 105 cm SSD.

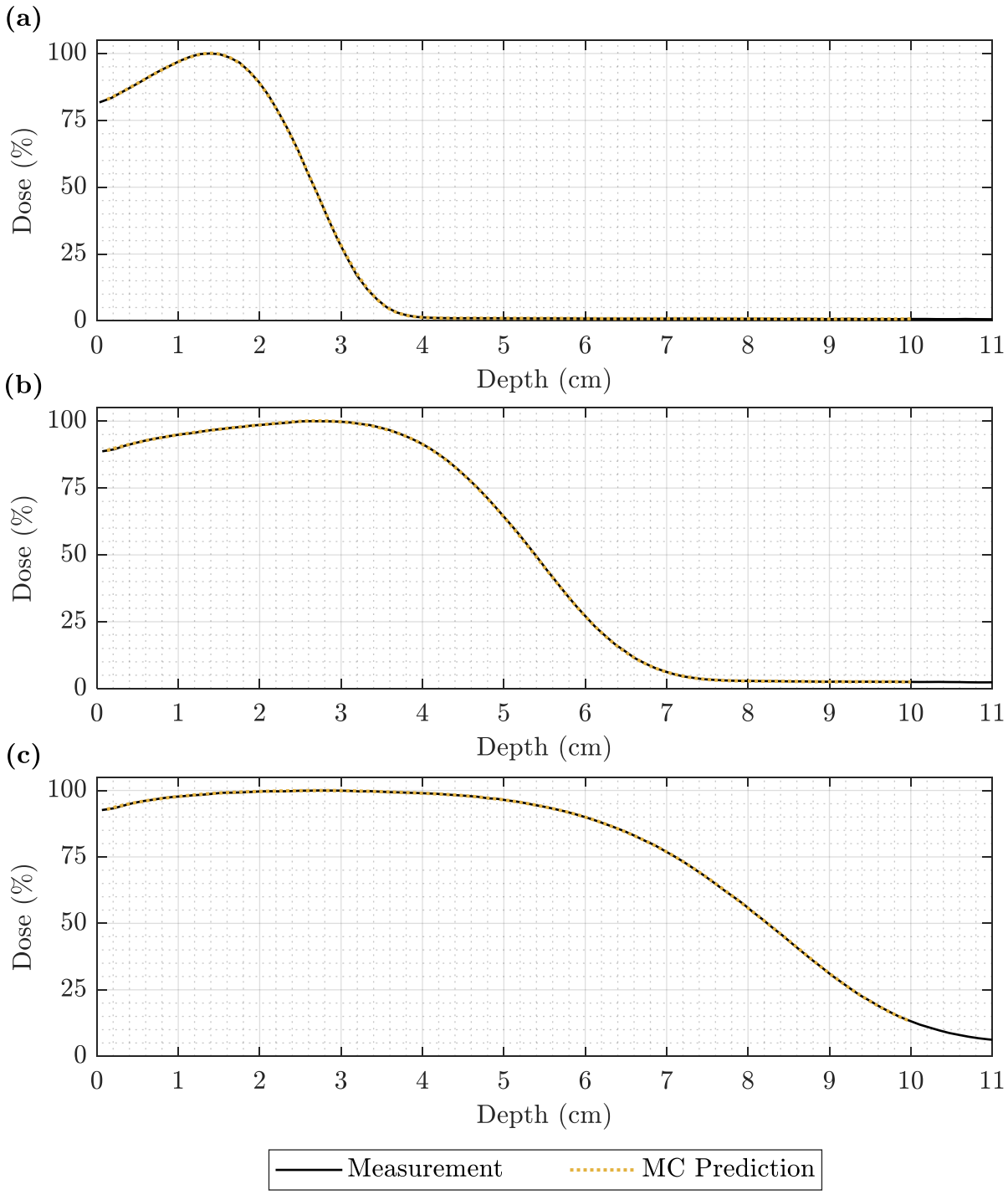

Figure D.18. PDD comparison of foam-only measurement and MC calculation for each beam energy at 110 cm SSD. Foam-only PDDs are plotted for measurement (solid black) and MC calculation (dotted yellow) at (a) 7, (b) 13, and (c) 20 MeV at 110 cm SSD.

Table D.2. Comparison of R_{90}, R_{50}, and R_{20} values for measurement and MC calculation under foam-only conditions. The measured and MC-calculated R_{90} and R_{50} values and their differences were determined under foam-only conditions at each setup.

SSD (cm)	Energy (MeV)	R_{90} (cm)			R_{50} (cm)			R_{20} (cm)		
		Meas.	MC	ΔR_{90}	Meas.	MC	ΔR_{50}	Meas.	MC	ΔR_{20}
100	7	1.98	1.99	-0.01	2.68	2.68	0.00	3.15	3.15	0.00
100	13	4.09	4.10	-0.01	5.39	5.39	0.00	6.23	6.23	0.00
100	20	5.98	5.98	0.00	8.27	8.27	0.00	9.59	9.58	0.01
105	7	1.97	1.98	-0.01	2.67	2.68	0.00	3.15	3.15	0.00
105	13	4.08	4.09	-0.01	5.39	5.39	0.00	6.24	6.24	0.00
105	20	6.01	6.01	0.00	8.27	8.28	-0.01	9.60	9.59	0.01
110	7	1.97	1.97	-0.01	2.68	2.68	0.00	3.15	3.15	0.00
110	13	4.08	4.08	0.00	5.38	5.38	0.00	6.24	6.23	0.00
110	20	6.00	6.01	0.00	8.24	8.24	-0.01	9.54	9.54	0.00

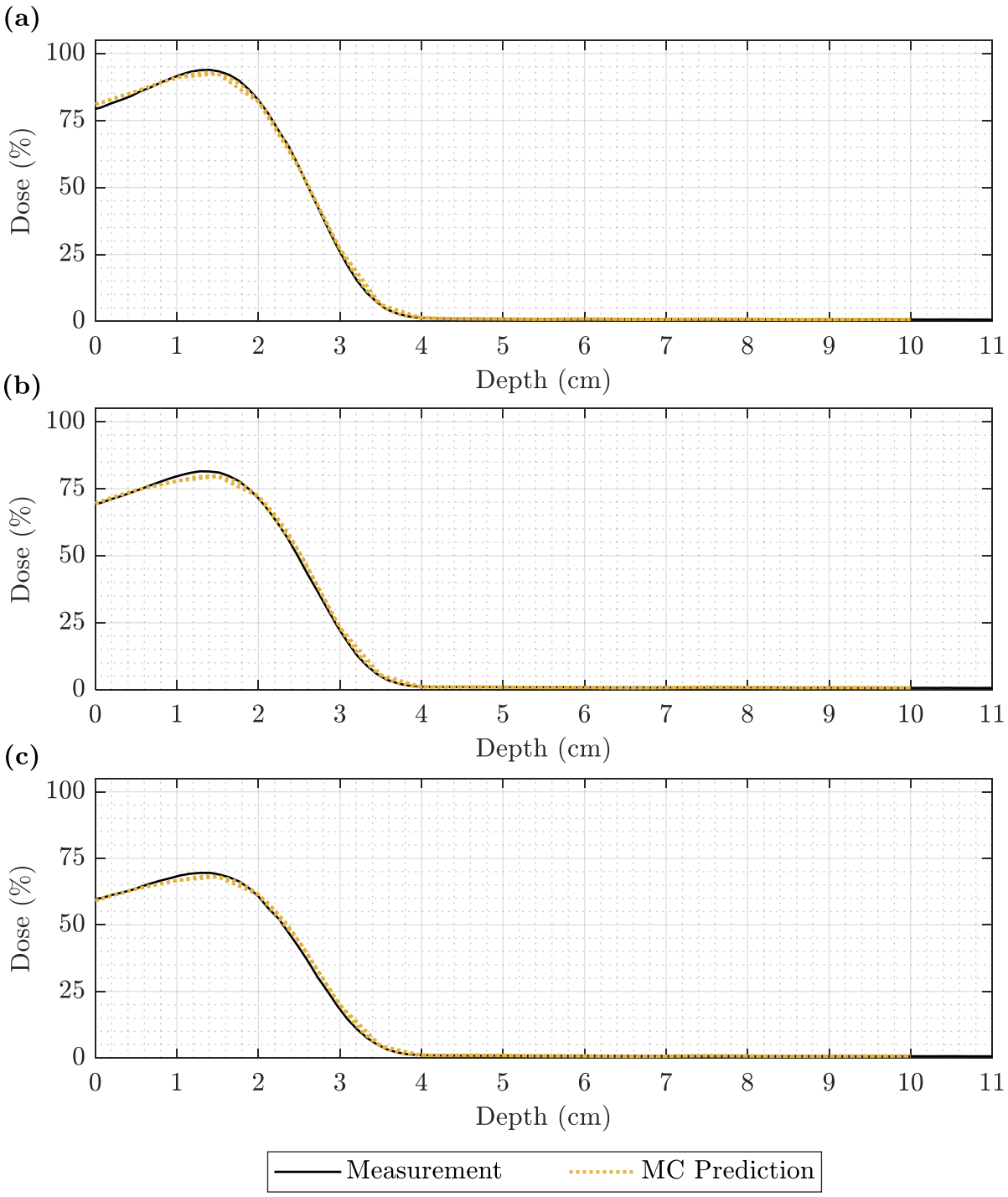

Figure D.19. PDD comparison of measurement and MC prediction at 7 MeV and 100 cm SSD. Measurement (solid black) is compared to the MC prediction (dotted yellow) for a 7 MeV beam at 100 cm SSD for (a) 0.158-cm, (b) 0.273-cm, and (c) 0.352-cm pins.

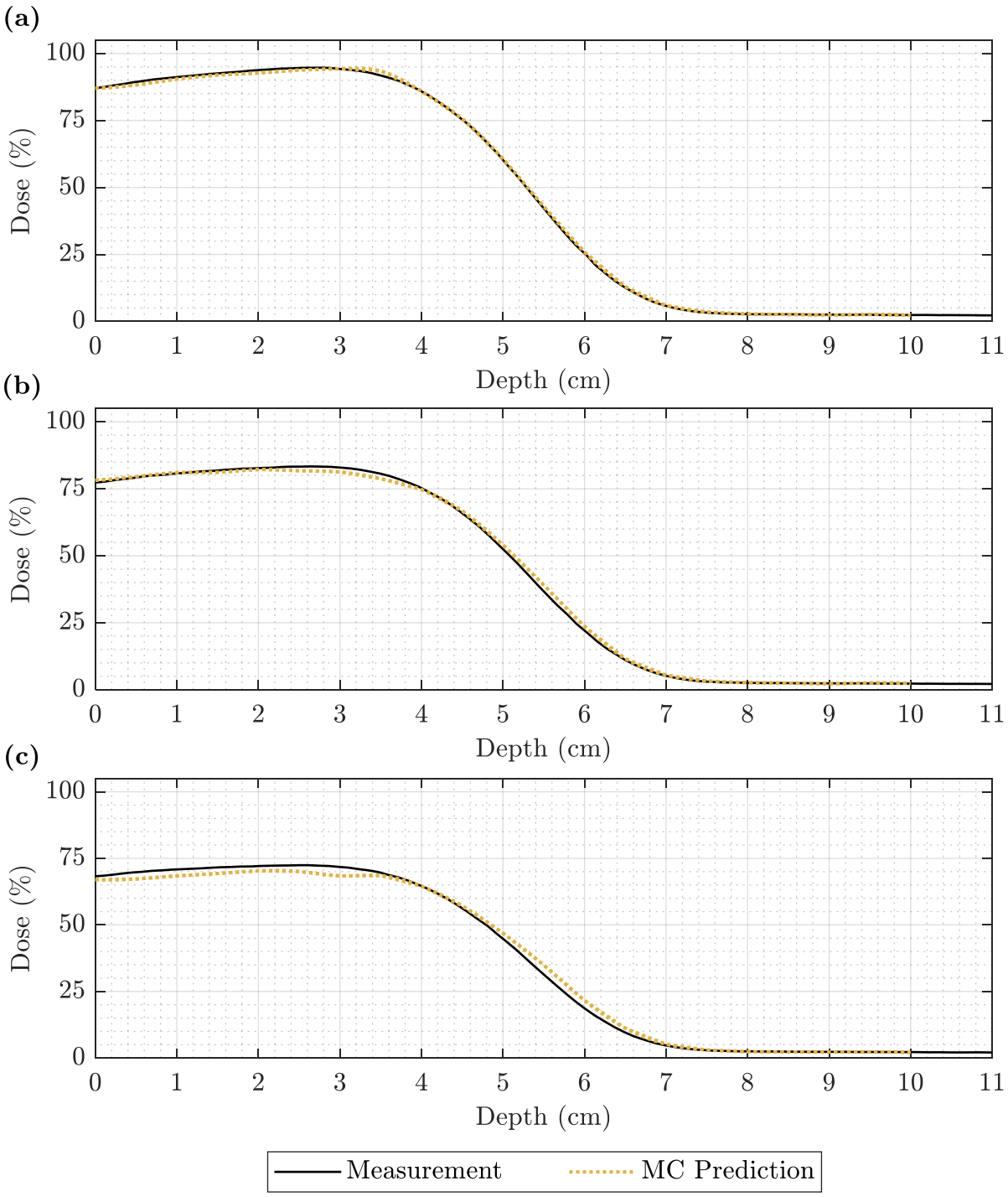

Figure D.20. PDD comparison of measurement and MC prediction at 13 MeV and 100 cm SSD. Measurement (solid black) is compared to the MC prediction (dotted yellow) for a 13 MeV beam at 100 cm SSD for (a) 0.158-cm, (b) 0.273-cm, and (c) 0.352-cm pins.

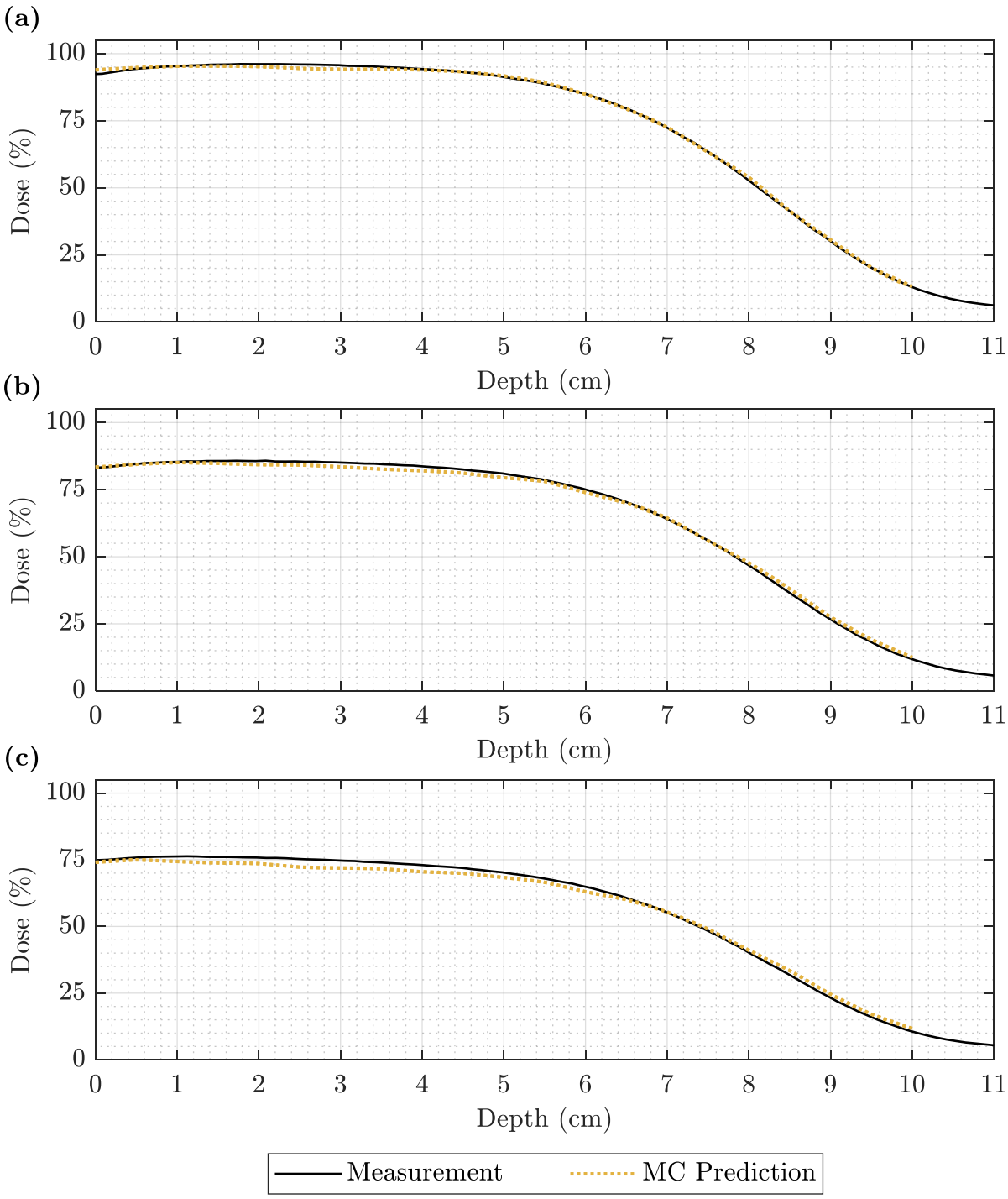

Figure D.21. PDD comparison of measurement and MC prediction at 20 MeV and 100 cm SSD. Measurement (solid black) is compared to the MC prediction (dotted yellow) for a 20 MeV beam at 100 cm SSD for (a) 0.158-cm, (b) 0.273-cm, and (c) 0.352-cm pins.

Table D.3. Comparison of R_{90}, R_{50}, and R_{20} values for measurement and MC prediction under modulated conditions. The measured and MC-estimated R_{90} and R_{50} values and their differences were determined under intensity modulators with pins of the indicated diameter. The average absolute difference between MC and measured R_{90}, R_{50}, and R_{20} were 0.08, 0.07, and 0.06 cm, respectively.

SSD (cm)	Energy (MeV)	d (cm)	R_{90} (cm)			R_{50} (cm)			R_{20} (cm)		
			Meas.	MC	ΔR_{90}	Meas.	MC	ΔR_{50}	Meas.	MC	ΔR_{20}
100	7	0.158	2.08	2.10	-0.02	2.71	2.73	-0.02	3.16	3.19	-0.03
100	7	0.273	2.30	2.37	-0.07	2.79	2.84	-0.04	3.20	3.24	-0.04
100	7	0.352	2.46	2.54	-0.08	2.88	2.93	-0.05	3.26	3.30	-0.04
100	13	0.158	4.31	4.33	-0.02	5.44	5.47	-0.03	6.27	6.29	-0.03
100	13	0.273	4.71	4.78	-0.08	5.59	5.68	-0.09	6.37	6.41	-0.04
100	13	0.352	5.00	5.15	-0.15	5.75	5.90	-0.16	6.48	6.60	-0.12
100	20	0.158	6.38	6.42	-0.04	8.34	8.37	-0.03	9.64	9.64	0.01
100	20	0.273	7.09	7.14	-0.06	8.58	8.67	-0.08	9.80	9.90	-0.09
100	20	0.352	7.58	7.67	-0.10	8.82	8.93	-0.11	10.02	10.19	-0.17
105	7	0.158	2.10	2.14	-0.04	2.71	2.73	-0.02	3.17	3.18	-0.01
105	7	0.273	2.30	2.32	-0.02	2.80	2.82	-0.02	3.22	3.24	-0.03
105	7	0.352	2.46	2.50	-0.04	2.87	2.92	-0.05	3.26	3.30	-0.04
105	13	0.158	4.32	4.28	0.04	5.45	5.48	-0.03	6.27	6.31	-0.04
105	13	0.273	4.70	4.73	-0.03	5.59	5.69	-0.10	6.37	6.45	-0.08
105	13	0.352	5.02	5.19	-0.17	5.76	5.92	-0.17	6.49	6.63	-0.14
105	20	0.158	6.46	6.52	-0.06	8.39	8.41	-0.03	9.66	9.66	0.00
105	20	0.273	7.14	7.21	-0.08	8.63	8.72	-0.10	9.85	9.87	-0.02
105	20	0.352	7.66	7.84	-0.19	8.88	9.01	-0.13	10.06	10.25	-0.20
110	7	0.158	2.11	2.14	-0.03	2.72	2.73	-0.01	3.16	3.17	0.00
110	7	0.273	2.29	2.35	-0.06	2.79	2.83	-0.04	3.21	3.23	-0.02
110	7	0.352	2.45	2.57	-0.12	2.86	2.92	-0.06	3.25	3.25	0.00
110	13	0.158	4.32	4.37	-0.05	5.45	5.48	-0.02	6.27	6.31	-0.04
110	13	0.273	4.70	4.77	-0.06	5.60	5.68	-0.08	6.37	6.47	-0.11
110	13	0.352	5.01	5.17	-0.16	5.75	5.90	-0.15	6.48	6.65	-0.17
110	20	0.158	6.43	6.50	-0.07	8.34	8.40	-0.05	9.62	9.66	-0.04
110	20	0.273	7.13	7.25	-0.12	8.60	8.70	-0.10	9.81	9.84	-0.03
110	20	0.352	7.67	7.89	-0.22	8.86	8.98	-0.13	10.05	10.05	0.00

Table D.4. Comparison of CAX dose values for measurement and MC prediction under modulated conditions. The measured and MC-estimated CAX dose values and their difference were determined under intensity modulators with pins of the indicated diameter. Values are normalized to maximum dose of the foam-only setup at the same beam energy and SSD conditions. The average magnitude difference in maximum dose was 1.6%.

SSD (cm)	Energy (MeV)	Diameter (cm)	Measured CAX Dose	MC-Estim. CAX Dose	Difference
100	7	0.158	93.9%	92.5%	-1.5%
100	7	0.273	81.5%	79.6%	-1.9%
100	7	0.352	69.5%	68.1%	-1.4%
100	13	0.158	94.7%	94.3%	-0.4%
100	13	0.273	83.4%	82.2%	-1.1%
100	13	0.352	72.4%	70.3%	-2.1%
100	20	0.158	96.1%	95.4%	-0.7%
100	20	0.273	85.8%	85.1%	-0.7%
100	20	0.352	76.3%	75.0%	-1.3%
105	7	0.158	93.6%	92.5%	-1.1%
105	7	0.273	81.8%	80.1%	-1.7%
105	7	0.352	70.3%	68.1%	-2.2%
105	13	0.158	94.7%	95.5%	0.9%
105	13	0.273	83.4%	82.3%	-1.1%
105	13	0.352	72.3%	69.9%	-2.3%
105	20	0.158	95.7%	94.0%	-1.7%
105	20	0.273	84.7%	82.5%	-2.2%
105	20	0.352	74.8%	71.2%	-3.6%
110	7	0.158	93.7%	92.1%	-1.6%
110	7	0.273	82.1%	81.2%	-0.9%
110	7	0.352	70.9%	67.4%	-3.5%
110	13	0.158	94.5%	94.1%	-0.4%
110	13	0.273	83.2%	81.2%	-2.0%
110	13	0.352	72.0%	69.6%	-2.4%
110	20	0.158	95.1%	94.9%	-0.2%
110	20	0.273	84.1%	82.5%	-1.7%
110	20	0.352	73.5%	70.3%	-3.2%

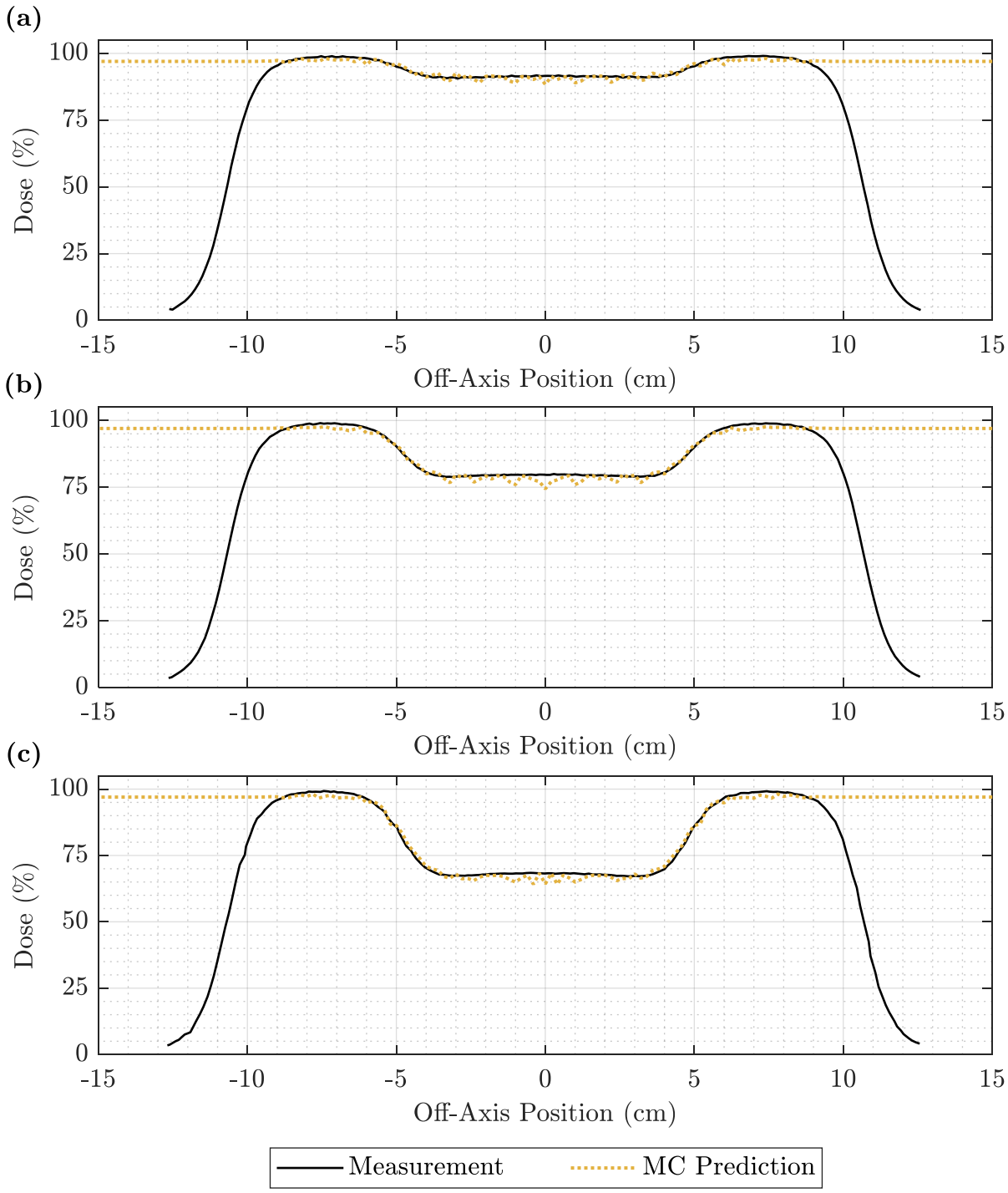

Figure D.22. Off-axis profile comparison of measurement and MC prediction for the 7 MeV beam at 100 cm SSD and 1.0 cm depth. Measurement (solid black) is compared to the MC prediction (dotted yellow) for a 7 MeV beam at 100 cm SSD for (a) 0.158-cm, (b) 0.273-cm, and (c) 0.352-cm pins at a depth of 1.0 cm.

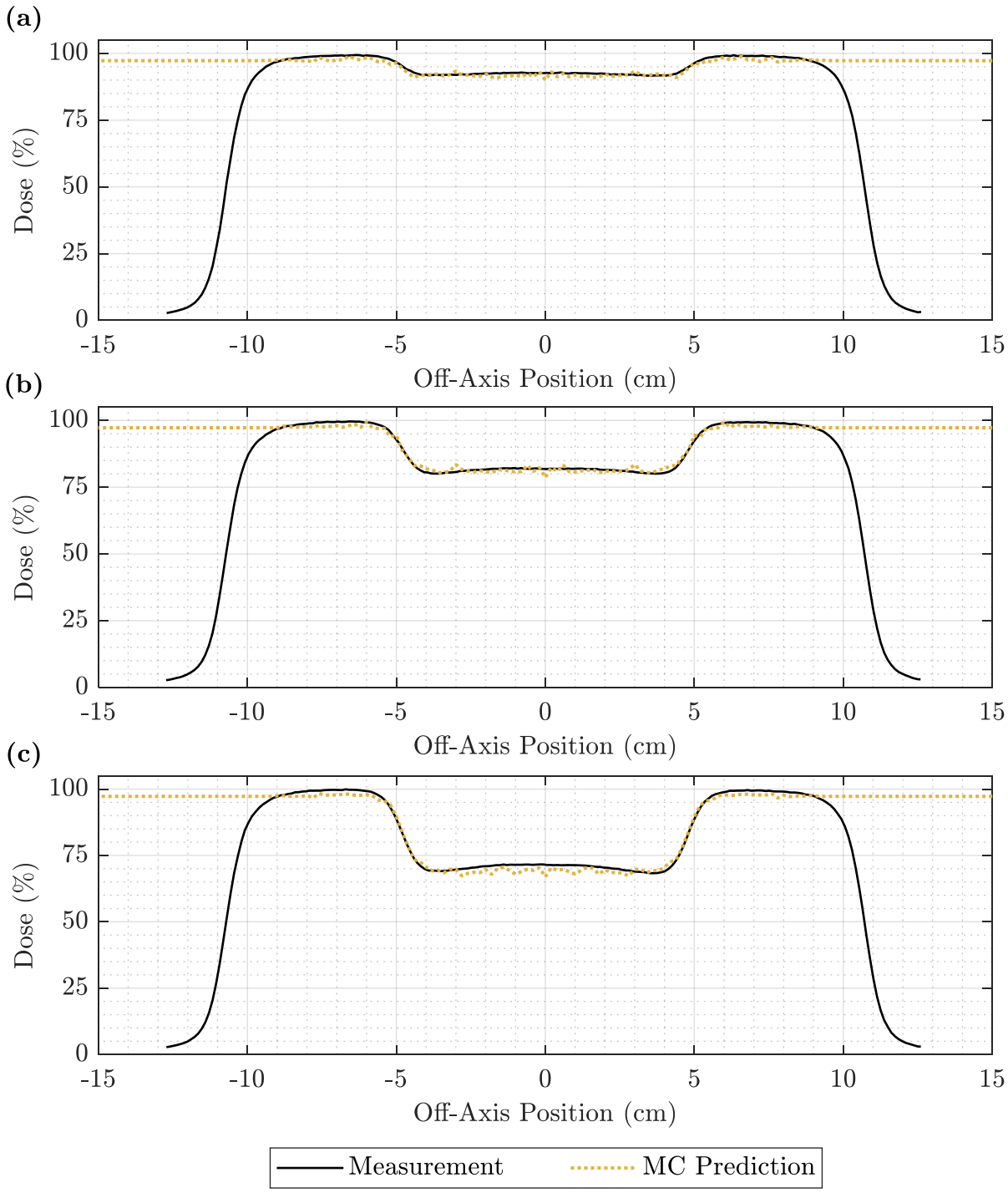

Figure D.23. Off-axis profile comparison of measurement and MC prediction for the 13 MeV beam at 100 cm SSD and 1.5 cm depth. Measurement (solid black) is compared to the MC prediction (dotted yellow) for a 13 MeV beam at 100 cm SSD for (a) 0.158-cm, (b) 0.273-cm, and (c) 0.352-cm pins at a depth of 1.5 cm.

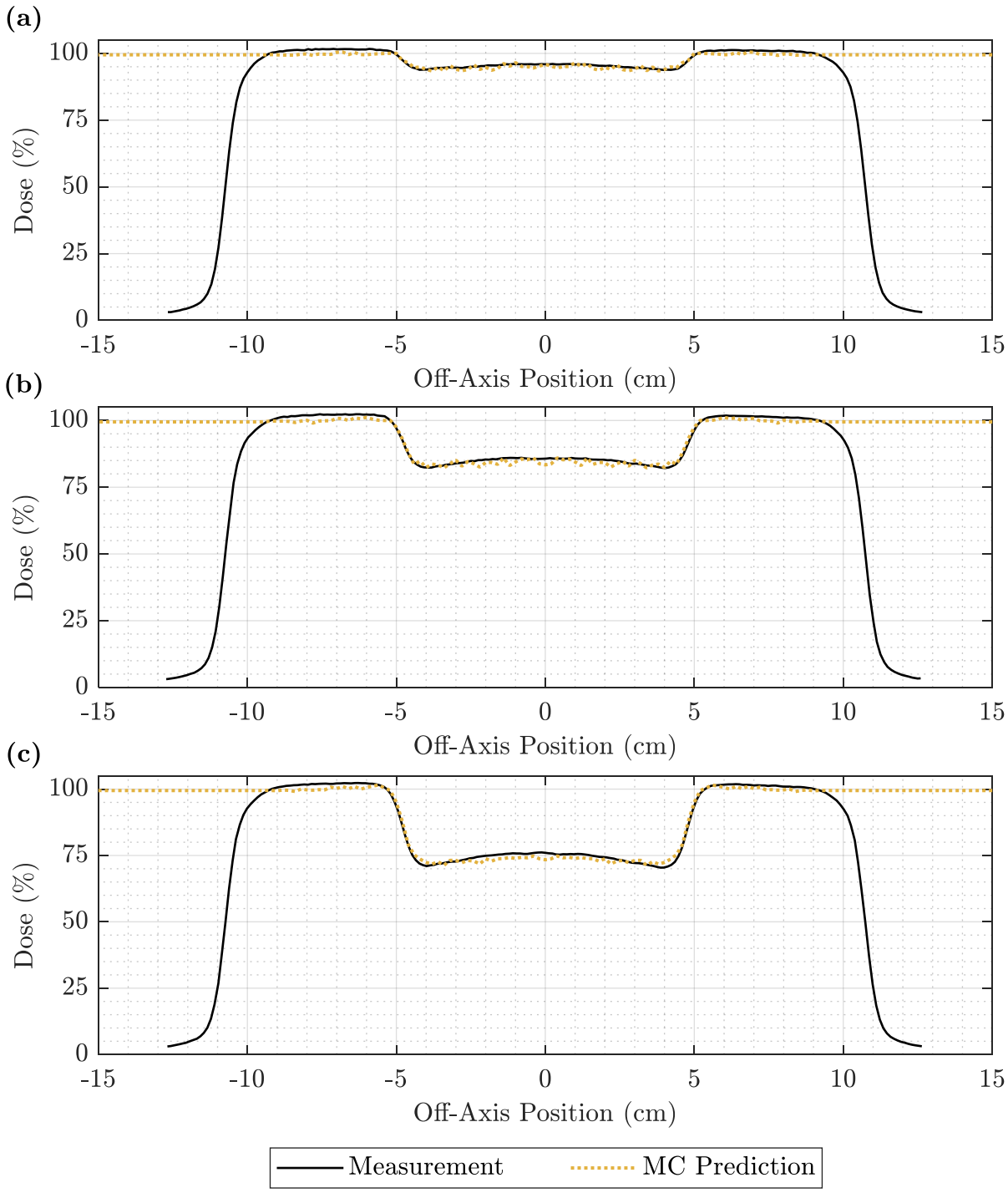

Figure D.24. Off-axis profile comparison of measurement and MC prediction for the 20 MeV beam at 100 cm SSD and 1.5 cm depth. Measurement (solid black) is compared to the MC prediction (dotted yellow) for a 20 MeV beam at 100 cm SSD for (a) 0.158-cm, (b) 0.273-cm, and (c) 0.352-cm pins at a depth of 1.5 cm.

Table D.5. Comparison of passing rates for MC-predicted modulated profiles under 3%/3mm DTA criteria. The MC-estimated dose distribution under a given pin arrangement was compared to the corresponding measurement with 3%/3mm DTA criteria up to 8 cm from CAX. Overall passing rates were evaluated. The average passing rate was 96.1%.

Energy (MeV)	Diameter (cm)	100 cm SSD	105 cm SSD	110 cm SSD
7	0.158	99.8%	99.7%	98.6%
7	0.273	97.3%	99.9%	94.0%
7	0.352	95.6%	94.3%	82.5%
13	0.158	99.7%	99.9%	99.7%
13	0.273	99.4%	99.0%	98.5%
13	0.352	90.4%	80.1%	91.3%
20	0.158	99.9%	99.1%	98.6%
20	0.273	99.7%	97.8%	96.2%
20	0.352	98.8%	90.9%	94.7%
	Average	97.8%	95.6%	94.9%

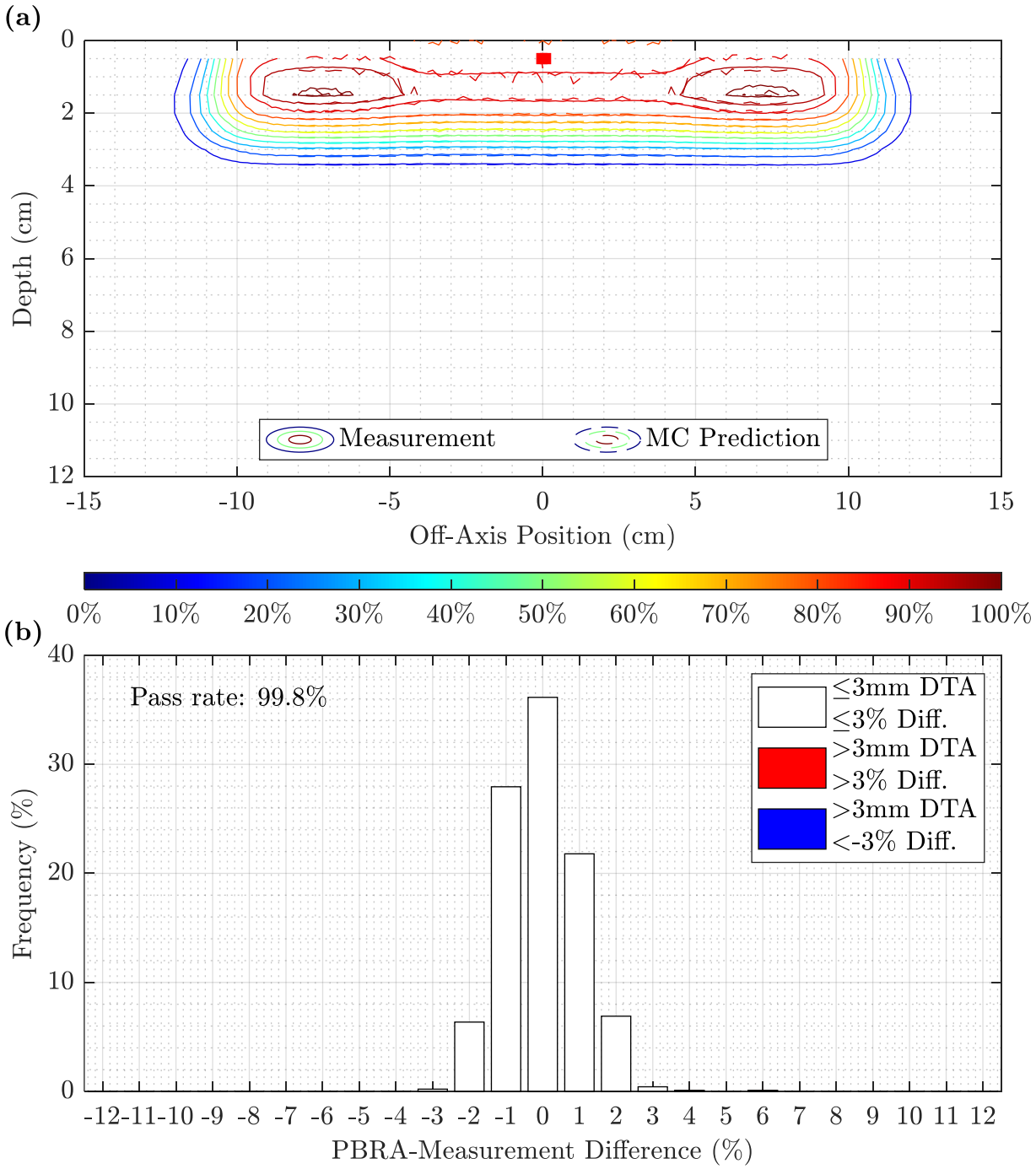

Figure D.25. Measurement and MC prediction isodose comparison and difference histogram for 0.158-cm pins at 7 MeV and 100 cm SSD. The isodose contours in (a) compare the measured (solid) and MC estimation (dashed) isodose distributions, and (b) contains the histogram of differences between measurement and MC prediction (Equation D.5) for 0.158-cm pins at 7 MeV and 100 cm SSD. In both (a) and (b), points at which the MC estimation underpredicted and overpredicted the dose relative to measurement are shown in blue and red, respectively. The 3%/3mm DTA criteria yielded a passing rate of 99.8% for points within 8 cm of CAX.

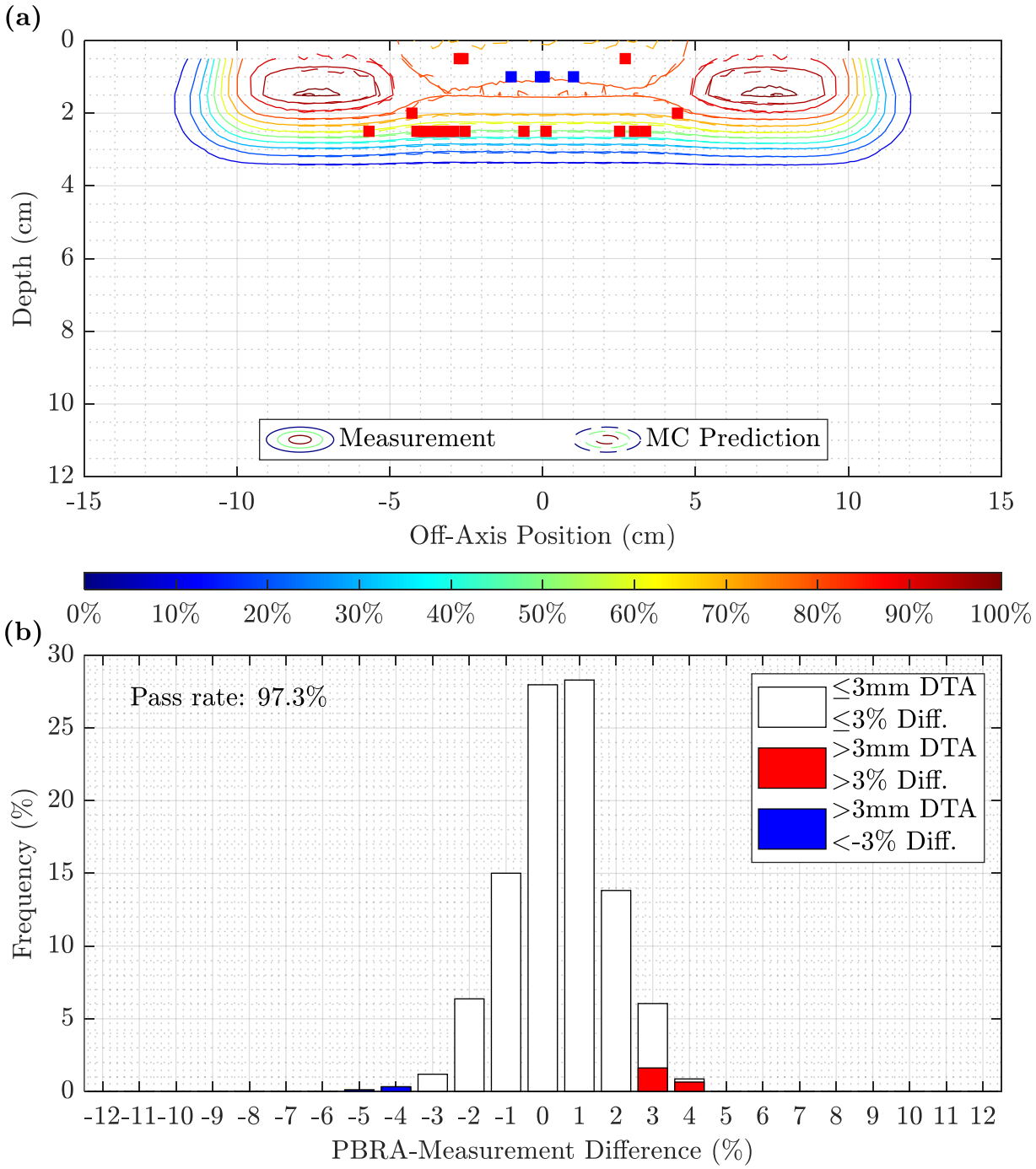

Figure D.26. Measurement and MC prediction isodose comparison and difference histogram for 0.273-cm pins at 7 MeV and 100 cm SSD. The isodose contours in (a) compare the measured (solid) and MC estimation (dashed) isodose distributions, and (b) contains the histogram of differences between measurement and MC prediction (Equation D.5) for 0.273-cm pins at 7 MeV and 100 cm SSD. In both (a) and (b), points at which the MC estimation underpredicted and overpredicted the dose relative to measurement are shown in blue and red, respectively. The 3%/3mm DTA criteria yielded a passing rate of 97.3% for points within 8 cm of CAX.

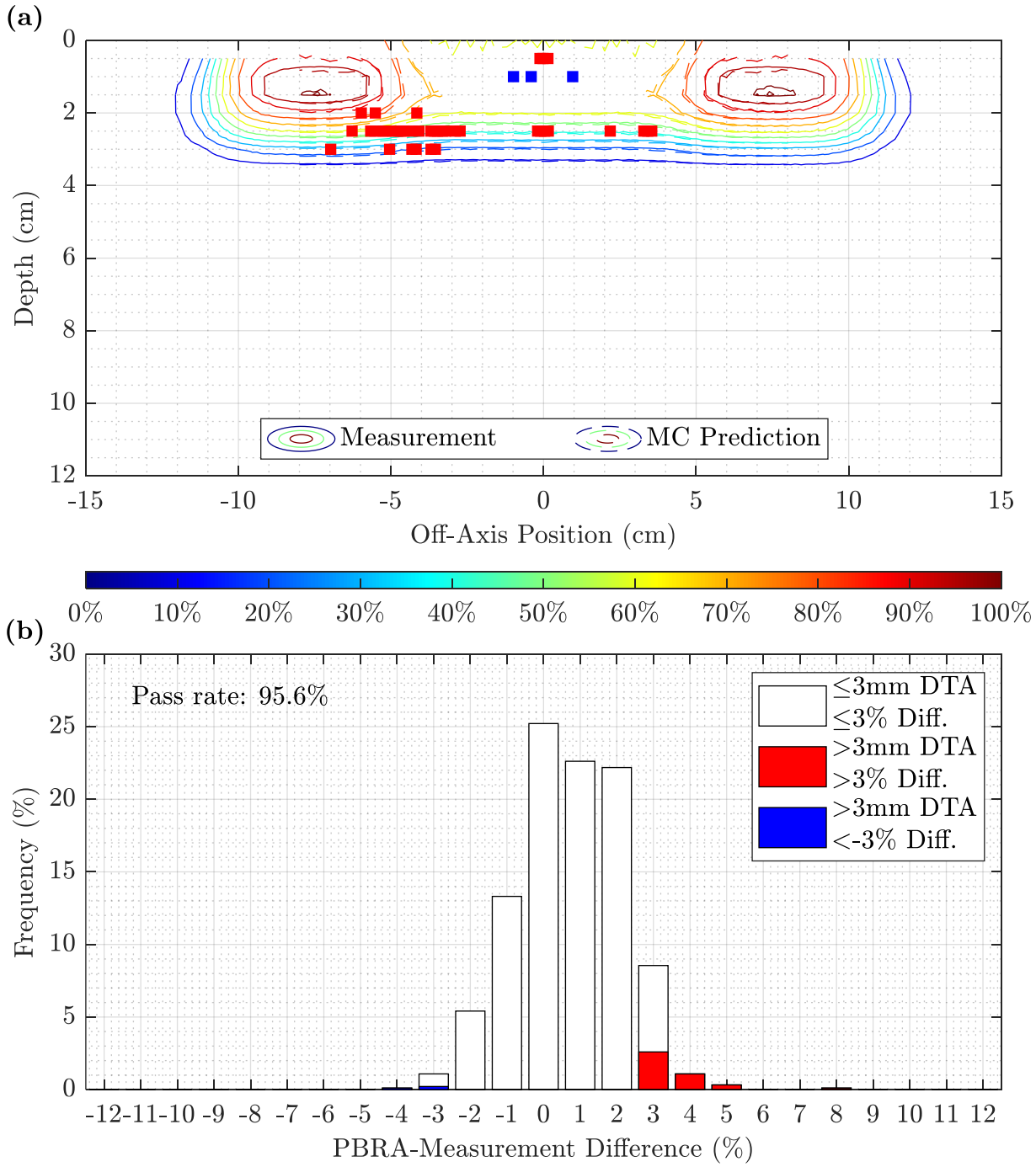

Figure D.27. Measurement and MC prediction isodose comparison and difference histogram for 0.352-cm pins at 7 MeV and 100 cm SSD. The isodose contours in (a) compare the measured (solid) and MC estimation (dashed) isodose distributions, and (b) contains the histogram of differences between measurement and MC prediction (Equation D.5) for 0.352-cm pins at 7 MeV and 100 cm SSD. In both (a) and (b), points at which the MC estimation underpredicted and overpredicted the dose relative to measurement are shown in blue and red, respectively. The 3%/3mm DTA criteria yielded a passing rate of 95.6% for points within 8 cm of CAX.

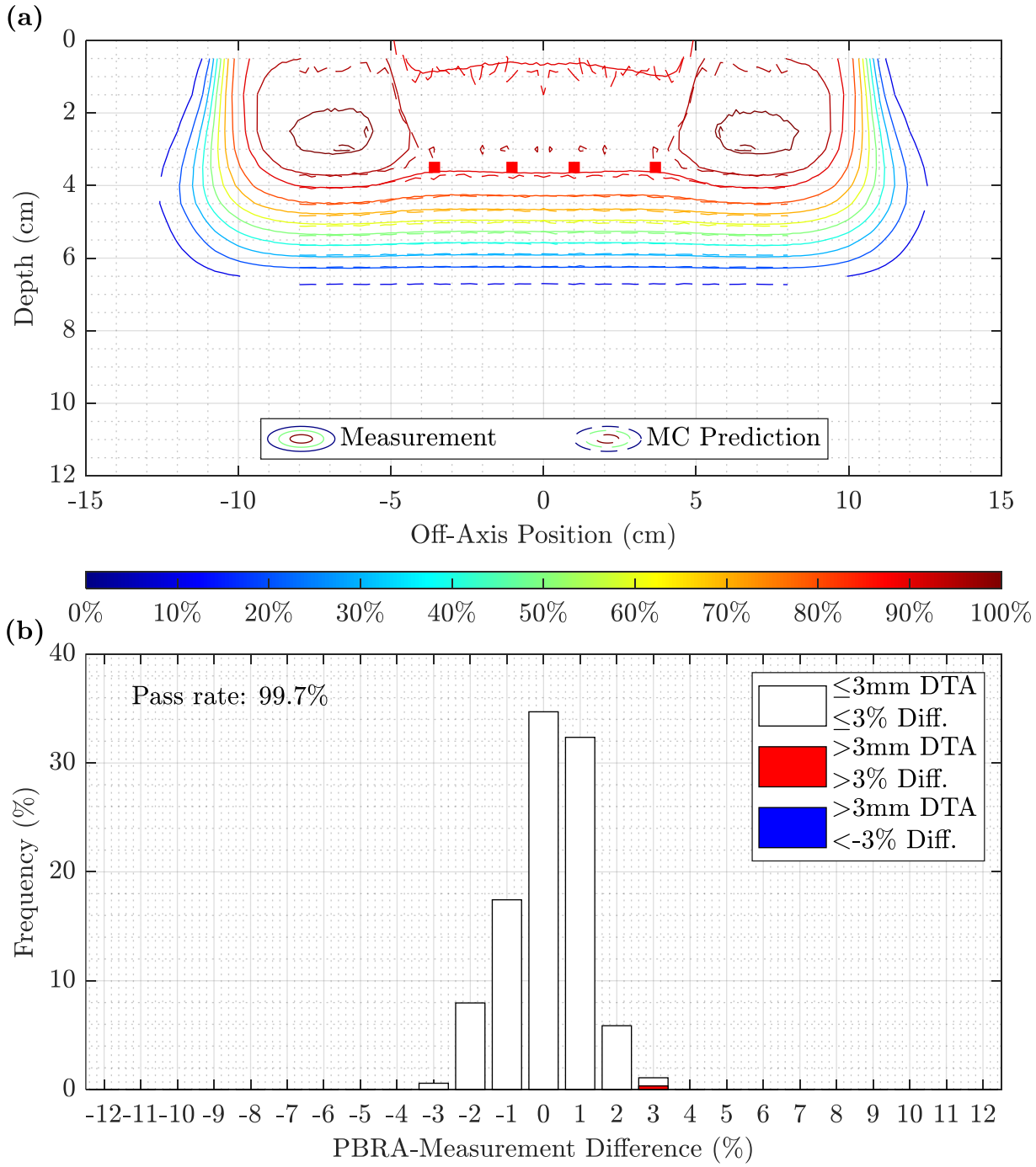

Figure D.28. Measurement and MC prediction isodose comparison and difference histogram for 0.158-cm pins at 13 MeV and 100 cm SSD. The isodose contours in (a) compare the measured (solid) and MC estimation (dashed) isodose distributions, and (b) contains the histogram of differences between measurement and MC prediction (Equation D.5) for 0.158-cm pins at 13 MeV and 100 cm SSD. In both (a) and (b), points at which the MC estimation underpredicted and overpredicted the dose relative to measurement are shown in blue and red, respectively. The 3%/3mm DTA criteria yielded a passing rate of 99.7% for points within 8 cm of CAX.

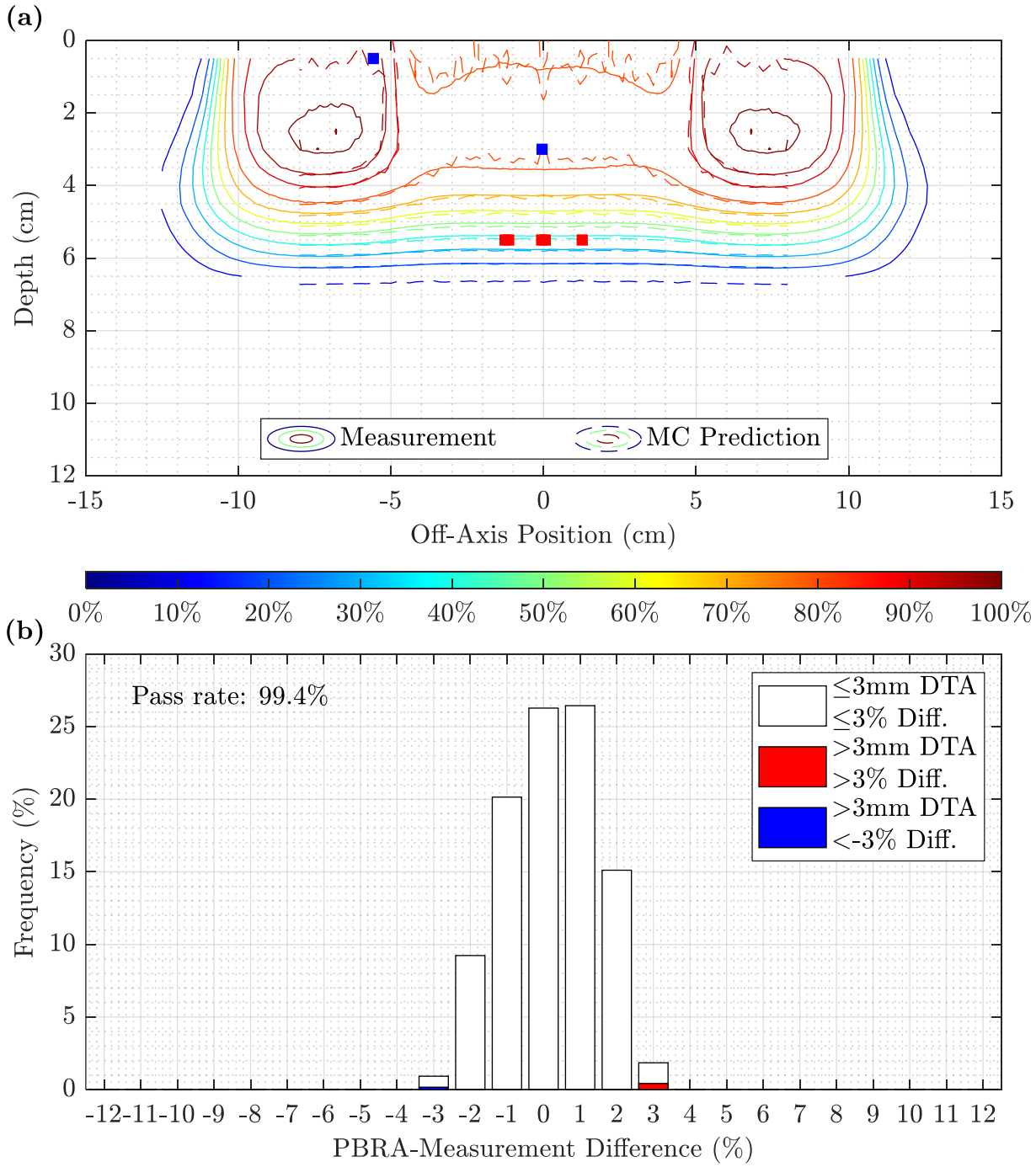

Figure D.29. Measurement and MC prediction isodose comparison and difference histogram for 0.273-cm pins at 13 MeV and 100 cm SSD. The isodose contours in (a) compare the measured (solid) and MC estimation (dashed) isodose distributions, and (b) contains the histogram of differences between measurement and MC prediction (Equation D.5) for 0.273-cm pins at 13 MeV and 100 cm SSD. In both (a) and (b), points at which the MC estimation underpredicted and overpredicted the dose relative to measurement are shown in blue and red, respectively. The 3%/3mm DTA criteria yielded a passing rate of 99.4% for points within 8 cm of CAX.

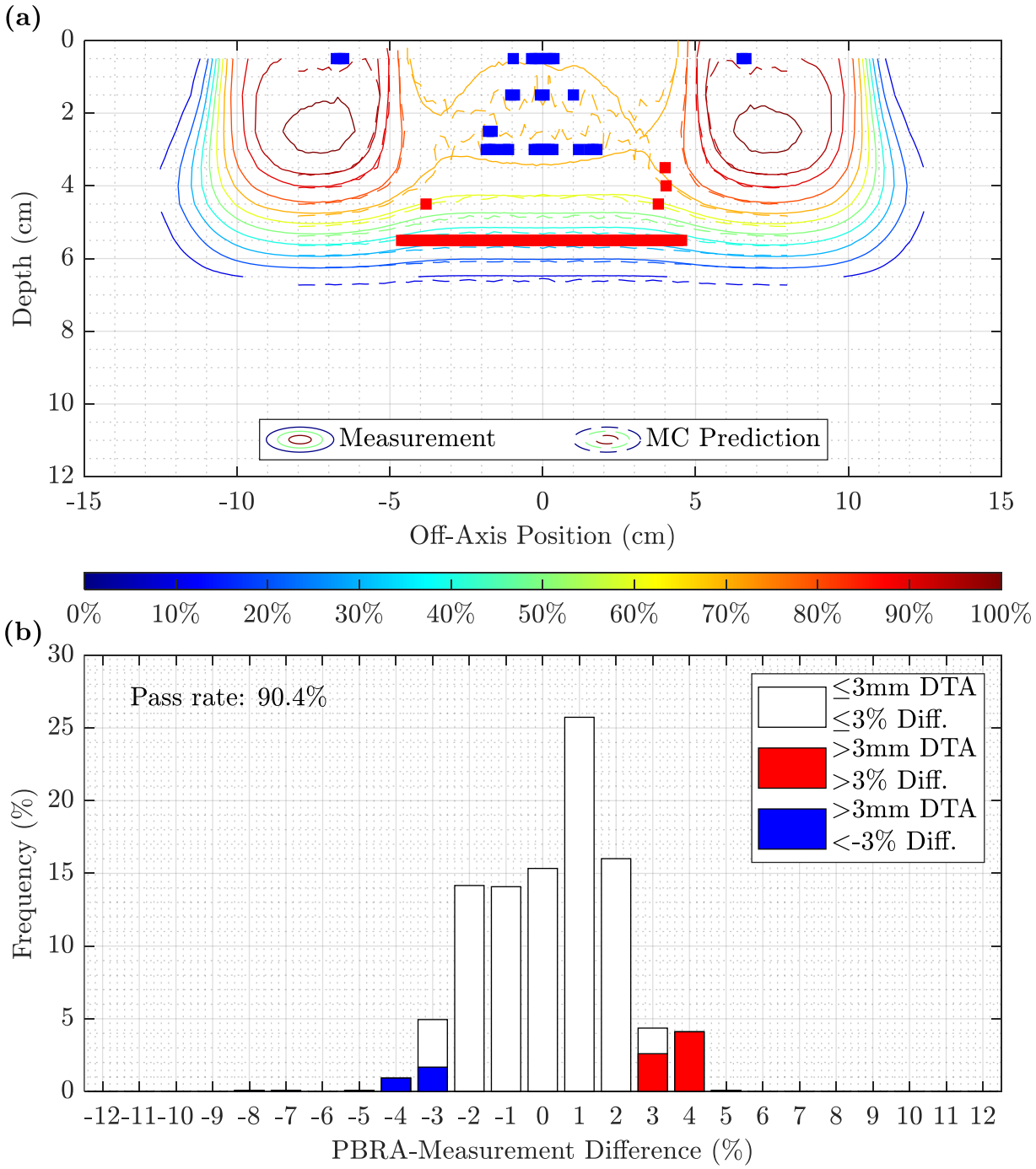

Figure D.30. Measurement and MC prediction isodose comparison and difference histogram for 0.352-cm pins at 13 MeV and 100 cm SSD. The isodose contours in (a) compare the measured (solid) and MC estimation (dashed) isodose distributions, and (b) contains the histogram of differences between measurement and MC prediction (Equation D.5) for 0.352-cm pins at 13 MeV and 100 cm SSD. In both (a) and (b), points at which the MC estimation underpredicted and overpredicted the dose relative to measurement are shown in blue and red, respectively. The 3%/3mm DTA criteria yielded a passing rate of 90.4% for points within 8 cm of CAX.

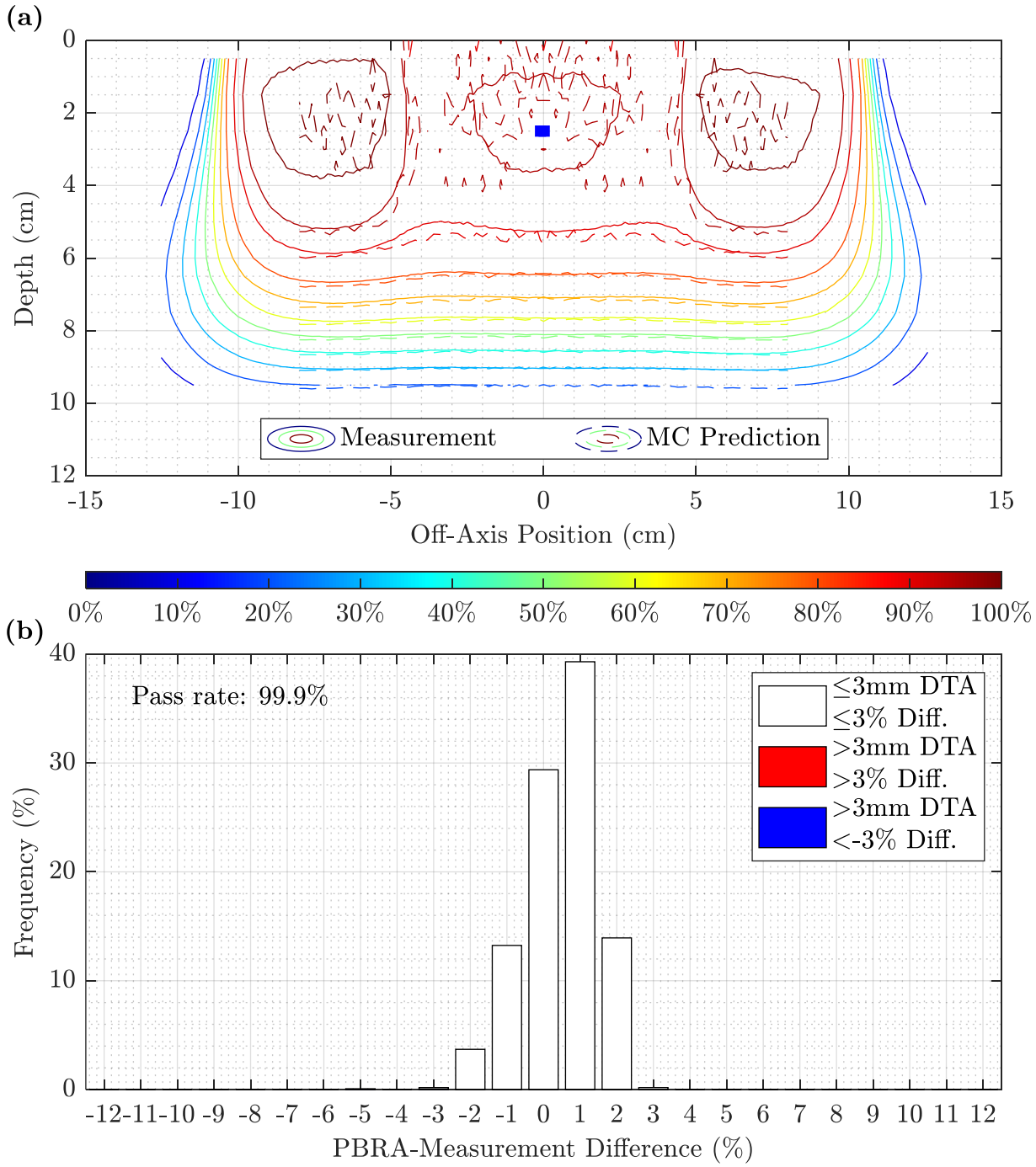

Figure D.31. Measurement and MC prediction isodose comparison and difference histogram for 0.158-cm pins at 20 MeV and 100 cm SSD. The isodose contours in (a) compare the measured (solid) and MC estimation (dashed) isodose distributions, and (b) contains the histogram of differences between measurement and MC prediction (Equation D.5) for 0.158-cm pins at 20 MeV and 100 cm SSD. In both (a) and (b), points at which the MC estimation underpredicted and overpredicted the dose relative to measurement are shown in blue and red, respectively. The 3%/3mm DTA criteria yielded a passing rate of 99.9% for points within 8 cm of CAX.

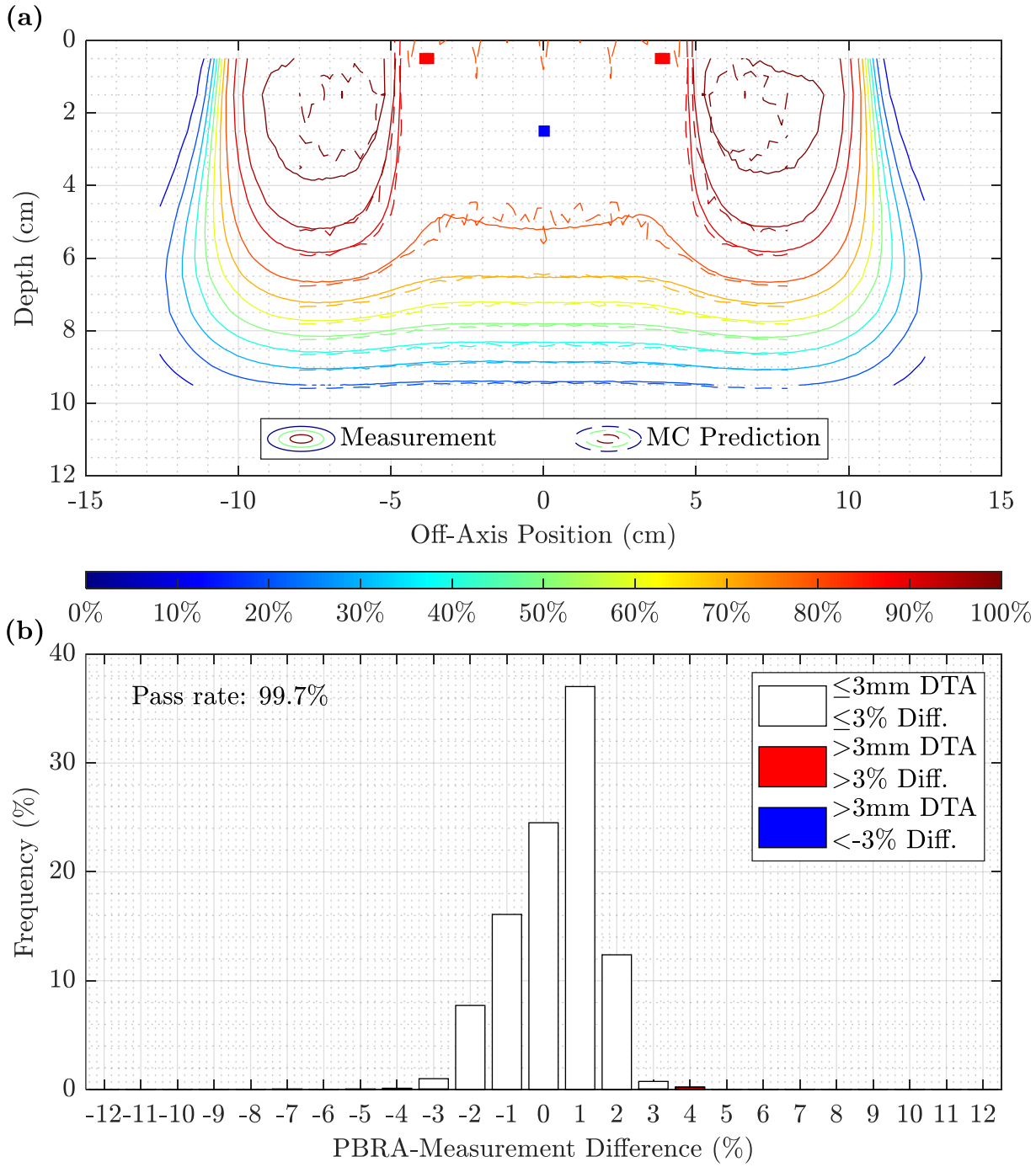

Figure D.32. Measurement and MC prediction isodose comparison and difference histogram for 0.273-cm pins at 20 MeV and 100 cm SSD. The isodose contours in (a) compare the measured (solid) and MC estimation (dashed) isodose distributions, and (b) contains the histogram of differences between measurement and MC prediction (Equation D.5) for 0.273-cm pins at 20 MeV and 100 cm SSD. In both (a) and (b), points at which the MC estimation underpredicted and overpredicted the dose relative to measurement are shown in blue and red, respectively. The 3%/3mm DTA criteria yielded a passing rate of 99.7% for points within 8 cm of CAX.

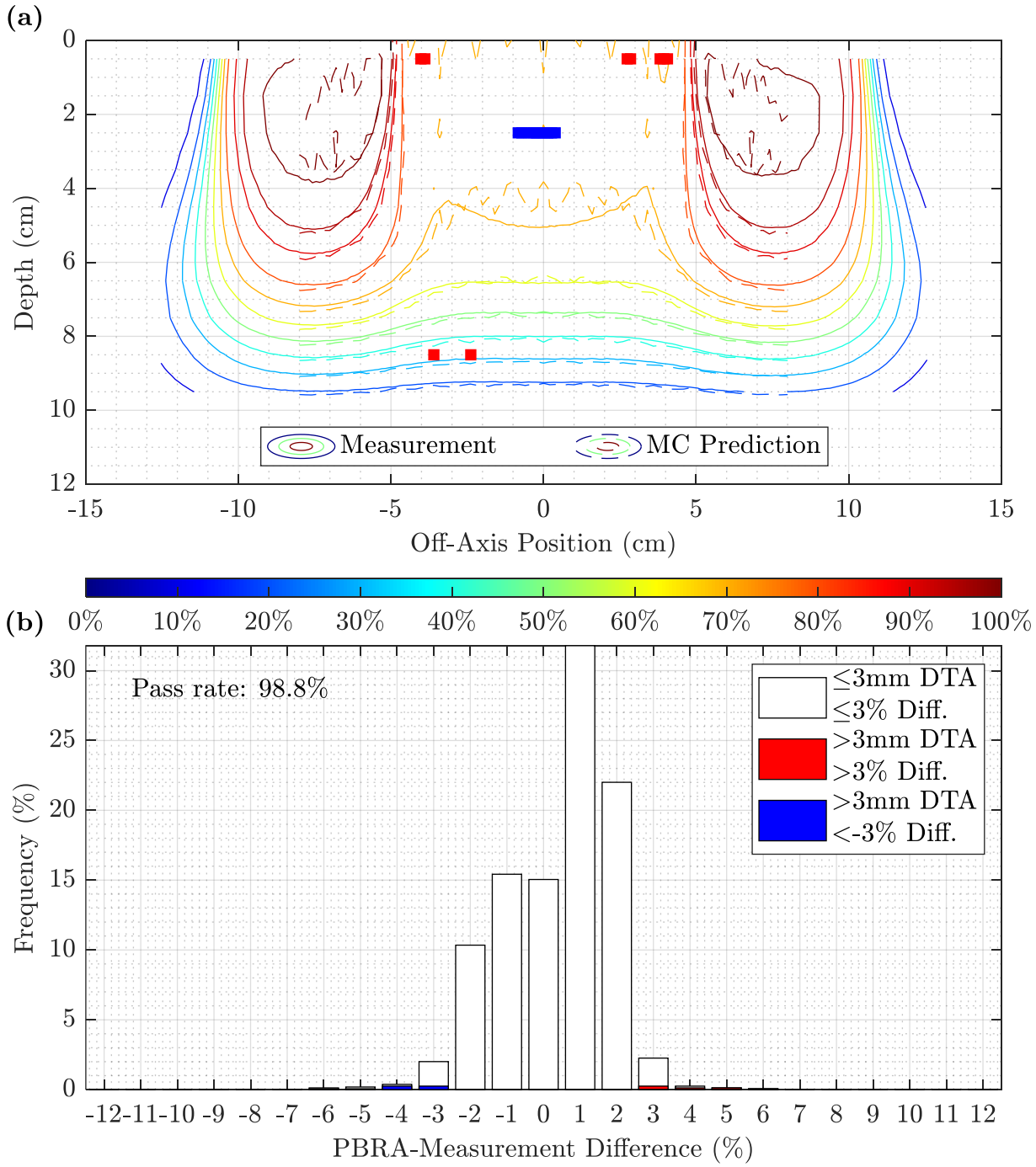

Figure D.33. Measurement and MC prediction isodose comparison and difference histogram for 0.352-cm pins at 20 MeV and 100 cm SSD. The isodose contours in (a) compare the measured (solid) and MC estimation (dashed) isodose distributions, and (b) contains the histogram of differences between measurement and MC prediction (Equation D.5) for 0.352-cm pins at 20 MeV and 100 cm SSD. In both (a) and (b), points at which the MC estimation underpredicted and overpredicted the dose relative to measurement are shown in blue and red, respectively. The 3%/3mm DTA criteria yielded a passing rate of 98.8% for points within 8 cm of CAX.

D.1.7. Discussion

The available component modules in EGSnrc cannot completely replicate the complex geometry of PRIME devices, so the model was necessarily limited to a single pin on CAX. The dose perturbation kernel method was adopted due to this shortcoming so that a reasonable estimate of dose under arbitrary PRIME devices could be calculated.

The average passing rate of the MC-estimated distributions was 96.1% compared to the average nominal PBRA passing rate of 98.1% for all setups, though the PBRA validation included all measured dose points, including those in the penumbra which the former comparison excluded.

In general, the CAX dose of measurement exceeds the MC prediction. One possibility is that the radial extent of the dose perturbation kernel (5 cm) was insufficiently low. As discussed earlier, the large-angle scatter, not accounted for by PBRA calculations, had an apparent effect on the modulated region, particularly at higher energies and larger pin diameters. The inadequate kernel distance could be compounded by the 14×14 cm^2 field size used in the MC calculations as 5 cm off-axis distance is near the penumbra. This dose fall-off can be seen near the end of the radial profiles (see Figure D.9) where dose fluctuates due to noise. Though the kernel is subtractive which should reduce the effect of this, the noise at larger radial distance is increased and incorporated into the dose estimation. The out-scatter contribution of an individual pin is small, but the cumulative effect of 247 pins could be more pronounced. The average out-scatter contribution of a single pin is a fraction of a percent, within the statistical error of the kernel, which is exacerbated by the field size used in the kernel determination.

Measured dose in the unmodulated field was generally greater than the MC prediction (Figures D.22-24). The differences could be due to the perturbation kernel limit of 5 cm being insufficient to capture the effect of large-angle scatter. It may also be due to scatter from the edges of the collimating insert (Rusk *et al*., 2016). In Equation D.5, the perturbation was subtracted from

the foam-only measured CAX PDD, but this assumes the dose is perfectly flat. Scatter off of the collimator would be more pronounced at the edges of the field, so the assumption does not hold.

In summary, the disagreement between MC and measurement in the modulated region was not understood and questions the accuracy of a PBRA model based on MC results. It was initially concluded that the MC estimation using the dose perturbation kernels might be insufficient to derive accurate corrections to the PBRA based on these limitations. However, after discovering the fabrication error in the PRIME devices, preliminary measurements with the replacement devices (Appendix E) showed good agreement with the MC prediction, so these issues may not be as significant as initially thought. It appears that the disagreement is due to an error in the divergence of the pins within the intensity modulators used for measurement.

D.2. Modification of PBRA parameters to match MC results

The in-scatter adjustments to the PBRA were presented in Chapter 2. In this section, the out-scatter component was inferred as the difference between in-scatter-adjusted PBRA calculation, which includes the effects of primary collimation and island block (pin) in-scatter, and the MC calculation, which contains full physics. The CAX dose resulting out-scatter component was parameterized by beam energy, SSD, and pin diameter so that the solution could be extended to intermediate conditions.

D.2.1. PBRA model

PBRA calculations were generated using an in-house research version of the PBRA for a 20×20 cm^2 field size at 7, 13, and 20 MeV and 100, 105, and 110 cm SSD. That version of the PBRA used Hilliard's modifications of increasing σ_{θ_x} by 50% and shifting the CAX PDD by reducing R_{90} by 0.1 cm to simulate the energy loss due to the foam. Dose calculations were made under two setups.

1. *Pin and foam.* At the level of the collimator insert, a single pin of a given diameter was placed on CAX. Calculations under this setup were made for both nominal and in-scatter-adjusted diameters (Table D.6) at nominal beam energies of 7, 13, and 20 MeV and SSDs of 100, 105, and 110 cm.
2. *Foam only.* No pin was included. Calculations were made at nominal beam energies of 7, 13, and 20 MeV and SSDs of 100, 105, and 110 cm.

Table D.6. Nominal and in-scatter-adjusted diameters used in PBRA calculations. The nominal pin diameters and their corresponding in-scatter-adjusted diameters are given for beam energies of 7, 13, and 20 MeV.

Energy (MeV)	d (cm)	d_{IS} (cm)
7	0.158	0.188
7	0.223	0.255
7	0.273	0.306
7	0.315	0.349
7	0.352	0.386
13	0.158	0.178
13	0.223	0.244
13	0.273	0.294
13	0.315	0.336
13	0.352	0.373
20	0.158	0.171
20	0.223	0.236
20	0.273	0.286
20	0.315	0.329
20	0.352	0.366

D.2.2. PBRA analysis

The PBRA calculated dose values in water every 0.5 cm with depth and laterally on a diverging grid which is defined at isocenter in 0.2-cm increments in the crossplane and inplane. To ensure the MC and PBRA calculations spatially coincided, PBRA dose values were linearly interpolated onto a uniform rectilinear grid corresponding to the MC calculation using an in-house script.

D_{max} values for foam-only were determined from a PDD averaged over the central 1×1 cm^2 for each energy and SSD combination. As was done with the MC calculation, a radial dose matrix was created for each PBRA dose calculation with a pin and normalized to the foam only D_{max} under the same energy and SSD conditions.

A radial dose perturbation kernel was calculated according to Equation D.1 for each combination of beam energy, SSD, and depth for both nominal and in-scatter-adjusted pin diameters. As with the MC kernels, this numerically describes how a single pin affects the dose distribution of an open field at a given distance (r, z) from the pin for each energy, SSD, and pin diameter combination.

D.2.3. PBRA PDD perturbation

PBRA PDD perturbations were calculated in the same manner as those using the MC kernels. At each beam energy and SSD combination for both the nominal and in-scatter-adjusted pin diameters, PBRA radial dose perturbation kernels were applied to calculate the dose under an 8.4×8.4 cm^2 matrix of pins of uniform diameter with blocks spaced every 0.6 cm on a square grid as shown in Figure D.4. A parallel beam was used for this calculation. The dose grid was comprised of uniformly spaced points of 0.2×0.2×0.5 cm^3. The dose perturbation matrix of a given setup was calculated by successively summing the kernel at all points within 5 cm radially from a given pin

position for all pins in the matrix according to Equation D.2 with f = 1.0 for a parallel beam. A PDD perturbation was calculated from the dose perturbation matrix as the average dose of the central 2×2 cm^2 cross section, or central 121 voxels as shown by Equation D.3 for each beam energy, SSD, and pin diameter combination.

D.2.4. Correction for out-scatter using MC

An empirical fit was derived to both smooth the MC results and parameterize the out-scatter dose. The radial dose perturbation kernels were extended to an 8.4×8.4 cm^2 matrix of pins spaced 0.6 cm on a rectilinear grid as illustrated in Figure D.4. For each beam energy and SSD combination, PDD perturbations were calculated for the central 2×2 cm^2 cross section as previously described by Equation D.3 using the nominal diameters for MC and in-scatter-adjusted diameters for the PBRA, contained in Table D.6. Since (1) the MC PDD perturbation contains both in-scatter and out-scatter effects, and (2) the adjusted PBRA incorporated only the in-scatter losses, their difference approximated the out-scatter dose. Thus, a PDD perturbation difference, ΔD, was calculated as the difference between the MC and in-scatter-adjusted PBRA PDD perturbations for each beam energy and pin diameter combination:

$$\Delta D(E, SSD, d, z) = \Delta PDD_{\mathrm{IS}}(E, SSD, d, z) - \Delta PDD_{\mathrm{MC}}(E, SSD, d, z), \qquad \text{D.6}$$

where E is the beam energy, d is the nominal block diameter, and z is the depth.

Upon examination of the data, an assumption was made that the out-scatter dose at the surface could be modeled as proportional to diameter (circumference). Since the out-scatter component must converge to 0 with decreasing diameter, the intercept of this linear fit was set to 0:

$$\Delta D(z = 0) = A_1 \cdot d. \qquad \text{D.7}$$

The A_1 fitting coefficients for the MC-PBRA PDD surface perturbation were parameterized according to the beam energy with the relationship determined by inspection:

$$A_1(E) = A_2 \cdot \sqrt{E}. \tag{D.8}$$

To smooth the noise in the MC PDD perturbation and parameterize the out-scatter dose, a straight line solution was imposed from the surface to a certain depth (approximately R_{90}) beyond which the out-scatter contribution is negligible. As discussed in Appendix C, the out-scatter spectrum differs significantly from the incident spectrum in that it is broader and has a lower mean energy. The domain of the fit was limited to a cutoff depth, z_{cutoff}, which represents the depth at which out-scattered electrons were assumed to have ranged out. A standard cutoff depth of R_{90} was chosen: 2.0, 4.0, and 6.0 cm for 7, 13, and 20 MeV, respectively.

The MC and in-scatter-adjusted PBRA approximately agree beyond z_{cutoff} since the out-scatter component goes to zero. That is, for this model:

$$\Delta PDD_{\text{IS}}(E, d, z \geq z_{\text{cutoff}}) = \Delta PDD_{\text{MC}}(E, d, z \geq z_{\text{cutoff}}). \tag{D.9}$$

Combining Equations D.7 and D.8 and forcing a linear fit to the cutoff depth yields the fitted MC-PBRA PDD perturbation difference, ΔD_{fit}:

$$\Delta D_{\text{fit}}(E, SSD, d, z) = \begin{cases} \left(1 - \dfrac{z}{B_1 \cdot E}\right)\left(B_2 \cdot \sqrt{E} \cdot d\right), & z \leq B_1 \cdot E \\ 0, & z > B_1 \cdot E \end{cases}, \tag{D.10}$$

where B_1 controls the depth dependence of the out-scatter, B_2 controls the magnitude of the out-scatter dose contribution, and both are functions of SSD. A set of coefficients was calculated for 100, 105, and 110 cm SSD.

Though the solution is depth-dependent due to the out-scattered energy spectrum, a single value of ΔD_{fit} was necessarily selected to determine the diameter correction. The average value of ΔD_{fit} between 1.0 cm depth and the convergence depth $B_1 \cdot E$, where ΔD_{fit} goes to 0, was taken:

$$\Delta D_{\text{shift}}(E, SSD, d) = \Delta D_{\text{fit}}(E, SSD, d, 1.0 \text{ cm})/2. \quad \text{D.11}$$

This dose shift was approximated as a change in *IRF*. The *IRF* with both the in-scatter and out-scatter modifications was then combined:

$$IRF_{\text{IS+OS}}(E, SSD, d) = IRF_{\text{IS}}(E, d) - \Delta D_{\text{shift}}(E, SSD, d). \quad \text{D.12}$$

The diameter corrected for in-scatter and out-scatter was determined by rearranging Equation 1.1 at a given beam energy, SSD, and pin diameter combination:

$$d_{\text{IS+OS}}(E, SSD, d) = (0.6 \text{ cm}) \left[\left(\frac{2\sqrt{3}}{\pi} \right) \left(1 - IRF_{\text{IS+OS}}(E, SSD, d) \right) \right]^{1/2}. \quad \text{D.13}$$

For each beam energy and nominal diameter, a corresponding diameter adjusted for both in-scatter and out-scatter was calculated for input into the IM-PBRA.

D.2.5. PBRA parameter modification results

Representative examples of the nominal and in-scatter-adjusted PBRA radial dose profiles and corresponding perturbation kernels are plotted to demonstrate dependence on beam energy (Figure D.34), SSD (Figure D.35), pin diameter (Figure D.36), and depth (Figure D.37). As observed with the MC kernels, the perturbation magnitude increased with both beam energy and pin diameter and decreased with increasing SSD and depth. The width (σ) of the kernels decreased with increasing energy, increased with increasing SSD and depth, and remained approximately constant with change in pin diameter.

The data of Tables D.7 and D.8 with the corresponding plots in Figure D.38 and Figure D.39 describe the empirical dependence of the out-scatter component on diameter and beam energy. Table D.7 contains the surface dose difference between the MC estimation and the in-scatter-adjusted PBRA calculation for each beam energy at 100 cm SSD, calculated from Equation D.6. The A_1 fitting coefficients, i.e. slopes of the linear fits applied to these data, are listed in Table D.8. The data of both of these tables are plotted in Figure D.38. Figure D.39.a plots the A_1 coefficients against beam energy. In deriving the global fit of Equation D.10, the out-scatter increased linearly with diameter and was approximately proportional to the square root of the beam energy. The fitting coefficients to the MC-PBRA PDD dose perturbation are listed in Table D.9 at each SSD. These coefficients are plotted against SSD in Figure D.39.b and Figure D.39.c with corresponding quadratic fits of

$$B_1(\mathrm{SSD}) = (-2.490 \times 10^{-3}) \cdot \mathrm{SSD}^2 + (4.991 \times 10^{-1}) \cdot \mathrm{SSD} - (2.478 \times 10^{1}) \qquad \text{D.14}$$

and

$$B_2(\mathrm{SSD}) = (-3.449 \times 10^{-3}) \cdot \mathrm{SSD}^2 + (9.733 \times 10^{-1}) \cdot \mathrm{SSD} - (6.531 \times 10^{1}). \qquad \text{D.15}$$

The PDD perturbations from the single-pin kernel extension to square pin matrices using the MC, nominal PBRA, and corresponding in-scatter-adjusted PBRA kernels are plotted in Figures D.40-48 for the smallest (0.158 cm), intermediate (0.273 cm), and largest (0.352 cm) pin diameters at each beam energy and SSD combination. The fitted MC perturbation for a given set of setup conditions is also plotted.

Tables D.10-12 contain the scatter correction terms for 100-110 cm SSD at all clinically available beam energies for each of the five nominal pin diameters. The in-scatter-adjusted quantities d_{IS} and IRF_{IS} were found according to the method outlined in Chapter 2, the dose shift

was determined by Equation D.11, and the fully corrected diameter was calculated using Equation D.13. The IS+OS-corrected diameter under the measurement-based method is also tabulated for comparison.

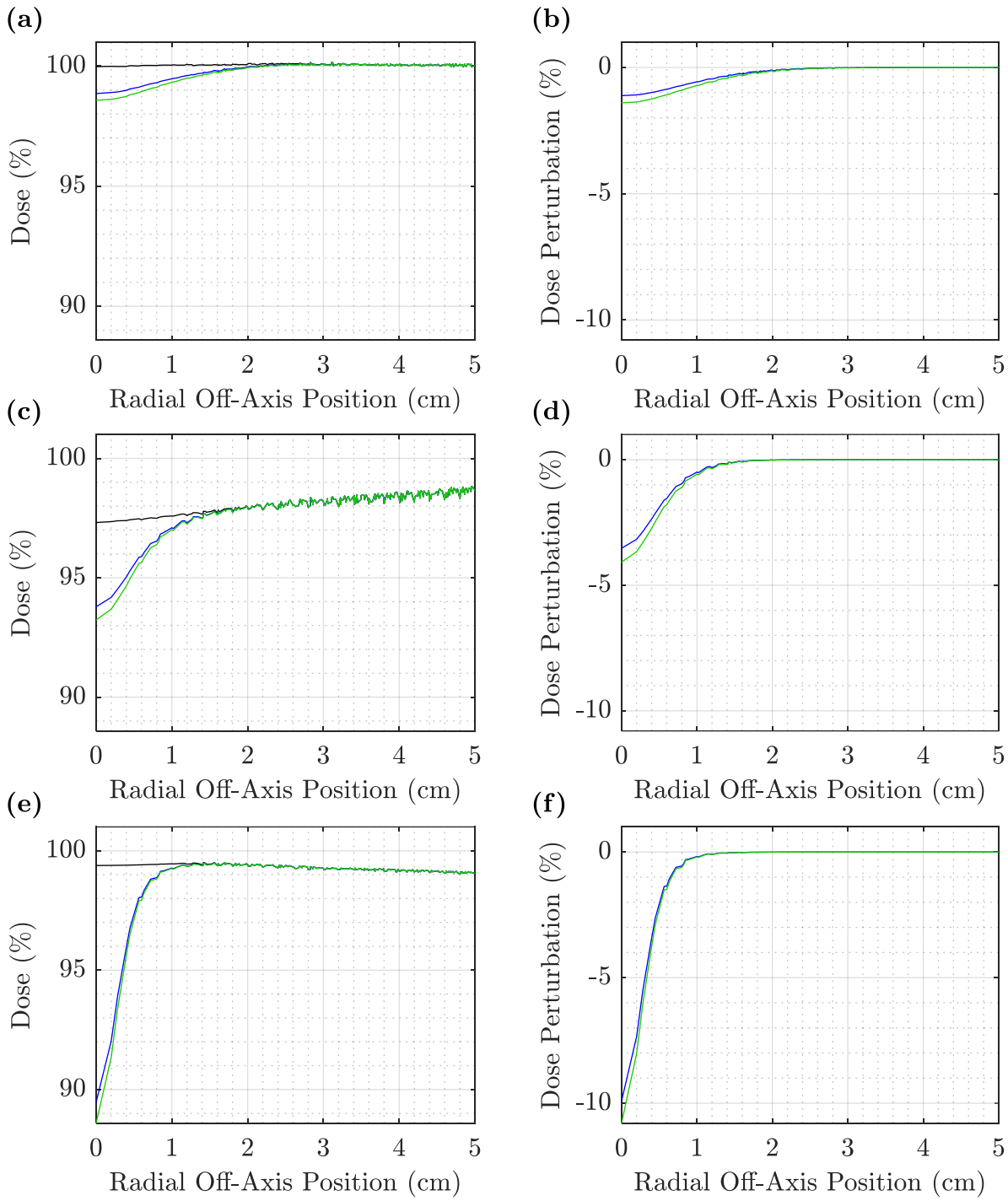

Figure D.34. Energy dependence of PBRA radial dose profiles and dose perturbation kernels at 7-20 MeV for a single 0.273-cm pin at 100 cm SSD at a depth of 1.5 cm. Radial dose profiles, in the first column, for foam only (black), nominal 0.273-cm single pin (blue), and corresponding in-scatter-adjusted pin (green) are shown at (a) 7, (c) 13, and (e) 20 MeV at 1.5 cm depth and 100 cm SSD. The radial dose perturbation is the difference between the foam and pin profiles, shown in the second column, for (b) 7, (d) 13, and (f) 20 MeV for the nominal (blue) and in-scatter-adjusted (green) pins.

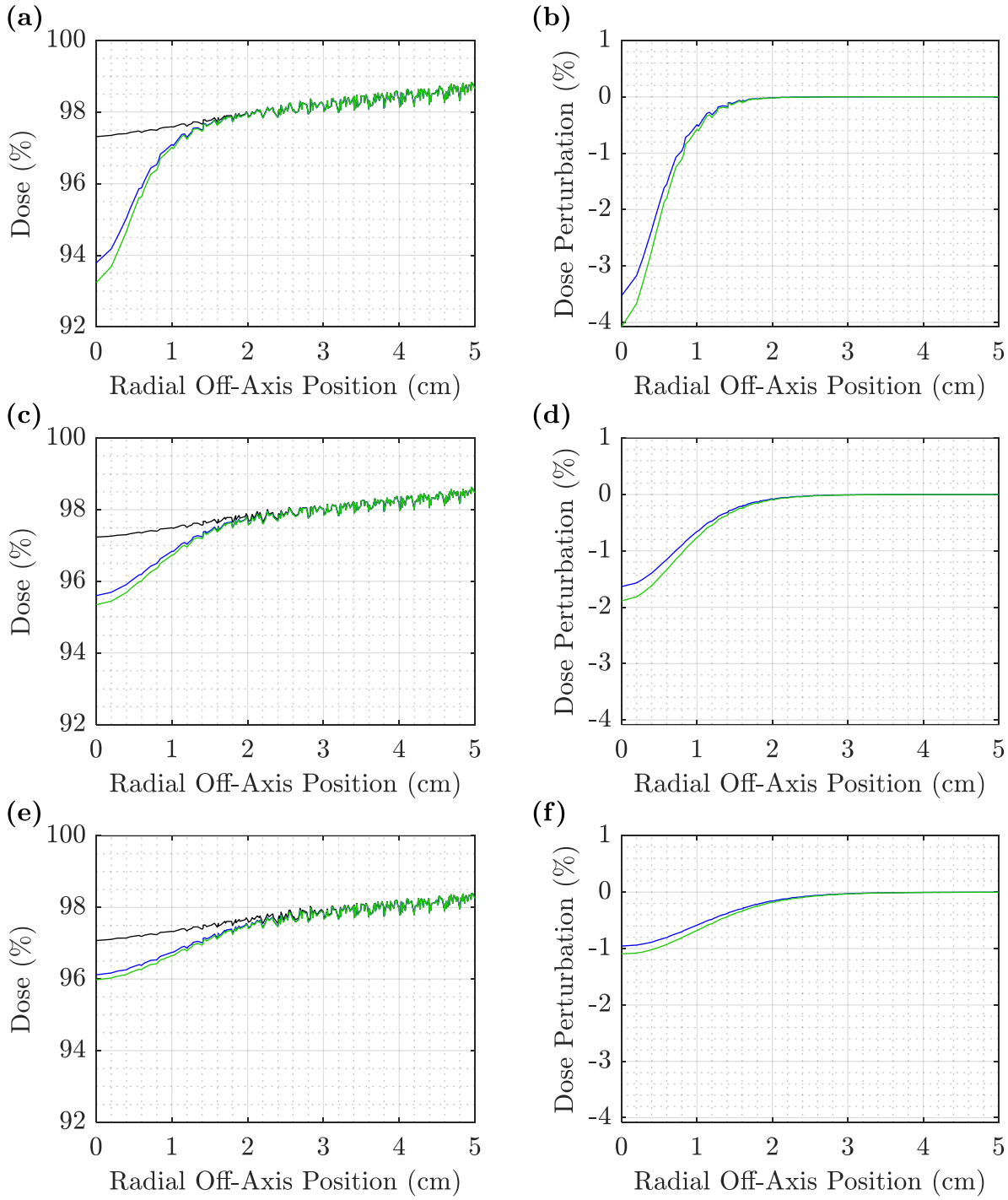

Figure D.35. SSD dependence of PBRA radial dose profiles and dose perturbation kernels at 13 MeV for a single 0.273-cm pin at 100-110 cm SSD at a depth of 1.5 cm. Radial dose profiles, in the first column, for foam only (black), nominal 0.273-cm single pin (blue), and corresponding in-scatter-adjusted pin (green) are shown at (a) 100, (c) 105, and (e) 110 cm SSD for a 13 MeV beam at 1.5 cm depth. The radial dose perturbation is the difference between the foam and pin profiles, shown in the second column, for (b) 100, (d) 105, and (f) 110 cm SSD for the nominal (blue) and in-scatter-adjusted (green) pins.

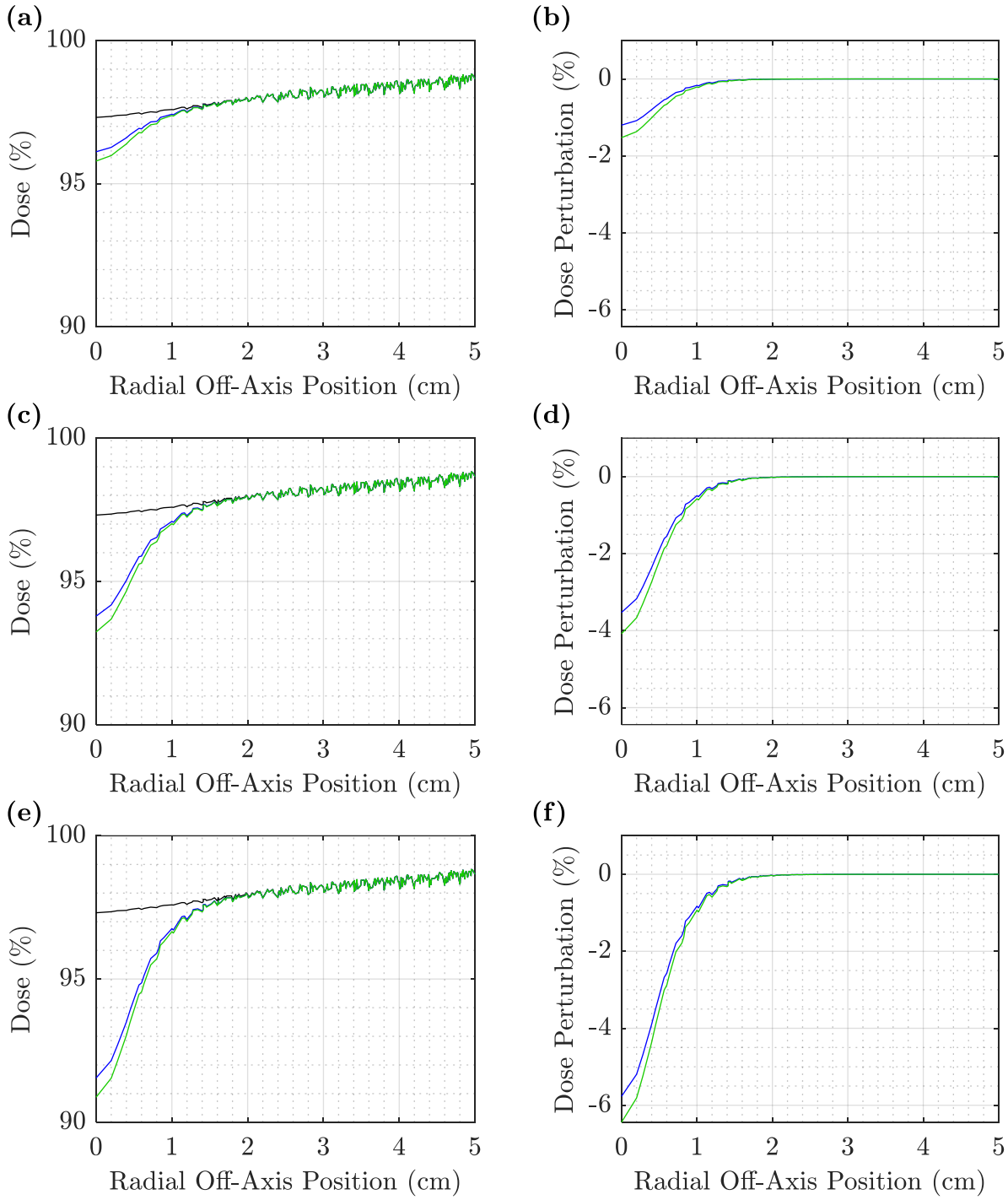

Figure D.36. Diameter dependence of PBRA radial dose profiles and dose perturbation kernels at 13 MeV for single pins 0.158-0.273 cm in diameter at 100 cm SSD at a depth of 1.5 cm. Radial dose profiles, in the first column, for foam only (black), nominal diameter (blue), and corresponding in-scatter-adjusted diameter (green) are shown at nominal diameters of (a) 0.158, (c) 0.273, and (e) 0.352 cm for a 13 MeV beam at 1.5 cm depth. The radial dose perturbation is the difference between the foam and pin profiles, shown in the second column, for diameters of (b) 0.158, (d) 0.273, and (f) 0.352 cm for the nominal (blue) and in-scatter-adjusted (green) pins.

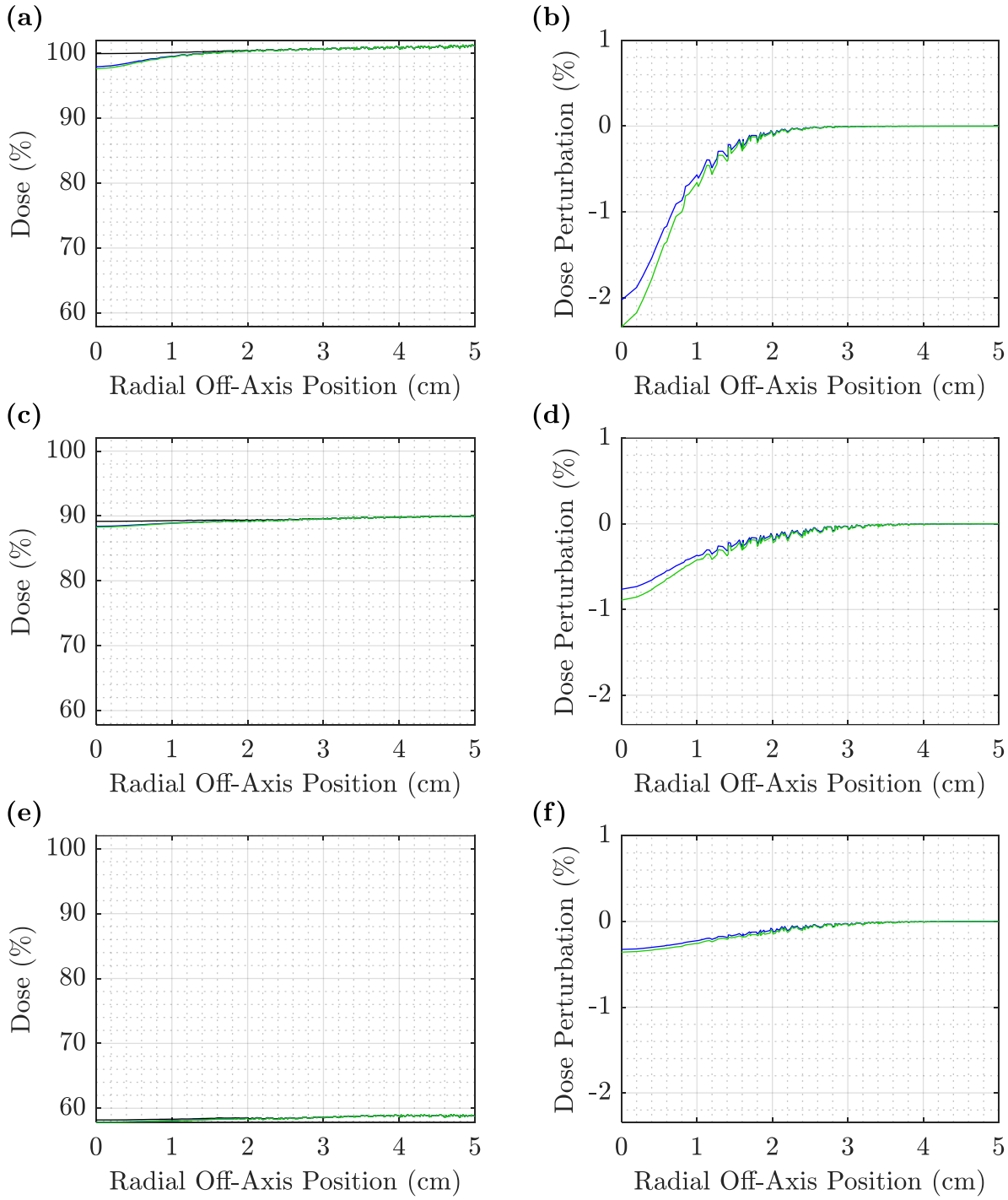

Figure D.37. Depth dependence of PBRA radial dose profiles and dose perturbation kernels at 13 MeV for a single pin 0.273-cm pin at 100 cm SSD at a depths of R_{100} to R_{50}. Radial dose profiles (first column) for foam only (black), 0.273-cm nominal diameter (blue), and corresponding in-scatter-adjusted diameter (green) are shown for a 13 MeV beam at 100 cm SSD at depths of (a) 2.5, (c) 4.0, and (e) 5.0, corresponding approximately to R_{100}, R_{90}, and R_{50}, respectively. The radial dose perturbation (second column) is the difference between the foam and pin profiles at depths of (b) 2.5, (d) 4.0, and (f) 5.0 cm for the nominal (blue) and in-scatter-adjusted (green) pins.

Table D.7: MC-PBRA PDD perturbation dose difference at surface for 7-20 MeV at 100 cm SSD. The surface dose differences were determined from the dose distributions evaluated for the rectilinear pin matrices (Figure D.4) using Equation D.6.

Diameter (cm)	Beam Energy (MeV)		
	7	13	20
0.158	0.79%	1.91%	1.95%
0.223	1.98%	2.30%	2.82%
0.273	1.07%	2.19%	3.02%
0.315	2.49%	2.57%	4.05%
0.352	2.08%	2.18%	3.88%

Table D.8. MC-PBRA PDD perturbation fitting coefficients at 7-20 MeV for 100 cm SSD. The fitting coefficients are derived from Equation D.7 using the data in Table D.7 at each energy and corresponding to the slopes in Figure D.38.

Beam Energy (MeV)	A_1 ($\% \cdot cm^{-1}$)
7	6.38
13	8.03
20	11.82

Table D.9. MC-PBRA PDD dose perturbation parameterization fitting coefficients at 100-110 cm SSD. The fitting coefficients at each SSD were determined by applying Equation D.10 to the MC-PBRA PDD differences (Figures D.40-48) at each beam energy and pin diameter combination up to a depth of R_{90} for the corresponding energy.

SSD (cm)	B_1 ($cm \cdot MeV^{-1}$)	B_2 ($\% \cdot MeV^{-1/2} \cdot cm^{-1}$)
100	+2.33E-01	-2.47E+00
105	+1.76E-01	-1.14E+00
110	-5.37E-03	+2.30E-02

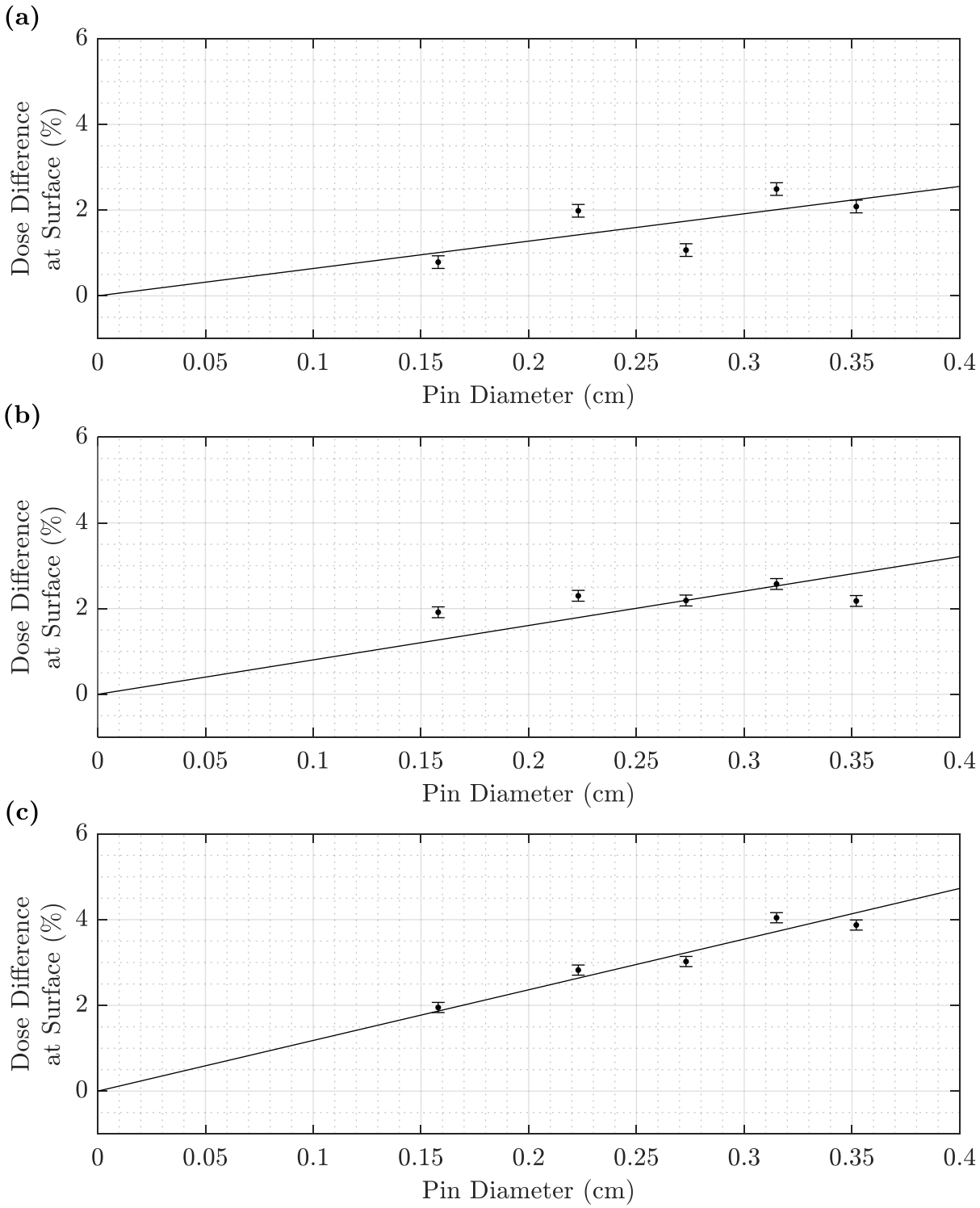

Figure D.38. MC-PBRA PDD perturbation at surface for 7-20 MeV at 100 cm SSD. The PDD perturbations at the surface are plotted against pin diameters for the (a) 7, (b) 13, and (c) 20 MeV beams. A linear fit is applied to each according to Equation D.7. The dose is expressed as a percent of D_{max} of the foam-only MC calculations. Plotted uncertainties of 1σ were determined from the MC calculations.

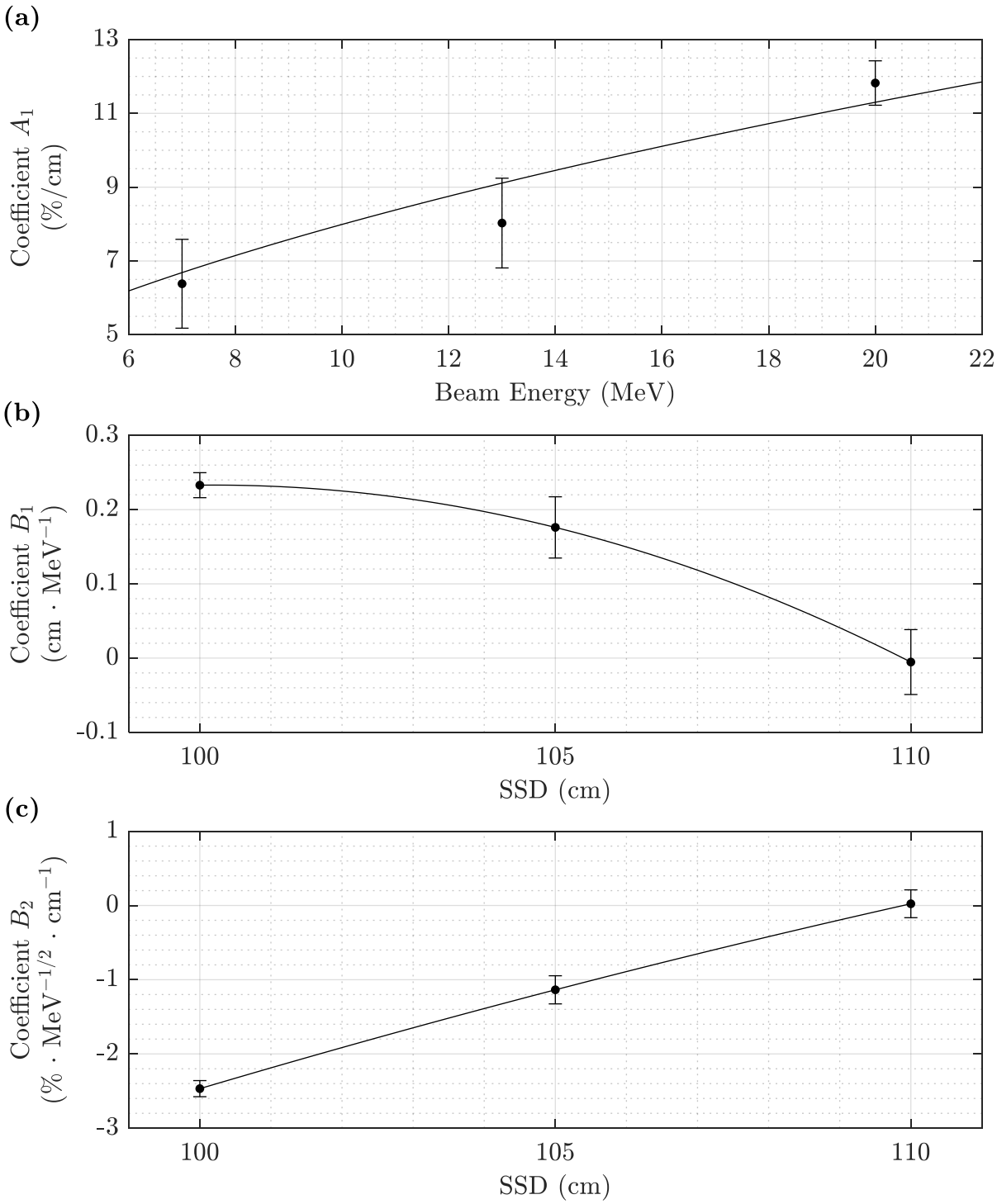

Figure D.39. Fitting coefficients for MC-based out-scatter correction. In (a), the MC-PBRA PDD surface perturbation for 7-20 MeV is plotted against beam energy with the corresponding fit from Equation D.8. The fitting coefficients B_1 and B_2 (Table D.9) of the parameterization of the MC-PBRA dose perturbation global fit (Equation D.10) are plotted in (b) and (c), respectively along with their corresponding quadratic fits to allow for interpolation between SSD values. Displayed uncertainties are 1σ.

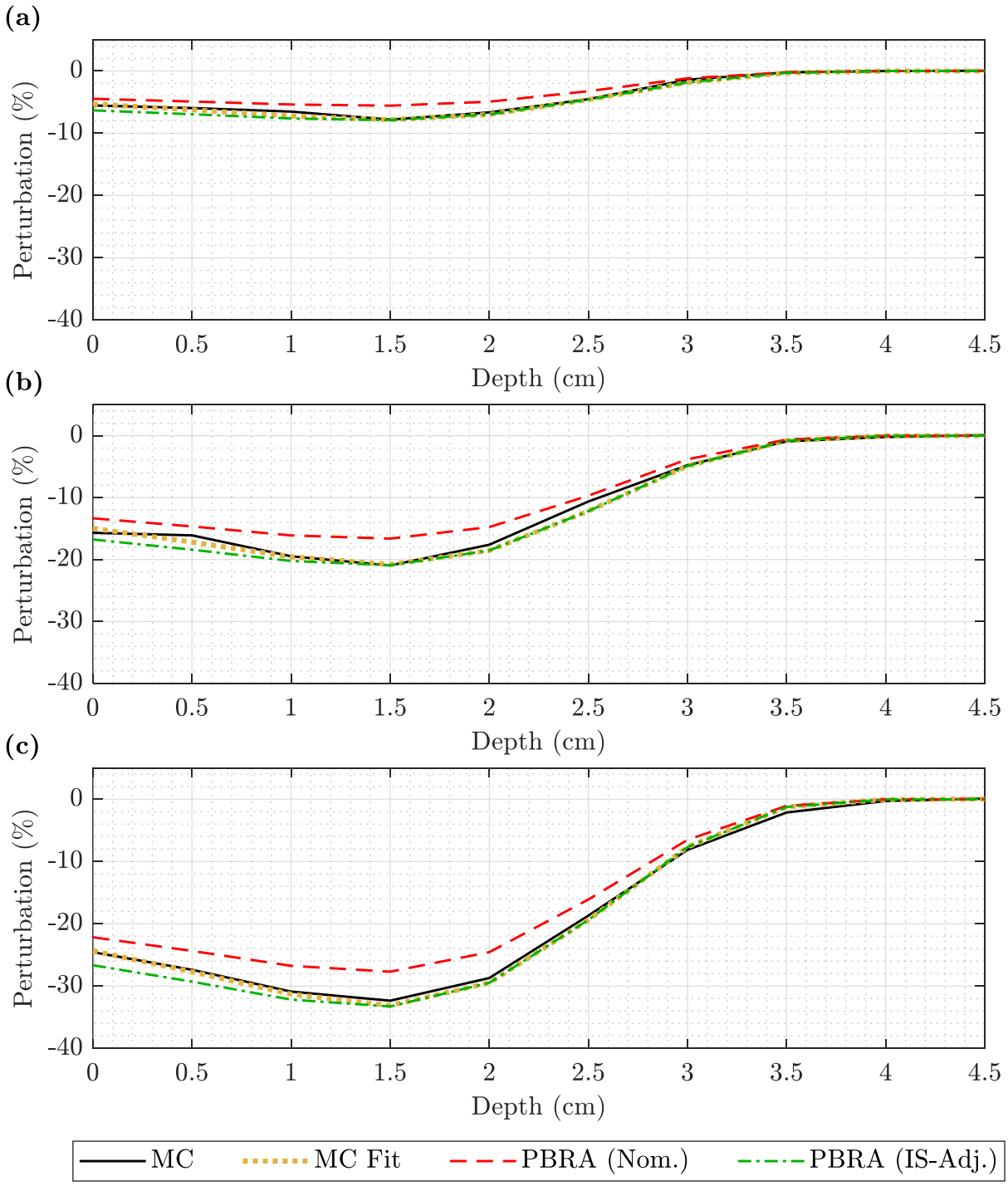

Figure D.40. Calculated PDD perturbations for square pin matrices at 7 MeV and 100 cm SSD. The PDD perturbations at 7 MeV and 100 cm SSD were calculated from the single-pin kernels of the MC (solid black), nominal PBRA (dashed red), and corresponding in-scatter-adjusted PBRA (dashed-dotted green) with the fitted MC (dotted yellow) determined at the given setup from Equation D.10 for rectilinear matrices (Figure D.4) with pins of uniform size: (a) 0.158, (b) 0.273, and (c) 0.352 cm in diameter.

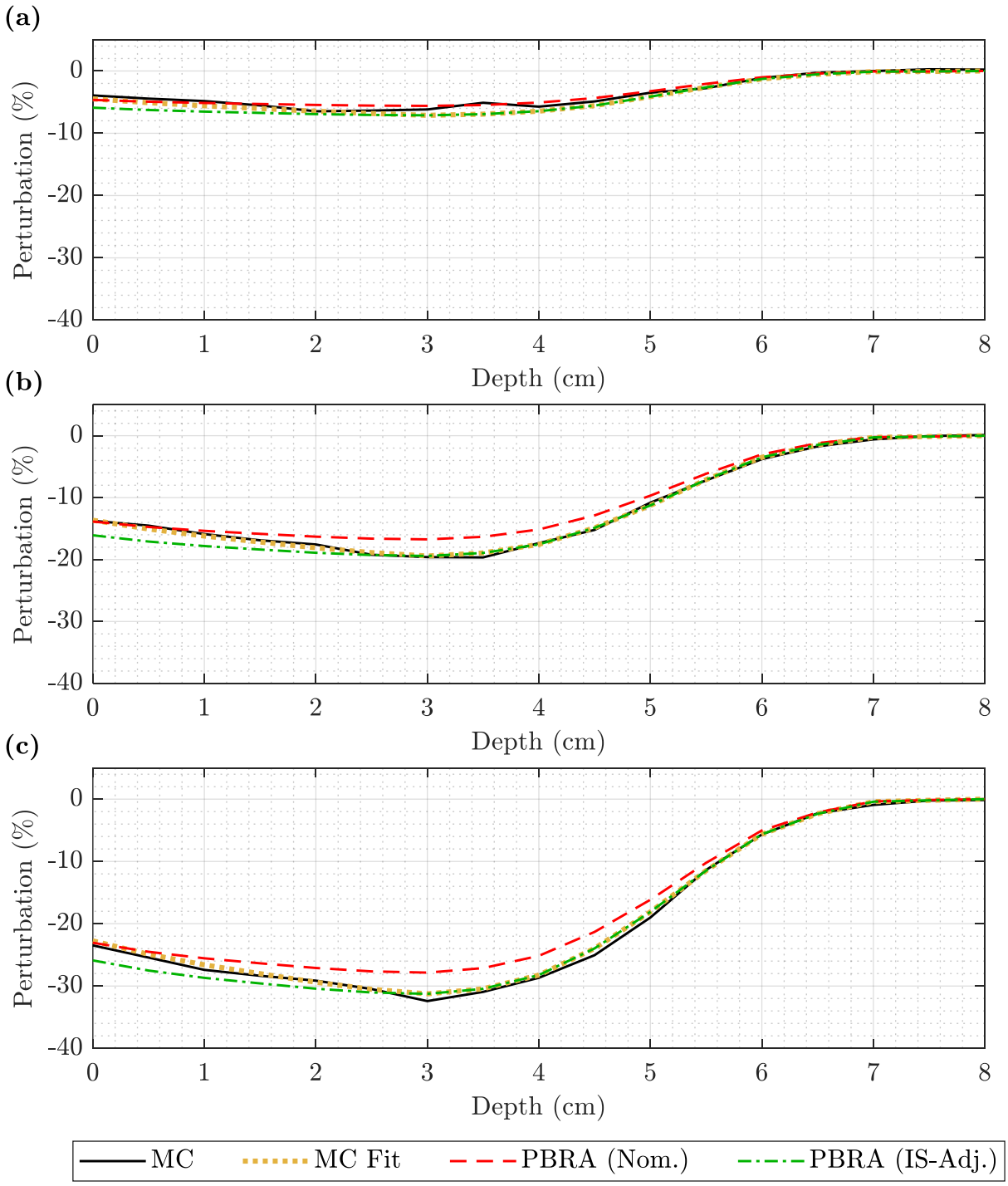

Figure D.41. Calculated PDD perturbations for square pin matrices at 13 MeV and 100 cm SSD. The PDD perturbations at 13 MeV and 100 cm SSD were calculated from the single-pin kernels of the MC (solid black), nominal PBRA (dashed red), and corresponding in-scatter-adjusted PBRA (dashed-dotted green) with the fitted MC (dotted yellow) determined at the given setup from Equation D.10 for rectilinear matrices (Figure D.4) with pins of uniform size: (a) 0.158, (b) 0.273, and (c) 0.352 cm in diameter.

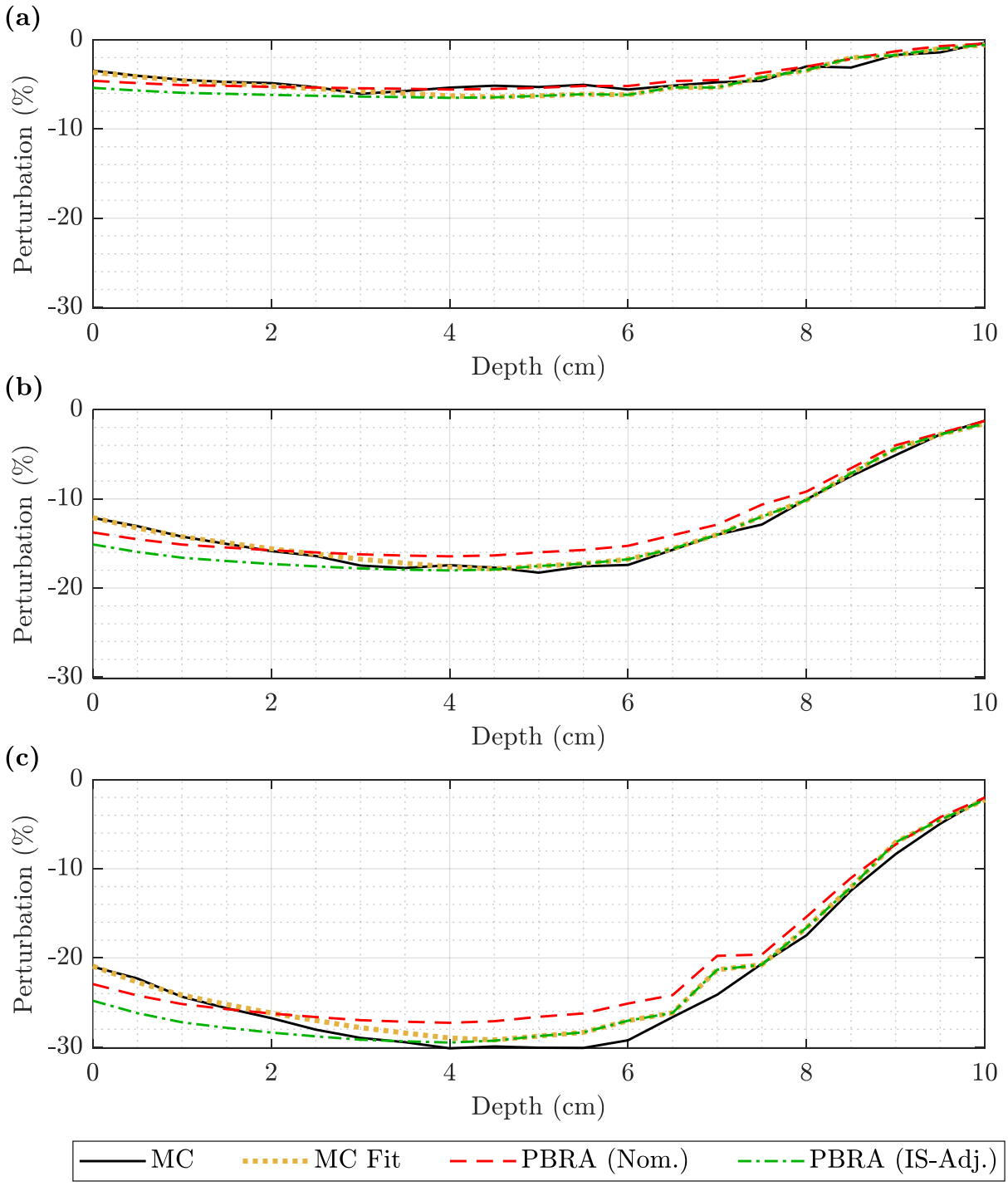

Figure D.42. Calculated PDD perturbations for square pin matrices at 20 MeV and 100 cm SSD. The PDD perturbations at 20 MeV and 100 cm SSD were calculated from the single-pin kernels of the MC (solid black), nominal PBRA (dashed red), and corresponding in-scatter-adjusted PBRA (dashed-dotted green) with the fitted MC (dotted yellow) determined at the given setup from Equation D.10 for rectilinear matrices (Figure D.4) with pins of uniform size: (a) 0.158, (b) 0.273, and (c) 0.352 cm in diameter.

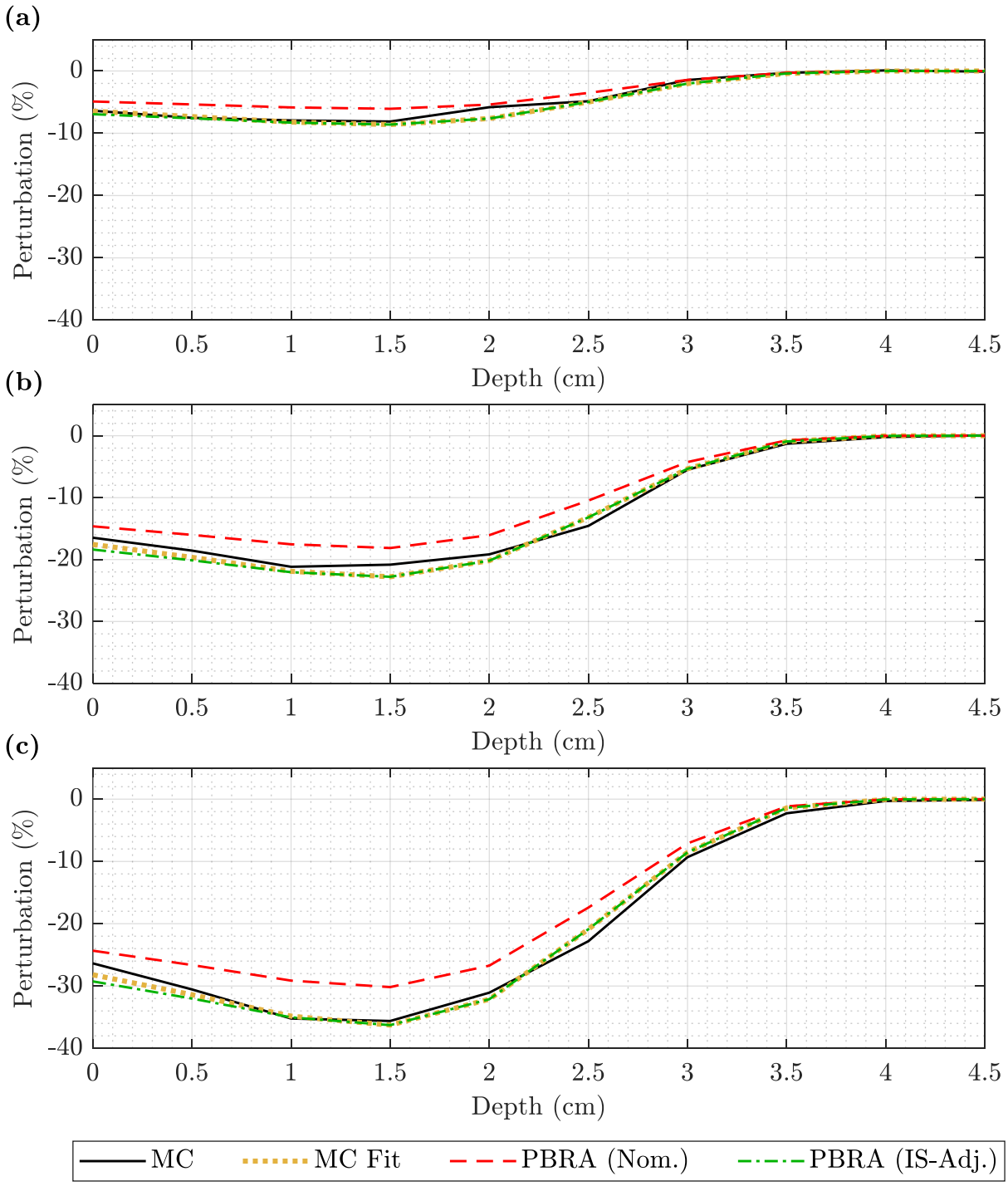

Figure D.43. Calculated PDD perturbations for square pin matrices at 7 MeV and 105 cm SSD. The PDD perturbations at 7 MeV and 105 cm SSD were calculated from the single-pin kernels of the MC (solid black), nominal PBRA (dashed red), and corresponding in-scatter-adjusted PBRA (dashed-dotted green) with the fitted MC (dotted yellow) determined at the given setup from Equation D.10 for rectilinear matrices (Figure D.4) with pins of uniform size: (a) 0.158, (b) 0.273, and (c) 0.352 cm in diameter.

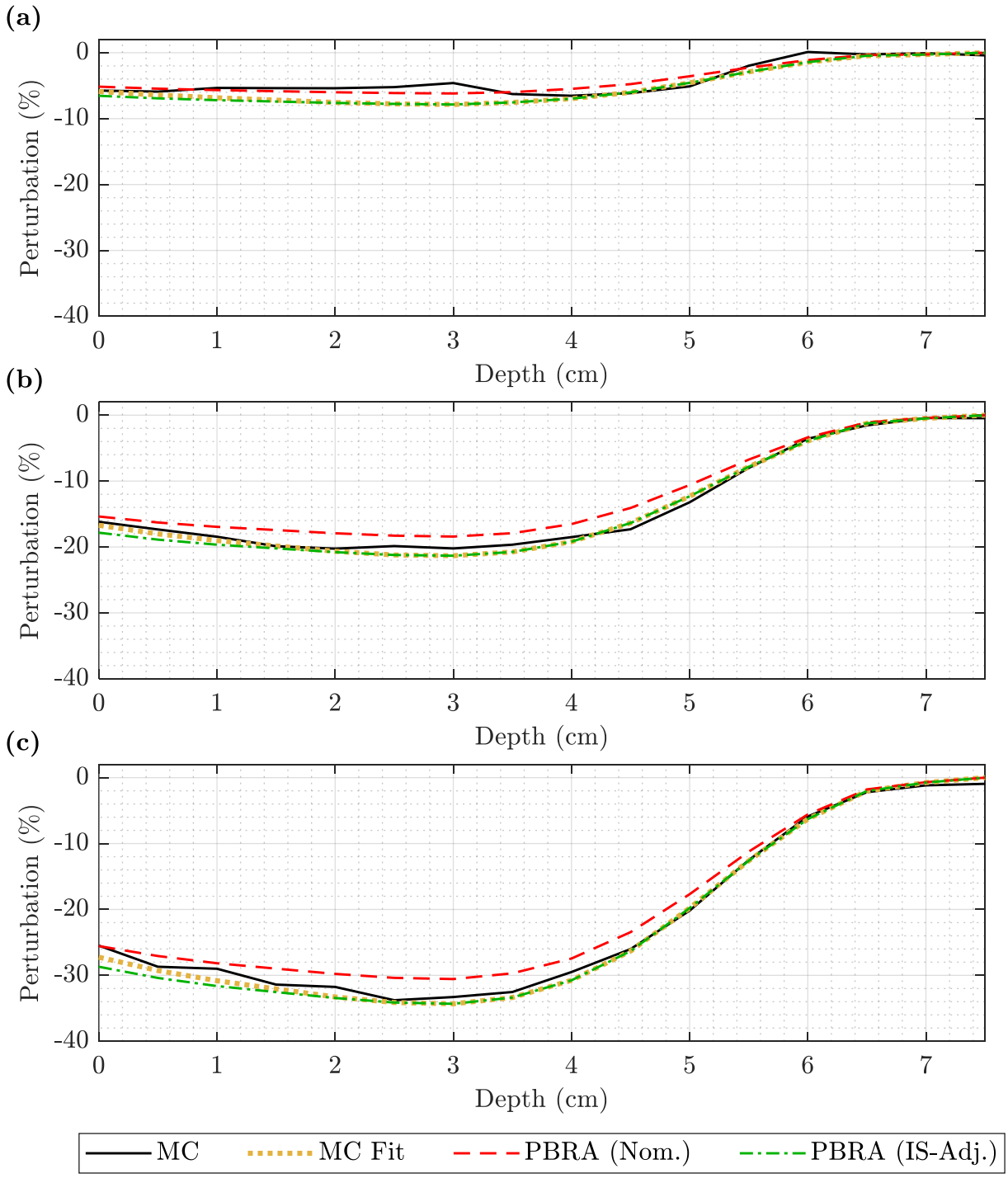

Figure D.44. Calculated PDD perturbations for square pin matrices at 13 MeV and 105 cm SSD. The PDD perturbations at 13 MeV and 105 cm SSD were calculated from the single-pin kernels of the MC (solid black), nominal PBRA (dashed red), and corresponding in-scatter-adjusted PBRA (dashed-dotted green) with the fitted MC (dotted yellow) determined at the given setup from Equation D.10 for rectilinear matrices (Figure D.4) with pins of uniform size: (a) 0.158, (b) 0.273, and (c) 0.352 cm in diameter.

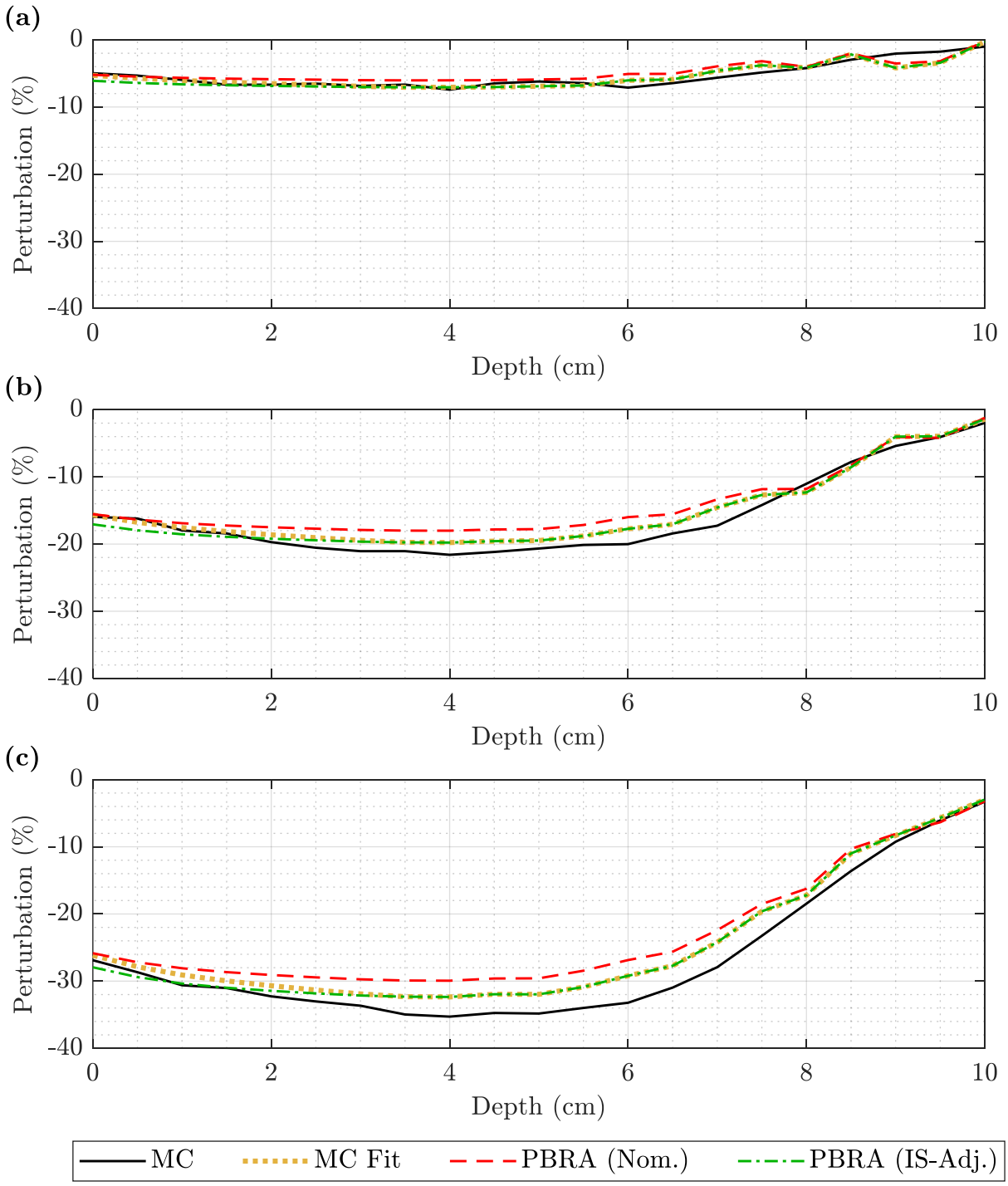

Figure D.45. Calculated PDD perturbations for square pin matrices at 20 MeV and 105 cm SSD. The PDD perturbations at 20 MeV and 105 cm SSD were calculated from the single-pin kernels of the MC (solid black), nominal PBRA (dashed red), and corresponding in-scatter-adjusted PBRA (dashed-dotted green) with the fitted MC (dotted yellow) determined at the given setup from Equation D.10 for rectilinear matrices (Figure D.4) with pins of uniform size: (a) 0.158, (b) 0.273, and (c) 0.352 cm in diameter.

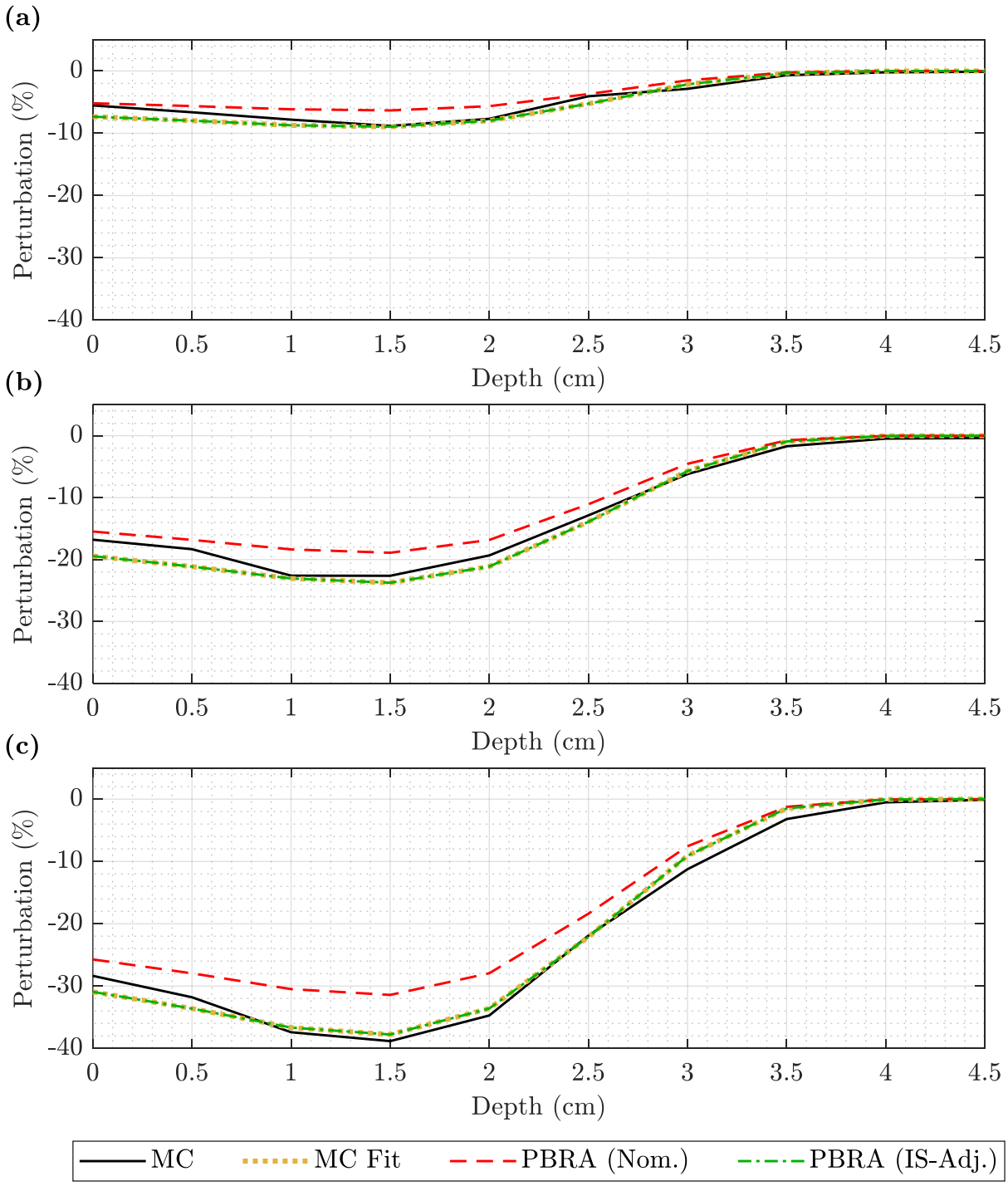

Figure D.46. Calculated PDD perturbations for square pin matrices at 7 MeV and 110 cm SSD. The PDD perturbations at 7 MeV and 110 cm SSD were calculated from the single-pin kernels of the MC (solid black), nominal PBRA (dashed red), and corresponding in-scatter-adjusted PBRA (dashed-dotted green) with the fitted MC (dotted yellow) determined at the given setup from Equation D.10 for rectilinear matrices (Figure D.4) with pins of uniform size: (a) 0.158, (b) 0.273, and (c) 0.352 cm in diameter.

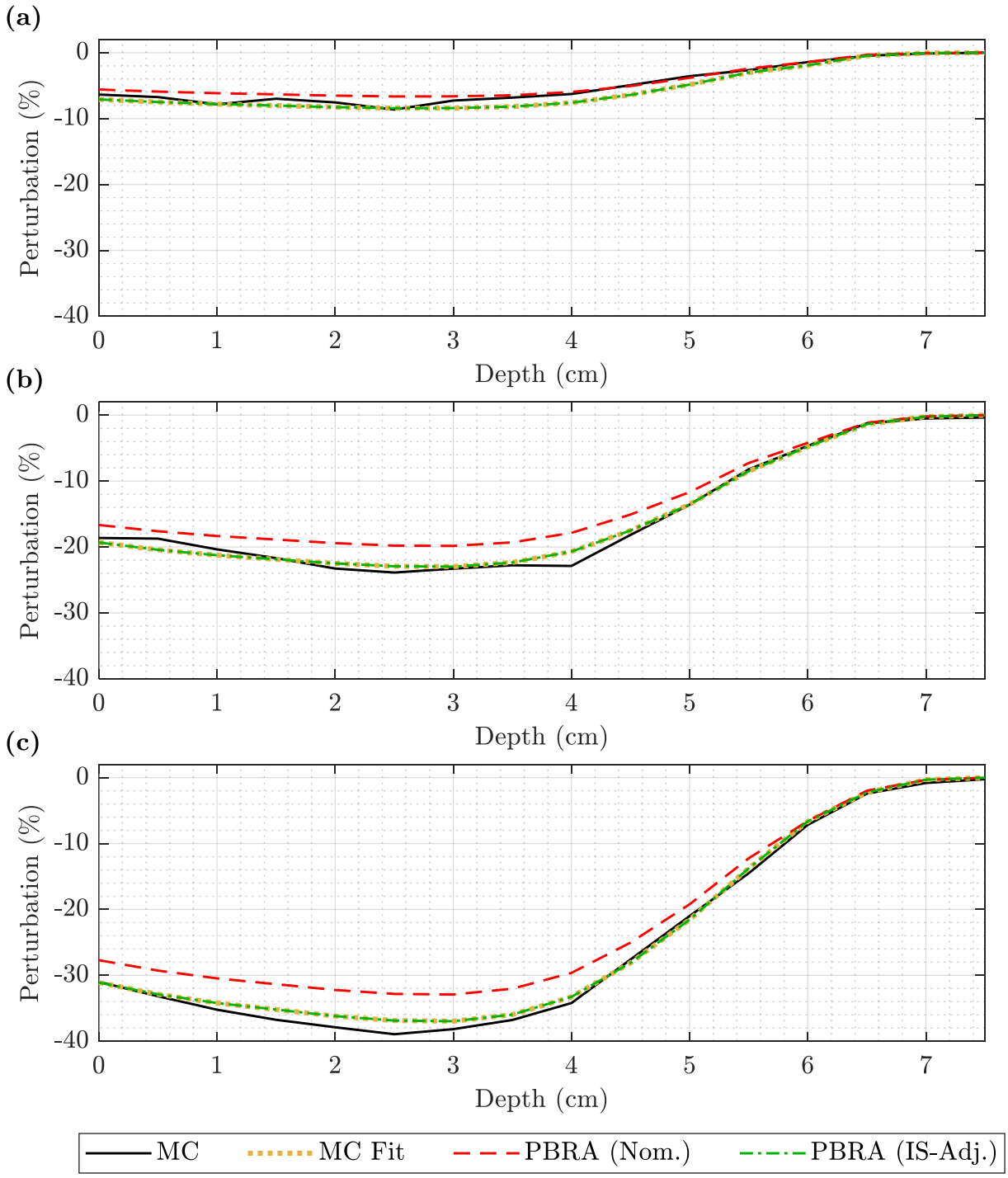

Figure D.47. Calculated PDD perturbations for square pin matrices at 13 MeV and 110 cm SSD. The PDD perturbations at 13 MeV and 110 cm SSD were calculated from the single-pin kernels of the MC (solid black), nominal PBRA (dashed red), and corresponding in-scatter-adjusted PBRA (dashed-dotted green) with the fitted MC (dotted yellow) determined at the given setup from Equation D.10 for rectilinear matrices (Figure D.4) with pins of uniform size: (a) 0.158, (b) 0.273, and (c) 0.352 cm in diameter.

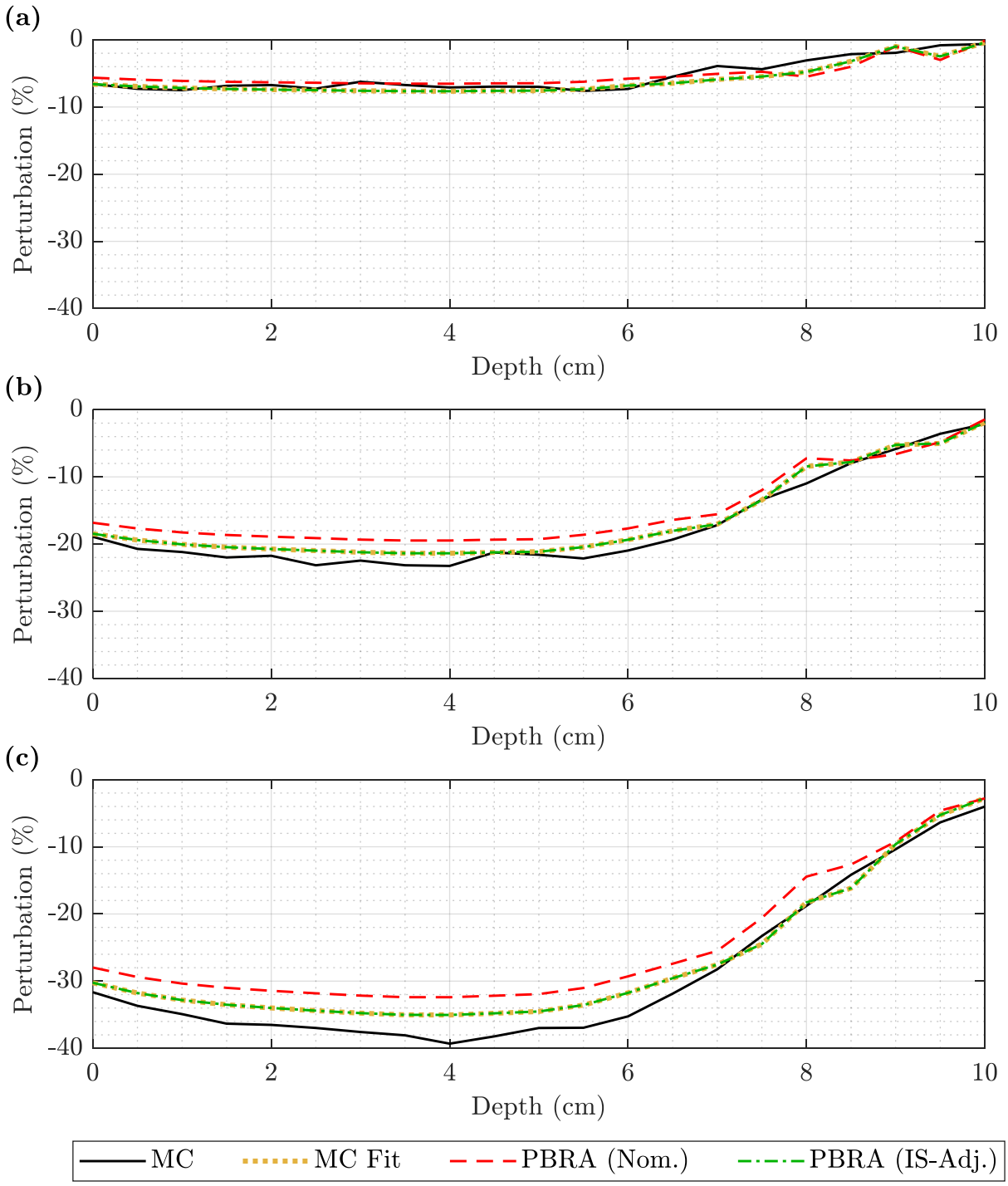

Figure D.48. Calculated PDD perturbations for square pin matrices at 20 MeV and 110 cm SSD. The PDD perturbations at 20 MeV and 110 cm SSD were calculated from the single-pin kernels of the MC (solid black), nominal PBRA (dashed red), and corresponding in-scatter-adjusted PBRA (dashed-dotted green) with the fitted MC (dotted yellow) determined at the given setup from Equation D.10 for rectilinear matrices (Figure D.4) with pins of uniform size: (a) 0.158, (b) 0.273, and (c) 0.352 cm in diameter.

Table D.10. MC-based scatter corrections for 100 cm SSD. Using the global fit of Equation D.10, the out-scatter dose shift was determined according to Equation D.11. This yielded an IRF corrected for both in-scatter and out-scatter from Equation D.12, from which the fully corrected (IS+OS) diameter was determined by Equation D.13. The IS+OS-corrected diameters using the measurement-based method are included for comparison.

Energy (MeV)	d (cm)	d_{IS} (cm)	IRF_{IS}	ΔD_{shift}	IRF_{IS+OS}	MC d_{IS+OS} (cm)	Meas. d_{IS+OS} (cm)
7	0.158	0.188	0.911	0.20%	0.913	0.186	0.173
7	0.223	0.255	0.836	0.28%	0.839	0.253	0.234
7	0.273	0.306	0.764	0.34%	0.767	0.304	0.281
7	0.315	0.349	0.693	0.39%	0.697	0.347	0.322
7	0.352	0.386	0.625	0.44%	0.629	0.384	0.357
9	0.158	0.184	0.915	0.30%	0.918	0.180	0.170
9	0.223	0.251	0.841	0.43%	0.845	0.248	0.232
9	0.273	0.301	0.772	0.52%	0.777	0.297	0.279
9	0.315	0.344	0.702	0.60%	0.708	0.340	0.320
9	0.352	0.381	0.634	0.67%	0.641	0.378	0.356
10	0.158	0.182	0.917	0.35%	0.921	0.178	0.169
10	0.223	0.248	0.845	0.49%	0.850	0.244	0.230
10	0.273	0.299	0.775	0.60%	0.781	0.295	0.278
10	0.315	0.341	0.707	0.70%	0.714	0.337	0.319
10	0.352	0.378	0.640	0.78%	0.648	0.374	0.354
11	0.158	0.180	0.918	0.39%	0.922	0.176	0.169
11	0.223	0.246	0.848	0.55%	0.854	0.241	0.229
11	0.273	0.296	0.779	0.68%	0.786	0.292	0.277
11	0.315	0.338	0.712	0.78%	0.720	0.334	0.317
11	0.352	0.376	0.644	0.87%	0.653	0.371	0.354
13	0.158	0.178	0.920	0.47%	0.925	0.173	0.168
13	0.223	0.244	0.850	0.66%	0.857	0.239	0.229
13	0.273	0.294	0.782	0.81%	0.790	0.289	0.277
13	0.315	0.336	0.716	0.93%	0.725	0.330	0.317
13	0.352	0.373	0.650	1.04%	0.660	0.367	0.353
16	0.158	0.174	0.924	0.57%	0.930	0.167	0.165
16	0.223	0.239	0.856	0.80%	0.864	0.232	0.227
16	0.273	0.290	0.788	0.98%	0.798	0.283	0.276
16	0.315	0.332	0.722	1.13%	0.733	0.325	0.317
16	0.352	0.369	0.657	1.27%	0.670	0.362	0.353
20	0.158	0.171	0.926	0.68%	0.933	0.163	0.164
20	0.223	0.236	0.860	0.96%	0.870	0.227	0.226
20	0.273	0.286	0.794	1.18%	0.806	0.278	0.275
20	0.315	0.329	0.727	1.36%	0.741	0.321	0.316
20	0.352	0.366	0.663	1.52%	0.678	0.357	0.351

Table D.11. MC-based scatter corrections for 105 cm SSD. Using the global fit of Equation D.10, the out-scatter dose shift was determined according to Equation D.11. This yielded an IRF corrected for both in-scatter and out-scatter from Equation D.12, from which the fully corrected (IS+OS) diameter was determined by Equation D.13. The IS+OS-corrected diameters using the measurement-based method are included for comparison.

Energy (MeV)	d (cm)	d_{IS} (cm)	IRF_{IS}	ΔD_{shift}	IRF_{IS+OS}	MC d_{IS+OS} (cm)	Meas. d_{IS+OS} (cm)
7	0.158	0.188	0.911	0.04%	0.911	0.188	0.170
7	0.223	0.255	0.836	0.06%	0.837	0.255	0.231
7	0.273	0.306	0.764	0.07%	0.765	0.306	0.280
7	0.315	0.349	0.693	0.08%	0.694	0.349	0.321
7	0.352	0.386	0.625	0.09%	0.626	0.385	0.356
9	0.158	0.184	0.915	0.10%	0.916	0.183	0.168
9	0.223	0.251	0.841	0.14%	0.842	0.250	0.230
9	0.273	0.301	0.772	0.17%	0.774	0.300	0.277
9	0.315	0.344	0.702	0.19%	0.704	0.343	0.319
9	0.352	0.381	0.634	0.22%	0.636	0.380	0.355
10	0.158	0.182	0.917	0.12%	0.918	0.180	0.167
10	0.223	0.248	0.845	0.17%	0.847	0.247	0.228
10	0.273	0.299	0.775	0.21%	0.777	0.297	0.276
10	0.315	0.341	0.707	0.24%	0.709	0.340	0.317
10	0.352	0.378	0.640	0.27%	0.643	0.377	0.353
11	0.158	0.180	0.918	0.14%	0.919	0.179	0.167
11	0.223	0.246	0.848	0.20%	0.850	0.244	0.227
11	0.273	0.296	0.779	0.25%	0.782	0.295	0.275
11	0.315	0.338	0.712	0.28%	0.715	0.336	0.315
11	0.352	0.376	0.644	0.32%	0.647	0.374	0.352
13	0.158	0.178	0.920	0.18%	0.922	0.176	0.166
13	0.223	0.244	0.850	0.25%	0.853	0.242	0.227
13	0.273	0.294	0.782	0.31%	0.785	0.292	0.275
13	0.315	0.336	0.716	0.36%	0.720	0.334	0.315
13	0.352	0.373	0.650	0.40%	0.654	0.371	0.351
16	0.158	0.174	0.924	0.23%	0.926	0.171	0.161
16	0.223	0.239	0.856	0.32%	0.859	0.236	0.223
16	0.273	0.290	0.788	0.40%	0.792	0.287	0.273
16	0.315	0.332	0.722	0.46%	0.727	0.329	0.313
16	0.352	0.369	0.657	0.51%	0.662	0.366	0.349
20	0.158	0.171	0.926	0.29%	0.929	0.168	0.156
20	0.223	0.236	0.860	0.40%	0.864	0.232	0.220
20	0.273	0.286	0.794	0.49%	0.799	0.283	0.271
20	0.315	0.329	0.727	0.57%	0.733	0.326	0.311
20	0.352	0.366	0.663	0.64%	0.669	0.362	0.345

Table D.12. MC-based scatter corrections for 110 cm SSD. Using the global fit of Equation D.10, the out-scatter dose shift was determined according to Equation D.11. This yielded an IRF corrected for both in-scatter and out-scatter from Equation D.12, from which the fully corrected (IS+OS) diameter was determined by Equation D.13. The IS+OS-corrected diameters using the measurement-based method are included for comparison.

Energy (MeV)	d (cm)	d_{IS} (cm)	IRF_{IS}	ΔD_{shift}	IRF_{IS+OS}	MC d_{IS+OS} (cm)	Meas. d_{IS+OS} (cm)
7	0.158	0.188	0.911	0.08%	0.912	0.187	0.173
7	0.223	0.255	0.836	0.11%	0.837	0.254	0.234
7	0.273	0.306	0.764	0.14%	0.765	0.305	0.281
7	0.315	0.349	0.693	0.16%	0.695	0.348	0.322
7	0.352	0.386	0.625	0.18%	0.627	0.385	0.357
9	0.158	0.184	0.915	0.07%	0.916	0.183	0.170
9	0.223	0.251	0.841	0.10%	0.842	0.250	0.232
9	0.273	0.301	0.772	0.12%	0.773	0.300	0.279
9	0.315	0.344	0.702	0.14%	0.703	0.343	0.320
9	0.352	0.381	0.634	0.16%	0.636	0.380	0.356
10	0.158	0.182	0.917	0.07%	0.918	0.181	0.169
10	0.223	0.248	0.845	0.10%	0.846	0.247	0.230
10	0.273	0.299	0.775	0.12%	0.776	0.298	0.278
10	0.315	0.341	0.707	0.14%	0.708	0.340	0.319
10	0.352	0.378	0.640	0.15%	0.642	0.377	0.354
11	0.158	0.180	0.918	0.07%	0.919	0.180	0.169
11	0.223	0.246	0.848	0.09%	0.849	0.245	0.229
11	0.273	0.296	0.779	0.11%	0.780	0.295	0.277
11	0.315	0.338	0.712	0.13%	0.713	0.337	0.317
11	0.352	0.376	0.644	0.15%	0.646	0.375	0.354
13	0.158	0.178	0.920	0.06%	0.921	0.178	0.168
13	0.223	0.244	0.850	0.09%	0.851	0.243	0.229
13	0.273	0.294	0.782	0.11%	0.783	0.293	0.277
13	0.315	0.336	0.716	0.12%	0.717	0.335	0.317
13	0.352	0.373	0.650	0.14%	0.651	0.372	0.353
16	0.158	0.174	0.924	0.06%	0.925	0.173	0.165
16	0.223	0.239	0.856	0.08%	0.857	0.238	0.227
16	0.273	0.290	0.788	0.10%	0.789	0.289	0.276
16	0.315	0.332	0.722	0.11%	0.723	0.332	0.317
16	0.352	0.369	0.657	0.12%	0.658	0.368	0.353
20	0.158	0.171	0.926	0.05%	0.927	0.171	0.164
20	0.223	0.236	0.860	0.07%	0.861	0.235	0.226
20	0.273	0.286	0.794	0.09%	0.795	0.285	0.275
20	0.315	0.329	0.727	0.10%	0.728	0.329	0.316
20	0.352	0.366	0.663	0.11%	0.664	0.365	0.351

D.2.6. Discussion

The MC-based dose estimation for multipin intensity modulators used a parallel beam so that the kernel spacing was consistent with the dose grid. PBRA calculations for multipin intensity modulators incorporate beam divergence, so, to simulate beam geometry similar to the MC, the kernel summation method was necessary. The observed MC and PBRA radial dose perturbation kernel tendencies were similar: increasing perturbation with beam energy and diameter, and decreasing amplitude with increasing SSD and depth.

The MC-estimated PDDs were noisy and required smoothing. Extension of the solution to energies without corresponding MC calculations was also necessary. The global fit addressed both of these issues. However, the MC prediction (Tables D.10-12) and measurement-based method (Tables 3.8-10) can differ by several percent, with the average dose corrections being 0.36% and 2.95%, respectively. The IS+OS diameters are also comparable to the in-scatter-adjustment, indicating that measurement dose will always be lower than the nominal PBRA calculation. Conversely, the measurement-corrected diameters may be smaller than nominal (i.e. more out-scatter), suggesting that the MC model insufficiently predicts out-scatter.

One issue with the pin matrix geometry used in calculating the dose shifts is the number of pins. The dose shifts here were derived using a square pin matrix (Figure D.4) so that the dose grid aligned with the kernel spacing and removed the need for interpolation. Due to the coincidence of the dose grid and kernel spacing, the parallel, rectilinear arrangement may have inadvertently overemphasized the dose perturbation directly beneath the pin where the dose reduction is greatest, resulting in smaller IS+OS diameters. This is further discussed in Appendix E.

D.3. Validation of the modified IM-BECT PBRA dose calculation

D.3.1. IM-PBRA calculations

For all corresponding measured setups, a PBRA dose distribution was calculated using the MC-based IS+OS diameters (Table D.13). The same plans and pin arrangements described in Section 3.1.8 were used. The measurement-based adjustments to the beam model were also used. Pin positions were corrected using the geometric factor of Equation 3.3 to account for beam divergence for the virtual source position. Dose values were normalized to the maximum CAX dose of the foam-only setup at the same beam energy and SSD conditions. Inplane profiles and CAX PDDs were extracted from the calculated distributions. Isodose contours in the *yz*-plane (x = 0 cm) were generated from the profiles.

Table D.13. Diameters corrected for in-scatter and out-scatter used in validation of MC-based IM-PBRA corrections. PBRA calculations were made using the IS+OS-corrected diameters and the same pin arrangements as the sample PRIME devices (Figure 3.1 and Figure 3.3).

Beam Energy (MeV)	Nominal Diameter (cm)	IS+OS-Corrected Diameters (cm)		
		100 cm SSD	105 cm SSD	110 cm SSD
7	0.158	0.186	0.188	0.187
7	0.273	0.304	0.306	0.305
7	0.352	0.384	0.385	0.385
13	0.158	0.173	0.176	0.178
13	0.273	0.289	0.292	0.293
13	0.352	0.367	0.371	0.372
20	0.158	0.163	0.168	0.171
20	0.273	0.278	0.283	0.285
20	0.352	0.357	0.362	0.365

D.3.2. Validation metrics

All validation metrics were evaluated for the dose distributions calculated with MC-based IS+OS-corrected and nominal pin diameters. For each combination of beam energy, SSD, and pin diameter, the passing rate for all measured dose points was calculated using 3%/3mm DTA criteria, and a dose difference histogram was generated. The maximum magnitude differences between measurement and PBRA calculations within the modulated volume ($|y| \leq 3.5$ cm and $z \leq R_p$) were evaluated according to Equations 4.1 and 4.2.

D.3.3. MC-modified IM-BECT PBRA dose calculation results

Table D.14 lists the passing rates of dose distributions calculated with nominal and IS+OS-corrected (both MC- and measurement-based) diameters. In all of the 27 measured combinations of beam energy, SSD, and island block diameter, the MC-based correction provided no improvement or worsened agreement over nominal PBRA calculation. The average passing rate decreased from 98.1% to 93.3%, with the worst-case being 83.3% with the MC-based corrected compared to 91.7% nominally. In cases with worsened agreement, the average decrease was -6.5% using the MC-based method.

Table D.15 contains the passing rates for points within the modulated volume ($|y| \leq 3.5$ cm and $z \leq R_p$). The average nominal and MC-based IS+OS-corrected PBRA passing rates were 96.2% and 66.7%, respectively. There was no improvement in 7 of 27 cases, all for the smallest pin diameter. In the remaining cases, the passing rate decreased by 41.8% on average. In the worst case at 7 MeV and 110 cm SSD for 0.352-cm pins, the passing rate in the modulated region decreased by 87.1% (see Figure D.69).

The measurement-based correction provided similar or better agreement with measurement than the MC-based correction. The measurement-based method yielded an average passing rate

5.2% greater than the MC-based method. At the smallest pin diameter, the overall (i.e. for the full dose distribution) passing rates of the correction methods were within 0.1% of one another except in one case (20 MeV and 100 cm SSD). In the extreme cases for the 0.273- and 0.352-cm pins, the passing rate with the measurement-based correction exceeded that with MC-based correction by 14.4% and 13.3%, respectively.

The maximum magnitude dose differences within the modulated region under nominal and MC-corrected diameters are shown in Table D.16. The spread of values worsened in all cases with the negative magnitude difference becoming more severe under the MC-based IS+OS correction.

Isodose comparisons of measurement to nominal and MC-corrected PBRA are plotted beside their difference histograms in Figures D.49-75. Points of failure within the corrected distribution are generally located in the modulated region.

Table D.14. Comparison of passing rates under 3%/3mm DTA criteria for nominal and MC-based IS+OS-corrected IM-PBRA calculations. PBRA calculations were compared to measurement for all points in the dose distribution with 3%/3mm DTA criteria, and overall passing rates were evaluated. The passing rates using measurement-based correction are included for comparison.

Energy (MeV)	SSD (cm)	*d* (cm)	Passing Rates				
			Nom.	MC-Based	Change	Meas-Based	Change
7	100	0.158	97.5%	97.4%	-0.1%	97.5%	0.0%
7	100	0.273	96.4%	87.2%	-9.2%	97.8%	1.4%
7	100	0.352	93.7%	83.3%	-10.4%	96.2%	2.5%
13	100	0.158	100.0%	100.0%	0.0%	100.0%	0.0%
13	100	0.273	100.0%	92.7%	-7.3%	100.0%	0.0%
13	100	0.352	96.5%	88.6%	-7.9%	93.9%	-2.6%
20	100	0.158	98.8%	98.6%	-0.2%	99.1%	0.3%
20	100	0.273	94.6%	92.9%	-1.7%	97.1%	2.5%
20	100	0.352	91.7%	89.8%	-1.8%	93.1%	1.4%
7	105	0.158	99.8%	99.8%	0.0%	99.8%	0.0%
7	105	0.273	99.1%	84.7%	-14.4%	99.1%	0.0%
7	105	0.352	96.6%	85.2%	-11.4%	97.9%	1.3%
13	105	0.158	100.0%	100.0%	0.0%	100.0%	0.0%
13	105	0.273	99.9%	92.7%	-7.2%	99.9%	0.0%
13	105	0.352	97.3%	88.3%	-9.1%	96.8%	-0.5%
20	105	0.158	99.4%	99.4%	0.0%	99.4%	0.0%
20	105	0.273	99.2%	96.1%	-3.1%	99.2%	0.0%
20	105	0.352	95.7%	91.1%	-4.6%	97.6%	1.9%
7	110	0.158	100.0%	100.0%	0.0%	100.0%	0.0%
7	110	0.273	99.9%	89.2%	-10.7%	99.9%	0.0%
7	110	0.352	97.9%	85.8%	-12.0%	99.2%	1.3%
13	110	0.158	100.0%	100.0%	0.0%	100.0%	0.0%
13	110	0.273	99.7%	94.0%	-5.7%	100.0%	0.3%
13	110	0.352	96.7%	89.6%	-7.1%	98.0%	1.3%
20	110	0.158	99.5%	99.5%	0.0%	99.5%	0.0%
20	110	0.273	99.3%	98.3%	-1.0%	99.4%	0.1%
20	110	0.352	98.7%	93.7%	-5.0%	98.3%	-0.4%
		Average	98.1%	93.3%	-4.8%	98.5%	0.4%

Table D.15. Comparison of passing rates within the modulated region under 3%/3mm DTA criteria for nominal and MC-based corrected IM-PBRA calculations. PBRA calculations were compared to measurement for all points in the modulated region ($|y| \leq 3.5$ cm and $z \leq R_p$) of the dose distribution with 3%/3mm DTA criteria, and the passing rates were evaluated. The passing rates using measurement-based correction are included for comparison.

Energy (MeV)	SSD (cm)	d (cm)	Passing Rates				
			Nom.	MC-Based	Change	Meas-Based	Change
7	100	0.158	100.0%	100.0%	0.0%	100.0%	0.0%
7	100	0.273	97.8%	32.8%	-65.1%	100.0%	2.2%
7	100	0.352	94.4%	11.6%	-82.8%	99.6%	5.2%
13	100	0.158	100.0%	100.0%	0.0%	100.0%	0.0%
13	100	0.273	100.0%	66.0%	-34.0%	100.0%	0.0%
13	100	0.352	84.7%	48.1%	-36.5%	89.1%	4.4%
20	100	0.158	98.5%	97.3%	-1.1%	100.0%	1.5%
20	100	0.273	83.5%	75.3%	-8.2%	95.0%	11.5%
20	100	0.352	70.9%	62.1%	-8.8%	87.7%	16.9%
7	105	0.158	100.0%	100.0%	0.0%	100.0%	0.0%
7	105	0.273	100.0%	20.2%	-79.8%	100.0%	0.0%
7	105	0.352	94.8%	10.8%	-84.1%	98.7%	3.9%
13	105	0.158	100.0%	100.0%	0.0%	100.0%	0.0%
13	105	0.273	100.0%	65.3%	-34.7%	100.0%	0.0%
13	105	0.352	91.4%	44.3%	-47.0%	92.9%	1.5%
20	105	0.158	100.0%	100.0%	0.0%	100.0%	0.0%
20	105	0.273	100.0%	84.7%	-15.3%	100.0%	0.0%
20	105	0.352	83.1%	60.2%	-23.0%	96.7%	13.6%
7	110	0.158	100.0%	100.0%	0.0%	100.0%	0.0%
7	110	0.273	100.0%	30.2%	-69.8%	100.0%	0.0%
7	110	0.352	97.8%	10.8%	-87.1%	100.0%	2.2%
13	110	0.158	100.0%	100.0%	0.0%	100.0%	0.0%
13	110	0.273	100.0%	70.0%	-30.0%	100.0%	0.0%
13	110	0.352	99.8%	47.8%	-52.0%	99.8%	0.0%
20	110	0.158	100.0%	100.0%	0.0%	100.0%	0.0%
20	110	0.273	100.0%	93.9%	-6.1%	100.0%	0.0%
20	110	0.352	99.4%	70.5%	-28.9%	100.0%	0.6%
		Average	96.2%	66.7%	-29.4%	98.5%	2.4%

Table D.16. Maximum magnitude dose differences in the modulated volume for MC-based corrections. The maximum magnitude differences between measurement an either nominal or MC-based IS+OS-corrected PBRA calculations were determined within the modulated region where the minimization routine was performed. Dose differences greater than 3% are shaded. The greatest dose difference for a given beam energy, SSD, and nominal diameter combination are bolded. Cases where there was no positive or negative difference are noted as "N/A".

SSD (cm)	Beam Energy (MeV)	d (cm)	Nominal		IS+OS-Corrected	
			$\Delta D^{+}_{\mathrm{mod}}$	$\Delta D^{-}_{\mathrm{mod}}$	$\Delta D^{+}_{\mathrm{mod}}$	$\Delta D^{-}_{\mathrm{mod}}$
100	7	0.158	2.3%	-0.7%	0.3%	**-2.9%**
100	7	0.273	3.3%	-1.1%	N/A	**-5.2%**
100	7	0.352	3.8%	-1.6%	N/A	**-6.9%**
100	13	0.158	2.1%	-1.7%	1.3%	**-2.9%**
100	13	0.273	2.4%	-2.9%	0.9%	**-4.9%**
100	13	0.352	2.8%	-4.5%	0.9%	**-7.0%**
100	20	0.158	1.2%	-3.6%	0.9%	**-4.0%**
100	20	0.273	1.2%	-6.3%	0.6%	**-6.9%**
100	20	0.352	1.9%	-8.9%	1.2%	**-9.8%**
105	7	0.158	2.6%	-0.6%	0.6%	**-2.9%**
105	7	0.273	2.4%	-1.1%	N/A	**-5.5%**
105	7	0.352	3.7%	-2.4%	N/A	**-7.8%**
105	13	0.158	2.1%	-1.2%	1.0%	**-2.6%**
105	13	0.273	2.6%	-2.4%	0.7%	**-4.8%**
105	13	0.352	3.0%	-3.7%	0.5%	**-6.8%**
105	20	0.158	1.0%	-1.7%	0.4%	**-2.5%**
105	20	0.273	1.9%	-2.4%	0.8%	**-3.7%**
105	20	0.352	1.8%	-4.5%	0.4%	**-6.2%**
110	7	0.158	**2.3%**	N/A	0.4%	-2.1%
110	7	0.273	2.2%	-0.6%	N/A	**-5.0%**
110	7	0.352	3.2%	-2.1%	N/A	**-7.5%**
110	13	0.158	2.0%	-0.7%	0.8%	**-2.3%**
110	13	0.273	2.7%	-2.0%	0.8%	**-4.6%**
110	13	0.352	3.0%	-2.8%	0.3%	**-6.3%**
110	20	0.158	1.7%	-1.2%	0.9%	**-2.2%**
110	20	0.273	2.0%	-1.9%	0.7%	**-3.5%**
110	20	0.352	2.5%	-3.1%	0.5%	**-5.3%**

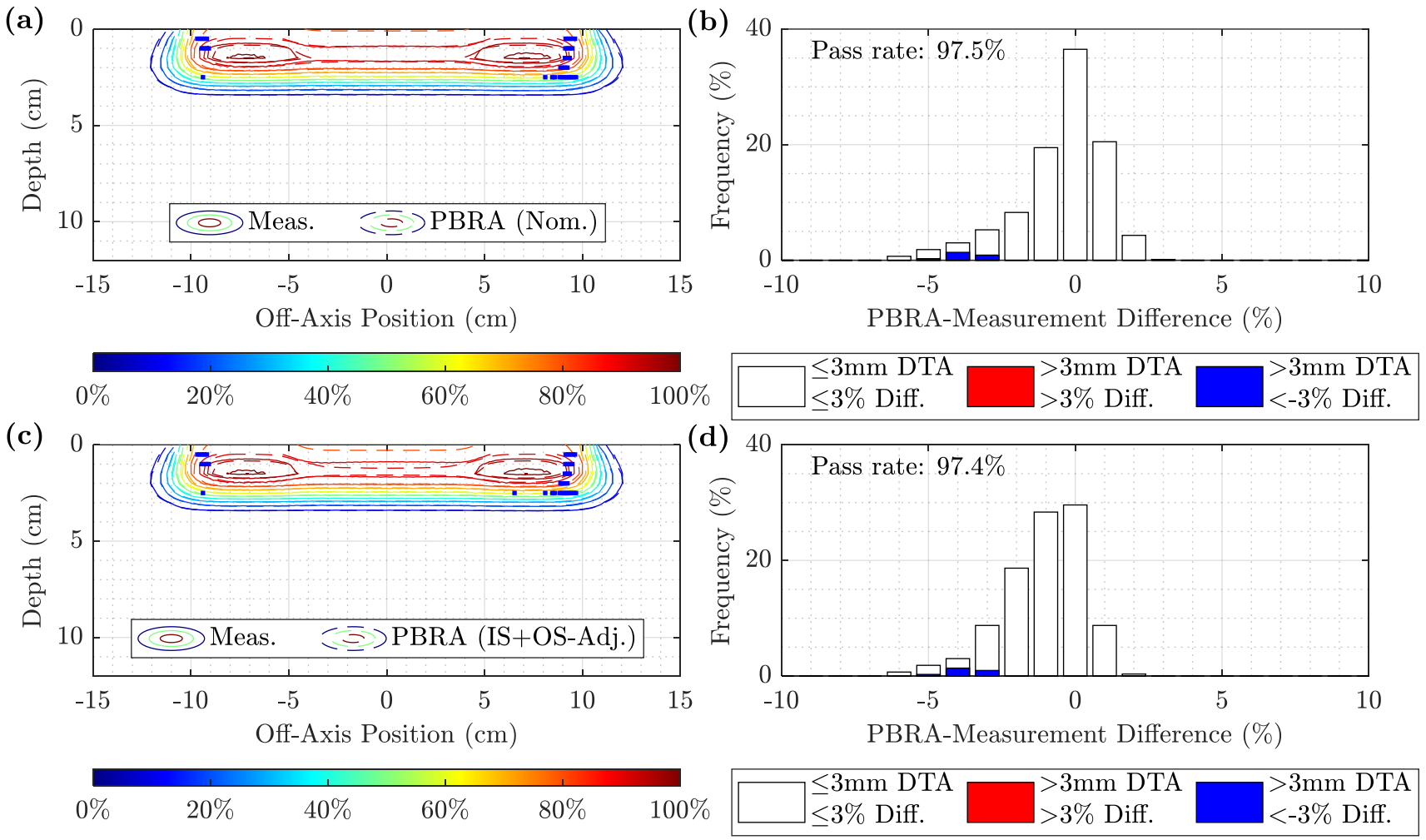

Figure D.49. Measured and PBRA-calculated isodose comparison and difference histograms for 0.158-cm pins at 7 MeV and 100 cm SSD using MC-based corrections. The isodose contours for measurement (solid) are compared to the PBRA calculations with (a) nominal and (c) MC-based IS+OS-corrected diameters. Difference histograms under 3%/3mm DTA criteria are plotted for (b) nominal and (d) MC-based IS+OS-corrected diameters. Points at which the PBRA underpredicted and overpredicted the dose relative to measurement are shown in blue and red, respectively. The nominal and corrected passing rates were 97.5% and 97.4%, respectively.

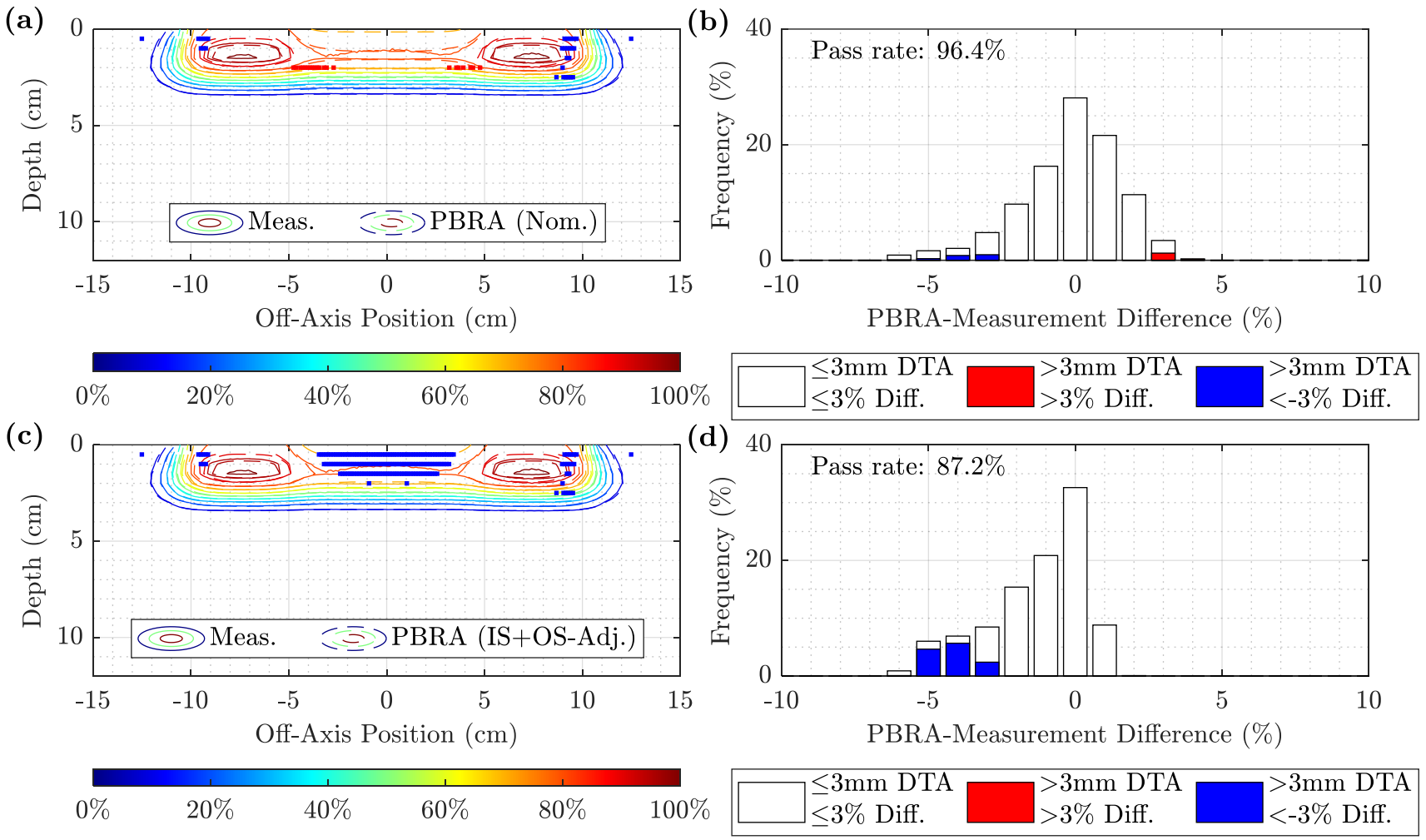

Figure D.50. Measured and PBRA-calculated isodose comparison and difference histograms for 0.273-cm pins at 7 MeV and 100 cm SSD using MC-based corrections. The isodose contours for measurement (solid) are compared to the PBRA calculations with (a) nominal and (c) MC-based IS+OS-corrected diameters. Difference histograms under 3%/3mm DTA criteria are plotted for (b) nominal and (d) MC-based IS+OS-corrected diameters. Points at which the PBRA underpredicted and overpredicted the dose relative to measurement are shown in blue and red, respectively. The nominal and corrected passing rates were 96.4% and 87.2%, respectively.

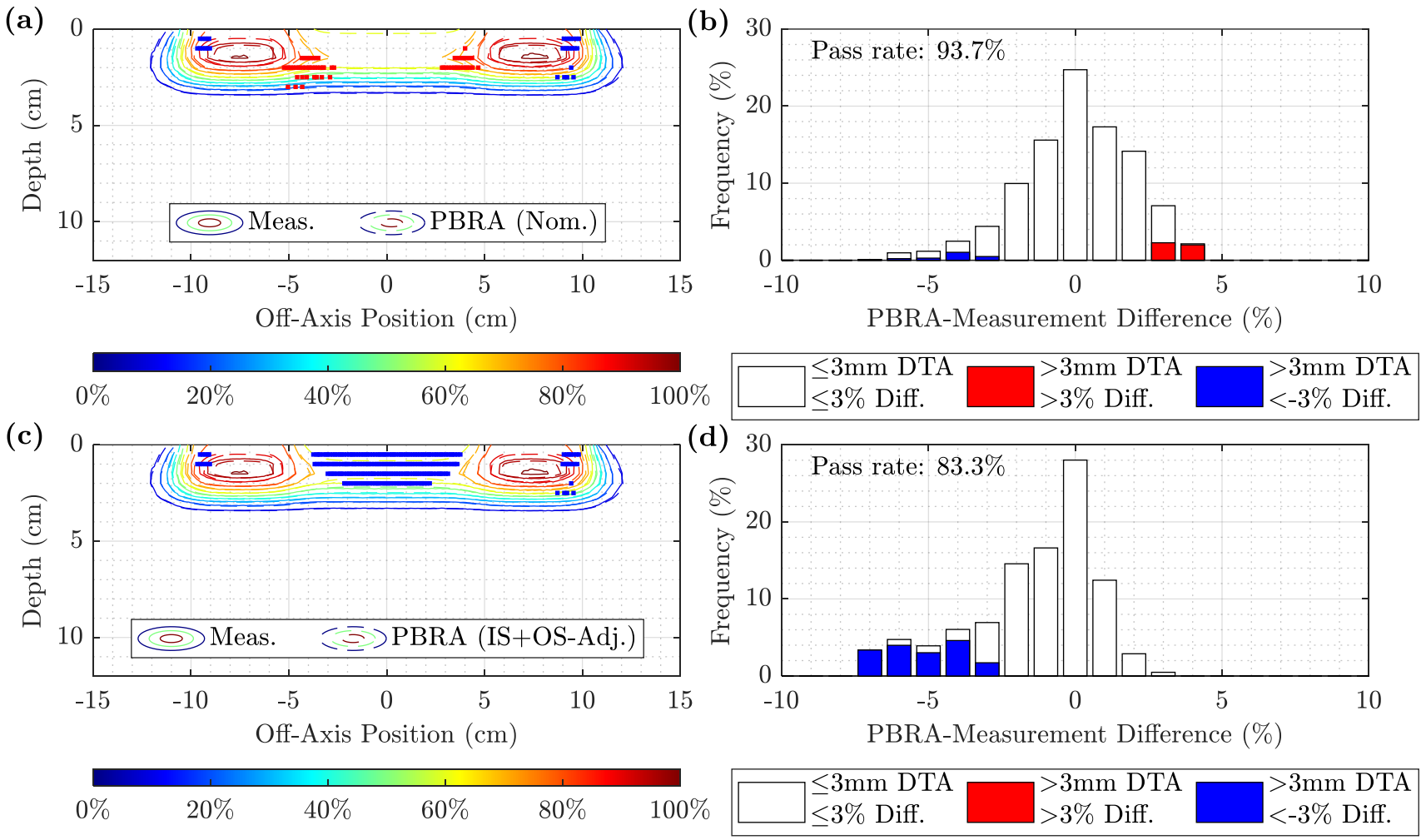

Figure D.51. Measured and PBRA-calculated isodose comparison and difference histograms for 0.352-cm pins at 7 MeV and 100 cm SSD using MC-based corrections. The isodose contours for measurement (solid) are compared to the PBRA calculations with (a) nominal and (c) MC-based IS+OS-corrected diameters. Difference histograms under 3%/3mm DTA criteria are plotted for (b) nominal and (d) MC-based IS+OS-corrected diameters. Points at which the PBRA underpredicted and overpredicted the dose relative to measurement are shown in blue and red, respectively. The nominal and corrected passing rates were 93.7% and 83.3%, respectively.

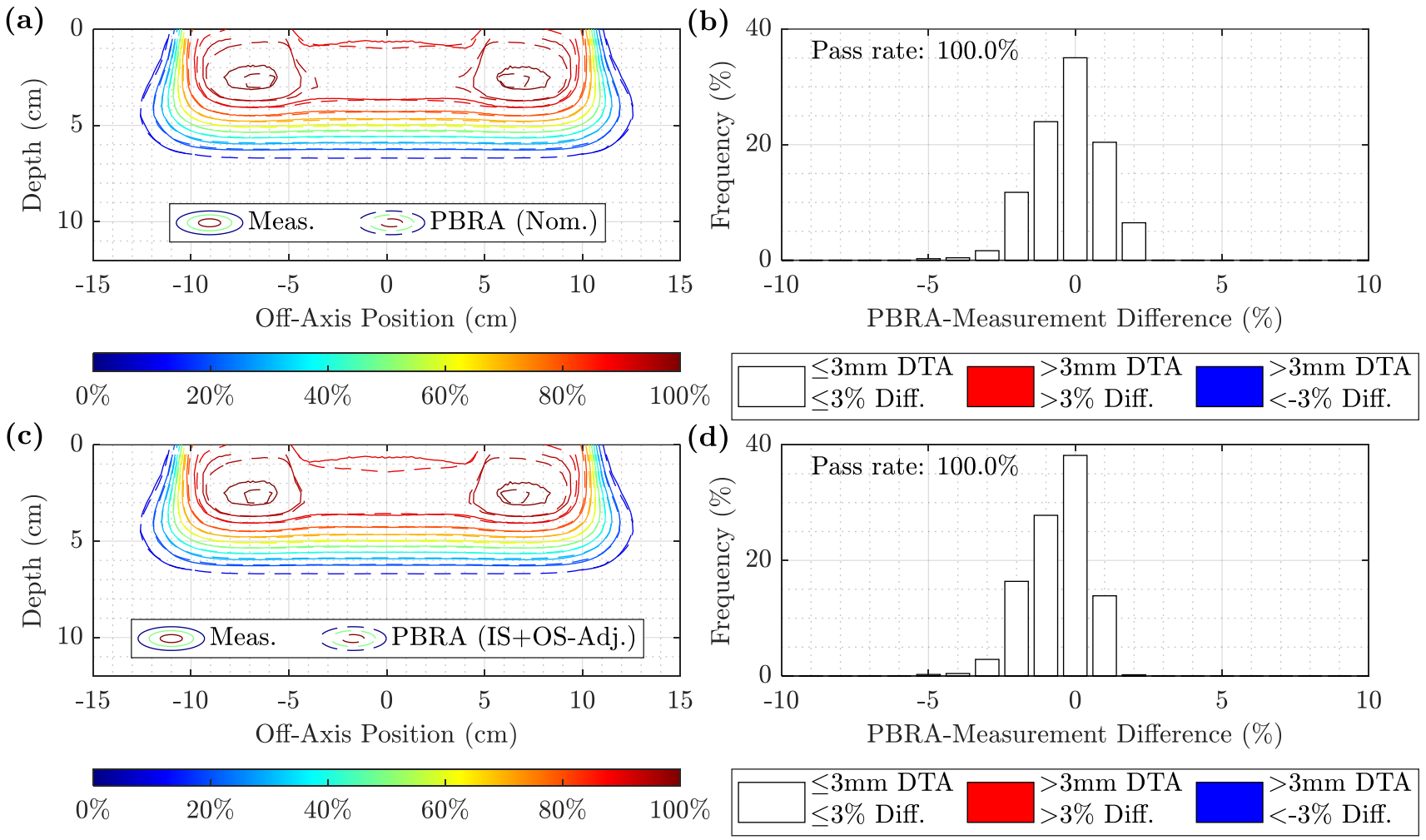

Figure D.52. Measured and PBRA-calculated isodose comparison and difference histograms for 0.158-cm pins at 13 MeV and 100 cm SSD using MC-based corrections. The isodose contours for measurement (solid) are compared to the PBRA calculations with (a) nominal and (c) MC-based IS+OS-corrected diameters. Difference histograms under 3%/3mm DTA criteria are plotted for (b) nominal and (d) MC-based IS+OS-corrected diameters. Points at which the PBRA underpredicted and overpredicted the dose relative to measurement are shown in blue and red, respectively. The nominal and corrected passing rates were both 100%.

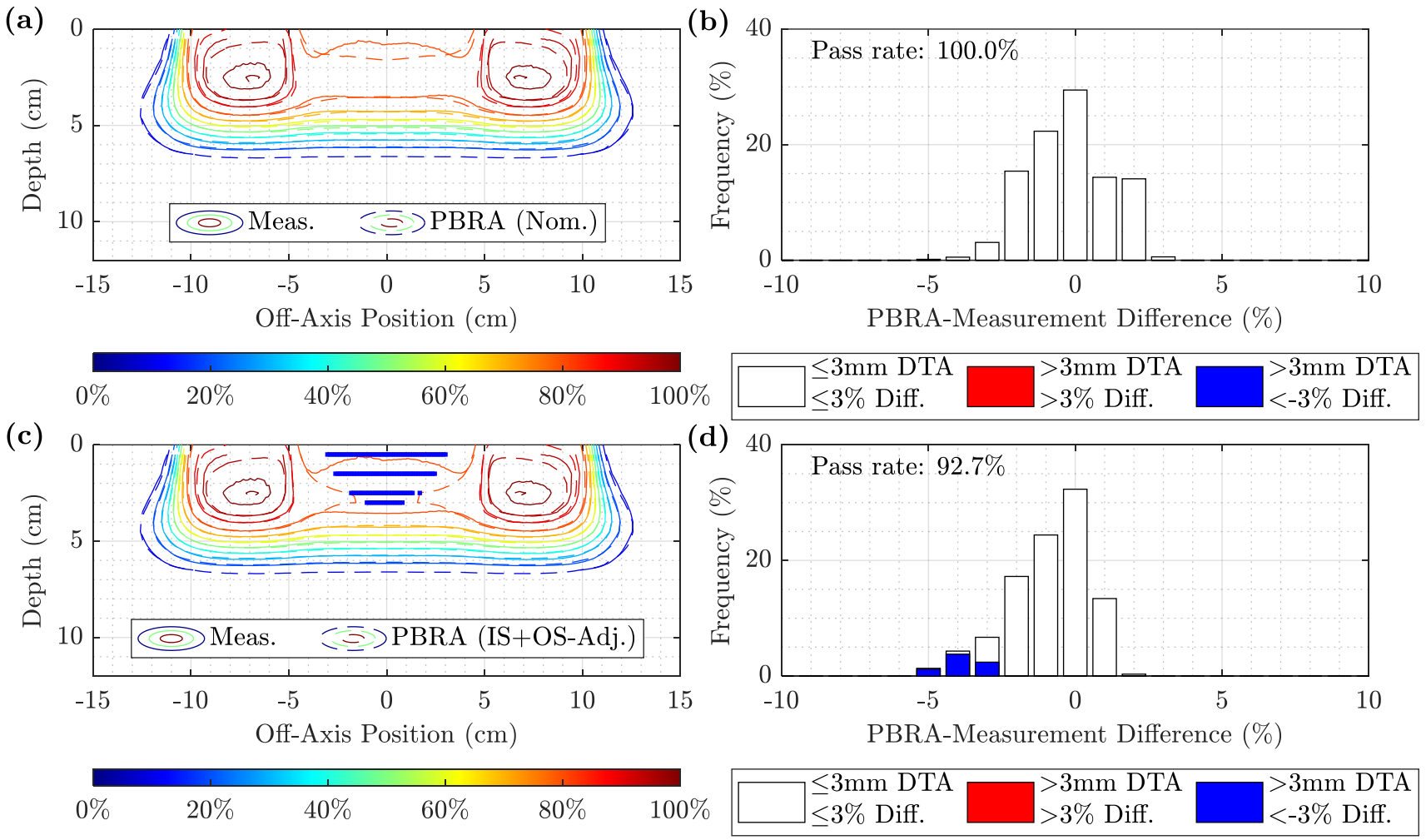

Figure D.53. Measured and PBRA-calculated isodose comparison and difference histograms for 0.273-cm pins at 13 MeV and 100 cm SSD using MC-based corrections. The isodose contours for measurement (solid) are compared to the PBRA calculations with (a) nominal and (c) MC-based IS+OS-corrected diameters. Difference histograms under 3%/3mm DTA criteria are plotted for (b) nominal and (d) MC-based IS+OS-corrected diameters. Points at which the PBRA underpredicted and overpredicted the dose relative to measurement are shown in blue and red, respectively. The nominal and corrected passing rates were 100% and 92.7%, respectively.

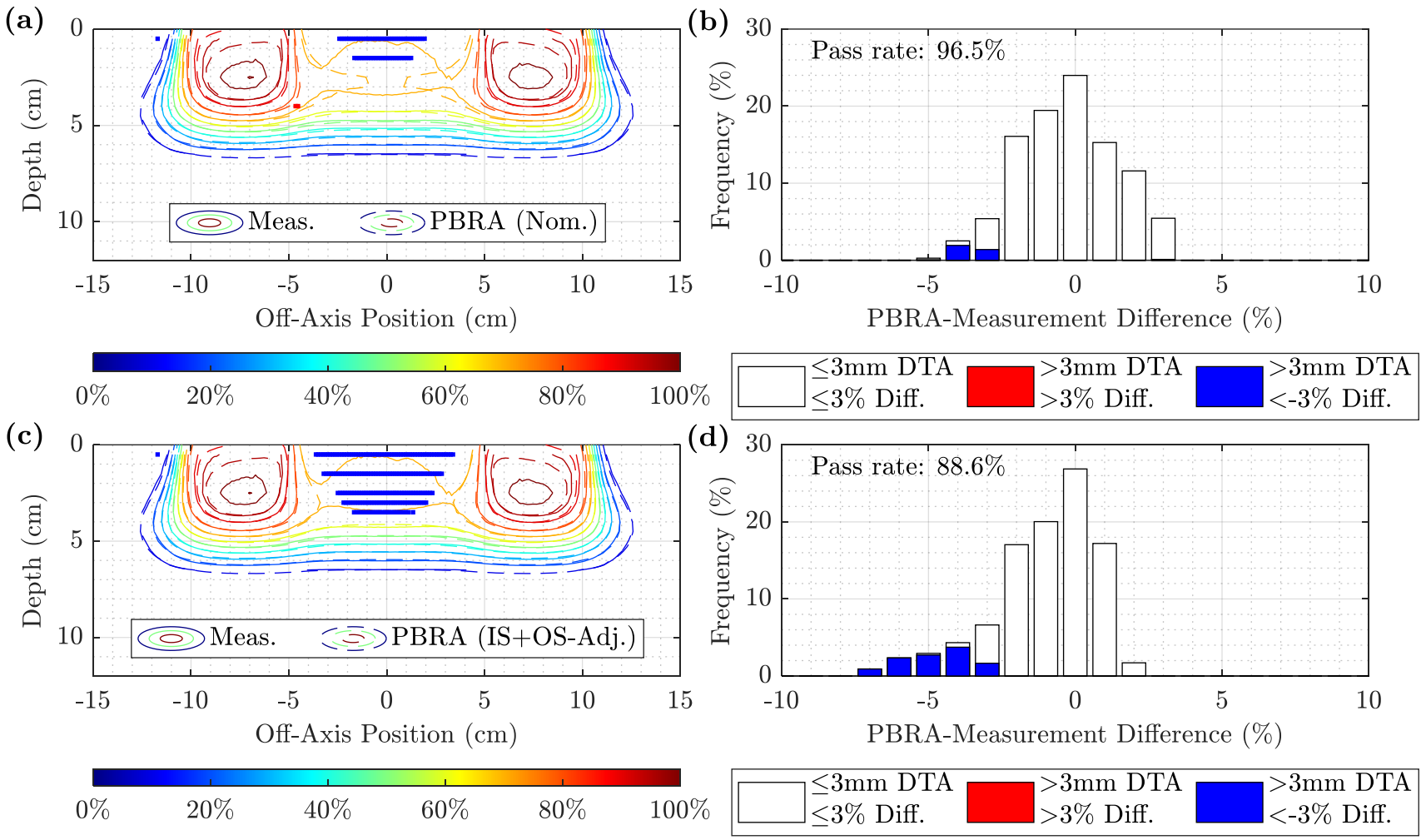

Figure D.54. Measured and PBRA-calculated isodose comparison and difference histograms for 0.352-cm pins at 13 MeV and 100 cm SSD using MC-based corrections. The isodose contours for measurement (solid) are compared to the PBRA calculations with (a) nominal and (c) MC-based IS+OS-corrected diameters. Difference histograms under 3%/3mm DTA criteria are plotted for (b) nominal and (d) MC-based IS+OS-corrected diameters. Points at which the PBRA underpredicted and overpredicted the dose relative to measurement are shown in blue and red, respectively. The nominal and corrected passing rates were 96.5% and 88.6%, respectively.

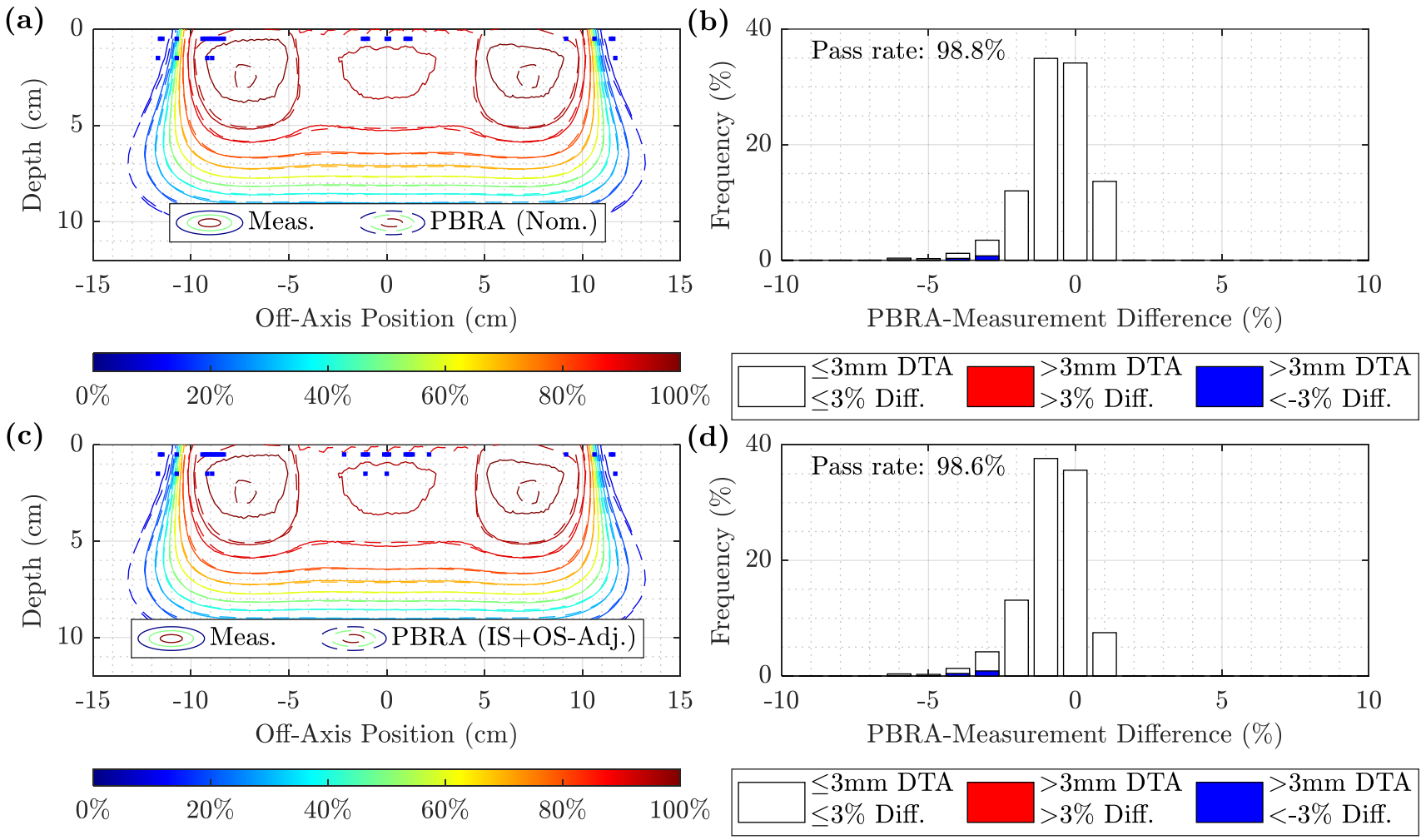

Figure D.55. Measured and PBRA-calculated isodose comparison and difference histograms for 0.158-cm pins at 20 MeV and 100 cm SSD using MC-based corrections. The isodose contours for measurement (solid) are compared to the PBRA calculations with (a) nominal and (c) MC-based IS+OS-corrected diameters. Difference histograms under 3%/3mm DTA criteria are plotted for (b) nominal and (d) MC-based IS+OS-corrected diameters. Points at which the PBRA underpredicted and overpredicted the dose relative to measurement are shown in blue and red, respectively. The nominal and corrected passing rates were 98.8% and 98.6%, respectively.

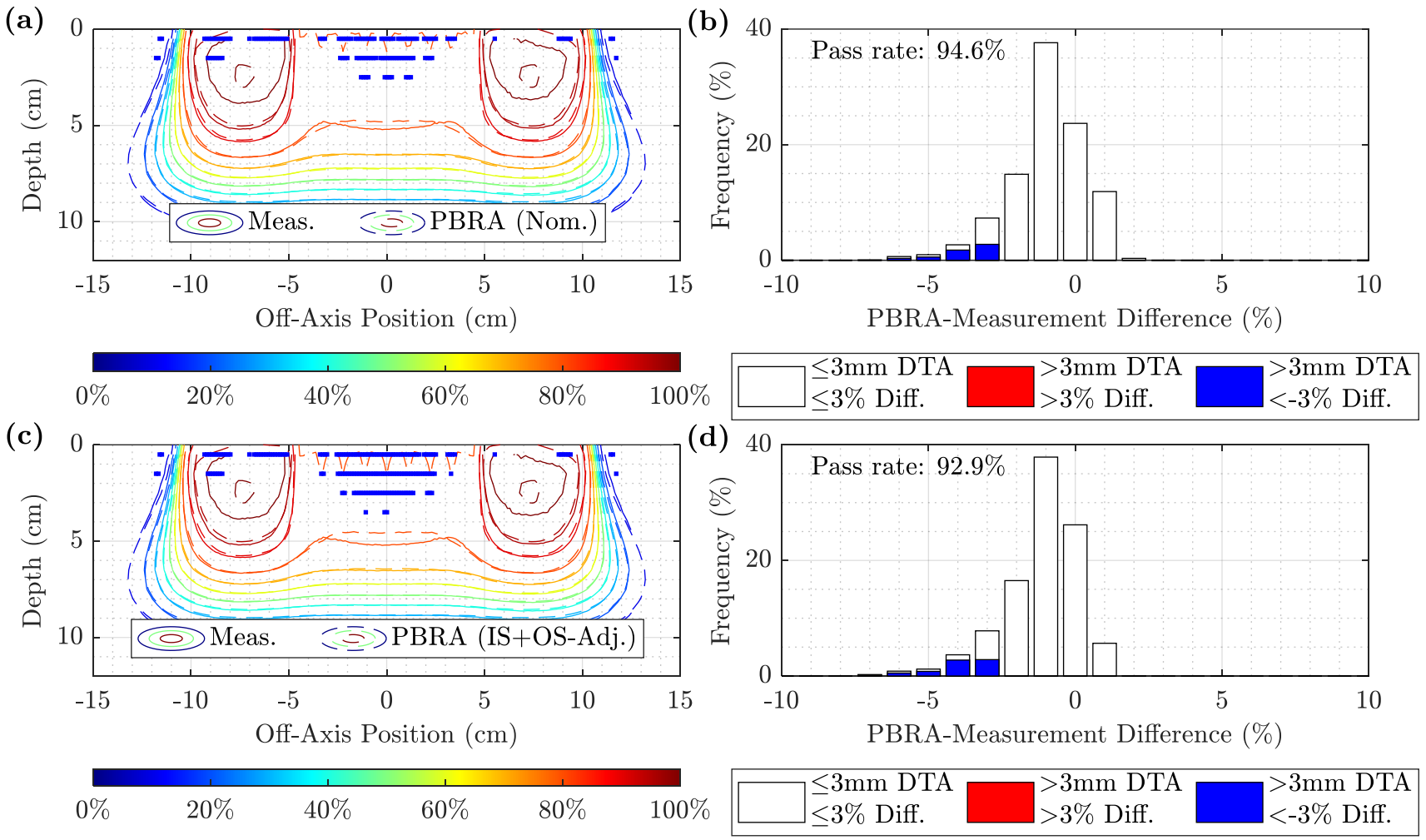

Figure D.56. Measured and PBRA-calculated isodose comparison and difference histograms for 0.273-cm pins at 20 MeV and 100 cm SSD using MC-based corrections. The isodose contours for measurement (solid) are compared to the PBRA calculations with (a) nominal and (c) MC-based IS+OS-corrected diameters. Difference histograms under 3%/3mm DTA criteria are plotted for (b) nominal and (d) MC-based IS+OS-corrected diameters. Points at which the PBRA underpredicted and overpredicted the dose relative to measurement are shown in blue and red, respectively. The nominal and corrected passing rates were 94.6% and 92.9%, respectively.

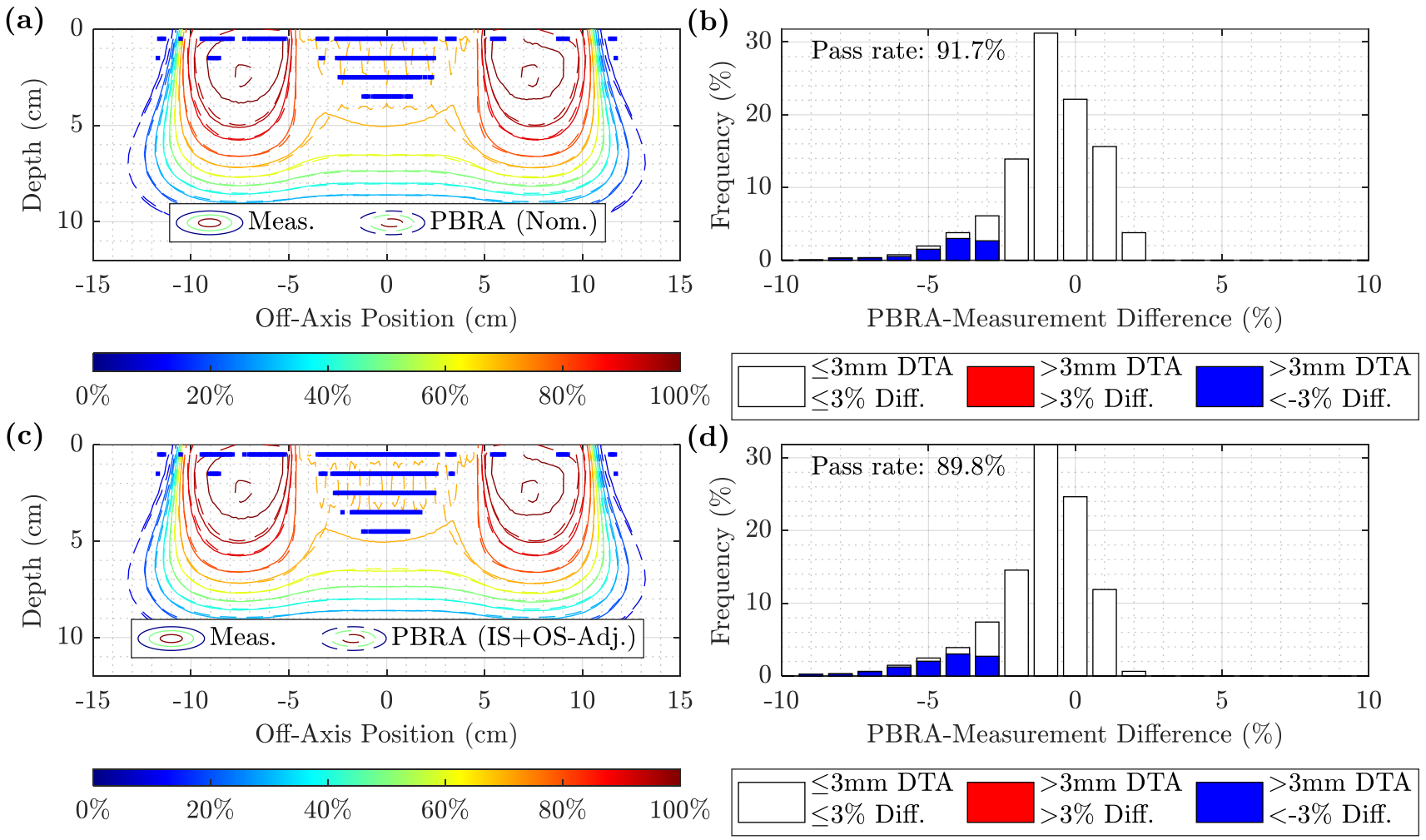

Figure D.57. Measured and PBRA-calculated isodose comparison and difference histograms for 0.352-cm pins at 20 MeV and 100 cm SSD using MC-based corrections. The isodose contours for measurement (solid) are compared to the PBRA calculations with (a) nominal and (c) MC-based IS+OS-corrected diameters. Difference histograms under 3%/3mm DTA criteria are plotted for (b) nominal and (d) MC-based IS+OS-corrected diameters. Points at which the PBRA underpredicted and overpredicted the dose relative to measurement are shown in blue and red, respectively. The nominal and corrected passing rates were 91.7% and 89.8%, respectively.

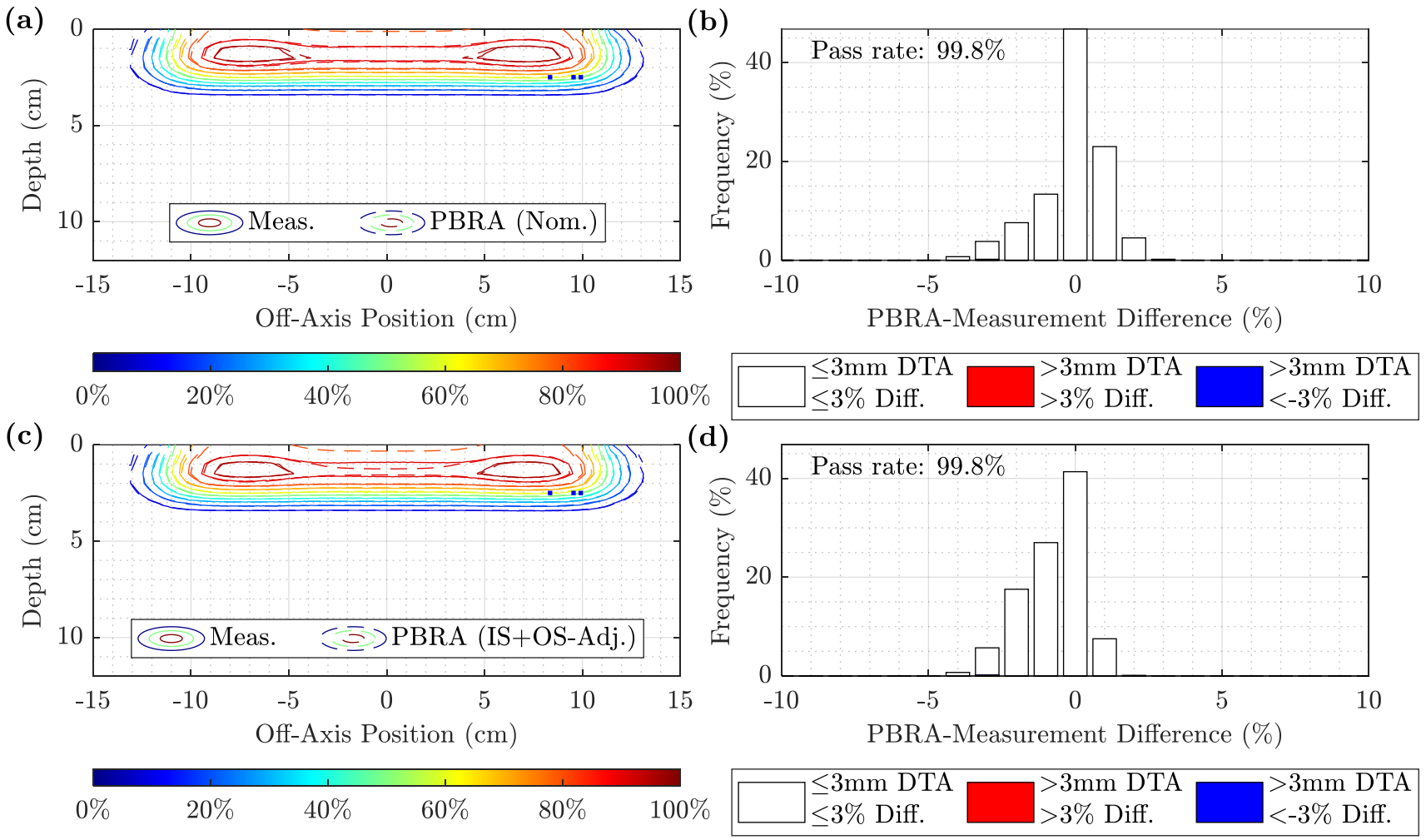

Figure D.58. Measured and PBRA-calculated isodose comparison and difference histograms for 0.158-cm pins at 7 MeV and 105 cm SSD using MC-based corrections. The isodose contours for measurement (solid) are compared to the PBRA calculations with (a) nominal and (c) MC-based IS+OS-corrected diameters. Difference histograms under 3%/3mm DTA criteria are plotted for (b) nominal and (d) MC-based IS+OS-corrected diameters. Points at which the PBRA underpredicted and overpredicted the dose relative to measurement are shown in blue and red, respectively. The nominal and corrected passing rates were both 99.8%.

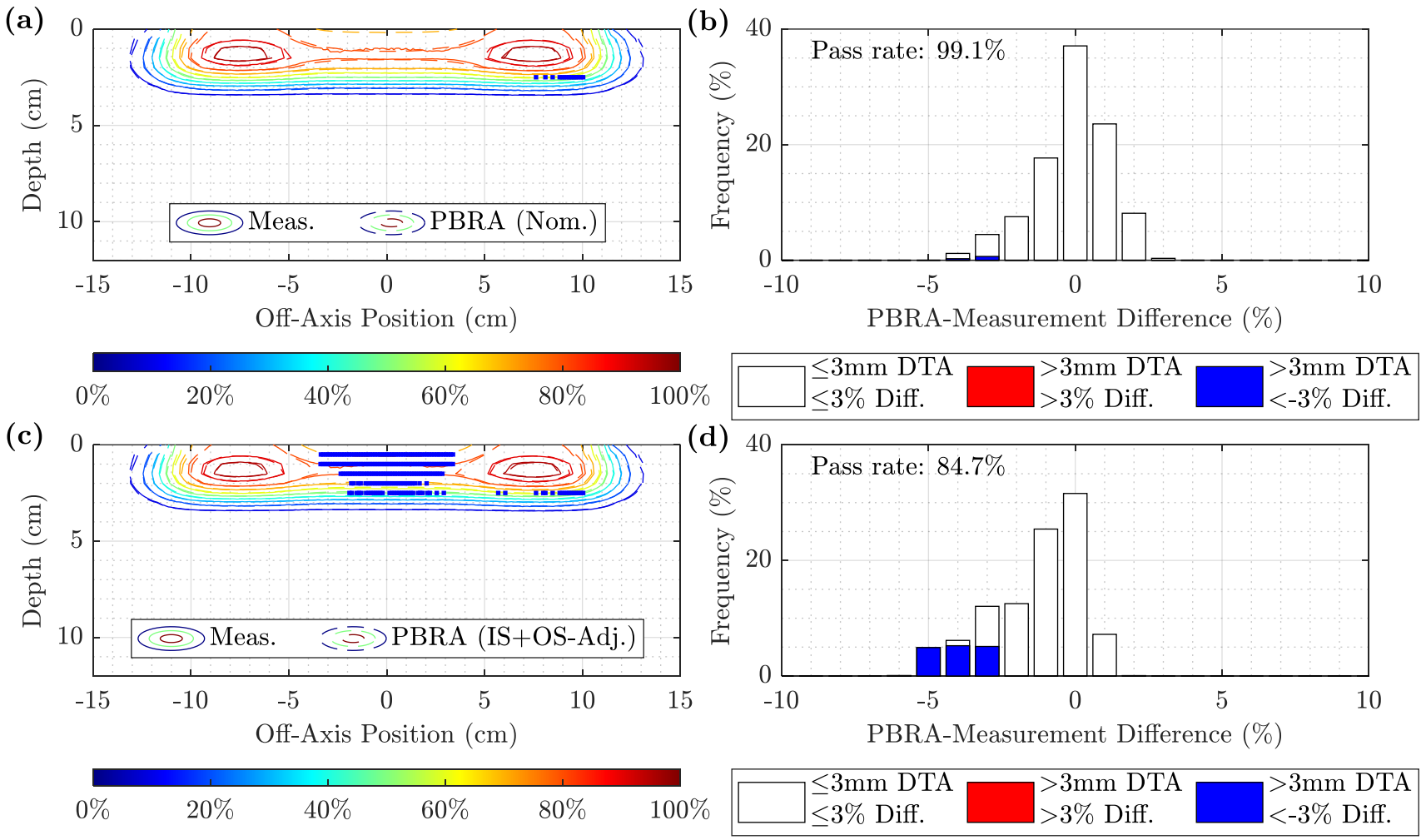

Figure D.59. Measured and PBRA-calculated isodose comparison and difference histograms for 0.273-cm pins at 7 MeV and 105 cm SSD using MC-based corrections. The isodose contours for measurement (solid) are compared to the PBRA calculations with (a) nominal and (c) MC-based IS+OS-corrected diameters. Difference histograms under 3%/3mm DTA criteria are plotted for (b) nominal and (d) MC-based IS+OS-corrected diameters. Points at which the PBRA underpredicted and overpredicted the dose relative to measurement are shown in blue and red, respectively. The nominal and corrected passing rates were 99.1% and 84.7%, respectively.

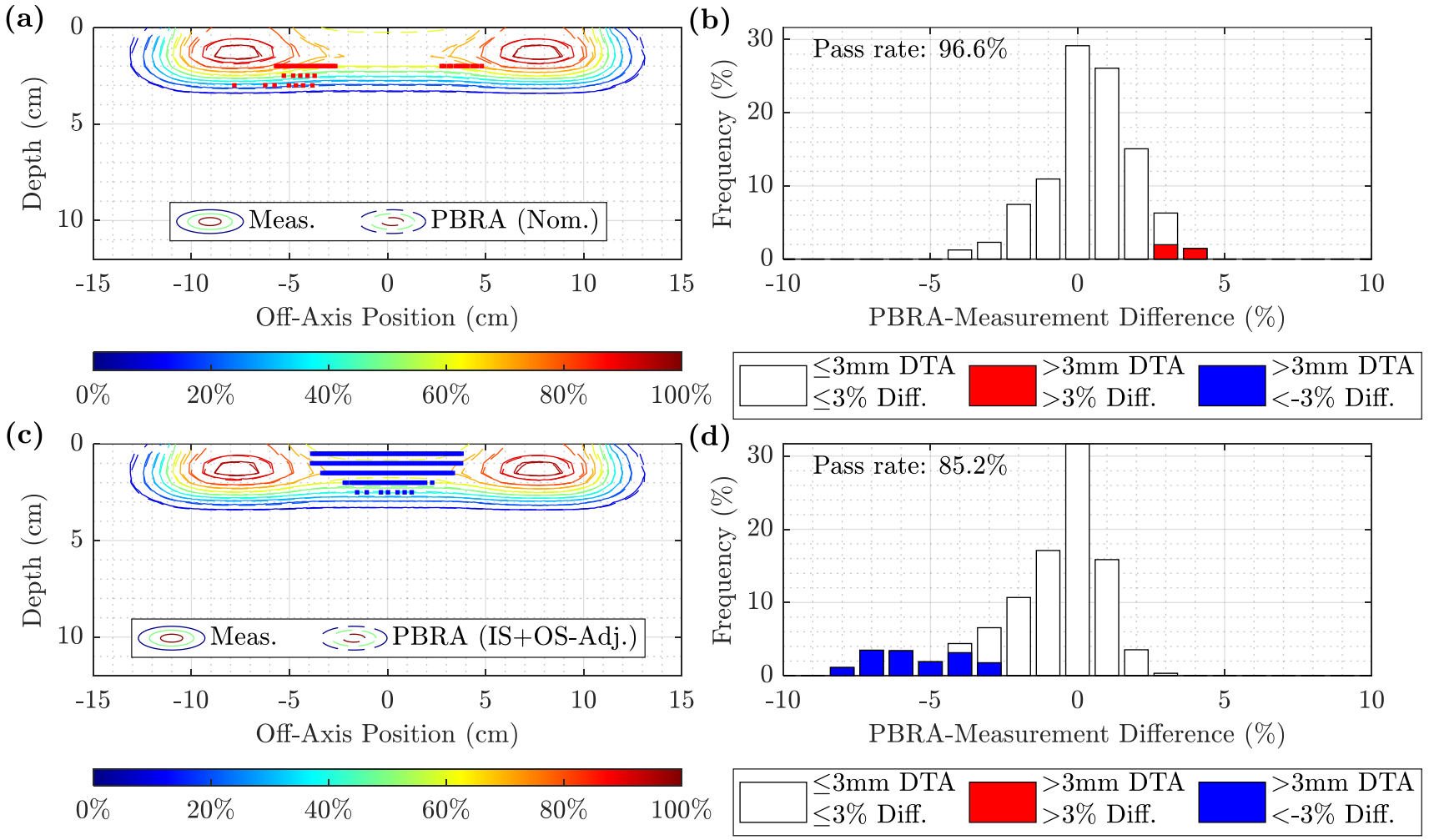

Figure D.60. Measured and PBRA-calculated isodose comparison and difference histograms for 0.352-cm pins at 7 MeV and 105 cm SSD using MC-based corrections. The isodose contours for measurement (solid) are compared to the PBRA calculations with (a) nominal and (c) MC-based IS+OS-corrected diameters. Difference histograms under 3%/3mm DTA criteria are plotted for (b) nominal and (d) MC-based IS+OS-corrected diameters. Points at which the PBRA underpredicted and overpredicted the dose relative to measurement are shown in blue and red, respectively. The nominal and corrected passing rates were 96.6% and 85.2%, respectively.

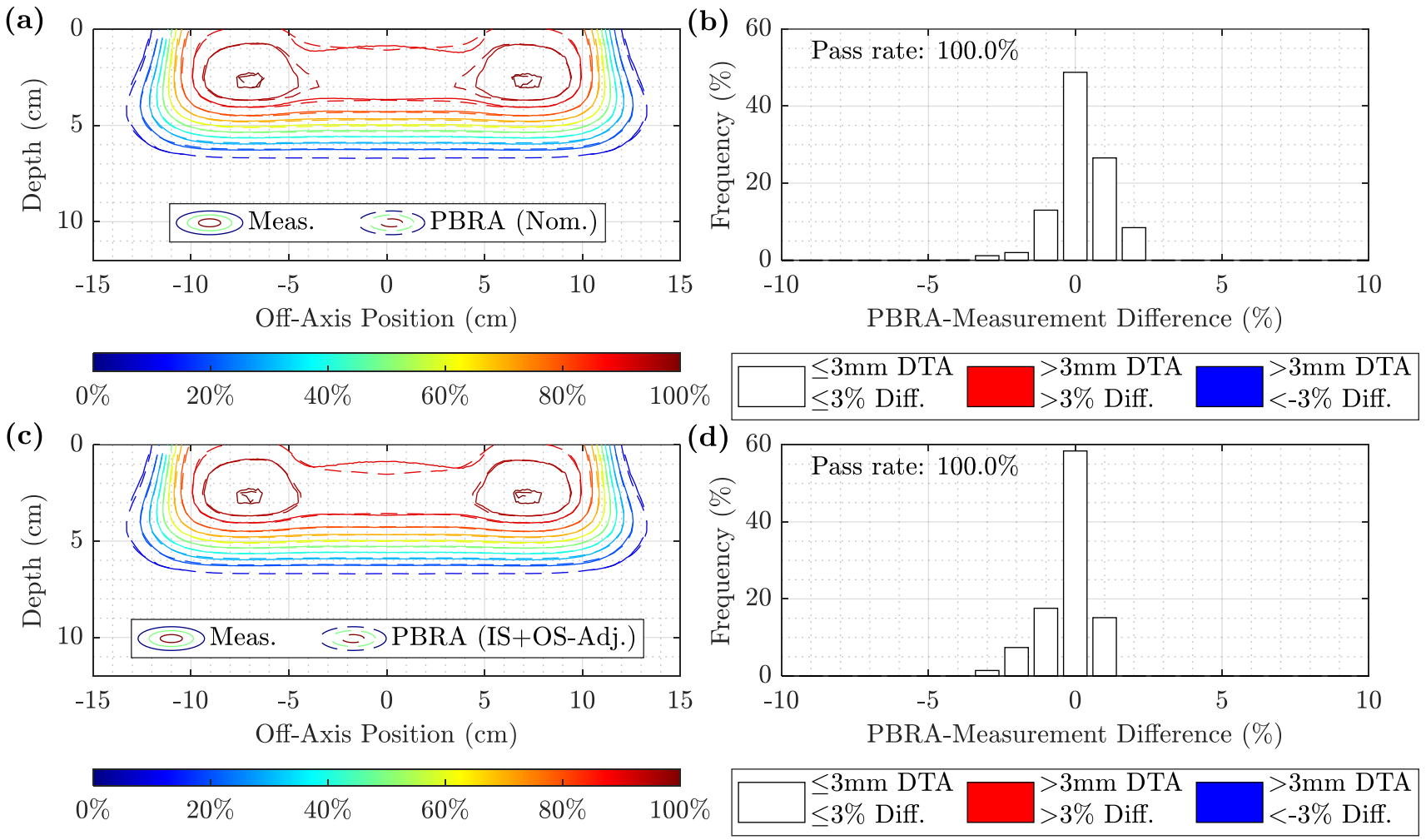

Figure D.61. Measured and PBRA-calculated isodose comparison and difference histograms for 0.158-cm pins at 13 MeV and 105 cm SSD using MC-based corrections. The isodose contours for measurement (solid) are compared to the PBRA calculations with (a) nominal and (c) MC-based IS+OS-corrected diameters. Difference histograms under 3%/3mm DTA criteria are plotted for (b) nominal and (d) MC-based IS+OS-corrected diameters. Points at which the PBRA underpredicted and overpredicted the dose relative to measurement are shown in blue and red, respectively. The nominal and corrected passing rates were both 100%.

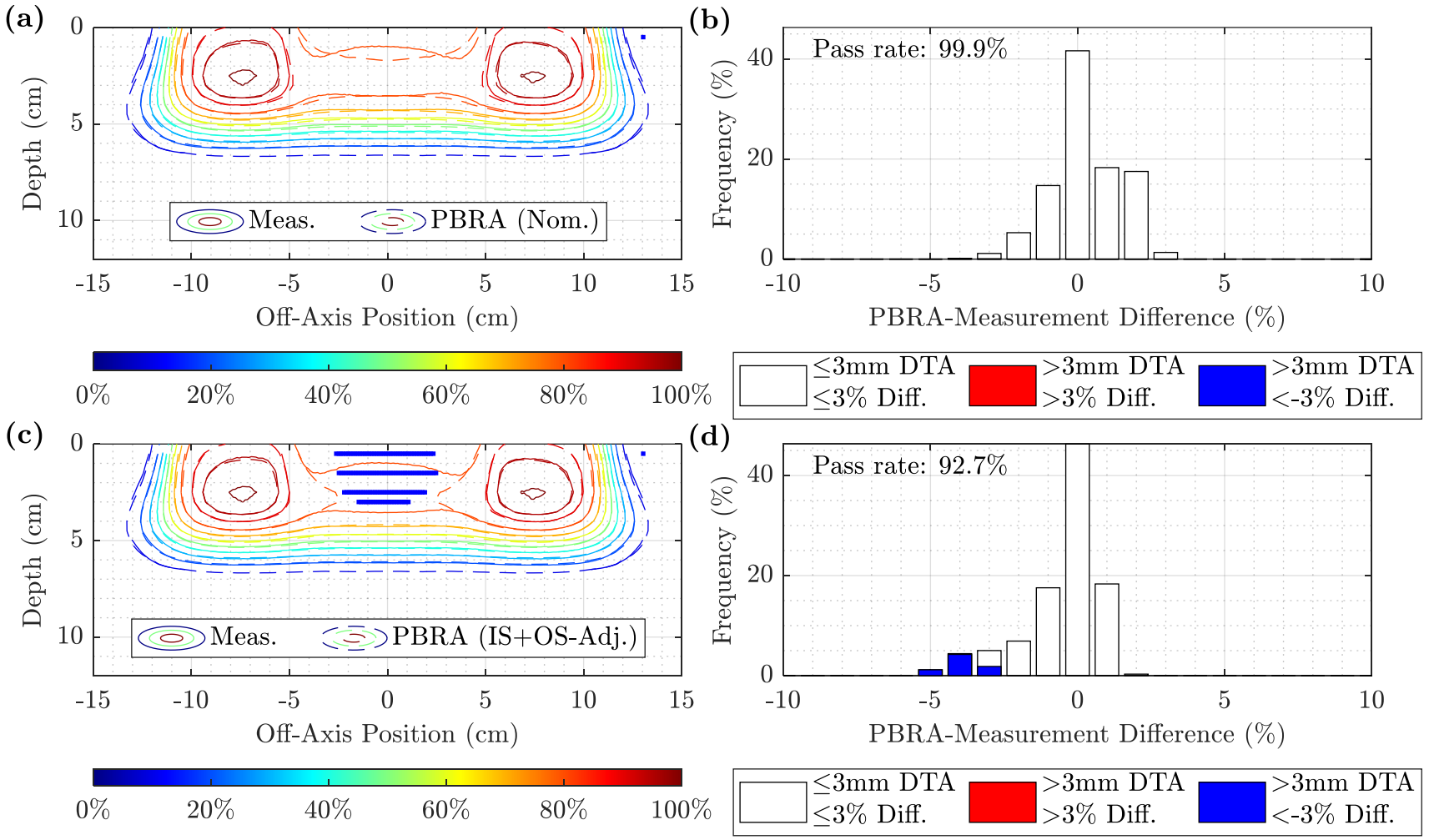

Figure D.62. Measured and PBRA-calculated isodose comparison and difference histograms for 0.273-cm pins at 13 MeV and 105 cm SSD using MC-based corrections. The isodose contours for measurement (solid) are compared to the PBRA calculations with (a) nominal and (c) MC-based IS+OS-corrected diameters. Difference histograms under 3%/3mm DTA criteria are plotted for (b) nominal and (d) MC-based IS+OS-corrected diameters. Points at which the PBRA underpredicted and overpredicted the dose relative to measurement are shown in blue and red, respectively. The nominal and corrected passing rates were 99.9% and 92.7%, respectively.

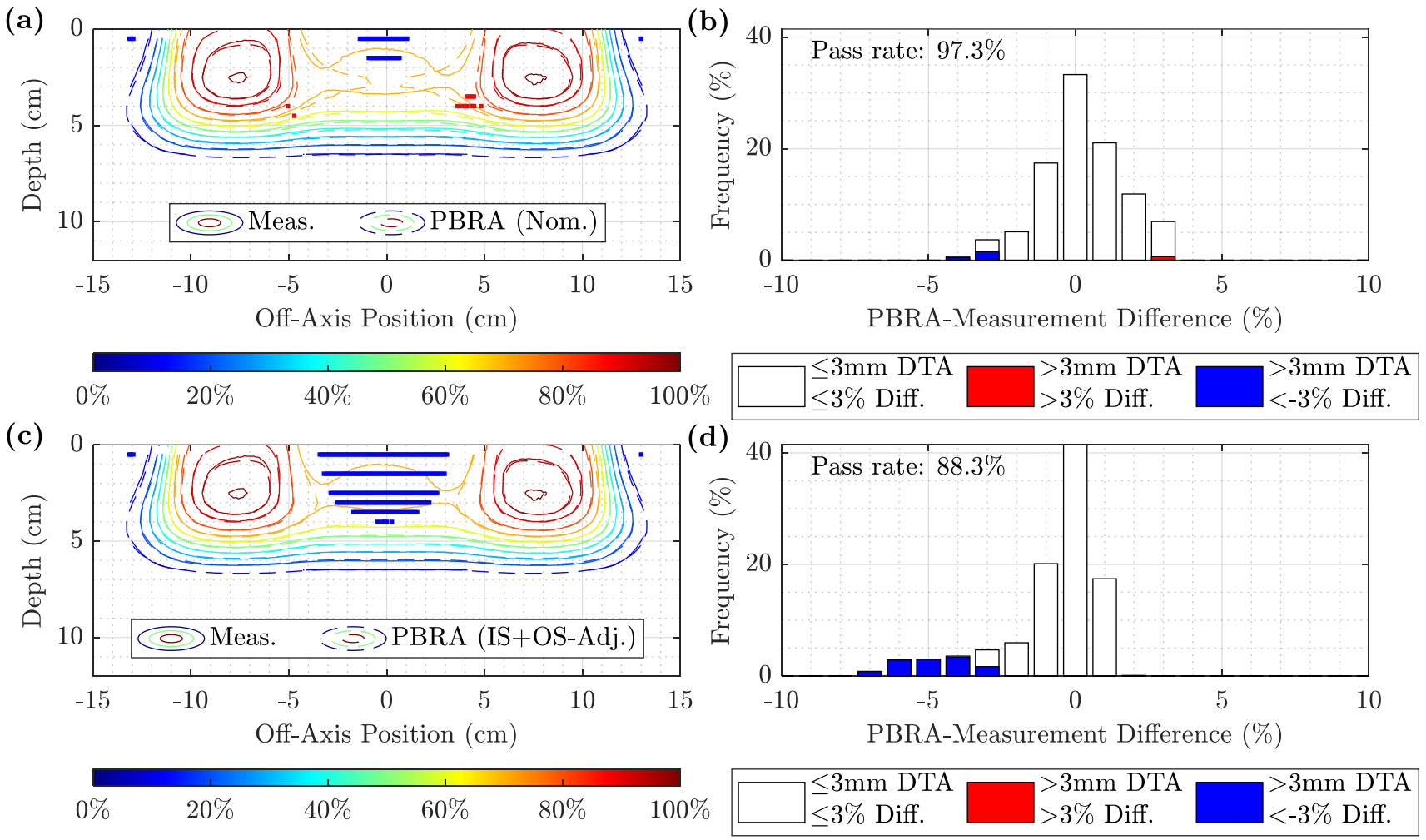

Figure D.63. Measured and PBRA-calculated isodose comparison and difference histograms for 0.352-cm pins at 13 MeV and 105 cm SSD using MC-based corrections. The isodose contours for measurement (solid) are compared to the PBRA calculations with (a) nominal and (c) MC-based IS+OS-corrected diameters. Difference histograms under 3%/3mm DTA criteria are plotted for (b) nominal and (d) MC-based IS+OS-corrected diameters. Points at which the PBRA underpredicted and overpredicted the dose relative to measurement are shown in blue and red, respectively. The nominal and corrected passing rates were 97.3% and 88.3%, respectively.

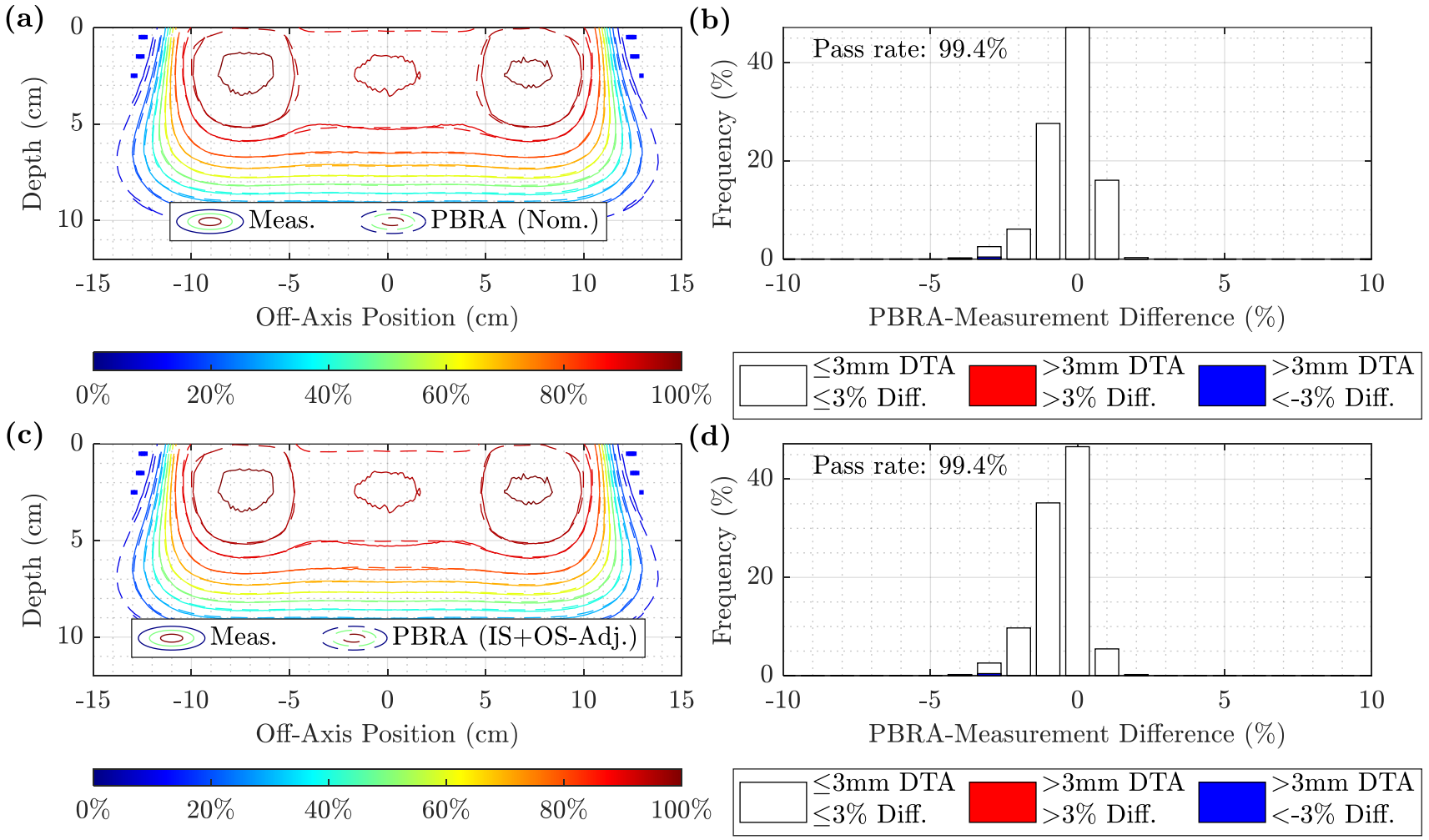

Figure D.64. Measured and PBRA-calculated isodose comparison and difference histograms for 0.158-cm pins at 20 MeV and 105 cm SSD using MC-based corrections. The isodose contours for measurement (solid) are compared to the PBRA calculations with (a) nominal and (c) MC-based IS+OS-corrected diameters. Difference histograms under 3%/3mm DTA criteria are plotted for (b) nominal and (d) MC-based IS+OS-corrected diameters. Points at which the PBRA underpredicted and overpredicted the dose relative to measurement are shown in blue and red, respectively. The nominal and corrected passing rates were both 99.4%.

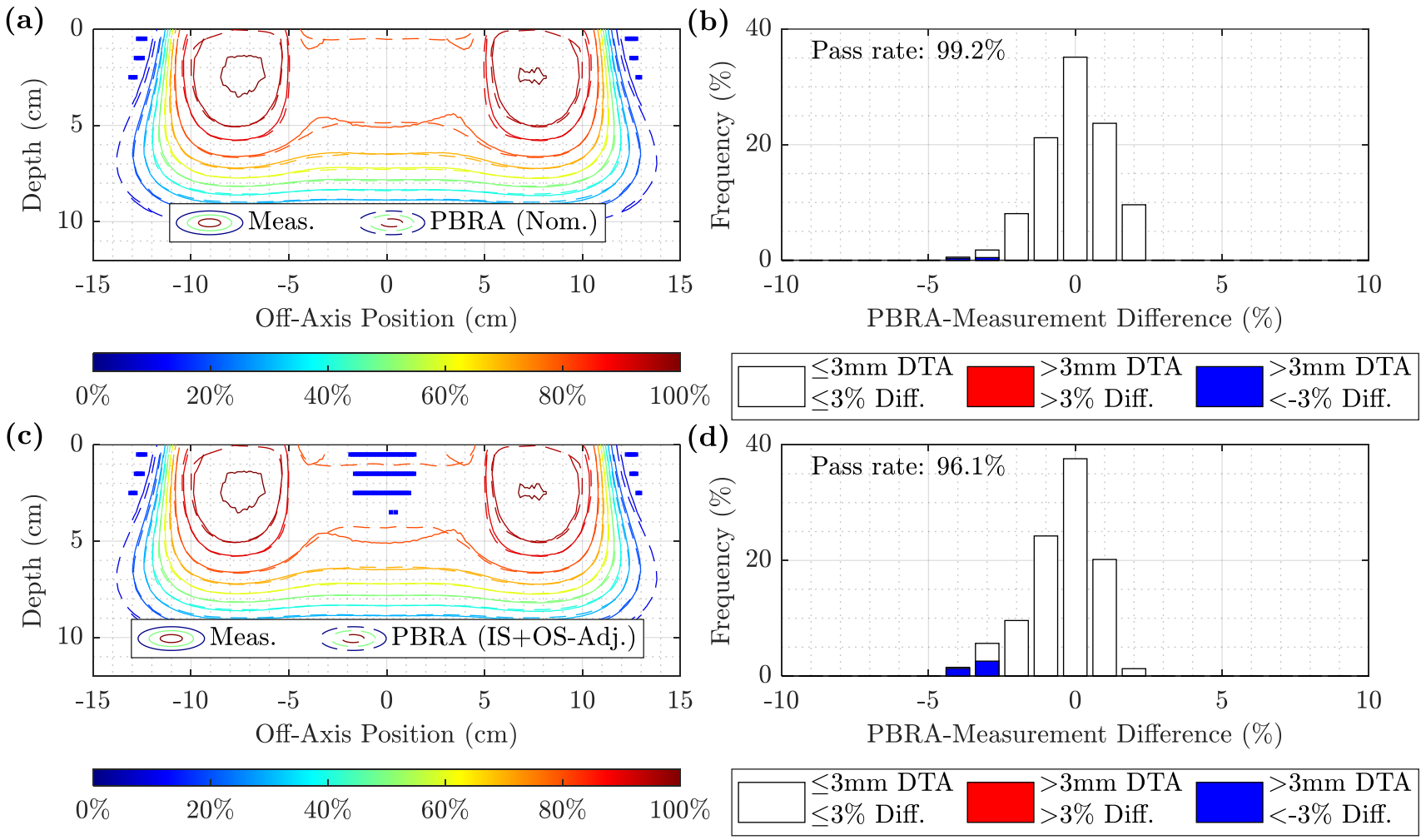

Figure D.65. Measured and PBRA-calculated isodose comparison and difference histograms for 0.273-cm pins at 20 MeV and 105 cm SSD using MC-based corrections. The isodose contours for measurement (solid) are compared to the PBRA calculations with (a) nominal and (c) MC-based IS+OS-corrected diameters. Difference histograms under 3%/3mm DTA criteria are plotted for (b) nominal and (d) MC-based IS+OS-corrected diameters. Points at which the PBRA underpredicted and overpredicted the dose relative to measurement are shown in blue and red, respectively. The nominal and corrected passing rates were 99.2% and 96.1%, respectively.

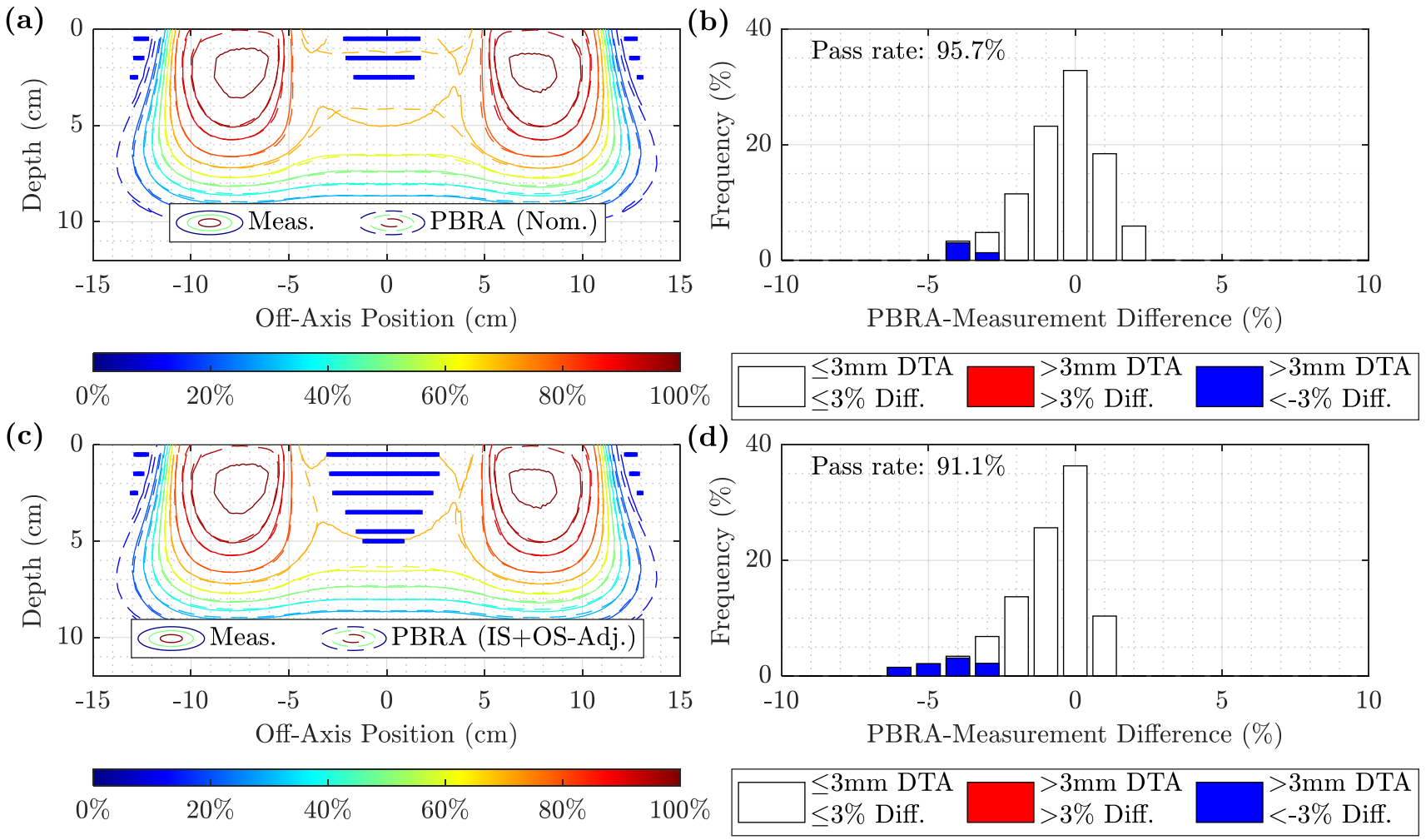

Figure D.66. Measured and PBRA-calculated isodose comparison and difference histograms for 0.352-cm pins at 20 MeV and 105 cm SSD using MC-based corrections. The isodose contours for measurement (solid) are compared to the PBRA calculations with (a) nominal and (c) MC-based IS+OS-corrected diameters. Difference histograms under 3%/3mm DTA criteria are plotted for (b) nominal and (d) MC-based IS+OS-corrected diameters. Points at which the PBRA underpredicted and overpredicted the dose relative to measurement are shown in blue and red, respectively. The nominal and corrected passing rates were 95.7% and 91.1%, respectively.

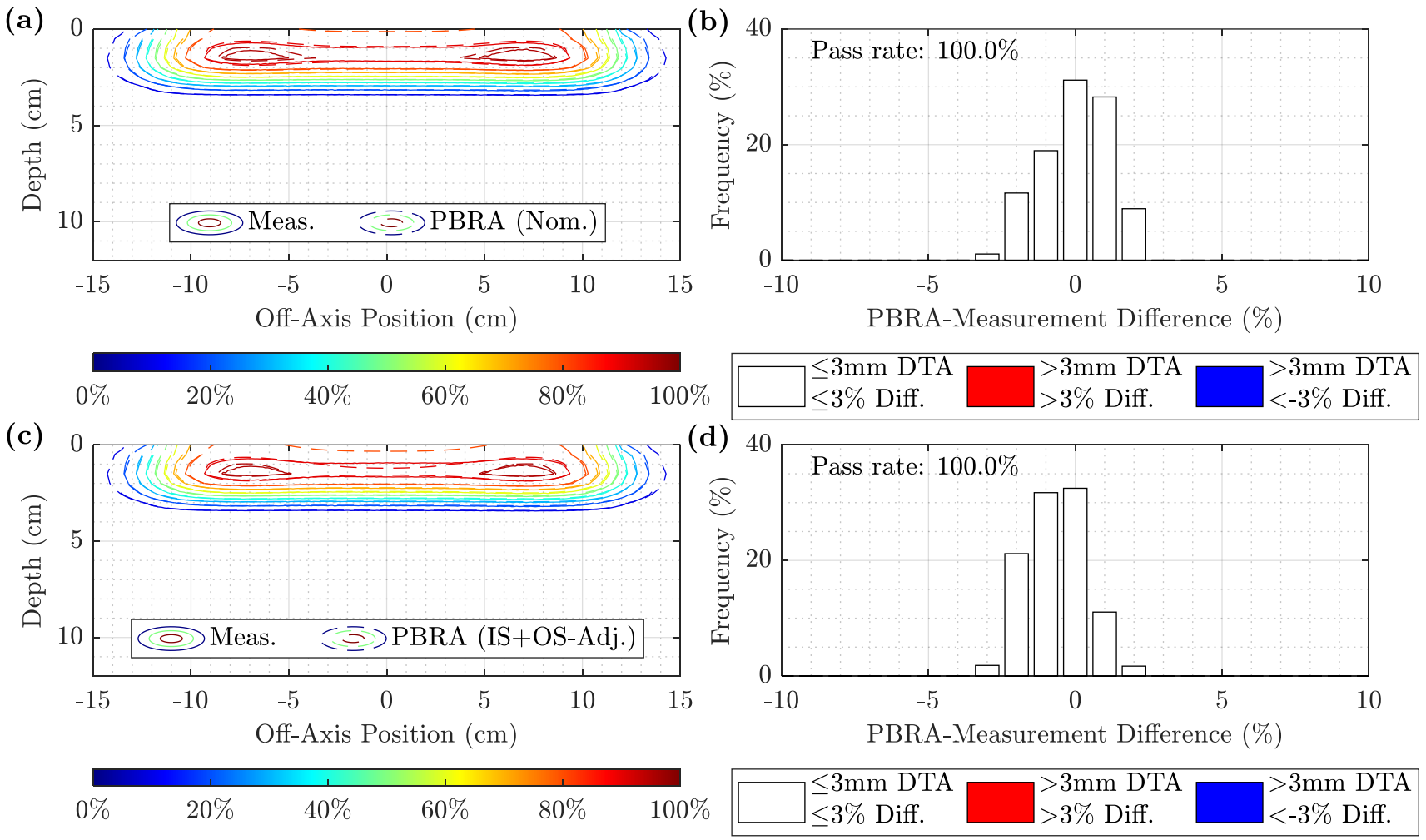

Figure D.67. Measured and PBRA-calculated isodose comparison and difference histograms for 0.158-cm pins at 7 MeV and 110 cm SSD using MC-based corrections. The isodose contours for measurement (solid) are compared to the PBRA calculations with (a) nominal and (c) MC-based IS+OS-corrected diameters. Difference histograms under 3%/3mm DTA criteria are plotted for (b) nominal and (d) MC-based IS+OS-corrected diameters. Points at which the PBRA underpredicted and overpredicted the dose relative to measurement are shown in blue and red, respectively. The nominal and corrected passing rates were both 100%.

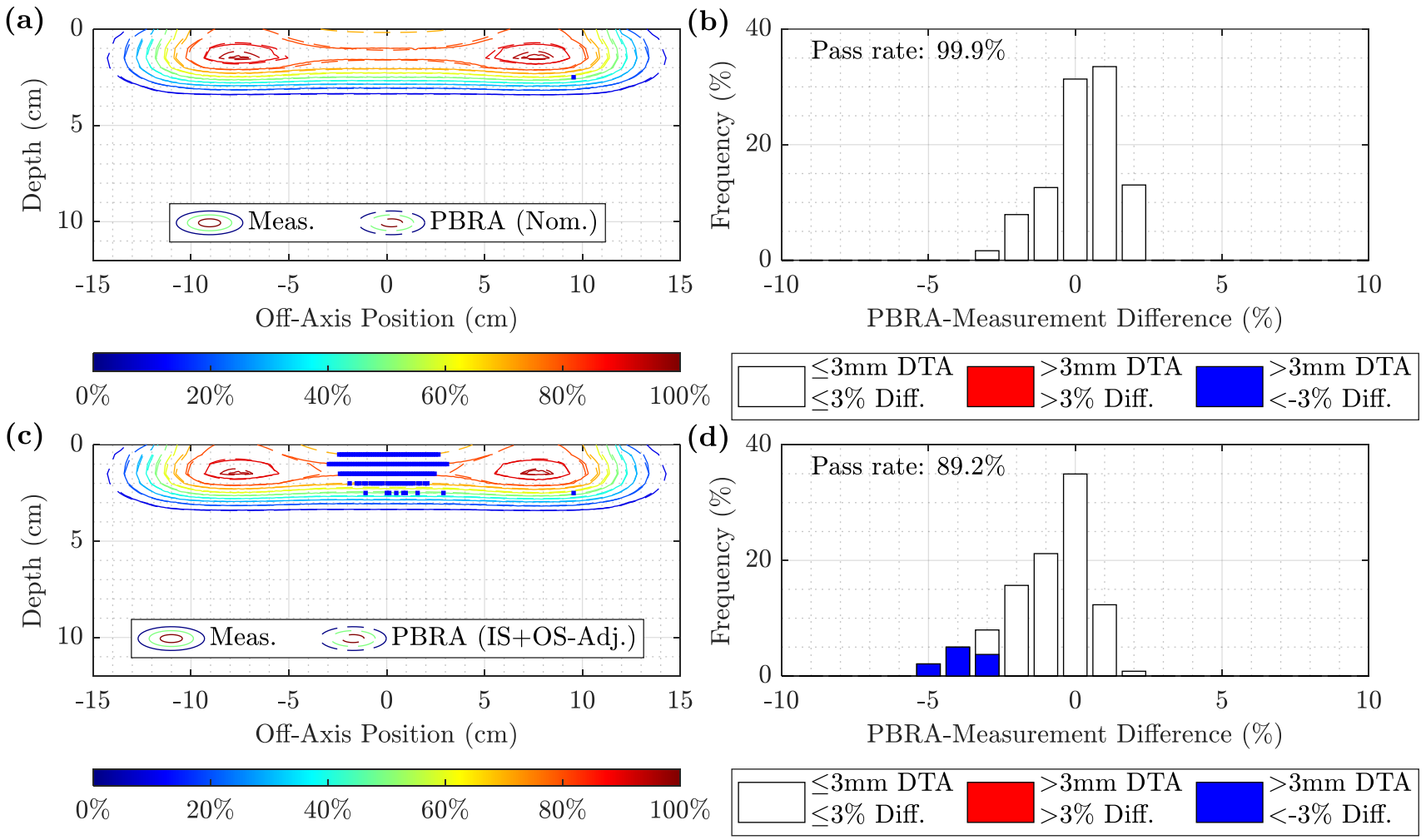

Figure D.68. Measured and PBRA-calculated isodose comparison and difference histograms for 0.273-cm pins at 7 MeV and 110 cm SSD using MC-based corrections. The isodose contours for measurement (solid) are compared to the PBRA calculations with (a) nominal and (c) MC-based IS+OS-corrected diameters. Difference histograms under 3%/3mm DTA criteria are plotted for (b) nominal and (d) MC-based IS+OS-corrected diameters. Points at which the PBRA underpredicted and overpredicted the dose relative to measurement are shown in blue and red, respectively. The nominal and corrected passing rates were 99.9% and 89.2%, respectively.

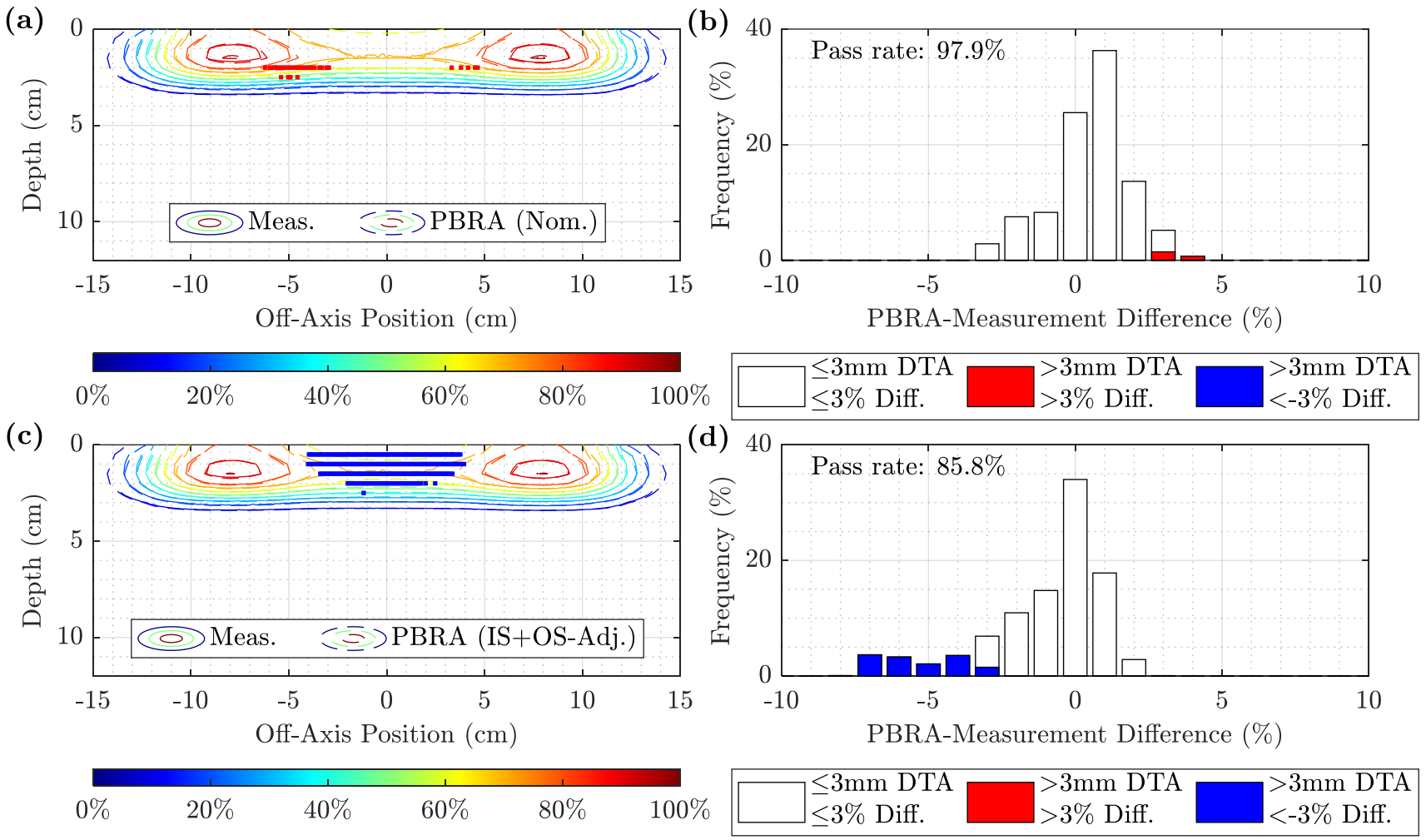

Figure D.69. Measured and PBRA-calculated isodose comparison and difference histograms for 0.352-cm pins at 7 MeV and 110 cm SSD using MC-based corrections. The isodose contours for measurement (solid) are compared to the PBRA calculations with (a) nominal and (c) MC-based IS+OS-corrected diameters. Difference histograms under 3%/3mm DTA criteria are plotted for (b) nominal and (d) MC-based IS+OS-corrected diameters. Points at which the PBRA underpredicted and overpredicted the dose relative to measurement are shown in blue and red, respectively. The nominal and corrected passing rates were 97.9% and 85.8%, respectively.

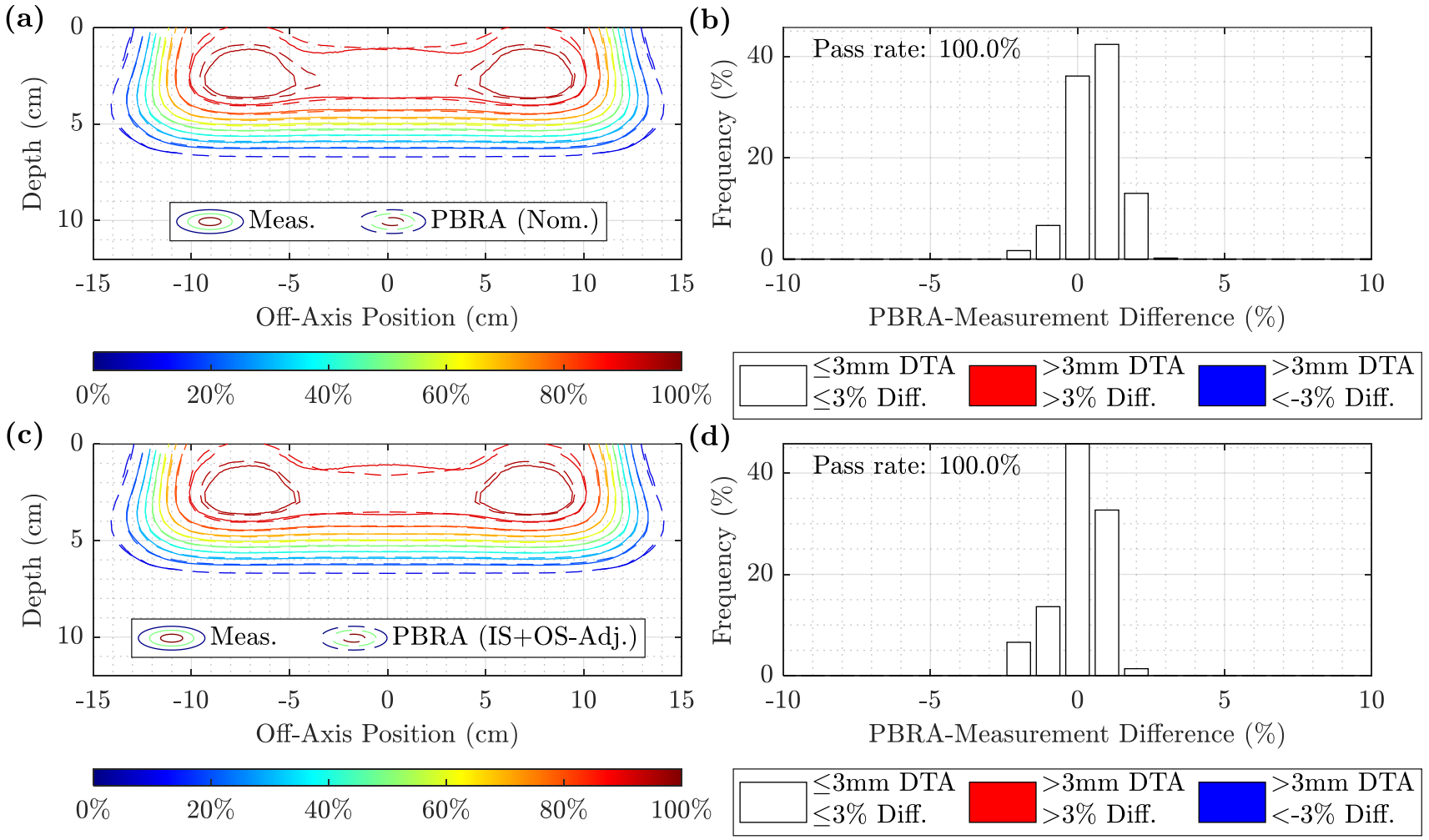

Figure D.70. Measured and PBRA-calculated isodose comparison and difference histograms for 0.158-cm pins at 13 MeV and 110 cm SSD using MC-based corrections. The isodose contours for measurement (solid) are compared to the PBRA calculations with (a) nominal and (c) MC-based IS+OS-corrected diameters. Difference histograms under 3%/3mm DTA criteria are plotted for (b) nominal and (d) MC-based IS+OS-corrected diameters. Points at which the PBRA underpredicted and overpredicted the dose relative to measurement are shown in blue and red, respectively. The nominal and corrected passing rates were both 100%.

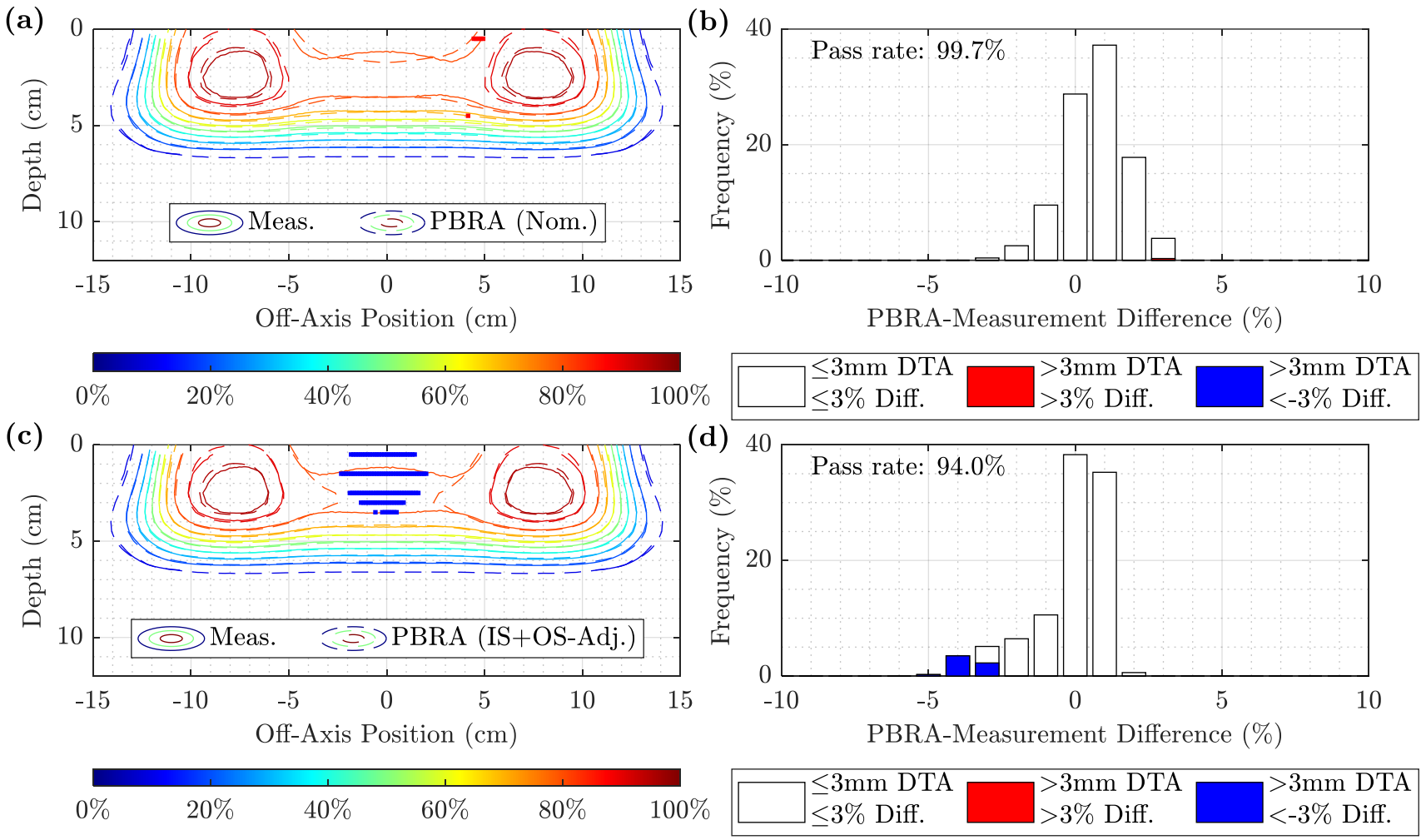

Figure D.71. Measured and PBRA-calculated isodose comparison and difference histograms for 0.273-cm pins at 13 MeV and 110 cm SSD using MC-based corrections. The isodose contours for measurement (solid) are compared to the PBRA calculations with (a) nominal and (c) MC-based IS+OS-corrected diameters. Difference histograms under 3%/3mm DTA criteria are plotted for (b) nominal and (d) MC-based IS+OS-corrected diameters. Points at which the PBRA underpredicted and overpredicted the dose relative to measurement are shown in blue and red, respectively. The nominal and corrected passing rates were 99.7% and 94.0%, respectively.

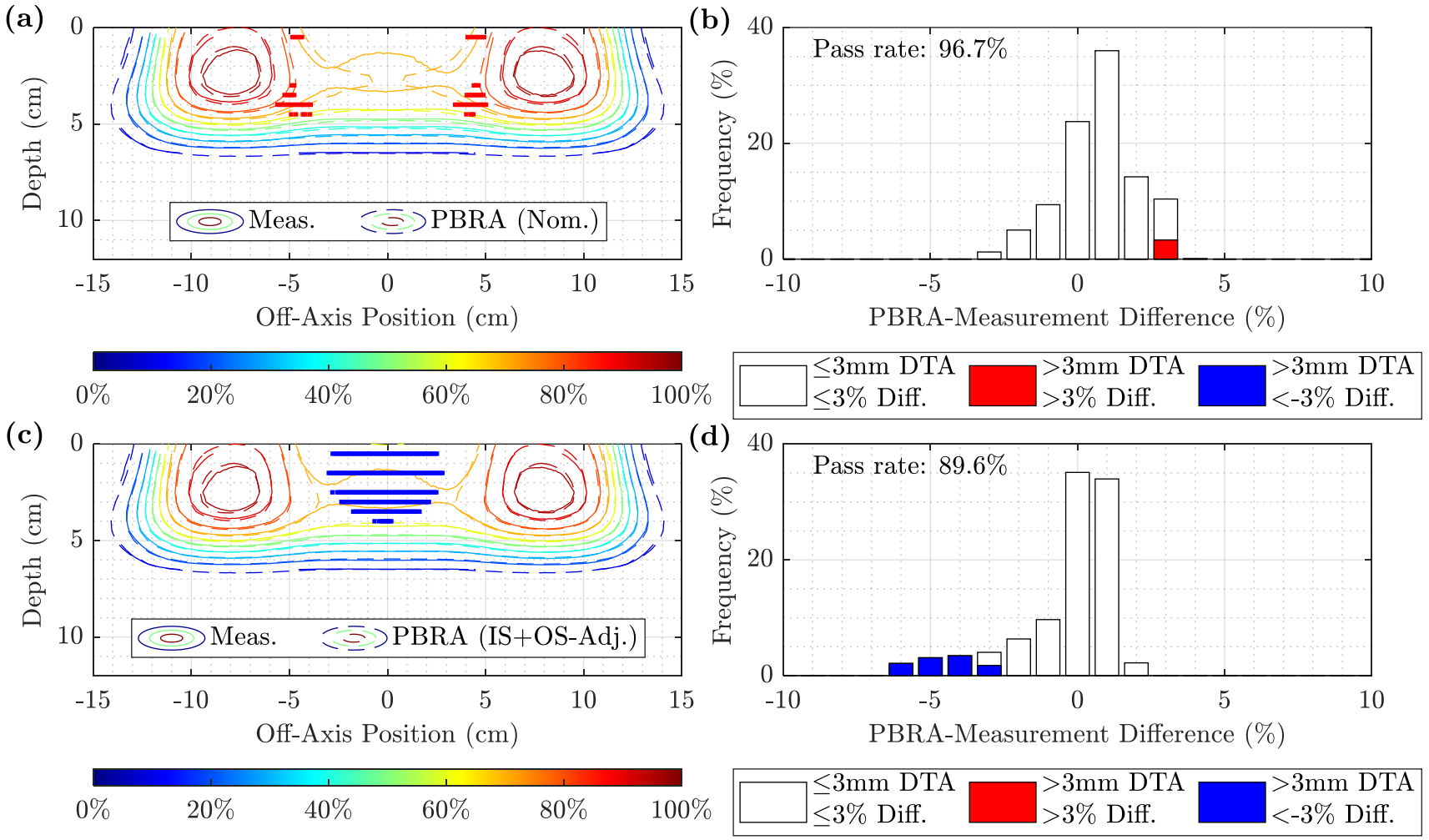

Figure D.72. Measured and PBRA-calculated isodose comparison and difference histograms for 0.352-cm pins at 13 MeV and 110 cm SSD using MC-based corrections. The isodose contours for measurement (solid) are compared to the PBRA calculations with (a) nominal and (c) MC-based IS+OS-corrected diameters. Difference histograms under 3%/3mm DTA criteria are plotted for (b) nominal and (d) MC-based IS+OS-corrected diameters. Points at which the PBRA underpredicted and overpredicted the dose relative to measurement are shown in blue and red, respectively. The nominal and corrected passing rates were 96.7% and 89.6%, respectively.

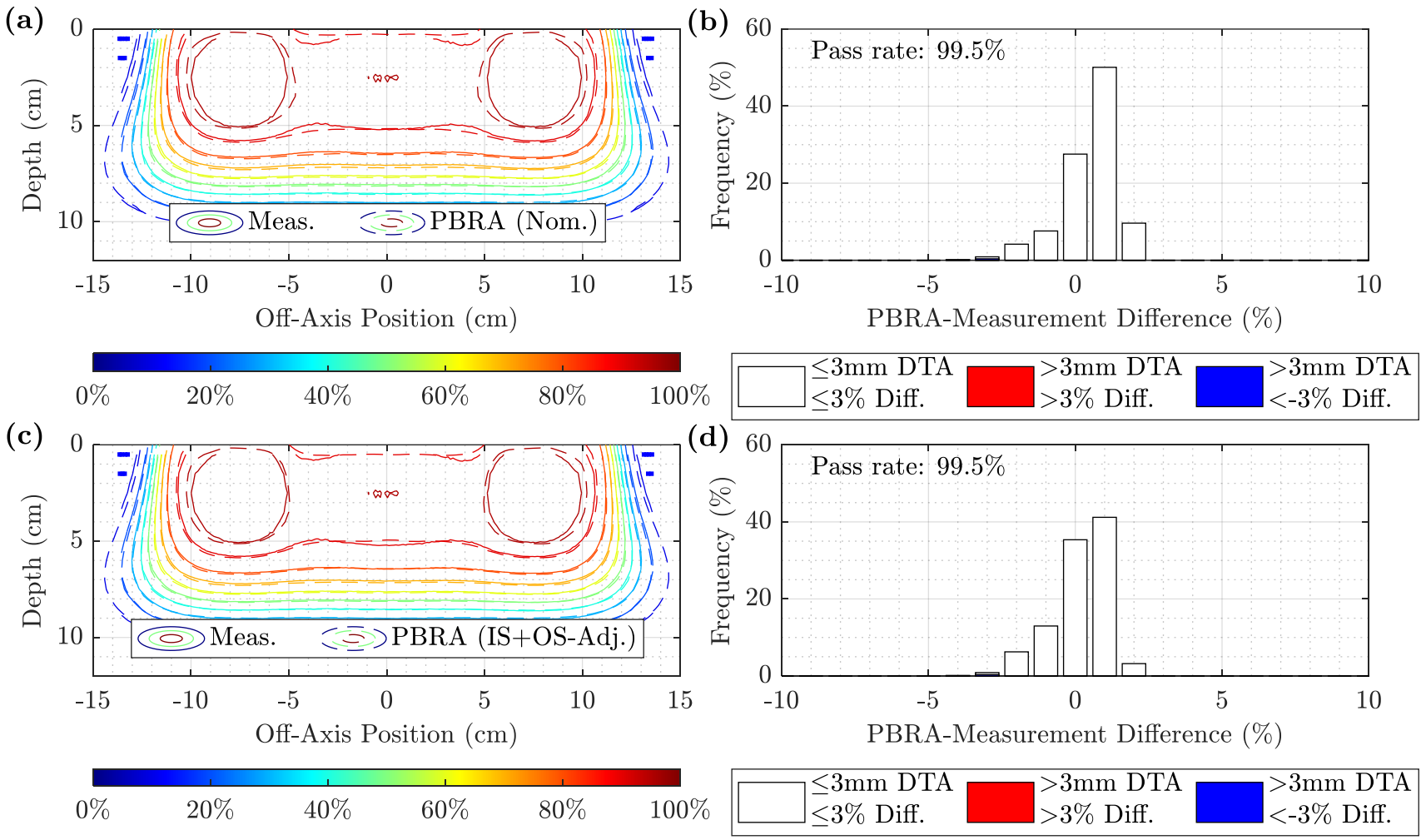

Figure D.73. Measured and PBRA-calculated isodose comparison and difference histograms for 0.158-cm pins at 20 MeV and 110 cm SSD using MC-based corrections. The isodose contours for measurement (solid) are compared to the PBRA calculations with (a) nominal and (c) MC-based IS+OS-corrected diameters. Difference histograms under 3%/3mm DTA criteria are plotted for (b) nominal and (d) MC-based IS+OS-corrected diameters. Points at which the PBRA underpredicted and overpredicted the dose relative to measurement are shown in blue and red, respectively. The nominal and corrected passing rates were both 99.5%.

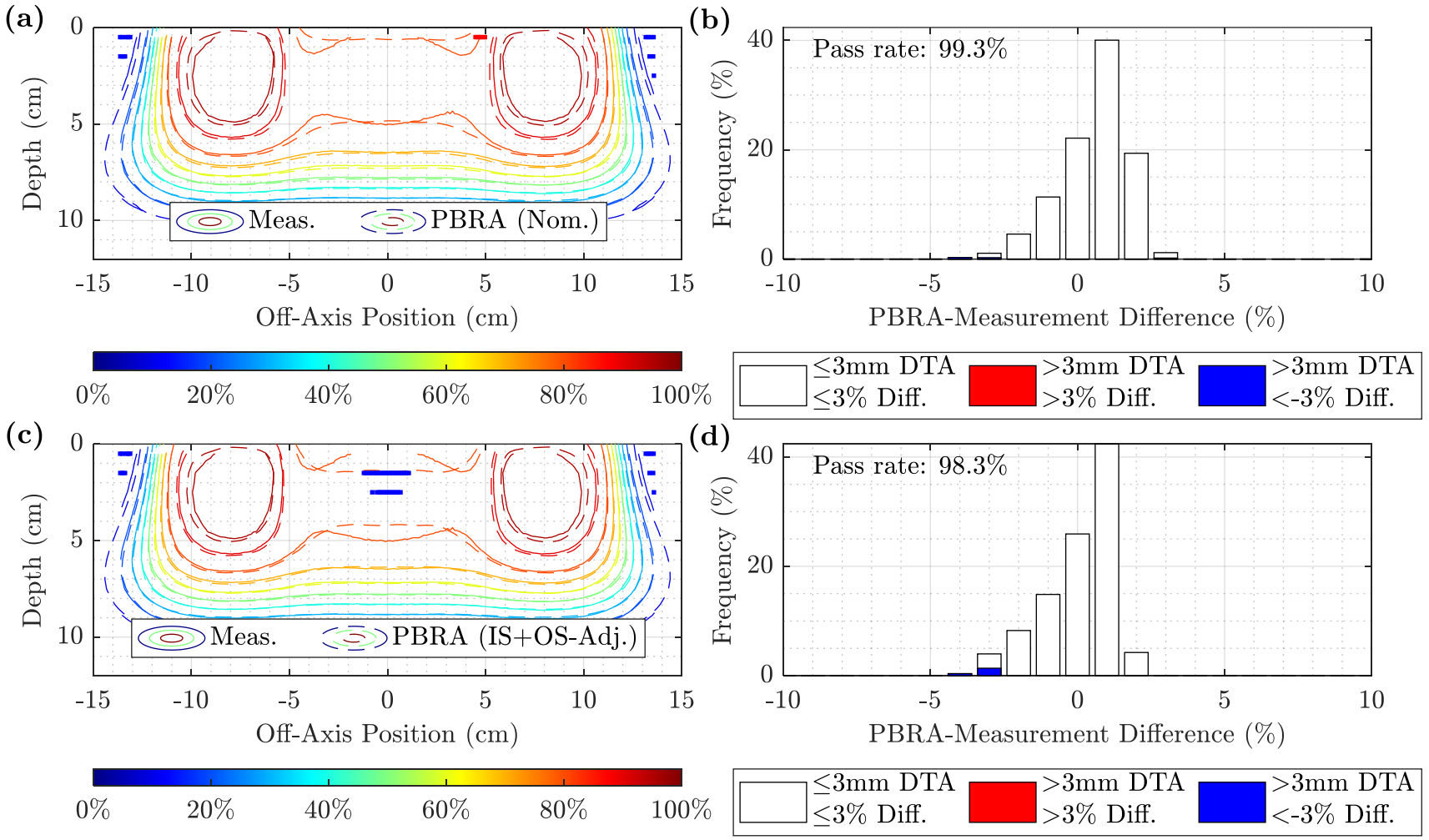

Figure D.74. Measured and PBRA-calculated isodose comparison and difference histograms for 0.273-cm pins at 20 MeV and 110 cm SSD using MC-based corrections. The isodose contours for measurement (solid) are compared to the PBRA calculations with (a) nominal and (c) MC-based IS+OS-corrected diameters. Difference histograms under 3%/3mm DTA criteria are plotted for (b) nominal and (d) MC-based IS+OS-corrected diameters. Points at which the PBRA underpredicted and overpredicted the dose relative to measurement are shown in blue and red, respectively. The nominal and corrected passing rates were 99.3% and 98.3%, respectively.

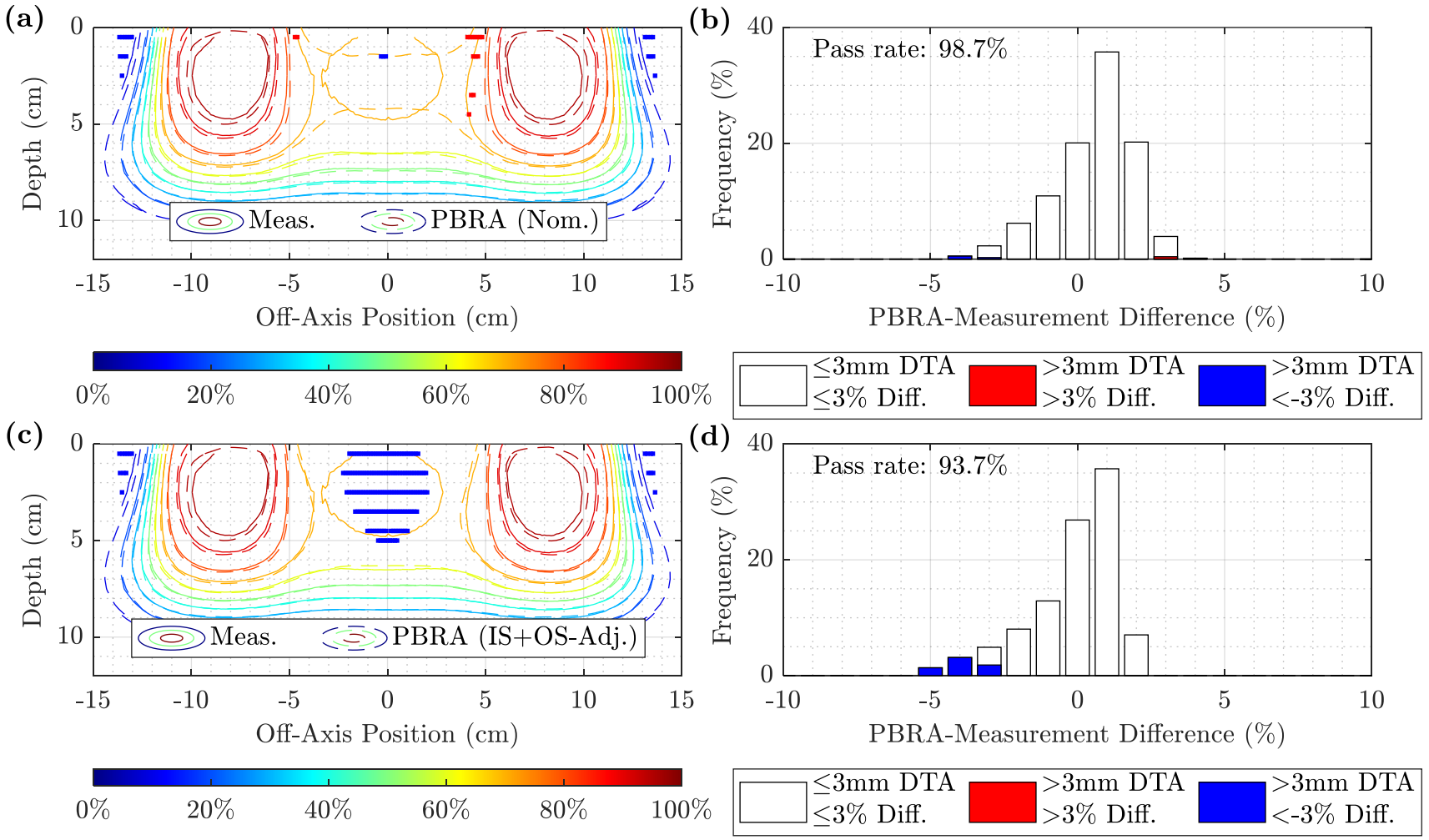

Figure D.75. Measured and PBRA-calculated isodose comparison and difference histograms for 0.352-cm pins at 20 MeV and 110 cm SSD using MC-based corrections. The isodose contours for measurement (solid) are compared to the PBRA calculations with (a) nominal and (c) MC-based IS+OS-corrected diameters. Difference histograms under 3%/3mm DTA criteria are plotted for (b) nominal and (d) MC-based IS+OS-corrected diameters. Points at which the PBRA underpredicted and overpredicted the dose relative to measurement are shown in blue and red, respectively. The nominal and corrected passing rates were 98.7% and 93.7%, respectively.

D.3.4. Discussion

The MC-based correction provided little to no improvement over the nominal diameters for any beam energy, SSD, and pin diameter combination. As seen in the MC-estimated and measured PDD and profile comparisons of Figures D.16-24, the MC method fails to predict the out-scatter dose accurately, particularly near CAX under the modulated region and near the surface. Similar passing rates at the smallest pin diameter are likely because the perturbation is relatively small and within the 3% criteria applied.

Originally based on this comparison, it was concluded that the MC-based corrections should not be used, i.e. the MC-based out-scatter corrections seemed insufficient for creating a suitable adjustment to the PBRA due to an inaccurate accounting for the out-scatter component. The MC-estimated distributions predicted a lower dose relative to measurement (Figures D.19-24) and nominal PBRA calculations (Figures D.49-75).

However, upon conclusion of this study, it was discovered that the island blocks used in this study were mistakenly fabricated with the axes of the cylindrical tungsten pins projected to a virtual source 93.4 cm downstream (i.e. converging) rather than 93.4 cm upstream (i.e. diverging) from the collimator. Based on data by Hilliard (2018), this error could increase measured CAX dose by as much as 4%. Hence, abandoning the MC correction method may not be necessary. However, measurements under a correctly fabricated device with diverging pins and reanalysis of the data will be required.

D.4. Effect of foam medium in MC model on in-scattering

The exact chemical composition of the machinable foam was unknown, so it was instead modeled in MC calculations (Figure D.2.a) as a 0.11-cm-thick water slab resulting in the same energy loss as the foam found by Hilliard (2018). However, this downstream placement results in

in-scatter being underestimated since the imbedding material is air rather than denser foam. Conversely, an upstream placement of the water slab would likely overestimate in-scatter losses. To determine the effect of this approximation, the in-scatter modeling of Chapter 2 was repeated treating the imbedding medium as air, and then the results were compared to those calculated under polyethylene (i.e. the results of Chapter 2).

D.4.1. Methods

The analysis of Chapter 2 was repeated, but the 0.6-cm of imbedding medium was taken to be air at SATP conditions (ρ = 1.2048×10^{-3} g·cm^{-3}) rather than polyethylene. The sigma terms with this consideration were calculated (Equation 2.15) at each beam energy in Table 2.3 using the mass scattering powers in Table D.17. The *f*-factors, in-scatter-adjusted diameters, and in-scatter-adjusted IRFs were then evaluated.

Table D.17. Mass scattering powers for air. The mass scattering powers for air are partially reproduced from Table 2.6 of ICRU 35 (Svensson *et al.*, 1984).

Beam Energy (MeV)	Mass Scattering Power (radians^2 · cm^2 · g^{-1})
6.0	1.70E-1
8.0	1.03E-1
10.0	6.98E-2
15.0	3.38E-2
20.0	2.01E-2

D.4.2. Results

The sigma terms for both air and polyethylene are contained in Table D.18. Taking the imbedding medium to be air has no effect on σ_x relative to the clinical value ($\sigma_{\theta_x,\text{clinical}} \cdot t$), whereas polyethylene increased the value by 10-13%.

Table D.19 lists the *f*-factors, in-scatter-adjusted diameters, and in-scatter-adjusted IRFs for both polyethylene and air imbedding media. The average and maximum differences in IRF_{IS} between the media are 0.003 and 0.006 relative to the open field planar fluence (1.000). Relative to the polyethylene IRF_{IS}, the average increase in IRF_{IS} was 0.4% under air and the maximum value was 0.9% for the extreme case (7 MeV and 0.352 cm), resulting in in-scatter-adjusted diameters of 0.386 cm with polyethylene and 0.383 cm with air.

Table D.18. Comparison of impact of machinable foam material on in-scatter sigma. The contribution of the foam is calculated by Equation 2.14 from the tabulated mass scattering power data in Table 2.2 for polyethylene and Table D.17 for air with intermediate values determined by interpolation. The RMS of the spatial distribution is evaluated using these data and Equation 2.15. The results with and without the foam in place are compared in the last two columns. The pin height, *t*, is 0.6 cm.

Beam Energy (MeV)	$\sigma_{\theta_x,\text{clinical}}$ (radians)	$\sigma_{x,\text{foam}}$ (cm)		σ_x (cm)		$\frac{\sigma_x}{\sigma_{\theta_x,\text{clinical}} \cdot t}$	
		Poly.	Air	Poly.	Air	Poly.	Air
7	0.0626	0.0184	0.0024	0.0418	0.0376	1.11	1.00
9	0.0535	0.0148	0.0019	0.0353	0.0322	1.10	1.00
10	0.0476	0.0134	0.0017	0.0315	0.0286	1.10	1.00
11	0.0420	0.0124	0.0016	0.0281	0.0253	1.12	1.00
13	0.0383	0.0107	0.0014	0.0253	0.0230	1.10	1.00
16	0.0296	0.0088	0.0011	0.0198	0.0178	1.11	1.00
20	0.0234	0.0072	0.0009	0.0158	0.0141	1.13	1.00

Table D.19. Comparison of in-scatter-adjusted diameters and IRFs for polyethylene and air imbedding materials for 7-20 MeV. The nominal pin diameters are tabulated. The f-factors are calculated from Equation 2.8 and the data in Table D.18 for beam energies 7-20 MeV. The in-scattered-adjusted diameters and IRFs were evaluated with these for Equations 2.10 and 2.11, respectively. The maximum difference in IRF_{IS} for air was 0.9% relative to IRF_{IS} for polyethylene.

Energy (MeV)	d (cm)	f		d_{IS} (cm)		IRF_{IS}	
		Poly.	Air	Poly.	Air	Poly.	Air
7	0.158	0.420	0.383	0.188	0.186	0.911	0.913
7	0.223	0.309	0.281	0.255	0.252	0.836	0.840
7	0.273	0.257	0.233	0.306	0.303	0.764	0.768
7	0.315	0.225	0.203	0.349	0.345	0.694	0.699
7	0.352	0.202	0.183	0.386	0.383	0.625	0.631
9	0.158	0.362	0.333	0.184	0.182	0.914	0.916
9	0.223	0.265	0.243	0.251	0.249	0.842	0.845
9	0.273	0.219	0.201	0.301	0.299	0.771	0.774
9	0.315	0.192	0.176	0.344	0.342	0.702	0.706
9	0.352	0.172	0.158	0.381	0.379	0.634	0.639
10	0.158	0.328	0.299	0.182	0.180	0.916	0.918
10	0.223	0.239	0.218	0.248	0.246	0.845	0.848
10	0.273	0.198	0.180	0.299	0.297	0.775	0.778
10	0.315	0.172	0.157	0.341	0.339	0.707	0.711
10	0.352	0.155	0.141	0.378	0.376	0.640	0.644
11	0.158	0.295	0.268	0.180	0.178	0.918	0.920
11	0.223	0.214	0.194	0.246	0.244	0.848	0.851
11	0.273	0.177	0.160	0.296	0.294	0.779	0.782
11	0.315	0.154	0.139	0.338	0.336	0.712	0.715
11	0.352	0.139	0.125	0.376	0.373	0.645	0.649
13	0.158	0.268	0.245	0.178	0.176	0.920	0.922
13	0.223	0.194	0.177	0.244	0.242	0.851	0.853
13	0.273	0.160	0.146	0.294	0.292	0.782	0.785
13	0.315	0.139	0.127	0.336	0.334	0.715	0.718
13	0.352	0.125	0.114	0.373	0.372	0.649	0.652
16	0.158	0.213	0.193	0.174	0.173	0.924	0.925
16	0.223	0.153	0.139	0.239	0.238	0.856	0.858
16	0.273	0.126	0.114	0.290	0.288	0.788	0.791
16	0.315	0.110	0.099	0.332	0.330	0.723	0.725
16	0.352	0.099	0.089	0.369	0.367	0.657	0.660
20	0.158	0.172	0.154	0.171	0.170	0.926	0.927
20	0.223	0.124	0.111	0.236	0.235	0.860	0.861
20	0.273	0.101	0.091	0.286	0.285	0.793	0.795
20	0.315	0.088	0.079	0.329	0.327	0.728	0.730
20	0.352	0.079	0.071	0.366	0.364	0.663	0.666

D.4.3. Discussion

Taking the foam medium as air had no effect on the RMS of the spatial distribution relative to the $\sigma_{\theta_x,\text{clinical}} \cdot t$ value, whereas the polyethylene increased the value by 10-13%. This was expected since the density of air is approximately two orders of magnitude less than that of the foam. At all energy and diameter combinations, IRF_{IS} for polyethylene is greater than that for air. This indicates that the MC calculations underestimate the in-scatter losses. The MC-PBRA difference used to parameterize out-scatter component (Equation D.6) is thus likely an overestimate of the actual value. Correcting the PBRA based on this difference could overcompensate for out scatter and yield corrections that are slightly smaller than optimal. However, this was not observed in the validations of this section, likely due to the issues explained in Appendix E. To improve accuracy, the foam could be simulated as closely to the physical dimensions as possible with the chemical composition set to that of polyethylene to be consistent with the assumption in Chapter 2.

Appendix E. Preliminary Analysis of PRIME Devices with Proper Pin Divergence

The island blocks comprising PRIME devices should be oriented such that the axes of the cylindrical pins are colinear with the rays diverging from the virtual source so that the solid angle subtended by the pin is consistent with the geometry of Equation 1.1. During fabrication, pins were aligned with a virtual source incorrectly positioned downstream from the collimator rather than upstream, so the blocks were converging with respect to the beam direction. Hilliard (2018) demonstrated that block orientation has a measurable impact on dose distributions. The converging blocks, which subtend an even greater solid angle than the parallel pins in the study by Hilliard, are expected to have a significant impact on the out-scatter correction adjustments in Aim 2 and Appendix D of this work.

E.1. Methods

Three replacement PRIME devices were fabricated with the same pin positions as the others, illustrated in Figure 3.3, each with pins of uniform diameters of 0.158, 0.273, and 0.352 cm. The pins of the new devices were oriented in a diverging fashion such that their axes back-projected to the virtual source. Using these and the foam-only modulators, the measurements discussed in Chapter 3 were repeated for 7, 13, and 20 MeV beams at 100 cm SSD only. For purposes of normalization, ionization ratios were measured at the depths indicated in Table 3.1 but in solid water rather than the water phantom under both sets of modulators: diverging and converging. PDDs and off-axis profiles were normalized as discussed in Section 3.1.6. Ionization ratios were calculated from Equation 3.1 and all PDDs were normalized in the same manner as done previously (Equation 3.2).

A partial re-analysis was performed for the 13 MeV beam and 0.352-cm pins only. PBRA calculations were repeated with the hexagonal pin matrix (Figure 3.3). Calculations were made

with corresponding nominal, in-scatter-adjusted, and IS+OS-corrected (both measurement- and MC-based) pin diameters. The measurement-based diameter corrections determined under the converging modulator, and not the measurements taken here, were used for PBRA calculations. The foam-only PDD measurements taken at the same time as the diverging modulator measurements were used as input into the PBRA. The geometric correction for the virtual source (Equation 3.3) was again applied to all PBRA calculations. To account for chamber alignment errors, the iterative normalization and R_{20} shifting were repeated. Measured isodose plots were generated from the inplane profiles as described in Section 3.1.7. MC dose distributions were estimated as described in Section D.1 using the hexagonal pin matrix (Figure 3.3) and the new foam-only measurements as input in Equation D.5. Measurements under the replacement modulator were compared using 3%/3 mm DTA criteria to the MC kernel prediction, nominal PBRA, measurement-based IS+OS PBRA, and MC-based IS+OS PBRA.

E.2. Results

Table E.1 compares the solid water ionization ratios measured under both the diverging and converging modulators. A smaller ratio was measured under the diverging arrangement in all cases; this is believed to be due to the off-axis pins for the converging arrangement scattering more electrons toward CAX.

Figures were generated at 13 MeV for the 0.352-cm-diameter pins to provide a preliminary comparison between modulator types and correction methods.

Figure E.1 compares measurement under the converging and diverging modulators to each other and the nominal and IS-PBRA. Measurement under the converging modulator exceeds that with the diverging modulator, most notably near CAX in the modulated region.

Figure E.2 compares diverging modulator measurement to MC estimation using the kernel method (Equation D.5). Agreement is very good within the modulated region, but worsens near the penumbra due to the infinite field simplification using this method, which does not model scatter from the edges of field cutouts. Figure E.3 compares the MC-estimated (i.e. Equation D.5) and measured isodose plots with the difference histogram under 3%/3mm DTA criteria. The MC perturbation method achieved a 99.5% passing rate for points within 8 cm of CAX up to R_p in depth with this beam energy, SSD, and diameter combination.

Figures E.4 and E.5 compare the measured isodose distribution to PBRA calculations with nominal diameters and IS+OS diameters determined using both measurement (Chapter 3) and MC (Appendix D) methods.

Table E.1. Comparison of normalization ratios in solid water at 100 cm SSD. The normalization ratios were computed according to Equation 3.1 for each setup at 100 cm SSD. "Div." and "Conv." indicate the ratios measured under the modulators with diverging and converging pin orientations, respectively. These were measured at physical depths of 1.7, 3.2, and 5.0 cm for the 7, 13, and 20 MeV beams, respectively.

Insert	7 MeV		13 MeV		20 MeV	
	Div.	Conv.	Div.	Conv.	Div.	Conv.
Foam Only	1.0000	1.0000	1.0000	1.0000	1.0000	1.0000
0.158-cm Pins	0.9235	0.9337	0.9353	0.9502	0.9410	0.9504
0.273-cm Pins	0.7940	0.8108	0.8159	0.8351	0.8298	0.8429
0.352-cm Pins	0.6644	0.6890	0.6947	0.7209	0.7153	0.7320

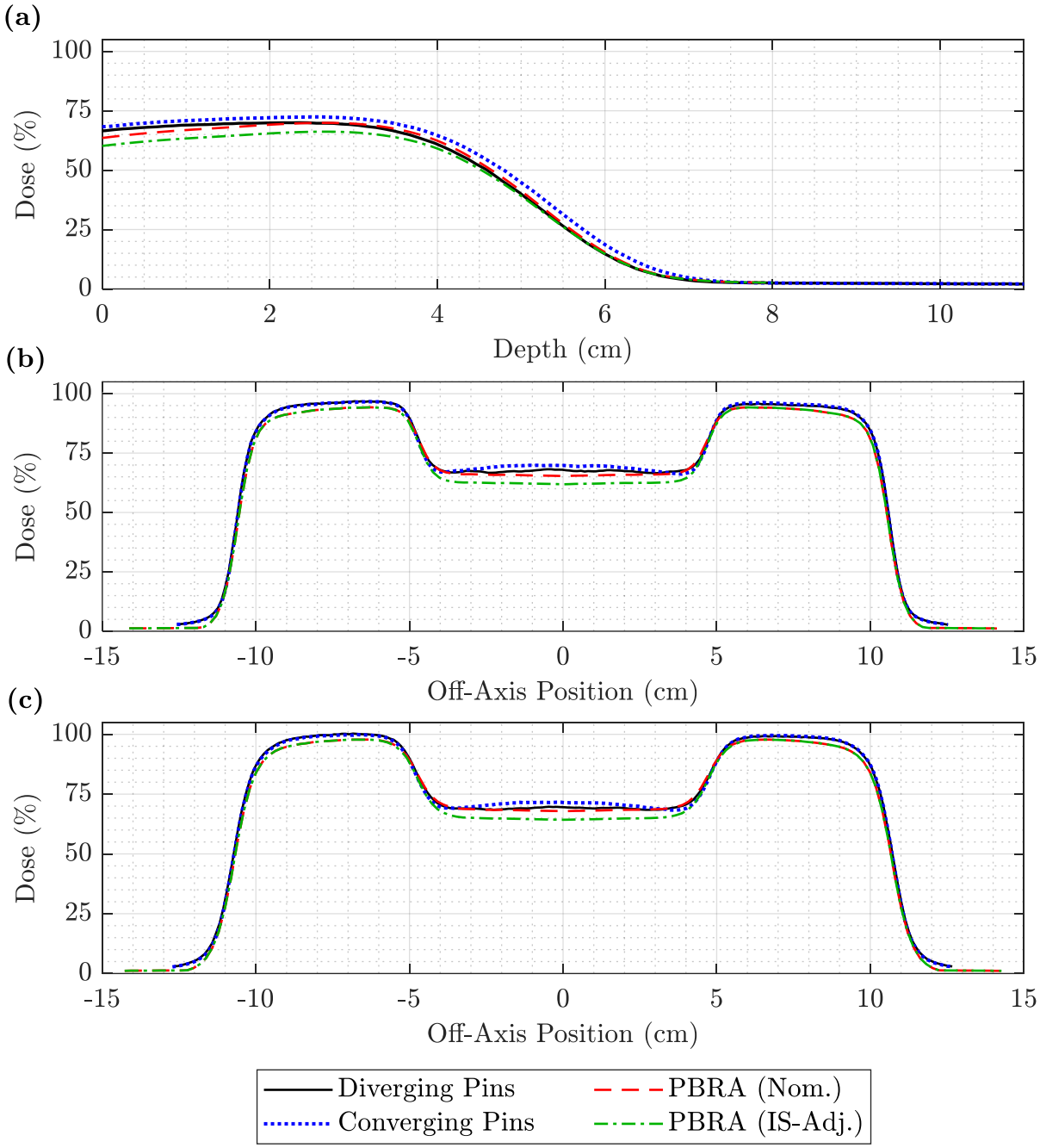

Figure E.1. PDD and off-axis profile comparison of measurement with diverging and converging modulators and nominal and IS-adjusted PBRA for the 13 MeV beam at 100 cm SSD with 0.352-cm pins. The PDD in (a) and off-axis profiles at depths of (b) 0.5, (c) 1.5, (d) 3.0, (e) 3.5, and (f) 4.0 cm compare measurement under modulators with diverging (solid black) and converging (dotted blue) pins to the nominal (dashed red) and IS-adjusted PBRA (dashed-dotted green) for a 13 MeV beam at 100 cm SSD for 0.352-cm-diameter pins.

(figure cont'd.)

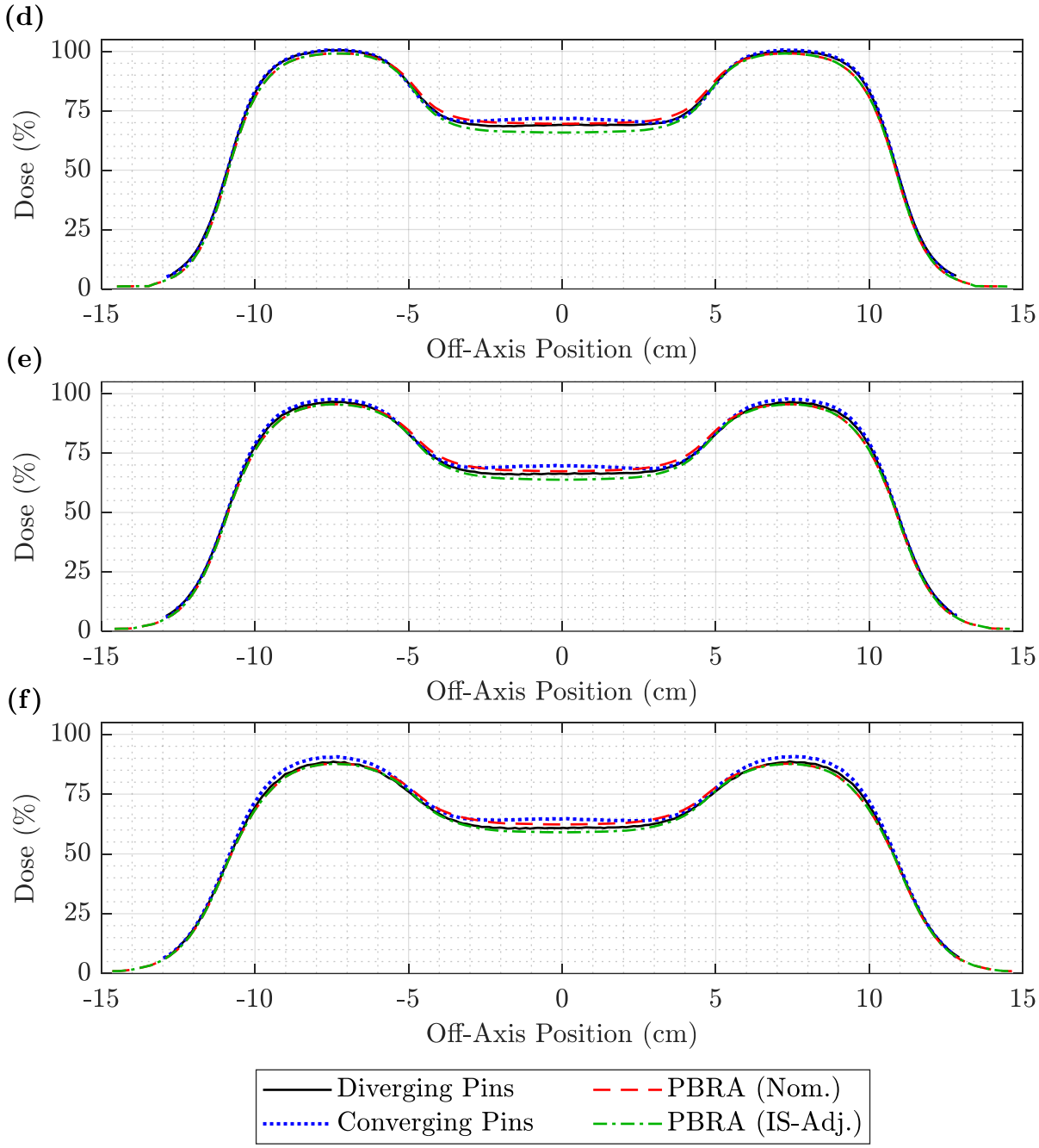
(d)
100
75
50
25
0
Dose (%)
-15
-10
-5
0
5
10
15
Off-Axis Position (cm)
(e)
100
75
50
25
0
Dose (%)
-15
-10
-5
0
5
10
15
Off-Axis Position (cm)
(f)
100
75
50
25
0
Dose (%)
-15
-10
-5
0
5
10
15
Off-Axis Position (cm)
Diverging Pins
Converging Pins
PBRA (Nom.)
PBRA (IS-Adj.)

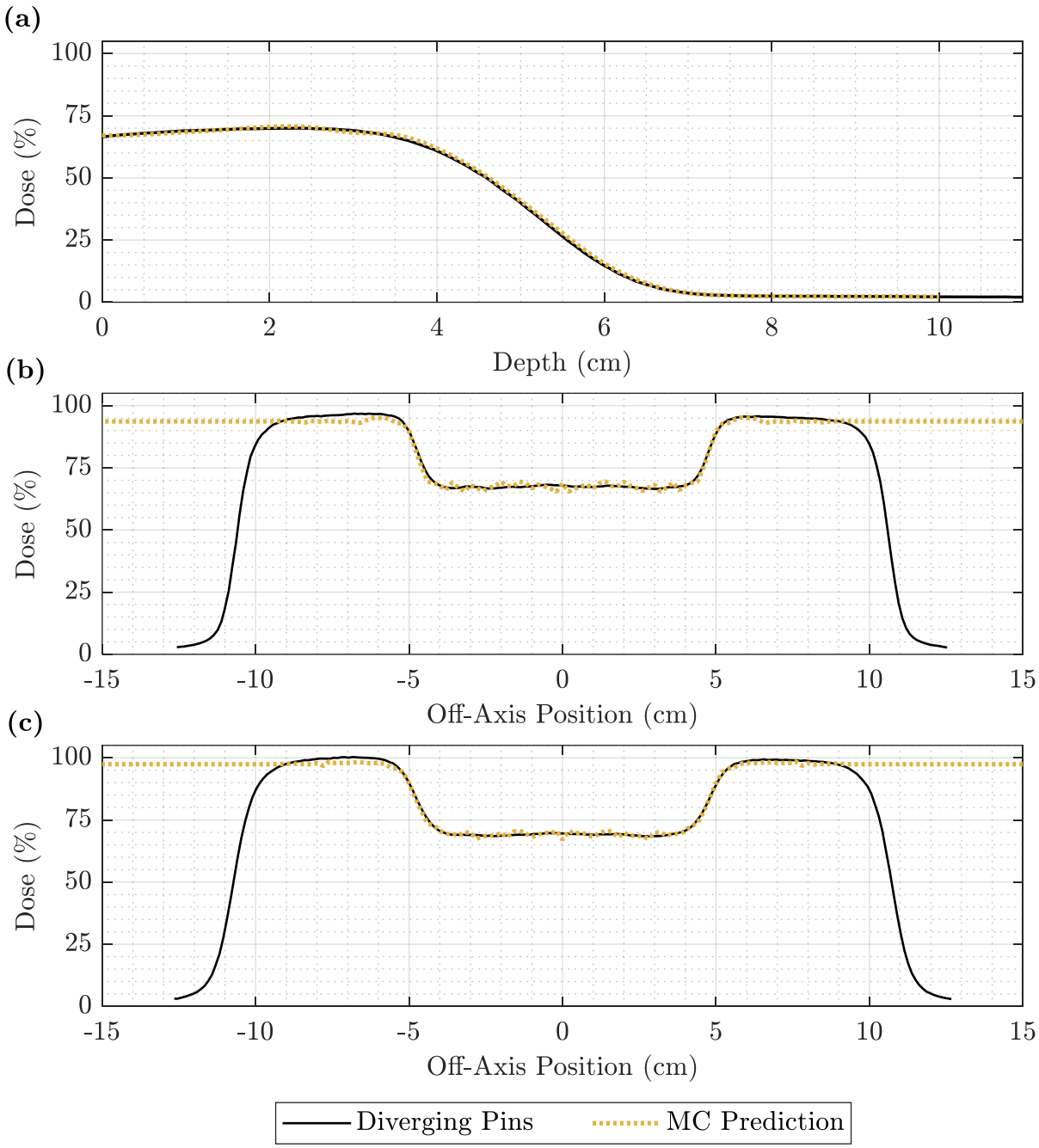

Figure E.2. PDD and off-axis profile comparison of measurement and MC prediction for the 13 MeV beam at 100 cm SSD and 0.352-cm pins. The PDD in (a) and off-axis profiles at depths of (b) 0.5, (c) 1.5, (d) 3.0, (e) 3.5, and (f) 4.0 cm compare measurement under the modulator with diverging pins (solid black) to the MC prediction (dotted yellow) for a 13 MeV beam at 100 cm SSD for 0.352-cm-diameter pins.

(figure cont'd.)

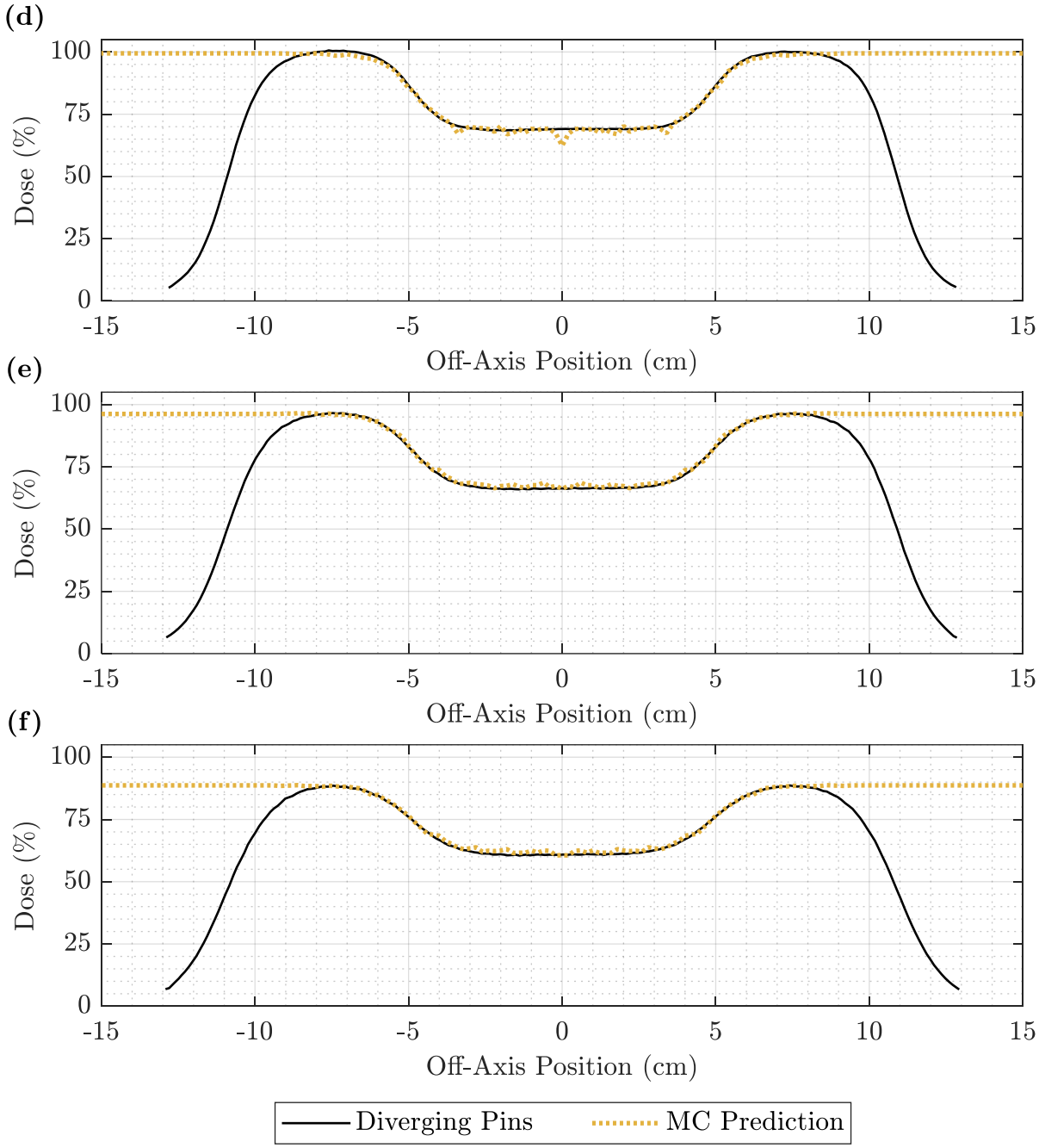
(d)
100
75
50
25
0
Dose (%)
-15
-10
-5
0
5
10
15
Off-Axis Position (cm)
(e)
100
75
50
25
0
Dose (%)
-15
-10
-5
0
5
10
15
Off-Axis Position (cm)
(f)
100
75
50
25
0
Dose (%)
-15
-10
-5
0
5
10
15
Off-Axis Position (cm)
Diverging Pins
MC Prediction

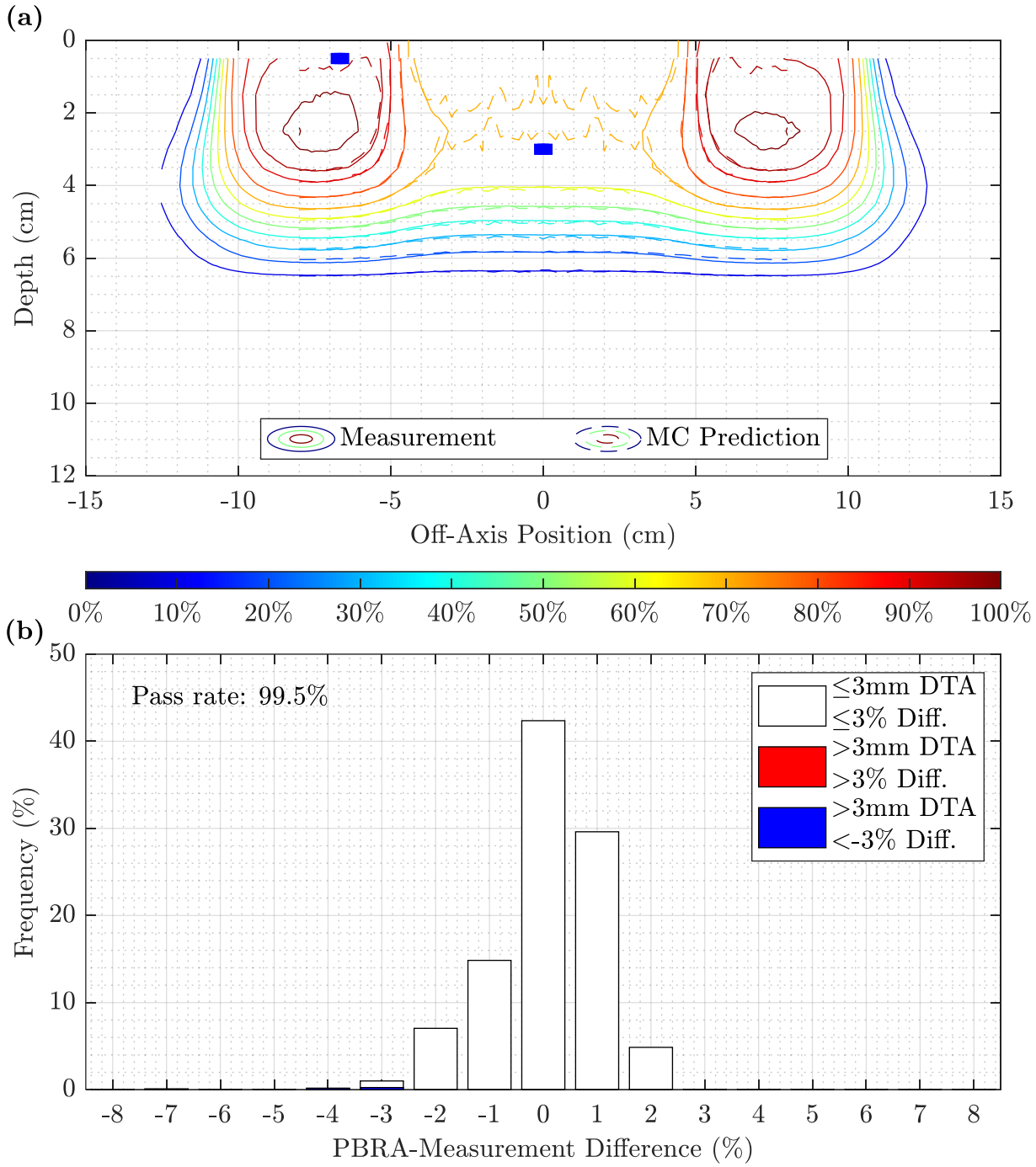

Figure E.3. Measurement and MC prediction isodose comparison and difference histogram for 0.352-cm pins at 13 MeV and 100 cm SSD. The isodose contours in (a) compare the measured (solid) and MC-estimated (dashed) isodose distributions, and (b) contains the histogram of differences between measurement and MC prediction for 0.352-cm pins at 13 MeV and 100 cm SSD. In both (a) and (b), points at which the MC estimation underpredicted and overpredicted the dose relative to measurement are shown in blue and red, respectively. The 3%/3mm DTA criteria yielded a passing rate of 99.5% for points within 8 cm of CAX and R_p in depth.

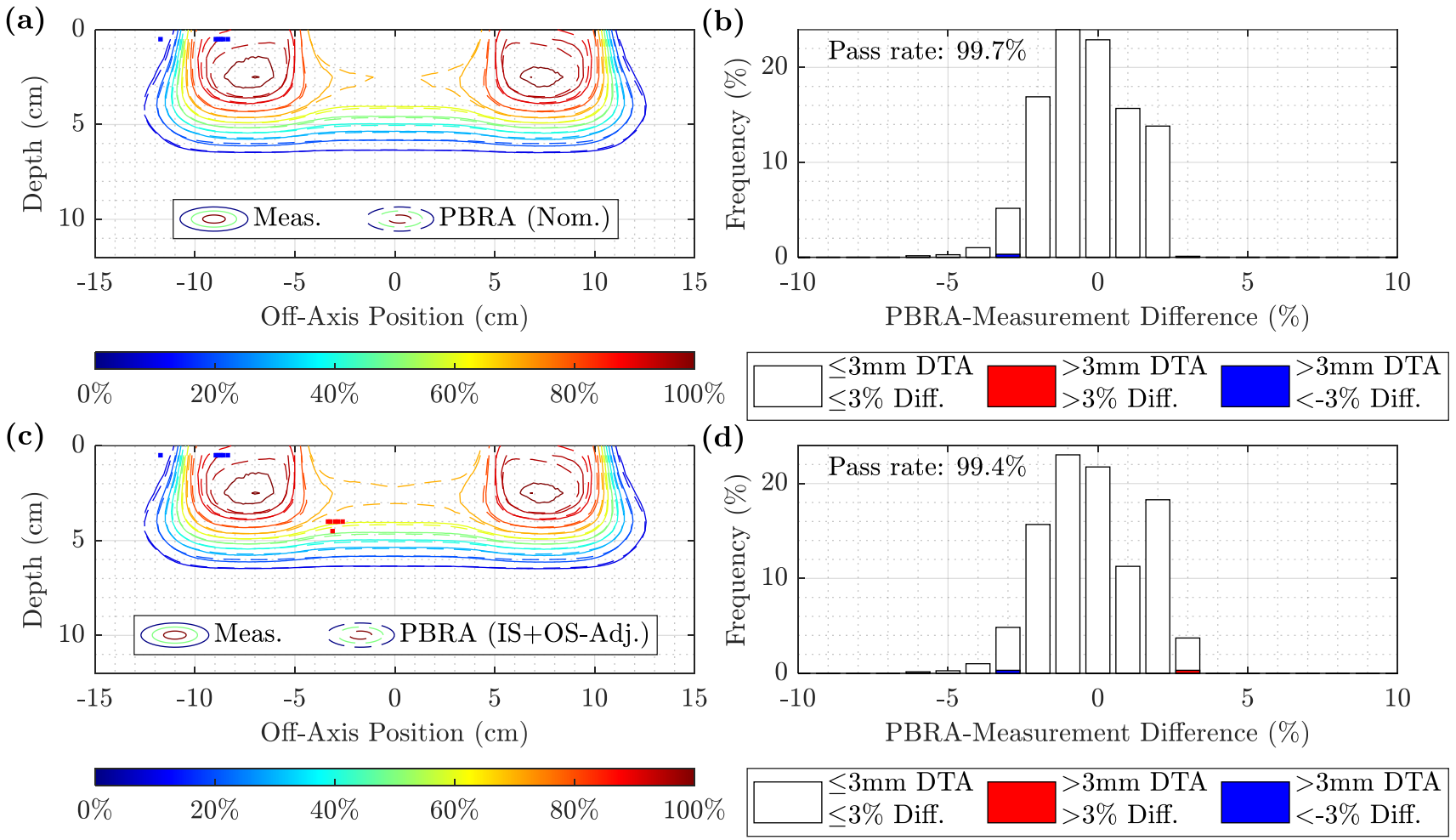

Figure E.4. Measured and PBRA-calculated isodose comparison and difference histogram for 0.352-cm pins at 13 MeV and 100 cm SSD under diverging modulators with measurement-based correction derived under converging modulators. The isodose contours for measurement (solid) are compared to the PBRA calculations with (a) nominal and (c) IS+OS-corrected (0.353 cm) pin diameters. Difference histograms under 3%/3mm DTA criteria are plotted for (b) nominal and (d) IS+OS-corrected PBRA diameters. Points at which the PBRA underpredicted and overpredicted the dose relative to measurement are shown in blue and red, respectively. The nominal and corrected passing rates were 99.7% and 99.4%, respectively.

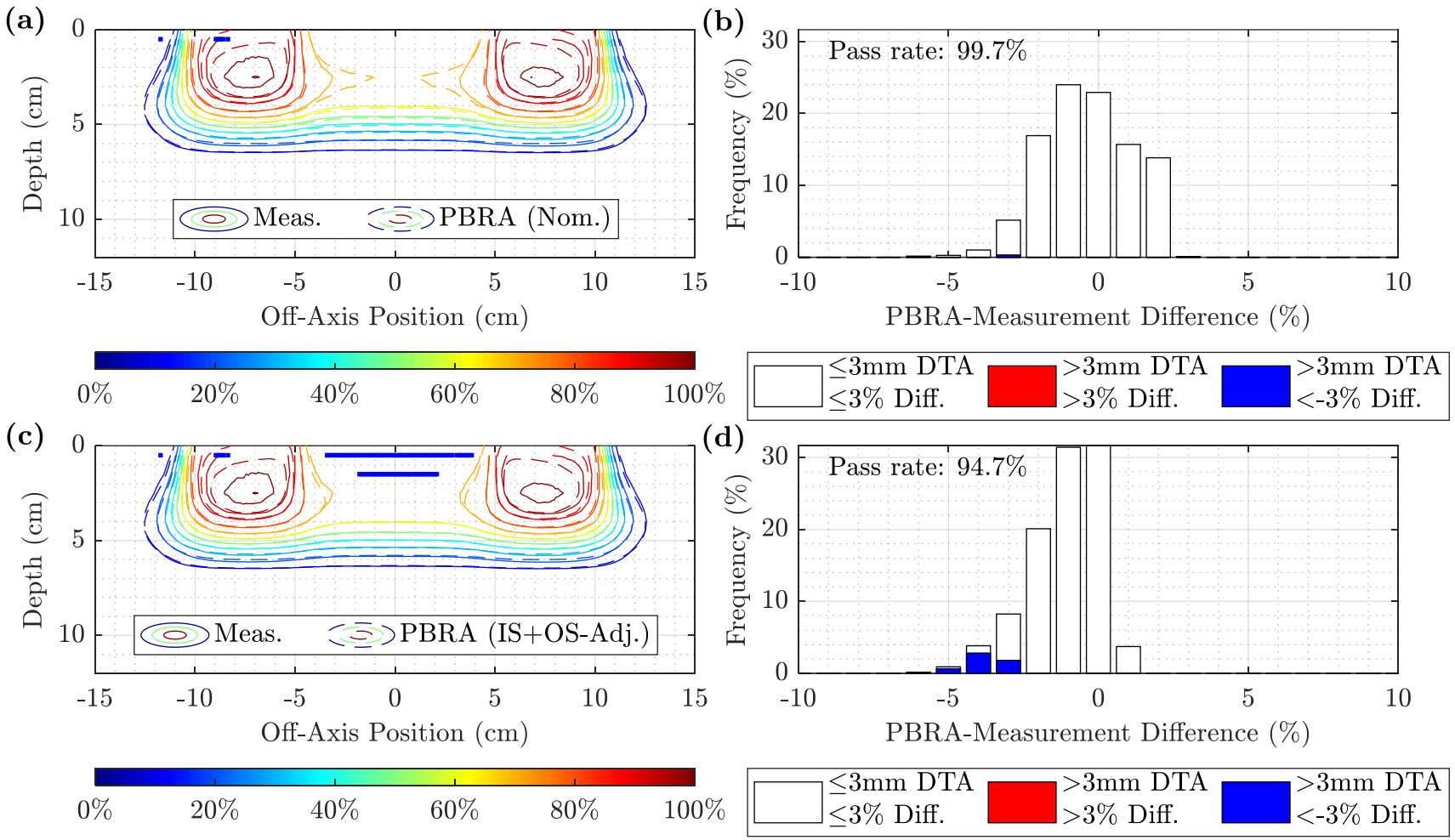

Figure E.5. Measured and PBRA-calculated isodose comparison and difference histogram for 0.352-cm pins at 13 MeV and 100 cm SSD under diverging modulators with MC-based PBRA correction. The isodose contours for measurement (solid) are compared to the PBRA calculations with (a) nominal and (c) IS+OS-corrected (0.367 cm) pin diameters. Difference histograms under 3%/3mm DTA criteria are plotted for (b) nominal and (d) IS+OS-corrected PBRA diameters. Points at which the PBRA underpredicted and overpredicted the dose relative to measurement are shown in blue and red, respectively. The nominal and corrected passing rates were 99.7% and 94.7%, respectively.

E.3. Discussion

The effect of pin orientation on electron absorption and scatter explored by Hilliard (2018) was approximately a 4% dose difference. That work compared diverging and parallel alignments at distances at least two times further from the beam CAX than in this work. Hence, the erroneous converging pin arrangement used in results reported here was hypothesized to have an approximately equal effect. Relative to pins diverging from the virtual source, the solid angle subtended by the converging pins increases with off-axis position, so the electron absorption will correspondingly increase with off-axis position. Consequently, dose near the edges of the modulated region will be lower than that near CAX. Slight inclination toward CAX of pins off CAX could also cause additional scattering that contributes to the dose on CAX. This behavior can be observed in the dose profiles in Figure E.1. Compared to diverging modulator dose, measured dose under the converging modulator increases near CAX and decreases near the edges of the modulated region. This results in profiles measured under the diverging modulator being comparatively flat and more closely resembling the PBRA-calculated profiles in shape. Converging measurements typically exceed the diverging measurements by a few percent, with the greatest differences near CAX. The ionization ratios in Table E.1 demonstrate that this can be as high as 2.5% at shallower depths. Since this region was used in determining the diameter corrections, the pin orientation will affect the diameter adjustments. Preliminary comparison between measurement and nominal PBRA calculations indicate that the nominal (i.e. uncorrected) PBRA might yield reasonably accurate calculations. Figure E.4 shows that the nominal PBRA passing rate was 99.7%. The passing rate derived under the converging modulator was lower (99.4%), suggesting that further optimization of pin diameters will be required.

The measured dose under both modulators in the unmodulated portion of the field (Figure E.1) is greater than calculation at shallow depths, suggesting the PBRA is not properly modeling scatter from the edges of the copper cutout (Rusk *et al*., 2016).

It was previously discussed that a single diameter scaling for a given set of conditions could be insufficient as PBRA calculations could not reproduce the behavior observed in the modulated region under the converging modulators, where the differences between CAX and off-axis dose in the modulated region could be as high as 6%. Measurements with the correct (diverging) modulators revealed that profiles were much flatter, and therefore a diameter scaling approach might be satisfactory to achieve a similar profile shape.

For both optimization method (MC- and measurement-based), dose in the unmodulated field exceeds calculation at shallow depths. The presence of this feature in both sets of profiles suggests that it is not an artifact of the pin orientation, but likely due to mainly scattering off of the island block edges.

The MC-based approach was initially abandoned due to substantial disagreement between MC estimation and measurement taken under the converging modulators. Figure E.2 suggests that agreement was significantly better than previously thought. However, the MC-based correction still yields a lower passing rate than nominal: 94.7% compared to 99.7% (Figure E.5). This may have been due to the geometry used to derive the correction, in which the rectilinear matrix approach (Figure D.4) possibly overestimated the matrix dose perturbation (Equations D.2 and D.3) as many dose calculation points were directly beneath pins where the magnitude of the kernels is most pronounced. This potential overweighting reduced the difference between the MC prediction and IS-PBRA from which the out-scatter component was estimated (Equation D.6). In some cases at 13 and 20 MeV, the MC-predicted PDD perturbation even exceeded that of the in-

scatter-adjusted PBRA (see Figures D.45, 47, and 48), so the out-scatter correction was minor, contrary to expectation at these energies. The out-scatter adjustment under the MC-based method was therefore suppressed, resulting in corrected diameters larger than nominal (i.e. less out-scatter) and often comparable to the in-scatter-adjusted values, as shown in Tables D.10-12. This can be observed by the shallow, colder region in Figure E.5.c. The good agreement between measurement and the MC estimation, shown in Figure E.3, calculated using the hexagonal matrix arrangement (Figure 3.3) and a diverging beam suggests that the MC-based approach could still be viable, although measurements will be required for final evaluation. The hexagonal arrangement, corresponding to measurement conditions, could be used with a diverging beam in future calculations of MC-based corrections.

Based on this preliminary study, further work will be required to improve the measurement-based corrections. The methodology described in Chapter 3 should be repeated with measurements under the correct modulators, but with measured profiles symmetrized. Also, for MC-based corrections, PDD perturbations should be based on a hexagonal pin arrangement with beam divergence to prevent biasing towards calculation points directly beneath the pin where the perturbation kernel is large.

References

Almond PR, Biggs PJ, Coursey BM, Hanson WF, Huq MS, Nath R, et al. AAPM's TG-51 protocol for clinical reference dosimetry of high-energy photon and electron beams. *Med Phys.* 1999;26(9):1847-70.

Boyd RA, Hogstrom KR, Rosen II. Effect of using an initial polyenergetic spectrum with the pencil-beam redefinition algorithm for electron-dose calculations in water. *Med Phys.* 1998;25(11):2176.

Chambers EL. Design of a passive intensity modulation device for bolus electron conformal therapy [Master's thesis]. Baton Rouge, LA: Louisiana State University; 2016.

Doiron J. Benefit of intensity modulated bolus electron conformal therapy for post mastectomy chest wall irradiation [Master's thesis]. Baton Rouge, LA: Louisiana State University; 2018.

Eldib AA, ElGohary MI, Fan J, Jin L, Li J, Ma CMC, et al. Dosimetric characteristics of an electron multileaf collimator for modulated electron radiation therapy. *J Appl Clin Med Phys.* 2010. p. 5-22.

Eley JG, Hogstrom KR, Matthews KL, Parker BC, Price MJ. Potential of discrete Gaussian edge feathering method for improving abutment dosimetry in eMLC-delivered segmented-field electron conformal therapy. *Med Phys.* 2011;38(12):6610-22.

Gaffney DK, Leavitt DD, Tsodikov A, Smith L, Watson G, Patton G, et al. Electron arc irradiation of the postmastectomy chest wall with CT treatment planning: 20-year experience. *Int J Radiat Oncol Biol Phys.* 2001;51(4):994-1001.

Gauer T, Albers D, Cremers F, Harmansa R, Pellegrini R, Schmidt R. Design of a computer-controlled multileaf collimator for advanced electron radiotherapy. *Phys Med Biol.* 2006;51(23):5987-6003.

Gerbi BJ, Antolak JA, Deibel FC, Followill DS, Herman MG, Higgins PD, et al. Recommendations for clinical electron beam dosimetry: Supplement to the recommendations of Task Group 25. *Med Phys*. 2009;36(7):3239-79.

Harris G. Development and validation of an electron Monte Carlo model for the Elekta Infinity accelerator [Master's thesis]. Baton Rouge, LA: Louisiana State University; 2012.

Hilliard EN. Verification and evaluation of a passive intensity modulation device for bolus conformal therapy [Master's thesis]. Baton Rouge, LA: Louisiana State University; 2018.

Hogstrom KR, Almond PR. Review of electron beam therapy physics. *Phys Med Biol* 2006;51(13):R455-R89.

Hogstrom KR, Antolak JA, Kudchadker R, Ma C, Leavitt D, editors. Modulated Electron Therapy. Intensity Modulated Radiation Therapy, The State of the Art: Proc 2003 AAPM Summer School; 2003. Madison, WI: Med Phys Publishing.

Hogstrom KR, Boyd RA, Antolak JA, Svatos MM, Faddegon BA, Rosenman JG. Dosimetry of a prototype retractable eMLC for fixed-beam electron therapy. *Med Phys.* 2004;31(3):443-62.

Hogstrom KR, Carver RL, inventors. Passive radiotherapy intensity modulator for electrons. US patent 10,751,549 B2. August 25, 2020.

Hogstrom KR, Carver RL, Chambers EL, Erhart K. Introduction to passive electron intensity modulation. *J Appl Clin Med Phys.* 2017;18(6):10-9.

Hogstrom KR, Mills MD, Almond PR. Electron beam dose calculations. *Phys Med Biol.* 1981;26(3):445-59.

Kawrakow I, Mainegra-Hin E, Rogers DW, Tessier F, Walters BRB. The EGSnrc code system: Monte Carlo simulation of electron and photon transport. Technical Report PIRS-701. Ottawa, Canada: National Research Council of Canada (NRCC); 2011.

Khan FM, Doppke KP, Hogstrom KR, Kutcher GJ, Nath R, Prasad SC, et al. Clinical electron-beam dosimetry: Report of AAPM Radiation Therapy Committee Task Group No. 25. *Med Phys*. 1991;18(1):73-109.

Kim MM, Kudchadker RJ, Kanke JE, Zhang S, Perkins GH. Bolus electron conformal therapy for the treatment of recurrent inflammatory breast cancer: a case report. *Med Dosim.* 2012;37(2):208-13.

Kudchadker RJ, Antolak JA, Morrison WH, Wong PF, Hogstrom KR. Utilization of custom electron bolus in head and neck radiotherapy. *J Appl Clin Med Phys*. 2003;4(4):321-33.

Kudchadker RJ, Hogstrom KR, Garden AS, McNeese MD, Boyd RA, Antolak JA. Electron conformal radiotherapy using bolus and intensity modulation. *Int J Radiat Oncol Biol Phys.* 2002;53(4):1023-37.

Lin J, Lin M-H, Hall A, Zhang B, Singh D, Regine WF. Comparison of bolus electron conformal therapy plans to traditional electron and proton therapy to treat melanoma in the medial canthus. *Pract Radiat Oncol*. 2016;6(2):105

Low DA, Starkschall G, Bujnowski SW, Wang LL, Hogstrom KR. Electron bolus design for radiotherapy treatment planning: bolus design algorimths. *Med Phys*. 1992;19(1):115-24.

Low DA, Starkschall G, Sherman NE, Bujnowski SW, Ewton JR, Hogstrom KR. Computer-aided design and fabrication of an electron bolus for treatment of the paraspinal muscles. *Int J Radiat Oncol Biol Phys*. 1995;33(5):1127-38

Łukowiak M, Jezierska K, Boehlke M, Więcko M, Łukowiak A, Podraza W, et al. Utilization of a 3D printer to fabricate boluses used for electron therapy of skin lesions of the eye canthi. *J Appl Clin Med Phys*. 2017;18(1):76-81.

Ma CM, Pawlicki T, Lee MC, Jiang SB, Li JS, Deng J, et al. Energy- and intensity-modulated electron beams for radiotherapy. *Phys Med Biol.* 2000. p. 2293-311.

Ma CM, Rogers DWO. BEAMDP as a General-Purpose Utility. Technical Report PIRS-0509(E). Ottawa, Canada: National Research Council of Canada (NRCC); 2020.

Million RM, Parsons JT, Bova FJ, Kalbaugh KJ. Electron beam: the management of head and neck cancer. *Front Radiat Ther Oncol.* 1991;25:107-27.

Opp D, Forster K, Li W, Zhang G, Harris EE. Evaluation of bolus electron conformal therapy compared with conventional techniques for the treatment of left chest wall postmastectomy in patients with breast cancer. *Med Dosim*. 2013;38(4):448-53.

Park K, Park S, Jeon MJ, Choi J, Kim JW, Cho YJ, et al. Clinical application of 3D-printed-step-bolus in post-total-mastectomy electron conformal therapy. *Oncotarget*. 2017;8(15):25660-8.

Perez CA, Lovett RD, Gerber R. Electron beam and x-rays in the treatment of epithelial skin cancer: dosimetric considerations and clinical results. *Front Radiat Ther Oncol.* 1991;25:90-106.

Perkins GH, McNeese MD, Antolak JA, Buchholz TA, Strom EA, Hogstrom KA. A custom-three dimensional electron bolus technique for optimization of postmastectomy irradiation. *Int J Radiat Oncol Biol Phys.* 2001;51(4):1142-1151.

Perrin DJ. Segmented field electron conformal therapy planning algorithm [Master's thesis]. Baton Rouge, LA: Louisiana State University; 2008.

Pitcher GM, Hogstrom KR, Carver RL. Improved electron collimation system design for Elekta linear accelerators. *J Appl Clin Med Phys*. 2017;18(5):259-70.

Recht A, Triedman SA, Harris JR. The 'boost' in the treatment of early-stage breast cancer: electrons versus interstitial implants. *Front Radiat Ther Oncol.* 1991;25:169-79.

Richaud P, Tapley N. Lateralized lesions of the oral cavity and oropharynx treated in part with the electron beam. *Int J Radiat Oncol Biol Phys.* 1979;5(4):461-5.

Richert JD, Hogstrom KR, Fields RS, Matthews KL, 2nd, Boyd RA. Improvement of field matching in segmented-field electron conformal therapy using a variable-SCD applicator. *Phys Med Biol.* 2007;52(9):2459-81.

Rogers DW, Walters B, Kawrakow I. BEAMnrc users manual. Ottawa, Canada: National Research Council of Canada (NRCC); 2011.

Rusk BD, Carver RL, Gibbons JP, Hogstrom KR. A dosimetric comparison of copper and Cerrobend electron inserts. *J Appl Clin Med Phys*. 2016;17(5):245-61.

Shiu AS, Hogstrom KR. Pencil-beam redefinition algorithm for electron dose distributions. *Med Phys*. 1991;18(1):7-18.

Su S, Moran K, Robar JL. Design and production of 3D printed bolus for electron radiation therapy. *J Appl Clin Med Phys*. 2014;15(4):194-211.

Svensson HA, P.; Brahme, A.; Dutreix, A.; Leetz, HK. ICRU Report 35: Radiation Dosimetry: Electron Beams with Energies Between 1 and 50 MeV. Bethesda, MD: International Commission on Radiation Units and Measurements; 1984.

Tapley NdV, Fletcher GH. Applications of the electron beam in the treatment of cancer of the skin and lips. *Radiology*. 1973;109(2):423-8.

Tapley NdV, Montague ED. Elective irradiation with the electron beam after mastectomy for breast cancer. *AJR Am*. 1976;126(1):127-34.

Vatanen T, Traneus E, Lahtinen T. Dosimetric verification of a Monte Carlo electron beam model for an add-on eMLC. *Phys Med Biol.* 2008;53(2):391-404.

Walters B, Kawrakow I, Rogers DW. DOSXYZnrc users manual. Ottawa, Canada: National Research Council of Canada (NRCC); 2011.

Wang CC. Intraoral cone for carcinoma of the oral cavity. *Front Radiat Ther Oncol.* 1991;25:128-31.

Zeidan OA, Chauhan BD, Estabrook WW, Willoughby TR, Manon RR, Meeks SL. Image-guided bolus electron conformal therapy - a case study. *J Appl Clin Med Phys*. 2011;12(1):68-75.

Vita

After graduating in physics from Portland State University in 2018, Joseph matriculated into the M.S. Medical Physics and Health Physics program at Louisiana State University. He plans to receive his master's degree in August 2021. In July 2021, he will join the medical physics residency program at the James Cancer Hospital at The Ohio State University in Columbus, Ohio.